COLLECTED PAPERS on Off-shell Science

Vol. 35

January 2020 – December 2020

Motoichi OHTSU[1,2]

1 Chief Director,
(General Incorporated Association)
Research Origin for Dressed Photon
2 Prof. Emeritus, The University of Tokyo
and Tokyo Institute of Technology

MEMBERS

[I] RESEARCH ORIGIN FOR DRESSED PHOTON (RODreP) *

Chief Director

Motoichi OHTSU**	(Dr. Eng.)	

Directors

Masayuki NAYA	(Dr. Eng.)	
Hirofumi SAKUMA	(PhD.)	(-June, 2020)
Hidefumi HORI	(Dr. Eng.)	(-June, 2020)
Teruo MURAKAMI		

Auditor

Satoshi SUGIURA

Advisors

Izumi OJIMA	(Dr. Sci.)
Junji MIYAHARA	(Dr. Eng.)
Masuo FUKUI	(Dr. Eng.)
Tadashi KAWAZOE	(Dr. Sci.)
Naoya TATE	(Dr. Eng.)

Senior Researcher

Kazuya OKAMURA	(Dr. Sci.)

Visiting Scientists

Hayato SAIGO	(Dr. Sci.) (Nagahama Inst. Bio-Sci. and Tech.)
Itsuki BANNO	(Univ. Yamanashi)
Hiroshi ANDO	(Dr. Sci.) (Chiba Univ.)
Suguru SANGU	(Dr. Eng.) (Ricoh Co. Ltd.)
Etsuo SEGAWA	(Dr. Eng.) (Yokohama National Univ.)
Leo MATSUOKA	(Dr. Eng.) (Hiroshima Inst. of Technol.)

Secretary

Mari KAZAMA

(*)（General Incorporated Association）Research Origin for Dressed Photon
(RODreP)
Phone: 090-1603-0562
E-mail: ohtsu@rodrep.or.jp
URL: http://www.rodrep.or.jp/
(new) http://jpn.rodrep.or.jp/
(Labs.)
c/o Bdg.1, Yokohama Research Center, NICHIA Corp.
3-13-19 Moriya-cho, Kanagawa-ku, Yokohama-shi, Kanagawa 221-0022, Japan
(Executive office)
Adthree Publishing Co., Ltd.
4-27-37 Higashi-Nakano, Nakano-ku, Tokyo164-0003, Japan

（一般社団法人）ドレスト光子研究起点
Phone: 090-1603-0562
E-mail: ohtsu@rodrep.or.jp
URL: http://www.rodrep.or.jp/
(new) http://jpn.rodrep.or.jp/
（研究所）
〒221-0022　神奈川県横浜市神奈川区守屋町 3－13－19
日亜化学工業（株）　横浜研究所　1 号館 1 階
（事務局）
〒164-0003　東京都中野区東中野 4 丁目 27-37
株式会社アドスリー

（**）Professor Emeritus, The University of Tokyo and Tokyo Institute of Technology
東京大学名誉教授、東京工業大学名誉教授

LIST OF PAPERS

[(pp. XX-XX); pages in this issue of the COLLECTED PAPERS**]**

[I] ORIGINAL PAPERS

[1] T. Kadowaki, T. Kawazoe, and M. Ohtsu, "SiC transmission-type polarization rotator using a large magneto-optical effect boosted and stabilized by dressed photons," *Sci. Reports*, (2020) 10: 12967.
https://doi.org/10.1038/s41598-020-69971-3

[2] H. Sakuma, I. Ojima, M. Ohtsu, and H. Ochiai, "Off-Shell Quantum Fields to Connect Dressed Photons with Cosmology," *Symmetry*, vol.12, no.8 (2020) 1244. DOI:10.3390/sym12081244

[II] PRESENTATIONS IN INTERNATIONAL CONFERENCES

N.A.

[III] REVIEW PAPERS

[1] M. Ohtsu, "History, current development, and future directions of near-field optical science," *Opto-Electronic Advances*, vol.3, no.3 (2020)190046.
DOI: 10.29026/oea.2020.190046

[IV] PREPRINT DEPOSITORIES

[Original papers]

[1] M. Ohtsu and T. Kawazoe, "Nutation in energy transfer of dressed photons between nano-particles," *Off-shell Archive* (May, 2020) OffShell: 2005O.001.v1.
DOI 10.14939/2005O.001.v1, http://offshell.rodrep.org/?p=274

[Review papers]

[1] M. Ohtsu, "Past, present, and future studies on the longitudinal electric field components of light," *Off-shell Archive* (June, 2020) OffShell: 2008R.001.v1.
DOI 10.14939/2008R.001.v1, http://offshell.rodrep.org/?p=318

[2] M. Ohtsu, “Errata: Route to Off-Shell Science,” *Off-shell Archive* (June, 2020) OffShell:2006R.001.v2.
DOI 10.14939/2008R.001.v2, http://offshell.rodrep.org/?p=304

[3] M. Ohtsu, “Route to Off-shell Science,” *Off-shell Archive* (June, 2020) OffShell: 2006R.001.v1.
DOI 10.14939/2006R.001.v1, http://offshell.rodrep.org/?p=283

[4] M. Ohtsu, “Progress in off-shell science in analyzing light–matter interactions for creating dressed photons,” *Off-shell Archive* (April, 2020) OffShell: 2004R.001.v1.
DOI 10.14939/2004R.001.v1, http://offshell.rodrep.org/?p=268

[5] M. Ohtsu, “The present and future of numerical simulation techniques for off-shell science,” *Off-shell Archive* (March, 2020) OffShell: 2003R.001.v1.
DOI 10.14939/2003R. 001.v1, http://offshell.rodrep.org/?p=259

[V] PUBLISHED BOOKS

[1] M. Ohtsu and I. Ojima (ed.), “Embarking on quantum fields --- Off-Shell Science Opened By Dressed Photons,” Asakura-Publishers, Tokyo (July, 2020), 225 pages
【大津元一、小嶋泉（編著、「ここからはじまる量子場―--ドレスト光子が開くオフシェル科学」、朝倉書店、東京、2020 年 7 月、225 ページ】

[VI] PRESENTATIONS IN DOMESTIC CONFERENCES

[1] T. Kadowaki, T. Kawazoe, and M. Ohtsu, “SiC polarization rotator using a magneto-optical effect induced by dressed photons,” Abstract of the 2020 IEICE Society Conference, September 15-18, 2020, Online meeting, paper number C3/4-9.
【門脇拓也、川添忠、大津元一、「ドレスト光子による磁気光学効果を使った SiC 偏光回転素子」、電子情報通信学会　2020 ソサエティ大会　2020 年 9 月 15-18 日、オンライン会議、講演番号 C3/4-9】

[2] I. Banno and M. Ohtsu, “Dressed Photons and Non-relativistic Nature of Material System,” Abstracts of the 67th Jpn. Soc. Appl. Phys. Spring Meeting, March 2020, Tokyo, Japan, paper number 14p-B309-10.
【坂野斎、大津元一、「ドレスト光子と物質系の非相対論性」、第 67 回応用物理学会春季学術講演会予稿集（東京、2020 年 3 月 12-15 日）、講演番号 14p-B309-10】

[3] H. Sakuma, I. Ojima, and M. Ohtsu, “Dressed photon study as the touchstone of developing quantum field theory,” Abstracts of the 67th Jpn. Soc. Appl. Phys. Spring Meeting, March 2020, Tokyo, Japan, paper number 14p-B309-11.
【佐久間弘文、小嶋泉、大津元一、「量子場理論に対する問題提起としてのドレスト光子研究」、第 67 回応用物理学会春季学術講演会予稿集（東京、2020 年 3 月 12-15 日）、講演番号 14p-B309-11】

[4] E. Segawa, R. Matsuoka, H. Saigo, S. Sangu, and M. Ohtsu, “A quantum walk simulation of autonomy in dressed photon energy transfer,”, Abstracts of the 67th Jpn.

Soc. Appl. Phys. Spring Meeting, March 2020, Tokyo, Japan, paper number 14p-B309-14.
【瀬川悦生、松岡雷士、西郷甲矢人、三宮俊、大津元一、「量子ウォークによるドレスト光子のエネルギー移動の自律性について」、第 67 回応用物理学会春季学術講演会予稿集（東京、2020 年 3 月 12-15 日）、講演番号 14p-B309-14】

[5] S. Sangu, H. Saigo, and M. Ohtsu, "Convergence Process to Steady States for Dressed-photon Energy Transfer," Abstracts of the 67th Jpn. Soc. Appl. Phys. Spring Meeting, March 2020, Tokyo, Japan, paper number 14p-B309-15.
【三宮俊、西郷甲矢人、大津元一、「ドレスト光子エネルギー移動における定常状態への収束過程」、第 67 回応用物理学会春季学術講演会予稿集（東京、2020 年 3 月 12-15 日）、講演番号 14p-B309-15】

[6] T. Kadowaki, T. Kawazoe, and M. Ohtsu, "Fabrication and evaluation of Si light emitting diode of 2 μ m-wavelength using dressed photons," Abstracts of the 67th Jpn. Soc. Appl. Phys. Spring Meeting, March 2020, Tokyo, Japan, paper number 14p-B309-16.
【門脇拓也、川添忠、大津元一、「ドレスト光子を用いた波長 2 μ m の Si 光ダイオードの作製と評価」、第 67 回応用物理学会春季学術講演会予稿集（東京、2020 年 3 月 12-15 日）、講演番号 14p-B309-16】

[7] M. Ohtsu, "Are the high-power light emitting devices by Si crystal LEDs or lasers? ---No, they are the PBD realized by dressed photons---," Proceedings of the LED General Forum 2020 " (Tokushima, February 29, 2020) paper number 2
[Invited presentation]
【大津元一、「シリコン結晶製の高光パワー発光素子は LED? レーザー？---いや、それはドレスト光子が創る新しい PBD---」、LED 総合フォーラム 2020in 徳 島（徳島、2020 年 2 月 29 日、講演番号 2）
【シンポジウム講演】

[8] M. Ohtsu, "Dressed photon phenomena that demand off-shell scientific theories," Workshop on Basic Mathematical Studies on Dressed Photon Phenomena (Univ.Kyusyu, IMI, February 13-14, 2020) paper number 1.
[Plenary presentation]
【大津元一、「ドレスト光子の性質とそれがもたらす新規な現象は新理論を求めている」、研究会「ドレスト光子に関する基礎数学的研究」（九州大学IMI、2020年2月13-14日）、講演番号1】
【特別講演】

[VII] AWARDS

N.A.

[VIII] APPENDIX

Publications and Presentations by RODreP members.

[I] ORIGINAL PAPERS

[1] M. Hamano and H. Saigo "Quantum Walk and Dressed Photon," Electron. Proc. in Theoretical Compt. Sci. (EPTCS), **315** (2020) pp.93-99.
(G. Di Molfetta, V. Kendon and Y. Shikano (Eds.): 9th International Conference on Quantum Simulation and Quantum Walks (QSQW 2020))
doi:10.4204/EPTCS.315.9

[II] PRESENTATIONS IN INTERNATIONAL CONFERENCES

[1] K. Okamura, "On the measurement of dressed photon,"
Abstract of The 2020 International Symposium on Nonlinear Theory and Its Applications (NOLTA2020), (Virtual Online Conference), November 16 – 19, 2020, Okinawa, Japan, (paper number C2L-B1) pp.327-329.
[2] L. Matsuoka, E. Segawa, K. Okamura, S. Sangu, and H. Saigo, "Development of a Mathematical Model Describing Dressed Photon PhenomenaBased on QuantumWalks on Self-Expanding Complex Networks,"
Abstract of The 2020 International Symposium on Nonlinear Theory and Its Applications (NOLTA2020), (Virtual Online Conference), November 16 – 19, 2020, Okinawa, Japan, (paper number C2L-B2) pp.330-332.
[3] E. Segawa and L. Matsuoka,"A discontinuity of dressed photon energy in the internal graph predicted by aquantum walk simulation,"
Abstract of The 2020 International Symposium on Nonlinear Theory and Its Applications (NOLTA2020), (Virtual Online Conference), November 16 – 19, 2020, Okinawa, Japan, (paper number C2L-B3) pp.333-335.
[4] S. Sangu and H. Saigo, "Numerical Analysis of Dressed-Photon Dynamics toward Its Control,"
Abstract of The 2020 International Symposium on Nonlinear Theory and Its Applications (NOLTA2020), (Virtual Online Conference), November 16 – 19, 2020, Okinawa, Japan, (paper number C2L-B4) pp.336-339.
[5] I. Ojima, "Dissipativity and Visibility of Macro,"
Abstract of the Virtual QBIC Workshop 2020, October 14 – 16, 2020, Noda, Japan, paper number 1.
[Invited presentation]

[III] REVIEW PAPERS

N.A.

[IV] PREPRINT DEPOSITORIES

N.A.

[V] PUBLISHED BOOKS

N.A.

[VI] PRESENTATIONS IN DOMESTIC CONFERENCES

[1] K. Okamura, “Dressed photon and measuring processes,” Abstracts of the 67th Jpn. Soc. Appl. Phys. Spring Meeting, March 2020, Tokyo, Japan, paper number 14p-B309-12.
【岡村和弥、「ドレスト光子と測定過程」、第 67 回応用物理学会春季学術講演会予稿集（東京、2020 年 3 月 12-15 日）、講演番号 14p-B309-12】

[2] H. Ando, “Dressed photons and indefinite metric,” Abstracts of the 67th Jpn. Soc. Appl. Phys. Spring Meeting, March 2020, Tokyo, Japan, paper number 14p-B309-13.
【安藤浩志、「ドレスト光子と不定計量」、第 67 回応用物理学会春季学術講演会予稿集（東京、2020 年 3 月 12-15 日）、講演番号 14p-B309-13】

[3] T. Kawazoe, “Time-resolved Measurement of Energy Transfer between CdSe Quantum Dots via Dressed Photon,” Abstracts of the 67th Jpn. Soc. Appl. Phys. Spring Meeting, March 2020,Tokyo, Japan, paper number 14p-B309-17.
【川添忠、「CdSe 量子ドット間のドレスト光子を介したエネルギー移動の時間分解計測」、第 67 回応用物理学会春季学術講演会予稿集（東京、2020 年 3 月 12-15 日）、講演番号 14p-B309-17】

[4] W. Nomura, Y. Tomita, T. Kawazoe, and T. Tadokoro, “Improvement of power generation efficiency of amorphous silicon cell by wavelength conversion film with nano-droplets,” Abstracts of the 67th Jpn. Soc. Appl. Phys. Spring Meeting, March 2020, Tokyo, Japan, paper number 14p-B309-18.
【野村航、冨田嘉崇、川添忠、田所貴志、「ナノドロップレット光波長変換膜による a-Si 太陽電池の発電効率向上」、第 67 回応用物理学会春季学術講演会予稿集（東京、2020 年 3 月 12-15 日）、講演番号 14p-B309-18】

[5] N. Tate, “Correlation analysis of the size-resonanced near-field optical signals for advanced physical security,” Workshop on Basic Mathematical Studies on Dressed Photon Phenomena (Univ.Kyusyu, IMI, February 13-14, 20202) paper number 2.
[Plenary presentation]
【竪直也、「先端物理セキュリティのための寸法共鳴近接場光信号の相関解析」、研究会「ドレスト光子に関する基礎数学的研究」（九州大学IMI、2020年2月13-14日）、講演番号2】
【特別講演】

[6] I. Ojima, “Dynamics of Micro-Macro Duality,” Workshop on Basic Mathematical Studies on Dressed Photon Phenomena (Univ.Kyusyu, IMI, February 13-14, 2020) paper number 3.

[Plenary presentation]
【小嶋泉、「ミクロ・マクロ双対のダイナミクス」、研究会「ドレスト光子に関する基礎数学的研究」（九州大学IMI、2020年2月13-14日）、講演番号3】
【特別講演】

[7] H. Ando, “Dressed photons and Electromagnetic fields from operator algebraic viewpoint,” Workshop on Basic Mathematical Studies on Dressed Photon Phenomena (Univ.Kyusyu, IMI, February 13-14, 2020) paper number 5.
【安藤浩志、「演算子代数の観点からのドレスト光子と電磁場」、研究会「ドレスト光子に関する基礎数学的研究」（九州大学IMI、2020年2月13-14日）、講演番号5】

[8] H. Saigo, “Dressed Photon and Quantum Walk,” Workshop on Basic Mathematical Studies on Dressed Photon Phenomena (Univ.Kyusyu, IMI, February 13-14, 2020) paper number 7.
【西郷甲矢人、「ドレスト光子と量子ウォーク」、研究会「ドレスト光子に関する基礎数学的研究」（九州大学IMI、2020年2月13-14日）、講演番号7】

[9] S. Sangu, ”Dynamics of dressed-photon population from the perspective of convergence to steady state,” Workshop on Basic Mathematical Studies on Dressed Photon Phenomena (Univ.Kyusyu, IMI, February 13-14, 2020) paper number 8.
【三宮俊､「定常状態への収束の観点からのドレスト光子数のダイナミクス」、研究会「ドレスト光子に関する基礎数学的研究」（九州大学IMI、2020年2月13-14日）、講演番号8】

[10] K. Okamura, ”Measurement of Dressed Photon,” Workshop on Basic Mathematical Studies on Dressed Photon Phenomena (Univ.Kyusyu, IMI, February 13-14, 2020) paper number 9.
【岡村和弥、「ドレスト光子の測定」、研究会「ドレスト光子に関する基礎数学的研究」（九州大学IMI、2020年2月13-14日）、講演番号9】

[11] H. Sakuma, “Review on Clebsch dual field and on the parallel between dynamical behavior of dressed photon and gravitational pseudo energy,” Workshop on Basic Mathematical Studies on Dressed Photon Phenomena (Univ.Kyusyu, IMI, February 13-14, 2020) paper number 11.
【佐久間弘文、「クレブシュ双対場、およびドレスト光子の動特性と重力擬エネルギーとの間の並行性について」、研究会「ドレスト光子に関する基礎数学的研究」（九州大学IMI、2020年2月13-14日）、講演番号11】

[12] I. Banno, “Non-relativistic Nature in Material Systems and the Dressed Photons,” Workshop on Basic Mathematical Studies on Dressed Photon Phenomena (Univ.Kyusyu, IMI, February 13-14, 2020) paper number 12.
【坂野斎、「物質系とドレスト光子の非相対論性」、研究会「ドレスト光子に関する基礎数学的研究」（九州大学IMI、2020年2月13-14日）、講演番号12】

[I] ORIGINAL PAPERS

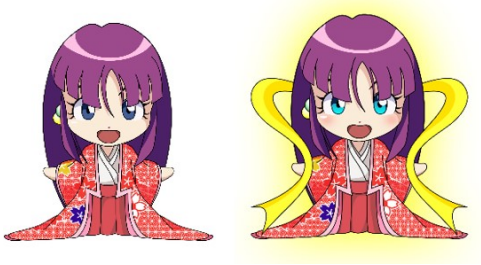

SCIENTIFIC REPORTS
nature research

Check for updates

OPEN

SiC transmission-type polarization rotator using a large magneto-optical effect boosted and stabilized by dressed photons

Takuya Kadowaki[1]✉, Tadashi Kawazoe[2] & Motoichi Ohtsu[3]

This paper reports the fabrication and operation of a transmission-type polarization rotator for visible light with a wavelength of 450 nm using indirect-transition-type semiconductor crystalline SiC in which Al atoms were implanted as a p-type dopant. A novel dressed-photon–phonon (DPP)-assisted annealing method was used for fabrication. The fabricated device exhibited a gigantic magneto-optical effect induced by interactions between photons, electrons, phonons, and magnetic fields in a nanometric space, mediated by dressed photons. The optical path length for polarization rotation was as short as the thickness of the p–n junction. It operated with a weak magnetic field on the order of mT, generated by injecting current to a ring-shaped electrode on the device surface. The Verdet constant was as large as 9.51×10^4 rad/T.m at a wavelength of 450 nm. SQUID measurements confirmed that the SiC crystal exhibited conspicuous ferromagnetic characteristics as a result of the DPP-assisted annealing. In this device, the dressed photons boosted the magnitude of the magneto-optical effect and stabilized the device operation of the polarization rotator.

Owing to recent progress in optical information processing technology, the demand for high-performance functional optical devices is increasing. Among such devices, a magneto-optical spatial light modulator and optical isolator using the magneto-optical effect are the most promising devices because they play essential roles in the control and processing of optical information[1–3]. However, since these devices have been conventionally fabricated using ferromagnetic materials such as yttrium iron garnet (YIG), one major problem is their large optical absorption in the visible range, originating from Fe atoms in the crystal[4]. On the other hand, even though this absorption is low in the case of optical isolators made of transparent magneto-optical materials such as terbium gallium garnet (TGG), the problem is their low polarization rotation capabilities[5], resulting in the need for a long optical path length to achieve the desired rotation. These technical situations indicate that it is not straightforward to find novel materials having both low absorption and high polarization rotation capability in the visible range. An additional problem is that an external coil or a bulky magnet is required to generate a strong magnetic field for the device operation.

In order to solve these problems, a visible reflection-type polarization rotator was developed by using a wide-bandgap ZnO semiconductor by employing fabrication and operation methods based on quite different principles from those used conventionally[6]. Even though ZnO is a semiconductor that does not exhibit any ferromagnetic characteristics, large polarization rotation was demonstrated by this device. This was attributed to the interaction between photons, electrons, phonons, and current-induced magnetic fields mediated by spatially localized dressed photons (DPs) created in the regions around dopants in a nanometric space (a detailed discussion of DPs is given in the "Basics" section below). However, the crystallographic properties of ZnO are not yet sufficiently high for this material to be used for advanced optical devices, even though it is transparent in the visible range. Also, it is not straightforward to grow p-type ZnO substrates even by using a recent sophisticated doping method[7].

On the other hand, since the wide bandgap semiconductor SiC has a high breakdown electric field strength, and p-type substrates have been grown by using recent advanced technology, it has been advantageously applied

[1]Nichia Corporation, 3-13-19 Moriya-cho, Kanagawa-ku, Yokohama, Kanagawa 221-0022, Japan. [2]Tokyo Denki University, 5 Senju-Asahi-cho, Adachi-ku, Tokyo 120-8551, Japan. [3]Research Origin for Dressed Photon, 3-13-19 Moriya-cho, Kanagawa-ku, Yokohama, Kanagawa 221-0022, Japan. ✉email: takuya.kadowaki@nichia.co.jp

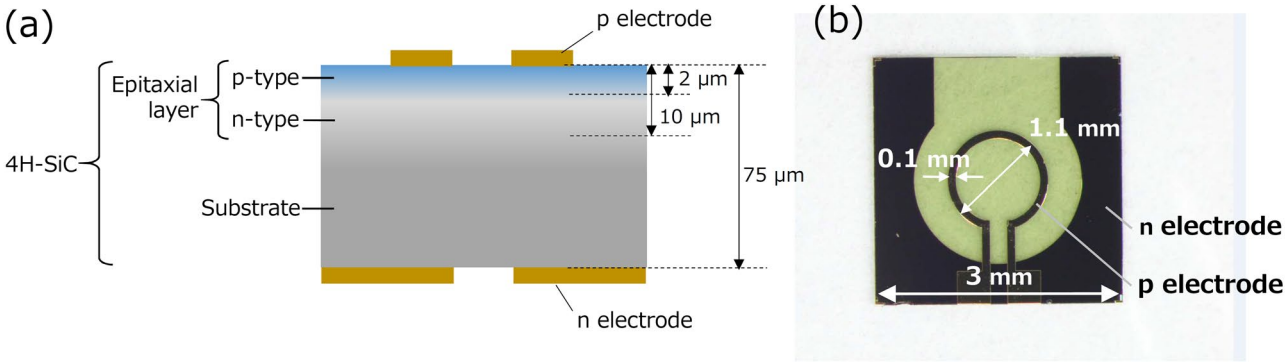

Figure 1. Profile of a polarization rotator using a 4H-SiC crystal. (**a**) Cross-sectional structure. (**b**) Optical microscope image.

to novel power electronic devices[8–10]. Due to the technical trends in these applications, it is expected that transparent SiC crystals exhibiting high crystallographic properties could be supplied in a sustainable manner from now on. By noting this advantage and expectation, basic experimental results on a reflection-type SiC polarization rotator for visible light with a wavelength of 450 nm have been recently reported by two authors (T.K. and M.O.) of this paper[11]. The fabrication and operation principles of this device are based on the concept of the DP and are equivalent to those of highly efficient silicon light-emitting devices (i.e., LEDs and LDs)[12–18],specifically, these Si devices emit photons with high efficiency by exchanging the momenta of the electrons in the conduction band with those of phonons, which are the constituent elements of the DPs.

This paper reports the fabrication and operation of a novel *transmission-type* polarization rotator for a wavelength of 450 nm using a single-crystal SiC.

Basics

The DP had previously been called an optical near field from the viewpoint of classical wave optics. However, as a result of more recent careful theoretical and experimental studies on light-matter interactions in a nanometric space based on quantum field theory, it was renamed as the DP due to its unique quantum optical nature. The detailed nature of the DP has been described in[19]. In summary, these studies indicate that the DP is a quantum field created as a result of the interaction between photons and electrons in a nanometric space. They have shown that the created DP could excite multi-mode coherent phonons in the crystal and couple with them, resulting in the creation of a novel quantum field called a dressed-photon–phonon (DPP)[20]. For device fabrication and operation, DPPs must be created efficiently in the semiconductor crystal. They can be created by autonomously controlling the spatial distribution of dopant atoms in the crystal using a DPP-assisted annealing method. In the annealing, Joule energy is generated by injecting a current into the p–n junction. Upon being heated by this Joule energy, the dopant atoms randomly diffuse in the crystal. During the heating, the crystal surface is irradiated with light that propagates through the crystal without absorption when its photon energy is lower than the bandgap energy of the crystal. As a result, the irradiated photons couple with electrons in a nanometric space at the dopant atoms to create DPs. Furthermore, the created DPs couple with multi-mode coherent phonons in the crystal, resulting in DPP creation.

Due to momentum exchange with phonons in the DPPs, the electrons in the conduction band recombine with positive holes to create photons, which is a stimulated emission process triggered by the irradiated light. Thus, the local diffusion efficiency of the dopant atoms decreases because a part of the Joule energy for heating is converted into the propagating photon energy and dissipates out from the crystal. By continuing the heating and dissipation processes above, the spatial distribution of the dopant atoms varies autonomously and gradually reaches a stationary state that is optimized for creating DPPs most efficiently. As a result, the device becomes optically active, allowing emission of light and/or rotation of the polarization of the incident light very effectively. When operating the device fabricated by using a SiC crystal, the DPPs are efficiently created at the optimally distributed dopant atoms by the incident light, and thus, the device exhibits a gigantic magneto-optical effect even though SiC is an indirect-transition-type semiconductor, and the polarization of the incident light is efficiently rotated. Detailed theoretical descriptions of the DPP-assisted annealing method and experimental results have been reported in previous papers by the research groups of some of the authors[21,22].

Experiment

Figure 1a schematically explains the cross-sectional structure of the SiC substrate. The (0001) planar surface of a 4H-SiC crystal was ion-implanted with a p-type dopant (Al atoms). After a ring-shaped electrode (outer diameter: 1.1 mm, line width: 0.1 mm) and a planar electrode were deposited on the top and bottom surfaces, respectively, the substrate was diced to form a 3 mm × 3 mm square device, as shown by the optical microscope image in Fig. 1b. In order to create the DPPs efficiently for fabrication and operation of the SiC device, the DPP-assisted annealing was employed (see "Methods" for details). A current was injected into the ring-shaped electrode for operating the fabricated device as a polarization rotator. Since a magnetic field was generated around this electrode, no external coils or bulky magnets were required to induce the magneto-optical effect.

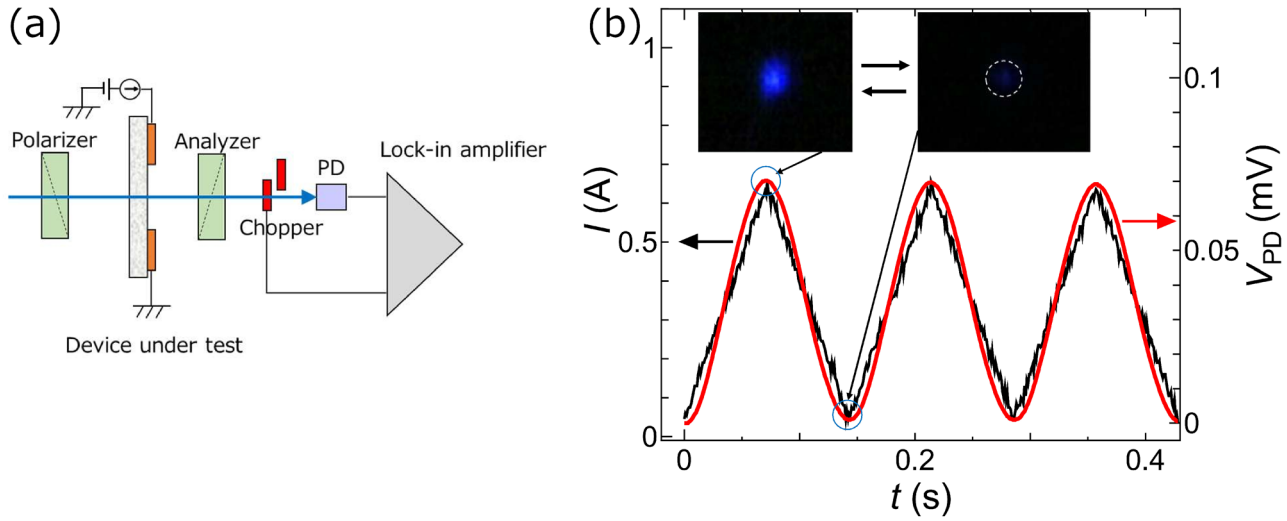

Figure 2. Evaluation of the polarization rotation characteristics. (**a**) Experimental setup. (**b**) Measured values of the temporal variation of the transmitted light intensity (V_{PD}: red curve). Black curve is that of the triangular current (I) injected to the ring-shaped electrode, whose frequency and amplitude were 7 Hz and 600 mA, respectively. The *inset* in this figure shows snapshots of the transmitted light spot.

The polarization rotation characteristics were evaluated for linearly polarized 450 nm-wavelength laser light that was normally incident on the device surface. A commonly used measurement system was employed for evaluation, as is schematically illustrated in Fig. 2a. Briefly, linearly polarized light with a spot diameter of 100 μm was incident on the center of the ring-shaped electrode. In order to exclude additional rotation of the polarization due to birefringence caused by the optical anisotropy of the 4H-SiC crystal, the propagation direction of the incident light was precisely adjusted to be normal to the crystal surface and also to be parallel to the C-axis of the 4H-SiC crystal.

A polarization selector was constructed used the crossed Nichol configuration by using a polarizer (prism beam splitter (PBS) with an extinction ratio of 1×10^{-3}) (Thorlabs: CCM1-PBS251/M) and an analyzer (polarizing plate) (Sigmakoki: SPF-30C-32). The device under evaluation was installed between them. The intensity of the light transmitted through the analyzer was measured by using a photodiode (Hamamatsu Photonics: S1226-18BK). For measuring with sufficiently high signal-to-noise ratio, a lock-in detection method was employed by using an optical chopper (frequency: 1.7 kHz) and a lock-in amplifier (Stanford Research Systems: SR830, time constant: 10 ms).

The red curve in Fig. 2b represents the measured values of the temporal variation of the transmitted light intensity. The black curve is that of the triangular current injected into the ring-shaped electrode. Its repetition frequency and amplitude were 7 Hz and 600 mA, respectively. The *inset* figures show snapshots of the transmitted light spot, which were taken by focusing and projecting the light beam on the screen. Polarization rotation can be clearly confirmed by comparing the images on the left and right in this inset, which were acquired at the top and bottom of the triangular current in this figure, respectively. The red curve shows that the transmitted light intensity varied by following the current variation, from which the polarization rotation angle of the transmitted light was quantitatively evaluated.

Discussion

Figure 3 shows the relation between the magnetic flux density ($B_\perp$) and the polarization rotation angle (θ_{rot}), which was estimated from V_{PD} of Fig. 2b using the standard method for polarization measurement: Before injecting the current to the device, the analyzer was rotated and the rotation angle vs V_{PD} was measured., i.e., by referring to the relation between the rotation angle vs V_{PD} measured by rotating the analyzer.

The red circles and black squares represent the relation acquired after and before DPP-assisted annealing, respectively. The reason for the polarization rotation even before the DPP-assisted annealing will be given later by referring to Fig. 4. The value of $B_\perp$ represents the vertical component of the magnetic flux density on the device surface, which was generated by the current injected into the ring-shaped electrode. Its value at the position of the transmitted light spot was evaluated to be 1.1 mT/A using a formula $B_\perp = \mu_0 I/d$, [where d is the ring diameter (1.1 mm)] derived from the Biot–Savart law. Also, from the slopes of the solid lines fitted to the measured values at $B_\perp < 0.3$ mT, the changes of the polarization angle per unit change of $B_\perp$ were evaluated to be 5.15×10^{-2} rad/mT and 1.09×10^{-1} rad/mT before and after DPP-assisted annealing, respectively. These values represent the magneto-optic sensitivity S represented in the unit of (rad/mT). The Verdet constant V was derived from the relation $V = S \times (dB_\perp/dI)$ and expressed in the unit (rad/A). Here, $dB_\perp/dI$ (= 1.1 mT/A) is the value of the vertical component of the magnetic flux density that was generated by 1-A current injected into the electrode. In order to change the unit (rad/A) of V to (rad/T.m), a common conversion formula 1 (A/m) = 1.26×10^{-6} (T) was used. As a result, The Verdet constant was expressed as $V = 8.73 \times 10^5 S$ (rad/T.m). By using this formula, the

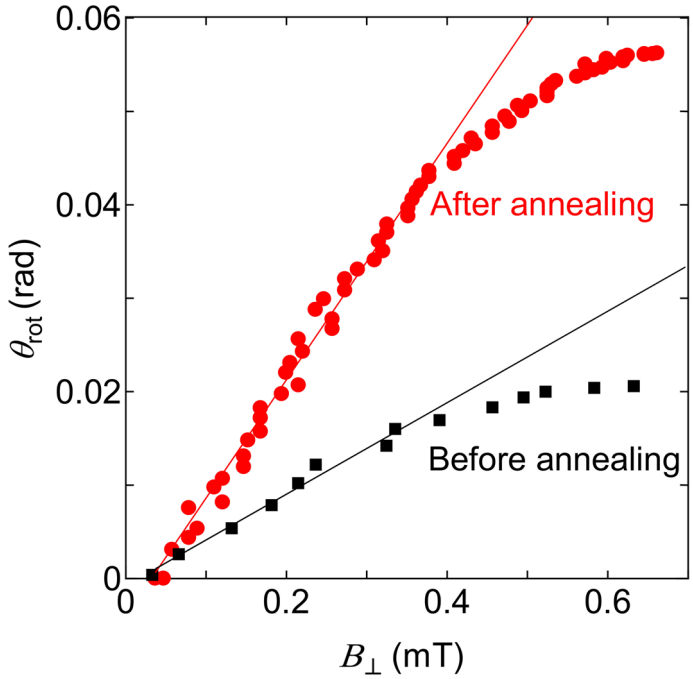

Figure 3. Measured relation between the magnetic flux density ($B_\perp$) and the polarization rotation angle (θ_{rot}). Closed red circles and black squares in the figure represent the device after and before DPP-assisted annealing, respectively. Solid lines were fitted to the measured values at $B_\perp < 0.3$ mT.

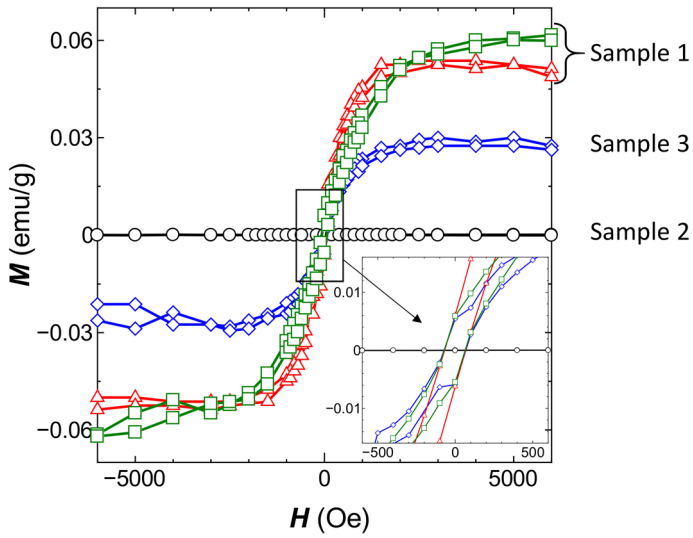

Figure 4. Relations between the applied magnetic field ***H*** (Oe) and the magnetization ***M*** (emu/g) at 300 K. Red triangles and green squares (Sample 1): A SiC crystal after DPP-assisted annealing with doping Al atoms, where the annealing times were 0.5 h and 72 h, respectively. Black circles (Sample 2): A SiC crystal without Al doping (no DPP-assisted annealing). Blue diamonds (Sample 3): A SiC crystal with Al doping (no DPP-assisted annealing). The *inset* shows the magnified relations near the origin of the graph.

values of the Verdet constant, before and after the DPP-assisted annealing, were derived as 4.49×10^4 rad/T.m and 9.51×10^4 rad/T.m, respectively.

The result showed a two-times increase in this constant, which originated from the increased contribution from the DPP due to the DPP-assisted annealing. The saturation of θ_{rot} seen at $B_\perp > 0.4$ mT in Fig. 3 was attributed to the temperature increases in the device due to the Joule-heat generated by current injection. As an evicence, it was estimated experimentally and by the thermal analysis simulation that crystal temperature increased up to 300 °C by 1 A current injection. The saturation in Fig. 3 was not due to the deterioration of the SiC crystal quality

but to the decreased efficiency of generating the magnetic field ($dB_{\perp}/dI$) by the current injected into the ring electrode. The reason for this is that, with the increase in temperature, a part of the current in the ring electrode leaked out to the SiC crystal due to the increases and decreases of the resistance of the metallic wire used for the ring electrode and that of the semiconductor SiC crystal, respectively. Thus, a part of the current in the ring electrode leaked out to the SiC crystal, resulting in a decrease in $dB_{\perp}/dI$. However, the performance of the device was evaluated in the region $B_{\perp} < 0.3$ mT, where it was free from the effects of temperature increases; i.e., the value of $dB_{\perp}/dI$ was maintained constant. For comparison, the Verdet constants of TGG, CeF_3, and PrF_3, which are the materials used for conventional optical isolators in the visible range, are on the order of 10^2 rad/T.m[23]. The above value of 9.51×10^4 rad/T.m is 10^2-times higher than this, by which a gigantic magneto-optical effect was confirmed. Furthermore, the above value is as high as that of the typical ferromagnetic YIG (10^5–10^6 rad/T.m) in the visible range[4].

In order to examine the origin of such a large polarization rotation capability realized by using the indirect-transition-type semiconductor SiC crystal, magnetization curves of a SiC single crystal (5 mm × 5 mm × 0.3 mm) after the DPP-assisted annealing (Sample 1) were acquired at a temperature of 300 K by using a SQUID (Quantum Design: MPMS with EverCool). For comparison, the magnetization curves were acquired also for a SiC crystal without Al doping (Sample 2) and for a SiC crystal doped with Al doping before DPP-assisted annealing (Sample 3). From preliminary measurements, it was confirmed that the values of the magnetization per unit mass M (emu/g) showed diamagnetic characteristics, that is, a linear dependence on the applied magnetic field $\boldsymbol{H}$ (Oe), in the range of -10 kOe $\leqq \boldsymbol{H} \leqq 10$ kOe. This dependence is reasonable because the SiC single crystal is a semiconductor.

For a more detailed discussion, Fig. 4 shows the magnified relation between $\boldsymbol{H}$ and $\boldsymbol{M}$ obtained by subtracting the contributions of the diamagnetic component from the measured values of $\boldsymbol{M}$. The curves in this figure have several typical characteristics: The values of $\boldsymbol{M}$ of Sample 1 (green squares and red triangles) are remarkably larger than those of other samples. Those of Sample 2 (black circles) are negligibly small. Sample 3 (blue diamonds) exhibit a certain amount of $\boldsymbol{M}$. The curves for Samples 1 and 3 show hysteresis characteristics. Furthermore, they exhibit a coercive force, as shown in the *inset* of Fig. 4. These characteristics indicate that the ferromagnetic characteristics were induced by doping Al atoms.

The saturated value of M of Sample 1 (green squares and red triangles) is about twice that of Sample 3. This figure also indicates that the saturated value increased with increasing DPP-assisted annealing time. This is the evidence that the large MO effect, realized by doping Al, was boosted by a factor of two by the DPP-assisted annealing. Thus, the fabricated device exhibited a larger MO effect than that exhibited by conventional materials, and this led to the large poralization-rotation of the transmitted visible light. It has been pointed out, based on a thermodynamic model for the two-level systems[21,24], that the Al dopants are apt to gradually diffuse in time due to the Joule energy generated by the current injected for operating the device. As a result, the magnitude of the MO effect, and thus the polarization-rotation angle, were apt to decrease gradually in time during the device operation. However, the DPP-assisted annealing could suppress this diffusion by forming an irreversible potential barrier to the Al dopants. As a result, even during the device operation, the spatial distribution of the Al dopants maintained the original profile that was formed by the DPP-assisted annealing. This indicates that the DPP-assisted annealing was indispensable in stabilizing the device operation.

As a reference, Song et al. have reported some ferromagnetic characteristics in SiC, which were attributed to doped Al atoms[25]. Although their specimens correspond to Sample 3 in the present study before the DPP-assisted annealing, they were prepared by sintering powdered silicon, carbon, and aluminum. Thus, that material is not suitable for use as a homogeneous and transparent material for the present polarization rotator in the visible range. In the present study, by employing DPP-assisted annealing, conspicuous ferromagnetic characteristics were induced in Sample 1 to realize a larger polarization rotation. The origins of such conspicuous characteristics are as follows: First, in Sample 3, the implanted Al atoms having a random spatial distribution form dimers (Al atom pairs), and the parallel spins in the pairs induce ferromagnetic characteristics. Second, in Sample 1, the spatial distribution of Al atoms was controlled autonomously by the DPP-assisted annealing, resulting in an increase in the number of Al atom pairs. Since it has been found that the triplet state of the electron orbital in an Al atom pair is more stable than the singlet state[26,27], the parallel spins induced more significant ferromagnetic characteristics[28]. Detailed discussions on these origins are currently underway.

Conclusion

This paper reported the fabrication and operation of a transmission-type polarization rotator for visible light with a wavelength of 450 nm using indirect-transition-type semiconductor crystalline SiC to which Al atoms were implanted as a p-type dopant. A novel DPP-assisted annealing method was used for fabrication. The fabricated device was much more compact than the conventional optical isolators because the optical path length required for the polarization rotation in the present device was as short as the thickness of the p–n junction. Also, for operating the fabricated device, no external coils or bulky magnets were required to apply a strong magnetic field to the device. A magnetic flux density as low as mT was sufficient, and this was generated by injecting current into a ring-shaped electrode on the device surface. The fabricated device exhibited a gigantic magneto-optical effect. Specifically, the Verdet constant was as large as 9.51×10^4 rad/T.m at a wavelength of 450 nm, which was 10^2-times higher that of TGG and as high as that of the typical ferromagnetic YIG in the visible range. Furthermore, SQUID measurements confirmed that the SiC crystal exhibited conspicuous ferromagnetic characteristics as a result of the DPP-assisted annealing. It is expected that this device can be used as an efficient transmission-type light modulator or an optical isolator for future information processing systems.

Methods

This section describes the process of fabricating the SiC device. For substrate preparation, first, an n-type 4H-SiC single-crystal was used, whose surface orientation was (0001). The n-type dopant (N atoms) density was 1×10^{18} cm^{-3}. Second, a 10 μm-thick n-type epitaxial layer (n-type dopant (N atoms) density 1×10^{16} cm^{-3}) was deposited on the crystal. Finally, in order to form a p–n junction, Al atoms serving as a p-type dopant were implanted into the (0001) surface by three-step ion implantation with acceleration energies of 700 keV, 350 keV, and 15 keV. The peak concentration was 1×10^{19} cm^{-3}. It was confirmed by preliminary experiments that the absorption coefficient of the SiC substrate was about 70 cm^{-1} at a wavelength of 450 nm. That is, an optical transmittance of the formed p–n homojunction (thickness: about 1 μm or less) was estimated to be as high as 99.3% at a wavelength of 450 nm. After ion-implantation of the Al dopants, post-implantation annealing was employed for crystallinity recovery. Specifically, the SiC crystal was annealed in a high-temperature furnace at 1,800 °C for five minutes. This was repeated two times. Since the highest temperature increase (300 °C) induced by the Joule energy during DPP-assisted annealing was much lower than 1,800 °C, its effect on further improvement of the crystal quality, and thus on the polarization rotation, was negligible.

After electrodes were formed on the top and bottom surfaces of the SiC substrate, the substrate was diced to form a device with dimensions of 3 mm × 3 mm. The ring-shaped p-electrode on the top surface was formed by a Cr/Au (100 nm/700 nm thick) film whose diameter and line width were 1.1 mm and 0.1 mm, respectively. The planar n-electrode on the bottom surface was a Cr/Pt/Au (30 nm/200 nm/700 nm thick) film with a 2 mm-diameter aperture at the center for allowing the incident light to pass through the device. These two electrodes were used for current injection to the p–n junction in the process of the DPP-assisted annealing. No ferromagnetic metals were used for these electrode materials, and it was confirmed that the metals used for the electrodes did not make any contribution to the magneto-optical effect exhibited by this device. For reference, GD-MS analysis (Nu Instruments: ASTRUM) confirmed that the concentration of the ferromagnetic metal impurity in the SiC crystal was as low as 0.036 ppm.

DPP-assisted annealing was carried out on the diced device: A forward bias voltage of 19 V (current density 0.022 A/mm^2) was applied for Joule heating. The top surface of the device was simultaneously irradiated with laser light (typical irradiation time is given in the caption for Fig. 4). The optical power and wavelength were 20 mW and 405 nm, respectively. By momentum exchange between the phonons in the DPP and the electrons in the conduction band, and electron–hole recombination, photon emission was realized, converting a part of the Joule energy to optical energy. Since the emitted photons propagated out from the device and dissipated, the diffusion rate of Al atoms was locally decreased and, as a result, the spatial distribution of Al atoms was controlled autonomously. This autonomous control played an essential role in the DPP-assisted annealing.

The device fabricated by this process operated as a polarization rotator by injecting current only to the ring-shaped p-electrode, while the planar electrode on the bottom surface was not used. It exhibited a gigantic magneto-optical effect in the visible range (wavelength, 450 nm) even though the SiC crystal was an indirect-transition-type semiconductor.

Received: 17 February 2020; Accepted: 20 July 2020
Published online: 31 July 2020

References

1. Cho, J. *et al.* Design, fabrication, switching, and optical characteristics of new magneto-optic spatial light modulator. *J. Appl. Phys.* **76**, 1910 (1994).
2. Park, J., Cho, J., Nishimura, K. & Inoue, M. Magnetooptic spatial light modulator for volumetric digital recording system. *Jpn. J. Appl. Phys.* **41**, 1813 (2002).
3. Villora, E. G. *et al.* Faraday rotator properties of $\{Tb_3\}[Sc_{1.95}Lu_{0.05}](Al_3)O_{12}$, a highly transparent terbium-garnet for visible-infrared optical isolators. *Appl. Phys. Lett.* **99**, 011111 (2011).
4. Hayashi, H. *et al.* Characteristics of Bi:YIG magneto-optic thin films fabricated by pulsed laser deposition method for an optical current transformer. *Jpn. J. Appl. Phys.* **41**, 410 (2002).
5. Slezak, O., Yasuhara, R., Lucianetti, A. & Mocek, T. Temperature-wavelength dependence of terbium gallium garnet ceramics Verdet constant. *Opt. Mater. Express* **6**(11), 3683 (2016).
6. Tate, N., Kawazoe, T., Nomura, W. & Ohtsu, M. Current-induced giant polarization rotation using a ZnO single crystal doped with nitrogen ions. *Sci. Rep.* **5**, 12762 (2015).
7. Lee, E.-C., Kim, Y.-S., Jin, Y.-G. & Chang, K. J. Compensation mechanism for N acceptors in ZnO. *Phys. Rev. B* **64**, 085120 (2001).
8. Itoh, A., Kimoto, T. & Matsunami, H. High performance of high-voltage 4H-SiC Schottky barrier diodes. *IEEE Electron Device Lett.* **16**, 280 (1995).
9. Matus, L. G., Powell, J. A. & Salupo, C. S. High-voltage 6H-SiC *p–n* junction diodes. *Appl. Phys. Lett.* **59**, 1770 (1991).
10. Kordina, O. *et al.* A 4.5 kV 6H silicon carbide rectifier. *Appl. Phys. Lett.* **67**, 1561 (1995).
11. Kawazoe, T., Tate, N. & Ohtsu, M. SiC magneto-optical current-transformer applicable to a polarization rotator using dressed photons. In *IDW'15 Proceedings* PRJ3-5L (2015).
12. Kawazoe, T., Mueed, M. A. & Ohtsu, M. Highly efficient and broadband Si homojunction structured near-infrared light emitting diodes based on the phonon-assisted optical near-field process. *Appl. Phys. B* **104**(4), 747–754 (2011).
13. Kawazoe, T., Ohtsu, M., Akahane, K. & Yamamoto, N. Si homojunction structured near-infrared laser based on a phonon-assisted process. *Appl. Phys. B* **107**, 659–663 (2012).
14. Tran, M. A., Kawazoe, T. & Ohtsu, M. Fabrication of a bulk silicon p–n homojunction-structured light-emitting diode showing visible electroluminescence at room temperature. *Appl. Phys. A* **115**, 105–111 (2014).
15. Kawazoe, T., Nishioka, K. & Ohtsu, M. Polarization control of an infrared silicon light-emitting diode by dressed photons and analyses of the spatial distribution of doped boron atoms. *Appl. Phys. A* **121**, 1409–1415 (2015).
16. Yamaguchi, M., Kawazoe, T., Yatsui, T. & Ohtsu, M. Spectral properties of a lateral p–n homojunction-structured visible silicon light-emitting diode fabricated by dressed-photon–phonon-assisted annealing. *Appl. Phys. A* **121**, 1389–1394 (2015).
17. Tanaka, H., Kawazoe, T., Ohtsu, M. & Akahane, K. Decreasing the threshold current density in Si lasers fabricated by using dressed-photons. *Fluoresc. Mater.* **1**, 1–7 (2015).

18. Ohtsu, M. & Kawazoe, T. Principles and practices of Si light emitting diodes using dressed photons. *Adv. Mater. Lett.* **10**, 860–867 (2019).
19. Ohtsu, M. History, current development, and future directions of near-field optical science. *Opto-Electron. Adv.* **3**, 190046 (2020).
20. Ohtsu, M. Dressed photon technology. *Nanophotonics* **1**, 83–97 (2012).
21. Ohtsu, M. *Silicon Light-Emitting Diodes and Lasers* 29–119 (Springer, Heidelberg, 2016).
22. Kim, J. H., Kawazoe, T. & Ohtsu, M. Dependences of emission intensity of Si light-emitting diodes on dressed-photon–phonon-assisted annealing conditions and driving current. *Appl. Phys. A* **123**, 606 (2017).
23. Molina, P., Vasyliev, V., Villora, E. G. & Shimamura, K. CeF_3 and PrF_3 as UV-Visible Faraday rotators. *Opt. Express* **19**(12), 11786 (2011).
24. Kim, J. H., Kawazoe, T. & Ohtsu, M. Optimization of dressed-photon–phonon-assisted annealing for fabricating GaP light-emitting diodes. *Appl. Phys. A* **121**, 1395–1401 (2015).
25. Song, B. *et al.* Observation of glassy ferromagnetism in Al-doped 4H-SiC. *J. Am. Chem. Soc.* **131**, 1376–1377 (2009).
26. Upton, T. H. Low-lying valence electronic states of the aluminum dimer. *J. Phys. Chem.* **90**, 754–759 (1986).
27. Rajca, A. Organic diradicals and polyradicals: from spin coupling to magnetism?. *Chem. Rev.* **94**, 871–893 (1994).
28. Ohtsu, M. *Silicon Light-Emitting Diodes and Lasers* 135–138 (Springer, Heidelberg, 2016).

Acknowledgements
We thanks to Prof. S. Nakagawa, Dr. Y. Takamura and Mr. M. Sato of Tokyo Institute of Technology for their technical supports on SQUID measurements.

Author contributions
T.K., T.K. and M.O. directed the project; T.K. fabricated the devices; T.K. and T.K. designed the experiments and performed optical characterizations; technical discussions were made by T.K., T.K. and M.O.

Competing interests
The authors declare no competing interests.

Additional information
Correspondence and requests for materials should be addressed to T.K.

Reprints and permissions information is available at www.nature.com/reprints.

Publisher's note Springer Nature remains neutral with regard to jurisdictional claims in published maps and institutional affiliations.

symmetry

MDPI

Article

Off-Shell Quantum Fields to Connect Dressed Photons with Cosmology

Hirofumi Sakuma [1,*,†], Izumi Ojima [1,†], Motoichi Ohtsu [1,†] and Hiroyuki Ochiai [2]

[1] Research Origin for Dressed Photon, Yokohama-shi, Kanagawa 221-0022, Japan; ojima@gaia.eonet.ne.jp (I.O.); ohtsu@rodrep.or.jp (M.O.)
[2] Institute of Mathematics for Industry, Kyushu University, Fukuoka-shi, Fukuoka 819-0395, Japan; ochiai@imi.kyushu-u.ac.jp
* Correspondence: sakuma@rodrep.or.jp
† These authors contributed equally to this work.

Received: 22 April 2020; Accepted: 21 July 2020; Published: 28 July 2020

Abstract: The anomalous nanoscale electromagnetic field arising from light–matter interactions in a nanometric space is called a dressed photon. While the generic technology realized by utilizing dressed photons has demolished the conventional wisdom of optics, for example, the unexpectedly high-power light emission from indirect-transition type semiconductors, dressed photons are still considered to be too elusive to justify because conventional optical theory has never explained the mechanism causing them. The situation seems to be quite similar to that of the dark energy/matter issue in cosmology. Regarding these riddles in different disciplines, we find a common important clue for their resolution in the form of the relevance of space-like momentum support, without which quantum fields cannot interact with each other according to a mathematical result of axiomatic quantum field theory. Here, we show that a dressed photon, as well as dark energy, can be explained in terms of newly identified space-like momenta of the electromagnetic field and dark matter can be explained as the off-shell energy of the Weyl tensor field.

Keywords: off-shell quantum field; space-like momentum; dressed photon; micro-macro duality; Clebsch dual field; Majorana fermion; the cosmological term; Weyl tensor; dark energy; dark matter

1. Introductory Review of Dressed Photon Technology

1.1. Broad Overview

Suppose that a nanometer-sized material (NM) is illuminated by propagating light whose diffraction-limited size is much larger than the size of the NM. Then, an anomalous non-propagating localized light field is generated around the NM, contrary to the accepted knowledge of optics. This non-propagating light field is called the optical near field [1], which is undetectable by a separately placed conventional photodetector. The studies on the optical near field initiated practically in the late 20th century have led, through trial-and-error approaches, to the novel concept of a quasi-particle created as a result of light–matter interaction in a nanometric space. This quasi-particle is figuratively called the dressed photon (DP), that is, a metaphoric expression of photon energy partly fused with the energies of the material involved in the interaction. Figure 1 shows typical experimental setups for creating a DP. Studies on DPs are now rapidly progressing, yielding innovative generic technologies [2] of "small light", which accomplish the impossible in a variety of application fields.

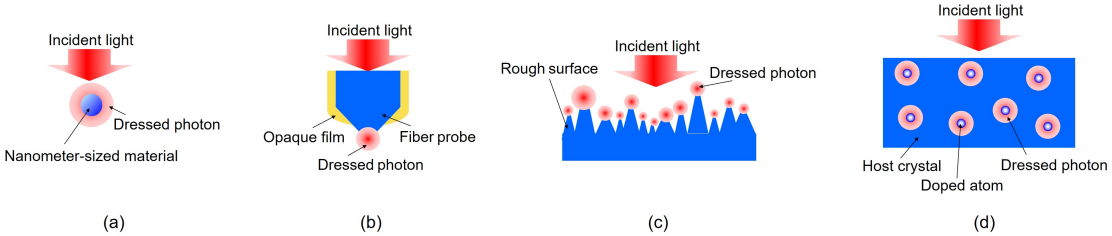

Figure 1. Typical experimental setups for creating a DP. (**a**) on a nanoparticle; (**b**) on the tip of a fiber probe; (**c**) on bumps of a rough material surface; (**d**) on doped atoms in a host crystal.

One should bear in mind, however, that the concept of a DP first proposed by one of the authors (M.O.) still seems to be either ignored or tacitly understood differently by the mainstream researchers in optical sciences because of the conceptual difficulty of dealing with off-shell quantities in the midst of field interactions. We think that this kind of refusal or confusion about DPs stems from a certain degree of ambiguity in using such an abstract expression as light–matter field interactions in a nanometric space; the main purpose of the above remark is not to criticize the incorrect usage of DPs in the literature but rather to promote renewed awareness that the issue of DP phenomena addressed here is a remarkable one that cannot be understood within the conventional framework of optical theory.

To elucidate the essence of the DP problem, we start by listing five conventional views in optics and briefly show how a DP violates them.

Five conventional common views in optics

I. Light is a propagating wave that fills a space. Its spatial extent (size) is much larger than its wavelength.
II. Light cannot be used for imaging and fabrication of sub-wavelength-sized materials. Furthermore, light cannot be used for assembling and operating sub-wavelength-sized optical devices.
III. For optical excitation of an electron, the photon energy must be equal to or higher than the energy difference between the relevant two electronic energy levels.
IV. An electron cannot be optically excited if the transition between the two electric energy levels is electric dipole forbidden.
V. Crystalline silicon has a very low light emission efficiency and is thus unsuitable for use as an active medium in light-emitting devices.

Contrary to I–V above, the intrinsic natures of DPs have enabled the advent of innovative technologies such as the following: (1) Nanometer-sized optical devices. These devices are operated on the basis of the spatially localized nature of DPs created on an NM (Figure 1a) and the autonomous DP energy transfer between NMs. These devices are based on the intrinsic nature of a DP that is contrary to I, II and IV. Integrated 2D arrays of NOT- and AND-logic gates operating at room temperature have been fabricated using InAs NMs [3]. (2) Nanofabrication technology, such as chemical vapor deposition and autonomous smoothing of a material surface (Figure 1b,c). These technologies are based on the intrinsic nature of a DP that is contrary to I–IV. Their details will be described in subsection 1.2 since the information on the maximum size of a DP will be used in Section 4 on cosmology. (3) Light-emitting devices using indirect-transition-type semiconductors. These devices are based on the intrinsic nature of a DP that is contrary to V. Infrared light-emitting diodes using crystalline silicon (Si) have been realized. For their fabrication, a method of DP-assisted annealing has been invented to autonomously control the spatial distribution of the dopant atoms on which DPs are created and localized (Figure 1d). Their output optical powers are as high as 2 W [4]. Infrared Si lasers have also been developed whose CW output optical power is as high as 100 W, and the threshold current density is as low as 60 A/cm [2] at room temperature [5]. Their high power and low energy consumption factors are 10^4 and 0.05, respectively, relative to those of the conventional single-stripe double heterojunction-structured semiconductor lasers fabricated using the direct-transition-type

compound InGaAsP. Furthermore, novel polarization rotators have been developed using crystalline SiC that exhibit a gigantic ferromagnetic magneto-optical effect [6].

1.2. Nanofabrication Technology and the Size of a DP

This subsection describes two examples of nanofabrication technology that provide key experimental data for theoretical discussions in Sections 2–4. In particular, the maximum size of a DP was determined by analyzing a large number of experimental results.

1.2.1. Photochemical Vapor Deposition

In this method, a material is grown by depositing atoms on a substrate. Gaseous molecules are dissociated when a DP is created, for example, on the fiber probe tip of Figure 1b. Atoms created by this dissociation are deposited on the substrate installed below the fiber probe tip. Since the size of a DP is equivalent to that of the fiber probe tip, a sub-wavelength-sized NM can be grown, which is contrary to common views I and II. Furthermore, the photon energy $h\nu_{in}$ of the light incident on the end of the fiber probe can be lower than the excitation energy E_{excite} of the electrons in the molecule, which is contrary to common view III. This phenomenon occurs because the energy $h\nu_{DP}$ of the created DP is given by the sum of $h\nu_{in}$, the energies of excitons and phonons in the fiber probe, and thus $h\nu_{DP} \geq E_{excite}$. For example, DP dissociated gaseous $Zn(C_2H_5)_2$ molecules (the wavelength λ_{excite} of light whose energy corresponds to E_{excite} was as short as 270 nm), thus depositing an NM composed of Zn atoms on a sapphire substrate. In contrast to common view III, blue incident light (wavelength $\lambda_{in} = 488$ nm $> \lambda_{excite}$) was used. Figure 2a shows 3D atomic force microscopic (AFM) images of the grown NMs [7]. Furthermore, the electric dipole-forbidden transition of electrons could be used for dissociation, which is contrary to common view IV. This approach was possible because the conventional long-wave approximation is not valid in the case of a DP due to its sub-wavelength size. For example, DPs dissociated optically inactive $Zn(acac)_2$ molecules, thus depositing Zn atoms, using visible incident light (457 nm wavelength) (Figure 2b) [8,9].

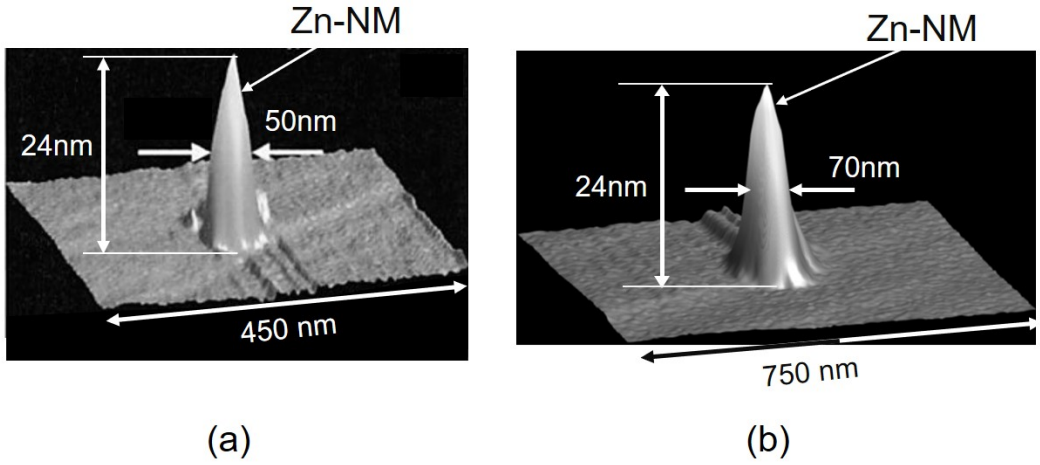

Figure 2. AFM images of Zn-NMs formed on a sapphire substrate. Dissociated molecules are (**a**) [7] $Zn(C_2H_5)_2$ and (**b**) [8] $Zn(acac)_2$. The values of the height and FWHM are given in each figure.

The maximum size of a DP was estimated by measuring temporal variations in the deposition rate of the number of Zn atoms and the full-width at half-maximum (FWHM) of the 3D image [10]. The results showed that, in the initial stage of deposition, the deposition rate and the FWHM increased monotonically with time. When the FWHM reached the size of the fiber probe tip, the deposition rate was the maximum, which is the phenomenon known as size-dependent resonance between the fiber probe tip and the size of the NM [11]. Then, the deposition rate monotonically decreased and approached a constant value. This result indicated that the size of the NM

asymptotically approached a certain value. Since the height of the NM monotonically increased with the deposition time, this approach indicated that the value of the FWHM approached a certain value. To confirm this indication, the maximum value of the FWHM was evaluated from the 3D images of the saturated-sized NMs. As a result, a value of 50–70 nm was obtained after compensating for the errors and inaccuracies in the experimental data. Figure 2a,b just show the images of the NMs with the maximum value of the FWHM. This maximum value also indicated that the maximum size of a DP is 50–70 nm because the size of the DP transferred from the fiber probe tip to the NM corresponds to the size of the NM. A series of experiments confirmed that this value was independent of the molecular species, the wavelength and power of the incident light, the conformation, and the size of the fiber probe tip.

1.2.2. Smoothing Material Surfaces

Galilei chemical-mechanically polished the lens surfaces of his telescope as early as the 17th century. Although this method is popularly used even now in industry, polishing 3D or microsurfaces using this method is difficult because it is a contact method that employs a polishing pad. Furthermore, small scratches are created on the surface during the polishing process. To solve these problems, a non-contact dry-etching method was invented using DPs [12]. Its principle is nearly the same as that of the photochemical vapor deposition above. That is, DPs are created on small bumps of the rough surface by light irradiation (Figure 1c). A gaseous Cl_2 molecule, as an example, is dissociated if it jumps into the DP field. Since the created Cl atom is chemically active, it etches the bump without using any devices such as a fiber probe. Thus, etching autonomously starts upon light irradiation, varying the conformation and size of the bumps, and stops when the surface becomes flat, i.e., when DPs are no longer created. A variety of 3D surfaces, such as convex surfaces, concave surfaces, and the side walls and inner wall of a cylinder, have been smoothed. The microsized side walls of the corrugations of a diffraction grating were also smoothed. This method has been applied to a variety of materials, such as glasses, crystals, ceramics, and plastics, to decrease the roughness to sub-nanometer. It has been employed in industry to increase the optical damage threshold of high-power UV laser mirrors [13], repair the surface of photomasks for UV lithography [14], and so on.

The maximum size of a DP was also evaluated by this method: Figure 3 shows the experimental results of polishing a plastic PMMA surface by dissociating O_2 molecules by DPs [15]. The wavelength λ_{excite} of light corresponding to the E_{excite} of the O_2 molecule was 242 nm. However, the wavelength λ_{in} of the incident light was as long as 325 nm ($>\lambda_{excite}$), contrary to common view III. The horizontal axis represents the period l of the surface roughness. The vertical axis is the standard deviation σ of the roughness acquired from the AFM images. Here, the ratio $\sigma_{after}/\sigma_{before}$ between the values before (σ_{before}) and after (σ_{after}) the etching is plotted on a logarithmic scale. This figure shows that $\sigma_{after}/\sigma_{before}$ was less than 1 in the range of $l <$ 50–70 nm, from which the maximum size of the DP is again confirmed to be 50–70 nm, as displayed by the grey band in this figure.

For comparison, in the case when $\lambda_{in} = 213$ nm ($<\lambda_{excite}$), which follows common view III, the value of $\sigma_{after}/\sigma_{before}$ was less than unity only in the range of $l > \lambda_{in}$. In contrast, $\sigma_{after}/\sigma_{before} > 1$ in the range of $l < \lambda_{in}$ was obtained. By comparing these results, etching by DPs is confirmed to be effective for selectively removing fine bumps of sub-wavelength size.

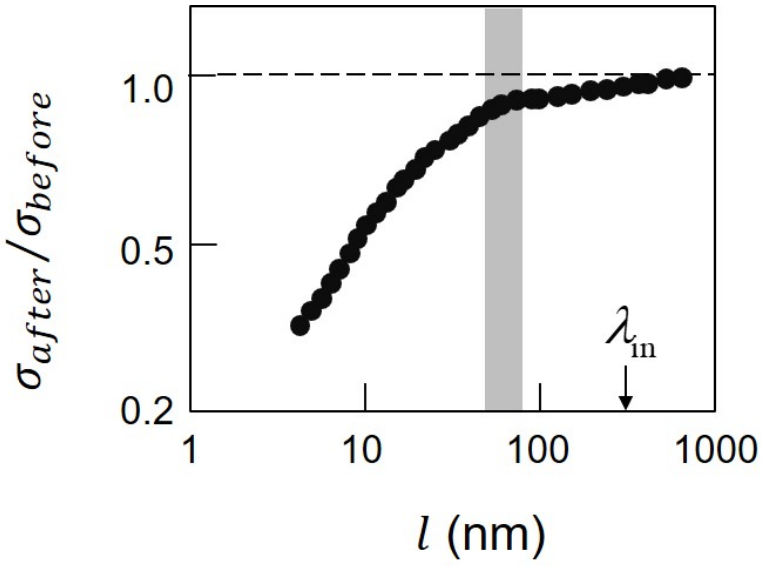

Figure 3. Ratio of the standard deviation of the roughness of a plastic PMMA surface before and after etching. The downward arrow represents the value of l that is equal to λ_{in}. The width of the grey band corresponds to the maximum size of the DP. The ratio $\sigma_{after}/\sigma_{before}$ was derived from the values of σ_{before} and σ_{after} given in Figure 4 of Ref. [15].

2. New Theory for Dressed Photon

2.1. Missing Aspect of Quantum Field Interaction Theory

In the usual quantum field theory (QFT), scattering processes are described by the LSZ reduction formulae [16], which determine the S-matrix elements $S_{\beta\alpha}$ connecting the in(-coming) and out(-going) scattering states, $|\alpha, in\rangle$ and $|\beta, out\rangle$, respectively, as on-shell projections of the time-ordered Green functions. This way of description is suitable for experimental situations satisfying the asymptotic completeness which means that interactions among fields can be reduced to scattering processes. In such situations, in-states $|\alpha, in\rangle \in \mathfrak{H}^{in}$ describe the states of on-shell particles in the Heisenberg picture in Hilbert space $\mathfrak{H}$ before the interaction at $t = -\infty$, and out-states $|\beta, out\rangle \in \mathfrak{H}^{out}$ representing the final states of on-shell particles after the interaction at $t = +\infty$, which can be determined by modeled scattering processes under the assumption $\mathfrak{H} = \mathfrak{H}^{in} = \mathfrak{H}^{out}$ of asymptotic completeness.

In the situations with asymptotic completeness being valid, all the discussions can safely be focused on the on-shell aspects in terms of the S-matrix for which the LSZ formulae in QFT are used commonly among particle physicists. In this case, however, an important issue has been forgotten regarding the roles played by off-shell Heisenberg fields at the center of given field interactions. We note here that the Greenberg and Robinson theorem [17,18] proved in axiomatic quantum field theory shows that an interaction among quantum fields must inevitably accompany space-like momentum supports whenever this interaction can non-trivially transform in-states of asymptotic field ϕ^{in} into out-states of asymptotic field ϕ^{out} describing particles with time-like momentum support. Note that space-like momentum here does not mean the presence of a tachyonic field [19] carrying unstable particles with space-like momenta.

Thus, the consequence of the axiomatic theory claiming the existence of space-like momentum support is a remarkable feature in sharp contrast to the conventional perturbative expansion method for field interactions, in which only on-shell particles with time-like or light-like momentum support are considered physical. This important result has been totally neglected thus far, perhaps owing to such prejudice that abstract consequences in mathematical theorems are irrelevant to specific physical aspects of interacting fields. In the following subsection, however, our discussion on DPs will exhibit the existence of space-like momentum supports in such a form linked to the existence

of well-known $U(1)$ gauge bosons mediating electromagnetic interactions as virtual photons. Since the notion of virtual photons is closely-linked to perturbative expansion methods not necessarily related to space-like momenta of the field under consideration, the term of virtual photons mentioned above is used in a loose sense. In what follows, we are going to reexamine the problem of electromagnetic interaction from the viewpoint of Micro-Macro duality theory to be touched upon shortly below in which not only microscopic "particle modes" but also macroscopic "non-particle condensates" play key roles to attain complete description of given electromagnetic fields.

2.2. Augmented Maxwell's Equation

In view of the unfamiliarity in the science community at large with the relevant subjects, we recapitulate the important points to make this article self-contained, on the basis of [5], the latest tutorial paper on DPs, which summarizes most of the results reported in a series of works [5,20–22]. In our new theory on DPs, we have introduced a new mathematical formulation called the Clebsch dual field, and some of the important outcomes derived from the formulation will be used in our arguments without detailed explanation; hence, we reserve the Method section until the end to give a revised concise explanation as background information for interested readers.

To identify precisely the nature of the problem under consideration, we emphasize first that quantum fields with infinite degrees of freedom are accompanied in general by disjoint representations [23], which are mutually separated by the absence of intertwiners, as the stronger, refined, and clear-cut version of unitary non-equivalence. For those who are familiar only with quantum mechanics with finite degrees of freedom, the existence of such disjoint representations may look like a pathology in the system with infinite degrees of freedom. However, the familiar situation encountered in the systems with finite degrees of freedom is, actually, an exceptional one specific to the finite system. The emergence of characteristic structures where "invisible"microscopic levels become "visible"to us is due to the sector structure arising from the spectral decomposition of the center of the observable algebra. Each sector labeled by macroscopic order parameters is mutually disjoint owing to the absence of intertwiners between different sectors at the microscopic level. This fact is the crux of the mathematically reformulated "quantum-classical"correspondence explained in the Micro-Macro duality proposed in [24,25] by one (I. O.) of the present authors.

Recall that, in the relativistically covariant formulation of the electromagnetic field, only transverse modes are considered physical and the longitudinal mode is eliminated as unphysical because of the indefiniteness of the metric of the longitudinal mode. At the classical macroscopic level, however, the Coulomb mode corresponding to the unphysical longitudinal mode plays the dominant role in electromagnetic interactions. The clue to resolving this contradiction related to the gap between microscopic and macroscopic worlds must lie in the disjointness of representations at the microscopic level and in the presence of space-like momentum support related to the former.

By one (I. O.) [26] of the authors, the important role played by macroscopic non-particle condensates (touched upon at the end of the preceding subsection) has first been discussed in electromagnetic theory in the attempt to reexamine the essence of Nakanish–Lautrup formalism [27] of abelian gauge theory: one of the remarkable points important for the present discussion on the classical Clebsch dual field is concerning the contrast between gauge invariance (in algebraic sense) and physicality of specific modes (changing from a representation to another, dependent on the choice of physical situations): in the usual treatment of gauge theories, it is believed that a physical quantity must be gauge invariant, on the basis of such algebraic judgment as whether $\tau_\Lambda(A) = A$ or not, in terms of the algebraic gauge transformation τ_Λ. In the actual situations, however, such gauge non-invariant quantities as the longitudinal Coulomb tail A^c and/or the Cooper pairs χ^c are to be treated as physical modes in spite of their gauge non-invariance! In order to treat correctly such gauge non-invariant physical modes, we need to introduce such viewpoint that a quantity A is physical or not in a given situation should be judged by means of the gauge transformation represented by a commutation relation at the operator level: $[Q_\Lambda, A] = 0$ or not, in each representation of physical

relevance, where Q_Λ denotes a conserved charge defined in the Nakanishi–Lautrup B-field formalism which generates an infinite-dimensional abelian Lie group of local gauge transformation. Thus, in spite of their gauge dependence, the Coulomb tail A^c or the Cooper pairs χ^c as c-number condensates become physical quantities owing to this commutativity. One should bear in mind that this point is helpful for reading Section 5 of Method on the formulation of the Clebsch dual field.

As to the electromagnetic 4-vector potential A_μ, one should also pay attention to the fact that it possesses a nonlocal off-shell (out-of-light-cone) characteristic in the sense that an observable quantity $\oint_\gamma A_\nu dl^\nu$ in the Aharonov–Bohm (AB) effect [28] does not correspond to the value of A_μ at a certain point in spacetime but to the integrated value along the Wilson loop γ is worth mentioning. Thus, motivated by the above-mentioned concept of disjoint representations and space-like momentum support, which seem to be closely linked to the nonlocal characteristic of A_μ, let us see how Maxwell's equation (1), represented in terms of vector potential A^μ, whose Helmholtz decomposition is given by (2), and the mixed form of energy-momentum (EM) tensor $T_\mu^{\ \nu}$ given in (3),

$$\partial_\nu F^{\mu\nu} = \partial_\nu(\partial^\mu A^\nu - \partial^\nu A^\mu) = [-\partial^\nu\partial_\nu A^\mu + \partial^\mu(\partial_\nu A^\nu)] = j^\mu, \tag{1}$$

$$A^\mu = \alpha^\mu + \partial^\mu\chi, \quad (\partial_\nu\alpha^\nu = 0, \ \ \partial_\nu A^\nu = \partial_\nu\partial^\nu\chi), \tag{2}$$

$$T_\mu^{\ \nu} = -F_{\mu\sigma}F^{\nu\sigma} + \frac{1}{4}\eta_\mu^{\ \nu}F_{\sigma\tau}F^{\sigma\tau}, \tag{3}$$

can be extended into a thus far unknown space-like 4-momentum sector of the electromagnetic field, where the notations are conventional and the sign convention of the Lorentzian metric ($\eta_{\mu\nu}$) signature $(+---)$ is employed.

In the Clebsch dual formulation, the 4-vector potential in the space-like sector is denoted by U_μ, and for the light-like case of $U^\nu(U_\nu)^* = 0$, where $*$ denotes a complex conjugate, this potential is parametrized in terms of a couple of Clebsch parameters λ and ϕ satisfying

$$U_\mu := \lambda\partial_\mu\phi, \ \ \partial^\nu\partial_\nu\lambda - (\kappa_0)^2\lambda = 0, \ \ \partial^\nu\partial_\nu\phi = 0, \tag{4}$$

$$C^\nu L_\nu = 0, \quad (C^\nu := \partial^\nu\phi, \ \ L_\nu := \partial_\nu\lambda), \tag{5}$$

where κ_0 is an important constant to be determined in Section 3. Our goal is to show that, as a dual of the Proca equation of the form $\partial^\nu\partial_\nu A^\mu + m^2A^\mu = 0$, the newly identified vector potential U^μ, called the Clebsch dual (electromagnetic wave) field, given by

$$\partial^\nu\partial_\nu U^\mu - (\kappa_0)^2U^\mu = 0, \quad \Longleftrightarrow \quad (\partial^\nu\partial_\nu A^\mu + m^2A^\mu = 0) \tag{6}$$

can satisfy "Maxwell's equation"in the space-like momentum sector and behaves like a classical version of a longitudinal virtual photon, which is shown in the Method section. While the space-like Klein Gordon (KG) equation in (4) is necessarily related to negative energy, this equation has been forgotten in the predominant arguments in the state vector space involving the Fock space structure equipped with the vacuum vector $|0\rangle$ characterized by $a|0\rangle = 0$ in terms of the annihilation operator a. However, this is not the whole story. Interestingly, if we move from the vacuum situation to thermal one, then we find that the modular inversion symmetry in the Tomita–Takesaki extension [29] of the thermal equilibrium, which can physically be interpreted as the right/left symmetry of the state vector of the Gibbs state, implies the existence of stable states with two-sided (positive and negative) energy spectra. Thus, one should not neglect the possibility that the two-sided "energy"as in (6) satisfies the stability of the Fock space structure.

As shown in the Method section, one of the important characteristics of the Clebsch dual field is that the field strength $S_{\mu\nu} := \partial_\mu U_\nu - \partial_\nu U_\mu$ corresponding to $F_{\mu\nu}$ is given by a simple bivector of

$$S_{\mu\nu} = L_\mu C_\nu - L_\nu C_\mu, \quad C^\nu L_\nu = 0. \tag{7}$$

In addition, it is shown in the Method section that the light-like ($U^\nu(U_\nu)^* = 0$) Clebsch dual field corresponding to the classical version of the $U(1)$ gauge boson can be extended to cover the gauge symmetry broken space-like $U^\nu(U_\nu)^* < 0$ case, in which both λ and ϕ satisfy the same space-like KG equation of (4). By this extension, the form of the EM tensor of the Clebsch dual field changes from (8) to the first equation in (9),

$$\hat{T}_\mu^{\ \nu} := S_{\mu\sigma}S^{\nu\sigma} = \rho C_\mu C^\nu, \ \ \rho := L^\nu L_\nu, \tag{8}$$

$$\hat{T}_\mu^{\ \nu} := S_{\mu\sigma}S^{\nu\sigma} - S_{\sigma\tau}S^{\sigma\tau}\eta_\mu^{\ \nu}/2, \iff G_\mu^{\ \nu} := R_\mu^{\ \nu} - Rg_\mu^{\ \nu}/2. \tag{9}$$

$\hat{T}_\mu^{\ \nu}$ in (9) becomes isomorphic to the Einstein tensor $G_\mu^{\ \nu}$ given in the second equation of (9) where $R_\mu^{\ \nu}$ denotes Ricci tensor defined as the contraction of Riemann curvature tensor of the form: $R_\mu^{\ \nu} := R_{\sigma\mu}^{\ \ \ \nu\sigma}$ and R is the scalar curvature defined as $R := R_\nu^{\ \nu}$. Riemann curvature tensor $R_{\alpha\beta\gamma\delta}$ satisfies the following properties:

$$R_{\beta\alpha\gamma\delta} = -R_{\alpha\beta\gamma\delta}, \quad R_{\alpha\beta\delta\gamma} = -R_{\alpha\beta\gamma\delta}, \quad R_{\gamma\delta\alpha\beta} = R_{\alpha\beta\gamma\delta}, \tag{10}$$

$$R_{\alpha\beta\gamma\delta} + R_{\alpha\gamma\delta\beta} + R_{\alpha\delta\beta\gamma} = 0, \quad \nabla_\nu G_\mu^{\ \nu} = 0. \tag{11}$$

where ∇_ν denotes a covariant derivative defined on a curved spacetime. Note that, if we define $\hat{R}_{\alpha\beta\gamma\delta}$ as $\hat{R}_{\alpha\beta\gamma\delta} := -S_{\alpha\beta}S_{\gamma\delta}$, then we readily see that it satisfies exactly the same equations as those in (10). The fact that $\hat{R}_{\alpha\beta\gamma\delta}$ also satisfies the first equation in (11) can be directly shown from (7), namely, $S_{\alpha\beta}$ is a simple bivector field. Since "Ricci tensor" $\hat{R}_\mu^{\ \nu}$ in this case is defined as $\hat{R}_\mu^{\ \nu} = \hat{R}_{\sigma\mu}^{\ \ \ \nu\sigma} = -S_{\sigma\mu}S^{\nu\sigma} = S_{\mu\sigma}S^{\nu\sigma}$ and "scalar curvature" $\hat{R}$ becomes $\hat{R}_\nu^{\ \nu} = S_{\sigma\tau}S^{\sigma\tau}$, we see that the first equation in (9) is rewritten as $\hat{T}_\mu^{\ \nu} = \hat{R}_\mu^{\ \nu} - \hat{R}\eta_\mu^{\ \nu}/2$ and is isomorphic to the second one. In addition, the divergence free condition $\partial_\nu \hat{T}_\mu^{\ \nu} = 0$ which qualifies $\hat{T}_\mu^{\ \nu}$ as the energy-momentum tensor of the Clebsch dual field corresponds to the second equation in (11). We conjecture that the above isomorphism (9) is a sort of "conjugated"manifestation of the isomorphism between the Coulomb force and the universal gravitation, since, as we already explained, the Clebsch dual field represents the longitudinal Coulomb modes of electromagnetic field. In addition, it also implies an intriguing possibility that *the quantization of the Clebsch dual field to be discussed in the following Section 3 is also closely related to that of spacetime.*

For a space-like case, when the λ and ϕ fields are given by plane waves of $\psi = \hat{\psi}_c \exp[i(k_\nu x^\nu)]$ satisfying (4), together with $\partial^\nu\psi\partial_\nu\psi^* = -(\kappa_0)^2(\hat{\psi}_c\hat{\psi}_c^*)$, we obtain $\hat{T}_\nu^{\ \nu} = -S_{\sigma\tau}S^{\sigma\tau}$ directly from (7) and (9), leading to showing that the trace of $\hat{T}_\nu^{\ \nu}$ defined as the norm of $\hat{T}_\nu^{\ \nu}$ ($||\hat{T}_\nu^{\ \nu}||$) is negative:

$$||\hat{T}_\nu^{\ \nu}|| := -S^{\sigma\tau}(S_{\sigma\tau})^* = 4(\kappa_0)^2[U^\nu(U_\nu)^*] = -2(\kappa_0)^4[\hat{\lambda}_c(\hat{\lambda}_c)^*][\hat{\phi}_c(\hat{\phi}_c)^*] < 0, \tag{12}$$

which will be used in Section 4 on cosmology.

3. Quantization of the Clebsch Dual Field and DP Model

Using the plane wave form mentioned above, L^μ derived from (4) satisfies

$$L^\nu L_\nu^* = -(\kappa_0)^2(\hat{\lambda}_c\hat{\lambda}_c^*) = const. < 0, \tag{13}$$

which shows that "momentum-like vector" $L^\mu = \partial^\mu\lambda$ lies in a submanifold of the Lorentzian manifold called de Sitter space in cosmology, which is a pseudo-hypersphere with radius $(\sqrt{\Lambda_{dS}})^{-1/2}$ embedded in R^5. The importance of this space in the context of spacetime quantization was first noted by Snyder [30], who proposed a quantization scheme with Planck length and the built-in Lorentz invariance based on the assumption that hypothetical momentum 5-vector $\hat{p}^\mu (0 \le a \le 4)$ in R^5 is constrained to lie on de Sitter space, *i.e.*, $\hat{p}^\nu\hat{p}_\nu^* = -\Lambda_{dS}$. The similarity between (13) and the de Sitter space structure of $\hat{p}^\nu\hat{p}_\nu^* = -\Lambda_{dS}$ seems to imply that the isomorphism (9) between $\hat{T}_\mu^{\ \nu}$ and $G_\mu^{\ \nu}$ derived for the classical field equation is valid also for quantized fields, which is surely an important issue to be investigated.

A particularly interesting point concerning this similarity is the following contrast: in Snyder's quantization scheme, the parameter Λ_{dS} does not explicitly appear although a Planck scale is introduced independently. On the contrary, $(\kappa_0)^2$ plays a key role in the Clebsch dual field. This observation suggests that conformal symmetry breaking related to (4) may be closely related to the dynamic origin of the cosmological constant Λ, which Snyder did not discuss. In this section, firstly, we will show that the introduction of κ_0 can be justified only when we consider the quantization of the Clebsch dual field. In addition, its physical implication for cosmology will be discussed in Section 4 from the viewpoint of simultaneous conformal symmetry breaking of electromagnetic and gravitational fields.

Note that $\hat{T}_\mu^{\ \nu} = \rho C_\mu C^{\ \nu}$ in (8) is isomorphic to the EM tensor of freely moving fluid particles, so the kinetic theory of molecules suggests that the ρ field can be quantized. Since the physical dimensions of $\rho C_\mu C^\nu = \rho \partial_\mu \phi \partial^\nu \phi$ and ϕ are the same as those of $F_{\mu\sigma}F^{\nu\sigma}$ and $F_{\mu\nu}$, respectively, using $\rho = L^\nu L_\nu$ given in (8), we see that L^μ has the dimension of length. Therefore, the quantization of ρ means that there exists a certain quantized length of which the inverse is κ_0. Now, let us consider the Dirac equation of the form

$$(i\gamma^\nu \partial_\nu + m)\Psi = 0, \tag{14}$$

which can be regarded as the "square root"of the time-like KG equation: $(\partial^\nu \partial_\nu + m^2)\Psi = 0$. Therefore, the Dirac equation for $(\partial^\nu \partial_\nu - (\kappa_0)^2)\Psi = 0$ must be $i(\gamma^\nu \partial_\nu + \kappa_0)\Psi = 0$. On the other hand, an electrically neutral Majorana representation exists for (14), in which all the values of the γ matrix become purely imaginary numbers such that this matrix has the form of $(\gamma^\nu_{(M)} \partial_\nu + m)\Psi = 0$, which is identical to the Dirac equation for the above space-like KG equation. The reason why we have introduced the Clebsch dual field as the space-like extension of the electrically neutral electromagnetic wave field is because the Greenberg and Robinson theorem mentioned in in Section 2.1 requires such a field for quantum field interactions, so that the above arguments suggest that Majorana field must be such a quantum field.

The Majorana field is fermionic with a half-integer spin 1/2, so the same state cannot be occupied by two fields according to Pauli's exclusion principle. A possible configuration of a couple of Majorana fields corresponding to the Clebsch dual field that behaves like a boson with spin 1 can be identified with the help of Pauli–Lubanski vector W_μ describing the spin states of moving particles. W_μ has the form of $W_\mu = M_{\mu\nu}p^\nu$, where $M_{\mu\nu}$ and p^ν are the angular and linear momenta of the Majorana field, respectively. Note that the two fields $M_{\mu\nu}$ and $N_{\mu\nu}$ can share the same W_μ such that

$$M_{\mu\nu}p^\nu = N_{\mu\nu}q^\nu = W_\mu \tag{15}$$

when their linear momenta p^μ and q^μ are orthogonal, i.e., $p^\nu q_\nu = 0$. Two Majorana fields satisfying this orthogonality condition can be combined, as in the case of a Cooper pair in the superconducting phenomenon, to form a vector boson with spin 1, which can be identified as the quantized Clebsch dual field satisfying the orthogonality condition in (5).

Now, we are ready to consider the mechanism through which a DP emerges. As a mathematically simple situation, let us consider the case in which the space-like KG Equation (4) is perturbed by the interaction with a point source $\delta(x^0)\delta(r)$, where r denotes the radial coordinate of a spherical coordinate system. The essential causal aspects of this problem were already investigated by Aharonov et al. [31], who showed that the resulting time-dependent behavior of the solution can be expressed by the superposition of a superluminal (space-like) stable oscillatory mode and a time-like linearly unstable mode whose combined amplitude spreads with a speed slower than the light velocity. A time-like unstable mode of the solution to (4) expressed in a polar coordinate system with spherical symmetry has the form of $\lambda(x^0, r) = \exp(\pm k_0 x^0)R(r)$, where $R(r)$ satisfies

$$R'' + \frac{2}{r}R' - (\hat{\kappa}_r)^2 R = 0, \quad (\hat{\kappa}_r)^2 := (k_0)^2 - (\kappa_0)^2 > 0, \tag{16}$$

whose solution becomes the Yukawa potential: $R(r) = \exp(-\hat{\kappa}_r r)/r$, which rapidly falls off as r increases. The nonzero component of the *deformed* Clebsch dual bivector field ${}^dS_{ab}$ derived by the combined use of (16) and (7) is ${}^dS_{0r}$, namely, ${}^dS^{\dagger}_{0r} := k_0 R' \exp(k_0 x^0)$ and ${}^dS_{0r} := -k_0 R' \exp(-k_0 x^0)$, which are, in the classical interpretation, growing and damping solutions. However, quantum mechanically, these two can be interpreted as follows. The transmutation from a space-like mode to a pair of these two time-like modes through the interaction with a point source can be regarded as a pair creation of Majorana particles: one going forward in time and the other antiparticle going backward in time. This pair creation is possible because the Clebsch dual field consists of a pair of Majorana fields. Since these modes are non-propagating, they are superimposed to yield a non-propagating light field called a DP that can be regarded as a pair annihilation. The energy density of the DP generated by these processes is given by $-({}^dS^{\dagger}_{0r})({}^dS_{0r}) = (k_0 R')^2$. If we use a natural unit system, then κ_0 possessing the dimension of m^{-1} may be regarded as an elemental block of DP energy. In subsection 1.2, we have observed that the maximum size of a DP is approximately 50 nm. Since this size can naturally be assumed to correspond to the minimum energy of the DP, we have $\mathrm{Min}[\hat{\kappa}_r] \approx \kappa_0 \approx (50\,\mathrm{nm})^{-1}$ using (16).

4. Connection with Cosmology

Since the spatial dimension of our physical spacetime is three, the maximum number of momentum vectors satisfying the orthogonality condition (15) is also three, that is, $M_{\mu\nu}p^{\nu} = N_{\mu\nu}q^{\nu} = L_{\mu\nu}r^{\nu} = W_{\mu}$, which indicates the existence of a compound state of Majorana fermions with spin 3/2 denoted by $|M3\rangle_g$. Note that this state can play the role of "the ground state"of the Clebsch dual field in the sense that Clebsch dual fields as extended virtual photons can be excited from any of the three different configurations of the "Clebsch dual structure" (15) embedded in $|M3\rangle_g$. Electromagnetic interactions are ubiquitous phenomena such that incessant occurrence of excitation–deexcitation cycles between "the ground"and non-ground states makes the former a fully occupied state from the viewpoint of a macroscopic time scale. In such a situation, $|M3\rangle_g$ would exist not as an extremely ephemeral virtual state but as a stable unseen off-shell state.

In order to apply our new idea on the Clebsch dual field to cosmological problems, we first point out that the formulation of it derived for Minkowski space in Sections 2 and 3 is readily generalized to cover the case of a curved spacetime for which the partial derivative ∂_μ of a given field defined on the former must be replaced by the covariant derivative ∇_μ of the field defined on the latter. At the end of Section 2, we have shown the isomorphsm between the energy-momentum tensor of Clebsch dual field and Einstein's field equation by utilizing $\hat{R}_{\mu\nu\rho\sigma} = -S_{\mu\nu}S_{\rho\sigma}$. It is clear that a curved spacetime does not create any problem for defining the skew-symmetric simple bivector field $S_{\mu\nu}$ and hence $\hat{R}_{\mu\nu\rho\sigma} = -S_{\mu\nu}S_{\rho\sigma}$. One of the notable problems we have in the case of dealing with a curved spacetime is that differential operators do not commute in general. For a given vector field V_μ on Minkowski space, we have $\partial^2_{\nu\rho}V_\mu = \partial^2_{\rho\nu}V_\mu$. On a curved spacetime, however, we have $\nabla_{\nu\rho}V_\mu = \nabla_{\rho\nu}V_\mu + V_\sigma R^{\sigma}{}_{\mu\nu\rho}$ where $R^{\sigma}{}_{\mu\nu\rho}$ denotes Riemann curvature tensor, so that the order of differentiation matters. The sole exception for this non-commuting rule is the case where a vector field V_μ is replaced by a scalar field S, for which we have $\nabla_\nu S = \partial_\nu S$ and $\nabla_{\nu\rho}S = \partial^2_{\nu\rho}S - \Gamma^{\sigma}{}_{\nu\rho}\partial_\sigma S = \nabla_{\rho\nu}S$ because the affin connection $\Gamma^{\sigma}{}_{\nu\rho}$ is symmetric with respect to the subscripts ν and ρ. Notice again that the skew-symmetric Clebsch dual field $S_{\mu\nu}$ given in (7) is a bivector field represented in terms of the exterior product of a couple of gradient vector $L_\mu = \partial_\mu\lambda = \nabla_\mu\lambda$ and $C_\mu = \partial_\mu\phi = \nabla_\mu\phi$. Therefore, while $S_{\mu\nu}$ only contains the first derivatives of scalar fields ϕ and λ, the entire formulation of the Clebsch dual field covering, for instance, $\nabla_\nu \hat{T}^{\nu}_{\mu}$ involves the first and second derivatives of them, for the latter of which the order of differentiation does not matter. We mentioned already that the simple bivector property of $S_{\mu\nu}$ is a crucial element for deriving the first equation in (11). In reference [5], we show that, not only for (11) but also for the other parts of the Clebsch dual formulation, the simple bivector property of $S_{\mu\nu}$ and the commutativity of the second derivatives of scalar fields λ and ϕ are essential elements. By using those properties, we can prove $\nabla_\nu \hat{T}^{\nu}_{\mu} = 0$ since, as far as the mathematical manipulations

are concerned, those in a curved spacetime are essentially similar to those in Minkowsky space. Thus, we show that the isomorphism (9) can be extended to that in a curved spacetime.

Having stated this, we now move on to the well-known isotropic spacetime structure employed in cosmological arguments:

$$ds^2 = (cdt)^2 - (R(t))^2 \left[\frac{dr^2}{1 - \xi r^2} + r^2(d\theta^2 + sin^2\theta d\phi^2) \right], \tag{17}$$

where ξ denotes the curvature parameter taking one of the triadic values of (0, +1, −1) and the other notations are conventional. The coordinate system employed in (17) is a unique co-moving (co-moving with matter) one singled out by Weyl's hypothesis on the cosmological principle with which the energy-momentum tensor $T_\mu^{\ \nu}$ of the universe becomes identical in form to the following one of the hydrodynamics:

$$T_\mu^{\ \nu} = \begin{pmatrix} \rho c^2 & 0 & 0 & 0 \\ 0 & -p & 0 & 0 \\ 0 & 0 & -p & 0 \\ 0 & 0 & 0 & -p \end{pmatrix}. \tag{18}$$

In addition, corresponding to (18), the components of metric tensor $g_{\mu\nu}$ can be chosen in such that off-diagonal elements of Einstein tensor $G_\mu^{\ \nu}$ are also zeros. A caveat in using this coordinate system for our Clebsch dual field is that, due to its space-like property, the energy-momentum tensor $\hat{T}_\mu^{\ \nu}$ of the Clebsch dual field to be given by (23) cannot be diagonalized as in the case of (18) since the field resides outside the familiar time-like universe. In spite of that, the above coordinates system introduced by Weyl is a quite informative one from the viewpoint of cosmological observations, so that we think one of the meaningful approaches to estimate the impact of $\hat{T}_\mu^{\ \nu}$ on our time-like universe would be to focus solely on its diagonal components, especially the trace $\hat{T}_\nu^{\ \nu}$ as the sum of them whose justification will be given shortly, projected on the four-dimensional "screen"spanned by the set of basis vectors of the Weyl coordinates.

In what follows, we are going to derive the energy-momentum tensor ((23) or (27)) directly related to a compound state of Majorana fermions $|M3\rangle_g$ referred to at the beginning of this section. To avoid misunderstanding of the characters of this tensor, the following remark on fermionic fields is important to be made in advance: in quantum theory, the time change of a state is described by the dynamics acting on the (C^*-)algebra of observables. The non-commutativity inherent to quantum theory requires the notions of quantum "observables"and "states"of a given system to be distinguished more clearly than in the classical case. Even in the classical Einstein field equation, it is true that "observables"or "physical quantities"(represented typically by the energy-momentum) and "states"(represented by the curvature of spacetime) are seen to occupy different places a way that the former and the latter appear in the right and the left hand sides of the equation, respectively. In regard to fermionic fields, we can say that, though state changes of fermionic fields are visible, the physical quantities satisfying Fermi statistics with anti-commutation relations cannot be visible. In the conventional quantum field theory, such invisible entities as fermionic fields were introduced as an ad hoc fashion and it is not until the advent of Doplicher-Haag-Roberts theory [32] that their existence was justified through a process of reconstructing the all the members of a standard formulation of the theory involving fermionic entities, just starting from the formalism consisting of only observable data structure in the context of Galois theory.

According to these arguments, the physical quantities associated with ((23) or (27)) derived from the spacelike Majorana fermionic field explained in Section 3 should be invisible in nature. The reason is as follows: the Clebsch dual field can be manipulated mathematically as if it is a classical field, similarly to the case of Schroedinger's wave equation. As far as the invisible nature of a spacelike 4 momentum vector is concerned, however, we have to take the above-mentioned property of Fermi statistics into consideration. (The close relation between the quantization of spacelike 4 momentum

and Fermi statistics was pointed out first by Feinberg [33].) The key question in our analysis on dark energy is, therefore, whether we can find observable quantities or not. Since the relevant criterion for singling out such quantities may change depending on the choices of situations and aspects, however, we have no choice but to make a good guess. The fact which seems to work as "the guiding principle"is that, within the framework of relativistic quantum field theory, any observable without exception associated with the given internal symmetry is the invariant under the action of transformation group materializing the symmetry under consideration. By extending this knowledge on the internal symmetry to the external (spacetime) one, we assume that the trace $\hat{T}_{\nu}^{\ \nu}$ as the invariant of general coordinate transformation is observable since it is directly related to the actual observable quantity of the expansion rate of the universe through the isomorphism (9) which has been shown to be valid for a curved spacetime through the arguments in the second paragraph in this section.

To implement our analyses on dark energy, for the sake of simplicity, we take two-stage approach I and II. In the first stage I, we confine the scope of our argument to sub-Hubble scales in which the spacetime of the isotropic universe can be regarded as Minkowski space in an approximate sense. Then, in the second stage II, we smoothly extend our argument beyond those limits to cover the entire curved spacetime.

Stage I analyses

Firstly, to incorporate the fundamental quantum condition of $E = h\nu$ into the Clebsch dual field, let us consider the light-like case given by (8), where we have $\hat{T}_{\mu}^{\nu} = \rho C_{\mu} C^{\nu} = (\partial_{\sigma}\lambda\partial^{\sigma}\lambda)\partial_{\mu}\phi\partial^{\nu}\phi$. Using plane wave expressions of

$$\phi = \hat{\phi}_c \exp(ik_{\nu}x^{\nu}), k_{\nu}k^{\nu} = 0;\ \lambda = iN_{\lambda}\hat{\lambda}_0 \exp(il_{\nu}x^{\nu}), l_{\nu}l^{\nu} = -(\kappa_0)^2, \tag{19}$$

where i, $\hat{\lambda}_0$ and N_{λ} denote the imaginary unit, the quantized elemental amplitude and the number of such an elemental mode, we obtain

$$(C_{\mu})^* C^{\nu} = k_{\mu}k^{\nu}\hat{\phi}_c(\hat{\phi}_c)^*,\ \ \rho = (iN_{\lambda})^2(\kappa_0)^{-2}. \tag{20}$$

In deriving the second equation of (20), $\hat{\lambda}_0(\hat{\lambda}_0)^* = (\kappa_0)^{-4}$ has been used since the dimension of $\hat{\lambda}_0$ is length squared. Now, we introduce Cartesian coordinates x^1, x^2, and x^3 such that the k vector for ϕ is parallel to the x^1 direction and consider a rectangular parallelepiped V spanned by the length vector $(1/k_1, 1, 1)$. Using (20) and $k_0 = \nu_0/c$ where c denotes the light velocity, the volume integration of $\hat{T}_0^0/(iN_{\lambda})^2$ over V as the energy per quantum becomes

$$\frac{1}{(iN_{\lambda})^2}\int_V \hat{T}_0^0 dx^1 dx^2 dx^3 = (\kappa_0)^{-2}\epsilon[\hat{\phi}_c(\hat{\phi}_c)^*]\frac{\nu_0}{c} \ \ \rightarrow \ \ h = \frac{1}{c}(\kappa_0)^{-2}\epsilon[\hat{\phi}_c(\hat{\phi}_c)^*], \tag{21}$$

from which the condition corresponding to $E = h\nu$ is identified as the second equation in (21), where ϵ denotes a unit square meter. For the non-light-like case of $U^{\nu}(U_{\nu})^* < 0$, using (12), since we have $||\hat{T}_{\nu}^{\ \nu}|| = -S^{\mu\nu}(S_{\mu\nu})^* = 2(iN_{\lambda})^2[\hat{\phi}_c(\hat{\phi}_c)^*]$, $||\hat{T}_{\nu}^{\ \nu}||_1 := -[S^{\mu\nu}(S_{\mu\nu})^*]_1$ defined as that for $(N_{\lambda})^2 = 1$ becomes

$$||\hat{T}_{\nu}^{\ \nu}||_1 = -[S^{\mu\nu}(S_{\mu\nu})^*]_1 = -2[\hat{\phi}_c(\hat{\phi}_c)^*]. \tag{22}$$

Since the Clebsch dual wave field, as in the case of an electromagnetic wave, has a propagating direction, to have isotropic radiation, we need three fields, any pair of which is mutually orthogonal. Such three fields are given, for instance, by (S_{23}, S_{02}), (S_{31}, S_{03}) and (S_{12}, S_{01}). $\hat{T}_{\mu}^{\ \nu}(3)$ derived by the superposition of these fields with $S_{23} = S_{31} = S_{12} = \sigma$ and $S_{01} = S_{02} = S_{03} = \tau$ turns out to be

$$\hat{T}_{\mu}^{\ \nu}(3) = \begin{pmatrix} -3\sigma^2 & -\tau\sigma & -\tau\sigma & -\tau\sigma \\ \tau\sigma & 2\tau^2-\sigma^2 & 0 & 0 \\ \tau\sigma & 0 & 2\tau^2-\sigma^2 & 0 \\ \tau\sigma & 0 & 0 & 2\tau^2-\sigma^2, \end{pmatrix}, \tag{23}$$

which is the energy-momentum tensor of the anti dark energy (dark energy with negative energy density, that is, $\hat{T}_0^0(3) = -3\sigma^2 < 0$) we propose in this paper. As we will see shortly, the dark energy (with positive energy density) ${}^*\hat{T}_{\mu}^{\ \nu}(3)$ given by (27) *having exactly the same trace as that of the anti dark energy* (23) can be introduced accordingly. Here, a remark must be made to clear the following point concerning different types of dark energy. Although the cosmological term $\lambda g_{\mu\nu}$ with $\lambda > 0$ is well-known and presumably the simplest candidate model of the dark energy, the up-to-date notion of dark energy includes presently-unknown entities other than $\lambda g_{\mu\nu}$. The present model ${}^*\hat{T}_{\mu}^{\ \nu}(3)$ now we are considering belongs to the latter type.

Stage II analyses

The above analyses in I shows that $\hat{T}_{\nu}^{\ \nu}(3) = -6\sigma^2 + 6\tau^2 = -6[\hat{\phi}_c(\hat{\phi}_c)^*]$. As we already pointed out, the isomorphism between $\hat{T}_{\mu}^{\ \nu}$ and $G_{\mu}^{\ \nu}$ in (9) can be extended to the one in a curved space-time. Using this relation, we can say that the existence of $\hat{T}_{\nu}^{\ \nu}(3)$ induces a constant negative scalar curvature in the universe. The configuration of such a universe is described as a four-dimensional hyper pseudo-sphere with a certain "radius" $3/\Lambda$ embedded in a fifth dimensional Minkowski space. This universe is known as de Sitter space whose metric invariant ds^2 can be rewritten with polar coordinates (r, θ, ϕ) as

$$ds^2 = (cdt)^2 - (R_0)^2 \exp\left(2\sqrt{\frac{\Lambda}{3}}ct\right)\{dr^2 + r^2(d\theta^2 + \sin^2\theta)d\phi^2\}, \tag{24}$$

where R_0 denotes a constant initial radius of the universe. By comparing (24) with (17), we see that the curvatue parameter ξ of de Sitter space is zero, which shows that the analyses in the first stage I can be extended smoothly to the second stage II. Since de Sitter space is a unique solution of the Einstein field equation for the cosmological term of $\Lambda g_{\mu\nu}$, we see that the impact of $\hat{T}_{\mu}^{\ \nu}(3)$ can be observed in a form of cosmological constant.

To the best of authors' knowledge, the observational data available to us on our expanding universe is the cosmological constant λ_{obs} derived on the assumption that the dark energy may be modeled by the cosmological term $\lambda g_{\mu\nu}$. If the dark energy is modeled by $\lambda_{obs} g_{\mu\nu}$, then the Einstein field equation with the sign convention of $R_{\mu\nu} = R^{\sigma}_{\mu\nu\sigma}$ becomes the first equation in (25), and if it is modeled by ${}^*\hat{T}_{\mu}^{\ \nu}(3)$, then the Einstein field equation becomes the second one in (25):

$$R_{\mu}^{\ \nu} - \frac{R}{2}g_{\mu}^{\ \nu} + \lambda_{obs} g_{\mu}^{\ \nu} = -\frac{8\pi G}{c^4}T_{\mu}^{\ \nu}, \quad R_{\mu}^{\ \nu} - \frac{R}{2}g_{\mu}^{\ \nu} = -\frac{8\pi G}{c^4}(T_{\mu}^{\ \nu} + {}^*\hat{T}_{\mu}^{\ \nu}(3)), \tag{25}$$

which suggests that one of the meaningful observational validations of our dark energy candidate model ${}^*\hat{T}_{\mu}^{\ \nu}(3)$ would be to compare the traces of $\lambda_{obs} g_{\mu}^{\ \nu}$ and $(-8\pi G/c^4){}^*\hat{T}_{\mu}^{\ \nu}(3)$. Since the trace of ${}^*\hat{T}_{\mu}^{\ \nu}(3)$ is the same as that of $\hat{T}_{\mu}^{\ \nu}(3)$, we see that, using (22), the magnitude of $\hat{T}_{\nu}^{\ \nu}(3)$ corresponding to the above-mentioned isotropic radiation is evaluated as $-3 \times 2[\hat{\phi}_c(\hat{\phi}_c)^*]$, whose numerical value can be derived by the use of (21), and the experimentally determined value of κ_0. Using $(\kappa_0)^{-1} \approx 50$ nm, we get $\lambda_{DP} := (-8\pi G/c^4)\hat{T}_{\nu}^{\ \nu}(3)/g_{\nu}^{\ \nu} \approx 2.47 \times 10^{-53} m^{-2}$, which may be regarded as the "reduced cosmological constant"of ${}^*\hat{T}_{\mu}^{\ \nu}(3)$, while the value of λ_{obs} derived by Planck satellite observations [34] is $\lambda_{obs} \approx 3.7 \times 10^{-53} m^{-2}$. Thus, we can say that $|M3\rangle_g$ is a promising candidate for dark energy.

Note that the energy density $\hat{T}_0^{\ 0}(3)$ in (23) is negative. In order to figure out the meaning of $\hat{T}_0^{\ 0}(3)$, let us consider a simple case of the on-shell condition of a real-valued 4-momentum vector $p_\mu = (p_0, p_1, p_2, p_3)$. Without the loss of generality, we can choose a coordinate system in which p_2 and p_3 vanish, so that we have

$$p^{\nu}p_{\nu} = (p_0)^2 - (p_1)^2 = \Pi = const. \tag{26}$$

Clearly, $(-p_0, -p_1)$ satisfies (26) when (p_0, p_1) is a solution to it. Since energy and time are canonically conjugate variables, the time evolution of a given dynamical system with negative energy (Hamiltonian) can be reinterpreted as the backward time evolution of the counterpart system with positive energy. We often encounter such reinterpretations in Feynman diagrams to distinguish the anti-particle arising from a pair creation, so that, at the microscopic quantum level, the emergence of negative energy does not create any fundamental problem, as we already referred to the two-sided energy spectra of the Tomita–Takesaki extension of the thermal equilibrium. At the macroscopic classical level, however, there is no hint of the existence of anti-matter in abundance. To explain it, the idea of a twin universe as the cosmic version of a pair creation was proposed by Petit [35], though the issue remains unsettled yet. Whatever the reason may be, the weak energy condition (positivity of the energy) in the classical general theory of relativity related to the stability of a given dynamical system under consideration must be tied to the matter (with positive energy) dominated property of our universe.

The simple argument on (26) suggests that the classically unfavorable negative property of $\hat{T}_0^{\ 0}(3)$ can be circumvented as follows. In (26), if we formally replace p_0 by ip_1 and p_1 by ip_0, then we readily see that (26) remains the same. This procedure can be applied to transform (23) into the following trace invariant (27). Notice that, with the Hodge dual exchanging between (σ, τ) and $(i\tau, i\sigma)$ in (23), which corresponds qualitatively to the above exchange between (p_0, p_1) and (ip_1, ip_0) because electric and magnetic fields respectively bear temporal and spatial attributes from the Lorentz group theoretical viewpoint, $\hat{T}_{\mu}^{\ \nu}(3)$ turns into the following ${}^*\hat{T}_{\mu}^{\ \nu}(3)$

$${}^*\hat{T}_{\mu}^{\ \nu}(3) = \begin{pmatrix} 3\tau^2 & \tau\sigma & \tau\sigma & \tau\sigma \\ -\tau\sigma & -2\sigma^2 + \tau^2 & 0 & 0 \\ -\tau\sigma & 0 & -2\sigma^2 + \tau^2 & 0 \\ -\tau\sigma & 0 & 0 & -2\sigma^2 + \tau^2, \end{pmatrix}, \tag{27}$$

in which the transformed 4-momentum vector density in the first row (in comparison to that in (23)), which changes the sign while the trace of it remains exactly the same as that of $\hat{T}_{\mu}^{\ \nu}(3)$ in (23). The sign change for the spatial components in the first row occurs in exactly the same manner as the one in (26), though the sign change for the temporal component differs from it. This is because, as we already pointed out, electric and magnetic field respectively bear temporal and spatial attributes, so that the appearance of τ in (27) is a consistent change in this respect. Thus, the physical meaning of the dual existence of (23) and (27) is that the notion of matter-antimatter duality can be extended to the dark energy model based on the Clebsch dual field. Notice that the diagonal components of ${}^*\hat{T}_{\mu}^{\ \nu}(3)$ resemble the artificial partition of the diagonal components of λg_{μ}^{ν} into $\rho_{\lambda} = \lambda c^4/(8\pi G)$ and $p_{\lambda} = -\lambda c^4/(8\pi G)$ (*cf.* (18)) already employed as the hypothetical equation of state of dark energy in the conventional cosmology.

In considering the problem of dark matter from the viewpoint of conformal symmetry breaking mentioned at the beginning of Section 3, we cast a spotlight on the Bel–Robinson tensor [36] $B_{\alpha\beta\gamma\delta}$ satisfying $\nabla^{\alpha}B_{\alpha\beta\gamma\delta} = 0$, where ∇^{α} denotes the covariant derivative. We can readily show that

$$\frac{1}{2}B_{\mu\nu\sigma}^{\ \ \ \sigma} = W_{\mu\alpha\beta\gamma}W_{\nu}^{\ \alpha\beta\gamma} - \frac{1}{4}g_{\mu\nu}W^2, \quad W^2 := W_{\alpha\beta\gamma\delta}W^{\alpha\beta\gamma\delta}, \tag{28}$$

where $W_{\alpha\beta\gamma\delta}$ denotes the Weyl tensor. A lengthy but straightforward calculation [37] shows that $B_{\mu\nu\sigma}^{\ \ \ \sigma}$ vanishes identically, which indicates that

$$g_{\mu\nu} = \frac{4W_{\mu\alpha\beta\gamma}W_{\nu}^{\ \alpha\beta\gamma}}{W^2}, \quad \text{if} \ \ W^2 \neq 0. \tag{29}$$

Since the magnitude of W^2 in the well-known Schwarzschild outer solution of a given star decreases monotonously along radius direction, for discussions on cosmological phenomena for which mass distributions can be approximated as that of continuous medium, we would have no need to worry about the singular point of $W^2 = 0$. Notice that (29) shows an intriguing possibility that we can figure out the physical meaning of the cosmological term $\lambda g_{\mu\nu}$ which remains a unsettled issue ever since the time of Einstein, though it is tentatively used as a dark energy model. The unique property of (29) that should be distinguished from the one of usual $g_{\mu\nu}$ as a metric tensor is the fact that the former can be defined in the spacetime whose dimension is larger than or equal to 4 because the Weyl tensor does not exist in the lower dimension and that it is directly related to gravitational field. Such being the case, we introduce a new notation $\hat{g}_{\mu\nu}$ to represent the right-hand side of (29).

In our preceding arguments on dark energy, we have shown a possibility that dark energy may be explained by a new model different from the cosmological term $\lambda g_{\mu\nu}$. If that is the case, then $\lambda g_{\mu\nu}$ must represent another phenomenon. Note that the magnitude W^2 measures the deviation of spacetime from the conformally flat FRW metric for the isotropic universe. Thus, a field whose energy-momentum tensor $\tilde{T}_{\mu\nu}$ having the following form:

$$\tilde{T}_{\mu\nu} = -\lambda \hat{g}_{\mu\nu}, \quad \lambda > 0 \tag{30}$$

would behave like a field with an attractive nature of gravity, that is to say, that it must work as the seed of galaxy formations, which suggests us to look into a possibility that $-\lambda \hat{g}_{\mu\nu}$ is one of the candidates of the dark matter model. One of the intriguing properties of $-\lambda \hat{g}_{\mu\nu}$ is that its form remains the same irrespective of the magnitude of W^2. Considering its attractive nature of gravity, the initial quite small magnitude $(W_{init})^2$ which seems to be relating to the observed slight density variations in the early universe identified by COBE mission would grow monotonously. Thus, $(W_{init})^2$ is a parameter playing a similar role as R_0 in (24) and the existence of $-\lambda \hat{g}_{\mu\nu}$ may be regarded as a major dynamical cause for monotonously increasing W^2 field.

The important question in fixing the dark matter model $-\lambda \hat{g}_{\mu\nu}$ is the determination of λ. For this problem, we think that the isomorphism between conformally broken space-like electromagnetic field (Clebsch dual field) and gravitational one (9) must play a key role. At the end of Section 2, we show that $||\hat{T}_{\nu}^{\nu}|$ in (12) is an elemental contribution of the former to the scalar curvature of spacetime. As we have already shown, the magnitude of this elemental contribution corresponds in the converted unit of cosmological constant to $\lambda_{DP}/3$ where λ_{DP} is the reduced cosmological constant of our dark energy model defined in the 6th line from Equation (25). Since (9) is the isomorphism between Clebsch dual field and Ricci part of gravitational field, it would be natural to assume that λ in $-\lambda \hat{g}_{\mu\nu}$ as a conformally broken scale parameter associated with Weyl part is equal to $\lambda_{DP}/3$, which we call simultaneous conformal symmetry breaking of electromagnetic and gravitational fields. As a partial justification of this hypothesis, we point out that the consensus ranges of the estimated percentage of dark energy and matter are $(68\% - 76\%; mean = 72\%)$ and $(20\% - -28\%; mean = 24\%)$, so that the coefficient $1/3$ of $\lambda_{DP}/3$ is consistent with the mean values of these ranges. In the limit of $W^2 \to 0$, where $\hat{g}_{\mu\nu} \to g_{\mu\nu}^{(FRW)}$, $-\lambda_{DP}\hat{g}_{\mu\nu}/3$ asymptotically approaches to the anti-de Sitter space extensively studied in the Maldacena duality [38]. Thus, if $-\lambda_{DP}\hat{g}_{\mu\nu}/3$ actually exists, then we can say that the anti-de Sitter space existed in the early universe.

5. Methods: Formulation of the Clebsch Dual Field

The quantization of the electromagnetic field cannot be performed without gauge fixing of some sort, which suggests that $\partial_\nu A^\nu$ can be specified in a physically meaningful fashion. We next discuss that the Feynman gauge first introduced by Fermi in the Lagrangian density L_{GF}, containing a gauge fixing term $-(\partial_\nu A^\nu)^2/2$ whose variation with respect to A_μ is the second equation in (31),

$$L_{GF} := -\frac{1}{4}F_{\mu\nu}F^{\mu\nu} - \frac{1}{2}(\partial_\nu A^\nu)^2 \quad \to \quad [\partial_\nu F^{\nu\mu} + \partial^\mu(\partial_\nu A^\nu)]\delta A_\mu = 0, \tag{31}$$

which is exactly such a gauge specification. Combining (1) and (31) with the well-documented equation $\partial_\nu T_\mu^{\ \nu} = F_{\mu\nu} j^\nu$ on the divergence of the EM tensor $T_\mu^{\ \nu}$ given by (3), we obtain

$$\partial^\nu \partial_\nu A^\mu = 0, \quad \text{and} \quad \partial_\nu T_\mu^{\ \nu} = F_{\mu\nu}(\partial^\nu \phi), \ (\phi := \partial_\nu A^\nu), \tag{32}$$

of which the second equation shows that the EM conservation $\partial_\nu T_\mu^{\ \nu} = 0$ holds well, even in the case of $\partial^\nu \phi \neq 0$, as long as the vector $\partial^\nu \phi$ is perpendicular to $F_{\mu\nu}$. In addition, directly from the second equation in (31), using the antisymmetry of $F^{\mu\nu}$, we have

$$\partial^\nu \partial_\nu \phi = 0. \tag{33}$$

Using Nakanishi–Lautrup (NL) B-field formalism mentioned in Section 2.2, we can show that (33) is the gauge-fixing condition we want to obtain. NL formalism realizes manifestly-covariant quantization of electromagnetic field in which the Lorentz gauge condition ($\partial_\nu A^\nu = 0$) can be *generalized* to the covariant linear gauges of the form:

$$L_B = B \partial_\nu A^\nu + \frac{\alpha}{2} B^2, \tag{34}$$

where L_B, B and α respectively denote a gauge-fixing Lagrangian density to be added to the gauge-invariant Lagrangian density $-F_{\mu\nu}F^{\mu\nu}/4$, NL B-field to be defined below and a real parameter. The gauge-fixing condition and B-field are given by

$$\partial_\nu A^\nu + \alpha B = 0, \quad \partial^\nu \partial_\nu B = 0. \tag{35}$$

In particular, the gauge-fixing condition with $\alpha = 1$ is known as the Feynman gauge and we readily show that the total Lagrangian density L_{GF} with this gauge becomes equal to the first equation in (31). The second equation in (35) is called a subsidiary condition necessary to identify the physically meaningful sector in which quantized transverse modes reside. Quantum mechanically, B-field is shown to be a physical quantity in the sense that it is "non-ghost"field though it is invisible.

Notice that the subsidiary condition on B given in (35) is identical to (33) on ϕ defined in (32) and the Feynman gauge shows that $\phi = \partial_\nu A^\nu = -B$. Since the classical physicality of ϕ in the sense of $\partial_\nu T_\mu^{\ \nu} = 0$ is assured by the orthogonality condition of $F_{\mu\nu} \perp \partial^\nu \phi$, we are going to look into this condition further. Using (2), the first equation in (32) can be regarded as a partial differential equation on α^μ given the above result of (33) specifying χ, namely,

$$\partial^\nu \partial_\nu \alpha^\mu_{(h)} = 0, \quad \partial^\nu \partial_\nu \alpha^\mu_{(i)} + \partial^\nu \partial_\nu (\partial^\mu \chi) = 0, \tag{36}$$

where $\alpha^\mu_{(h)}$ and $\alpha^\mu_{(i)}$ denote homogeneous and inhomogeneous solutions, respectively. $\alpha^\mu_{(h)}$ obviously represents a transverse mode, and the second equation gives, in hydrodynamic terms, a balance between rotational and irrotational modes. The existence of such a balance is well documented in the hydrodynamic literature explaining the mathematical description of irrotational motion of a two-dimensional incompressible fluid. Due to the irrotationality of the motion, the velocity vector (v_1, v_2) is expressed in terms of the gradient of the vector potential $\hat{\phi}$, namely, $(v_1 = \partial_1 \hat{\phi}, v_2 = \partial_2 \hat{\phi})$; on the other hand, the incompressibility of the fluid makes its motion non-divergent such that (v_1, v_2) is alternatively expressed as $(v_1 = -\partial_2 \hat{\psi}, v_2 = \partial_1 \hat{\psi})$, where $\hat{\psi}$ denotes a streamfunction. Equating these two, we obtain $\partial_1 \hat{\phi} = -\partial_2 \hat{\psi}, \partial_2 \hat{\phi} = \partial_1 \hat{\psi}$, showing that $\hat{\phi}$ and $\hat{\psi}$ satisfy the Cauchy–Riemann relation in complex analysis. This example serves as a useful reference in proving that *a null vector current $\partial^\mu \phi$ propagating along the x^1 axis perpendicular to $F_{\mu\nu}$ can be reinterpreted as the current of the longitudinal (x^1-directed) electric field*, of which a detailed explanation is given in reference [21] and the existence of such longitudinally propagating electric field was actually reported by [39]. Thus, based on the above

arguments on ϕ and B, we can say that they are physically meaningful key quantities in formulating the Clebsch dual field.

The orthogonality condition $F_{\mu\nu}(\partial^\nu\phi) = 0$ derived by (32) is mathematically equivalent to the relativistic hydrodynamic equation of motion of a barotropic (isentropic) fluid [40]: $\omega_{\mu\nu}(wu^\nu) = 0$, where $\omega_{\mu\nu} := \partial_\mu(wu_\nu) - \partial_\nu(wu_\mu)$, u^ν and w are the vorticity tensor, 4-velocity, and proper enthalpy density of the fluid, respectively. This observation suggests that we look into the unknown form of 4-vector potential U_μ relating to a longitudinal virtual photon that may have space-like momentum by the method of Clebsch parametrisation [41]:

$$U_\mu = \lambda\partial_\mu\phi, \tag{37}$$

where the two scalars λ and ϕ become canonically conjugate variables in the parametrized Hamiltonian isentropic vortex dynamics. Now, let us determine the λ field by referring to the following structures of electromagnetic waves: (1) $\partial^\sigma\partial_\sigma F_{\mu\nu} = 0$ and (2) $F_{\mu\nu}$ is advected along a longitudinal null Poynting 4-vector. Corresponding to these structures, we introduce, with a constant κ_0 to be determined, a space-like KG equation $\partial^\nu\partial_\nu\lambda - (\kappa_0)^2\lambda = 0$ (the middle equation of (4)) with the directional constraint $C^\nu\partial_\nu L_\mu = 0$, where $C^\nu := \partial^\nu\phi$ and $L_\mu := \partial_\mu\lambda$. Multiplying this constraint by L^μ and C^μ yields

$$L^\mu(C^\nu\partial_\nu L_\mu) = 0 \rightarrow\ C^\nu\partial_\nu(L^\mu L_\mu) = 0; C^\mu(C^\nu\partial_\nu L_\mu) = 0\ \rightarrow\ C^\nu\partial_\nu(C^\mu L_\mu) = 0,$$

which shows that $\rho := L^\nu L_\nu$ and $C^\nu L_\nu$ are advected along C^μ. In particular, if C^μ and L_μ are perpendicular at the initial time, then they remain so after that. Thus, as an important constraint, we can introduce

$$C^\nu L_\nu = 0. \tag{38}$$

The main results of the Clebsch dual formulation can be summarized as follows by classifying this formulation into two categories: *i.e.*, [I] the light-like ($U^\nu(U_\nu)^* = 0$) case possessing "gauge symmetry (GS)"in the sense of (33) and [II] the space-like ($U^\nu(U_\nu)^* < 0$) case with broken GS.

Category I.

(1) The field strength $S_{\mu\nu} := \partial_\mu U_\nu - \partial_\nu U_\mu$ corresponding to $F_{\mu\nu}$ is given by a simple bivector with the important orthogonality condition that cannot be satisfied when L^μ is a time-like vector:

$$S_{\mu\nu} = L_\mu C_\nu - L_\nu C_\mu, \quad C^\nu L_\nu = 0. \tag{39}$$

(2) U_μ is a tangential vector along a null geodesic satisfying the following wave equation:

$$U^\nu\partial_\nu U_\mu = -S_{\mu\nu}U^\nu = 0, \iff \partial^\nu\partial_\nu U^\mu - (\kappa_0)^2 U^\mu = 0. \tag{40}$$

(3) The EM tensor corresponding to (3) with the opposite sign can be defined together with its conservation law. In references [5,20–22] referred to at the beginning of subsection 4, this sign change is not properly accounted for, which should be fixed as a typo. The sign change is necessary because we are dealing with the negative energy that can be clearly seen in the ρ field in (41),

$$\hat{T}^\nu_\mu = S_{\mu\sigma}S^{\nu\sigma} = \rho C_\mu C^\nu,\ \rho := L^\nu L_\nu;\ \ \partial_\nu\hat{T}^\nu_\mu = S_{\mu\sigma}\partial_\nu S^{\nu\sigma} = S_{\mu\sigma}(\kappa_0)^2 U^\sigma = 0. \tag{41}$$

The first equation in (41) clearly shows that the Clebsch wave field has the dual representation of a wave, $S_{\mu\sigma}S^{\nu\sigma}$, and longitudinally moving particles, $\rho C_\mu C^\nu$ with negative "density"ρ ($L^\nu(L_\nu)^* < 0$ because L^ν is a space-like vector), which corresponds to an unphysical longitudinal mode in QED. Equation (40) proves (6) in subsection 2.2. Thus, we have shown that *the Clebsch dual field given in (6) possessing space-like momentum characteristics carries a longitudinally propagating electric field satisfying*

"gauge invariant"condition (33), which implies that the quantization of the Clebsch dual field gives an alternative representation of a $U(1)$ gauge boson that emerges in the perturbative calculations in QED.

Category II.

(1) U_μ that is advected by U^μ along a geodesic is redefined.

$$U_\mu := \frac{1}{2}(\lambda C_\mu - \phi L_\mu), \implies U^\nu \partial_\nu U_\mu = -S_{\mu\nu}U^\nu + \frac{1}{2}\partial_\mu(U^\nu U_\nu) = 0, \tag{42}$$

$$\partial^\nu \partial_\nu \lambda - (\kappa_0)^2\lambda = 0, \ \ \partial^\nu \partial_\nu \phi - (\kappa_0)^2\phi = 0, \ \ C^\nu L_\nu = 0. \tag{43}$$

The form of $S_{\mu\nu}$ given in (39) remains unchanged by (42).

(2) The EM tensor satisfying the conservation law of $\partial_\nu \hat{T}^\nu_\mu = 0$ is redefined.

$$\hat{T}^\nu_\mu = \hat{S}_{\mu\sigma}{}^{\nu\sigma} - \frac{1}{2}\hat{S}_{\alpha\beta}{}^{\alpha\beta}\eta^\nu_\mu, \quad \hat{S}_{\alpha\beta\gamma\delta} := S_{\alpha\beta}S_{\gamma\delta}. \tag{44}$$

$\hat{S}_{\alpha\beta\gamma\delta}$ defined above has the same antisymmetric properties as the Riemann tensor $R_{\alpha\beta\gamma\delta}$ including the first Bianchi identity, $S_{\alpha[\beta\gamma\delta]} = 0$, which holds well since $S_{\mu\nu}$ is a bivector field given by (39). Thus, $\hat{T}^\nu_\mu$ given in (44) becomes isomorphic to Einstein tensor $G^\nu_\mu := R^\nu_\mu - Rg^\nu_\mu/2$, where the Ricci tensor $R_{\mu\nu}$ is defined as $R_{\mu\nu} := R^\sigma_{\mu\nu\sigma}$.

6. Conclusions

In this article, we have discussed the important role played by the space-like 4-momentum in electromagnetic field interactions and found that the space-like momentum field is embodied by the Majorana fermion, of which time-like modes are now attracting the attention of scientists in the field of solid-state physics [42]. The investigation of the Majorana field unexpectedly opened up a new dynamic channel through which we have identified the causes of the three enigmatic phenomena of DPs, dark energy, and dark matter. The former are generated by the pair annihilation of unstable time-like Majorana particles, while the two fields in the latter come into existence as the compound ground state $|M3\rangle_g$ of the Majorana field and the revised cosmological term $-\lambda_{DP}g_{\mu\nu}/3$ through the simultaneous conformal symmetry breaking in electromagnetic and gravitational fields.

Our interpretation on dark matter defined as $-\lambda_{DP}g_{\mu\nu}/3$ with (29) is consistent with the fact that it can provide the triggering mechanism of galaxy clustering formation since non-zero W^2 in (29) acts as the core stuff of such dynamical processes. If we regard such galaxy clustering formations as the time evolution of material subsystems in the universe, then we can say that the simultaneous existence of the dark matter and energy sustains such subsystems'evolutions, respectively, as the unseen driving forces of attraction and repulsion with different magnitude, both of which are external to the subsystems in the sense that they are not bound to the time-like sectors in the spacetime. Their remarkable abundance ratios in comparison to a negligible one of ordinary matter suggests an extended thermodynamical viewpoint in which the evolution of material subsystems in the universe can be compared to the "heat engines"working between a couple of "heat reservoirs"with higher and lower temperature, which correspond respectively to the dark matter with positive energy and the negative dark energy.

Author Contributions: H.S. contributed to the basic structure of this article as well as to the Clebsch dual representation applied to the discussions of dressed photons and cosmology. I.O. contributed to providing the knowledge on fundamental quantum field theory which gives the justification of introducing Clebsch dual representation to electromagnetic field interactions and also to the improvement of the basic structure of the article. M.O. contributed to the experimental achievements on dressed photon phenomena. H.O. contributed to the derivation of Equation (29), which suggests the physical meaning of the cosmological term. All authors have read and agreed to the published version of the manuscript.

Funding: This research received no external funding.

Acknowledgments: This research was partially supported in the form of collaboration with the Institute of Mathematics for Industry, Kyushu University. We thank the anonymous reviewer for his questions and comments, which helped us to improve the quality of this article.

Conflicts of Interest: The authors declare no conflict of interest.

References

1. Ohtsu, M.; Kobayashi, K. *Optical Near Fields*; Springer: Berlin, Germany 2004; pp. 11–51.
2. Ohtsu, M. *Dressed Photons*; Springer: Berlin, Germany, 2014; pp. 89–214.
3. Kawazoe, T.; Ohtsu, M.; Aso, S.; Sawado, Y.; Hosoda, Y.; Yoshizawa, K.; Akahane, K.; Yamamoto, N.; Naruse, M. Two-dimensional array of room-temperature nano-photonic logic gates using InAs quantum dots in mesa structures. *Appl. Phys. B* **2011**, *103*, 537–546. [CrossRef]
4. Ohtsu, M.; Kawazoe, T. Principles and practices of Si light emitting diodes using dressed photons. *Adv. Mater. Lett.* **2019**, *10*, 860–867. [CrossRef]
5. Ohtsu, M.; Ojima, I.; Sakuma, H. *Progress in Optics*; Visser, T., Ed.; Elsevier: Amsterdam, The Netherlands, 2019; Chapter 1, Volume 62, pp. 45–97.
6. Ohtsu, M. *Silicon Light-Emitting Diodes and Lasers*; Springer: Berlin, Germany, 2016; Chapter 8, pp. 121–138.
7. Kawazoe, T.; Kobayashi, K. Nonadiabatic photodissociation process using an optical near field. *J. Chem. Phys.* **2005**, *122*, 024715. [CrossRef] [PubMed]
8. Kawazoe, T.; Ohtsu, M. Adiabatic and nonadiabatic nanofabrication by localized optical near fields. *Proc. SPIE* **2004**, *5339*, 619–630.
9. Kawazoe, T.; Kobayashi, K.; Ohtsu, M. Near-field optical chemical vapor deposition using $Zn(acac)_2$ with a non-adiabatic photochemical process. *Appl. Phys. B* **2006**, *84*, 247–251. [CrossRef]
10. Ohtsu, M.; Kawazoe, T. Experimental Estimation of the Maximum Size of a Dressed Photon. 2018. Available online: http://offshell.rodrep.org/?p=98 (accessed on 16 February 2018).
11. Sangu, S.; Kobayashi, K.; Ohtsu, M. Optical near fields as photon-matter interacting systems. *J. Microsc.* **2001**, *202*, 279–285.
12. Yatsui, T.; Hirata, K.; Nomura, W.; Tabata, Y.; Ohtsu, M. Realization of an ultra-flat silica surface with angstrom-scale average roughness using nonadiabatic optical near-field etching. *Appl. Phys. B* **2008**, *93*, 55–57. [CrossRef]
13. Hirata, K. Realization of high-performance optical element by optical near-field etching. *Proc. SPIE* **2011**, *7921*, 79210M.
14. Teki, R.; Kadaksham, A.J.; Goodwin, F.; Yatsui, T.; Ohtsu, M. Dressed-photon nanopolishing for EUV mask substrate defect mitigation. In Proceedings of the Society of Photo-Optocal Instrumentation Engineers (SPIE) Advanced Lithography, San Jose, CA, USA, 24–28 February 2013; Paper 8679-14.
15. Yatsui, T.; Nomura, W.; Ohtsu, M. Realization of ultraflat plastic film using Dressed-Photon-Phonon-Assisted selective etching of nanoscale structures. *Adv. Opt. Technol.* **2015**, *2015*, 701802. [CrossRef]
16. Lehmann, H.; Symanzik, K.; Zimmerman, W. Zur Formulierung quantisierter Feldtheorien. *Nuovo Cim.* **1955**, *1*, 425. [CrossRef]
17. Jost, R. *The General Theory of Quantized Fields*; American Mathematical Society: Providence, RI, USA, 1963.
18. Dell'Antonio, G.F. Support of a field in p space. *J. Math. Phys.* **1961**, *2*, 759–766. [CrossRef]
19. Bers, A.; Fox, R.; Kuper, C.G.; Lipson, S.G. The impossibility of free tachyons. In *Relativity and Gravitation*; Kuper, C.G., Peres, A., Eds.; Gordon and Breach Science Publishers: New York, NY, USA, 1971.
20. Sakuma, H.; Ojima, I.; Ohtsu, M. Dressed photons in a new paradigm of off-shell quantum fields. *Progr. Quantum Electron.* **2017**, *55*, 74–87. [CrossRef]
21. Sakuma, H.; Ojima, I.; Ohtsu, M. Gauge symmetry breaking and emergence of Clebsch-dual electromagnetic field as a model of dressed photons. *Appl. Phys. A* **2017**, *123*, 750. [CrossRef]
22. Sakuma, H. Virtual Photon Model by Spatio-Temporal Vortex Dynamics. In *Progress in Nanophotonics*; Yatsui, T., Ed.; Springer: Cham, Switzerland, 2018; Volume 5, pp. 53–77.
23. Ojima, I. A unified scheme for generalized sectors based on selection criteria—order parameters of symmetries and of thermal situations and physical meanings of classifying categorical adjunctions. *Open Syst. Inf. Dyn.* **2003**, *10*, 235–279. [CrossRef]

24. Ojima, I. Micro-macro duality in quantum physics. In Proceedings of the International Conference on Stochastic Analysis: Classical and Quantum, Meijo University, Nagoya, Japan, 1–5 November 2004; World Scientific: Singapore, 2005; pp. 143–161.
25. Ojima, I. Micro-Macro duality and emergence of macroscopic levels. *Quantum Probab. White Noise Anal.* **2008**, *21*, 217–228.
26. Ojima, I. Nakanishi-Lautrup B-Field, Crossed Product & Duality. *RIMS Kokyuroku* **2006**, *1524*, 29–37.
27. Nakanishi, N.; Ojima, I. *Covariant Operator Formalism of Gauge Theories and Quantum Gravity*; World Scientific: Singapore, 1990.
28. Aharonov, Y.; Bohm, D. Significance of electromagnetic potentials in the quantum theory. *Phys. Rev.* **1959**, *115*, 485–491. [CrossRef]
29. Bratteli, O.; Robinson, D. *Operator Algebra and Statistical Mechanics*, 2nd ed.; Springer: Berlin, Germany, 1987; Volume 1.
30. Snyder, H.S. Quantized space-time. *Phys. Rev.* **1947**, *71*, 38. [CrossRef]
31. Aharonov, Y.; Komar, A.; Susskind, L. Superluminal behavior, causality, and instability. *Phys. Rev.* **1969**, *182*, 1400–1402. [CrossRef]
32. Doplicher, S.; Haag, R.; Roberts, J.E. Fields, observables and gauge transformations I & II. *Comm. Math. Phys.* **1969**, *13*, 1–23.
33. Feinberg, G. Possibility of Faster-Than-Light Particles. *Phys. Rev.* **1967**, *159*, 1089–1105. [CrossRef]
34. Liu, H. Available online: https://www.quora.com/What-is-the-best-estimate-of-the-cosmological-constant (accessed on 15 April 2020).
35. Petit, J.P. Twin Universes Cosmology. *Astrophys. Space Sci.* **1995**, *226*, 273–307. [CrossRef]
36. Jezierski, J.; Lukasik, M. Conformal Yano-Killing tensor for the Kerr metric and conserved quantities. *arXiv* **2005**, arXiv:gr-qc/0510058.
37. Sakuma, H.; Ochiai, H. Note on the Physical Meaning of the Cosmological Term. OffShell: 1909O.001.v2. 2019. Available online: http://offshell.rodrep.org/?p=249 (accessed on 15 April 2020).
38. Maldacena, J. The large N limit of superconformal field theories and supergravity. *Adv. Theor. Math. Phys.* **1998**, *2*, 231–252. [CrossRef]
39. Cicchitelli, L.; Hora, H.; Postle, R. Longitudinal field components for laser beams in vacuum. *Phys. Rev. A* **1990**, *41*, 3727–3732. [CrossRef] [PubMed]
40. Landau, L.D.; Lifshitz, E.M. Fluid Mechanics. In *Course of Theoretical Physics*, 2nd ed.; Elsevier: Oxford, UK, 1987; Volume 6.
41. Lamb, S.H. *Hydrodynamics*, 6th ed.; Cambridge University Press: Cambridge, UK, 1930.
42. Kasahara, K.; Ohnishi, T.; Mizukami, Y.; Tanaka, O.; Sixiao, M.; Sugii, K.; Kurita, N.; Tanaka, H.; Nasu, J.; Motome, Y.; et al. Majorana quantization and half-integer thermal quantum Hall effect in a Kitaev spin liquid. *Nature* **2018**, *559*, 227–231. [CrossRef]

[II] PRESENTATIONS

IN INTERNATIONAL CONFERENCES

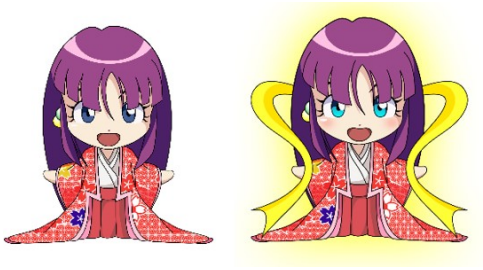

[III] REVIEW PAPERS

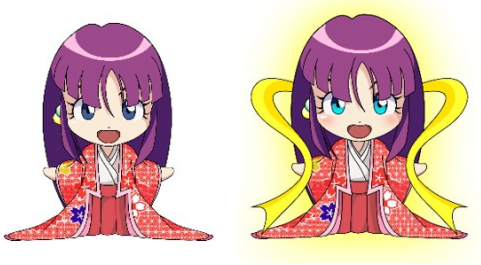

Opto-Electronic Advances

OE Historical

2020, Vol. 3, No. 3

DOI: 10.29026/oea.2020.190046

History, current developments, and future directions of near-field optical science

Motoichi Ohtsu*

This paper reviews the science of the optical near-field (ONF), which is created and localized in a nanometer-sized material (NM) or on its surface. It is pointed out that work on near-field optics was started in order to break through the diffraction limit in optical microscopy and had already come to an end without giving answers to the essential questions on the origin of the near-field optical interaction. However, recent studies have reincarnated these studies and identified the ONF as an off-shell quantum field. Based on this identification, a novel science called off-shell science has started on the basis that the dispersion relation between energy and momentum is invalid for the ONF. This quantum field is called the dressed photon because it is created as a result of the interaction between photons and electrons (or excitons) in a NM and, thus, it accompanies the energies of electrons or excitons. In reviewing current developments, this paper presents fifteen novel phenomena that are contrary to the common views in conventional optical science. Novel technologies developed by applying these phenomena are also reviewed. These include: nanometer-sized optical devices, nano-fabrication technology, and energy conversion technology. High-power Si light emitting diodes, Si lasers, and SiC polarization rotators are reviewed as examples of electrical to optical energy conversion. For future directions, this paper also reviews novel theoretical studies that have commenced recently by relying on physical and mathematical bases.

Keywords: dressed photon; off-shell science; interaction; uncertainty principle; silicon laser

Ohtsu M. History, current developments, and future directions of near-field optical science. *Opto-Electron Adv* **3**, 190046 (2020).

Introduction

The relatively new optical science of dressed photons (DPs) has seen rapid progress recently. The DP is a quantum field created in a complex system composed of photons and electrons (or excitons) in a nanometer-sized material. The fruits of this science have been applied to develop generic technologies (for example, nanometer-sized optical devices, information processing systems using these devices, nano-fabrication technology, and energy conversion technology) to realize disruptive innovations. Furthermore, studies on off-shell science have commenced. Off-shell science is a novel optical science including studies on the DP. The origin of this science can be found in near-field optics, which was actively investigated in the 1980s and 1990s after a long period of incubation since the 1920s. Studies on near-field optics started with the aim of achieving disruptive innovations in optical science, especially in optical microscopy. Extensive studies were carried out in the 1980s and 1990s, and they have mostly already come to an end. However, basic studies exploring the nature of the optical near field (ONF) were steadily continued by a small number of scientists, and near-field optics was reincarnated as a novel science of the DP. This science involves the study of light-matter interactions in a nanometer-sized space and explores novel applications that are contrary to those in conventional optical science and technology.

The author of this paper (M.O.) has been engaged in work on near-field optics for over three decades, spurred by a simple and intuitive desire to miniaturize the dimensions of light[1,2]. He pioneered DP science based on the long-term accumulation of his studies. Since the circumstances at the end and subsequent reincarnation of near-field optics mentioned above may not be widely known, especially by the young scientists, this paper

Research Origin for Dressed Photon, 3-13-19 Moriya-cho, Kanagawa-ku, Yokohama, Kanagawa 221-0022, Japan.
*Correspondence: M Ohtsu, E-mail: ohtsu@nanophotonics.t.u-tokyo.ac.jp
Received: 23 December 2019; Accepted: 30 January 2020; Published: 20 March 2020

starts by reviewing the history of near-field optics. Next, current developments in studies on the DP are reviewed. Finally, possible directions for the future are suggested.

History

To start a review on the history of near-field optics, first, the principles of creating and detecting the ONF should be explained: Scattered light is created when a nanometer-sized material (NM1) is illuminated by light. It should be noted that another form of electromagnetic field is also created in NM1 or on its surface. This field is called the ONF. The ONF is localized on NM1, and its spatial extent (size) is equivalent to the size of NM1. The ONF cannot be detected by a conventional photodetector installed far from NM1 because it does not propagate to the far field. To detect it, a second nanometer-sized material (NM2) is inserted into the ONF. The ONF is disturbed by NM2 and is converted to scattered light that propagates to the far field, and is thus detected by a photodetector.

Since the size of the ONF is equivalent to the size of NM1, it is expected that one can use the ONF to break through the diffraction limit which determines the spatial resolution in optical microscopy. In such a system, the ONF on NM1 works as a light source for acquiring an optical microscope image of NM2. Based on this expectation, research on near-field optics was started with the aim of realizing this breakthrough, and a great deal of effort was made to create an ONF whose size Δx is much smaller than the wavelength λ of light ($\Delta x<<\lambda$).

Since conventional optical theories were used in the early studies on near-field optics, the momentum p of the electromagnetic field has been treated as a definite quantity even though it is accompanied by a small uncertainty Δp due to quantum fluctuations. However, it should be pointed out that Heisenberg's uncertainty principle $\Delta p{\cdot}\Delta x \geq h/2\pi$ (where h is Planck's constant) indicates a large uncertainty Δp ($\Delta p>>p$) because of the relation $\Delta x<<\lambda$ above.

Modern studies are treating the ONF as a quantum field with a large energy uncertainty ΔE as well as a large Δp. In particular, by examining the light-matter interactions in nanometer-sized spaces, a variety of novel phenomena that are contrary to those in conventional optical phenomena have been discovered. That is to say, near-field optics was reincarnated as a novel optical science, and the ONF was renamed the DP. Taking note of this reincarnation, the history of near-field optics is reviewed in the following.

It has been recognized that the classical period of near-field optics started in the 1920s to 1950s, with proposals that it be applied to high-resolution optical microscopy to achieve resolutions beyond the diffraction limit[3–5]. Diffraction and radiation of the electromagnetic field from a small aperture were analyzed based on classical electromagnetic field theory[6,7]. Instead of using NM1 mentioned above, a small aperture was used for experimental demonstrations in the microwave frequency region[8].

In the 1980s and 1990s, experimental demonstrations in the optical frequency region were finally made by several scientists around the world, including the author of this paper (M.O.). These include a method of acquiring an optical microscope image of sub-wavelength sized materials by scanning an aperture or a probe. The equipment assembled for this imaging was named an ONF microscope, a scanning near-field optical microscope, or a near-field scanning optical microscope[9]. It was used for acquiring high-resolution images beyond the diffraction limit[10–13]. In the early stages of these studies, since the performance of the aperture or probe was not sufficiently high, it was not straightforward to acquire sufficiently high-resolution images. However, the advent of high-quality fiber probes enabled high-resolution imaging and quantitative analysis of the acquired images[14]. High-precision technology for fabricating and using high-quality fiber probes propelled the development of ONF microscopy, allowing it to join the family of scanning tunneling microscopy (STM)[15–20]. In parallel with these experimental studies, the ONF microscopes mentioned above were used to acquire images of chemical and biological specimens[21–23] and to analyze the optical properties of materials[24,25]. These microscopes are now commercially available[26]. Evaluation of the spatial resolution of such microscopes[27], spectral analysis of the ONF[28], and a proposal for a self-consistent theory including many body effects[29] have also been made.

For promoting studies on near-field optics, a compact international workshop was held in 1992[9]. Theoretical pictures of the ONF were drawn in this workshop based on the conventional optical method using the dispersion relation between the momentum and energy of light. Based on future outlooks for near-field optics in a panel discussion at this workshop chaired by the author (M.O.), an international near-field optics conference was organized, which is periodically held even now. To promote studies also in the Asia-Pacific region, the author (M.O.)

organized the Asia-Pacific Near-field Optics Workshop in 1996[30]. After this workshop, the Asia-Pacific Near-field Optics Conference was organized and is still periodically held.

In the studies above, since the ONF and relevant phenomena have been discussed in the framework of conventional wave-optics, and the electromagnetic origin of the ONF, and especially the origin of the light-matter interactions in nanometer-sized space, have remained unrevealed. However, a salvation was that quantum theoretical studies were started as a first step in revealing the nature of these interactions[31,32].

Although near-field optics had succeeded in breaking through the diffraction limit by the 1990s, a technical problem was that the data acquisition time was too long because the fiber probe had to be slowly scanned under precise feedback servo-control. Furthermore, since other members of the STM family (such as atomic force microscopes and scanning electron tunneling microscopes) had already realized spatial resolutions as high as or higher than that of ONF microscopes, it was not straightforward to make the prominent performance of ONF microscopes appealing to nonprofessional users. A more essential problem was that the image-acquiring process in an ONF microscope disturbed the electron energies in the specimen. This is because the image is acquired by using the near-field optical interaction between the tip of the fiber probe and the specimen. In other words, NM1 (the tip of the fiber probe) and NM2 (the specimen) are not independent of each other but are combined via the near-field optical interaction. Thus, even though a high spatial resolution beyond the diffraction limit was realized, the problem was that the profile of the acquired image did not have a direct correlation with that of a conventional optical microscopic image. On the whole, the classical studies of the ONF in the 1980s and 1990s did not give any clear answers to the essential questions, "What is the origin of the near-field optical interaction?" and "What kind of optical scientific revolution could near-field optics have made?" By recognizing that these questions had been neglected, the application of the ONF to microscopy, i.e., the study of near-field optics in the classical period, effectively came to an end.

However, even after this end, basic studies on the concepts and principles of the ONF were steadily continued by a small number of scientists. In relation to these studies, experiments on controlling atomic motion with high spatial resolution were carried out in a high vacuum[33]. Thanks to these continuous studies, a modern period of studies has started via transient studies named nano-optics or nanophotonics[34,35]. As a result, novel optical science and technology, based on the DP, have emerged as the reincarnation of classical near-field optics. These will be reviewed in the next section.

Current developments

From the current studies of the DP as the reincarnation of classical near-field optics, novel phenomena that are contrary to those accepted in conventional optical science have been found. This section presents these phenomena and their applications to novel technologies.

A name change: optical near field to dressed photon

In order to review the current developments in studies on the DP, five common views that have been accepted for a long time in conventional optical science are listed here: [a] Light is a propagating wave that fills a space. Its spatial extent (size) is much larger than its wavelength. [b] Light cannot be used for imaging and fabrication of sub-wavelength sized materials. Furthermore, it cannot be used for assembling and operating sub-wavelength sized optical devices. [c] For optical excitation of an electron, the photon energy must be equal to or higher than the energy difference between the relevant two electronic energy levels. [d] An electron cannot be optically excited if the transition between the two electronic energy levels is electric-dipole forbidden. [e] Crystalline silicon has a very low light emission efficiency, and thus, it is unsuitable for use as an active medium for light emitting devices.

The origin of these common views is attributed to the dispersion relation of the photon, which definitely fixes the relation between energy E and momentum p. In the case where light propagates in a vacuum, the dispersion relation is linear ($E=cp$, where c is the speed of light). By noting that momentum is a three-dimensional vector, this relation is geometrically represented by a circular cone. In the case of propagation in a material, this relation is geometrically represented by a paraboloid. This circular cone and paraboloid have been called the mass-shell, and thus, propagating light is considered to be an electromagnetic field in the on-shell state ("on-shell field" for short) because it is on the mass-shell. Even though the quantum fluctuations of the light have to be taken into account, conventional optical science has treated light in the on-shell state. Thus, this science can be called on-shell science. The common views [a]–[e] above are for light in

the on-shell state, and they have become accepted in on-shell science.

Contrary to propagating light in the on-shell state described above, the ONF is in the off-shell state, which deviates from the circular cone and the paraboloid above. This is because its sub-wavelength size Δx ($<<\lambda$), being contrary to the common view [a] above, produces a large momentum uncertainty Δp ($\Delta p>>p$) due to the Heisenberg's uncertainty principle $\Delta p\cdot\Delta x\geq h/2\pi$.

Since p and E are mutually dependent, the electromagnetic field in the off-shell state ("off-shell field" for short) also has a large uncertainty ΔE ($>>E$) in the energy. Thus, Heisenberg's uncertainty principle ($\Delta E\cdot\Delta t\geq h/2\pi$) also gives $\Delta t\leq h/2\pi E$. This indicates the short duration of the field, which corresponds to the nature of a virtual photon. Due to the two large uncertainties (Δp and ΔE), the science of the ONF belongs to the category of off-shell science[36]. It should be noted that the natures of on-shell and off-shell fields are contrary to each other. The off-shell field is created neither in a vacuum nor in a super-wavelength sized macroscopic material. Instead, this field exhibits the following phenomenon: [**Phenomenon 1**] *The off-shell field is created and localized on a sub-wavelength material.*

Since this field is created as a result of the interactions between photons and electrons (or excitons) in a NM, it is the electromagnetic field that accompanies the electronic or excitonic energy. Thus, this field has been named the DP[36]. In other words, the DP is the quantum field created in a complex system composed of photons and electrons (or excitons) in a NM. It has a sub-wavelength size and short duration. By using the DP, novel phenomena (including Phenomenon 1 above) that are contrary not only to the common view [a] but also to common views [b]–[e] have been found. Disruptive innovations in application technologies have been realized by applying these phenomena; and these technologies are presented in this section.

Theoretical studies have been carried out to draw the following two physical pictures of the DP:

1) Creation and annihilation of the DP

Creation and annihilation operators are required to describe the energy exchange during light-matter interactions. In the case of the DP, however, the problem was that the DP has a sub-wavelength size. This meant that one could not define a virtual cavity, and thus, could not define the mode of the field for deriving its Hamiltonian. As an urgent solution to this problem, the conventional theories of quantum optics were modified and applied to express photons of sub-wavelength size as a superposition of an infinite number of modes that interacted with the excitons of infinite energy levels in the NM[36]. As a result, creation and annihilation operators of the DP were derived, which were expressed by the sum of the operators of the photon of an infinite number of electromagnetic modes and those of the exciton of an infinite number of energy levels. This means that the photon "dressed" the exciton energy, and thus, this quantum field was named the DP[36]. It should be noted that this summation and dressing results in a broadband spectrum of the created DP even if a narrow-spectrum single-mode photon is incident on the NM.

As an example of further dressing of the material energy, the coupling between the DP and phonon has been found: After a DP is created on an atom in a crystal under light illumination, it hops to the adjacent atom and excites a crystal-lattice vibration, creating phonons. The DP couples with these phonons and accompanies their energies. The creation and annihilation operators of this coupled state were expressed as the product of the DP operators above and the displacement operator of multi-mode phonons[37], which indicated that the DP couples with the multi-mode coherent phonons.

2) Spatial localization of the DP

In order to detect the DP that is created and localized on NM1, the DP must be converted to propagating scattered light. This can be performed by inserting NM2 into the DP field. Propagating scattered light is created by this insertion, and it reaches a photodetector in the far-field where it is detected. Although NM1 and NM2 may be considered as a light source and a detector in this process, one should note the following two phenomena. The first one is [**Phenomenon 2**] *The DP energy transfers back and forth between the two NMs.* Due to this transfer, the light source and detector above are not independent of each other but are coupled in the nanometer-sized space, and thus, they cannot be distinguished as individual elements. The second one is [**Phenomenon 3**] *The DP field is conspicuously disturbed and demolished by inserting NM2 for detection.*

By noting these two phenomena, spatial localization of the DP has been studied for a system composed of two NMs between which the DP energy is transferred[31,38]. This study assumed that a nanometer-sized subsystem (composed of two NMs and the DP) was buried in a macroscopic subsystem (composed of a macroscopic host

material, incident light, and scattered light). Since the light-matter interaction in the nanometer-sized subsystem is the main subject of the study, the effects originating from the surrounding macroscopic subsystem were renormalized by the projection operator method.

By assuming also that the exciton-polariton in the macroscopic subsystem follows a paraboloidal dispersion relation, the magnitude of the effective interaction energy between the two NMs, mediated by the localized DP, was derived. It was represented by a Yukawa function whose spatial extent corresponded to the size of the NM. This indicates that the size of the DP corresponded to that of the NM. Although this spatial localization feature has been empirically known from experimental studies on the ONF, it was successfully formulated by the renormalization above. Furthermore, the following phenomenon was also formulated[38]: [**Phenomenon 4**] *The efficiency of the DP energy transfer between two NMs is highest when the sizes of the NMs are equal.* This phenomenon was named size-dependent resonance, and is nothing more than the momentum-conservation law for the DP energy transfer.

Although the long-wavelength approximation has been popularly used in conventional optical scientific studies on light-matter interactions, they are invalid in the case of the DP because its spatial extent, derived above, is much shorter than the wavelength of light. Due to this invalidity, a phenomenon that is contrary to the common view [d] was found: [**Phenomenon 5**] *An electric-dipole forbidden transition is allowed in off-shell science.*

The two physical pictures above have been actively used to propel experimental studies on the DP by using semiconductor NMs, organic NMs, and gaseous molecules. The light–matter interactions involving these specimens were analyzed by considering the discrete energy levels of the electrons or the excitons in the materials. By applying the results of these studies, novel technologies have been developed to bring about disruptive innovations.

In comparison with the studies above, extensive studies have been carried out using metallic NMs or films, resulting in the realization of a novel technology named plasmonics, which uses the interaction between light and the plasmonic oscillation of free electrons in a metal[39]. This technology employs light-scattering phenomena that occur by controlling the dispersion relation of the polariton-plasmon. Since the collective motion of the electrons in metals is involved in this phenomenon, optical energy is converted promptly to plasma oscillation energy. Furthermore, since the phase-relaxation time of the electrons is very short, the unique properties of light, such as its quantum properties, are promptly lost in the metal. Therefore, to analyze the plasmonic phenomena, it is sufficient to use conventional wave-optical quantities, such as refractive index, wave-number, guiding mode, and the dispersion relation. In other words, these analyses are still based on wave optics, i.e., on-shell science.

Application to novel technologies

Even though the theoretical studies carried out so far were for the purpose of finding an urgent solution to the problems noted above, they have ingeniously contributed to the realization of innovative generic technologies, including novel nanometer-sized optical devices, nano-fabrication technology, and energy-conversion technology. Among them, this section reviews a few examples and presents novel phenomena that originate from the intrinsic nature of the DP and are contrary to the common views [a]–[e].

Nanometer-sized optical devices and their applications

This section reviews novel nanometer-sized optical functional devices, named DP devices, developed by using semiconductor NMs. They have enabled the transmission and readout of optical signals by DP energy transfer and subsequent dissipation. The operation of the DP devices was analyzed by using a quantum mechanical master equation based on a density matrix formulation[40]. Practical NOT logic gate and AND logic gate devices that operated at room temperature have been fabricated by using InAs NMs[41]. One advantage of these devices was that their extremely small sizes (20–50 nm side length in the case of the logic gate devices using InAs NMs) were far beyond the diffraction limit, contrary to the common view [b]. Other advantages were their superior performance levels and unique functionalities, such as single-photon operation[42], extremely low energy consumption[43], and autonomous energy transfer[44]. These advantages originated from the unique operating principles of DP devices achieved by exploiting Phenomena 4 and 5. Furthermore, a phenomenon inherent to off-shell science was used for the device operation: [**Phenomenon 6**] *The DP energy transfers among NMs autonomously.*

Novel information processing systems have been proposed by using DP devices[45]. The first example is a non-Von Neumann computing system utilizing DP energy transfer. The ability to solve a decision making problem[46] and an intractable computational problem[47] has

been demonstrated. The second example is an information security system that uses Phenomenon 4. This system has realized a lock-and-key[48]. Furthermore, a hierarchical hologram[49] has been developed using the following phenomenon that originates from the size-dependent resonance (Phenomenon 4): [**Phenomenon 7**] *The DP energy transfer exhibits hierarchical features.*

Nano-fabrication technology

This section starts by reviewing an example of nano-fabrication technology that uses a fiber probe or an aperture. The specific natures of the DP relevant to this technology, and that are contrary to the common view [b], are also demonstrated. Next, a more practical technology is reviewed, in which neither the fiber probe nor aperture is required.

1) Technology using a fiber probe or an aperture

This part reviews photochemical vapor deposition (PCVD) based on a DP–molecule interaction, as an example in which a fiber probe is used. It involves molecular dissociation by the DP and subsequent deposition of the dissociated atoms on a substrate.

$Zn(C_2H_5)_2$ ("DEZn" for short) was adopted as a specimen molecule. A DP was created on the tip of the fiber probe by irradiating the end of the fiber probe with light. Gaseous DEZn molecules, filled in a vacuum chamber, dissociated when these molecules jumped into the DP field. Here, the tip of the fiber probe and the molecule correspond to NM1 and NM2, respectively. The dissociated Zn atom subsequently landed on the substrate. After a short migration on the substrate, the Zn atom was adsorbed on the substrate. By repeating these dissociation and deposition processes, the number of adsorbed Zn atoms increased, resulting in the deposition of Zn atoms and the formation of a nanometer-sized metallic Zn-NM on the substrate.

For comparison, in the case of dissociating the DEZn molecules by using conventional propagating light, the wavelength was required to be shorter than 270 nm (photon energy 4.59 eV) for exciting an electron in the DEZn molecule (refer to the common view [c]). By noting this requirement, the following ingenious contrivances (i)-(iii) were employed in order to confirm that the DEZn molecules were dissociated only by the DP in the PCVD above.

(i) The wavelength of the propagating light for creating the DP was set longer than 270 nm, contrary to the common view [c]. As a result, it was expected that the DEZn molecules would not be dissociated even if they were irradiated with the propagating light that leaked out from the tip of the fiber probe into the vacuum. Instead, it was expected that the DEZn molecules would be dissociated only by the DP on the tip due to the following phenomenon: [**Phenomenon 8**] *The photon energy hv can be lower than the excitation energy of the electron* $E_{ex}-E_g$, *where* E_{ex} *and* E_g *are the energies of the excited and ground states of the electron, respectively.* That is, since the created DP is the quantum field accompanying the energies of the excitons ($E_{exciton}$) and phonons (E_{phonon}) at the tip of the fiber probe, its energy is expressed as $h\nu_{DP}=h\nu+E_{exciton}+E_{phonon}$. Thus, even though $h\nu<E_{ex}-E_g$, the DP energy $h\nu_{DP}$ can be larger than $E_{ex}-E_g$ ($h\nu_{DP}\geq E_{ex}-E_g$), which enables the dissociation of DEZn molecules[50].

(ii) In order to insure that the contribution of the propagating light was excluded (refer to (i)), an unreliable fiber probe was used to intentionally cause the propagating light to leak out from the taper and tip of the fiber probe into the vacuum. That is, the fiber probe used here was fabricated by heating and mechanically pulling the fiber to form a sharp tip. This was a very primitive method in comparison with the high-precision and highly reproducible selective etching method[14,16]. Thus, high-precision control of the size, cone angle, and throughput were not expected. In addition, the probe was not coated with a metallic film, allowing the propagating light to leak out.

(iii) For further insurance, the DEZn molecules were replaced by zinc-bis(acetylacetonate) ("$Zn(acac)_2$" for short) molecules[51]. $Zn(acac)_2$ is a well-known optically inactive molecule that has never been shown to be dissociated by propagating light. However, it was expected, from Phenomenon 5, that it could be dissociated by the DP.

Figures 1(a) and 1(b) show images of a Zn-NM formed on a sapphire substrate by dissociating DEZn molecules; these images were acquired by using a shear-force microscope[50]. The wavelengths of the propagating light for creating the DP were as long as 488 and 684 nm, respectively, which indicates that the contribution from the propagating light was excluded due to contrivances (i) and (ii) above. Figure 1(c) shows an image of a three-dimensional Zn-NM formed on a sapphire substrate, where DEZn molecules were replaced by $Zn(acac)_2$ molecules based on contrivances (ii) and (iii)[51]. The wavelength of the propagating light for creating the DP was 457 nm. Figure 1

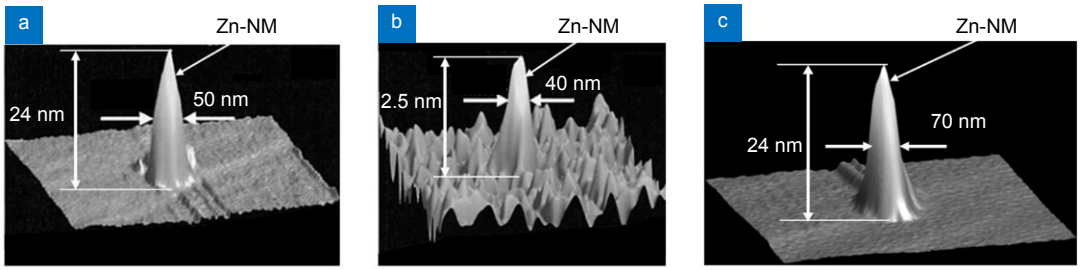

Fig. 1 | Shear-force microscopic images of Zn-NMs formed on a sapphire substrate. Dissociated molecules are DEZn ((**a**) and (**b**)) and $Zn(acac)_2$ (**c**). The wavelengths of the propagating light for creating the DP were 488 nm (a), 684 nm (b), and 457 nm (c).

demonstrates that the presented PCVD using the DP is contrary to the common views [b]–[d].

It should be pointed out that the maximum size $a_{DP,Max}$ of the DP was estimated from the experimental results of the PCVD above[52]. For this estimation, Fig. 2 was acquired and shows the dependence of the rate R of depositing Zn atoms on the full-width at the half maximum (FWHM) of the formed Zn-NM. Here, the value of the FWHM increased with increasing deposition time. Closed circles and squares represent the experimental values[53]. The solid curve is the theoretical one fitted to them[54]. This figure shows that the rate R took the maximum when the FWHM was equal to the tip diameter $2a_p$ of the fiber probe (a_p=4.4 nm: tip radius). This was due to the size-dependent resonance of the DP energy transfer between the tip of the fiber probe and the formed Zn-NM (Phenomenon 4). Although further increases in the deposition time increased the size of the Zn-NM, the value of R decreased. Finally, the size and conformation of the Zn-NM reached stationary states, and the value of the

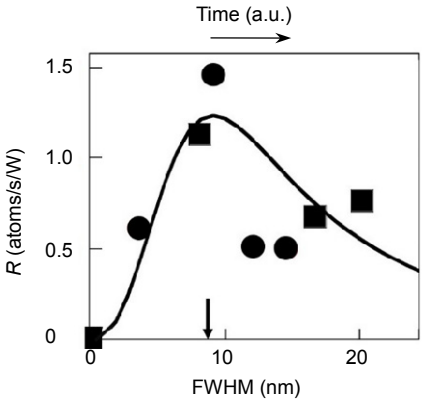

Fig. 2 | Dependence of the deposition rate *R* (atoms/s/W) on the FWHM of the Zn-NM. FWHM increased with increasing deposition time. The number of atoms deposited per unit time was normalized to the irradiated light power (W) to derive the rate R. The wavelength of the propagating light for creating the DP was 325 nm. Closed circles and squares represent the measured values when the powers of the light incident to the fiber probe were 5 μW and 10 μW, respectively. The downward arrow represents the value of $2a_p$.

FWHM saturated. Figure 1 shows the profiles acquired after this saturation.

It should be noted that the FWHM values in Fig. 1 were 50–70 nm even though the controllability of the tip diameter of the fiber probe was low (contrivance (ii) above). They were independent of the tip diameter, the wavelength and the power of the light used for irradiating the end of the fiber probe, and the species of molecules used. A larger FWHM was not realized even by increasing the deposition time. Here, it should also be noted, based on the Yukawa function and Phenomenon 4, that the spatial profile and size of the DP transferred from the tip of the fiber probe corresponded to those of the NM deposited on the substrate. From these results, the values of the FWHM in the shear-force microscopic images in Fig. 1 indicate the following phenomenon: [**Phenomenon 9**] *The maximum size $a_{DP,Max}$ of the DP is 50–70 nm.*

By using the nano-fabrication technology above, a variety of two-dimensional patterns have been formed by scanning a fiber probe, like a picture drawn with a single stroke of the pen[55]. However, the total scanning time increased with larger pattern sizes, which decreased the working efficiency. To increase the efficiency, a novel lithography technology has been developed in which the fiber probe was replaced by a two-dimensional photo-mask. A small pattern was formed on the material surface by exposing the thin photoresist film by the DP that was created on the apertures of the photo-mask. For this creation, visible light was used as a light source. Although its wavelength was longer than that of the ultraviolet light required for exposing photoresist in conventional photolithography, it was allowed to be used due to Phenomenon 8[56]. Furthermore, an optically inactive photoresist material ZEP-520, popularly used for electron-beam lithography, has been used based on Phenomenon 5. A fully automatic practical photolithography machine has been developed and was used to form a diffraction grating pattern with a half-pitch as narrow as 22 nm[57]. It also

produced a two-dimensional array of the DP devices[58], and practical devices for soft X-rays (a Fresnel zone plate[59] and a diffraction grating[60]).

2) Technology not using a fiber probe or an aperture

This part reviews a novel autonomous nano-fabrication technology that requires neither fiber probes nor apertures, resulting in drastic increases in the working efficiency. A representative example is autonomous smoothing of a material surface: The material to be smoothed is installed in a vacuum chamber, and the chamber is also filled with gaseous molecules. By irradiating the material surface with light, the DP is created at the tips of the bumps on the rough material surface. That is, the bumps play the role of a fiber probe for creating the DP. If the molecules jump into the DP field, they are dissociated, as was the case of the PCVD in 1). The chemically active atoms, created as a result of this dissociation, selectively etch the tips of the bumps away, while the flat part of the surface remains unetched. The etching autonomously starts by light irradiation and the surface roughness decreases gradually as etching progresses. The etching autonomously stops when the bumps are annihilated and the DP is not created anymore.

The disc surface of a synthetic silica substrate (30 mm diameter) was etched by using gaseous Cl_2 molecules. Although light with a wavelength shorter than 400 nm was required for conventional photo-dissociation (common view [c]), the present method used visible light with a wavelength of 532 nm based on Phenomenon 8. Etching by active Cl atoms decreased the surface roughness to as low as 0.13 nm. A laser mirror was produced by coating a high-reflection film on the smoothed substrate surface, and its damage threshold to the high-power ultraviolet laser light pulses was evaluated. The threshold value was confirmed to be as high as twice that of the commercially available strongest mirror whose substrate surface was polished by a conventional chemical-mechanical polishing technology[61].

Gaseous O_2 molecules can be also used for autonomous etching because the O atoms created by the dissociation are chemically active. The advantage is that etching can be carried out in atmospheric conditions by using O_2 molecules in air, and thus, a vacuum chamber is not required. Figure 3(a) shows experimental results of etching a plastic PMMA surface by using O_2 molecules[62]. Although ultraviolet light with a wavelength shorter than 242 nm was required for the conventional photo-dissociation, light with a wavelength of 325 nm was used here due to Phenomenon 8. For comparison, Fig. 3(b) shows the result of the etching by using conventional photo-dissociation, for which the wavelength of the light used was as short as 213 nm.

In Figs. 3(a) and (b), the surface roughness was evaluated from its standard deviation $\sigma(l)$, by referring to the square root of the variance that has been popularly used for evaluating the frequency fluctuations of microwave oscillators and lasers[63]. The horizontal axis l represents the period of the roughness on the surface. The vertical axis is the value of $\sigma(l)$ acquired from the AFM image. Here, the ratio $\sigma_{\rm after}/\sigma_{\rm before}$ between the values before ($\sigma_{\rm before}$) and after ($\sigma_{\rm after}$) the etching is plotted in a logarithmic scale (This ratio was derived from the values $\sigma_{\rm before}$ and $\sigma_{\rm after}$ in Fig. 4 in ref.[62]). Figure 3(a) shows that $\sigma_{\rm after}/\sigma_{\rm before}<1$ in the range $l<\lambda$ (λ is the wavelength of the light radiated for creating the DP, identified by a downward arrow in this figure), by which the contribution of the sub-wavelength sized DP is confirmed. Drastic decreases in $\sigma_{\rm after}/\sigma_{\rm before}$ can be seen in the range l<50–70 nm, from which Phenomenon 9 regarding the maximum size of the DP is confirmed again. In

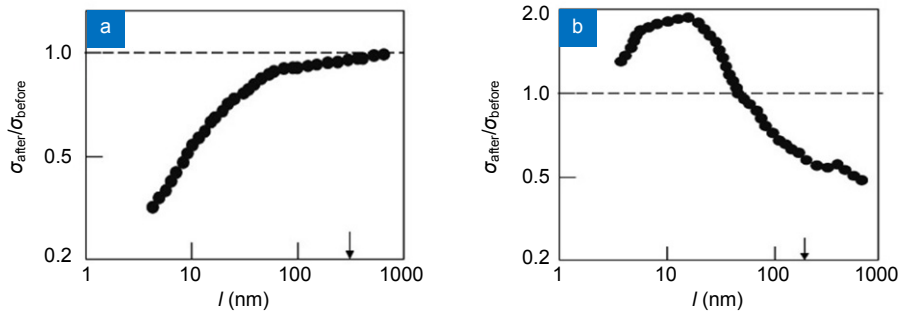

Fig. 3 | The ratio of the standard deviation of the roughness of the PMMA surface before and after etching. (**a**) and (**b**) are the results acquired by illuminating the surface with light having wavelengths of 325 nm and 213 nm, respectively. The downward arrows represent the values of *l* that are equal to the wavelengths above.

contrast to Fig. 3(a), Fig. 3(b) shows that $\sigma_{\rm after}/\sigma_{\rm before}<1$ in the range $l>\lambda$. This means that the etching was effective in the super-wavelength range. On the contrary, $\sigma_{\rm after}/\sigma_{\rm before}>1$ in the sub-wavelength range, indicates that the surface roughness was increased by the etching. By comparing the two figures, it is confirmed that the etching by the DP is effective for selectively removing bumps of sub-wavelength size.

Since the DPs are always created on the tip of the bump on the material surface under light irradiation, the present autonomous etching has been applied to a variety of surface profiles. These included a convex surface, a concave surface, and the inner surface of a cylinder. As an example, this etching has smoothed the side surface of a diffraction grating composed of parallel linear corrugated patterns[64] and the surface of a photo-mask used for conventional ultraviolet lithography[65]. Furthermore, a variety of materials have been smoothened, such as the surfaces of GaN crystals[66], transparent ceramics[67], and diamonds[68]. These achievements demonstrated the prominent capability of the present autonomous smoothing technology, achieved by exploiting the DP.

Energy conversion

Since the DP field has a broad spectrum, the novel phenomena of energy up- and down-conversion are expected. Three kinds of such energy conversions are reviewed in this section.

1) Conversion from optical to optical energy

Energy up-conversion, i.e., the conversion from infrared to visible light, has been realized. In this process, phonons in the DP provided their energies to the electrons in NMs. NMs of DCM, coumarine 540A, and stilbene 420 dye molecules were used as specimens for demonstrating the up-conversion. By irradiating them with infrared light of 0.8–1.3 μm wavelength, the DP created on one NM was transferred to the adjacent NMs. These NMs received the DP energy that contained the phonon energy, and thus, they respectively emitted red, green, and blue light[69,70]. This conversion method has been applied to measure infrared optical pulse shapes[71].

Energy down-conversion has also been realized by using an autonomously grown optically curable resin[72] that contains NMs of ZnO and DCM[73]. The DP energy transferred from the ZnO-NM to the DCM-NM and subsequent dissipation, as with the transfer in the nanometer-sized optical devices, realized energy down-conversion: By irradiating the film with ultraviolet light of 300–350 nm wavelength, visible light of 560 nm wavelength was emitted. The conversion efficiency was evaluated to be as high as 90%–95%.

As an application of this down-conversion, a novel plastic film was fabricated by dispersing ZnO and DCM NMs into it[73]. By putting this film on the surface of a commercially available Si solar cell battery (surface area of 156 mm×156 mm and nominal electrical power generation efficiency of 18.1%), the electrical power generation efficiency was evaluated to be 20.0%. To achieve further increases, another type of film was fabricated by replacing the DCM NMs with BBQ dye NMs. As a result, ultraviolet light of 300–350 nm wavelength was efficiently converted to visible light of 450 nm wavelength. By putting this film on the surface of the Si solar battery above, the electrical power generation efficiency was evaluated to be as high as 20.2%. It should be pointed out that an efficiency higher than 20% has never been achieved with conventional solitary Si solar batteries.

2) Conversion from optical to electrical energy

Novel devices for optical to electrical energy conversion that exhibited the energy up-conversion feature originating from the DP have been fabricated. One example is a photovoltaic device using an organic thin film of P3HT. By depositing Ag nanoparticles on the device surface using a novel DP-assisted rf-sputtering method, the conformation of the electrode surface was autonomously controlled[74]. Another example is a Si-photodiode in which the spatial distribution of doped boron (B) atoms was autonomously controlled by a novel DP-assisted annealing[75]. A detailed explanation of this annealing will be given in 3) below. In these two examples, efficient energy up-conversion was realized even when the incident photon energy was lower than the bandgap energy of the semiconductor materials used for the devices. Furthermore, optical amplification was confirmed, which originated from stimulated emission triggered by the DP.

3) Conversion from electrical to optical energy

This part reviews Si light-emitting diodes (LEDs), Si lasers, and SiC polarization rotators as examples of the conversion from electrical to optical energy. Phenomena contrary to the common view [e] are also demonstrated.

Crystalline Si has long been a key material supporting the development of modern technology for more than half a century because of its numerous advantages, such as Si′s abundance in the earth′s crust, and its widespread use for electronics. However, because Si is an indirect-transition-type semiconductor, it has been considered to

be unsuitable for light-emitting devices: Since the bottom of the conduction band and the top of the valence band in Si are at different positions in reciprocal lattice space, the momentum conservation law requires an interaction between an electron–hole pair and phonons for radiative recombination. However, the probability of this interaction is very low.

Nevertheless, Si has been the subject of extensive study for the fabrication of light-emitting devices. These include studies using porous Si[76], a super-lattice structure of Si and SiO_2[77], and so on. However, the devices fabricated in these studies have some limitations, such as low efficiency, the need to operate at low temperature, complicated fabrication processes, and the difficulty of current injection. Experimental work on a novel technology named silicon photonics has recently progressed[78]. Although sophisticated passive optical devices such as optical waveguides and optical switches have been developed, Si light-emitting devices have not been dealt with.

The problems above have been solved by using the DP because the phonons in the DP can provide momenta to the electron to satisfy the momentum conservation law[79]. For fabrication, the DPs were created by irradiating a Si crystal with light, as was the case in the previous parts 1) and 2). For the device operation, DPs were created by electronic excitation, unlike the optical excitations in the case of the previous parts.

① Infrared Si-LEDs

Fabrication and operation methods are reviewed here by taking an infrared Si-LED as a first example. An n-type Si substrate was used, in which as atoms or Sb atoms were doped. As the first step, the substrate surface was transformed to a p-type material by implanting B atoms, forming a p-n homojunction. Metallic films were coated on the substrate surfaces to serve as electrodes.

As the next step, this substrate was processed by a novel fabrication method named DP-assisted annealing: By current injection, Joule heat was generated, which caused the B atoms to diffuse. During this Joule-annealing, the substrate surface was irradiated with infrared light (for example, 1.342 μm-wavelength light). Because its photon energy $h\nu_{\mathrm{anneal}}$ (=0.925 eV) was sufficiently lower than the bandgap energy E_{g} (=1.12 eV) of Si, the light could penetrate into the Si substrate without suffering absorption. Then, the light reached the p-n homojunction to create the DP on the B atom. The created DP localized at this impurity B atom, which manifested the following phenomenon: [**Phenomenon 10**] *The DP is created and localized at a singularity such as a nanometer-sized particle or impurity atom in a material.*

The phonons in the created DP can provide momenta to the electron nearby to satisfy the momentum conservation law, resulting in radiative recombination for photon emission. This is stimulated emission triggered by the irradiated infrared light. The emitted light propagated out from the crystal to the outside, which indicated that part of the Joule energy used for diffusing the B atoms was dissipated in the form of optical energy, resulting in local cooling that locally decreased the diffusion rate. As a result, by the balance between heating by the Joule energy and cooling by the stimulated emission, the spatial distribution of B atoms varied and reached a stationary state autonomously. This stationary state was expected to be the optimum for efficient creation of the DPs and for efficient LED operation because the probability of spontaneous emission was proportional to that of the stimulated emission described above.

The optimum condition for the DP-assisted annealing has been found based on a two-level system model. That is, the optimum ratio between the irradiated photon number and the injected electron number per unit time was 1:1[80]. After the DP-assisted annealing, the Huang-Rhys factor, a parameter representing the magnitude of the coupling between electron–hole pairs and phonons, was experimentally evaluated to be 4.08[81]. This was 10^2–10^3 times higher than that before the DP-assisted annealing. It was also found that the DPs coupled with the coherent phonons of the longitudinal optical mode[82].

The device fabricated above was operated as an LED by simple current injection, similar to the case of operating conventional LEDs. By injecting a current of 3.0 A into a device with an areal size of 0.35 mm×0.35 mm, a CW output optical power as high as 2.0 W was obtained at a substrate temperature of 77 K. A power as high as 200 mW was obtained even at room temperature (283 K)[83]. These results confirmed that the following phenomenon occurs: [**Phenomenon 11**] *The spatial distribution of B atoms varies and reaches a stationary state autonomously due to DP-assisted annealing, resulting in strong light emission from the Si crystal.*

Figure 4 shows the light emission spectra of the fabricated Si-LED acquired at a temperature of 283 K and an injection current of 2.45 A[83]. This figure clearly shows high spectral peaks at E_{g}–$3E_{\mathrm{phonon}}$, E_{g}–$6E_{\mathrm{phonon}}$, and E_{g}–$9E_{\mathrm{phonon}}$ (refer to the arrows A–C), where E_{phonon} is a phonon energy.

It should be noted that the photon energy emitted from the conventional LEDs was governed by E_g. However, in the present Si-LED, the energy difference between $h\nu_{anneal}$ and E_g was compensated by the created phonon energy. The origin of this compensation was attributed to the spatial distribution of B atoms that was autonomously controlled during the DP-assisted annealing. For this control, the irradiated light served as a source for creating the DP during the DP-assisted annealing. It has been theoretically confirmed that the DP, after being created and localized on the B atom (Phenomenon 10), coupled more efficiently with localized phonons than with non-localized ones. It has been also confirmed that a B atom-pair served as a resonant cavity to confine and localize phonons, resulting in localized phonon creation[84].

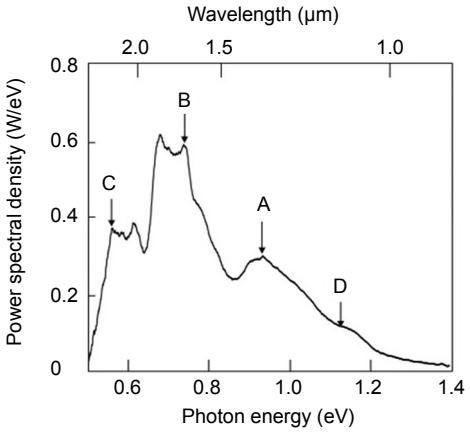

Fig. 4 | Light emission spectra of the Si-LED. The substrate temperature and the injection current were 283 K and 2.45 A, respectively. Downward arrows A–D represent the spectral peaks at E_g–3E_{phonon}, E_g–6E_{phonon}, E_g–9E_{phonon}, and E_g, respectively.

For comparing these theoretical confirmations with experimental results, the three-dimensional spatial distribution of B atoms at the p-n homojunction was acquired by atom probe field ion microscopy of sub-nanometer spatial resolution. By analyzing the acquired data, it was found that the B atoms were apt to form pairs with a length d=3a (a (=0.54 nm) is the lattice constant of the Si crystal), and the formed pairs were apt to orient along a plane parallel to the top surface of the Si crystal[85]. That is, the following phenomenon was found: [**Phenomenon 12**] *The length and orientation of the B atom-pair in a Si crystal are autonomously controlled by the DP-assisted annealing.*

It should be noted that the Si crystal is composed of multiple cubic lattices, and the value of the required phonon momentum has to be h/a for the radiative recombination of the electron (at the bottom of the conduction band at the X-point in reciprocal space) and the positive hole (at the top of the valence band at the Γ-point) to take place. It should be also noted that the value of the phonon momentum is $h/3a$ when the phonon localizes at the B atom-pair with d=3a. By comparing these values of momenta, it is found that the DP created and localized at this B atom-pair provides three phonons for recombination. As a result, the emitted photon energy $h\nu_{em}$ is expressed as $h\nu_{em}$= E_g–3E_{phonon}. By substituting the values of E_g (= 1.12 eV) and the relevant optical mode phonon energy E_{phonon} (=65 meV) into this equation, the value of $h\nu_{em}$ is derived to be 0.93 eV, which is nearly equal to the photon energy $h\nu_{anneal}$ (=0.95 eV) irradiated during the DP-assisted annealing. This numerical relation is consistent with the spectral feature in Fig. 4. This indicates that the irradiated light served as a breeder that created a photon with energy $h\nu_{em}$=$h\nu_{anneal}$ and manifested the following phenomenon: [**Phenomenon 13**] *A light emitting device fabricated by DP-assisted annealing exhibits photon breeding (PB) with respect to photon energy; i.e., the emitted photon energy* $h\nu_{em}$ *is equal to the photon energy* $h\nu_{anneal}$ *used for the annealing.*

The peaks B and C in this figure are the second and third harmonics of the phonon contributions, respectively. PB was observed also with respect to the photon spin. That is, the polarization direction of the emitted light was identical to that of the light irradiated during the DP-assisted annealing[85].

② Visible LEDs

The second example is visible LEDs fabricated by using crystalline Si and that exhibit the PB phenomenon. Specifically, blue, green, and red light-emitting LEDs were fabricated by radiating blue, green, and red light, respectively, during the DP-assisted annealing[86]. A lateral p-n homojunction structure was developed in order to increase the efficiency of extracting the visible light from the Si crystal[87].

A variety of visible LEDs have been developed by using crystalline SiC even though it is also a well-known indirect transition-type semiconductor. They were fabricated by irradiating them with UV-violet, bluish-white, blue, and green light during the DP-assisted annealing. The fabricated devices emitted UV-violet, bluish-white, blue, and green light, respectively[88].

③ Infrared Si-lasers

The third example is high-power infrared Si-lasers. A

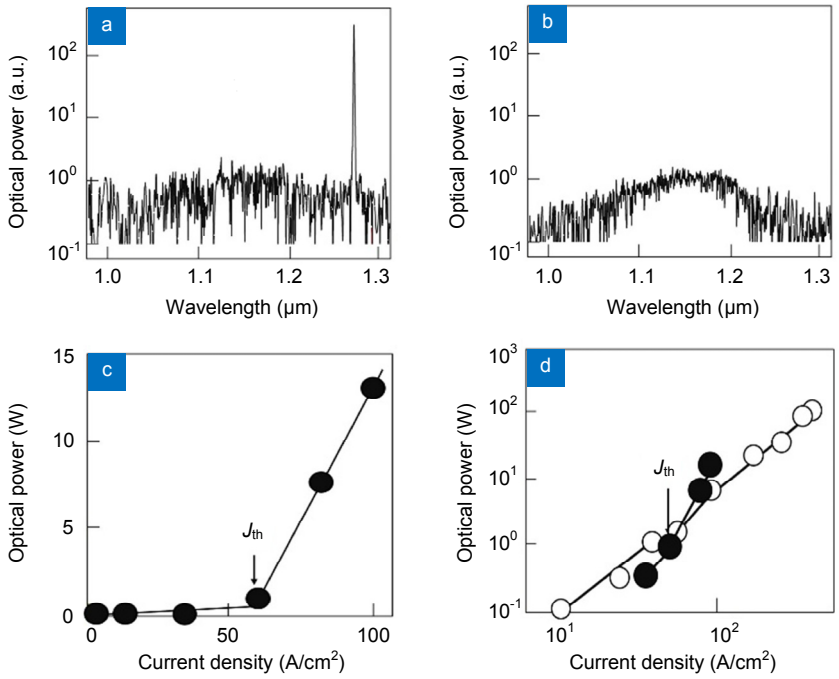

Fig. 5 | Light emission spectra and output optical power of Si lasers. (**a**), (**b**) Spectral profiles above and below the threshold, respectively, of a 550 μm-length device with a ridge waveguide. The threshold current density was 1.1 A/cm^2 under CW operation at room temperature (25 ℃). (**c**), (**d**) Relation between the injected current density and the output optical powers of 15 mm-long and 30 mm-long devices, respectively. J_{th} is the threshold current density. Closed circles in (d) are a copy of those in (c).

simple ridge waveguide (10 μm-width and 2 μm-height) was built-in, and the cleaved facets were used as mirrors of a Fabry-Perot cavity (550 μm-cavity length)[89]. DP-assisted annealing was carried out by injecting 1.3 μm-wavelength light into the cavity through one of the end facets. Figures 5(a) and 5(b) show the light emission spectra of the fabricated device acquired under CW operation at room temperature (25 ℃). Above the threshold, a sharp lasing spectrum was observed (Fig. 5(a)), which demonstrated single-mode oscillation even though the cavity length was as long as 550 μm. The origin of this single-mode oscillation was that the low infrared absorption by the Si provided a low threshold for the principal longitudinal mode at the peak of the optical amplification gain spectrum and, as a result, the gains for other modes were depleted by this principal mode due to nonlinear mode competition. The spectral profile below the threshold (Fig. 5(b)) does not show any amplified spontaneous emission spectra, which is evidence of gain depletion due to the mode competition above. The lasing wavelength, shown in Fig. 5(a), was 1.271 μm, which was approximately equal to that of the light irradiated during the DP-assisted annealing, from which PB was also confirmed.

By modifying the device structure above, high-power infrared laser devices were fabricated. The ridge waveguide was not built into them because further increases in the optical confinement efficiency were not expected in this waveguide as long as the device had a p-n homojunction. Instead, the cavity length was increased to 15 mm to realize high-power lasing by utilizing the very low infrared absorption of crystalline Si. Figure 5(c) shows that an output optical power as high as 13 W was obtained at the injected current density of 100 A/cm^2 [90]. The threshold current density J_{th} was as low as 60 A/cm^2. The lasing wavelength was 1.34 μm. As is shown in Fig. 5(d), an output optical power higher than 100 W was obtained recently by further increases in the cavity length to 30 mm[91]. By summarizing the experimental results of the first to the third examples above, the following phenomenon that is contrary to the common view [e] was confirmed: [**Phenomenon 14**] *By DP-assisted annealing, a Si crystal works as a high-power light emitting device even though it is an indirect transition-type semiconductor.*

④ Polarization rotators

The last example is polarization rotators fabricated by using a SiC crystal. The fabrication method was equivalent to that of the visible SiC-LEDs of the second example: By implanting Al atoms into an n-type SiC substrate, the substrate surface was transformed to a p-type material,

forming a p-n homojunction. By the DP-assisted annealing, during which the substrate surface was irradiated with the 405 nm-wavelength light, diffusion of Al atoms was autonomously controlled to realize the optimum spatial distribution of Al atoms for light emission. As a result, the device worked as a visible LED.

In order to use it as a polarization rotator, an H-shaped electrode was installed on the top surface. By current injection to this electrode, electrons were injected into the p-n homojunction and a magnetic field was generated. It is expected that this current injection rotated the polarization of the light incident into the device. Linearly polarized 405 nm-wavelength light was made normally incident on the top surface of this device. This was because, due to PB, it was also expected that the rotation angle was the largest when its wavelength was identical to that of the light irradiated during the DP-assisted annealing.

Meeting the expectations above, the polarization angle of the incident light actually rotated after propagating through the device. The Verdet constant was evaluated to be 660 deg/A from the measured values of the polarization rotation angle. This is 10^5–10^6 times those of conventional paramagnetic materials that are transparent in the visible region. The Faraday rotation angle was also as large as 2480 deg/cm. These large values demonstrated that the present SiC crystal exhibited a gigantic magneto-optical effect. Furthermore, the remanent magnetization was 0.36 mT, which corresponded to those in conventional ferromagnetic materials[92]. The experimental results above indicated that the presently used SiC crystal acquired novel properties, equivalent to those of ferromagnetic materials.

In order to find the origin of such novel ferromagnetic properties, a magnetization curve was acquired at 27 ℃. Closed squares in Fig. 6 are the acquired values. They were fitted by the curve A and clearly exhibited a hysteresis characteristic, which is inherent to ferromagnetic materials. The values of the magnetization were very small before the DP-assisted annealing, as shown by open circles and the curve B. By comparing these measured values, the following novel phenomenon was confirmed: [**Phenomenon 15**] *The semiconductor SiC crystal was made to behave as a ferromagnet as a result of the DP-assisted annealing and exhibited a gigantic magneto-optical effect in the visible region.*

The origin of this behavior has been attributed to the Al atom-pairs that were autonomously formed as a result of the DP-assisted annealing. That is, the ferromagnetic characteristic likely originated from the two electrons with parallel spins in the triplet state of the electron orbital in an Al atom-pair, which was more stable than the singlet state.

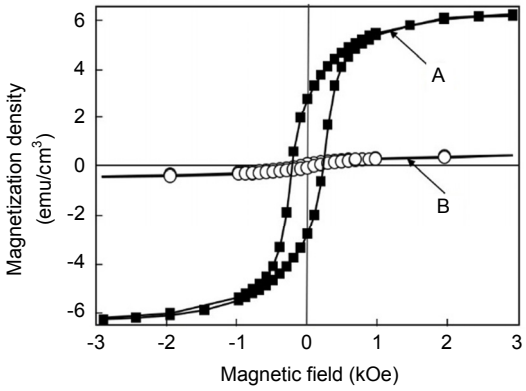

Fig. 6 | Magnetization curve for the SiC crystals, measured at 27 ℃. Closed squares and open circles are the results acquired after and before the DP-assisted annealing, respectively. They are fitted by the curves A and B, respectively.

At the end of this part it should be pointed out that similar polarization rotators have also been fabricated by using ZnO crystals based on the same principle as in the SiC crystals above[93].

Future directions

The studies reviewed in this paper identified the DP as a quantum field that is created as a result of the light-matter interaction in a nanometer-sized space. However, they also presented at least two theoretical difficulties. One was that the mode of the electromagnetic field could not be defined. The other was that the description of the spatial localization of the DP required the surrounding macroscopic subsystem to have a parabolic dispersion relation. As an urgent solution to overcome these difficulties, the theoretical methods in on-shell science were modified and applied to tentatively describe the physical nature of the DP.

Although the theoretical studies above were at a standstill, experimental studies have found the novel Phenomena 1–15. It should be noted that they cannot be described by conventional optical theories. This is because these theories treat only photons in a vacuum (free photons) and in a macroscopic material, whose dispersion relation is given by the mass-shell ("on-shell" for short). It has been popularly known that massless particles with non-zero spin, such as free photons, cannot be localized

in space in the sense that the position operator cannot be defined[94]. However, it turns out to be natural to consider localized photons when the effective mass of photons, created by light–matter interactions, is taken into account. Especially in the case of NMs, space–time localization and energy–momentum fluctuations constitute novel aspects of light. A photon in such a context is called a DP.

For a theoretical definition of the DP and for describing the Phenomena 1–15 above, the "off-shell" nature of the interaction has to be considered. That is, the DP is an off-shell quantum field that conspicuously deviates from the mass-shell. As has been well known, quantum field theories cannot be formulated without off-shell entities. In other words, the traditional particle description has failed to treat the quantum field of a composite system. Hence, DPs must be entities that are very different from Einstein's quanta of light or free photons.

Here, a fundamental question arises: How can the DP be described as an individual entity? As long as one sticks to the notion of individual entities as irreducible on-shell particles, it is impossible to treat the DP as an individual entity. However, a more general perspective, advocated by Ojima[95], has shown that macroscopic physical phenomena can emerge out of a condensation of microscopic off-shell entities.

By following this perspective, a basic idea can be proposed: In the interaction between light and NMs, certain families of modes of the composite system will behave as individuals. This behavior suggests that the DP is the quantum field of a composite system in which an electromagnetic field and an electron (or an exciton) interact in a nanometer-sized space. Furthermore, it is a virtual field localized in the nanometer-sized space within a short time duration. Thus, the DP is a quantum field whose nature is contrary to that of an on-shell photon. This means that conventional optical theories are incapable of giving a systematic description of Phenomena 1–15. Fortunately, however, several hints have been given to construct novel theories for describing the phenomena above by noting that the virtual photon plays an essential role in the electromagnetic Coulomb interactions. They are:

[A] The longitudinal mode of an electromagnetic field (the longitudinal wave) contributes to the Coulomb interaction[96].

[B] The field interaction accompanies the 4-momentum[97].

[C] Although the spacelike field is not spatially localized because it behaves as a stable wave, it becomes unstable and can localize if it interacts with a timelike field[98].

By referring to these hints, novel theoretical studies have commenced by relying on physical bases[99]. One is the theory using electromagnetic response functions based on classical electromagnetics. The other is the theory based on spatio-temporal vortex hydrodynamics supported by the relativity theory[100].

Furthermore, mathematics-based theoretical studies are in progress that will serve as invaluable guides for gaining a deep understanding of the concepts of the physics-based theories for the phenomena that originate from the DP[99]. Examples of these theories are the quantum probability theory and the quantum measurement theory. Also demonstrated is a theory based on micro–macro duality, which serves as a foundation for embarking on theoretical studies of off-shell science.

One of the promising future direction of DP science is to propel the theoretical studies above in collaboration with experimental ones. By using the fruits of these studies, further developments of application technologies are expected, resulting in further disruptive innovations.

Summary

This paper reviewed the progress in optical sciences dealing with the ONF. After the introduction, it pointed out that the ONF was an electromagnetic field that is created and localized in an NM, or on its surface, under light illumination.

Next, it reviewed the classical studies of the ONF that explored the possibilities of creating and using the ONF. It described that the studies on the ONF, called the near field optics, started for realizing disruptive innovation by breaking through the diffraction limit of optical microscopy. Its methodology was proposed in the 1920s to 1950s, and experimental demonstrations were carried out in the 1980s and 1990s. It was pointed out that the classical studies of the ONF had already come to an end without answering the essential questions on the origin of the near-field optical interaction.

However, even after this end, basic studies on the ONF were steadily continued by a small number of scientists. These included studies on the concepts and principles of the ONF, with the aim of answering the questions above. As a result, the ONF was identified as an off-shell quantum field, i.e., a virtual field localized in a nanometer-sized space within a short time duration. Based on

this identification, a novel off-shell science has started by noting that the dispersion relation between the energy and momentum was invalid for the ONF. This quantum field is now called the DP because it is created as a result of the interaction between photons and electrons (or excitons) in a NM, and thus, it accompanies the energies of electrons or excitons. In the other words, the DP is a quantum field created in a system composed of electromagnetic fields and NMs.

Novel Phenomena 1–15 were reviewed that have been found in a series of experimental studies on the DP. Phenomena 1–5 are general in concepts. Phenomena 6–7 are observed in novel photonic devices and in information processing, and 8–9 are in nano-fabrication. Phenomena 10–15 correspond to novel observations in energy conversion of light emitting semiconductors by utilizing DP. They are contrary to the common views that have been accepted for a long time by conventional optical science. By applying these phenomena, a variety of technologies have been developed. These include nanometer-sized optical devices (including their applications to information transmission and processing systems), nano-fabrication technology (photochemical vapor deposition, lithography, and smoothing of material surfaces), and three kinds of energy conversion technologies. Among these energy conversion technologies, the electrical to optical energy conversion used a DP that was created as a result of electrical excitation by current injection. This conversion realized high-power light emitting diodes and lasers by using crystalline Si, which is a typical indirect-transition-type semiconductor. A polarization rotator was realized by using crystalline SiC (also an indirect-transition-type semiconductor) that exhibited a gigantic magneto-optical effect.

Finally, the advent of novel theories was reviewed. These included a theory using electromagnetic response functions, a theory based on spatio-temporal vortex hydrodynamics supported by relativity theory, quantum probability theory, quantum measurement theory, and a theory based on micro–macro duality.

References

1. Ohtsu M. *Near-Field Nano/Atom Optics and Technology* (Springer, Berlin, 1998).
2. Zhu X, Ohtsu M. *Near-Field Optics*: *Principles and Applications* (World Scientific, Singapore, 2000).
3. Ohtsu M. From classical to modern near-field optics and the future. *Opt Rev* **21**, 905–910 (2014).
4. Synge E H. A suggested method for extending microscopic resolution into the ultra-microscopic region. *Lond Edinb Dublin Phil Mag J Sci* **6**, 356–362 (1928).
5. O'Keefe J A. Resolving power of visible light. *J Opt Soc Am* **46**, 359 (1956).
6. Bethe H A. Theory of diffraction by small holes. *Phys Rev* **66**, 163–182 (1944).
7. Bouwkamp C J. On the diffraction of electromagnetic waves by small circular disks and holes. *Philips Res Rep* **5**, 401–422 (1950).
8. Ash E A, Nicholls G. Super-resolution aperture scanning microscope. *Nature* **237**, 510–512 (1972).
9. Pohl D W, Courjon D. *Near Field Optics* (Kluwer, Dordrecht, 1993).
10. Pohl D W, Denk W, Lanz M. Optical stethoscopy: image recording with resolution λ/20. *Appl Phys Lett* **44**, 651–653 (1984).
11. Lewis A, Isaacson M, Harootunian A, Muray A. Development of a 500 Å spatial resolution light microscope: I. Light is efficiently transmitted through λ/16 diameter apertures. *Ultramicroscopy* **13**, 227–231 (1984).
12. Fischer U C. Optical characteristics of 0.1 μm circular apertures in a metal film as light sources for scanning ultramicroscopy. *J Vac Sci Technol B* **3**, 386–390 (1985).
13. Betzig E, Isaacson M, Lewis A. Collection mode near-field scanning optical microscopy. *Appl Phys Lett* **51**, 2088–2090 (1987).
14. Mononobe S, Saiki T. Chs. 3 and 4 in *Near-Field Nano/Atom Optics and Technol* . (ed Ohtsu M. Springer Tokyo, 1998).
15. Betzig E, Trautman J K, Harris T D, Weiner J S, Kostelak R L. Breaking the diffraction barrier: optical microscopy on a nanometric scale. *Science* **251**, 1468–1470 (1991).
16. Pangaribuan T, Yamada K, Jian S D, Ohsawa H, Ohtsu M. Reproducible fabrication technique of nanometric tip diameter fiber probe for photon scanning tunneling microscope. *Jpn J Appl Phys* **31**, L1302–L1304 (1992).
17. Malmqvist L, Hertz H M. Trapped particle optical microscopy. *Opt Commun* **94**, 19–24 (1992).
18. van Hulst N F, Moers M H P, Noordman O F J, Tack R G, Segerink F B et al. Near-field optical microscope using a silicon-nitride probe. *Appl Phys Lett* **62**, 461–463 (1993).
19. Zenhausern F, Martin Y, Wickramasinghe H K. Scanning interferometric apertureless microscopy: optical imaging at 10 angstrom resolution. *Science* **269**, 1083–1085 (1995).
20. Guerra J M. Photon tunneling microscopy. *Appl Opt* **29**, 3741–3752 (1990).
21. Betzig E, Chichester R J. Single molecules observed by near-field scanning optical microscopy. *Science* **262**, 1422–1425 (1993).
22. Xie X S, Dunn R C. Probing single molecule dynamics. *Science* **265**, 361–364 (1994).
23. Maheswari R U, Mononobe S, Tatsumi H, Katayama Y, Ohtsu M. Observation of subcellular structures of neurons by an illumination mode near-field optical microscope under an optical feedback control. *Opt Rev* **3**, 463–467 (1996).
24. Levy J, Nikitin V, Kikkawa J M, Awschalom D D, Samarth N. Femtosecond near-field spin microscopy in digital magnetic heterostructures. *J Appl Phys* **79**, 6095–6100 (1996).
25. Saiki T, Nishi K, Ohtsu M. Low temperature near-field photoluminescence spectroscopy of InGaAs single quantum dots. *J Appl Phys* **37**, 1638–1642 (1998).
26. Narita Y, Murotani H. Submicrometer optical characterization of the grain boundary of optically active Cr^{3+} doped polycrystalline Al_2O_3 by near-field spectroscopy. *Am Mineral* **87**, 1144–1147 (2002).

27. Isaacson M, Cline J, Barshatzky H. Resolution in near-field optical microscopy. *Ultramicroscopy* **47**, 15–22 (1992).
28. Wolf E, Nieto-Vesperinas M. Analyticity of the angular spectrum amplitude of scattered fields and some of its consequences. *J Opt Soc Am* **2**, 886–890 (1985).
29. Girard C, Courjon D. Model for scanning tunneling optical microscopy: a microscopic self-consistent approach. *Phys Rev B* **42**, 9340–9439 (1990).
30. Eah S K, Jhe W, Saiki T, Ohtsu M. Study of quantum optical effects with scanning near-field optical microscopy In *Proceedings of the First Asia-Pacific Workshop on Near Field Optics* (1996).
31. Kobayashi K, Ohtsu M. Quantum theoretical approach to a near-field optical system. *J Microsc* **194**, 249–254 (1999).
32. Kobayashi K, Sangu S, Ito H, Ohtsu M. Near-field optical potential for a neutral atom. *Phys Rev A* **63**, 013806 (2001).
33. Ito H, Nakata T, Sakaki K, Ohtsu M, Lee K I et al. Laser spectroscopy of atoms guided by evanescent waves in micron-sized hollow optical fibers. *Phys Rev Lett* **76**, 4500–4503 (1996).
34. Ohtsu M, Kobayashi K, Kawazoe T, Sangu S, Yatsui T. Nanophotonics: design, fabrication, and operation of nanometric devices using optical near fields. *IEEE J Sel Top Quantum Electron* **8**, 839–862 (2002).
35. Ohtsu M. *Handbook of Nano-Optics and Nanophotonics* (Springer, Heidelberg, New York, 2013).
36. Ohtsu M, Yatsui T. P*rogress in Nanophotonics 4* (Springer, Heidelberg, 2017).
37. Tanaka Y, Kobayashi K. Spatial localization of an optical near field in one-dimensional nanomaterial system. *Physica E* **40**, 297–300 (2007).
38. Sangu S, Kobayashi K, Ohtsu M. Optical near fields as photon-matter interacting systems. *J Microsc* **202**, 279–285 (2001).
39. Maier S A, Brongersma M L, Kik P G, Meltzer S, Requicha A A G et al. Plasmonics—A route to nanoscale optical devices. *Adv Mater* **13**, 1501–1505 (2001).
40. Sangu S, Kobayashi K, Shojiguchi S, Ohtsu M. Logic and functional operations using a near-field optically coupled quantum-dot system. *Phys Rev B* **69**, 115334 (2004).
41. Kawazoe T, Ohtsu M, Aso S, Sawado Y, Hosoda Y et al. Two-dimensional array of room-temperature nanophotonic logic gates using InAs quantum dots in mesa structures. *Appl Phys B* **103**, 537–546 (2011).
42. Kawazoe T, Tanaka S, Ohtsu M. Single-photon emitter using excitation energy transfer between quantum dots. *J Nanophoton* **2**, 029502 (2008).
43. Naruse M, Holmström P, Kawazoe T, Akahane K, Yamamoto N et al. Energy dissipation in energy transfer mediated by optical near-field interactions and their interfaces with optical far-fields. *Appl Phys Lett* **100**, 241102 (2012).
44. Naruse M, Leibnitz K, Peper F, Tate N, Nomura W et al. Autonomy in excitation transfer via optical near-field interactions and its implications for information networking. *Nano Commun Netw* **2**, 189–195 (2011).
45. Naruse M, Tate N, Aono M, Ohtsu M. Information physics fundamentals of nanophotonics. *Rep Prog Phys* **76**, 056401 (2013).
46. Kim S J, Naruse M, Aono M, Ohtsu M, Hara M. Decision maker based on nanoscale photo-excitation transfer. *Sci Rep* **3**, 2370 (2013).
47. Aono M, Naruse M, Kim S J, Wakabayashi M, Hori H et al. Amoeba-inspired nanoarchitectonic computing: solving intractable computational problems using nanoscale photoexcitation transfer dynamics. *Langmuir* **29**, 7557–7564 (2013).
48. Tate N, Sugiyama H, Naruse M, Nomura W, Yatsui T et al. Quadrupole-dipole transform based on optical near-field interactions in engineered nanostructures. *Opt Express* **17**, 11113–11121 (2009).
49. Tate N, Naruse M, Yatsui T, Kawazoe T, Hoga M et al. Nanophotonic code embedded in embossed hologram for hierarchical information retrieval. *Opt Express* **18**, 7497–7505 (2010).
50. Kawazoe T, Kobayashi K, Takubo S, Ohtsu M. Nonadiabatic photodissociation process using an optical near field. *J Chem Phys* **122**, 024715 (2005).
51. Kawazoe T, Kobayashi K, Ohtsu M. Near-field optical chemical vapor deposition using $Zn(acac)_2$ with a non-adiabatic photochemical process. *Appl Phys B* **84**, 247–251 (2006).
52. Ohtsu M, Kawazoe T. Experimental estimation of the maximum size of a dressed photon. (2018); http://doi.org/10.14939/1802R.001.v1.
53. Lim J, Yatsui T, Ohtsu M. Observation of size-dependent resonance of near-field coupling between a deposited Zn dot and the probe apex during near-field optical chemical vapor deposition. *IEICE Trans Electron* **E88-C**, 1832–1835 (2005).
54. Kobayashi K, Sangu S, Ohtsu M, Ch 5 in *Progress in Nano-Electro-Optics* (Springer, Heidelberg, 2003).
55. Polonski V V, Yamamoto Y, Kourogi M, Fukuda H, Ohtsu M. Nanometric patterning of zinc by optical near-field photochemical vapour deposition. *J Microsc* **194**, 545–551 (1999).
56. Yonemitsu H, Kawazoe T, Kobayashi K, Ohtsu M. Nonadiabatic photochemical reaction and application to photolithography. *J Luminesc* **122–123**, 230–233 (2007).
57. Inao Y, Nakasato S, Kuroda R, Ohtsu M. Near-field lithography as prototype nano-fabrication tool. *Microelectron Eng* **84**, 705–710 (2007).
58. Kawazoe T, Kobayashi K, Akahane K, Naruse M, Yamamoto N et al. Demonstration of nanophotonic NOT gate using near-field optically coupled quantum dots. *Appl Phys B* **84**, 243–246 (2006).
59. Kawazoe T, Takahashi T, Ohtsu M. Evaluation of the dynamic range and spatial resolution of nonadiabatic optical near-field lithography through fabrication of Fresnel zone plates. *Appl Phys B* **98**, 5–11 (2010).
60. Koike M, Miyauchi S, Sano K, Imazono T. Ch. 9 in *Nanophotonics and Nanofabrication*. (ed Ohtsu M. Wiley-VCH, 2009).
61. Hirata K. Realization of high-performance optical element by optical near-field etching. *Proc SPIE* **7921**, 79210M (2011).
62. Yatsui T, Nomura W, Ohtsu M. Realization of ultraflat plastic film using dressed-photon–phonon-assisted selective etching of nanoscale structures. *Adv Opt Technol* **2015**, 701802 (2015).
63. Allan D W. Statistics of atomic frequency standards. *Proc IEEE* **54**, 221–230 (1966).
64. Yatsui T, Hirata K, Tabata T, Miyake Y, Akita Y et al. Self-organized near-field etching of the sidewalls of glass corrugations. *Appl Phys B* **103**, 527–530 (2011).
65. Teki R, John Kadaksham A, House M, Harris-Jones J, Ma A et al. Alternative smoothing techniques to mitigate EUV substrate defectivity. *Proc SPIE* **8322** 83220B (2012).
66. Yatsui T, Nomura W, Stehlin F, Soppera O, Naruse M et al. Challenges in realizing ultraflat materials surfaces. *Beilstein J Nanotechnol* **4**, 875–885 (2013).
67. Nomura W, Yatsui T, Yanase Y, Suzuki K, Fujita M et al. Repair-

ing nanoscale scratched grooves on polycrystalline ceramics using optical near-field assisted sputtering. *Appl Phys B* **99**, 75–78 (2010).
68. Yatsui T, Nomura W, Naruse M, Ohtsu M. Realization of an atomically flat surface of diamond using dressed photon-phonon etching. *J Phys D* **45**, 475302 (2012).
69. Kawazoe T, Fujiwara H, Kobayashi K, Ohtsu M. Visible light emission from dye molecular grains via infrared excitation based on the nonadiabatic transition induced by the optical near field. *IEEE J Sel Top Quant Electron* **15**, 1380–1386 (2009).
70. Fujiwara H, Kawazoe T, Ohtsu M. Nonadiabatic multi-step excitation for the blue–green light emission from dye grains induced by the near-infrared optical near-field. *Appl Phys B* **98**, 283–289 (2010).
71. Fujiwara H, Kawazoe T, Ohtsu M. Nonadiabatic nondegenerate excitation by optical near-field and its application to optical pulse-shape measurement. *Appl Phys B* **100**, 85–91 (2010).
72. Tate N, Naruse M, Liu Y, Kawazoe T, Yatsui T et al. Experimental demonstration and stochastic modeling of autonomous formation of nanophotonic droplets. *Appl Phys B* **112**, 587–592 (2013).
73. Yatsui T. *Progress in Nanophotonics 5* (Springer, 2018).
74. Yukutake S, Kawazoe T, Yatsui T, Nomura W, Kitamura K et al. Selective photocurrent generation in the transparent wavelength range of a semiconductor photovoltaic device using a phonon-assisted optical near-field process. *Appl Phys B* **99**, 415–422 (2010).
75. Tanaka H, Kawazoe T, Ohtsu M. Increasing Si photodetector photosensitivity in near-infrared region and manifestation of optical amplification by dressed photons. *Appl Phys B* **108**, 51–56 (2012).
76. Hirschman K D, Tsybeskov L, Duttagupta S P, Fauchet P M. Silicon-based visible light-emitting devices integrated into microelectronic circuits. *Nature* **384**, 338–341 (1996); http://doi.org/10.1038/384338a0.
77. Lu Z H, Lockwood D J, Baribeau J M. Quantum confinement and light emission in SiO_2/Si superlattices. *Nature* **378**, 258–260 (1995); http://doi.org/10.1038/378258a0.
78. Milosevic M M, Chen X, Cao W, Runge A F J, Franz Y et al. Ion implantation in silicon for trimming the operating wavelength of ring resonators. *IEEE J Sel Top Quant Electron* **24**, 8200107 (2018); http://doi.org/10.1109/JSTQE.2018.2799660.
79. Kawazoe T, Mueed M A, Ohtsu M. Highly efficient and broadband Si homojunction structured near-infrared light emitting diodes based on the phonon-assisted optical near-field process. *Appl Phys B* **104**, 747–754 (2011).
80. Kim J H, Kawazoe T, Ohtsu M. Optimization of dressed-photon—phonon-assisted annealing for fabricating GaP light-emitting diodes. *Appl Phys A* **121**, 1395–1401 (2015).
81. Yamaguchi M, Kawazoe T, Ohtsu M. Evaluating the coupling strength of electron–hole pairs and phonons in a 0.9 μm-wavelength silicon light emitting diode using dressed-photon-phonons. *Appl Phys A* **115**, 119–125 (2014).
82. Wada N, Tran M A, Kawazoe T, Ohtsu M. Measurement of multimode coherent phonons in nanometric spaces in a homojunction-structured silicon light emitting diode. *Appl Phys A* **115**, 113–118 (2014).
83. Ohtsu M, Kawazoe T. Principles and practices of Si light emitting diodes using dressed photons. *Adv Mater Lett* **10**, 860–867 (2019).
84. Tanaka Y, Kobayashi K. Optical near field dressed by localized and coherent phonons. *J Microsc* **229**, 228–232 (2008).
85. Kawazoe T, Nishioka K, Ohtsu M. Polarization control of an infrared silicon light-emitting diode by dressed photons and analyses of the spatial distribution of doped boron atoms. *Appl Phys A* **121**, 1409–1415 (2015).
86. Tran M A, Kawazoe T, Ohtsu M. Fabrication of a bulk silicon p-n homojunction-structured light-emitting diode showing visible electroluminescence at room temperature. *Appl Phys A* **115**, 105–111 (2014).
87. Yamaguchi M, Kawazoe T, Yatsui T, Ohtsu M. Spectral properties of a lateral p-n homojunction-structured visible silicon light-emitting diode fabricated by dressed-photon—phonon-assisted annealing. *Appl Phys A* **121**, 1389–1394 (2015).
88. Ohtsu M. *Silicon Light-Emitting Diodes and Lasers* (Springer, Heidelberg, 2016).
89. Kawazoe T, Ohtsu M, Akahane K, Yamamoto N. Si homojunction structured near-infrared laser based on a phonon-assisted process. *Appl Phys B* **107**, 659–663 (2012).
90. Kawazoe T. High power Silicon laser based on the dressed photon technology. In *Proceedings of 2017 International Conference on Solid State Devices and Materials* 413–414 (2017).
91. Ohtsu M, Ojima I, Sakuma H. Ch 1, Vol 62 in *Progress in Optics* (ed Visser T. Elsevier, 2019)
92. Ohtsu M. Ch 6 and Ch 8 in *Silicon Light-Emitting Diodes and Lasers* (Springer, Heidelberg, 2016).
93. Tate N, Kawazoe T, Nomura W, Ohtsu M. Current-induced giant polarization rotation using a ZnO single crystal doped with nitrogen ions. *Sci Rep* **5**, 12762 (2015).
94. Newton T D, Wigner E P. Localized states for elementary systems. *Rev Mod Phys* **21**, 400–406 (1949).
95. Ojima I. Micro-macro duality in quantum physics. Ch 12 in *Stochastic Analysis: Classical and Quantum-Perspectives of White Noise Theory* (ed T Hida. World Scientific, 2005).
96. Ojima I. Nakanishi-Lautrup, B-field, crossed product and duality. In *Research on Quantum Field Theory*, *RIMS Workshop* (2006).
97. Dell' Antonio G F. Support of a field in *p* space. *J Math Phys* **2**, 759–766 (1961).
98. Aharonov Y, Komar A, Susskind L. Superluminal behavior, causality, and instability. *Phys Rev* **182**, 1400–1403 (1969).
99. Yatsui T. Vol 5 in *Progress in Nanophotonics* (Springer, 2018).
100. Ohtsu M, Ojima I, Sakuma H. Ch 2, Vol 64 in *Progress in Optics* (ed Visser T D. Elsevier, 2019).

Competing interests

The author declares no competing financial interests.

[IV] PREPRINT DEPOSITORIES

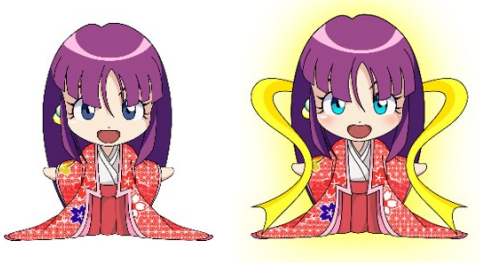

Nutation in energy transfer of dressed photons between nano-particles

M. Ohtsu[1] and T. Kawazoe[2]

[1]Research Origin for Dressed Photon,
3-13-19 Moriya-cho, Kanagawa-ku, Yokohama, Kanagawa 221-0022 Japan

[2]Tokyo Denki University,
5 Senju-Asahi-cho, Adachi-ku, Tokyo 120-8551, Japan
(Present affiliation: Nichia Corp. 13-19, 3, Moriya-Cho, Kanagawa-Ku, Yokohama-Shi, Kanagawa 221-0022 Japan)

Abstract

Experimental results on the temporal behavior of dressed photon (DP) energy transfer are presented. Nanometer-sized particles (NPs) of cubic CuCl crystals grown in a NaCl crystal were used as the sample for the experiments. By measuring the temporal variations of the photoluminescence (PL) intensities emitted from these NPs, unique characteristics of DP energy transfer were found. Namely, the PL intensities exhibited nutation that originated from the bidirectional DP energy transfer between the small and large NPs. The period of the nutation was 50 ps. The periodic variation of the PL intensity emitted from the small NP had a phase lag of $\pi/3$ behind that from the large NP. The duration of the forward DP energy transfer was longer than that of the backward transfer. The difference between these times resulted in temporal modulation of the PL intensities. The temporal variations exhibited additional pulsatory variations whose period was one-*fourth* the nutation period.

1. Introduction

A dressed photon (DP) is an off-shell quantum field created by the interactions among photons, electrons, and phonons in a nanometer-sized space [1-4]. During DP energy transfer between nanometer-sized particles (NPs), the energy is dissipated by transformation to the energies of propagating free photons. These energy transfer and dissipation processes have been used to detect the DP, and have been applied to realize innovative nanometer-sized optical devices, nanometer-resolution fabrication technologies, energy conversion devices, and so on [5,6].

The novel phenomena of size-dependent resonance and autonomy in the DP energy transfer have been experimentally observed [7]. Further experimental studies have identified that the spatio-temporal properties of these phenomena corresponded to the quantum walk (QW) process [8]. Based on this identification, novel studies on quantum probability theory have commenced recently [9].

This paper presents the results of experiments on the temporal behavior of DP energy transfer carried out in order to promote these studies, especially to establish theoretical models of the QW.

2. Experimental methods

This paper presents experimental results that correspond to the QW system in Fig. 1. Two semiconductor NPs played the roles of nodes 1 and 2. The DP, transferred between these NPs bidirectionally, played the role of a link. The light incident into and emitted from the NPs played the role of the input and output signals, respectively. The sample used for the experiments consisted of cubic NPs of CuCl crystals (volume density of $2\times10^{17}/\mathrm{cm}^3$) that were grown in a NaCl crystal (Fig. 2(a)). The average center-to-center distance between the adjacent NPs was 12 nm, which was estimated by assuming that the random spatial distribution of the grown NPs was a Weibull distribution.

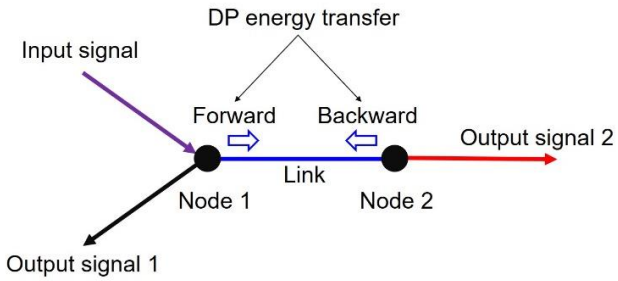

Fig. 1 The QW system to be experimentally realized in the present paper.

Two of the NPs in the NaCl crystal were used as nodes 1 and 2. As is schematically explained by Fig. 2(b), they were small and large cubic CuCl-NPs (NP_S and NP_L, respectively). Pulsed light (10 ps pulse width and 381 nm wavelength) was used as the input signal. For the output signals 1 and 2, photoluminescences (PLs) emitted from the excitons in NP_S and NP_L, respectively, were used. Quantum states of these excitons were identified by a set of three quantum numbers (1,1,1). The wavelengths of these PLs were 383 nm and 385 nm, respectively. The sample temperature was maintained at 80 K.

Two strategies, **(S1)** and **(S2),** were planned to experimentally realize the system of Fig. 1 by using the sample in Fig. 2(a):

(S1) For selective application of the input signal only to node 1:

As is schematically explained by Fig. 2(b), a pair of NPs, consisting of NP_S and NP_L, with $a_{S,eff}$: $a_{L,eff} = 1:\sqrt{2}$, was used. Here, $a_{S,eff}$ and $a_{L,eff}$ are the effective side lengths, representing the spatial extent of the quantum field of the exciton. The required length ratio was achieved by selectively using NP_S and NP_L of 3.9 nm (= $a_{S,eff}$) and 5.5 nm(= $a_{L,eff}$), respectively[1)]. Their center-to-center distance was 12 nm, estimated as described above.

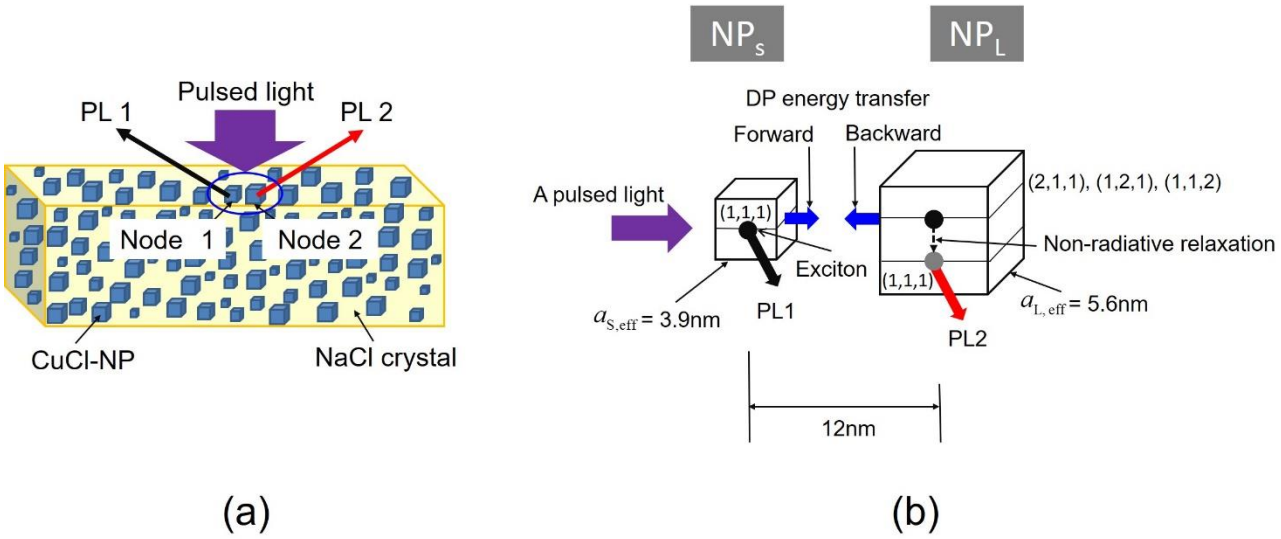

Fig. 2 The sample used for the experiments.

(a) Cubic NPs of CuCl crystals grown in a NaCl crystal. (b) Small and large cubic CuCl-NPs (NP_S and NP_L, respectively), used as nodes 1 and 2 in Fig. 1.

By irradiating the sample with pulsed light, an exciton was excited to the (1,1,1) state of NP_S. It should be noted that, because of the length ratio above, the energies of the triply degenerate states (2,1,1), (1,2,1), and (1,1,2) in NP_L were equal to that of the (1,1,1) state of NP_S. However, even under such resonant condition, the exciton could not be exited to these states because they are electric dipole-forbidden states with respect to propagating light. This indicated that the incident light was effective to excite the exciton only in NP_S, realizing selective application of the input signal to node 1.

1) Their geometrical side lengths were 4.6 nm (= a_S) and 6.3 nm (= a_L), respectively.

(S2) For distinguishing between output signals 1 and 2:

[Output signal 1]

The PL emitted from the exciton in the (1,1,1) state of NP_S was used as output signal 1. It should be noted that this exciton also creates a DP.

[Output signal 2]

{Creation} The energy of the DP, created by the exciton of the (1,1,1) state in NP_S, transferred to NP_L and excited the exciton to the triply degenerate states (2,1,1), (1,2,1), and (1,1,2). This excitation was possible because these states were electric-dipole allowed states with respect to the nanometer-sized DP. In other words, the long-wavelength approximation, popularly employed in conventional optical science, was violated by the DP. The exciton excited by the DP above emitted the PL. It also created the DP, and its energy transferred back to NP_S, resulting in bidirectional DP energy transfer between NP_S and NP_L. This transfer phenomenon has been called nutation.

{Measurement} It might be possible to use the PL emitted from NP_L as output signal 2. However, its wavelength was equal to that of output signal 1 due to the resonance condition above. Therefore, output signal 2 could not be distinguished from output signal 1, and thus, it could not be selectively measured. For selective measurement, a rapid non-radiative relaxation, specific to the CuCl-NPs, was used by de-exciting the exciton from the triply degenerate states to the state (1,1,1), allowing subsequent emission of the PL. Its wavelength (385 nm) was longer than that (383 nm) of output signal 1 due to the energy dissipation by the non-radiative radiation. Although the magnitude of this dissipation was as low as 1/100 times the photon energies of output signal 1, it was sufficiently large to allow output signals 1 and 2 to be distinguished. Thus, this PL could be used as output signal 2.

As a result of the planned strategies **(S1)** and **(S2)** above, the realized system of Fig. 2(b) exhibited the following differences **(D1)** – **(D3)** from the system of Fig.1. They were:

(D1) Node 2 was split into three because of the triple degeneracy of the exciton state in NP_L.

(D2) A part of the DP energy dissipated at node 2 due to the non-radiative relaxation of the exciton in NP_L .

(D3) Since the effective side lengths ($a_{S,\mathrm{eff}}$ and $a_{L,\mathrm{eff}}$) of NP_S and NP_L were different from each other, the magnitudes of the created DP energies and their spatial extents, represented by a Yukawa-type function $V(r)$ ($V(r) \propto \exp(-r/a)/r$, where a is the size of the NP), were different. Thus, their DP energy transfer times, being inversely proportional to $V(r)$, were different. That is, since $a_{S,\mathrm{eff}} < a_{L,\mathrm{eff}}$, the transfer time of the forward path of the link (from NP_S to NP_L) was longer than that of the backward path (from NP_L to NP_S).

By noting the differences **(D1) - (D3)**, Fig. 1 was revised to Fig. 3(a). However, for a basic discussion of the QW process, it should be possible to approximate Fig. 3(a) by the simpler system of Fig. 3(b) because of the sufficiently low magnitude of the energy dissipation in **(D2)**.

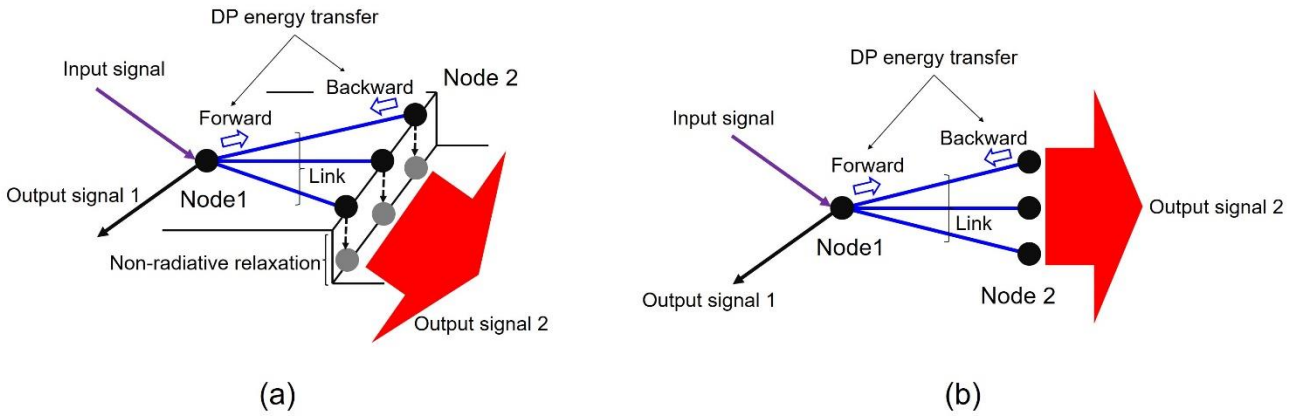

Fig. 3 The revised QW system.

3. Experimental results and discussions

The black and red curves in Fig. 4 represent the measured temporal variations of the outputs 1 and 2, respectively. They were the PL intensities emitted from the (1, 1, 1) states of the excitons in NP_S and NP_L. They exhibited monotonic decreases with time, which originated from the conventional radiative relaxation. In the time span 0–500 ps immediately after applying the pulsed input signal, the temporal decrease was attributed to the QW process and was fitted by $\exp(-t)$ [9]. The subsequent decrease in the time span from 500 ps to 4 ns was slower and was fitted by $\exp\left(-\sqrt{t}\right)$, which was attributed to the random walk process. Since the present paper focuses on the phenomena relevant to the QW process, especially on the nutation of the DP energy transfer, experimental results acquired in the time span 0–500 ps were analyzed. For these analyses, Fig. 5 was acquired by expanding the horizontal axis of Fig. 4.

The black and red curves in Fig. 5 indicate the temporal variations of the DP energy transfer of the forward and backward paths, respectively. Their pulsatory variations represent nutation with a period of 50 ps. This value of the period was compatible with the period (40 ps) that was estimated from the relation between the center-to-center distance (10 nm) and the transferred DP energy (1×10^{-4} eV) [10].

Figure 5 indicates the following unique characteristics **(C1)**–**(C3)** of DP energy transfer:

(C1) The phases of the pulsatory variations of the two curves are different from each other: In order to estimate the magnitude of this difference, the Fourier components of the 50 ps-period were extracted from these curves and are shown in Fig. 6. The black and red curves in this figure represent nutation, and the sinusoidal variation of the black curve had a phase lag of $\pi/3$ behind that of the red curve. This lag originated from the triply degenerate states of the exciton in NP_L (**(D1)** in Section 2). That is, the *triple* degeneracy caused a lag of one-*third* of π [2]. In other words,

within one-*third* of the DP energy transfer time of the backward path, the (1,1,1) state in NP_S was promptly occupied by the exciton that was initially created in the triply degenerate states in NP_L.

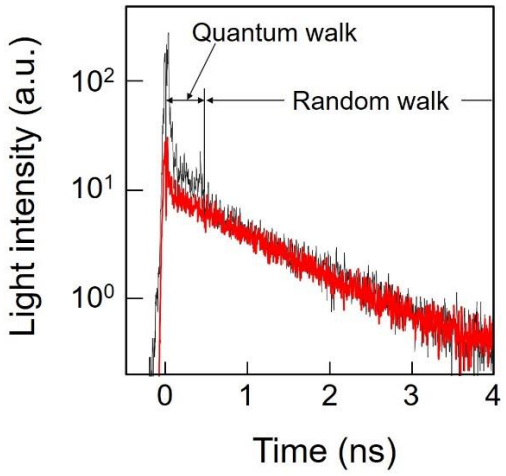

Fig. 4 The measured temporal variations of the two PLs.
The black and red curves represent outputs 1 and 2, respectively.

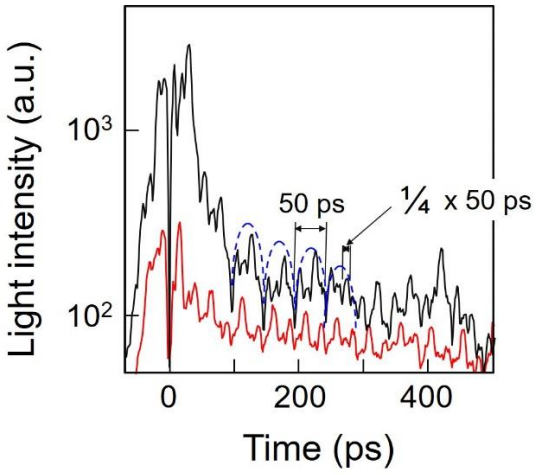

Fig. 5 The measured temporal variations of the two outputs.
They are the experimental results in the time span as short as 0–500 ps in Fig. 4

Since the DP energy was bidirectionally transferred between NP_S and NP_L, the profiles of the two curves in Fig. 6 should be anti-correlated, and thus, their phase difference should be as large as π. However, the phase lag was found to be $\pi/3$. The reason for this discrepancy was considered to be as follows: Since a large number of CuCl-NPs were buried in the NaCl crystal, the DP energies could transfer not only between NP_S and NP_L but also between multiple NP_Ls (or between multiple NP_Ss). Furthermore, it was confirmed by analyzing the measured absorption spectral profile of the sample that the number of NP_Ls was larger than the number of NP_Ss. This

indicated that the DP energy transfer between neighboring NP_Ls could contribute to the phase difference between the two curves. However, since the phase of the DP energy transfer between these NP_Ls is random, the anti-correlation characteristics did not clearly appear, and thus, the phase difference was maintained as small as $\pi/3$.

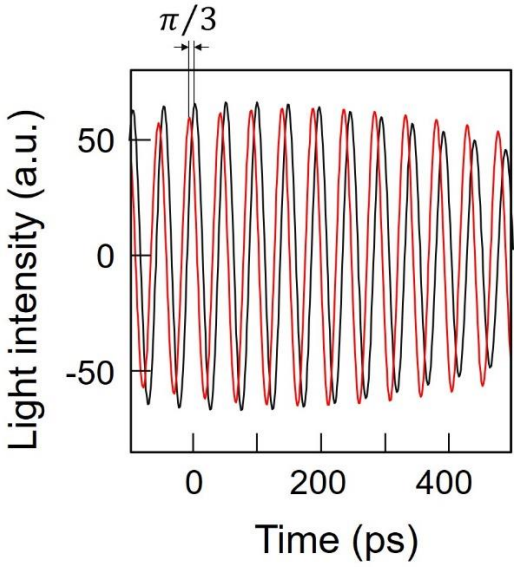

Fig. 6 The measured temporal variations of the two outputs.
They are the Fourier components of the 50 ps-period, extracted from the two curves in Fig. 5.

---

2) This kind of phase lag has never been observed when a large number of NPs is used as the macroscopic material system for inducing conventional optical phenomena. This is because the NPs in this system have been approximated as a coupled quantum state having a singlet state of the exciton.

(C2) The pulsatory variations of the PL intensities were modulated (blue broken curve in Fig. 1): This was attributed to the fact that the transfer time along the forward path was longer than that along the backward path (**(D3)** in Section 2).

(C3) Additional pulsatory variations existed whose period was one-*fourth* that of the nutation: Such a short period was attributed to the fact that, among the *four* energy levels (the (1,1,1) state level in NP_S and the triply degenerate states in NP_L) relevant to the bidirectional DP energy transfer, only the (1,1,1) state in NP_S was initially occupied by an exciton at the commencement of the nutation.

Figure 7 shows the Fourier spectral profiles of the two curves in Fig. 5. The spectral peak (A) at 20 GHz corresponded to the nutation period of 50 ps. Because the profiles of the measured pulsatory variations deviated from sinusoidal curves, the spectral peak (B) of the second-order higher harmonic can be seen. The absence of the third-order spectral peak was attributed to the modulation in the PL intensity mentioned in **(C2)**. In other words, the odd-order higher harmonics

were missing due to the difference between the forward and backward transfer times. The spectral peak (C) was attributed to the superposition of the fourth-order higher harmonic and the additional pulsatory variations whose period was one-*fourth*, as mentioned in **(C3)**.

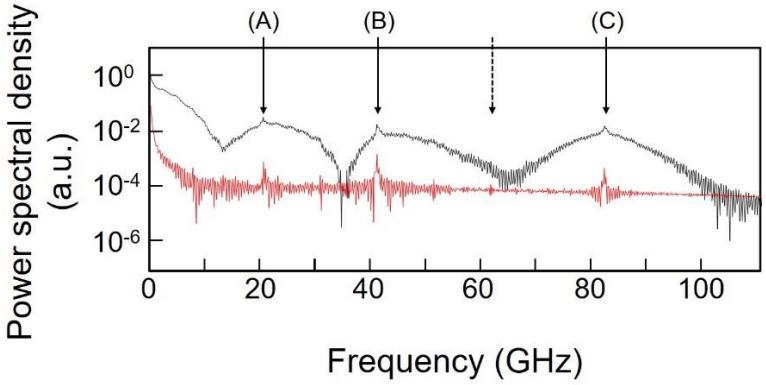

Fig. 7 The Fourier spectral profiles of the two curves in Fig. 5.

4. Summary

This paper presented experimental results on the temporal behavior of DP energy transfer in order to promote studies on the QW process. Cubic NPs of CuCl crystals grown in a NaCl crystal were used as the sample for the experiments. By measuring the temporal variations of the PL intensities emitted from these NPs, unique characteristics of DP energy transfer were found. They were:

[1] The PL intensities exhibited nutation that originated from the bidirectional DP energy transfer between the small and large NPs. The period of the nutation was 50 ps.

[2] The periodic variation of PL intensity emitted from the small NP had a phase lag of $\pi/3$ behind that from the large NP. This lag originated from the triple degenerate states of the exciton in the large NP.

[3] The duration of the forward DP energy transfer was longer than that of the backward transfer. This was attributed to the difference in the magnitudes of the created DP energies localized at the small and large NPs. This difference temporally modulated the PL intensities.

[4] The spectral profile exhibited additional pulsatory variations whose period was one-*fourth* the nutation period because the (1,1,1) state in the small NP was initially occupied by an exciton at the commencement of the nutation.

Acknowledgements

The authors thank Profs. H. Saigo (Nagahama Inst. Bio-Sci. and Technol.) and E. Segawa (Yokoyama Natnl. Univ.) for their valuable comments and discussions on the quantum walk process.

References

[1] M. Ohtsu, “History, current development, and future directions of near-field optical science,” Opto-Electronic Advances, Vol.3, No.3 (2020)190046.

[2] M. Ohtsu, *Dressed Photons* (Springer, Heidelberg, 2014) pp.1-36.

[3] M. Ohtsu, “Progress in off-shell science in analyzing light–matter interactions for creating dressed photons,” *Off-shell Archive* (April, 2020). OffShell: 2004.R.001.v1. **DOI** 10.14939/2004R.001.v1, http://offshell.rodrep.org/?p=268

[4] M. Ohtsu, I. Ojima, and H. Sakuma, “Dressed Photon as an Off-Shell Quantum Field,” Prog. in Opt. **64** (ed. by T.D. Visser) (Elsevier, Amsterdam, 2019) pp.45-97.

[5] M. Ohtsu, *Dressed Photons* (Springer, Heidelberg, 2014) pp.89-214.

[6] M. Ohtsu, Silicon Light-Emitting Diodes and Lasers, (Springer, Heidelberg, 2016) pp.1-138.

[7] M. Ohtsu, Historical Review of Dressed Photons: Experimental Progress and Required Theories, Prog. in Nanophotonics 5 (ed. by T. Yatsui) (Springer, Heidelberg,2018) pp.1-51.

[8] M. Ohtsu, T. Kawazoe, and H. Saigo,“Spatial and Temporal Evolution of Dressed Photon Energy Transfer,” *Off-shell Archive* (October, 2017). OffShell: 1710.R.001.v1. **DOI** 10.14939/ 1710R.001.v1 http://offshell.rodrep.org/?p=79

[9] H. Saigo, Quantum Probability for Dressed Photons: The Arcsine Law in Nanophotonics, Prog. in Nanophotonics 5 (ed. by T. Yatsui) (Springer, Heidelberg,2018) pp.79-106.

[10] T.Kawazoe, K. Kobayashi, J. Lim, Y. Narita, and M. Ohtsu, "Direct Observation of Optically Forbidden Energy Transfer between CuCl Quantum Cubes via Near-Field Optical Spectroscopy,” Phys. Rev. Lett., vol.88, no.6 (2002) 067404-1～067404-4

Past, present, and future studies on the longitudinal electric field components of light

M. Ohtsu

Research Origin for Dressed Photon,

3-13-19 Moriya-cho, Kanagawa-ku, Yokohama, Kanagawa 221-0022 Japan

Abstract

Unlike a planar lightwave, a tightly focused light beam has longitudinal components of the electric field (LCEF) that are polarized along the propagation direction. This article reviews the past and present status of theoretical and experimental studies on the LCEF. By pointing out that the LCEF is an essential constituent element of the dressed photon (DP), the future outlook of these studies for advancing DP science and its applications is discussed.

1. Introduction

Elementary textbooks on optics study planar lightwaves of infinitely large cross-section that propagate through space in a vacuum or in a macroscopic material [1]. In this picture, light has been recognized as a transverse wave composed of transverse electric fields that are polarized in a plane normal to its propagation direction.

In contrast, a typical laser light beam has a finite cross-sectional size. Furthermore, it can be decreased to a size as small as the optical wavelength when it is focused by a lens with a high numerical aperture (NA). In such a tightly focused situation, the light beam around the focal plane is no longer a planar lightwave, and thus, it is not a transverse wave either. Instead, it can have longitudinal components of the electric field (LCEF) that are polarized along the propagation direction.

Studies on the LCEF had already commenced before the advent of lasers. Subsequently, the concept of the LCEF was applied to microscopy, spectroscopy, and material processing technology, bringing about novel experimental results that are impossible to achieve when only the transverse components of the electric field are used. Theoretical analyses of the interaction between the LCEF and matter in a microscopic space are indispensable for understanding these experimental results. However, such analyses have not been actively carried out. In fact, the gauge for the vector potential for describing the LCEF has not yet been adequately determined. Furthermore, even though a high-intensity LCEF is required to acquire experimental results in a reproducible manner, this requirement has not been met because of the technical difficulties involved in fabricating a high-NA

lens. A further difficulty was that experimental methods for suppressing the transverse field components have not yet been developed.

Even with these difficulties, theoretical and experimental studies on the generation and application of the LCEF are continuously progressing, and they have given some hints for achieving advances in optical science. To realize these advances, it should be pointed out that off-shell science has elucidated that the LCEF is an essential constituent element of the dressed photon (DP) [2]. The DP is a quantum field created in a complex system composed of photons and electrons (or excitons) in a nanometer-sized space [3]. The fruits of this science have been applied to the development of generic technologies (for example, nanometer-sized optical devices, information processing systems using these devices, nano-fabrication technology, and energy conversion technology) which have realized disruptive innovations.

Section 2 of this article reviews the past and present status of studies on the LCEF. In Section 3, the future outlook of these studies for advancing DP science and its applications is discussed. Section 4 presents concluding remarks.

2. Past and present

Even before the advent of lasers, the behavior of the LCEF had been studied by theoretically analyzing the structure of light near the focus of an aplanatic system [4]. Subsequent studies found that this behavior in the focal plane showed a resemblance to the well-known picture of the lines of force emanated from an oscillating electric dipole [5]. In particular, along the direction of the azimuthal line, $\psi=0$, the transverse electric field was found to be strictly zero, indicating that the electric field was purely longitudinal. This implied the possibility of generating the LCEF while suppressing transverse components. Furthermore, it was expected that an LCEF as high as 10^5 V/cm could be attained by focusing a laser beam, and this could be used for accelerating charged particles.

The exact Maxwellian formulation for the LCEF was developed by using the angular spectrum method in order to derive the Maxwellian stress tensor of the nonlinear force [6]. The results were compared with experimentally acquired data on the energy of electrons emitted from a laser-irradiated tenuous plasma. The results agreed with each other, thus demonstrating the polarization independence of the energy if all components of the Gaussian beam, including the LCEF, are used to constitute the Maxwellian stress tensor. From this demonstration, it was confirmed that the LCEF significantly contributed to the light–matter interaction even though the intensity of the LCEF was low compared with its transverse counterparts. Encouraged by this confirmation, researchers developed interferometric techniques to convert a linearly polarized laser beam into a radially polarized one with uniform azimuthal intensity. As a result, it was demonstrated that the radially polarized focused beam had sufficiently high-intensity LCEF for accelerating charged particles [7].

The LCEF has been applied to spectroscopy of a single fluorescent molecule [8]. In that

study, the molecule was excited by a focused laser beam, and the orientation of the absorption dipole moment was determined by mapping the spatial distribution of the electric field components. As a result, it was found that an annular illumination geometry strongly enhanced the LCEF in the vicinity of a planar dielectric/air interface, where the intensity became as high as those of other components. The method of geometrical optics was used to qualitatively analyze the spatial features of the enhanced LCEF.

The method of vector-wave optics was used for detailed analyses of the spatial features of the light field in an image space for application to fluorescence correlation spectroscopy and single-molecule fluorescence detection with a confocal microscope [9]. Furthermore, the rotational dynamics of a fluorescent single molecule on a material surface were investigated by polarization spectroscopy, which succeeded in evaluating the intensity of the LCEF at the focal plane [10]. With the aim of advancing these applications, radially polarized cylindrical-vector beams were found to be advantageous for generating a high-intensity LCEF near the focal plane [11]. Furthermore, it was found that, as its cross-sectional size decreased, the intensity of the LCEF increased and finally exceeded that of the transverse field.

In order to confirm the contribution of the LCEF to light–matter interactions, spectroscopic measurements on a single trapped $^{40}Ca^{+}$ ion were carried out [12]. For triggering the Zeeman-split $^{40}Ca^{+}$ quadrupole $S_{1/2}$-$D_{5/2}$ transition, the $^{40}Ca^{+}$ ion was illuminated with twisted light having opposite orbital and spin angular momenta. The acquired experimental data were compared with a theoretical model in which the LCEF was taken into account. The results agreed with each other, thus confirming the significant contribution of the LCEF to the light–matter interaction. A chip-scale sensor was recently developed for experimentally analyzing the orbital angular momenta of this type of light [13,14].

The interaction between tightly focused ultrashort optical pulses and transparent media was used to imprint their local polarizations in the focal region [15]. By referring to the experimental results of this imprinting, complex polarization states, including the LCEF, were investigated. As a result, it was confirmed that a small crater on the fused silica surface was formed by the contribution from the LCEF, which demonstrated a novel material ablation mechanism due to the LCEF.

As reviewed above, in conjunction with experimental studies, theoretical studies of tightly focused light beams have demonstrated the importance of taking the LCEF into account for analyzing light–matter interactions. It has also been demonstrated that the LCEF can even dominate the interaction with matter. Following these demonstrations, there is currently substantial interest in structured light, that is, customized light fields generated to suit specific needs in applications of the LCEF [16,17].

It should be pointed out that reports on theoretical and experimental studies of the LCEF have not been found in the field of quantum electrodynamics. Although the LCEF has been briefly described in relevant articles [18,19], the vector potentials and interaction Hamiltonian have been discussed only by using conventional Coulomb and Lorenz gauges.

3. Future outlook

This section presents some comments regarding references [6], [8-10], [12], and [13]. Based on these comments, the future outlook of each of these studies for advancing DP science and its applications is discussed.

<Reference [6]>

[Comments]

From a theoretical basis derived by using the angular spectrum method, reference [6] claimed that the LCEF significantly contributed to the light–matter interaction. It should be noted that this method was based on a concept from on-shell science called linear causality. This reference also claimed that, as a logical consequence derived using Maxwell's equations, the intensity of the LCEF increased with decreasing cross-sectional size of the light. Figure 1 briefly explains the relation between the cross-sectional size and the intensity of the LCEF. This figure shows that the cross-sectional size discussed in this reference (also in [4,5,7-17]) was larger than the wavelength of the light. In other words, it was a discussion of a situation below the diffraction limit, which means that the LCEF was investigated using the conventional on-shell scientific method. This reference did not describe the reason why the nonlinear ponderomotive force induced the polarization-independency of the electron energy even though the intensity of the LCEF was low. Furthermore, this reference did not discuss the light–matter (electron) interaction in a microscopic space.

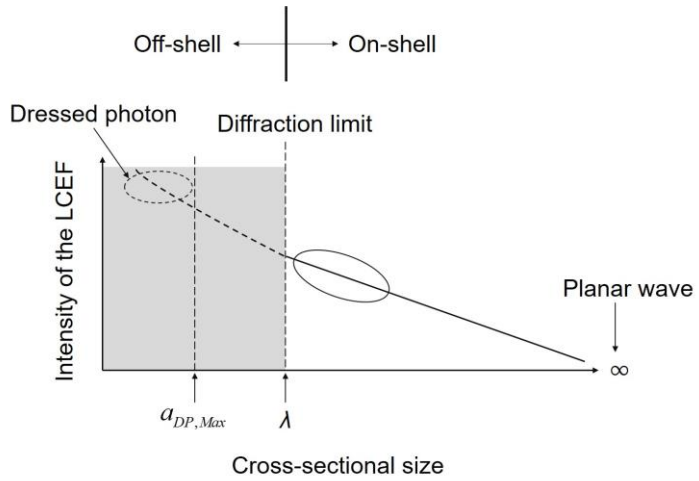

Fig.1 Relation between the cross-sectional size of light and the intensity of the LCEF.

λ is the wavelength of light. $a_{DP,Max}$ is the maximum size (50-70 nm) of the DP [2,3]. The solid ellipse represents the area of the relation that was dealt with in references [4-17]. The broken ellipse is for the DP.

[Outlook]
Figure 1 clearly shows that this reference did not deal with the DP because its maximum size, $a_{DP,Max}$ (=50–70 nm), was much smaller than the wavelength of the light [2,3]. Off-shell science is required to deal with the LCEF in the DP. It is expected that the magnitude of the light–matter interaction originating from the DP increases due to its small cross-sectional size. Off-shell science is also required to describe such a large magnitude.

<References [8-10]>
[Comments]
References [8-10] described that the LCEF generated in the near-field regions at the surfaces of high-NA lenses were applied to microscopy and spectroscopy. Thus, these applications may be called near field optics. However, even though their resolutions were improved, they were still limited by the diffraction of light. That is, these applications still stayed within the region of on-shell science.
[Outlook]
Even though the behaviors of the LCEF discussed in these references were governed by diffraction, the results gave some hints for achieving advances in off-shell science. Progress in off-shell science is expected by taking advantage of these hints.

<Reference [12]>
[Comments]
Reference [12] used the vector potential to describe the light–matter interaction. However, it was based on the Lorenz gauge, which is commonly used for the transverse wave. Furthermore, this reference claimed that the quadrupole transition matrix elements vanished at first order in the coordinates. However, this claim is true only when the long-wavelength approximation is valid. This reference also discussed the interaction between twisted light and a single trapped ion (a simple specimen for spectroscopy) by using the orbital and spin angular momenta. It should be noted that these discussions were based on on-shell science because they relied on these definitely identified momenta.
[Outlook]
In the case where the DP is involved in a light–matter interaction in microscopic space, the long-wavelength approximation turns out to be invalid due to the small size of the DP, beyond the diffraction limit. Thus, the quadrupole transition matrix elements can have non-zero values [2,3]. Progress in off-shell science is required to investigate the novel phenomena occurring under this invalid condition. Furthermore, in the case where the DP is involved in the interaction above, the momenta cannot be defined due to the small size of the DP, beyond the diffraction limit. Under such undefined conditions, violation of the selection rules and allowance of the electric dipole forbidden transition can be observed [2,3]. Off-shell science is required also for describing the phenomena

occurring under these conditions.

<Reference [13]>

[Comments]

Reference [13] used light with a wavelength shorter than the absorption-edge wavelength of the relevant matter. This is a method popularly used in on-shell science.

[Outlook]

In the case where the DP is used for imprinting, a technical advantage is that longer-wavelength light can also be used as a source for creating the DP [2,3]. Off-shell science is required to describe the physical processes in such DP-imprinting.

4. Concluding remarks

Even though the mechanism of generating the LCEF and the contribution of the LCEF to the light–matter interactions have been elucidated by modern optical science, the claim that "light is a transverse wave" continues to be seen even now. It is seen even in advanced textbooks on optics. A plausible reason for such a claim is that studies on the microscopic nature of light–matter interactions have not yet been fully developed. Further progress of optical science is required to advance these studies. By noting that the LCEF is an essential constituent element of the DP and that the magnitude of the DP–electron interaction can be very large in a nanometer-size space, off-shell scientific studies on the DP may open a new route to elucidate the intrinsic nature of the LCEF.

Acknowledgements

The author thanks Dr. H. Sakuma (Research Origin for Dressed Photon) for his valuable comments on the contribution of the LCEF to the DP.

References

[1] M. Born and E. Wolf, *Principles of Optics*, the 4th edition, (Pergamon Press, Oxford, 1970) p.52.

[2] H. Sakuma, I. Ojima, M. Ohtsu, and H. Ochiai, "Off-Shell Quantum Fields to Connect Dressed Photons with Cosmology," *Symmetry*, **12**, 1244 (2020).

[3] M. Ohtsu, "History, current development, and future directions of near-field optical science," *Opto-Electronic Advances*, **3**, 190046 (2020).

[4] B. Richards and E. Wolf, "Electromagnetic diffraction in optical systems. ii. Structure of the image field in an aplanatic system, " *Proc. Royal Soc*. A **253**, 358-379 (1959).

[5] A. Boivin and E. Wolf, "Electromagnetic field in the neighborhood of the focus of a coherent beam," Phys. Rev. B **138**, 1561-1565 (1965).

[6] C. Cicchitelli, H. Hora, and R. Postle, "Longitudinal field components for laser beam in vacuum," *Phys. Rev.* A **41**,

3727-3732 (1990) .

[7] S.C. Tidwell, D.H. Ford, and W.D. Kimura, "Generating radially polarized beams interferometrically," *Appl. Opt.* **29**, 2234-2239 (1990).

[8] B. Sick, B. Hecht, and L. Novotny, "Orientational imaging of single molecules by annular illumination," *Phys. Rev. Lett*. **85**, 4482-4485 (2000).

[9] J. Enderlein, "Theoretical study of detection of a dipole emitter through an objective with high numerical aperture," *Opt. Lett*. **25**, 634-636 (2000).

[10] T. Ha, T.A. Laurence, D.S. Chemla, and S. Weiss, "Polarization spectroscopy of single fluorescent molecules, " *J. Phys. Chem.* B **103**, 6839-6850 (1999).

[11] K.S. Youngworth and T.G. Brown, "Focusing of high numerical aperture cylindrical vector beams," *Opt. Express* **7**, 77-87 (2000).

[12] G.F. Quinteiro, F. Schmidt-Kaler, and C.T. Schmiegelow, "Twisted-light-ion interaction: The role of longitudinal fields," *Phys. Rev. Lett.* 119, 253203 (2017).

[13] H.M. Hill, "Chip-scale sensor detects light's orbital angular momentum," *Phys. Today*, **73** (2020) 18-20.

[14] Z. Ji, W. Liu, S. Krylyuk, X. Fan, Z. Zhang, A. Pan, L. Feng, A. Davydov, and R. Agarwal, "Photocurrent detection of the orbital angular momentum of light," *Science*, **368** (2020) pp. 763-767.

[15] C. Hnatovsky, V. Shvedov, W. Krolikowski, and A. Rode, "Revealing local field structure of focused ultrashort pulses, " *Phys. Rev. Lett.* 106, 123901 (2011).

[16] F. Maucher, S. Skupin, S.A. Gardiner, and I.G. Hughes, "Shaping the longitudinal electric field component of light," *Proc. SPIC 10935, Complex Light and Optical Forces XIII*, 193502 (1 March 2019); DOI: 10.1117/12/2512112

[17] A. Forbes, "Structured light," *Optics and Photonics News*, June 2020, 24-31.

[18] C. Cohen-Tannoudji, J. Dupont-Roc, G. Grynberg, *Photons and Atoms*, John Wiley & Sons, New York, 1989.

[19] C. Cohen-Tannoudji, J. Dupont-Roc, G. Grynberg, *Atom-Photon Interactions*, John Wiley & Sons, New York, 1998.

Errata: Route to Off-Shell Science

M. Ohtsu

Research Origin for Dressed Photon,

3-13-19 Moriya-cho, Kanagawa-ku, Yokohama, Kanagawa 221-0022 Japan

References [28], [29], and [31] of [Section 6] in *Off-shell Archive* (June, 2020), OffShell: 2006R.001.v1. **DOI**: 10.14939/2006R.001.v1. http://offshell.rodrep.org/?p=283 should be corrected as

[28] H. Tanaka, T. Kawazoe, and M. Ohtsu, "Large scale pn homojunction infrared Si laser for a high optical output power," *Abstract of the 63st JSAP Spring Meeting*, March 2016, Tokyo, Japan, paper number 19a-S622-8.

[29] H. Tanaka, T. Kawazoe, M. Ohtsu, K. Akahane, and N. Yamamoto, "A luminescence spectrum of a broad area Si laser for a high optical output power," *Abstract of the 76th JSAP Autumn Meeting*, September 2015, Nagoya, Japan, paper number 16p-2G-8.

[31] T. Kawazoe, S. Sugiura, and M. Ohtsu, "Fabrication of a high power homojunctin silicon laser," *Abstract of the 64th JSAP Spring Meeting*, March 2017, Yokoyama, Japan, paper number 15a-F202-9.

Route to Off-Shell Science

M. Ohtsu

Research Origin for Dressed Photon,
3-13-19 Moriya-cho, Kanagawa-ku, Yokohama, Kanagawa 221-0022 Japan

Abstract

This article reviews the experimental and theoretical studies under development and shows the route that should be taken to establish off-shell science in the future. Section 1 reviews the past and present of the science and technology of the DP. It presents the reasons why the off-shell scientific theory is required. As the bases of these reasons, fifteen experimentally observed unique phenomena that originate from the DP are presented (their details will be reviewed in Sections 2–6). Section 2 reviews the nature of the DP by presenting experimental results. Theoretical results describing them are also presented. However, it should be pointed out that these theories are no more than urgent theoretical solutions based on on-shell scientific methods. Sections 3–5 review a variety of disruptive innovations realized by using DPs: nano-optical devices (Section 3), nano-fabrication technology (Section 4), and optical energy conversion technology (Section 5). Section 6 reviews light-emitting diodes, lasers, and polarization rotators whose operating principles are based on the nature of the DP. Finally, Section 7 reviews the theoretical approaches to off-shell science. They are theories based on spatio-temporal vortex hydrodynamics, quantum probability, quantum walk, quantum measurement, and micro-macro duality. Appendix A reviews the results of numerical simulations for the experimental results in Sections 5 and 6. They rely on statistical mechanics and complex-systems science to derive urgent solutions. The problems with these on-shell science-based simulations are presented. Appendix B provides a supplementary explanation of the theory based on spatio-temporal vortex hydrodynamics reviewed in Section 7.

1 History, current developments, and problems

The relatively new optical science of dressed photons (DPs) has seen rapid progress recently. The DP is a quantum field created in a complex system composed of photons and electrons (or excitons) in a nanometer-sized particle (NP). The fruits of this science have been applied to develop generic technologies (for example, nanometer-sized optical devices, information processing systems using these devices, nano-fabrication technology, and energy conversion technology) to realize disruptive innovations. Furthermore, studies on off-shell science have commenced. Off-shell science is a novel

optical science including studies on the DP. The origin of this science can be found in near-field optics [1]. Studies on near-field optics started with the aim of achieving disruptive innovations in optical science, especially in optical microscopy. Basic studies exploring the nature of the optical near field (ONF) were steadily continued, and near-field optics was reincarnated as a novel science of the DP. This science involves the study of light-matter interactions in a nanometer-sized space and explores novel applications that are contrary to those in conventional optical science and technology.

1.1 Past and present

To start a review on the past and present of the optical science of DPs, first, the principles of creating and detecting the ONF should be explained: Scattered light is created when a nanometer-sized material (NP1) is illuminated by light (Fig.1.1(a)). It should be noted that another form of electromagnetic field is also created in NP1 or on its surface. This field is called the ONF. The ONF is localized on NP1, and its spatial extent (size) is equivalent to the size of NP1. The ONF cannot be detected by a conventional photodetector installed far from NP1 because it does not propagate to the far field. To measure it, a second nanometer-sized material (NP2) is inserted into the ONF (Fig.1.1(b)). The ONF is disturbed by NP2 and is converted to scattered light that propagates to the far field, and is thus measured by a photodetector.

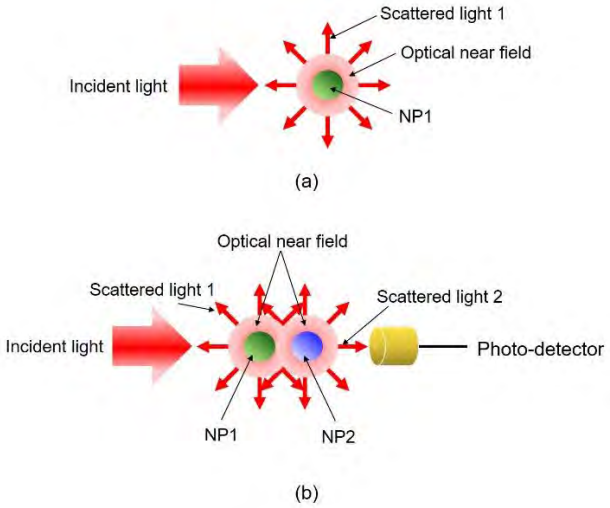

Fig.1.1 Creation (a) and measurement (b) of the optical near field.

Since the size of the ONF is equivalent to the size of NP1, it is expected that one can use the ONF to break through the diffraction limit which determines the spatial resolution in optical microscopy. In such a system, the ONF on NP1 works as a light

source for acquiring an optical microscope image of NP2. Based on this expectation, research on near-field optics was started with the aim of realizing this breakthrough, and a great deal of effort was made to create an ONF whose size Δx is much smaller than the wavelength λ of light ($\Delta x << \lambda$).

Since conventional optical theories were used in the early studies on near-field optics, the momentum p of the electromagnetic field has been treated as a definite quantity even though it is accompanied by a small uncertainty Δp due to quantum fluctuations. However, it should be pointed out that Heisenberg's uncertainty principle $\Delta p \cdot \Delta x \geq h/2\pi$ (, where h is Planck's constant) indicates a large uncertainty Δp ($\Delta p >> p$) because of the relation $\Delta x << \lambda$ above.

Modern studies are treating the ONF as a quantum field with a large energy uncertainty ΔE as well as a large Δp. In particular, by examining the light-matter interactions in nanometer-sized spaces, a variety of novel phenomena that are contrary to those in conventional optical phenomena have been discovered. That is to say, near-field optics was reincarnated as a novel optical science, and the ONF was renamed the DP.

In the studies above, since the ONF and relevant phenomena have been discussed in the framework of conventional wave-optics, the electromagnetic origin of the ONF, and especially the origin of the light-matter interactions in nanometer-sized space, have remained unrevealed. However, a salvation was that quantum theoretical studies were started as a first step in revealing the nature of these interactions [2,3].

Although near-field optics had succeeded in breaking through the diffraction limit by the 1990s, an essential problem was that the image-acquiring process in an ONF microscope disturbed the electron energies in the specimen. This is because the image is acquired by using the near-field optical interaction between the tip of the fiber probe and the specimen (Section 1.2.1). In other words, NP1 (the tip of the fiber probe) and NP2 (the specimen) are not independent of each other but are combined via the near-field optical interaction. Thus, even though a high spatial resolution beyond the diffraction limit was realized, the problem was that the profile of the acquired image did not have a direct correlation with that of a conventional optical microscopic image (Section 2.2.1). On the whole, the classical studies of the ONF did not give any clear answers to the essential questions, "What is the origin of the near-field optical interaction?" and "What kind of optical scientific revolution could near-field optics have made?" By recognizing that these questions had been neglected, the application of the ONF to microscopy, i.e., the study of near-field optics in the classical period, effectively came to an end.

However, even after this end, basic studies on the concepts and principles of the ONF were steadily continued. In relation to these studies, experiments on controlling atomic motion with high spatial resolution were carried out in a high vacuum [4]. Thanks to these continuous studies, a modern period of studies has started via transient studies named nano-optics or nanophotonics [5,6]. As a result, novel optical science and technology, based on the DP, have emerged as the reincarnation of classical near-field optics.

From the current studies of the DP as the reincarnation of classical near-field optics, novel phenomena that are contrary to those accepted in conventional optical science have been found. In order to review the current developments in studies on the DP, five common views that have been accepted for a long time in conventional optical science are listed here:

[a] Light is a propagating wave that fills a space. Its spatial extent (size) is much larger than its wavelength.

[b] Light cannot be used for imaging and fabrication of sub-wavelength sized materials. Furthermore, it cannot be used for assembling and operating sub-wavelength sized optical devices.

[c] For optical excitation of an electron, the photon energy must be equal to or higher than the energy difference between the relevant two electronic energy levels.

[d] An electron cannot be optically excited if the transition between the two electronic energy levels is electric-dipole forbidden.

[e] Crystalline silicon has a very low light emission efficiency, and thus, it is unsuitable for use as an active medium for light emitting devices.

The origin of these common views is attributed to the dispersion relation of the photon, which definitely fixes the relation between energy E and momentum p. In the case where light propagates in a vacuum, the dispersion relation is linear ($E=cp$, where c is the speed of light). By noting that momentum is a three-dimensional vector, this relation is geometrically represented by a circular cone. In the case of propagation in a material, this relation is geometrically represented by a paraboloid. This circular cone and paraboloid have been called the mass-shell (Fig.1.2), and thus, propagating light is considered to be an electromagnetic field in the on-shell state ("on-shell field" for short) because it is on the mass-shell. Even though the quantum fluctuations of the light have to be taken into account, conventional optical science has treated light in the on-shell state. Thus, this science can be called on-shell science. The common views **[a]-[e]** above are for light in the on-shell state, and they have become accepted in on-shell science.

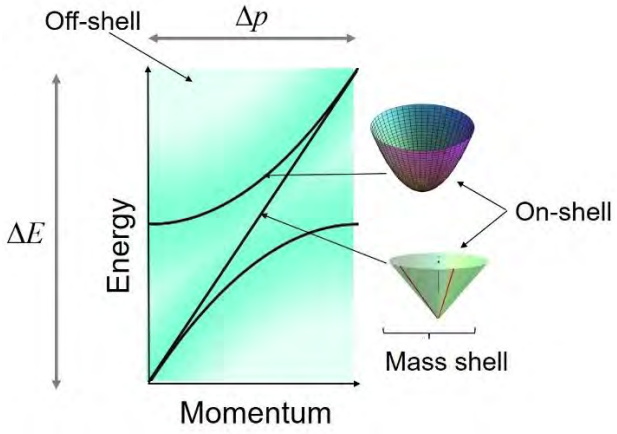

Fig.1.2 Mass shell (on-shell) and off-shell in the dispersion relation. **Off-shell[17]**

Contrary to propagating light in the on-shell state described above, the ONF is in the off-shell state, which deviates from the circular cone and the paraboloid above. This is because its sub-wavelength size Δx ($<<\lambda$), being contrary to the common view **[a]** above, produces a large momentum uncertainty Δp ($\Delta p >> p$) due to the Heisenberg's uncertainty principle $\Delta p \cdot \Delta x \geq h/2\pi$,.

Since p and E are mutually dependent, the electromagnetic field in the off-shell state ("off-shell field" for short) also has a large uncertainty ΔE ($>> E$) in the energy. Thus, Heisenberg's uncertainty principle ($\Delta E \cdot \Delta t \geq h/2\pi$) also gives $\Delta t \ll h/2\pi E$. This indicates the short duration of the field, which corresponds to the nature of a virtual photon. Due to the two large uncertainties (Δp and ΔE), the science of the ONF belongs to the category of off-shell science [7]. It should be noted that the natures of on-shell and off-shell fields are contrary to each other. The off-shell field is created neither in a vacuum nor in a super-wavelength sized macroscopic material. Instead, this field exhibits the following phenomenon:

[Phenomenon 1] The off-shell field (DP) is created and localized on a sub-wavelength material.

Since this field is created as a result of the interactions between photons and electrons (or excitons) in an NP, it is the electromagnetic field that accompanies the electronic or excitonic energy. Thus, this field has been named the DP [7]. In other words, the DP is the quantum field created in a complex system composed of photons and electrons (or excitons) in an NP. It has a sub-wavelength size and short duration. By using the DP, novel phenomena (including Phenomenon 1 above) that are contrary not only to the common view **[a]** but also to common views **[b]** – **[e]** have been found.

Table 1.1 summarizes fifteen novel phenomena originating from DPs [1]. Even though novel theories on light-matter interactions are required to analyze these phenomena, on-shell science has never met this requirement. However, disruptive innovations in application technologies have been realized by applying these phenomena (Sections 3 - 5).

Table 1.1 Fifteen novel phenomena originating from DPs

No.	Phenomenon
1	The off-shell field (DP) is created and localized on a sub-wavelength material.
2	The DP energy transfers back and forth between the two NPs.
3	The DP field is conspicuously disturbed and demolished by inserting NP2 for measurement.
4	The DP energy transfers among NPs autonomously.
5	The efficiency of the DP energy transfer is highest when the sizes of the fiber tip and the NP (NP1 and NP2) are equal.
6	The DP energy transfer exhibits hierarchical features.
7	The DP is created and localized at a singularity such as a nanometer-sized particle or impurity atom in a material.
8	An electric-dipole forbidden transition is allowed in off-shell science.
9	The irradiation photon energy $h\nu$ can be lower than the excitation energy of the electron $E_{ex} - E_g$, where E_{ex} and E_g are the energies of the excited and ground states of the electron, respectively.
10	The maximum size $a_{DP,Max}$ of the DP is 50–70 nm.
11	By DP-assisted annealing, a Si crystal works as a high-power light emitting device even though it is an indirect transition-type semiconductor.
12	The spatial distribution of B atoms varies and reaches a stationary state autonomously due to DP-assisted annealing, resulting in strong light emission from the Si crystal.
13	The length and orientation of the B atom-pair in a Si crystal are autonomously controlled by the DP-assisted annealing.
14	A light emitting device fabricated by DP-assisted annealing exhibits photon breeding (PB) with respect to photon energy; i.e., the emitted photon energy $h\nu_{em}$ is equal to the photon energy $h\nu_{anneal}$ used for the annealing.
15	The semiconductor SiC crystal was made to behave as a ferromagnet as a result of the DP-assisted annealing and exhibited a gigantic magneto-optical effect in the visible region.

1.2 A link to novel theories

A dressed photon (DP) exists in an off-shell area that is displaced from the mass-shell. To analyze its physical properties in detail, which will open up a new field of off-shell science, a novel theory that describes the micro-macro duality of quantum fields is essential [8]. In order to develop such a theory, this section reviews the requirements in theoretical studies, which have been identified from experimental results accumulated for more than a quarter of a century. For this review, a fiber probe is adopted as a representative device to create and measure the DP [9]. Since this device has a simple structure, it should be possible to analyze the transformation of an electromagnetic (EM) field between micro- and macroscopic systems, which will open up a new field of off-shell science.

1.2.1 Principles of creation and measurement of the dressed photon

In order to create such a small DP, a fiber probe has been used, as is schematically explained by Fig. 1.3(a) [10]. The operating mode of the fiber probe in this figure is called the illumination mode (I-mode) [11], in which the tail of the fiber probe is illuminated with propagating light (the EM field on shell) to create a DP at the nanometric tip of the probe.

Since the created DP is localized on the tip, it is measured by inserting a sonde into the DP for acquiring the response from the DP. That is, the DP is measured by acquiring its response to a stimulus applied from the outer system. A nano-particle (NP) has been used as such a sonde (Fig. 1.3(b)). By putting this NP in close proximity to the tip of the fiber probe, the DP energy transfers between the fiber probe tip and the NP, resulting in excitation of an electron (or an exciton) in the NP. The excited electron can create a photon. Since this photon is a conventional scattered light field on shell, it can be measured by a conventional photo-detecting device, and thus, the response can be acquired. In this I-mode, the fiber probe and NP respectively play the roles of a light source and a detector for creating and measuring the DP.

It is possible to exchange the roles of the fiber probe and the NP: First, the NP is illuminated by propagating light to create the DP (Fig. 1.4(a)). Next, a fiber probe, which is used as a sonde, is brought close to the NP (Fig. 1.4(b)). The DP energy thus transfers between the NP and fiber probe tip, resulting in excitation of an electron in the tip of the fiber probe. The excited electron can create a photon, i.e., scattered light. Since this scattered light is guided through the fiber probe and reaches its tail, it can be detected by a conventional photo-detecting device, and thus, the response can be acquired. The

operating mode of the fiber probe in this figure is named the collection mode (C-mode) [11].

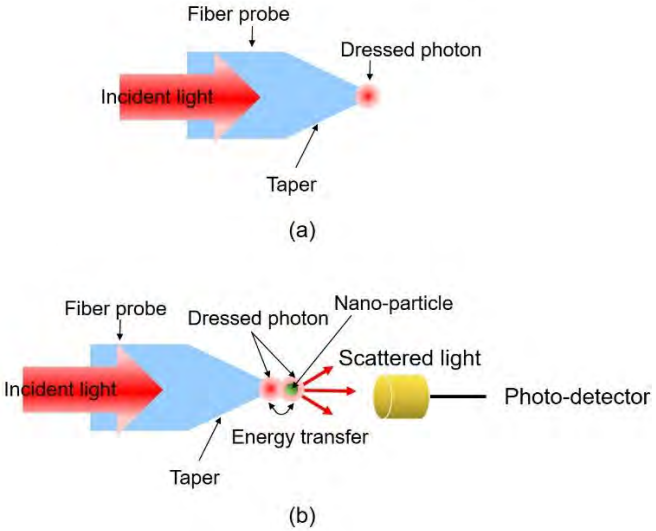

Fig.1.3 Illumination mode for the fiber probe operation.
(a) For creating the DP. (b) For measuring the DP.

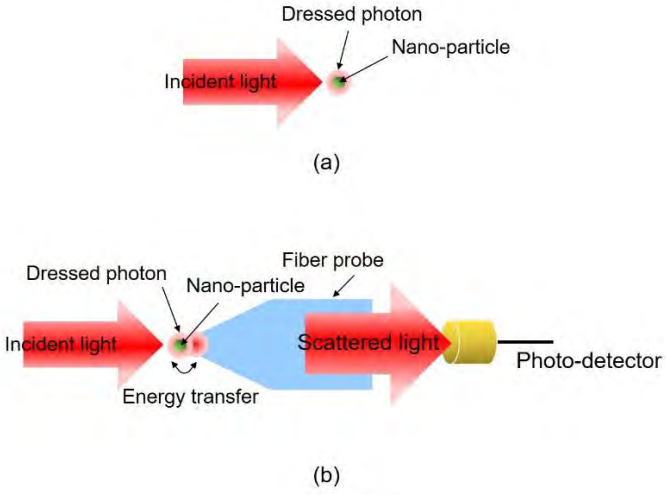

Fig.1.4 Collection mode of the fiber probe operation.
(a) For creating the DP. (b) For measuring the DP.

1.2.2 Performance of fiber probes

As is summarized in Fig. 1.5(a), a variety of fiber probes have been developed so far, some of which have been commercially available [9]. The size and conformation of the

tip and taper of the fiber probe have been empirically controlled during the fabrication process, resulting in sufficiently high efficiencies for creating and measuring DPs for practical use. These high efficiencies are indispensable for reliable conversion of the EM field from macro- to microscopic systems and also from micro- to macroscopic systems, respectively, in the case of the I- and C-modes.

Figure 1.5(b) represents the efficiency of measuring the DP acquired when the fiber probe was used in the I-mode [12]. This efficiency is expressed as the "throughput", which is the ratio between the measured optical power and the optical power incident at the tail of the fiber probe. The horizontal axis is the diameter d_f of the foot of the taper protruding from an opaque metallic film, which was deposited for blocking unwanted scattered light. In these old experimental results, it should be pointed out that a certain amount of unwanted scattered photons was measured simultaneously with the DP when d_f was larger than 100 nm. This signal mixing was due to insufficient shielding resulting from the immature metallic film coating technology available at the time.

It should be noted that the spatial resolution of this novel microscope and spectrometer are determined by the value of the tip radius, a_p. Detailed discussions of the special resolution, and also of the image contrast, are given in Section 2.2.1 [13].

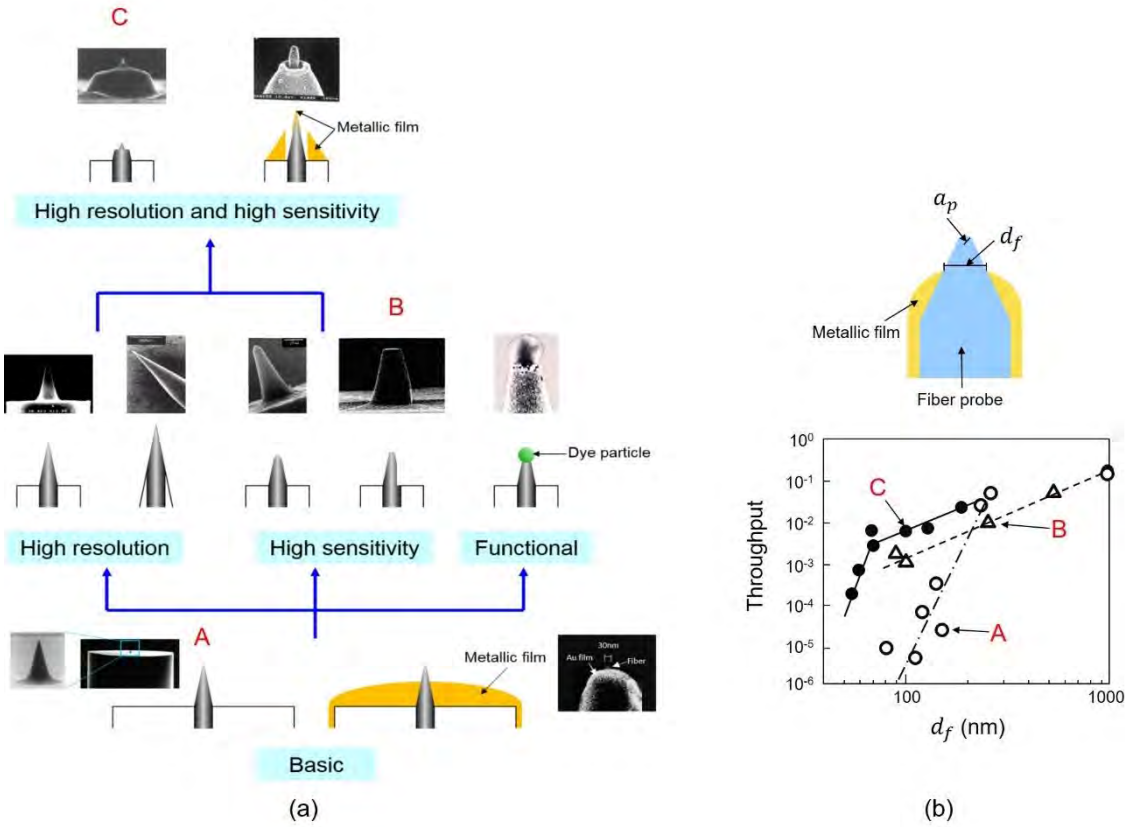

Fig. 1.5 Developed fiber probes.

(a) Cross-sectional profiles and scanning electron microscopic images. (b) The efficiency of measuring the DP. d_f is the foot diameter of the taper protruding from an opaque metallic film. Open circles, open triangles, and closed circles represent the experimental results measured for the fiber probes A, B, and C in (a), respectively.

1.2.3 Using nano-particles

A novel method has been developed recently in order to replace the role of the fiber probe operating in the I-mode by an NP, as is schematically explained by Fig. 1.6(a). In this scheme, an NP is illuminated by propagating light to create a DP. One may worry that the creation efficiency will be very low because the interface between the macro- and microscopic systems, i.e., the taper of the fiber probe in Fig. 1.3, is missing in this configuration. However, novel interface devices, such as a nano-optical condenser and an energy transmitter (Sections 3.2 and 3.3, respectively) [14], have been developed by using multiple NPs, enabling drastic increases in efficiency.

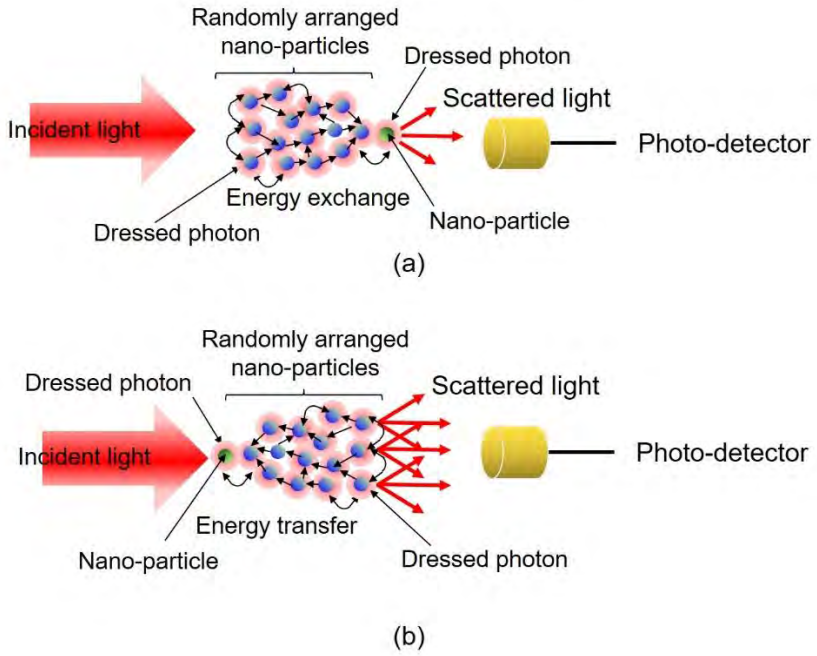

Fig. 1.6 Nano-particles for creation and measurement of the DP.

The multiple randomly arranged NPs correspond to the taper of the fiber probe.(a) For creating the DP. (b) For measuring the DP.

The replacement mentioned above has been realized also for the C-mode: As is schematically explained by Fig. 1.6(b), in this scheme, multiple NPs are arranged around the NP on which the DP is originally created. As a result, the DP energy transfers between the center NP and the surrounding multiple NPs to excite an electron. The excited electron can subsequently create scattered light, which can be acquired by a conventional photo-detecting device.

Although NP1 and NP2 may be considered as a light source and a detector in this process, one should note the following two phenomena. The first one is

[Phenomenon 2] The DP energy transfers back and forth between the two NPs.

Due to this transfer, the light source and detector above are not independent of each other but are coupled in the nanometer-sized space, and thus, they cannot be distinguished as individual elements. The second one is

[Phenomenon 3] The DP field is conspicuously disturbed and demolished by inserting NP2 for detection.

It should be pointed out that a specific phenomenon of autonomous DP energy exchange has been observed among multiple randomly arranged NPs (Section 2.2.2) [14]. That is, it has been experimentally confirmed that the optimum route was

autonomously selected for the DP energy transfer in the nano-optical condenser and energy transmitter devices:

[Phenomenon 4] The DP energy transfers among NPs autonomously.

1.2.4 Requirements for novel theories

The gray cone in the diagram of Fig. 1.7 represents the area in which the DP measuring efficiency is high, which was empirically found through experimental work on fabricating and using an I-mode fiber probe. Here, a_p is the tip radius, a_s is the radius of the spherical NP, a_s / a_p is their ratio, and θ is the cone angle of the taper. It should be pointed out that the efficiency is the highest when $a_s / a_p = 1$, which is due to the size-dependent resonance feature of the DP energy exchange [15]:

[Phenomenon 5] The efficiency of the DP energy transfer is highest when the sizes of the fiber tip and the NP (NP1 and NP2) are equal.

A similar conical area can be derived also for the C-mode. A novel theory is required since one of the major requests from experimentalists is to find the optimum condition for realizing the highest efficiency of creation and measurement of DPs. It is expected that Fig. 1.7 will serve as a reference to find this condition.

To find the optimum condition, it should be also noted that the detailed profile of the tip and taper of the fiber probe are not smooth but have some roughness on their surfaces, as is schematically shown in Fig. 1.8. Specifically, Fig. 1.8(a) represents a conical surface profile with a smooth surface, which can be observed from a far field view point. However, the NP in Fig. 1.3(b), which is installed in the near field of the fiber probe surface, may see a magnified surface and find a lot of bumps (Fig. 1.8(b)), on which multiple DPs with a variety of sizes are created. That is, a hierarchy exists in the DP measurement, which depends on the position and size of the NP to be used as a sonde for the measurement:

[Phenomenon 6] The DP energy transfer exhibits hierarchical features.

A novel theory that can describe this hierarchy, as well as the autonomy, is needed.

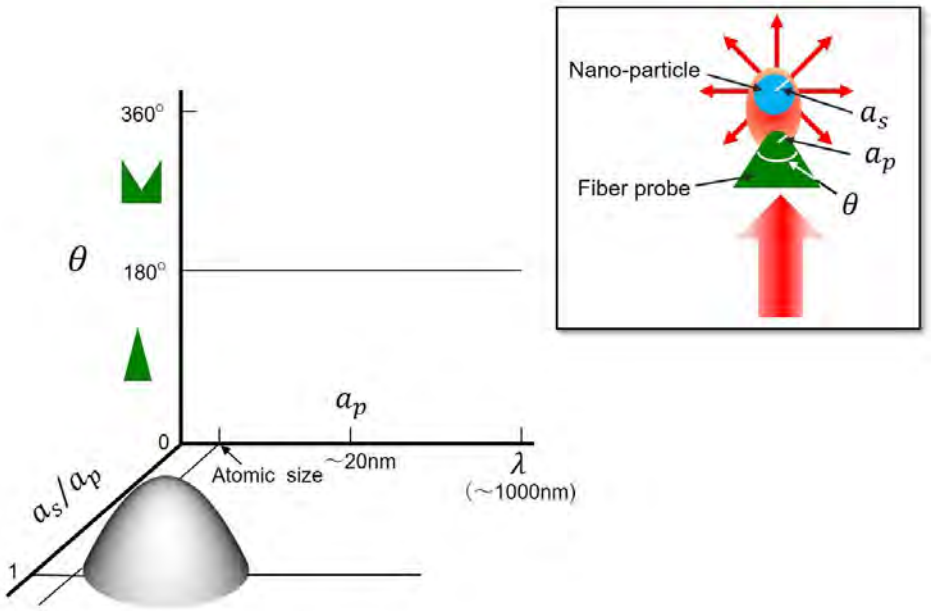

Fig. 1.7 Diagram for representing the area in which the efficiency of measuring the DP is high.

λ is the wavelength of the light incident on the fiber probe.

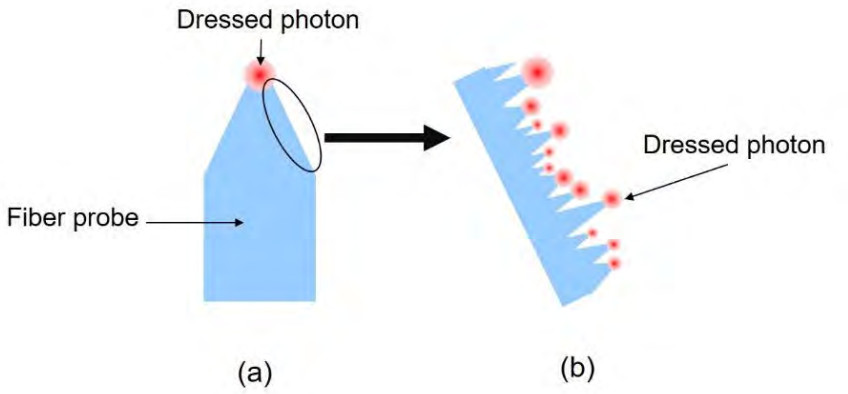

Fig. 1.8 Hierarchy of measuring the DP created on the tip and taper of the fiber probe.

(a) Cross-sectional profile of the tip and taper of the fiber probe.(b) Magnified profile of (a).

1.3 Strategies for novel theories

This section presents problems to be solved, which have been requested by experimentalists. Some promising novel theoretical methods for solving these problems are reviewed.

1.3.1 Problems to be solved

In the case where the I-mode is used by illuminating the tail of the fiber probe with propagating light, it is advantageous to create:

(A) a small DP for achieving high-spatial-resolution measurement,

and

(B) a high energy DP for achieving high-sensitivity measurement.

In order to find the criteria for designing a fiber probe for creating these DPs, the following two-step theoretical calculation ought to be carried out (Fig. 1.9). That is, the problems to be solved are

(1) 1st step: Three kinds of EM fields in the taper have to be derived. They are

a) Propagating light, which is guided through the taper (on-shell EM field).

b) Scattered light, which is dissipated via radiation from the taper (on-shell EM field).

c) A DP (off-shell EM field), whose size is equivalent to the size of the taper (Section 2.1.2) [15].

(2) 2nd step: The DP on the tip of the fiber probe has to be derived.

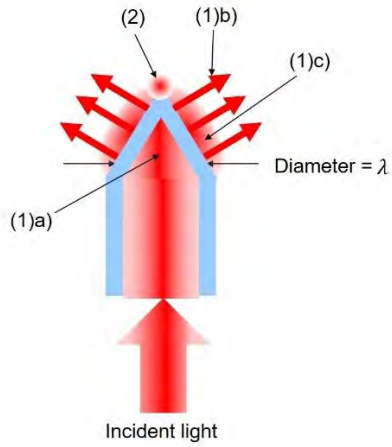

Fig. 1.9 Two-steps for theoretical calculation.

λ is the wavelength of the light incident on the fiber probe.

The DP in **(2)** is created as a result of the DP energy transfer from the fields **(1a)** and **(1c)**. It means that the conformation and structure of the taper play essential roles in creating the DP of **(A)** and **(B)** on the tip. In other words, it is essential to optimize the magnitude of the energy dissipated from the taper, which is the magnitude of the energy of the field **(1b)**.

It should be pointed out that this taper is the interface between micro- and macroscopic systems (i.e., between the tip and the tail of the fiber probe), and thus, it plays an essential role in the micro–macro duality. However, EM fields in the taper have

never been correctly described by the conventional on-shell EM field theories because these theories cannot be applied to the taper due to its sub-wavelength diameter. Namely, a method of numerical analysis based on Maxwell's equations (for example, the Finite Difference Time Domain (FDTD) method) is not suitable for deriving the EM field of **(1b)** and **(1c)** [16]. In particular, in the case of **(1c)**, the use of the FDTD method is useless because it does not take into account the longitudinal component of the electric field [17].

1.3.2 Expected theoretical methods

Several novel theoretical methods have been proposed to solve the problems presented in Section 1.3.1. This section reviews these methods. Figure 1.7 shows that the highest efficiency was obtained in the case of $a_s / a_p = 1$, due to Phenomenon 5. This case corresponds to the case where the magnitude of the energy dissipation from the taper (the scattered light energy of **(1b)** in Section 1.3.1) takes the minimum. Therefore, in order to find the creation methods **(A)** and **(B)** in Section 1.3.1, it is essential to explore the conformation and size of the fiber probe which maximize the difference between the energy of the DP localized at the tip and the energy lost due to dissipation at the taper. For this exploration, Fig. 1.10(a) was derived, in which the value of a_s / a_p in Fig. 1.7 was replaced by the magnitude of the energy loss E_d (magnitude of the light energy scattered from the taper). It should be noted that this figure uses the energy dissipation rate $\eta_d \left(= E_d / E_i\right)$, which is defined by the ratio between E_d and the energy E_i of the light incident on the tail of the fiber probe. For this replacement, a semi-quantitative relation between a_s / a_p and η_d was derived based on Fig. 2.6 of ref. [15], which is shown by Fig. 1.10(b).

Here, the problem is that the conventional on-shell EM field theories cannot be used to evaluate the magnitude E_d of energy dissipation because the taper is of sub-wavelength size. To solve this problem, it would be advantageous to use the concept of effective mass of the EM field instead of using the conventional method. This may enable estimation of the magnitude of the energy dissipation by assuming that the energy dissipation takes place during the process of transforming the massless free photon (on-

shell) to the off-shell photon with a finite mass.

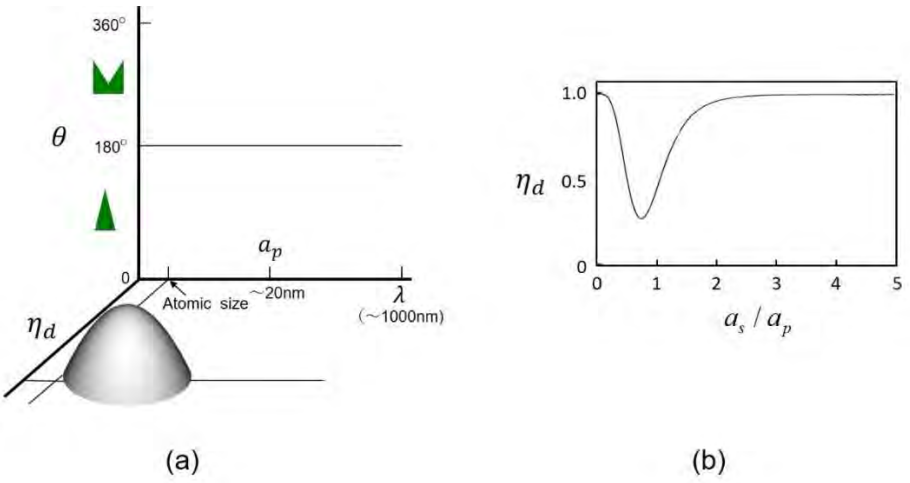

Fig.1.10 Diagram for representing the area in which the efficiency of measuring the DP is high. (a) The ratio of the sizes a_s / a_p in Fig. 1.7 is replaced by the energy dissipation rate η_d. (b) The relation between a_s / a_p and η_d used for illustrating (a).

The Clebsch dual field theory (Section 6.1) was developed for this estimation by noting the duality between the fields in the spacelike and timelike areas in the Minkowski spacetime (Fig.6.1) [8,18]. Applying the Minkowski spacetime ~~diagram~~ to the I-mode reveals that the EM fields in the lightlike, timelike, and spacelike domains correspond to the propagating light incident on the tail of the fiber probe, the scattered light radiating from the taper of the fiber, and the DP created on the tip of the fiber probe, respectively, as is schematically explained by Fig. 1.11(a). In the case of the C-mode, this correspondence is also explained by Fig. 1.11(b). Since the lightlike field creates a pair consisting of timelike and spacelike fields, the creation rate of the spacelike field can be maximized by minimizing the creation rate of the timelike field. As a result, the DPs in **(A)** and **(B)** in Section 1.3.1 can be efficiently created. It should be pointed out that the hierarchy explained in Fig. 1.8 can be described by including the nonlinear interaction in the theoretical approach.

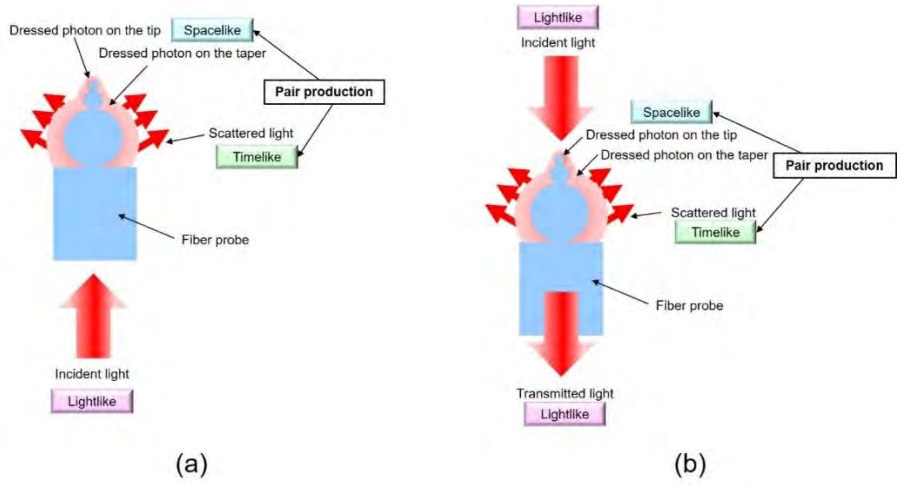

Fig.1.11 Electromagnetic fields in the lightlike, timelike, and spacelike domains. (a) Illumination mode (transformation from macro- to microscopic systems). (b) Collection mode (transformation from micro- to macroscopic systems).

It should be noted that the gray cones in Figs. 1.7 and 1.10(a) have asymmetric profiles. This is because the DP is intrinsically created on the tip of the fiber probe, which has a translationally asymmetric profile. Theoretical models for the off-shell EM field should be developed based on this asymmetry. For this advanced theoretical model, use of the quadrality scheme [19] based on category theory is expected to be a promising approach for describing the transformation of the microscopic DP to the macroscopic system. Furthermore, a novel measurement theory should be constructed by noting that the fiber probe and NP in Figs. 1.3(b) and 1.4(b) form a composite system originating from the DP energy exchange. Tomita's decomposition theorem [20] is expected to be promising for this construction. Further advances in these theoretical studies (Section 6) are expected to lead to developments in the field of off-shell science.

2. Nature of the dressed photon

This section reviews the results of theoretical and experimental studies on the unique nature of the DP. First, Section 2.1 reviews the results of theoretical studies on the creation, annihilation, and spatial localization of the DP. It should be noted that these studies give no more than urgent solutions based on the methods of on-shell science. Next, Sections 2.2 and 2.3 review the spatial and temporal evolutions of DP energy transfer. Finally, Section 2.4 reviews the energy disturbance that occurs by measuring the DP. It should also be noted that the experimental results presented in Sections 2.2–

2.4 cannot be theoretically explained as long as the methods of on-shell science are used.

2.1 Creation, annihilation, and localization of the dressed photon

Creation and annihilation operators are required to describe the energy exchange during light-matter interactions. In the case of the DP, however, the problem was that the DP has a sub-wavelength size. This meant that one could not define a virtual cavity, and thus, could not define the mode of the field for deriving its Hamiltonian.

2.1.1 Creation and annihilation of the dressed photon

As an urgent solution to this problem, the conventional theories of quantum optics (on-shell science) were modified and applied to express photons of sub-wavelength size as a superposition of an infinite number of photon modes ($\hat{a}_{\boldsymbol{k}\lambda}$: annihilation operator. $\hat{a}^{\dagger}_{\boldsymbol{k}\lambda}$: creation operator. $\boldsymbol{k}$: the wave-vector. $w_{\boldsymbol{k}}$: angular frequency. l : polarization state. $\hbar\omega_{\boldsymbol{k}}$: energy.) that interacted with the excitons of infinite energy levels in the NP [1].

By diagonalizing the Hamiltonian operator, annihilation and creation operators ($\tilde{a}$ and $\tilde{a}^{\dagger}$, respectively) of the novel quasi-particle were derived, which represented the quantum state of the coupled photon and electron–hole pairs as a result of their interaction in the nanometric space:

$$\tilde{a}=\sum_{\boldsymbol{k}\lambda}\left\{\hat{a}_{\boldsymbol{k}\lambda}-iN_{\boldsymbol{k}}\sum_{\alpha>F,\beta<F}\left(\rho^{*}_{\alpha\beta\lambda}(\boldsymbol{k})\hat{b}_{\alpha\beta}+\rho^{*}_{\beta\alpha\lambda}(\boldsymbol{k})b^{\dagger}_{\alpha\beta}\right)\right\}, \tag{2.1}$$

and

$$\tilde{a}^{\dagger}=\sum_{\boldsymbol{k}\lambda}\left\{\hat{a}^{\dagger}_{\boldsymbol{k}\lambda}+iN_{\boldsymbol{k}}\sum_{\alpha>F,\beta<F}\left(\rho_{\alpha\beta\lambda}(\boldsymbol{k})\hat{b}^{\dagger}_{\alpha\beta}+\rho_{\beta\alpha\lambda}(\boldsymbol{k})b_{\alpha\beta}\right)\right\}, \tag{2.2}$$

where $\rho_{\alpha\beta\lambda}(\boldsymbol{k})$ is the spatial Fourier transform of the electric dipole moment. These operators are represented by the sum of the operators for the photons of the infinite number of modes and for the electron–hole pairs of the infinite number of energy levels. Because of this summation, this quasi-particle was named the dressed photon (DP), i.e., a photon dressed by the material excitation energy (Fig. 2.1)[2].

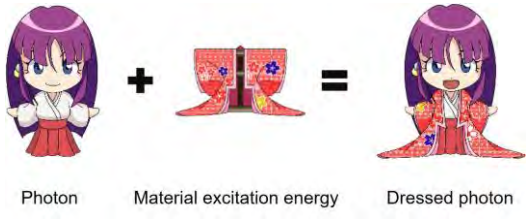

Fig.2.1 Illustrative explanation of the dressed photon.

It should be noted that this summation and dressing results in a broadband spectrum of the created DP even if a narrow-spectrum single-mode photon is incident on the NP.

As an example of further dressing of the material energy, coupling between the DP and phonon has been found: After a DP is created on an atom in a crystal under light illumination, it hops to the adjacent atom and excites a crystal-lattice vibration, creating phonons. The DP couples with these phonons and accompanies their energies. The creation and annihilation operators of this coupled state were expressed as the product of the DP operators above and the displacement operator of multi-mode phonons [3]:

$$\hat{\alpha}_i = \tilde{a}_i \exp\left\{\sum_{p=1}^{N} \frac{\chi_{ip}}{\Omega_p}\left(\hat{c}_p^{\dagger} - \hat{c}_p\right)\right\}, \tag{2.3}$$

$$\hat{\alpha}_i^{\dagger} = \tilde{a}_i^{\dagger} \exp\left\{-\sum_{p=1}^{N} \frac{\chi_{ip}}{\Omega_p}\left(\hat{c}_p^{\dagger} - \hat{c}_p\right)\right\}, \tag{2.4}$$

which indicated that the DP couples with the multi-mode coherent phonons. Here, $\tilde{a}_i$ and $\tilde{a}_i^{\dagger}$ respectively denote the annihilation and creation operators of a DP with energy $\hbar w$ at site i in the lattice. $\hat{c}_p$ and $\hat{c}_p^{\dagger}$ are respectively the annihilation and creation operators of the phonon of mode p. $\hbar\Omega_p$ is the phonon energy, and is $\hbar\chi_{ip}$ the DP–phonon interaction energy.

It should be noted that this function creates a multi-mode phonon with a coherent state. In other words, the DP excites a multi-mode coherent phonon, which couples with the DP to form a quasi-particle that is a novel form of DP. Further theoretical studies found that the created DP localized on an impurity atom in a lattice site or on the edge of the nanomaterial tip when the DP–phonon interaction energy was sufficiently high:

[Phenomenon 7] The DP is created and localized at a singularity such as a nanometer-sized particle or impurity atom in a material.

2.1.2 Spatial localization of the dressed photon

In order to detect the DP that is created and localized on NP1, the DP must be converted to propagating scattered light. This can be performed by inserting NP2 into the DP field. Propagating scattered light is created by this insertion, and it reaches a photodetector in the far-field where it is detected.

By noting the Phenomena 2 and 3 in Section 1.2.3, spatial localization of the DP has been studied for a system composed of two NPs between which the DP energy is transferred [4,5]. This study assumed that a nanometer-sized subsystem (composed of two NPs and the DP) was buried in a macroscopic subsystem (composed of a macroscopic host material, incident light, and scattered light). Since the light-matter interaction in the nanometer-sized subsystem is the main subject of the study, the effects originating from the surrounding macroscopic subsystem were renormalized by the projection operator method.

By assuming also that the exciton-polariton in the macroscopic subsystem follows a paraboloidal dispersion relation, the magnitude of the effective interaction energy between the two NPs, mediated by the localized DP, was derived. It was represented by a Yukawa function whose spatial extent corresponded to the size of the NP:

$$Y(r) = \frac{\exp(-r/a)}{r}, \tag{2.5}$$

where r is the distance from the center of the NP, and a represents the extent of localization, which is equivalent to the size of the NP [6]. This indicates that the size of the DP corresponded to that of the NP. Although this spatial localization feature has been empirically known from experimental studies on the ONF, it was successfully formulated by the renormalization above.

2.2 Spatial evolution of DP energy transfer

Experimental studies have found Phenomenon 5 that was named size-dependent resonance, and is nothing more than the momentum-conservation law for the DP energy transfer [7].

Although the long-wavelength approximation has been popularly used in conventional optical scientific studies on light-matter interactions, they are invalid in the case of the DP because its spatial extent (eq.(2.5)) is much shorter than the wavelength of light. Due to this invalidity, a phenomenon that is contrary to the common view **[d]** in Section 1.1 was found:

[Phenomenon 8] An electric-dipole forbidden transition is allowed in off-shell science.

Phenomena 5 and 8 have been actively used to propel experimental studies on the DP by using semiconductor NPs, organic NPs, and gaseous molecules. The light–matter interactions involving these specimens were analyzed by considering the discrete energy levels of the electrons or the excitons in the materials. By applying the results of these studies, novel technologies have been developed to bring about disruptive innovations.

In comparison with the studies above, extensive studies have been carried out using metallic NPs or films, resulting in the realization of a novel technology named plasmonics, which uses the interaction between light and the plasmonic oscillation of free electrons in a metal [8]. This technology employs light-scattering phenomena that occur by controlling the dispersion relation of the polariton-plasmon. Since the collective motion of the electrons in metals is involved in this phenomena, optical energy is converted promptly to plasma oscillation energy. Furthermore, since the phase-relaxation time of the electrons is very short, the unique properties of light, such as its quantum properties, are promptly lost in the metal. Therefore, to analyze the plasmonic phenomena, it is sufficient to use conventional wave-optical quantities, such as refractive index, wave-number, guiding mode, and the dispersion relation. In other words, these analyses are still based on wave optics, i.e., on-shell science.

This section reviews these features and points out that a theoretical treatment of them is necessary for realizing future progress in DP science and technology [9].

2.2.1 Size-dependent resonance

As a preliminary discussion on hierarchy, this section starts by reviewing the efficiency of the DP energy transfer between the two spherical NPs (NP1 and NP2, with radii a_1

and a_2, respectively: Fig.2.2(a)). Section 2.1.2 presented the Yukawa function that represented the magnitude of the interaction energy between the two NPs mediated by a DP [4]. As a result of the interaction, propagating light was created from the NPs and could be detected by a conventional photo-detector installed in the far field. The intensity of this light is shown in Fig. 2.2(b) [5]. The two curves in this figure show that the efficiency resonantly takes the maximum when $a_1 = a_2$. This feature has been called size-dependent resonance, which represents the momentum conservation law during the DP energy transfer.

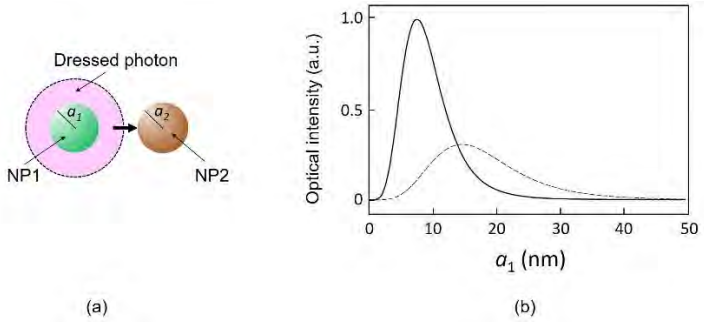

Fig. 2.2 Size-dependent momentum resonance.

(a) Two spherical NPs and their radii. (b) Relation between the radius and the detectable intensity of the propagating light. The solid and broken curves represent the calculated values for a_2 =10 and 20 nm, respectively. The surface-to-surface separation between the two NPs is 1 nm.

This resonance feature has been confirmed by several experiments on scanning probe microscopy: DPs have been used in a novel microscope and a spectrometer with ultrahigh spatial resolution beyond the diffraction limit of light. The NPs in Figs. 1.3(a) and 1.4(a) correspond to the specimens to be measured by these instruments. In the I-mode, the DP on the tip of the fiber probe serves as a light source to illuminate the specimen. In the C-mode, the light source is the DP on the NP, which is picked up by the fiber probe.

In order to analyze the spatial resolution and contrasts of the acquired microscopic and spectroscopic images, the cross-sectional profile of the fiber probe is shown in Fig. 2.3(a) [10,11]. Here, a_p is the tip radius, d_f is the diameter of the foot of the taper protruding from an opaque metallic film, which is deposited for blocking the propagating scattered light, and θ is the cone angle. The spatial resolution of the measurement is governed by the size of the DP created on the tip, which is equivalent to the tip radius a_p, because the spatial profile of the DP field is represented by the

Yukawa function.

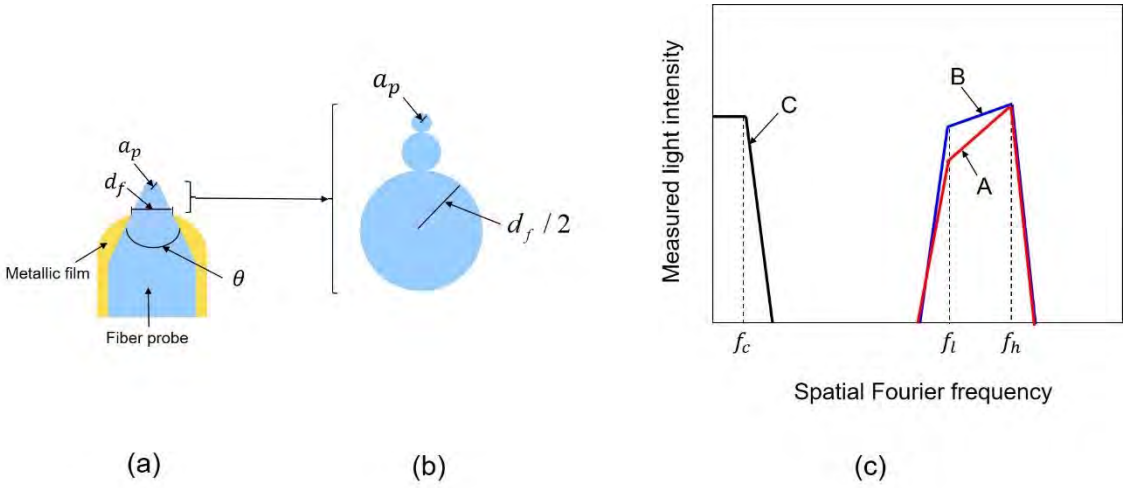

Fig. 2.3 A fiber probe and spatial Fourier spectra of the acquired image.
(a) Cross-sectional profile of the fiber probe. (b) A taper approximated by a chain of spheres.(c) Spatial Fourier spectrum of the image acquired in the Collection mode. Lines A and B correspond to the fiber probe with small and large cone angles θ, respectively. Line C represents the spectrum acquired by a conventional optical microscope.

Here, the contributions from the DPs created on the taper have to be also considered for evaluating the contrast of the acquired image. For this consideration, Fig. 2.3(b) schematically explains that the taper is approximated as a chain of small spheres which are connected in order to increase the radius, from a_p up to $d_f / 2$. These spheres receive the DP energy created on the NP in the case of the C-mode, whereas they create the DP on their surfaces in the case of the I-mode. Therefore, in the case of the C-mode, due to the size-dependent resonance feature of the DP energy transfer (Phenomenon 5), high-efficiency measurement is achieved if the size of the DP on the NP falls between a_p and $d_f / 2$. This means that this efficiency has the characteristics of a spatial band-pass filter. Its spatial Fourier spectra are shown by the lines A and B in Fig. 2.3(c). They show that the C-mode can detect a DP whose size falls within the pass band of this spatial filter (i.e., between a_p and $d_f / 2$). Its high-frequency cutoff f_h is proportional to a_p^{-1}, showing that the spatial resolution is determined by a_p. On the

other hand, the low-frequency cutoff f_l is proportional to d_f^{-1}.

Figure 2.3(c) shows that with a smaller θ (line A), a lower efficiency is exhibited at f_l than that with a larger θ (line B), because the sphere of radius $d_f/2$ is farther from the tip in the case of a smaller θ. This means that the sharper fiber probe can achieve higher selectivity in measuring the DP with a size as small as the tip radius a_p. In other words, the high-spatial-resolution component in the image is acquired with higher contrast. In the case of the I-mode, the lines A and B represent the size dependence of the DP energy created on the fiber probe; that is, a DP with a size ranging from a_p to $d_f/2$ is efficiently created.

A conventional optical microscope collects propagating light scattered from the specimen with convex lenses for acquiring an image of the specimen. The spatial Fourier spectrum of the acquired image is represented by the line C in Fig. 2.3(c). Due to the diffraction limit of light, it has the characteristics of a low-pass filter, whose high-frequency cutoff f_c is determined by the wavelength λ of the light, i.e., is proportional to λ^{-1}.

By comparing the lines A, B, and C, it is confirmed that the spatial resolution of the microscope using DPs is much higher than that of the conventional microscope because $a_p \ll \lambda$ ($f_h \gg f_c$), which is the origin of the name “ultrahigh spatial resolution microscope”

It should be noted here that the spatial Fourier spectral characteristics of the microscopic images acquired by this ultrahigh spatial resolution microscope and the conventional optical microscope do not have any strong correlation between each other. In other words, the images acquired by these microscopes are totally different from each other, in addition to the ultrahigh spatial resolution feature of the former. This is because their spatial filtering characteristics are different; i.e., band-pass filtering and low-pass filtering. By noting the size-dependent resonance feature of the DP energy transfer (Phenomenon 5), it should be pointed out that the microscope using DPs acquires an image of the fiber probe tip itself instead of an image of the specimen NP.

2.2.2 Autonomy

Experiments have observed unique characteristics of the DP energy transfer among NPs. From these characteristics, it appears as if DP energy transfer occurs of its own will, and thus this behavior has been called autonomy (Phenomenon 4). The origins of this autonomy have been attributed to the size-dependent momentum resonance and hierarchy. Furthermore, based on this autonomous behavior, the DP behaves like an organism. That is, the DP seems to indicate two things of its own will. They are:

{1} The DP indicates its existence to the macroscopic system most effectively.

The experimental ground for this indication is:

The DP in the nanometer-sized system autonomously selects the route for transferring its energy so as to maximize the power of the generated propagating light (the output signal) (Section 3.3)

{2} The DP indicates that it minimizes the magnitude of the energy dissipation of the macroscopic system by removing the DP energy from the nanometer-sized system most effectively.

The experimental grounds for this indication are:

- -The DP autonomously annihilates so as to minimize the energy dissipation of incident light during the process of etching a bump on a material surface (Section 4.2).
- -The DP autonomously modifies the spatial distribution of silver (Ag) particles so as to maximize the output photocurrent when the input light has the same photon energy as that of the light irradiated during the device fabrication* (photon breeding**) (Section 5.2).
- -The DP autonomously modifies the spatial distribution of boron (B) atoms so as to maximize the emitted light power whose photon energy is equivalent to that of light irradiated during the device fabrication* (photon breeding**) (refer to Section 5.3)

As an urgent theoretical analysis of the experimental results that originated from the autonomy, a random walk model has been used for numerical simulation techniques relying on conventional statistical mechanics and complex-system science. The results are reviewed in Appendix A.

(*) Sections 5.2 and 5.3 reveal that the spatial distributions of the B and Ag atoms, respectively, were controlled by the DP. Furthermore, these atoms form pairs, and these pairs induce photon breeding. This induction is analogous to the induction of the self-duplicating function originating from the pair of helices in DNA.

(**) The photon breeding indicates that the light emitted from the device is a replica of the light irradiated on the crystal during the device fabrication. That is, the emitted light is self-duplicated by the irradiated light, which suggests that the behavior of the DP is analogous to that of organisms.

2.2.3 Hierarchy

The bandwidth of curve A of Fig.2.3(c) depended on the profile and size of the tapered part of the conical fiber probe. This dependence indicated that the characteristics of the acquired image also depended on the distance between the fiber probe and the specimen. In order to confirm this dependence, the left parts of Figs. 2.4 (a) and (b) show images of flagellar filaments of salmonella bacteria on a glass substrate, acquired by scanning a fiber probe [12]. The probe–flagellum separations were 15 nm and 65 nm, respectively. It can be seen that the diameters of the filament-like structures in Fig. 2.4(a) are smaller than those in (b).

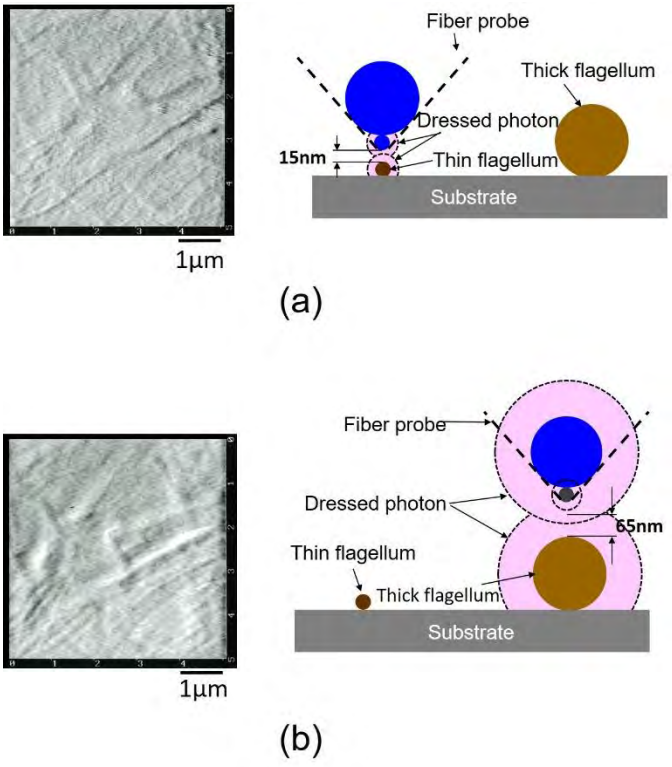

Fig. 2.4 Images of the flagella of salmonellae and schematic explanation of the setups used to acquire them.

(a) and (b) represent the cases with probe-flagellum separations of 15 and 65 nm, respectively.

In order to identify the origin of the difference in diameter, the right parts of Figs. 2.4(a) and (b) schematically show the modeled setups used to acquire these images. The probe is approximated as two blue spheres, where the smaller sphere represents the apex of the probe, and the larger sphere is placed on the smaller sphere. The pink circles in the right part of Fig. 2.4(a) show the DP field created on the smaller sphere and extending to the flagellum when the probe–flagellum separation is short. This means that a high-spatial-resolution image can be acquired by the DP field on the smaller sphere due to the size-dependent momentum resonance with the flagella, even though the image is partly superposed with the low-spatial-resolution image acquired by the DP field on the larger sphere. On the other hand, as shown in the right part of Fig. 2.4(b), the DP field on the smaller sphere does not extend to the flagella when the probe–flagellum separation is large. Only the DP on the larger sphere extends to the flagella so as to be involved in the imaging due to the size-dependent momentum resonance, whereby a low-spatial-resolution image is acquired.

In what follows, the main discussions on hierarchy can be started based on the size-dependent resonance (Phenomenon 5). Here, it is assumed that two spherical NPs (NP1 and NP2 with radii a_1 and a_2, respectively) are installed in close proximity to each other (Fig. 2.5). It is also assumed that two more NPs (NP1' and NP2', with radii $a_1'(>a_1)$ and $a_2'(>a_2)$, respectively) are installed in proximity to NP1 and NP2. The size-dependent resonance realizes efficient energy transfer of the DP on NP1 to NP2 when $a_1 = a_2$. Although the energy on NP1' is also efficiently transferred to NP2' when $a_1' = a_2'$, the efficiency of the DP energy transfer to NP2 is low due to the size difference ($a_2 \neq a_2'$). The efficiency of the transfer from NP1 to NP2' is also low. That is, the channels of the DP energy transfer between the different-sized pairs do not exhibit any crosstalk. This feature of DP energy transfer without any crosstalk is called hierarchy (Phenomenon 6). It means that different energy transfers occur independently for different material sizes. A hierarchical memory has been developed by using this hierarchy feature [13].

For further discussions on hierarchy, one should consider the "size" of the material. In the case of a spherical NP, its size is represented by its radius. However, even though it is recognized as a sphere when it is viewed in the far field, its surface often has roughness when it is viewed in the near field. That is, the recognized shape and size depend on the separation between the NP and the observer. The hierarchy is

related to these separation-dependencies. If the surface of the above-mentioned spherical NP is divided into small parts, and they are approximated as spheres whose radii are equivalent to the size of the roughness, discussions equivalent to those of the original spherical NP can be made. The concept of hierarchy is established by assuming that the spatial features of the divided parts are equivalent to those of the original spherical NP.

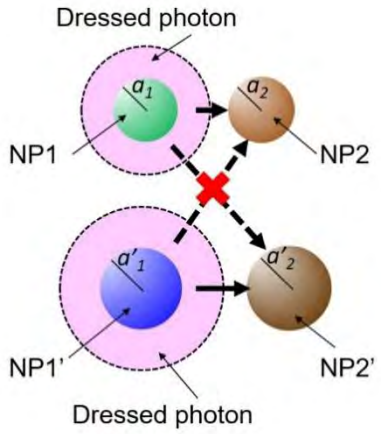

Fig. 2.5 Schematic explanation of hierarchy.

However, this division cannot be repeated infinitely. The minimum size of the NP to be divided obviously corresponds to the size of an atom, for which the discussions of hierarchy above are valid. On the other hand, experimental studies have estimated that the maximum size of the DP was 50-70 nm (Phenomenon 10: Section 4.1)[14], which corresponds to the maximum size of the NP for which discussions of hierarchy are valid.

2.3 Temporal evolutions of DP energy transfer

This section reviews experimental results on the temporal behavior of DP energy transfer between NPs. They are on the nutation and radiative relaxation.

The sample used for the experiments consisted of cubic NPs of CuCl crystals (volume density of $2 \times 10^{17}/\mathrm{cm}^3$) that were grown in a NaCl crystal (Fig. 2.6(a)). The average center-to-center distance between the adjacent NPs was 12 nm, which was estimated by assuming that the random spatial distribution of the grown NPs was a Weibull distribution.

Two of the NPs in the NaCl crystal were used, as is schematically explained by Fig. 2.6(b). They were small and large cubic CuCl-NPs (NP_S and NP_L, respectively). Pulsed light (10 ps pulse width and 381 nm wavelength) was used as the input signal.

For the output signals 1 and 2, photoluminescences (PL1 and PL2) emitted from the excitons in NP_S and NP_L, respectively, were used. Quantum states of these excitons were identified by a set of three quantum numbers (1,1,1). The wavelengths of these PLs were 383 nm and 385 nm, respectively. The sample temperature was maintained at 80 K.

Two strategies, **(S1)** and **(S2),** were planned:

(S1) For selective application of the input signal only to NP_S :

As is schematically explained by Fig. 2.6(b), a pair of NPs, consisting of NP_S and NP_L, with $a_{S,\mathrm{eff}} : a_{L,\mathrm{eff}} = 1:\sqrt{2}$, was used. Here, $a_{S,\mathrm{eff}}$ and $a_{L,\mathrm{eff}}$ are the effective side lengths, representing the spatial extent of the quantum field of the exciton. The required length ratio was achieved by selectively using NP_S and NP_L of 3.9 nm ($=a_{S,\mathrm{eff}}$) and 5.5 nm($=a_{L,\mathrm{eff}}$), respectively[1)]. Their center-to-center distance was 12 nm, estimated as described above.

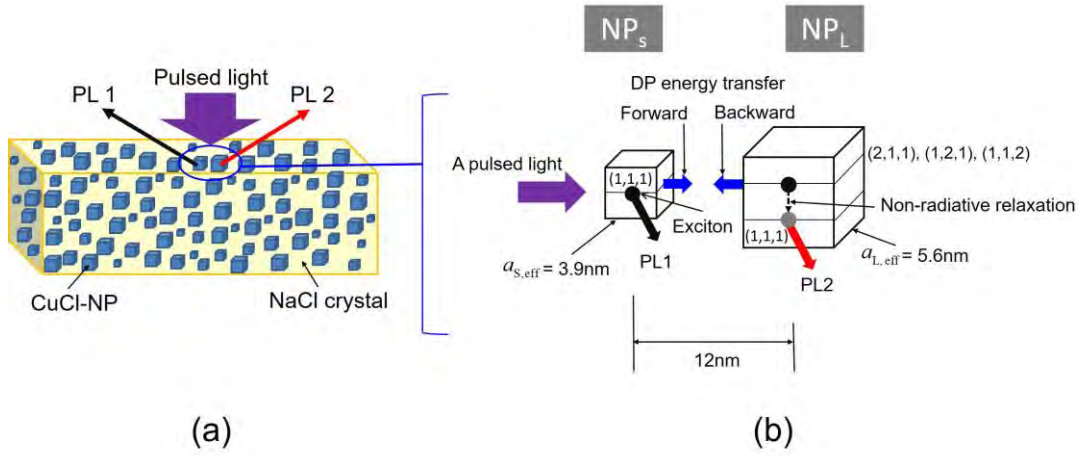

Fig. 2.6 The sample used for the experiments.

(a) Cubic NPs of CuCl crystals grown in a NaCl crystal. (b) Small and large cubic CuCl-NPs (NP_S and NP_L, respectively).

By irradiating the sample with pulsed light, an exciton was excited to the (1,1,1) state of NP_S. It should be noted that, because of the length ratio above, the energies of the triply degenerate states (2,1,1), (1,2,1), and (1,1,2) in NP_L were equal to that of the (1,1,1) state of NP_S. However, even under such resonant condition, the exciton could not be exited to these states because they are electric dipole-forbidden states with respect to

propagating light. This indicated that the incident light was effective to excite the exciton only in NP_S.

(S2) For distinguishing between output signals 1 and 2:

[Output signal 1]

The PL1 emitted from the exciton in the (1,1,1) state of NP_S was used as output signal 1. It should be noted that this exciton also creates a DP.

[Output signal 2]

{Creation} The energy of the DP, created by the exciton of the (1,1,1) state in NP_S, transferred to NP_L and excited the exciton to the triply degenerate states (2,1,1), (1,2,1), and (1,1,2). This excitation was possible because these states were electric-dipole allowed states with respect to the nanometer-sized DP. In other words, the long-wavelength approximation, popularly employed in conventional optical science, was violated by the DP. The exciton excited by the DP above emitted the PL. It also created the DP, and its energy transferred back to NP_S, resulting in bidirectional DP energy transfer between NP_S and NP_L (Phenomenon 2). This transfer phenomenon has been called nutation.

{Measurement} It might be possible to use the PL emitted from NP_L as output signal 2. However, its wavelength was equal to that of output signal 1 due to the resonance condition above. Therefore, output signal 2 could not be distinguished from output signal 1, and thus, it could not be selectively measured. For selective measurement, a rapid non-radiative relaxation, specific to the CuCl-NPs, was used by de-exciting the exciton from the triply degenerate states to the state (1,1,1), allowing subsequent emission of the PL2. Its wavelength (385 nm) was longer than that (383 nm) of output signal 1 due to the energy dissipation by the non-radiative radiation. Although the magnitude of this dissipation was as low as 1/100 times the photon energies of output signal 1, it was sufficiently large to allow output signals 1 and 2 to be distinguished.

The black and red curves in Fig. 2.7 represent the measured temporal variations of the outputs 1 and 2, respectively. They were the PL intensities emitted from the (1, 1, 1) states of the excitons in NP_S and NP_L. They exhibited monotonic decreases with time.

First, to study the nutation of the DP energy transfer, experimental results acquired in the time span 0–500 ps, immediately after applying the pulsed input signal, were analyzed [15]. For these analyses, Fig. 2.8 was acquired by expanding the horizontal axis of Fig. 2.7.

The black and red curves in Fig. 2.8 indicate the temporal variations of the DP energy transfer of the forward and backward paths, respectively. Their pulsatory variations represent nutation with a period of 50 ps. This value of the period was

compatible with the period (40 ps) that was estimated from the relation between the center-to-center distance (10 nm) and the transferred DP energy (1×10^{-4} eV) [16].

Figure 2.8 indicates the following unique characteristics **(C1)–(C3)** of DP energy transfer:

(C1) The phases of the pulsatory variations of the two curves are different from each other: In order to estimate the magnitude of this difference, the Fourier components of the 50 ps-period were extracted from these curves and are shown in Fig. 2.9. The black and red curves in this figure represent nutation, and the sinusoidal variation of the black curve had a phase lag of $\pi/3$ behind that of the red curve. This lag originated from the triply degenerate states of the exciton in NP_L (refer to **(D1)**). That is, the *triple* degeneracy caused a lag of one-*third* of π[2)]. In other words, within one-*third* of the DP energy transfer time of the backward path, the (1,1,1) state in NP_S was promptly occupied by the exciton that was initially created in the triply degenerate states in NP_L.

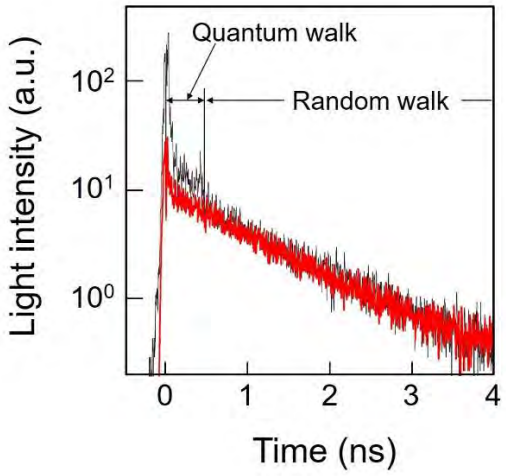

Fig. 2.7 The measured temporal variations of the two PLs.
The black and red curves represent outputs 1 and 2, respectively.

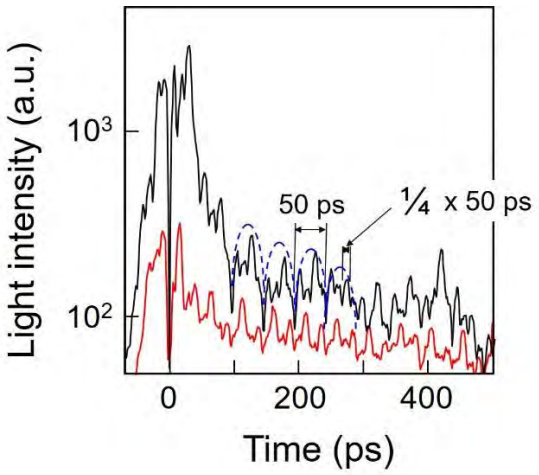

Fig. 2.8 The measured temporal variations of the two outputs.

They are the experimental results in the time span as short as 0–500 ps in Fig. 4

Since the DP energy was bidirectionally transferred between NP_S and NP_L, the profiles of the two curves in Fig. 2.9 should be anti-correlated, and thus, their phase difference should be as large as π. However, the phase lag was found to be $\pi/3$. The reason for this discrepancy was considered to be as follows: Since a large number of CuCl-NPs were buried in the NaCl crystal, the DP energies could transfer not only between NP_S and NP_L but also between multiple NP_LS (or between multiple NP_SS). Furthermore, it was confirmed by analyzing the measured absorption spectral profile of the sample that the number of NP_LS was larger than the number of NP_SS. This indicated that the DP energy transfer between neighboring NP_LS could contribute to the phase difference between the two curves. However, since the phase of the DP energy transfer between these NP_LS is random, the anti-correlation characteristics did not clearly appear, and thus, the phase difference was maintained as small as $\pi/3$.

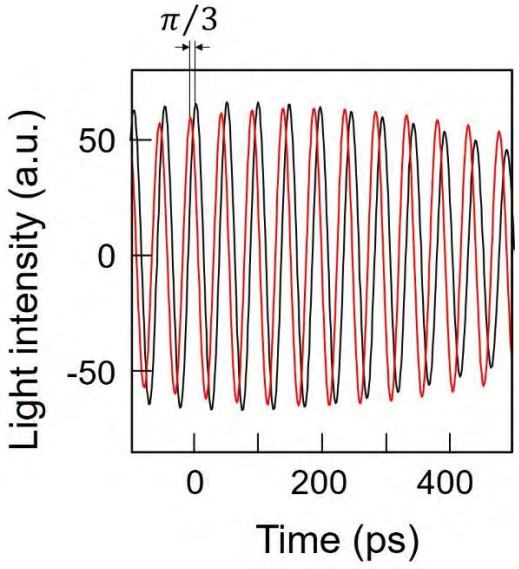

Fig. 2.9 The measured temporal variations of the two outputs.

They are the Fourier components of the 50 ps-period, extracted from the two curves in Fig. 2.8.

(C2) The pulsatory variations of the PL intensities were modulated (blue broken curve in Fig. 2.8): This was attributed to the fact that the transfer time along the forward path was longer than that along the backward path.

(C3) Additional pulsatory variations existed whose period was one-*fourth* that of the nutation: Such a short period was attributed to the fact that, among the *four* energy levels (the (1,1,1) state level in NP_S and the triply degenerate states in NP_L) relevant to the bidirectional DP energy transfer, only the (1,1,1) state in NP_S was initially occupied by an exciton at the commencement of the nutation.

Figure 2.10 shows the Fourier spectral profiles of the two curves in Fig. 2.8. The spectral peak (A) at 20 GHz corresponded to the nutation period of 50 ps. Because the profiles of the measured pulsatory variations deviated from sinusoidal curves, the spectral peak (B) of the second-order higher harmonic can be seen. The absence of the third-order spectral peak was attributed to the modulation in the PL intensity mentioned in **(C2)**. In other words, the odd-order higher harmonics were missing due to the difference between the forward and backward transfer times. The spectral peak (C) was attributed to the superposition of the fourth-order higher harmonic and the additional pulsatory variations whose period was one-*fourth*, as mentioned in **(C3)**.

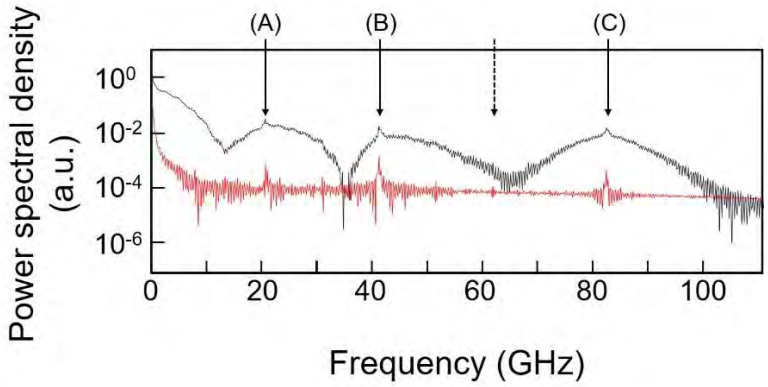

Fig. 2.10 The Fourier spectral profiles of the two curves in Fig. 5.

Off-shell[2]

Second, for studying the radiative relaxation process in Fig.2.7, black squares in Fig.2.11 show the measured temporal evolution of the PL2 in the time span as long as 0 – 10 ns [17]. The blue curve represents the temporal evolution expressed as $\exp\left(-t/\tau_{f1}\right)$, where τ_{f1} is the fall time, depending on the magnitude of the transferred DP energy. This curve agrees with the black squares only for an initial stage as short as $0 \le t \le 2$ ns. On the other hand, the red curve represents the temporal evolution expressed as $\exp\left(-\sqrt{t/\tau_{f2}}\right)$, where the fall time τ_{f2} is the radiative relaxation rate from the (1,1,1) state in NP_L. This agrees with the black squares for a wide range of time periods up to 10 ns. The component expressed as $\exp\left(-\sqrt{t/\tau_{f2}}\right)$ can be suppressed by decreasing the device temperature.

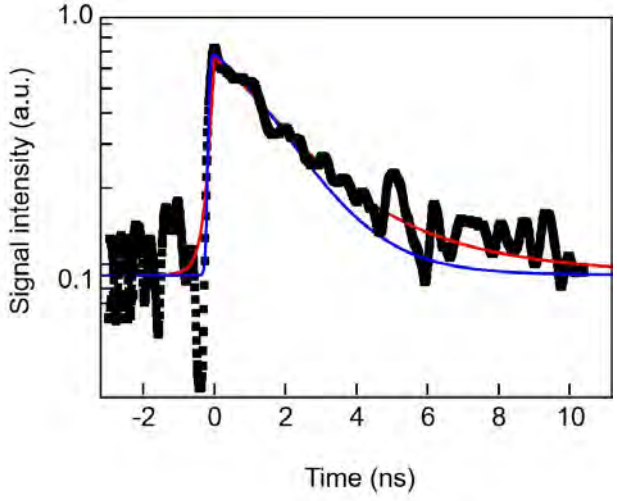

Fig. 2.11 Temporal evolution of the light intensity emitted from the CuCl NP_L for $0 \le t \le 10$ns.

The temporal evolutions shown in Fig. 2.11 have several common features even though the materials used are different:

(1) The temporal evolution expressed as $\exp\left(-t/\tau_{f1}\right)$ originated from the DP energy transfer between NPs. The rise time τ_r also originates from this transfer.

(2) The temporal evolution expressed as $\exp\left(-\sqrt{t/\tau_{f2}}\right)$ originated from the radiative relaxation in each NP.

Features (1) and (2) above represent unique phenomena which are different from each other. The former is exactly the novel off-shell scientific phenomenon [18]. The latter is no more than a conventional on-shell phenomenon. The fact that these temporal evolutions are respectively expressed as $\exp\left(-t/\tau_{f1}\right)$ and $\exp\left(-\sqrt{t/\tau_{f2}}\right)$ suggests that they correspond to the quantum walk [19] and the random walk relaxation processes, respectively. As for the former process, it should not be considered as a mere random walk because its energy transportation is linearly dependent on time, not on the square root of time.

---

1) Their geometrical side lengths were 4.6 nm (= a_S) and 6.3 nm (= a_L), respectively.

2) This kind of phase lag has never been observed when a large number of NPs is used as the macroscopic material system for inducing conventional optical phenomena. This is because the NPs in this system have been approximated as a coupled quantum state having a singlet state of the exciton.

2.4 Energy disturbance by measurement

This section shows that the energies of the DP and the exciton in the NP are disturbed by the measurement (Phenomenon 3) [20]. It should be pointed out that, due to the correlation between energy and momentum, their momenta should also be disturbed even though the size-dependent resonance phenomenon exists (Phenomenon 5).

Experimental results are presented to demonstrate the energy disturbance by using two kinds of NPs as specimens.

[1] The first specimen contained GaN-NPs [21,22] that were buried immediately under the surface of an AlN substrate. Their diameters were 50–70 nm, and their heights were 7–10 nm. Figure 2.12(a) shows the photoluminescence (PL) spectral profile acquired by

radiating pulsed light of with a wavelength of 267 nm (photon energy 4.655 eV) using a conventional microscope (on-shell science).

Since the peak energies of the narrow PL spectra from the GaN-NPs depended on their scattering sizes, the spectrum in Fig. 2.12(a) corresponded to the envelope of these scattered narrow spectra from a large number of the GaN-NPs, and thus, its width was very large. On the other hand, in the case where the fiber probe was used (off-shell sciene), it was expected that a few narrow spectra emitted from a few NPs located under the probe tip would be resolved.

However, as shown in Fig. 2.12(b), only an extremely narrow PL spectrum that originated from a single NP located exactly under the probe tip was acquired. This was because the DP energy was preferentially transferred from this NP to the probe tip most efficiently. This indicates that the DP energy transfers from other NPs, located slightly away from the probe tip, were suppressed, indicating that the linear relation between the cause and effect of the DP energy measurement was lost, thus indicating energy disturbance of the excitons and also the DP.

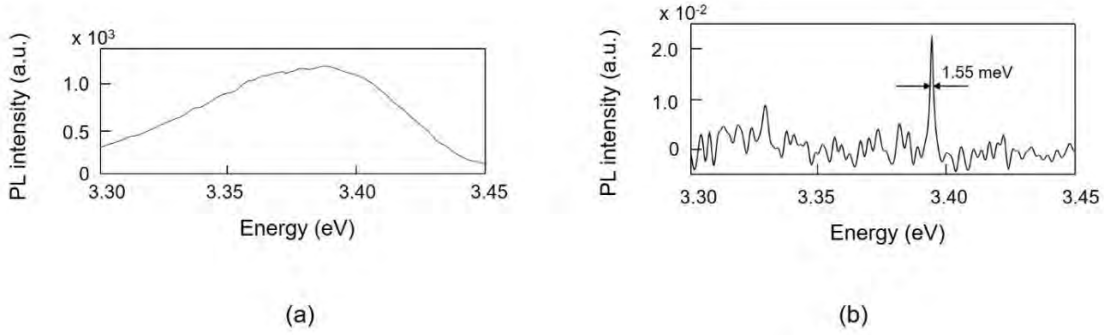

Fig. 2.12 PL spectral profiles from GaN-NPs, obtained using methods of on-shell science (a) and off-shell science (b).

[2] The second specimen contained nanometer-sized rings (NR) of GaAs that were buried immediately under the surface of an AlGaAs substrate (Fig. 2.13) [23]. Their diameters were in the range of 30–50 nm. The average thickness was 23 nm. It should be pointed out that the lowest excited energy level of the exciton in the NR is electric-dipole forbidden.

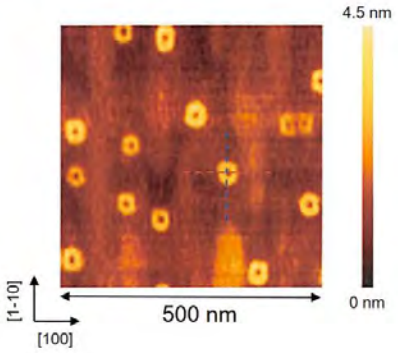

Fig. 2.13 Atomic force microscope image of GaAs-NRs.

PL emission spectra from these NRs were acquired by using the fiber probe. Here, the NRs were irradiated with a short optical pulse (400 nm wavelength, 25 ps duration, and 87 MHz repetition rate) in order to measure the temporal variation of the emitted light intensity. From these measurements, light emission from the electric-dipole forbidden energy level was clearly seen at a temperature of 7 K (Phenomenon 8); such an effect has never been seen using the methods of on-shell science. This is evidence of violation of the long-wavelength approximation.

Figure 2.14(a) shows the temporal variation of the light intensity emitted from the electric-dipole forbidden level, which demonstrated an emission lifetime of 305 ps when the probe–specimen distance was 5 nm. Such a short lifetime indicates that the fiber probe disturbed the exciton energy and also the DP to trigger light emission from the forbidden state. As shown in Fig. 2.14(b), decreases of the fiber-specimen distance decreased the emission lifetime to 260 ps. This decrease in the lifetime indicates that the energy disturbance was enhanced by decreasing the probe–specimen distance.

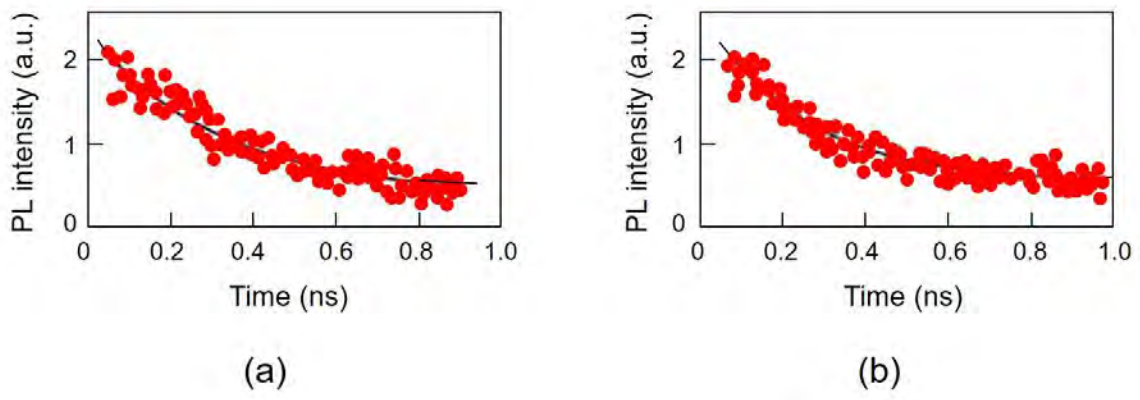

Fig. 2.14 Temporal variation of the light intensity emitted from the electric-dipole forbidden energy level. Red circles represent the measured value. Black curves are the exponential functions fitted to them. (a) The probe–specimen distance was 5 nm. The emission lifetime estimated from the fitted curve was

305 ps.

(b) The probe–specimen distance was <5 nm. The emission lifetime estimated from the fitted curve was 260 ps.

3 Nano-optical devices based on the nature of the dressed photon

Dressed photons have ingeniously contributed to the realization of innovative generic technologies. Among them, this section reviews novel nanometer-sized optical devices and demonstrates Phenomena in Table 1.1 that originate from the intrinsic nature of the DP and are contrary to the common views **[a]–[d]** in Section 1.1.

Novel nanometer-sized optical functional devices, named DP devices, have been developed by using semiconductor NPs [1]. They have enabled the transmission and readout of optical signals by DP energy transfer (Phenomenon 2) and subsequent dissipation. The operation of the DP devices was tentatively analyzed to derive an urgent solution by using an on-shell scientific quantum mechanical master equation based on a density matrix formulation (on-shell science) [2].

3.1 Logic gates

Novel AND and NOT logic gate devices operated by the DP energy transfer and dissipation (Fig.2.6(b)). Practical NOT logic gate and AND logic gate devices that operated at room temperature have been fabricated by using InAs NPs [3]. Figure 3.1 demonstrates the structure and operation of these devices that were fabricated by integrating size-controlled semiconductor NPs on a substrate [4].

One advantage of these devices was that their extremely small sizes (20–50 nm side length in the case of Fig. 3.1 using InAs NPs) were far beyond the diffraction limit, contrary to the common view **[b]** in Section 1.1. Other advantages were their superior performance levels and unique functionality, such as autonomous energy transfer (Section 3.3) [5], single-photon operation (Section 3.5.1) [6], and extremely low energy consumption (Section 3.5.2) [7]. These advantages originated from the unique operating principles of DP devices achieved by exploiting Phenomena 4, 5, and 8.

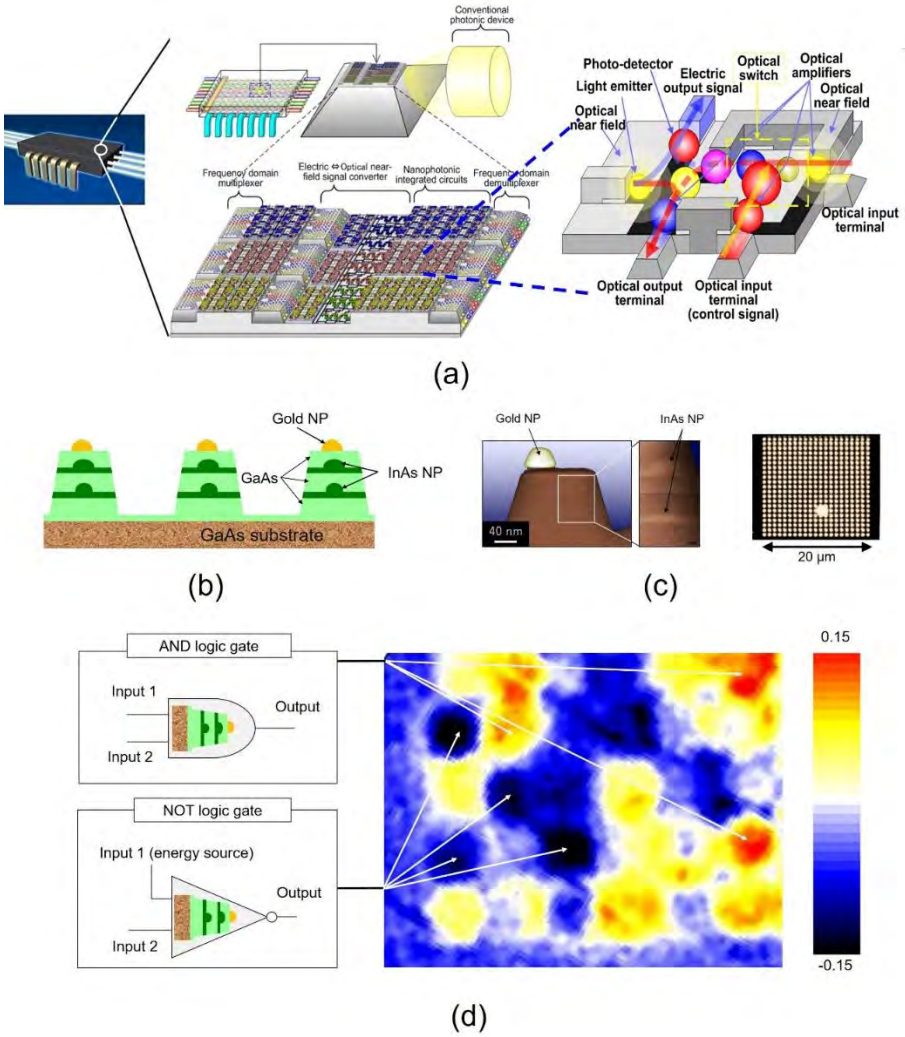

Fig. 3.1 Dressed photon devices.

(a) Prototype of integrated circuit composed of DP devices.

(b) Cross-sectional structure of mesa-shaped NOT logic gate composed of InAs NPs.

(c) Scanning transmission electron microscope image of structure in (b) (left) and optical microscope image of a two-dimensional array of structures in (b) (right).

(d) Measured spatial distribution of the output signal intensity from a two-dimensional array of fabricated devices composed of InAs NPs.

Novel information processing systems have been proposed by using DP devices [8]. The first example is a non-Von Neumann computing system utilizing DP energy transfer. The ability to solve a decision making problem [9] and an intractable computational problem [10] has been demonstrated. The second example is an information security system that uses Phenomenon 5. This system has realized a lock-and-key [11]. Furthermore, a hierarchical hologram [12] has been developed using the

Phenomenon 6 that originates from the size-dependent resonance (Phenomenon 5):

3.2 Nano-optical condenser

A nano-optical condenser that converts propagating light to DPs with high efficiency has been developed on the basis on the unique spatial evolution features of the DP energy transfer [13]. In order to construct this device, a large number of small nano-particles (NP_S) are used, and one large nano-particle (NP_L) is installed at the center, as shown in Fig. 3.2(a). Moreover, medium-sized nano-particles (NP_M) are installed in the intervening spaces. Since the sizes of these NPs are tuned so that the quantized exciton energy levels are resonant with each other, as was the case between the two NPs in Fig. 2.6(b), when an exciton is created in NP_S by irradiation with propagating light, the DP energy is transferred from NP_S to NP_M. After this transfer, relaxation promptly occurs in NP_M, and subsequently, the energy is transferred from NP_M to NP_L. After relaxation in NP_L, the output signal is generated from the exciton in the energy level (1,1,1). Here, since the energy level (1,1,1) in NP_S is tuned to the photon energy of the incident propagating light, almost all the incident propagating light energy can be absorbed by a large number of NP_Ss.

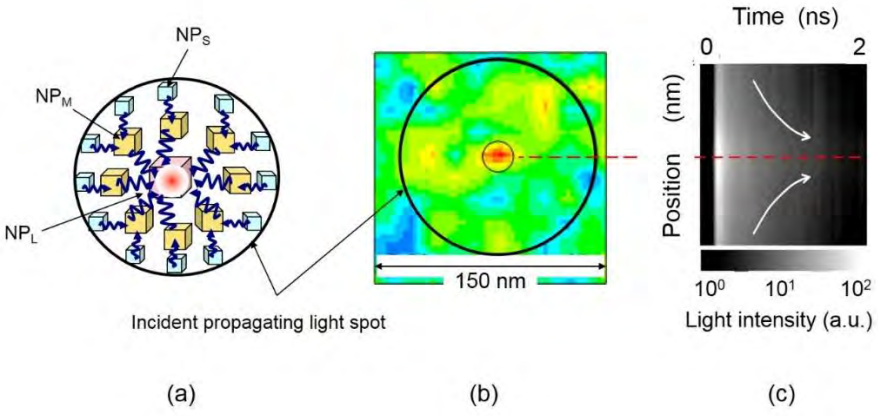

Fig. 3.2 Nano-optical condenser.

(a) Structure of the device. (b) and (c) show the spatial distribution and temporal evolution of the light intensity emitted from CuCl NPs, respectively.

Furthermore, since the energy dissipation in this system is due to the non-radiative relaxation in NP_M and NP_L, its magnitude is very small. As a result, a high efficiency is expected for concentrating the energy of the incident propagating light at NP_L.

Figure 3.2(b) shows an observed near field optical microscopic image of the

spatial distribution of the DP energy by applying propagating light with a wavelength of 385 nm to cubic CuCl NPs in an NaCl host crystal. The bright spot at the center corresponds to the place at which the incident light energy was condensed at NP_L, which had a side length of 8 nm. Its diameter was about 20 nm, including the size of the probe apex used for the microscope, which governs the resolution of the measurement. The light power in this spot was more than five-times higher than that of the light power emitted from NP_L when it was isolated from the NPs. From these results, it is confirmed that this device worked as a high-efficiency optical condenser beyond the diffraction limit. This novel device has also been called an optical nano-fountain [13].

The high performance of this device can be confirmed by comparing it with a conventional convex lens. When propagating light is focused by a convex lens, the theoretical spot diameter at the focal plane is expressed as λ / NA, which corresponds to the diffraction limit of a focused light beam. Here, λ is the wavelength of the incident light, and NA is a parameter called the numerical aperture, which depends on the shape and material of the lens, being smaller than unity. By substituting the spot diameter in Fig. 3.2(b) into this formula, we fid that NA is more than 40, which is much larger than that of a conventional convex lens.

Figure 3.2(c) shows the measured spatial and temporal evolutions of the light intensity. The horizontal axis at the top of the figure represents time, and the vertical axis represents the radial position in polar coordinates centered at NP_L. The brightness gradation is proportional to the number of emitted photons, from which one can find that the energy is condensed at NP_L with a time constant as short as 2 ns.

Because of the extremely low energy dissipation due to the relaxation from the upper to lower energy levels in NP_M and NP_L, the efficiency of optical energy concentration can be higher than 0.9. The energy transfer process in the nano-optical condenser described above is similar to that in photosynthetic bacteria [14], whose high energy transfer efficiency is receiving attention as a novel system function inherent to such complex systems in a nano-scale space [15,16].

3.3 Energy transmitter

An energy transmitter is used to transmit a signal from one DP device to another, corresponding to the function of a metallic wire in an electrical circuit or an optical waveguide in a conventional optical integrated circuit. It should meet the following two requirements:

(1) Signal reflection from the DP devices connected to the tail of this transmitter must

be avoided to achieve stable uni-directional energy transmission.

(2) Transmission loss must be sufficiently low to realize a long transmission length.

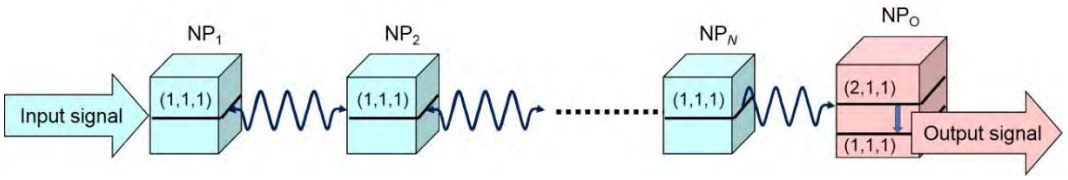

Fig. 3.3 Structure of energy transmitter.

Figure 3.3 shows the structure of an energy transmitter that was developed to meet these requirements. It is composed of an array of N NPs of the same size (NP_1 – NP_N), and a large NP (NP_O) installed at the end of this array. In the case of using cubic NPs, as an example, an exciton is created in energy level $(1,1,1)$ in NP_1 by applying an input signal, i.e., by irradiating NP_1 with propagating light. This light is converted to a DP and is transferred to energy level $(1,1,1)$ in NP_N, and nutation occurs among the N NPs. As a result, these NPs are coupled with each other. If the size of NP_O is tuned so that its triply degenerated electric dipole-forbidden levels ((2,1,1), (1,2,1), and (1,1,2) are resonant with the energy level of this coupled state of the N NPs, nutating energy is transferred to the triply degenerated upper energy levels in NP_O, and by subsequent relaxation to the lower energy level $(1,1,1)$. Finally, the light is emitted from the exciton in level (1,1,1) and is used as the output signal.

The device in Fig. 3.3 meets requirement **(1)** above because the exciton cannot be excited to the triply degenerated upper energy levels in NP_O even if the exciton is created in the lower energy level (1,1,1) in NP_O by back-transfer of the signal from the DP devices installed at the stage after NP_O. Thus, the energy is not back-transferred from NP_O to NP_1 – NP_N.

It can be easily found that requirement **(2)** is met because the magnitude of the energy dissipated during the non-radiative relaxation from upper to lower levels in NP_O is as low as 20 meV, which is much lower than the photon energy of the light radiated onto the device.

For device fabrication, it is much easier to randomly disperse NP_1 – NP_N and NP_O on a substrate than to arrange them accurately so as to maintain a constant separation. Figure 3.4(a) schematically explains this configuration [17], in which small NPs are randomly dispersed along the x-, y-, and z-axes, and are used as NP_1 – NP_N, whose numbers of rows are denoted by N_x, N_y, and N_z, respectively. NP_O is installed among the dispersed small NPs. NP_1 and NP_O are respectively denoted by NP_{in}

and NP_{out} in this figure.

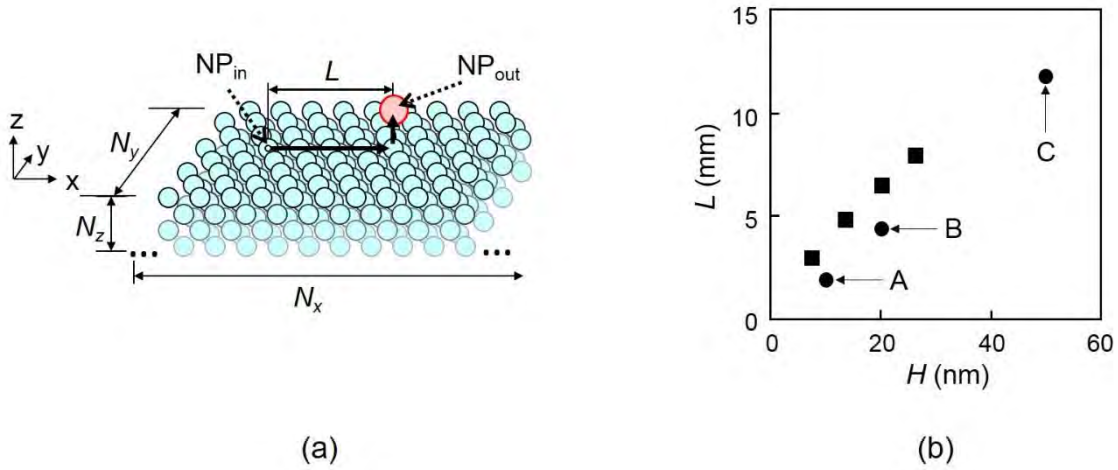

Fig. 3.4 Calculated results for NPs dispersed on a planar substrate.

(a) Arrangement of multiple small NPs (NP_S) and one larger NP (NP_L).

(b) Dependence of the energy transfer length L on the thickness H of the small NP layers.

For experiments, spherical CdSe NPs were used for simplicity of material preparation. The diameters of NP_1 – NP_N were maintained at 2.8 nm, whereas that of NP_O was 4.1 nm in order to satisfy the resonance condition of the exciton energy levels. These spherical CdSe NPs were dispersed on a SiO_2 substrate, and the average separation between the adjacent NPs was arranged to be close to 7.3 nm in order allow efficient DP energy transfer. Moreover, the thickness of the NP layers, H in Fig. 3.4(a), was fixed to 10 nm, 20 nm, and 50 nm, which is proportional to the number of rows N_z of NP_1 – NP_N along the z-axis. These devices are denoted by A, B, and C, respectively.

By applying propagating light with a wavelength of 473 nm, the energy transfer length L was measured as a function of H. The results are shown in Fig. 3.4(b), from which the values of L for devices A, B, and C were found to be 1.92 μm, 4.40 μm, and 11.8 μm, respectively. These are much longer than the wavelength of the incident light, which also meets requirement **(2)** above. This figure shows that these measured values agree with the values calculated by using the rate equations representing DP energy transfer between two adjacent NPs. It also shows that L increases with increasing H, i.e., with increasing N_z. By these experimental results, the autonomous DP energy transfer (Phenomenon 4) was confirmed.

It has been found that this autonomous DP energy transfer showed the following characteristics **[C1]** and **[C2]** [1,18], suggesting that there exists an optimum arrangement of the NPs that give indication **{1}** in Section 2.2.2.

[C1] The efficiency in energy transfer is highest when $N \cong 4$: The DP energy transfer from multiple NP_Ss to one NP_L has been analyzed in order to present an urgent solution [5]. As is schematically explained by Fig. 3.5(a), the device under analysis contained N small NPs (NP_S) and one large NP (NP_L). By assuming that each NP_S was initially occupied by an exciton, quantum master equations for the density matrices were solved to derive the occupation probability of the exciton in energy level (1,1,1) of NP_L. The time-integrated value of this probability is proportional to the output signal intensity. This intensity was calculated as a function of the number N of CdSe NP_S. The calculated results are indicated by closed circles in Fig. 3.5(b) and show that the efficiency of energy transfer was highest when $N \cong 4$. Since the radiative relaxation rate from the lower energy level of NP_L took a finite value, the DP energy was not transferred to NP_L until the exciton in energy level (1,1,1) was annihilated, and as a result, the energy was dissipated from NP_S if N was too large. Therefore, the output signal intensity did not increase if too many NP_S were installed around an NP_L, which meant that the efficiency of the energy transfer to NP_L decreased when $N > 4$. Small and large spherical CdSe NPs (2.0 nm and 2.8 nm diameters, respectively) were used to experimentally measure the magnitude of the energy transferred from NP_S to NP_L [15]. The results are represented by the closed squares in Fig. 3.5(b). They show that the output signal intensity was highest at $N \cong 4$, in agreement with the calculated results.

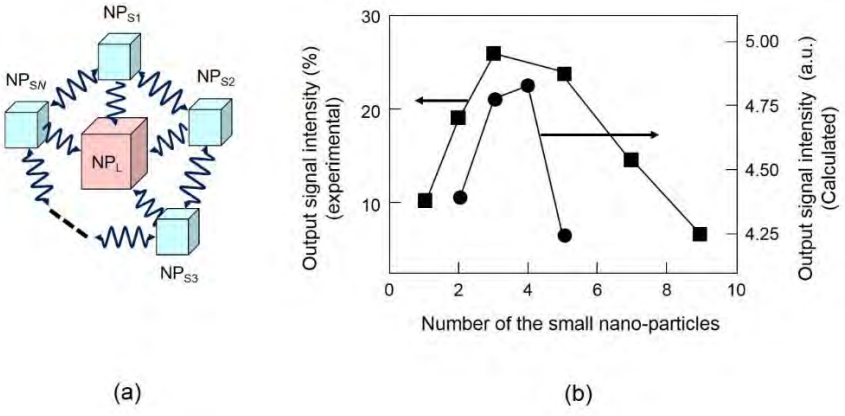

Fig. 3.5 Autonomy of the DP energy transfer.

(a) Layout of NPs. (b) Dependences of the output signal intensities emitted from CdSe NP on the ratio of the number of NP_Ss to that of NP_L.

[C2] If the interaction between NP_L and one of the NP_Ss is degraded or lost, the DP energy at this NP_S does not transfer to the other NP_Ss but is efficiently stored in this NP_S until the DP energy is transferred to NP_L. This efficient storage indicates that the

transferred energy autonomously searches for unoccupied NP_Ss in the system: Let us assume that the interaction between some NP_S and NP_L may be degraded or lost because of size-detuning of the NPs, fluctuations in the separations between the NPs, or deterioration of the NP materials. In the case of a pentagonal layout, as shown in Fig. 3.6(a), there can be seven degraded configurations: By referring to system E0 as the one without any degradation, system E1 represents the layout in which the interaction between one NP_S and NP_L is degraded or lost (represented by the red mark × between NP_{S1} and NP_L in this figure). Systems E2 and E2' have two degraded interactions. Figure 3.6(b) shows the time-integrated values of the occupation probability of the exciton in NP_L for the eight systems (E0–E5). This figure shows that system E5 does not generate any output signals because the interaction between NP_S and NP_L is completely lost. In contrast, the output signal intensities from systems E1–E4 with degraded interactions are larger than that from system E0. In particular, the value of the output signal intensity from system E2 is 1.64-times larger than that from system E0. Moreover, the autonomy in the DP energy transfer can be understood from Fig. 3.6(c). This figure shows the temporal evolutions of the occupation probabilities of excitons in the energy levels of five NP_S in system E2, in which two interactions are degraded (NP_{S2}–NP_L and NP_{S3}–NP_L). The energy levels in all the NP_Ss are initially occupied by excitons, and afterward for several nanoseconds, the occupation probabilities in NP_{S2} and NP_{S3} remain high, which means that the DP energy does not transfer to the other NP_Ss but is efficiently stored in this NP_S until the DP energy is transferred to NP_L. On the other hand, Fig. 3.6(d) shows the time evolutions of the occupation probabilities in the case of system E0, in which the energy levels of three NP_Ss (NP_{S1}, NP_{S3}, and NP_{S4}) are initially occupied by excitons. It is found from this figure that the occupation probabilities for NP_{S2} and NP_{S5} increased within 2 ns even though they were initially zero. This means that the transferred DP energy autonomously searches for unoccupied NP_Ss in the system.

Characteristics [C1] and [C2] originating from the autonomy in the DP energy transfer can be applied to novel information technologies: Since the phenomenon of autonomous DP energy transfer between NPs is similar to the inherent behaviors of amoeba used for bio-computing [10], several simulations have been carried out for applying this phenomenon to novel non-von Neumann type computing systems in order to solve constraint satisfaction problems, Boolean satisfiability problems, and decision making problems [19].

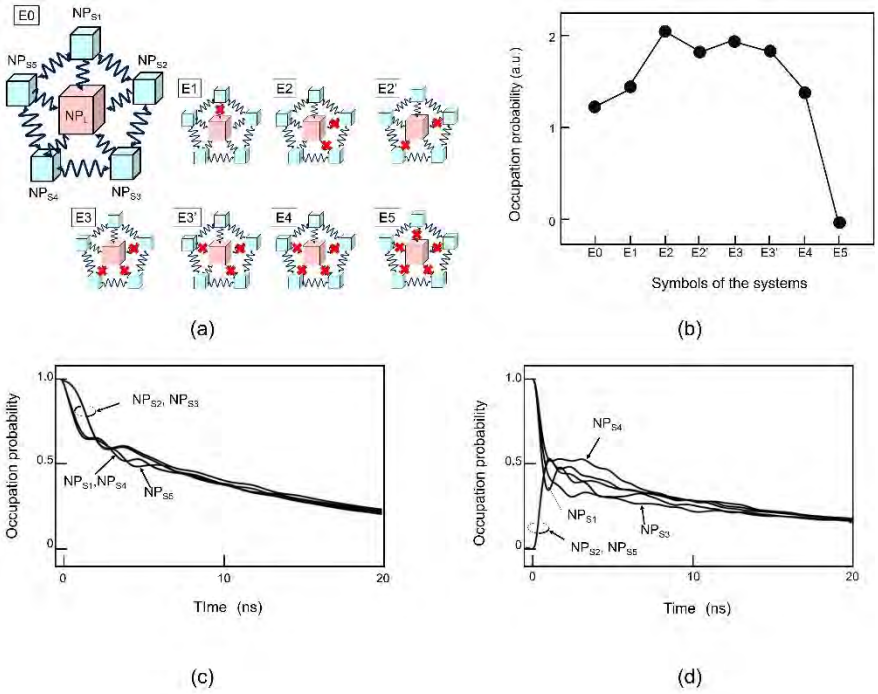

Fig. 3.6 Degraded or lost interaction between NP_S and NP_L.

(a) Layout of the NPs. (b) Time-integrated values of the occupation probabilities for systems E0 to E5. (c), (d) Temporal evolutions of the occupation probabilities of the exciton in the energy levels in five NP_Ss in systems E2 and E0, respectively.

3.4 Optical buffer memory device

Figure 3.7 schematically explains the structure and operation of the optical buffer memory device [20]. For holding the input optical signal in this device, nutation of the DP energy transfer between two NPs of equal side length was used, as is shown in Fig. 3.7(a). The buffering time corresponds to the cycle time of the nutation. To read out the held signal, a NOT logic gate (Section 3.1), whose operation was based on DPs [21], was installed in proximity to the two NPs (Fig.3.7(b)). Application of a readout optical pulse to the NOT logic gate created output photons that propagated out from the device.

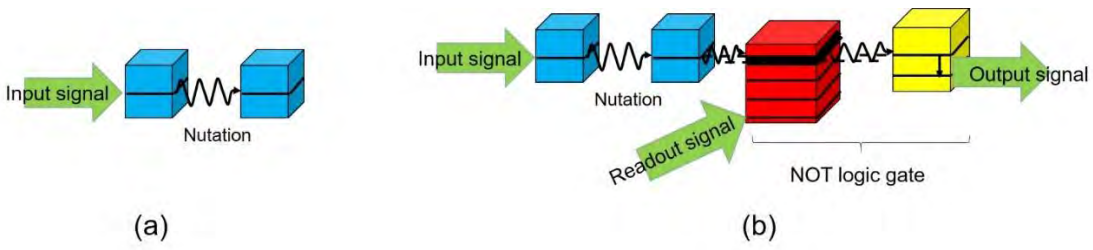

Fig. 3.7 An optical buffer memory device.

(a) Holding an optical signal by means of nutation of the DP energy between two NMs.

(b) Acquiring an optical signal by applying a readout optical pulse to the NOT logic gate.

CuCl NPs were used for demonstrating the device operation. Pump-probe spectroscopy was used for acquiring spectral data, where the pump and probe pulses corresponded to the optical input and readout pulses, respectively. Their pulse widths were 2 ps. Figure 3.8(a) is the spatial distribution of the light intensity emitted by illuminating the NPs with 325 nm-wavelength light. Figure 3.8(b) represents the spectral profile of the light emitted from NPs located in the area surrounded by a broken circle in Fig. 3.8(a). The peaks A and B correspond to the input signal (the illuminated light) and the light applied for readout, respectively. The peak C is the output signal, by which the operation of the optical buffer memory was successfully confirmed.

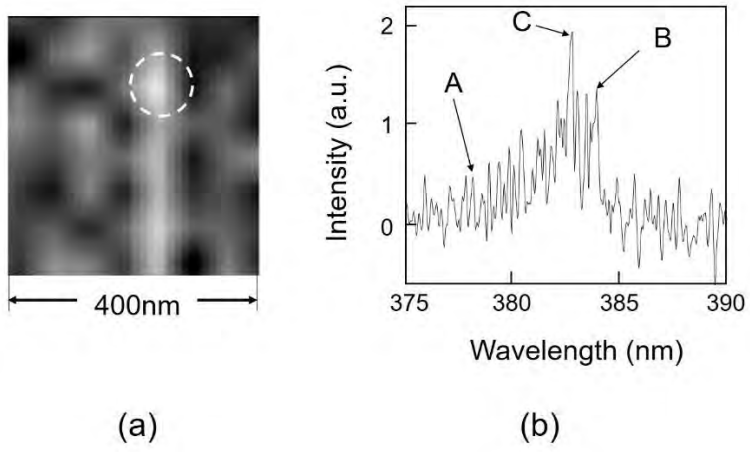

Fig. 3.8 Result of experiments using CuCl NPs.

(a) Spatial distribution of the emitted light intensity.

(b) Spectral profile of the emitted light acquired from the area surrounded by a broken circle in (a). Peaks A and B correspond to the illuminated light and the light for readout, respectively. Peak C is the output signal.

Figure 3.9 is the temporal variation of the output signal intensity plotted as a function of the time delay, i.e. the time difference between the applications of the input and readout pulses to the device. Curves A and B represent the experimental values. Curve C is the theoretical curve fitted to them by using three numerical values. They were (1) a decay time constant of 600 ps, which corresponded to the time required for the DP energy transfer observed at $0 \le t \le 300\text{ps}$, (2) a decay time constant of 1300 ps,

which corresponded to the radiative relaxation observed at $t \geq 300\text{ps}$, and (3) a nutation cycle (refer to Section 2.3) of 155 ps.

The curve C exhibits a pulsating feature, taking a first local maximum immediately after the readout pulse is applied. This corresponded to the first output signal. Subsequently, a series of output signals repeatedly appeared with a period of 150 ps, which corresponded to the nutation cycle. Even though the device was as small as 29 nm, such a long period was successfully realized. This novel function, made possible by DPs, has never been seen before in conventional optical devices.

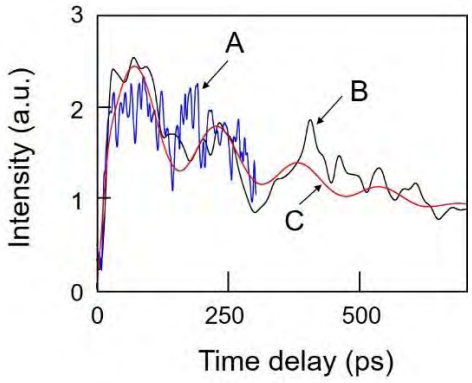

Fig. 3.9 Temporal variation of the output signal intensity as a function of the time delay. Curves A and B represent the experimental results. Curve C is the theoretical curve fitted to the curves A and B.

3.5 Superior performance levels and unique functionality of DP devices

As examples of the superior performance levels and unique functionality of the DP devices, this section demonstrates single-photon operation and extremely low-energy consumption [20].

3.5.1 Sigle-photon operation

After an exciton is created by injecting a photon to the input terminal NP of the DP device, a photon is created by subsequent DP energy transfer to the output terminal NP and relaxation. Thus, the DP device is expected to be operated by a single photon. This single-photon operation has been confirmed by photon correlation experiments [22]. As shown in Fig. 3.10(a), two cubic CuCl NPs (NP_S and NP_L) (refer to Fig.2.6(b)) were used.

Figure 3.10(b) shows the experimental results [6]. The horizontal and vertical axes represent the time difference between the detections by two photodetectors and the cross-correlation coefficient between the two detected light intensities. When the time difference was zero, the value of the measured cross-correlation coefficient was nearly zero, which meant that the quantum state of the photon was in an anti-bunching state. From these experimental results, the probability of occurrence of the single-photon emission event was estimated to be as high as 99.3%.

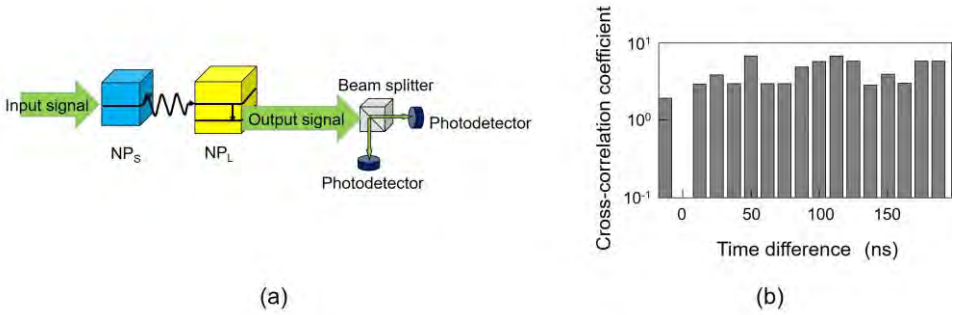

Fig. 3.10 Experimental results for single-photon operation.

(a) Setup of photon correlation experiment.

(b) Measured dependence of the cross-correlation coefficient on the time difference between the detections by two photodetectors.

Such a high probability of single-photon emission is due to the following blockade mechanisms: If two excitons are created in the NP_S by a single input photon, the exciton energy of the lowest excited level decreases by about 30 meV due to coupling of the two excitons. Thus, this exciton energy is detuned from the input signal energy and also from the exciton energy of the second-lowest excited level in the NP_L. As a result, the creation of two excitons in the NP_S is not allowed, and DP energy transfer from the NP_S to the NP_L is blocked. Due to this blockade mechanism, DP energy transfer to the NP_L is allowed only when one exciton is created in the NP_S. As a result, only a single photon is emitted from the NP_L.

3.5.2 Low-energy consumption

Very low energy dissipation and consumption capabilities are expected due to the single-photon operation of the DP device above. As a first step to confirm these capabilities, the magnitude of the energy dissipation is discussed in comparison with that of conventional electronic devices. For operating an electronic device, electrical wires are required to connect with a power supply and other devices. This means that the

magnitude of the energy dissipation is governed not only by the electronic device itself but also by other elements, including wires, and load resistances that consume a large amount of energy. In contrast, since the DP device does not require electrical or optical wires, the energy is dissipated only in the DP device due to relaxation from a higher to a lower energy level in an NP. The rate of this relaxation is about 1×10^{11} s^{-1} in the case of a CuCl NP. Based on this value, the magnitude of the energy dissipated in the DP device was estimated to be extremely low, namely, 10^4 times lower than that of a CMOS logic gate [23]. The energy transfer process in the DP device is similar to that observed in a photosynthetic bacterium [14]. Because of its high energy transfer efficiency, this process is receiving attention as a novel optical function that is inherent to complex systems in nano-scale spaces [15].

As a second step, the magnitude of the energy consumption is discussed by estimating the magnitude of the driving energy and dissipated energy from the viewpoint of transmitting significant information to a receiver [7]. For this estimation, a basic optical information transmission system is considered, as illustrated in Fig. 3.11. It is composed of an input interface (a nano-optical condenser) to convert the input propagating light to a DP, a NOT logic gate [21], and an output interface. The CuCl NPs in Fig. 3.10 is replaced by InAs NPs for enabling practical room-temperature operation. The output interface is composed of a gold NP to convert the created DP to propagating light [4] that reaches a photodetector. Then, it is converted to an electrical signal.

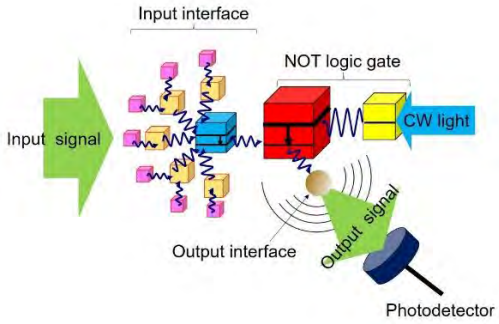

Fig. 3.11 A system composed of an input interface, a NOT logic gate, an output interface, and a photodetector.

The intensity of the propagating light (the output signal) is required to be sufficiently high in order to achieve detection with a sufficiently large signal-to-noise ratio for definitely recognizing the transmitted information. To meet this requirement, it was estimated that the magnitude of energy consumption must be larger than 140 eV, which was approximately equal to the experimentally estimated value (156 eV). In this

estimation, the magnitude of the energy consumption at the output interface was found to be the largest. That in the input interface was smaller. It should be emphasized that the magnitude in the NOT logic gate was too small to be neglected. For comparison, the magnitude of the energy consumption of a CMOS logic gate, to which a load impedance is connected, was estimated to be 6.3 MeV [24]. Since the value estimated above (140 eV) is about 10^4 times smaller, it is confirmed that the energy consumption of the system in Fig. 3.11 is extremely low.

Finally, the signal processing rate of the NOT logic gate in Fig. 3.11 was estimated by noting that this rate depended on (1) the DP energy transfer time from the input NP to the output NP, (2) the number of photons required to recognize a one-bit signal with a conventional receiver, and (3) the efficiency of the output interface. By using 50 ps [4], 100, and 0.45 for these values, respectively, the signal processing rate was estimated to be as high as 90 Mb/s. If one can utilize the device redundancy of multiple identical devices operating in parallel, the minimum duration for a single information bit can be shortened, allowing further increases in the signal processing rate.

From the estimations described above, it was confirmed that the energy consumed by DP devices was extremely low, which means that a higher degree of integration of these devices can be expected as compared with that of conventional electronic devices. Also, the much higher degree of integration compared with conventional optical devices will enable the construction of novel integrated systems that are not possible as long as conventional electrical or optical devices are used. That is, one can be released from the commonly held view in conventional technology that "light should be used for communication because of its high propagation speed, while electrons should be used for computing because of their small size."

A DP computer using DP devices has been proposed as an example of the novel systems that can be constructed when released from this common view [25]. It should be noted that DP computing is completely different from conventional optical computing [26], which carries out digital information processing using several technologies based on spatially parallel processing utilizing the wave optical properties of propagating light, for example, holography. In contrast, DP computing carries out digital processing of time-sequential signals, which has never been possible by using conventional optical devices and propagating light.

4 Nano-fabrication technology based on the nature of the dressed photon

This section reviews novel nano-fabrication technology and demonstrates Phenomena

in Table 1.1 that originate from the intrinsic nature of the DP [1,2]. It starts by reviewing an example of nano-fabrication technology that uses a fiber probe or an aperture. The specific natures of the DP relevant to this technology, and that are contrary to the common views **[a]–[d]** in Section 1.1, are also demonstrated. Next, a more practical technology is reviewed, in which neither the fiber probe nor aperture is required.

4.1 Technology using a fiber probe or an aperture

This part reviews photochemical vapor deposition (PCVD) based on a DP–molecule interaction in which a fiber probe is used. It involves molecular dissociation by the DP and subsequent deposition of the dissociated atoms on a substrate.

$Zn(C_2H_5)_2$ ("DEZn" for short) was adopted as a specimen molecule. A DP was created on the tip of the fiber probe by irradiating the end of the fiber probe with light. Gaseous DEZn molecules, filled in a vacuum chamber, dissociated when these molecules jumped into the DP field (Fig.4.1(a)). Here, the molecule corresponds to the NP in Fig.1.3(b). The dissociated Zn atom subsequently landed on the substrate. After a short migration on the substrate, the Zn atom was adsorbed on the substrate. By repeating these dissociation and deposition processes, the number of adsorbed Zn atoms increased, resulting in the deposition of Zn atoms and the formation of a metallic Zn-NP on the substrate (Fig.4.1(b)).

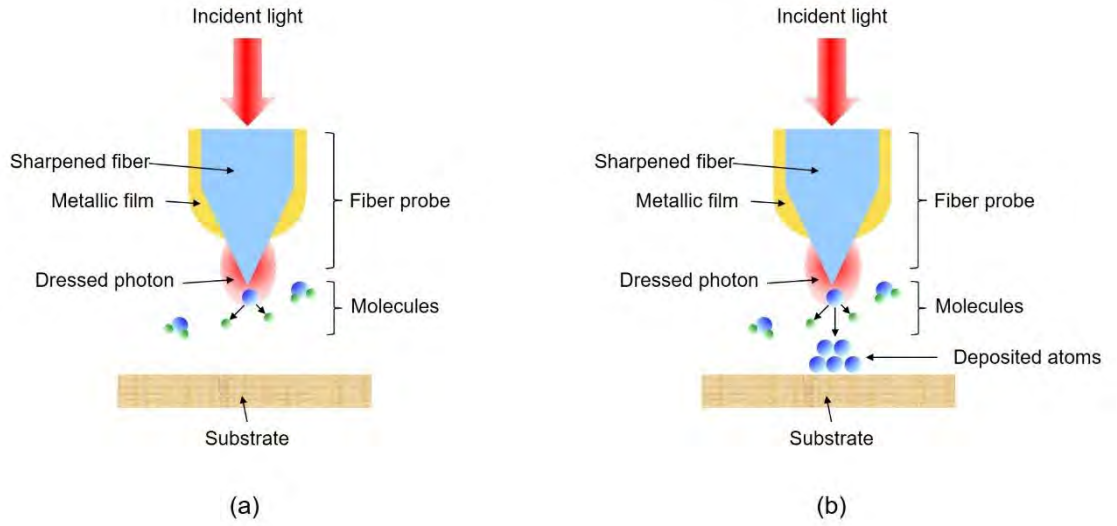

Fig. 4.1 Photochemical vapor deposition based on DP–molecule interaction.
(a) Dissociation of molecules. (b) Deposition of the dissociated atoms.

For comparison, in the case of dissociating the DEZn molecules by using conventional propagating light, the wavelength was required to be shorter than 270 nm (photon energy 4.59 eV) for exciting an electron in the DEZn molecule (refer to the common view **[c]**). By noting this requirement, the following ingenious contrivances **(i)-(iii)** were employed in order to confirm that the DEZn molecules were dissociated only by the DP in the PCVD above (Fig.4.2).

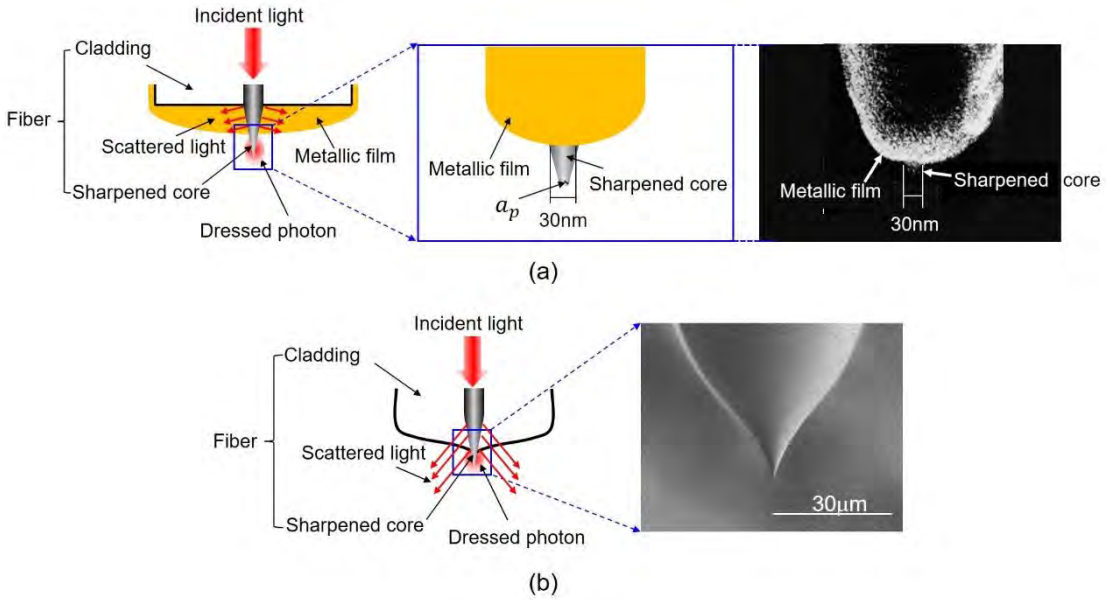

Fig. 4.2 Structures and scanning electron microscopic images of fiber probes.
(a) A high-precision fiber probe, which has been popularly used for high-spatial-resolution microscopy and spectroscopy. a_p is the radius of curvature of the tip. (b) A primitive fiber probe, which was used for the present experiments.

(i) The wavelength of the propagating light for creating the DP was set longer than 270 nm, contrary to the common view **[c]**. As a result, it was expected that the DEZn molecules would not be dissociated even if they were irradiated with the propagating light that leaked out from the tip of the fiber probe into the vacuum. Instead, it was expected that the DEZn molecules would be dissociated only by the DP on the tip due to the following phenomenon:

[Phenomenon 9] *The irradiation photon energy* $h\nu$ *can be lower than the excitation energy of the electron* $E_{ex} - E_g$, *where* E_{ex} *and* E_g *are the energies of the excited and ground states of the electron, respectively.*

That is, since the created DP is the quantum field accompanying the energies of the

excitons ($E_{exciton}$) and phonons (E_{phonon}) at the tip of the fiber probe, its energy is expressed as $h\nu_{DP} = h\nu + E_{exciton} + E_{phonon}$. Thus, even though $h\nu < E_{ex} - E_g$, the DP energy $h\nu_{DP}$ can be larger than $E_{ex} - E_g$ ($h\nu_{DP} \geq E_{ex} - E_g$), which enables the dissociation of DEZn molecules [3].

(ii) In order to insure that the contribution of the propagating light was excluded (refer to **(i)**), an unreliable fiber probe was used to intentionally cause the propagating light to leak out from the taper and tip of the fiber probe into the vacuum. That is, the fiber probe used here was fabricated by heating and mechanically pulling the fiber to form a sharp tip. This was a very primitive method in comparison with the high-precision and highly reproducible selective etching method [4,5]. Thus, high-precision control of the size, cone angle, and throughput were not expected. In addition, the probe was not coated with a metallic film, allowing the propagating light to leak out.

(iii) For further insurance, the DEZn molecules were replaced by zinc-bis(acetylacetonate) ("$Zn(acac)_2$" for short) molecules [6]. $Zn(acac)_2$ is a well-known optically inactive molecule that has never been shown to be dissociated by propagating light. However, it was expected, from Phenomenon 8, that it could be dissociated by the DP.

Figures 4.3(a) and (b) show images of a Zn-NP formed on a sapphire substrate by dissociating DEZn molecules; these images were acquired by using a shear-force microscope [3]. The wavelengths of the propagating light for creating the DP were as long as 488 and 684 nm, respectively, which indicate that the contribution from the propagating light was excluded due to contrivances **(i)** and **(ii)** above. Figure 4.3(c) shows an image of a three-dimensional Zn-NM formed on a sapphire substrate, where DEZn molecules were replaced by $Zn(acac)_2$ molecules based on contrivances **(ii)** and **(iii)** [6]. The wavelength of the propagating light for creating the DP was 457 nm. Figure 4.3 demonstrates that the presented PCVD using the DP is contrary to the common views **[a]**–**[d]**.

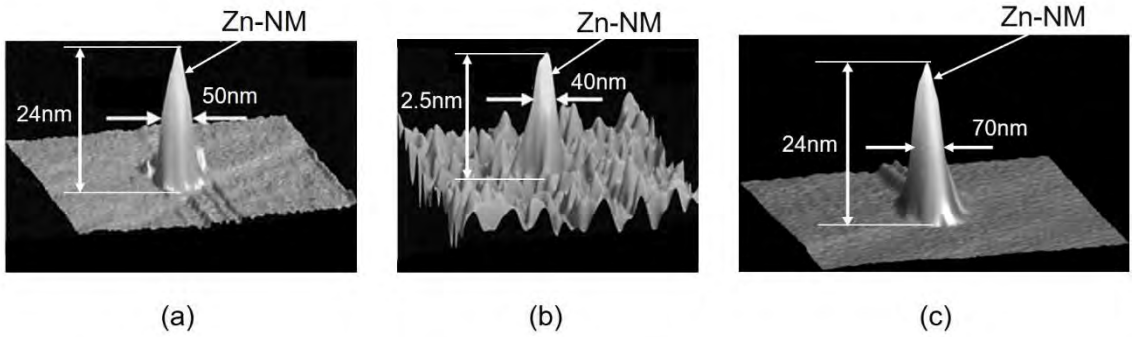

Fig. 4.3 Shear-force microscopic images of Zn-NPs formed on a sapphire substrate. Dissociated molecules are DEZn ((a) and (b)) and $Zn(acac)_2$ (c). The wavelengths of the propagating light for creating the DP were 488nm (a), 684 nm (b), and 457 nm (c).

It should be pointed out that the maximum size $a_{DP,Max}$ of the DP was estimated from the experimental results of the PCVD above [1]. For this estimation, Fig. 4.4 was acquired and shows the dependence of the rate R of depositing Zn atoms on the full-width at the half maximum (FWHM) of the formed Zn-NP. Here, the value of the FWHM increased with increasing deposition time. Closed circles and squares represent the experimental values [7]. The solid curve is the theoretical one fitted to them [8]. This figure shows that the rate R took the maximum when the FWHM was equal to the tip diameter $2a_p$ of the fiber probe (a_p =4.4 nm: tip radius). This was due to the size-dependent resonance of the DP energy transfer between the tip of the fiber probe and the formed Zn-NP (Phenomenon 5). Although further increases in the deposition time increased the size of the Zn-NP, the value of R decreased. Finally, the size and conformation of the Zn-NP reached stationary states, and the value of the FWHM saturated. Figure 4.3 shows the profiles acquired after this saturation.

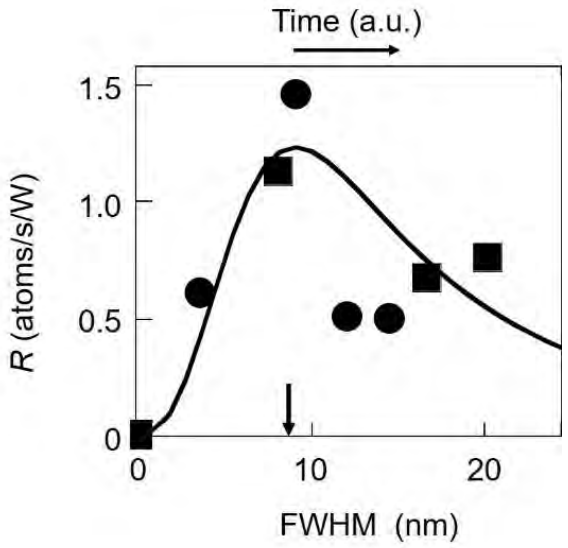

Fig. 4.4 Dependence of the deposition rate R (atoms/s/W) on the FWHM of the Zn-NP. FWHM increased with increasing deposition time. The number of atoms deposited per unit time was normalized to the irradiated light power (W) to derive the rate R. The wavelength of the propagating light for creating the DP was 325 nm. Closed circles and squares represent the measured values when the powers of the light incident to the fiber probe were 5 μ W and 10 μ W, respectively. The downward arrow represents the value of $2a_p$.

It should be noted that the FWHM values in Fig. 4.3 were 50–70 nm even though the controllability of the tip diameter of the fiber probe was low (contrivance **(ii)** above). They were independent of the tip diameter, the wavelength and the power of the light used for irradiating the end of the fiber probe, and the species of molecules used. A larger FWHM was not realized even by increasing the deposition time. Here, it should also be noted, based on the Yukawa function and Phenomenon 5, that the spatial profile and size of the DP transferred from the tip of the fiber probe corresponded to those of the NP deposited on the substrate. From these results, the values of the FWHM in the shear-force microscopic images in Fig. 4.3 indicate the following phenomenon:

[Phenomenon 10] *The maximum size* $a_{DP,Max}$ *of the DP is 50–70 nm.*

By using the nano-fabrication technology above, a variety of two-dimensional patterns have been formed by scanning a fiber probe, like a picture drawn with a single stroke of the pen [9]. However, the total scanning time increased with larger pattern sizes, which decreased the working efficiency. To increase the efficiency, a novel lithography technology has been developed in which the fiber probe was replaced by a two-dimensional photo-mask. A small pattern was formed on the material surface by

exposing the thin photoresist film by the DP that was created on the apertures of the photo-mask. For this creation, visible light was used as a light source. Although its wavelength was longer than that of the ultraviolet light required for exposing photoresist in conventional photolithography, it was allowed to be used due to Phenomenon 9 [10]. Furthermore, an optically inactive photoresist material ZEP-520, popularly used for electron-beam lithography, has been used based on Phenomenon 8. A fully automatic practical photolithography machine has been developed and was used to form a diffraction grating pattern with a half-pitch as narrow as 22 nm [11]. It also produced a two-dimensional array of the DP devices reviewed in Section 3.1 [12], and practical devices for soft X-rays (a Fresnel zone plate [13] and a diffraction grating [14]).

4.2 Technology not using a fiber probe or an aperture

This part reviews a novel autonomous nano-fabrication technology that requires neither fiber probes nor apertures, resulting in drastic increases in the working efficiency. A representative example is autonomous smoothing of a material surface: The material to be smoothed is installed in a vacuum chamber, and the chamber is also filled with gaseous molecules. By irradiating the material surface with light, the DP is created at the tips of the bumps on the rough material surface. That is, the bumps play the role of a fiber probe for creating the DP. If the molecules jump into the DP field, they are dissociated, as was the case of the PCVD in Section 4.1. The chemically active atoms, created as a result of this dissociation, selectively etch the tips of the bumps away, while the flat part of the surface remains unetched. The etching autonomously starts by light irradiation and the surface roughness decreases gradually as etching progresses. The etching autonomously stops when the bumps are annihilated and the DP is not created anymore.

The disc surface of a synthetic silica substrate (30 mm diameter) was etched by using gaseous Cl_2 molecules. Although light with a wavelength shorter than 400 nm was required for conventional photo-dissociation (common view **[c]**), the present method used visible light with a wavelength of 532 nm based on Phenomenon 9. Etching by active Cl atoms decreased the surface roughness to as low as 0.13 nm. A laser mirror was produced by coating a high-reflection film on the smoothed substrate surface, and its damage threshold to the high-power ultraviolet laser light pulses was evaluated. The threshold value was confirmed to be as high as twice that of the commercially available strongest mirror whose substrate surface was polished by a conventional chemical-mechanical polishing technology [15].

Gaseous O_2 molecules can be also used for autonomous etching because the O atoms created by the dissociation are chemically active. The advantage is that etching can be carried out in atmospheric conditions by using O_2 molecules in air, and thus, a vacuum chamber is not required. Figure 4.5(a) shows experimental results of etching a plastic PMMA surface by using O_2 molecules [16]. Although ultraviolet light with a wavelength shorter than 242 nm was required for the conventional photo-dissociation, light with a wavelength of 325 nm was used here that was due to Phenomenon 9. For comparison, Fig. 4.5(b) is the result of the etching by using conventional photo-dissociation, for which the wavelength of the light used was as short as 213 nm.

In Figs. 4.5(a) and (b), the surface roughness was evaluated from its standard deviation $\sigma(l)$, by referring to the square root of the variance that has been popularly used for evaluating the frequency fluctuations of microwave oscillators and lasers [17]. The horizontal axis l represents the period of the roughness on the surface. The vertical axis is the value of $\sigma(l)$ acquired from the atomic-force microscopic image. Here, the ratio $\sigma_{after}/\sigma_{before}$ between the values before (σ_{before}) and after (σ_{after}) the etching is plotted in a logarithmic scale (This ratio was derived from the values σ_{before} and σ_{after} in Fig. 4 in ref. [16]). Figure 4.5(a) shows that $\sigma_{after}/\sigma_{before}<1$ in the range $l<\lambda$ (λ is the wavelength of the light radiated for creating the DP, identified by a downward arrow in this figure), by which the contribution of the sub-wavelength sized DP is confirmed. Drastic decreases in $\sigma_{after}/\sigma_{before}$ can be seen in the range $l<$ 50–70 nm, from which Phenomenon 10 is confirmed again. In contrast to Fig. 4.5(a), Fig. 4.5 (b) shows that $\sigma_{after}/\sigma_{before}<1$ in the range $l>\lambda$. This means that the etching was effective in the super-wavelength range. On the contrary, $\sigma_{after}/\sigma_{before}>1$ in the sub-wavelength range, which indicates that the surface roughness was increased by the etching. By comparing the two figures, it is confirmed that the etching by the DP is effective for selectively removing bumps of sub-wavelength size.

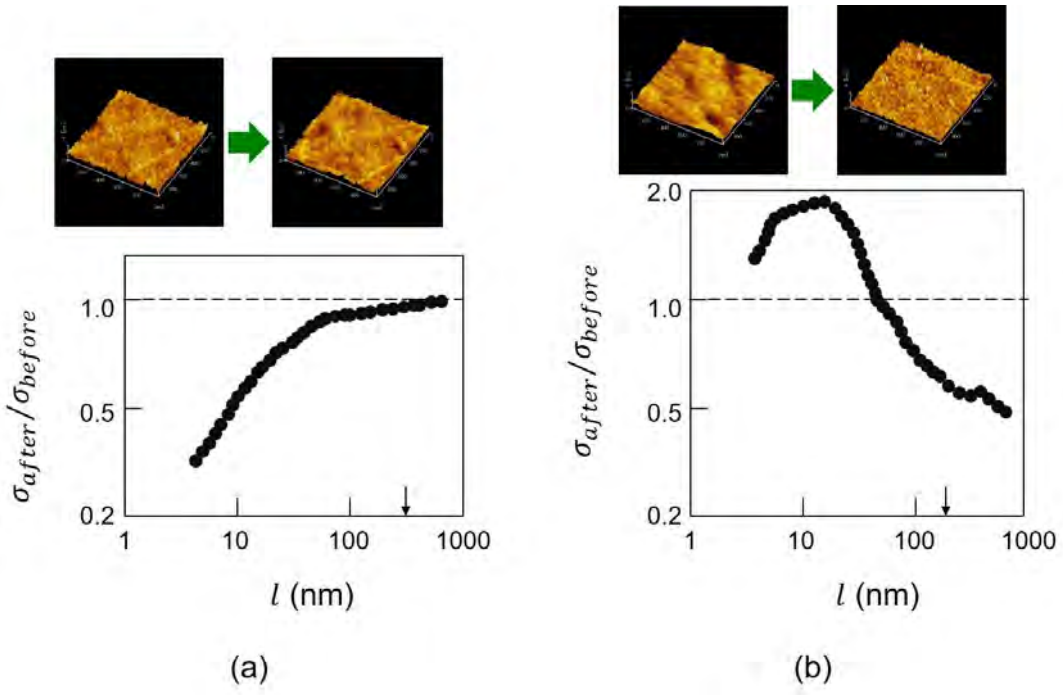

Fig. 4.5 The ratio of the standard deviation of the roughness of the PMMA surface before and after etching.

(a) and (b) are the results acquired by illuminating the surface with light having wavlengths of 325 nm and 213 nm, respectively. The downward arrows represent the values of l that are equal to the wavelengths above.

Since the DPs are always created on the tip of the bump on the material surface under light irradiation, the present autonomous etching has been applied to a variety of surface profiles. These included a convex surface, a concave surface, and the inner surface of a cylinder. As an example, this etching has smoothed the side surface of a diffraction grating composed of parallel linear corrugated patterns [18] and the surface of a photo-mask used for conventional ultraviolet lithography [19]. Furthermore, a variety of materials have been smoothened, such as the surfaces of GaN crystals [20], transparent ceramics [21], and diamonds [22]. These achievements demonstrated the prominent capability of the present autonomous smoothing technology, achieved by exploiting the DP.

5 Optical energy conversion based on the nature of the dressed photon

Since the DP field has a broad spectrum, as was described in Section 3, the novel phenomena of energy up- and down-conversion are expected. This section reviews

experimental results of such optical energy conversions and describes the phenomena in Table 1.1 that originate from the intrinsic nature of the DP and are contrary to the common views **[c]–[e]** in Section 1.1.

5.1 Conversion to optical energy

Optical energy up-conversion, i.e., the conversion from infrared to visible light, has been realized. In this process, phonons in the DP provided their energies to the electrons in NPs. NPs of DCM, coumarine 540A, and stilbene 420 dye molecules were used as specimens for demonstrating the up-conversion. By irradiating them with infrared light of 0.8–1.3 μm wavelength, the DP created on one NP was transferred to the adjacent NPs. These NPs received the DP energy that contained the phonon energy, and thus, they respectively emitted red, green, and blue light [1,2]. This conversion method has been applied to measure infrared optical pulse shapes [3].

Energy down-conversion has also been realized by using NPs in a plastic film and in an autonomously grown optically curable resin. Their experimental results are reviewed in this section.

5.1.1 Nanoparticles in a plastic film

A novel thin film was invented recently, which efficiently converts ultraviolet (UV) photon energy to visible photon energy by means of DP energy transfer and dissipation [4]. It has been used to drastically improve the electrical power generation efficiency of a solar cell battery.

Transparent silicone or ethylene-vinyl acetate (EVA) was used as the film material, with a thickness of 10 μ m. ZnO semiconductor NPs (average size and number density are 3–5 nm and 10^{17} to 10^{18} /cm^3, respectively) and DCM dye NPs (weight density 3–5 mg/cm^3) were dispersed in this film. It is required that the separation between the ZnO- and DCM-NPs be as close as possible to their sizes in order to transfer the DP energy between them. The number density and weight density above meet this requirement [5,6].

The roles of the ZnO- and DCM-NPs in this film are to absorb UV light and emit visible light, respectively. They correspond respectively to NP_S and NP_L in Fig. 2.6(b). That is, UV light absorption excites an electron in the ZnO-NP to create the DP. Then, the DP energy is transferred to the DCM NP, resulting in excitation of the electron in the DCM-NP. This electron dissipates a small amount of its energy by relaxing to a

lower energy level, emitting visible light.

For the DP energy transfer, an electronic dipole-forbidden transition (Phenomenon 8) is utilized. Furthermore, since the magnitude of the energy dissipation above is very low, very high-efficiency optical energy conversion can be realized.

Figures 5.1(a) and (b) show the electronic energy levels in the ZnP- and DCM-NPs for UV light absorption and visible light emission, respectively. They are:

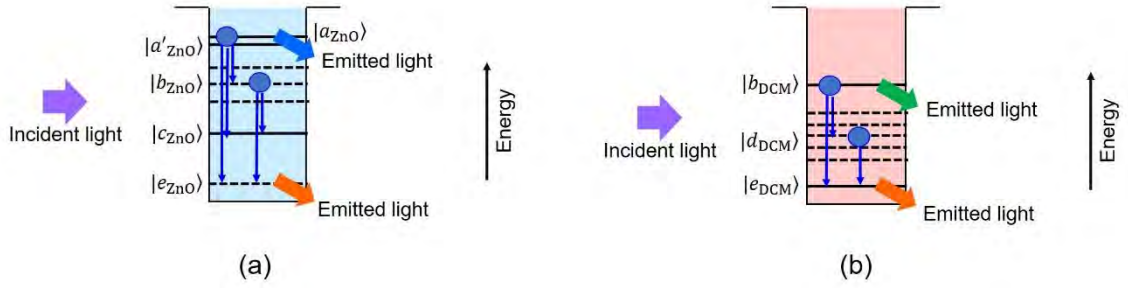

Fig. 5.1 Electronic energy levels in NPs.

(a) In a ZnO-NP.

$|a_{ZnO}\rangle$: An energy level of the electron in the conduction band. $|a'_{ZnO}\rangle$: An electric dipole-allowed energy level in the conduction band.

$|b_{ZnO}\rangle$: Several energy levels in the bandgap, which originate from impurity atoms in the ZnO-NP.

$|c_{ZnO}\rangle$: An electric dipole-allowed level of the energy levels $|b_{ZnO}\rangle$.

$|e_{ZnO}\rangle$: An electric dipole-forbidden level of the energy levels $|b_{ZnO}\rangle$.

(b) In a DCM-NP.

$|b_{DCM}\rangle$: An electric dipole-allowed level.

$|d_{DCM}\rangle$: Electric dipole-forbidden energy levels, which originate from the impurity atoms in the DCM-NP.

$|e_{DCM}\rangle$: An electric dipole-allowed level of the energy levels $|d_{DCM}\rangle$. It is resonant with the energy level $|e_{ZnO}\rangle$ in the ZnO-NP.

The UV light absorption and visible light emission processes in the ZnO NP and DCM NP, are:

[In ZnO-NP (Fig. 5.1(a))]

An electron in the ZnO-NP is excited to the energy level $|a_{ZnO}\rangle$ by UV light absorption.

This excited electron has a higher probability of UV light emission than that of relaxation to a lower energy level. Thus, the conversion efficiency from UV light to visible light is low.

[In DCM-NP (Fig. 5.1(b))].
After an electron in the DCM-NP is excited to a higher energy level by UV light absorption, it relaxes to an electric dipole-forbidden energy level, which is a triplet energy level. Thus, the conversion efficiency from UV light to visible light is low.

However, in the case where both the ZnO- and DCM-NPs are dispersed in the film, the light absorption and emission processes are remarkably different from those above. They are (Fig. 5.2): An electron in the ZnO-NP is excited to the energy level $|a_{\mathrm{ZnO}}\rangle$ by UV light absorption. It subsequently relaxes to the lower energy levels $|b_{\mathrm{ZnO}}\rangle$, $|c_{\mathrm{ZnO}}\rangle$, or $|e_{\mathrm{ZnO}}\rangle$. Then, a DP is created, and its energy is transferred to the resonant energy levels $|b_{\mathrm{DCM}}\rangle$, $|d_{\mathrm{DCM}}\rangle$, or $|e_{\mathrm{DCM}}\rangle$ in the DCM-NP. As a result, an electron is excited to these levels and emits visible light. This visible light emission realizes a high efficiency of energy conversion from UV light to visible light. It should be noted that the DP energy can be transferred back from the DCM- to the ZnO-NPs even though the electron in the DCM -NPs relaxes to the triplet energy level. This back transfer contributes to further increases in the energy conversion efficiency.

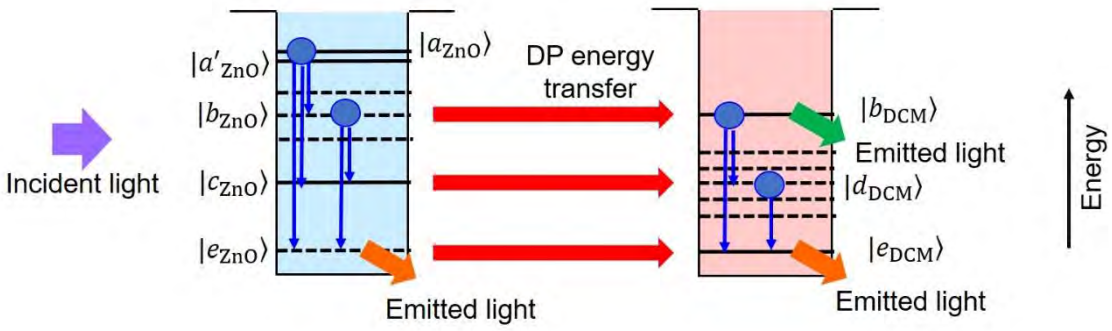

Fig. 5.2 Light absorption and emission of a film in which ZnO- and DCM-NPs are dispersed.

Figure 5.3 shows measured excitation spectra, in which the horizontal axis represents the wavelength of the light incident on the film, and the vertical axis is the intensity of the visible light (wavelength 560 nm) emitted from the electron in the energy level $|e_{\mathrm{DCM}}\rangle$ of the DCM NP. Figures 5.3(a) and (b) show the results acquired when only the ZnO- and DCM-NPs are dispersed in the film, respectively. Figure 5.3 (c) shows those when both ZnO- and DCM-NPs are dispersed. Comparing the areas below the

curves in these figures, the efficiency of the conversion from UV light to visible light (wavelength 560 nm) energy in Fig. 5.3(c) is estimated to be at least 10-times higher than that in Fig. 5.3(a) or (b).

Furthermore, a bump A on the curve in Fig. 5.3(c) represents that the efficiency of the visible light emission is selectively enhanced when the incident UV light is resonant with the energy level $|a_{\mathrm{ZnO}}\rangle$ of the ZnO-NP. Furthermore, the bumps B and C also represent that the efficiency is selectively enhanced when the incident light is resonant with the energy level $|b_{\mathrm{ZnO}}\rangle$ or $|c_{\mathrm{ZnO}}\rangle$ of the ZnO-NP. These selective enhances are due to the DP energy transfer to the energy levels $|b_{\mathrm{DCM}}\rangle$ or $|d_{\mathrm{DCM}}\rangle$ of the DCM NPs, and subsequent relaxation to the energy level $|e_{\mathrm{DCM}}\rangle$.

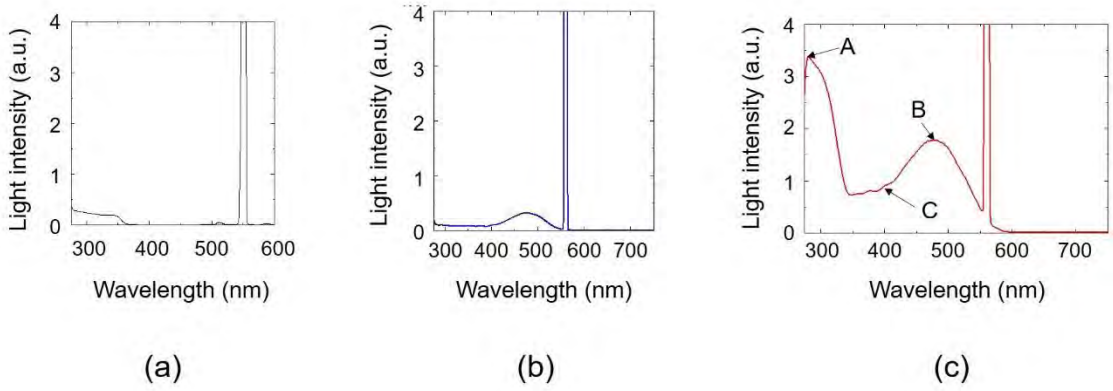

Fig. 5.3 Excitation spectra.

(a) and (b) The results acquired when only the ZnO- and DCM-NPs are dispersed in the film, respectively.
(c) The result when both ZnO- and DCM-NPs are dispersed.

Figure 5.4 shows the measured relation between the incident UV light intensity (wavelength 325 nm) and the efficiency of the energy conversion to visible light (wavelength 560 nm). It shows that the measured efficiency is proportional to the square of the incident UV light intensity. This is because the conversion efficiency is proportional to the product of the numbers of DPs created in the ZnO- and DCM-NPs.

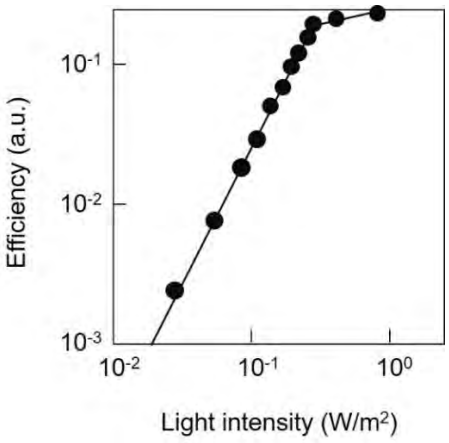

Fig. 5.4 Measured relation between the incident UV light intensity (wavelength 325 nm) and the efficiency of the energy conversion.

Figure 5.5 shows the temporal evolution of the light intensity emitted from the film when a propagating light pulse (pulse width: 2 ps) was applied to the NPs. Figures 5.5(a) and (b) were acquired when only the ZnO- and DCM-NPs were respectively dispersed in the film. They are nothing more than the intensities of the light emitted from the ZnO- and DCM-NPs, respectively, as a result of conventional fluorescence (radiative relaxation process in Section. 2.3). The rise time τ_r of the light intensity is as short as 10 ps in Figs. 5.5(a) and (b). On the other hand, the fall time τ_f is as long as 15 ns and 1.4 ns, respectively, which corresponds to the radiative relaxation rate.

Figure 5.5(c) shows the results acquired when both ZnO- and DCM-NPs are dispersed in the film. Figure 5.5(d) is a schematic explanation of the curves in Fig. 5.5(c). The time constant τ_r in this figure represents the rise time. Two constants τ_{f1} and τ_{f2} represent two different fall times. Figure 5.5(c) shows that the values of τ_r and τ_{f1} are 100–150 ps. These correspond to the DP energy transfer times from the ZnO- to DCM-NPs, which are much longer than the fluorescence rise times in Figs. 5.5 (a) and (b).

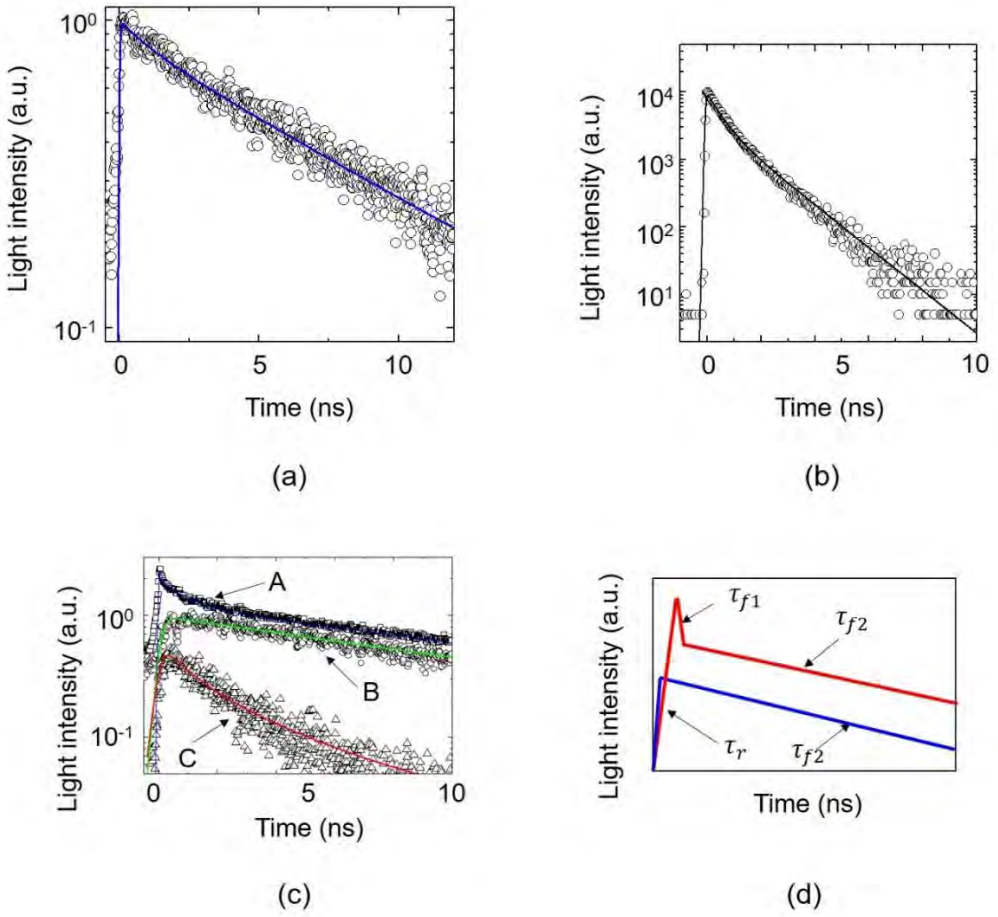

Fig. 5.5 Temporal evolutions of the light intensity emitted from the film.

Similar to the fall time of the curves in Figs. 5.5(a) and (b), the fall time τ_{f2} is 15 ns, which is much longer than τ_{f1}. This fall time τ_{f2} corresponds to the value of the radiative relaxation rate. It means that, after the DP energy transfer, conventional florescence occurs in the case where both the ZnO and DCM NPs are dispersed in the film. It should be noted that Figs. 5.5(a) and (b) do not have the temporal behaviors represented by the time constants τ_r and τ_{f1}. It should be pointed out that the temporal evolutions shown in Fig.5.5(c) also have two features given at the end of Section 2.3. They are: (1) The temporal evolution expressed as $\exp\left(-t/\tau_{f1}\right)$ originated from the DP energy transfer between NPs, and (2) The temporal evolution expressed as

$\exp\left(-\sqrt{t/\tau_{f2}}\right)$ originated from the radiative relaxation in each NP.

It is expected that the optical energy conversion efficiency of the film is as high as 90%–95% by referring to the large difference between the DP energy transfer time (τ_r, τ_{f1} = 100–150 ps) and the lifetime (τ_{f2} = 15 ns) for fluorescent light emission from the DCM NP. Based on this expectation, a novel film was fabricated for converting UV light energy (wavelength 300–350 nm) to visible light energy (wavelength 560 nm) by dispersing ZnO- and DCM-NPs (Fig. 5.6(a)) [7]. By putting this film on the surface of a commercially available Si solar cell battery (surface area 156 mm × 156 mm, nominal electrical power generation efficiency 18.1 %), the electrical power generation efficiency was measured to be as high as 20.0 %, which is an increase of 1.9 % compared with the nominal efficiency mentioned above.

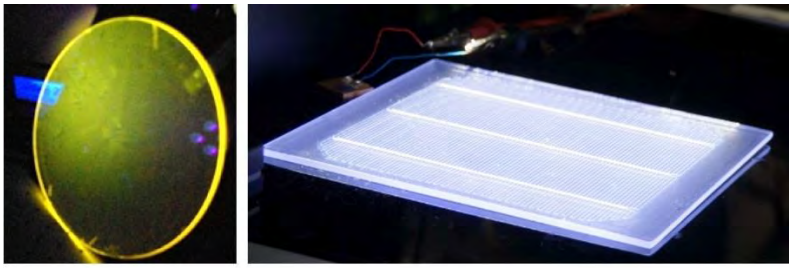

(a) (b)

Fig. 5.6 Photographic images of the film.

The film is 10 μ m thick and is coated on the front surface of a glass substrate. After an index-matching oil is coated on the rear surface, it is placed on a solar cell battery surface.

(a) ZnO- and DCM-NPs are dispersed in the film. (b) ZnO- and BBQ-NPs are dispersed in the film.

To realize an even higher increase, another type of film was recently developed by replacing the DCM-NPs with BBQ dye NPs (Fig. 5.6(b)), which allowed UV light in the wavelength range 300–350 nm to be efficiently converted to visible light with a wavelength of 450 nm [8]. By putting this film on the surface of the Si solar battery above, the electrical power generation efficiency was measured to be as high as 20.2 %, which is an increase of 2.1 % compared with the nominal efficiency mentioned above.

It should be pointed out that the efficiencies higher than 20% realized by these films have never been achieved with conventional solitary Si solar batteries. The technical details of the method of fabricating these films will be published elsewhere.

5.1.2 Nano-droplets

A nano-droplet (ND) is a small particle of resin in which semiconductor NPs are encapsulated [9]. Table 5.1 shows four pairs of NPs (NP1 and NP2) that were encapsulated [10-13]. For forming the ND, these NPs were dispersed into a solution of ultraviolet (UV)-setting resin or thermosetting resin to allow the NPs to undergo Brownian motion.

Table 5.1 ~~3.1~~ Pairs of NPs and resins used to form the ND.

NP1	NP2	Regin	Reference
CdSe	ZnO	UV-setting	[10]
CdSe	ZnO	UV-setting	[11]
CdSe	CdS	UV-setting	[12]
CdSe	CdS	Thermosetting	[13]

This solution was irradiated with visible light whose photon energy was resonant with the exciton energy, $E_{1\text{exciton}}$, in NP1 in order to excite the exciton. Here, it should be noted that the exciton in NP2 was not excited because its energy, $E_{2\text{exciton}}$, was much higher than the photon energy of the irradiated visible light. The exciton excited in NP1 created a DP, which could transfer to NP2 because its energy was as high as $E_{2\text{exciton}}$ due to the contribution of the energies of the exciton and phonon (Phenomenon 9). This transfer took place only when the size of NP2 was equivalent to that of NP1 (size-dependent resonance: Phenomenon 5). The transferred DP subsequently excited an exciton in NP2, resulting in the creation of another DP. The UV-setting resin solution was finally cured by this DP because the energy of the DP had been increased to an energy as high as the UV photon energy, also due to the contribution of the energies of the exciton and phonon. The spatial extent of the cured UV-setting resin solution was limited by that of the DPs on NP1 and NP2 (Section 2.1.2).

NP1 and NP2 were encapsulated in a small particle of the cured resin called an ND, as schematically illustrated in Fig. 5.7(a) [11]. The optical microscope images in Fig. 5.7(b) demonstrated that a large number of spherical NDs were formed. They also demonstrated that the conformations and sizes of these NDs were homogenous, and this was attributed to the autonomous control of the Brownian motion of the NPs and the DP energy transfer.

It should be pointed out that the ND could be formed even by replacing the UV-setting resin solution with an optically transparent thermosetting resin. It has been known that the photon–electron interaction in such a resin is electric-dipole forbidden, and thus, this resin is optically transparent. However, the DP turned the transition to an electric-dipole allowed transition (Phenomenon 8), resulting in curing of the resin and formation of the ND. The formed ND can be advantageously used due to the optical transparent nature of the cured resin. It is expected that quantum walk theory will describe the autonomous control of the Brownian motion and DP energy transfer in the process of forming the ND.

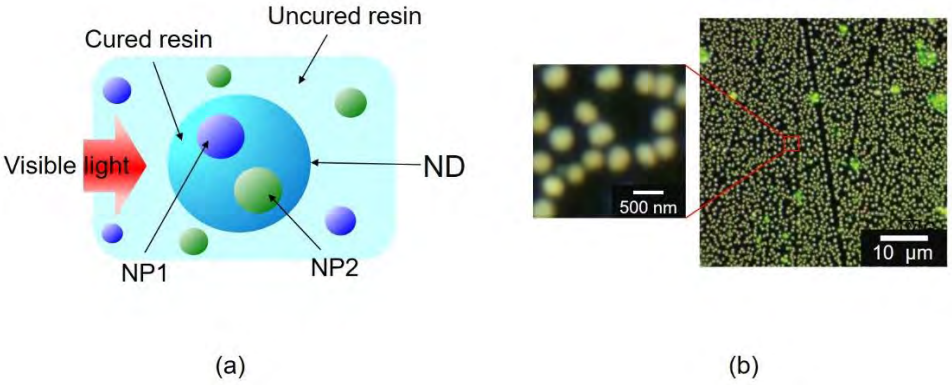

Fig.5.7 Schematic explanation of a nano-droplet (ND).
(a) Principles of formation. (b) Optical images of formed NDs.

NDs formed in this way have been used for optical energy down-conversion to generate visible light under UV light irradiation [11]. It should be noted that the direction of the DP energy transfer for this conversion was opposite to the one for forming the ND. That is, NP2 absorbed the irradiated UV light to create a DP that was subsequently transferred to NP1 to generate visible light. Figure 5.8 represents the photoluminescence (PL) spectra emitted from four independent NDs [10]. It shows that their spectral profiles, including spectral peaks and widths, were equivalent to each other. They were well-fitted to the Lorentzian curve. From these spectral features, homogeneity of the optical properties of these NDs was confirmed.

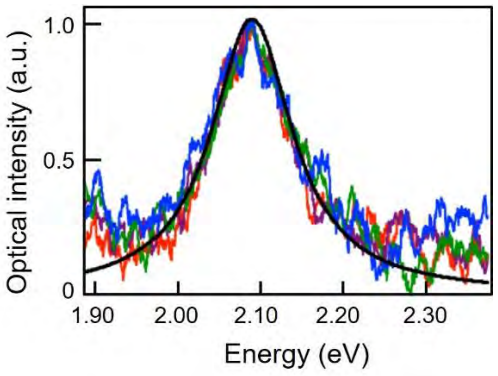

Fig.5.8 PL spectra from the NDs.

CdSe and ZnO were used as NP1 and NP2, respectively. They were encapsulated in a UV-setting resin. Red, green, blue and violet curves are the spectra from four independent NDs acquired under light irradiation with a photon energy of 3.06 eV. The solid curve is a Lorentz function fitted to these curves.

5.2 Conversion to electrical energy

Novel devices for optical to electrical energy conversion that exhibited the energy up-conversion feature originating from the DP have been fabricated. The first example is a photovoltaic device using organic molecules of poly(3-hexylthiophene) (P3HT). By depositing Ag particles on the device surface using a novel DP-assisted rf-sputtering method, the conformation of the electrode surface was autonomously controlled [14]. The second example is a Si-photodiode in which the spatial distribution of doped boron (B) atoms was autonomously controlled by a novel DP-assisted annealing [15]. A detailed explanation of this annealing will be given in Section 6. In these two examples, efficient energy up-conversion was realized even when the incident photon energy was lower than the bandgap energy of the semiconductor materials used for the devices. Furthermore, optical amplification was confirmed, which originated from stimulated emission triggered by the DP.

This section reviews experimental results for the first example above [16]. Autonomously created DPs were utilized for fabrication and operation of this device in order to realize a high conversion efficiency. The fabrication and operation can be summarized as follows.

5.2.1 Fabrication

A P3HT film was used as a p-type semiconductor having a bandgap energy, E_g, of 2.18

eV, and therefore, the cutoff-wavelength, λ_c, for optical to electrical energy conversion was 570 nm. A ZnO film was used as an n-type semiconductor (E_g=3.37 eV, λ_c=367 nm). A transparent ITO film and an Ag film were used as two electrodes. The principal features of this photovoltaic device originated from the P3HT because a depletion layer of the pn-junction was formed inside the P3HT. Films of ITO, ZnO, P3HT, and Ag were deposited successively on a sapphire substrate to thicknesses of 200 nm, 100 nm, 50 nm, and several nm, respectively, in order to make a preliminary device (Fig. 5.9).

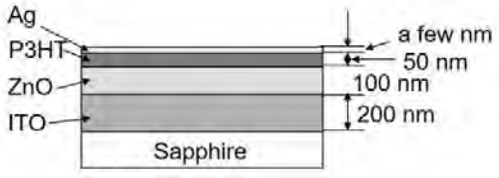

Fig. 5.9 Preliminary photovoltaic device using an Ag film as an electrode.

On the Ag film of the preliminary device, Ag particles were deposited by the method shown in Fig. 5.10: While Ag particles were being deposited by RF-sputtering, the surface of the Ag film was irradiated with light to create DPs, and a reverse bias voltage, V_b, was applied to the pn-junction. Here, the wavelength λ_0 of the irradiation light was longer than λ_c. As an example, λ_0 was set to 660 nm, and V_b was -1.5 V.

The fabrication principle was such that the autonomously created DPs and the reverse bias voltage controlled the amount of Ag particles that flew into and out of the Ag film surface. The fabrication process was as follows:

(1) Creation of electron–hole pairs by the DPs (Fig. 5.11(a)): The DPs were created at bumps on the Ag film surface by the irradiation light. If the field of the DPs extended to the pn-junction, electrons were excited to create electron–hole pairs even though the photon energy of the irradiation light was lower than E_g. This unique excitation was possible due to the contribution of the energy of the phonon that was a constituent element of the DP.

(2) Charging the Ag film (Fig. 5.11(b)): The created electron–hole pairs were annihilated by the electric field generated by the reverse bias voltage, and the positive holes were attracted to the Ag film electrode. As a result, the Ag film was positively charged.

(3) Autonomous control of Ag particle deposition (Fig. 5.11(c)): The Ag particles

striking the Ag film surface were positively charged because they passed through an Ar plasma for RF-sputtering. Therefore, these Ag particles were repulsed from the area of the Ag film surface that was locally positively charged as a result of efficient creation of DPs in steps **(1)** and **(2)**. As a result, the repulsed Ag particles were deposited on other areas of the Ag film surface.

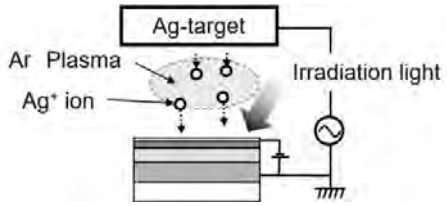

Fig. 5.10 Deposition of Ag particles by RF-sputtering under light irradiation.

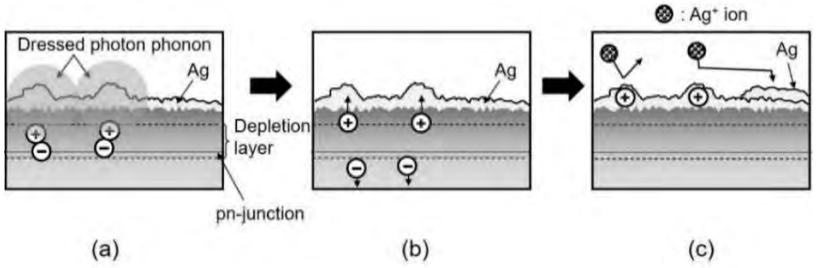

Fig. 5.11 Principle of controlling the amount of Ag particles that flew into and out of the Ag film surface.

(a), (b), (c) represent the creation of electron-hole pairs by the DP, charging of the Ag film, and autonomous control of the Ag particle deposition, respectively.

By steps **(1)**–**(3)**, a unique surface morphology was formed on the Ag film, which was governed by the spatial distribution of the DPs. The fabrication process finished autonomously once the spatial distribution of the created DPs reached a stationary state.

Table 5.2 summarizes the values of the irradiation light power, P, and the reverse bias voltage, V_b, for three devices A, B, and C. Figure 5.12 shows scanning electron microscope (SEM) images of the Ag film surfaces. The images show that the surfaces of devices B and C (Figs. 5.12(b) and (c)) were rougher than that of device A (Fig. 5.12(a)) due to the larger Ag-NPs grown on the surface. The lower parts in Figs. 5.12(b) and (c) show histograms of the distribution of NP diameters, derived by assuming spherical NP shapes. The solid curves are lognormal functions fitted to these histograms. In Fig. 5.12(b), the average and the standard deviation of the diameter were 90 nm and 64 nm, respectively, whereas they were respectively 86 nm and 32 nm in Fig.

5.12(c). By comparing these values, it was found that the standard deviation decreased with increasing light power, P, which meant that a surface morphology with unique-sized NPs was autonomously formed due to the high irradiation power. A unique feature of the histograms in Figs. 5.12(b) and (c) was the bumps, identified by downward arrows, that deviated from the lognormal functions.

Table 5.2 The values of the irradiation light power, P, and the reverse bias voltage, V_b, for device fabrication.

Name of device	Irradiation light power, P	Reverse bias voltage, V_b
A(1)	0	0
B	50 mW	-1.5 V
C	70 mW	-1.5 V

(1) A is a reference device that was fabricated to compare its performance with that of devices B and C.

5.2.2 Operation

To operate the device fabricated above, it was irradiated with light from the rear surface of the sapphire substrate (Fig. 5.13). Since the spatial distributions of the DPs created on the Ag-NPs in Figs. 5.12(b) and (c) depended on the NP sizes (the average diameters of the NPs were 90 nm and 86 nm, respectively), the DP fields of devices B and C extended to the pn-junctions because the sum of the thicknesses of the Ag film and the P3HT was less than 70 nm. As a result, electron–hole pairs were created by these DPs when the device was irradiated with light*. Even though the photon energy of the irradiation light was lower than E_g, optical to electrical energy up-conversion was expected thanks to the energy of the phonons, constituent elements of the DP. Furthermore, it was expected that the efficiency of creating the electron–hole pairs would be highest when the irradiation light wavelength was equal to the wavelength, λ_0, of the light irradiated during the fabrication process. This phenomenon is called the photon breeding (PB) effect [17], and will be reviewed also in Section 6.

(*) In the case of device A, on the other hand, the field of the DPs did not reach the pn-junction because the Ag film was too thick (800 nm) to allow electron–hole pairs to be created.

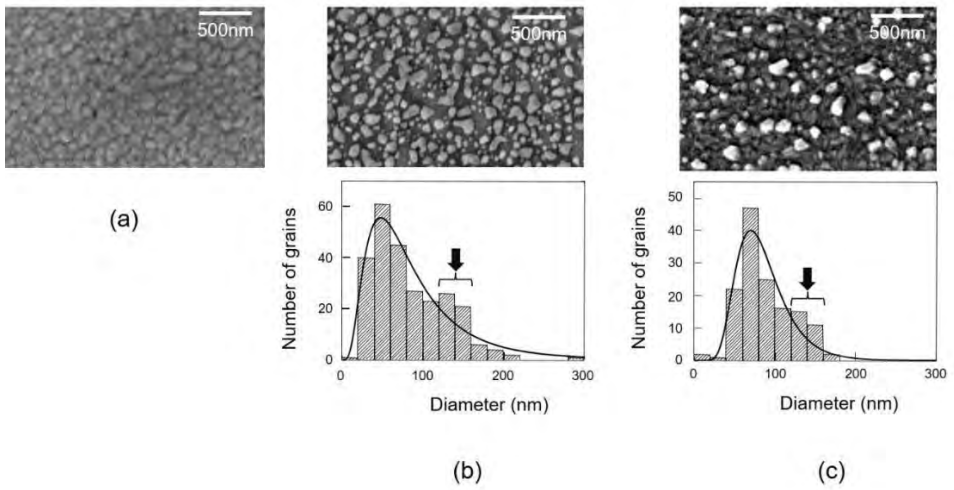

Fig. 5.12 Scanning electron microscopic images of Ag film surfaces.
(a), (b), and (c) show images of devices A, B, and C, respectively. Lower parts of (b) and (c) show histograms of the distribution of the Ag-NP diameters. The downward arrows represent the bumps on the histograms.

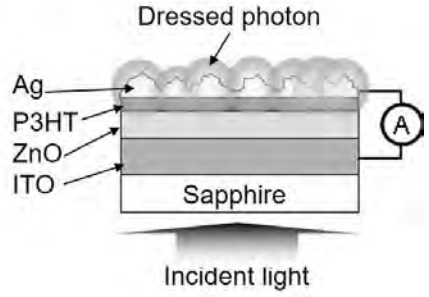

Fig. 5.13 Operation of the fabricated photovoltaic device.

Figure 5.14 shows the measured dependence of the generated photocurrent density on the irradiation light wavelength. The wavelength range of the measurement was 580–670 nm, which was longer than the wavelength λ_c (=570 nm) of the P3HT. Curve A in this figure shows a very low photocurrent density generated from device A. Curves B and C are for devices B and C, respectively. They show that photocurrents were generated even with irradiation light wavelengths longer than λ_c.

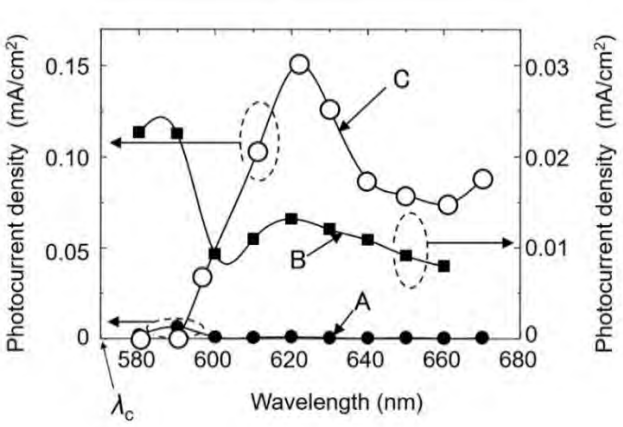

Fig.5.14 Relation between the incident light wavelength and the photocurrent density.
Curves A, B, and C represent the measured results for devices A, B, and C, respectively.

Curve C has a peak at 620 nm*, clearly confirming the PB effect. Wavelength selectivity was not so clearly seen in curve B (device B) compared with curve C, because of the lower light power (50 mW) irradiated during the fabrication process for device B. The clear wavelength selectivity of curve C was due to the efficient creation of DPs by the higher irradiation power (70 mW).

(*) The peak wavelength (620 nm) of curve C was 40 nm shorter than the wavelength, λ_0 (=660 nm), of the irradiation light used in the fabrication process. This difference in wavelength originated from the DC Stark effect induced by the reverse bias voltage, V_b, applied during the fabrication process.

---

6 Light-emitting diodes, lasers, and polarization rotators based on the nature of the dressed photon

This section reviews Si light-emitting diodes (LEDs), Si lasers, and SiC polarization rotators. For comparison with Section 5, it should be pointed out that they are examples of devices that convert electrical energy to optical energy. Phenomena contrary to the common view **[e]** are also demonstrated.

Crystalline Si has long been a key material supporting the development of modern technology for more than half a century because of its numerous advantages, such as Si's abundance in the earth's crust, and its widespread use for electronics. However, because Si is an indirect-transition-type semiconductor, it has been considered

to be unsuitable for light-emitting devices: Since the bottom of the conduction band and the top of the valence band in Si are at different positions in reciprocal lattice space, the momentum conservation law requires an interaction between an electron–hole pair and phonons for radiative recombination. However, the probability of this interaction is very low.

Nevertheless, Si has been the subject of extensive study for the fabrication of light-emitting devices. These include studies using porous Si [1], a super-lattice structure of Si and SiO_2 [2], and so on. However, the devices fabricated in these studies have some limitations, such as low efficiency, the need to operate at low temperature, complicated fabrication processes, and the difficulty of current injection. Experimental work on a novel technology named silicon photonics has recently progressed [3]. Although sophisticated passive optical devices such as optical waveguides and optical switches have been developed, Si light-emitting devices have not been dealt with.

The problems above have been solved by using the DP because the phonons in the DP can provide momenta to the electron to satisfy the momentum conservation law [4]. As a result, the following phenomenon that is contrary to the common view **[e]** was confirmed:

[Phenomenon 11] By DP-assisted annealing, a Si crystal works as a high-power light emitting device even though it is an indirect transition-type semiconductor.

6.1 Si-LEDs

Fabrication and operation methods are reviewed here by taking an infrared Si-LED [5]. An n-type Si substrate was used, in which As atoms or Sb atoms were doped. As the first step, the substrate surface was transformed to a p-type material by implanting B atoms, forming a p-n homojunction. Metallic films were coated on the substrate surfaces to serve as a mesh- electrode (Fig. 6.1).

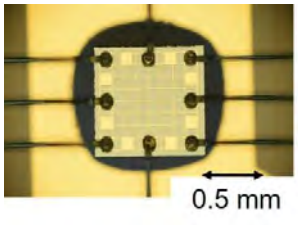

Fig. 6.1 Photographic profile of the fabricated mesh-electrode type LED.

As the next step, this substrate was processed by a novel fabrication method named DP-assisted annealing: By current injection, Joule heat was generated, which

caused the B atoms to diffuse. During this Joule-annealing, the substrate surface was irradiated with infrared light (for example, 1.342 μ m-wavelength light). Because its photon energy $h\nu_{anneal}$ (=0.925eV) was sufficiently lower than the bandgap energy E_g (=1.12eV) of Si (Phenomenon 9), the light could penetrate into the Si substrate without suffering absorption. Then, the light reached the p-n homojunction to create the DP on the B atom. The created DP localized at this impurity B atom, which manifested Phenomenon 7.

The phonons in the created DP can provide momenta to the electron nearby to satisfy the momentum conservation law, resulting in radiative recombination for photon emission. This is stimulated emission triggered by the irradiated infrared light. The emitted light propagated out from the crystal to the outside, which indicated that part of the Joule energy used for diffusing the B atoms was dissipated in the form of optical energy, resulting in local cooling that locally decreased the diffusion rate. As a result, by the balance between heating by the Joule energy and cooling by the stimulated emission, the spatial distribution of B atoms varied and reached a stationary state autonomously. This stationary state was expected to be the optimum for efficient creation of the DPs and for efficient LED operation because the probability of spontaneous emission was proportional to that of the stimulated emission described above.

The optimum condition for the DP-assisted annealing has been found based on a two-level system model. That is, the optimum ratio between the irradiated photon number and the injected electron number per unit time was 1:1 [6]. After the DP-assisted annealing, the Huang-Rhys factor, a parameter representing the magnitude of the coupling between electron–hole pairs and phonons, was experimentally evaluated to be 4.08 [7]. This was 10^2–10^3 times higher than that before the DP-assisted annealing. It was also found that the DPs coupled with the coherent phonons of the longitudinal optical mode [8].

The device fabricated above was operated as an LED by simple current injection, similar to the case of operating conventional LEDs. By injecting a current of 3.0 A into a flip-chip type device with an areal size of 0.35 mm $\times$ 0.35 mm (Fig. 6.2), a CW output optical power as high as 2.0 W was obtained at a substrate temperature of 77 K. A power as high as 200 mW was obtained even at room temperature (283 K) [9]. These results confirmed that the following phenomenon occurs:

[Phenomenon 12] The spatial distribution of B atoms varies and reaches a stationary state autonomously due to DP-assisted annealing, resulting in strong light emission from the Si crystal.

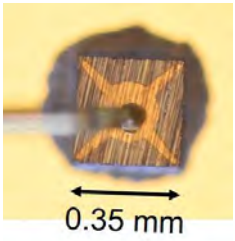

Fig. 6.2 Photographic profile of the fabricated flip-chip type LED.

Figure 6.2 shows the light emission spectra of the fabricated Si-LED acquired at a temperature of 283 K and an injection current of 2.45 A [9]. This figure clearly shows high spectral peaks at $E_g - 3E_{phonon}$, $E_g - 6E_{phonon}$, and $E_g - 9E_{phonon}$ (refer to the arrows A -C), where E_{phonon} is a phonon energy.

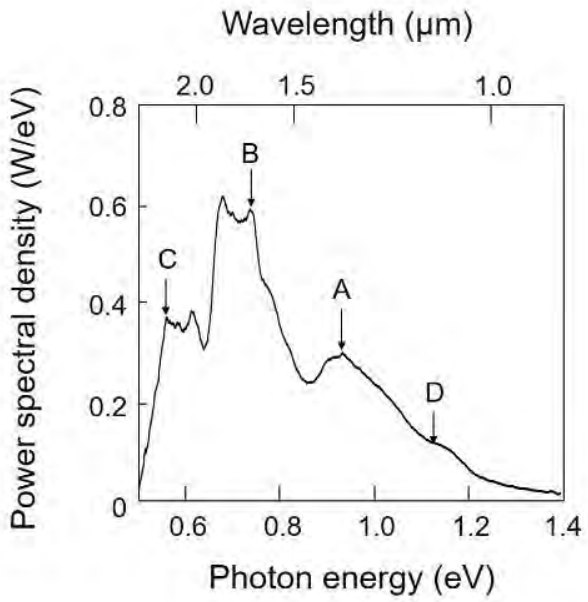

Fig. 6.3 Light emission spectra of the Si-LED.

The substrate temperature and the injection current were 283 K and 2.45 A, respectively. Downward arrows A – D represent the spectral peaks at $E_g - 3E_{phonon}$, $E_g - 6E_{phonon}$, $E_g - 9E_{phonon}$, and E_g, respectively.

It should be noted that the photon energy emitted from the conventional LEDs

was governed by E_g. However, in the present Si-LED, the energy difference between $h\nu_{anneal}$ and E_g was compensated by the created phonon energy. The origin of this compensation was attributed to the spatial distribution of B atoms that was autonomously controlled during the DP-assisted annealing. For this control, the irradiated light served as a source for creating the DP during the DP-assisted annealing. It has been theoretically confirmed that the DP, after being created and localized on the B atom (Phenomenon 7), coupled more efficiently with localized phonons than with non-localized ones. It has been also confirmed that a B atom-pair served as a resonant cavity to confine and localize phonons, resulting in localized phonon creation [10].

For comparing these theoretical confirmations with experimental results, the three-dimensional spatial distribution of B atoms at the p-n homojunction was acquired by atom probe field ion microscopy of sub-nanometer spatial resolution. By analyzing the acquired data, it was found that the B atoms were apt to form pairs with a length $d = 3a$ (a (=0.54 nm) is the lattice constant of the Si crystal), and the formed pairs were apt to orient along a plane parallel to the top surface of the Si crystal [11] (Fig. 6.4(a)). That is, the following phenomenon was found:

[Phenomenon 13] *The length and orientation of the B atom-pair in a Si crystal are autonomously controlled by the DP-assisted annealing.*

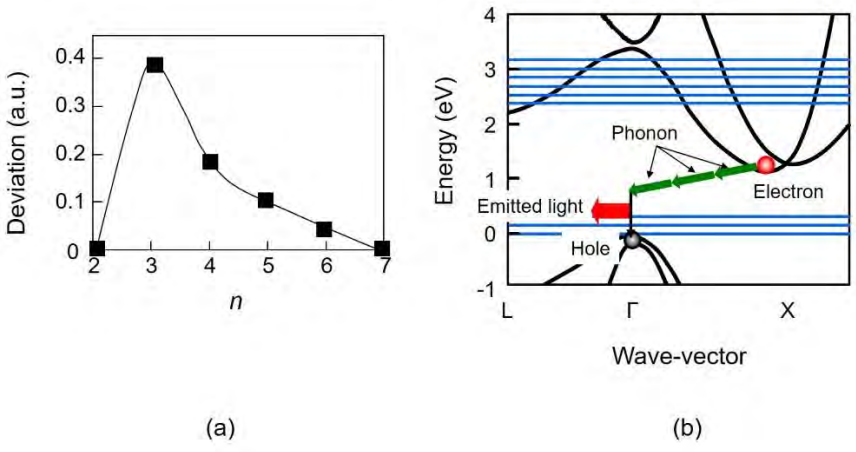

Fig. 6.4 Relation between $n(=d/a)$ and the deviation of the number of B atom pairs from the Weibull distribution .

(a) Measured results. (b) The energy band diagram of Si and schematic explanation of light emission.

It should be noted that the Si crystal is composed of multiple cubic lattices, and the value of the required phonon momentum has to be h/a for the radiative

recombination of the electron (at the bottom of the conduction band at the X-point in reciprocal space) and the positive hole (at the top of the valence band at the Γ-point) to take place. It should be also noted that the value of the phonon momentum is $h/3a$ when the phonon localizes at the B atom-pair with $d = 3a$. By comparing these values of momenta, it is found that the DP created and localized at this B atom-pair provides three phonons for recombination (Fig. 6.4 (b)). As a result, the emitted photon energy $h\nu_{em}$ is expressed as $h\nu_{em} = E_g - 3E_{phonon}$. By substituting the values of E_g (= 1.12eV) and the relevant optical mode phonon energy E_{phonon} (=65meV) into this equation, the value of $h\nu_{em}$ is derived to be 0.93 eV, which is nearly equal to the photon energy $h\nu_{anneal}$ (=0.95 eV) irradiated during the DP-assisted annealing. This numerical relation is consistent with the spectral feature in Fig. 6.3. This indicates that the irradiated light served as a breeder that created a photon with energy $h\nu_{em} = h\nu_{anneal}$ and manifested the following phenomenon:

[Phenomenon 14] A light emitting device fabricated by DP-assisted annealing exhibits photon breeding (PB) with respect to photon energy; i.e., the emitted photon energy $h\nu_{em}$ is equal to the photon energy $h\nu_{anneal}$ used for the annealing.

The peaks B and C in this figure are the second and third harmonics of the phonon contributions, respectively. PB was observed also with respect to the photon spin. That is, the polarization direction of the emitted light was identical to that of the light irradiated during the DP-assisted annealing [11].

Visible LEDs have been also fabricated by using crystalline Si and that exhibit the PB phenomenon. Specifically, blue, green, and red light-emitting LEDs were fabricated by radiating blue, green, and red light, respectively, during the DP-assisted annealing [12]. A lateral p-n homojunction structure was developed in order to increase the efficiency of extracting the visible light from the Si crystal [13].

A variety of visible LEDs have been developed by using crystalline SiC even though it is also a well-known indirect transition-type semiconductor. They were fabricated by irradiating them with UV-violet, bluish-white, blue, and green light during the DP-assisted annealing. The fabricated devices emitted UV-violet, bluish-white, blue, and green light, respectively [14].

6.2 Si-lasers

Crystalline Si has been the subject of extensive research for use in fabricating lasers since it shows excellent compatibility with electronic devices [15]. For example, there have been several reports of basic devices that have been demonstrated, including Raman lasers [16] and lasers utilizing quantum size effects in Si [17]. However, parameters such as the operating temperature, efficiency, wavelength, optical power and so forth are still not adequate for practical adoption of these devices.

Optical gain occurs if the device operation satisfies the Bernard–Duraffourg inversion condition [18]. Furthermore, if the device has an optical cavity structure for confining the emission energy, and if the optical gain is larger than the cavity loss, there is a possibility of laser oscillation occurring as a result of stimulated emission [19].

6.2.1 Single-mode lasers

This section reviews the fabrication and operation of single-mode Si-laser devices [20,21]. The first part is devoted to the basic devices. The second part reviews an improved device structure for decreasing the threshold current density.

a. Basic devices

An As-doped n-type Si crystal was used as a device substrate. The electrical resistivity was 10 Ω cm, and the thickness was 625 μm. A part of this crystal was further doped with B atoms by ion implantation to form a p-type layer. The concentration of B atoms was 1×10^{19} cm^{-3} [21]. After forming a p–n homojunction, an ITO film was deposited on the p-layer side of the Si substrate, and an Al film was deposited on the n-substrate side for use as electrodes in the process of annealing described below. Subsequently, the Si crystal was diced to form a device. For DP-assisted annealing, the substrate was irradiated with infrared laser light having a photon energy $h\nu_{anneal}$ of 0.94 eV (1.32 μm wavelength) and a power density of 200 mW/cm^2, during which annealing was performed by injecting a forward-bias current of 1.2 A to generate Joule-heat, causing the B atoms to diffuse.

Next, the ITO electrode and the Al electrode were removed by etching. Then, a ridge waveguide was fabricated by conventional photolithography. After that, an Al film was deposited by DC sputtering. The substrate was then polished to a thickness of 100 μm, and an Al film was deposited also on the reverse side of the Si substrate. These Al films were used as electrodes for injecting a current to drive the fabricated laser device. The sample was cleaved to various lengths, and the cleaved end-facets served as cavity mirrors.

Figure 6.5(a) illustrates the device structure. Secondary ion mass spectrometry measurements confirmed that the active layer formed in the p–n homojunction was located at a depth of 1.5–2.5 μm from the surface of the Si substrate. This corresponds to the bottom of the ridge waveguide. Figure 6.5(b) shows an SEM image of a fabricated device, from which the width and thickness of the ridge waveguide constituting the cavity were confirmed to be 10 μm and 2 μm, respectively. Several devices were fabricated, whose cavity lengths L were 250–1000 μm.

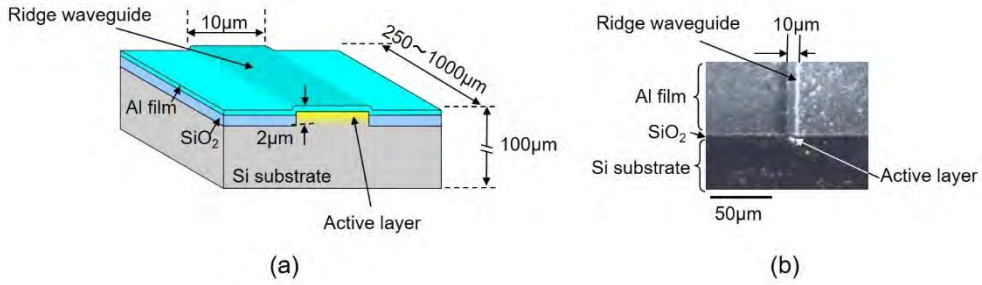

Fig. 6.5 The profile of a Si laser device.

(a) Schematic illustration of the structure. (b) An SEM image of a fabricated Si laser device.

Light emission spectral profiles were measured for the Si laser with L=500 μm. The results are shown in Fig.6.6, where the threshold current density J_{th} was 1.1 kA/cm^2. Above the threshold for lasing (at an injection current of 57 mA), a sharp laser oscillation spectrum was observed, as shown in Fig. 6.6(a). Its wavelength was 1.271 μm, which was evidence of photon breeding (PB) [22]. The full width at half maximum (FWHM) was 0.9 nm or less, which was limited by the resolution of the measurement equipment. The sharp spectral peak in Fig. 6.6(a) represents the CW laser oscillation

with a single longitudinal mode that was realized even though the waveguide was as long as 500 μm. Its origin was that the low infrared absorption by the Si provided a low threshold for the principal longitudinal mode at the optical gain spectral peak and, as a result, the gains for other modes were depleted by this principal mode due to nonlinear mode competition [23,24]. Below the threshold (at an injection current of 55 mA (Fig. 6.6(b)), there existed only a wide, low-power spectrum that originated from the amplified spontaneous emission (ASE).

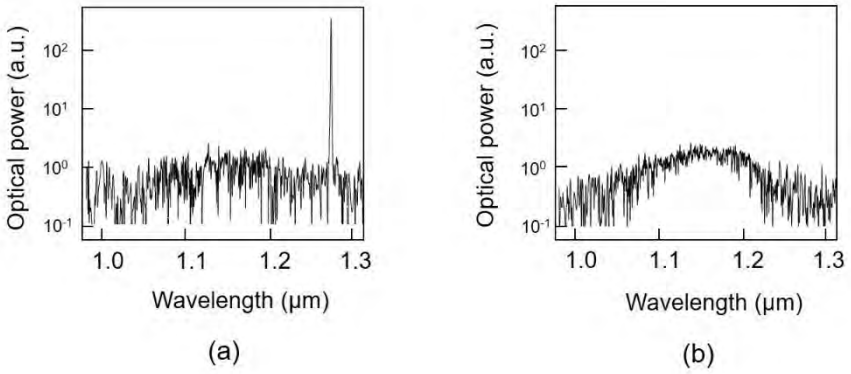

Fig. 6.6 Light emission spectral profiles of the Si laser with a cavity length of 550 μm.

(a) Above the threshold. (b) Below the threshold.

b. Decreasing the threshold current density

This part reviews the design and fabrication of an improved device with a higher optical confinement factor for reducing J_{th} [21]. In designing the device structure, the value of the transparent current density J_{tr} was estimated to be 5.0 A/cm^2 [25-27]. Through this estimation, the differential gain coefficient g was also estimated to be 38.4 cm/A.

By using these estimated values and the formula in ref. [27], J_{th} was estimated to be 2.6 kA/cm^2, where α_{int}=1.6 × 10^{-5} cm^{-1} (internal optical loss coefficient), Γ=4.7 × 10^{-4} (optical confinement factor), L=250 μm, and $R_1 = R_2$=0.31 (reflectivities of the two end-facets of the waveguide) were also used.

Since G for the device in Fig. 6.5 was very low (4.7×10^{-4}), further decreases in J_{th} were expected by increasing G. Based on this expectation, the dependence of J_{th} on G was numerically calculated, which suggested that J_{th} decreased to less than 1/100th that of the device in Fig. 6.5, i.e., to 8.8 A/cm^2, by increasing G to 0.16.

By following this suggestion and using the numerical values above, an improved device with a larger G was designed. Its cross-sectional profile is schematically illustrated in Fig. 6.7. The device layer was 15 μm thick, which was realized by using a silicon-on-insulator (SOI) substrate. The thickness and width of the ridge waveguide were 2 μm and 8 μm, respectively.

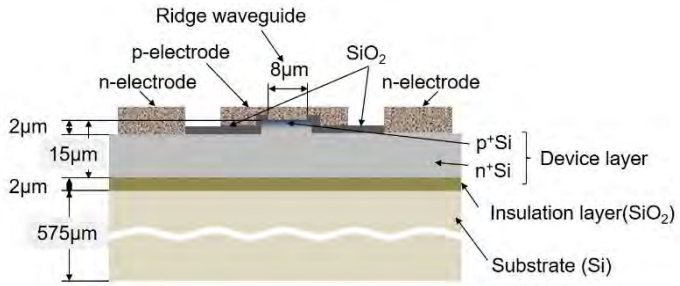

Fig. 6.7 A cross-sectional profile of the improved device.

The SOI substrate consisted of a device layer, an insulating layer made of SiO_2, and a Si support substrate. The device layer was P-doped n-type Si with a resistivity of 2.0×10^{-2} – 3.4×10^{-2} Ωm. The thicknesses of the insulation layer and the Si support substrate were 2 μm and 575 μm, respectively. Figure 6.8 shows an SEM image of an end-facet of the waveguides.

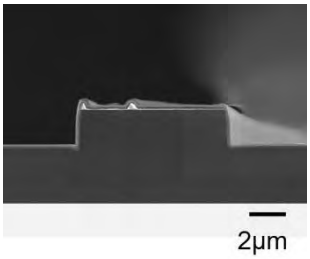

Fig. 6.8 An SEM image of the end-facet of the waveguide of the fabricated device.

DP-assisted annealing was adopted by injecting a current pulse (1 kHz repetition frequency, 100 μs pulse width, 77.5 A/cm^2 peak current density, 3.2 V peak voltage). The substrate was irradiated with infrared laser light (1.31 μm wavelength, 1 mW

power) during this current injection. The annealing time was 1.5 hours.

Figure 6.9 shows the light emission spectral profiles that were acquired at room temperature (25 °C). The vertical axis of this graph is a logarithmic scale. Figure 6.9(a) shows the profile above the threshold for lasing (J =42 A/cm^2). Here, J_{th} was 40 A/cm^2, as will be presented below. The sharp spectral peak at a wavelength of 1.40 μm represents the CW laser oscillation with a single longitudinal mode. Figure 6.9(b) shows the spectral profile below the threshold (J =38 A/cm^2), in which no ASE spectra are seen because of the gain depletion due to the mode competition.

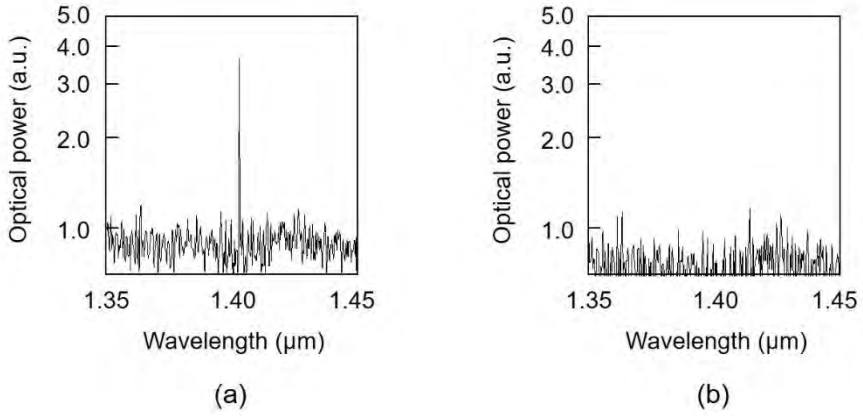

Fig. 6.9 Light emission spectral profiles.

(a) Above the threshold. (b) Below the threshold.

The value of J_{th} was found to be 40 A/cm^2 [21], which is 1/28th that of the device in Fig. 6.5. A possible reason why this value of J_{th} was still higher than the designed value (8.8 A/cm^2) is that the actual value of α_{int} was still higher than the value used for the device design. It should be possible to decrease this value further by improving the fabrication process.

6.2.2 High-power lasers

Section 6.2.1a reviewed devices with a narrow ridge waveguide. They realized single-longitudinal mode lasing with a very low J_{th} by constant current injection at room temperature. Due to such prominent features, it was expected that these devices could be used as light sources for information transmission systems, information processing systems, and sensing systems. On the other hand, to apply them to machining and processing systems, high optical output power is required. This section reviews recent progress in fabricating and operating high-power Si laser devices designed to meet this requirement.

Section 6.2.1a demonstrated that low J_{th} was achieved, which suggested that the present fabrication method had the capability to realize a device with a high optical output power driven by a fairly low J. Based on this suggestion, novel high-power laser devices were designed and fabricated by referring to the values of physical quantities evaluated in Section 6.2.1a. Here, to ensure a large total optical gain, a Si crystal with a large cross-section and long length, and without a waveguide structure, was employed. Employing such a large Si crystal can be more advantageous than increasing the optical confinement factor of a small waveguide because, and due to the p-n homojunction-structure in the Si crystal, an extremely high optical confinement cannot be expected even by further modification of the waveguide configuration.

Figure 6.10 shows the cross-sectional structure of the Si crystal used as the laser medium (1 mm width, 150 μm thickness) that was designed for realizing high-power light emission [28]. The length L of the crystal was 15 mm, as seen in the photograph in Fig. 6.11(a). The two end-facets of the crystal were cleaved for use as laser cavity mirrors. An As-doped n-type epitaxial Si film (10 μm thickness, 10 Ω cm resistivity) was grown on a Sb-doped n-type Si crystal substrate (15 mΩ cm resistivity). A part of this film was further doped with B atoms by ion implantation to form a p-type layer. The concentration of B atoms was 1×10^{19} cm^{-3}. The thickness of the B-doped p-type layer was 1.2 μm. After depositing Cr/Pt/Au films for use as electrodes, the device was installed in a heat sink made of copper plates, as shown in Fig. 6.11(b). For DP-assisted annealing, one end-facet was irradiated with infrared laser light having $h\nu_{anneal}$ of 0.95 eV (1.31 μm wavelength) and a power of 200 mW, during which annealing was performed by injecting a forward-bias current of 5 A.

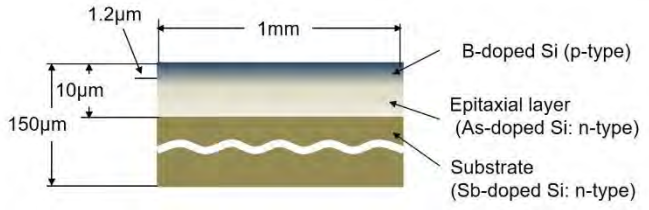

Fig. 6.10 Cross-sectional profile of the Si crystal used as a laser medium and the laser cavity.

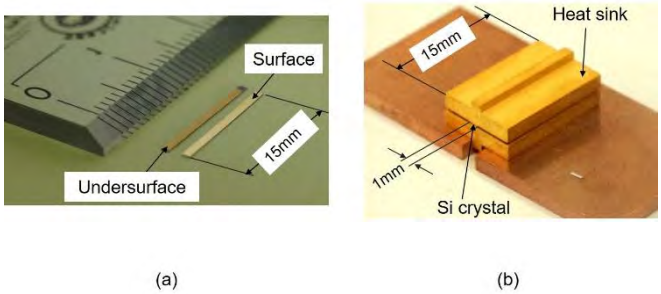

Fig. 6.11 Photograph of the laser device.

(a) The Si crystal. (b) A heat sink, in which the Si crystal is installed.

By substituting physical quantities evaluated in Section 6.2.1a into a conventional rate equation for a laser light intensity, the relation between J and the optical output power P_{out} emitted from one end-facet of the device was derived, as shown in Fig. 6.12 [28]. This figure shows that J_{th} is about 100 A/cm^2. Since the electrodes may be damaged when J increases to 1 kA/cm^2, which corresponds to the output power of 200 W in Fig. 6.12, the present study aimed at safely realizing the highest output power of 100 W to avoid the type of damage mentioned above.

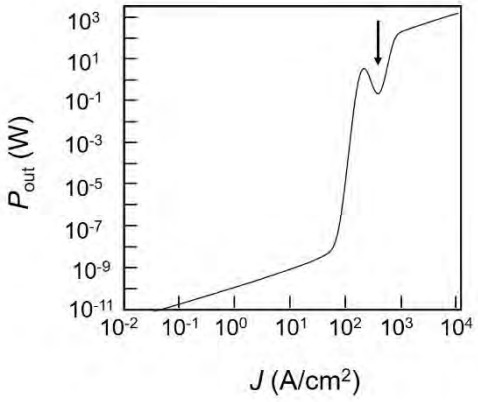

Fig. 6.12 Calculated relation between J and P_{out} of the fabricated device (L =15 mm).

The downward arrow indicates the dip originating from the saturated absorption feature of the device.

Figure 6.13 shows the light emission spectral profile above the lasing threshold for lasing under constant current injection at room temperature [29]. In contrast to those in Figs. 6.6(a) and 6.9(a), it has three spectral peaks A, B, and C. This multi-wavelength operation was attributed to the multiple transverse and longitudinal modes that were allowed to exist in the present primitive large laser cavity. The spectral peak A is located at a wavelength of 1.31 μm. This is identical to the wavelength of the light irradiated during the DP-assisted annealing, which is direct evidence for photon breeding (PB). The spectral peak B is a phonon sideband, which was generated by creating an LO-mode phonon with an energy of 40 meV at the X-point in the electronic energy band diagram. The spectral peak C is also a phonon sideband, which was generated by creating a TO-mode phonon with an energy of 60 meV.

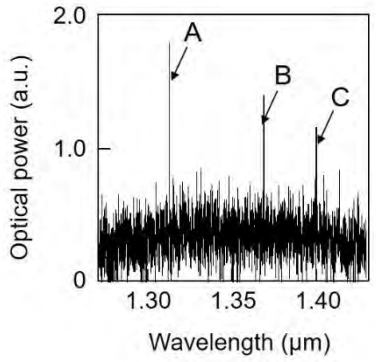

Fig. 6.13 Light emission spectral profiles.

The wavelength of the spectral peak A is identical to that of the light irradiated during the DP-assisted annealing. The spectral peaks B and C are phonon sidebands, which were generated by creating LO-mode and TO-mode phonons, respectively.

The closed squares in Fig. 6.14 represent the measured relation between J and P_{out}. The value of P_{out} took a maximum value of 110 mW at J =33 A/cm^2 (5 A injection current). This value is more than 10-times higher than that of a conventional double heterojunction-structured InGaAsP/InP laser (10 mW at 1.3 μm wavelength: SLT1130 series manufactured by Sumitomo Electric). By taking the optical output power radiated from the other end-facet into account, the maximum total optical output power was 220 mW.

Figure 6.14 also shows that J_{th} was 12 A/cm^2, which was lower than that described in Section 6.2.1a (40 A/cm^2). The origin of such a low J_{th} in the present device is attributed to the large total optical gain due to a large laser medium.

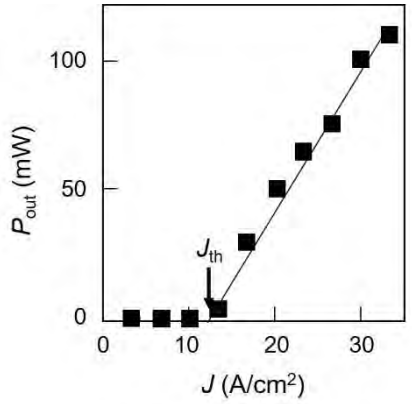

Fig. 6.14 Measured relation between J and P_{out} emitted from one end-facet of the Si crystal.

The slope of the line fitted to the closed squares indicates that the external differential quantum efficiency was 9.0% in the case where the total optical output power was radiated from the two end-facets. This is higher than the efficiency of a conventional double heterojunction-structured InGaAsP/InP laser (7% at 1.3 μm wavelength: SLT1130 series manufactured by Sumitomo Electric).

Figure 6.15(a) shows a dazzling infrared radiation pattern from the end-facets, acquired by an infrared camera, which demonstrates the high output optical power. Figure 6.15(b) is an image of the light scattered from the surface of a screen installed at a position 20 cm away from the laser. The image is spatially modulated, i.e., speckles are clearly seen, which demonstrates a high spatial coherence of the output infrared light beam.

Fig. 6.15 Images of the output infrared light.

(a) Radiation pattern of the infrared light emitted from the end-facet. (b) The speckles in the light pattern

scattered from the screen surface.

Based on the experimental results above, the structures of the device and heat sink were improved to attain the 100 W output power. The improvement was achieved by carrying out the following three steps.

As the first step, the structure of the heat sink was improved to increase the heat dissipation efficiency [30,31]. Furthermore, in order to reduce the heat generation, the device was driven by injecting a pulsed current with a duty ratio of 10:1. Since the pulse width was as large as 2 ms and the repetition frequency was as low as 50 Hz, this pulse current can be considered as a quasi-constant current.

The relation between J and P_{out} is shown in Fig. 6.16(a) and was consistent with the one estimated by the simulation (Fig. 6.12). This figure shows that the highest output power was 13 W (emitted from one end-facet). The value of J_{th} was maintained as low as 53 A/cm^2.

As the second step, the optical reflection-loss of the cavity was decreased by coating reflection films on the two end-facets of the cavity (the reflectivities were R_1 =70 % and R_2=100 %) [32]. As a result, the value of J_{th} was decreased to 27 A/cm^2 (threshold current was 4 A), which was half of that in the first step. As shown in Fig. 6.16(b), the noise magnitude originated from the spontaneous emission below the threshold decreased to 1/10th to 1/100th that in the first step.

As the last step, the implantation depth of the p-type dopant atoms was decreased from 2 μm to less than 1 μm so as to allow the device to be operated by a triangular-wave injection current (1 Hz repetition frequency). It should be pointed out that injection of such slow triangle-wave current is equivalent to constant current injection. The device length L was increased to 30 mm. Figure 6.16 (c) shows the experimental results, demonstrating that the highest power achieved was 100 W. Through the comparison with the values represented by closed squares in this figure (the same as those in Fig. 6.16(a)), it was confirmed that the value of J_{th} was maintained as low as the value realized in the first step.

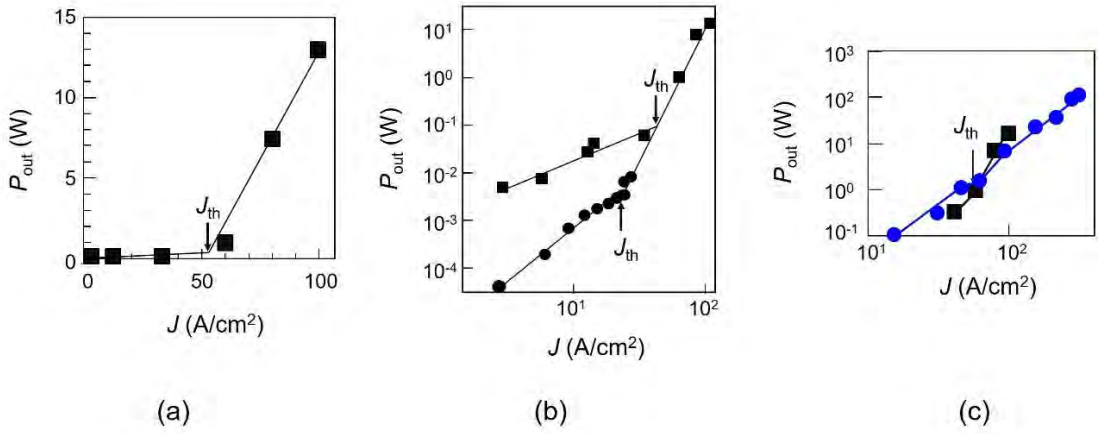

Fig. 6.16 Measured relation between J and P_{out} emitted from one end-facet of the Si crystal.

(a) The first step. (b) Closed circles are for the second step. Closed squares are identical to those in (a).

(c) Blue circles are for the last step. black squares are identical to those in (a).

An optical output power higher than 100 W and precise control of the lasing wavelength as well as lasing modes are expected by modifying the device structure and the parameters for the DP-assisted annealing. Visible lasers are also expected to be fabricated by using crystalline SiC, also an indirect transition-type semiconductor that has been employed for fabricating visible LEDs [33].

6.2.3 Comparison with other type of lasers

The experimental results in Section 6.2.2 demonstrated that high P_{out} and low J_{th} were simultaneously realized as a result of the large optical gain and also the very low infrared absorption loss. Experimental progress made towards achieving this is summarized in Fig. 6.17.

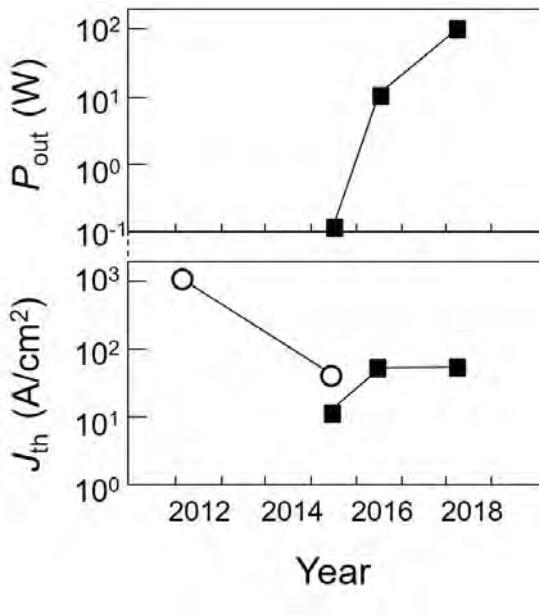

Fig. 6.17 Progress in increasing P_{out} and decreasing J_{th},.

Open circles and closed squares are for single-mode lasers (Section 6.2.1a) and high-power lasers (Section 6..2.2), respectively.

Since a Si bulk crystal without a waveguide structure was used in Section 6.2.2, the structure of the present device is more similar to those of solid-state and gas lasers than those of conventional double heterojunction-structured semiconductor lasers [34,35]. Further similarities with solid-state and gas lasers can be found by referring to the magnitude of infrared absorption loss: In the case of solid-state and gas lasers, electronic transitions in the electronically isolated ions, atoms, and molecules are used for lasing. Therefore, even though direct electric current injection to these laser media is difficult, the absorption loss per unit volume is very low. Thus, a high optical output power can be obtained by increasing the size of the laser medium even though the photon density of the lasing light is low.

On the other hand, in the case of conventional semiconductor lasers, coupled electrons and holes in the conduction and valence bands, respectively, have been used for lasing. Therefore, direct electric current injection to the laser medium is easy. An additional advantage is that the laser medium can be very small. However, the problem is that the absorption loss per unit volume is large, making it impossible to achieve high P_{out} and low J_{th} even though the photon density of the lasing light is high.

Considering the discussions above, the present Si laser is found to be similar to solid-state and gas lasers because an electronically isolated DP is used, which keeps the absorption loss per unit volume very low. Thus, the value of J_{th} can be decreased. Furthermore, the value of P_{out} can be greatly increased by increasing the size of the laser medium even though the photon density of the lasing light is low. An additional advantage is that electrons can be easily supplied by direct electric current injection, due to a low recombination loss in the Si crystal.

Finally, it should be pointed out that, early in the study of semiconductor lasers, it was found that the absorption loss in indirect transition-type semiconductors was low at low temperature, which was advantageous for inverting the electron population for lasing [36]. However, the disadvantage was that the magnitude of the population inversion was not sufficiently large for ensuring a large optical gain. Since this finding, it has been believed for a long time that indirect transition-type semiconductors were not appropriate for use as laser media. Instead, direct transition-type semiconductors have been predominantly used until now [37]. However, DP technology has realized the manifestation of large optical gain in indirect transition-type semiconductors, which is the secret to the dramatically high P_{out} and low J_{th} values realized by the present device made of Si crystal.

6.3 Polarization rotators

This section briefly describes the SiC device structure for the optical polarization rotator [38]. An n-type 4H-SiC crystal with a resistivity of 25m Ωcm and (0001) surface orientation was used. A 500 nm-thick n-type buffer layer was deposited on this crystal, after which a 10 μm-thick n-type epitaxial layer (n-type dopant (N atoms) density 1×10^{16} cm^{-3}) was deposited. The surface of the 4H-SiC crystal was then implanted with an p-type dopant (Al atoms) by ion implantation. To activate the Al ions for forming a p-n homojunction, thermal annealing was performed for 5 min. at 1800 °C. After this, a second thermal annealing was performed under the same conditions as above.

Although the structure was almost the same as that of the SiC-LED described in Section 6.1, it was inverted, resulting in the SiC substrate being the top layer. Furthermore, an H-shaped electrode formed of a Cr/Pt/Au (100 nm/150 nm/200 nm thick) stripe film was deposited on the top surface. A homogeneous electrode formed of

Cr/Ni/Au (100 nm/150 nm/200 nm thick) was deposited on the bottom surface. After this, the 4H-SiC crystal was diced to form a device with an area of $500\ \mu m \times 500\ \mu m$. Figures 6.18(a) and (b) show the cross-sectional structure of a fabricated device and a photograph of the device taken from above, respectively.

For the DP-assisted annealing, a forward bias voltage of 12 V (current density 45 A/cm^2) was applied to the device to bring about annealing due to Joule-heat, which caused the Al atoms to diffuse. During this process, the device was irradiated from the top surface with laser light (optical power 20 mW) having a wavelength of 405 nm. As a result, the device worked as an LED by momentum exchange between the electrons in the conduction band and the multimode coherent phonons in the DP.

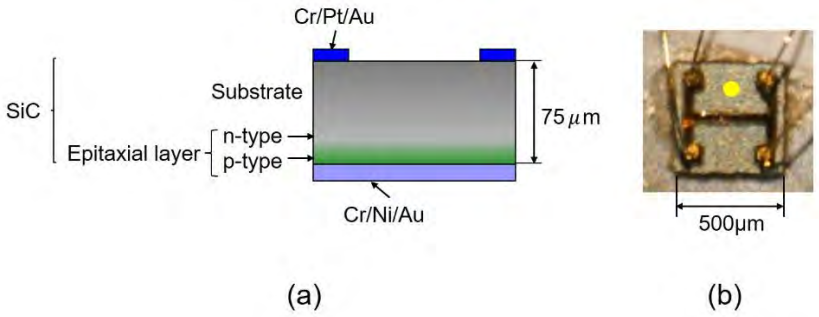

Fig. 6.18 Cross-sectional profile (a) and photograph (b) of a polarization rotator using a 4H-SiC crystal. The yellow circle represents the cross-sectional position of the incident light beam.

To operate the device as an optical polarization rotator, a current was injected to the H-shaped electrode to inject electrons and to generate a magnetic field, simultaneously. In order to measure the polarization rotation angle θ_{rot}, linearly polarized 405 nm-wavelength light was made normally incident on the top surface of this device. The yellow circles in Fig. 6.18(b) represents the cross-section of the incident light beam. The value of the magnetic flux density $\boldsymbol{B}_{\perp}$ normal to the top surface at this spot was evaluated to be 1.8 mT, where the injection current I was 30 mA. That is, the relation

$$\frac{dB_{\perp}}{dI} = 0.06 \text{ (T/A)} \qquad (6.1)$$

holds.

The relation between $\boldsymbol{B}_{\perp}$ and θ_{rot} was measured by the experimental setup of Fig.6.19(a), and the results are represented by the red circles in Fig.6.19(b). The solid line B was fitted to these circles. From the slope of the line B, the relation

$$\frac{d\theta_{rot}}{dB_{\perp}} = 2.2 \times 10^{3} \text{ (deg/T)} \tag{6.2}$$

is derived.

From eqs. (6.1) and (6.2), the relation

$$\frac{d\theta_{rot}}{dI} = 660 \text{ (deg/A)} \tag{6.3}$$

is derived. This value corresponds to the Verdet constant, which was 10^5-10^6 times higher those of conventional paramagnetic materials that are transparent in the visible region [39]. This means that the present SiC crystal exhibited a gigantic magneto-optical effect.

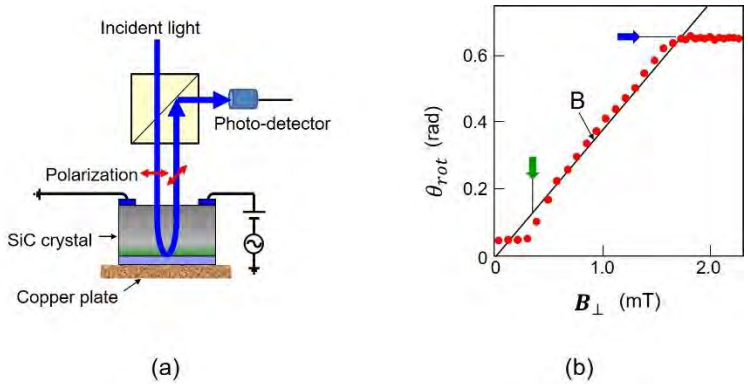

Fig. 6.19 Measured relation between $\boldsymbol{B}_{\perp}$ and θ_{rot}.
(a) Experimental setup to measure the value of θ_{rot}. (b) The relation between $\boldsymbol{B}_{\perp}$ and θ_{rot}. (The unit (π rad) written along the vertical axis of Fig. 2 in ref.[40], and also that of Fig. 8.18(b) in ref. [41], is wrong. The correct unit (rad) is written on the vertical axis above.)

The right-pointing blue arrow in this figure indicates that θ_{rot} saturated as $\boldsymbol{B}_{\perp}$ increased, as has been widely observed in conventional ferromagnetic materials. The saturated value was 0.65 rad (=37 deg). The total optical path length of the incident light propagating through the SiC crystal was 150 μm because the crystal thickness was 75 μm, as shown in Fig. 6.18(a). Thus, the saturated value, normalized to the unit optical path length, corresponding to the Faraday rotation angle [39], was as large as 2480 deg/cm. Furthermore, the downward green arrow indicates the threshold value of $\boldsymbol{B}_{\perp}$, which was 0.36 mT. This value corresponds to the remanent magnetization in conventional ferromagnetic materials, and was as large as those values. The two arrows suggest that the presently used SiC crystal acquired novel properties, equivalent to those of ferromagnetic materials.

In order to find the origin of such novel ferromagnetic properties, a

magnetization curve was acquired uisng a SQUID [40]. The results are given in Fig. 6.20. Here, the applied magnetic field $\boldsymbol{H}$ (Oe) was proportional to the current injected to the H-shaped electrode. Closed squares in this figure are the acquired values. They were fitted by the curve A and clearly exhibited a hysteresis characteristic, which is inherent to ferromagnetic materials. Since these results were acquired at 27 °C, it was confirmed that the Curie temperature was estimated to be higher than 27 °C. The values of the magnetization were very small before the DP-assisted annealing, as shown by open circles and the curve B.

By comparing the black squares and red open circles, the following novel phenomenon was confirmed:

[Phenomenon 15] The semiconductor SiC crystal was made to behave as a ferromagnet as a result of the DP-assisted annealing and exhibited a gigantic magneto-optical effect in the visible region.

This behavior originated from the formation of Al atom pairs, autonomously formed as a result of the DP-assisted annealing. This origin can be understood by referring to the following two research findings: (1) It has been found that the triplet state of the electron orbital in an Al atom pair is more stable than the singlet state [42]. (2) Two electrons with parallel spins in the triplet state induce the ferromagnetic characteristic [43].

At the end of this part it should be pointed out that similar polarization rotators have also been fabricated by using ZnO crystals based on the same principle as in the SiC crystals above [44].

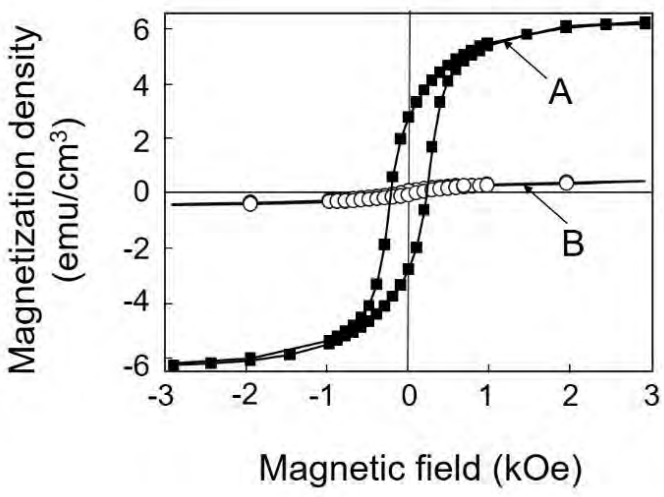

Fig. 6.20 Magnetization curve for the SiC crystals, measured at 27 °C.

Closed squares and open circles are the results acquired after and before the DP-assisted annealing, respectively. They are fitted by the curves A and B, respectively.

7 Embarking on theoretical studies for off-shell science

The studies reviewed in previous sections identified the DP as a quantum field that is created as a result of the light-matter interaction in a nanometer-sized space. However, they also presented at least two theoretical difficulties (Sections 2.1 and 2.2). One was that the mode of the electromagnetic field could not be defined. The other was that the description of the spatial localization of the DP required the surrounding macroscopic subsystem to have a parabolic dispersion relation. As an urgent solution to overcome these difficulties, the theoretical methods in on-shell science were modified and applied to tentatively describe the physical nature of the DP.

Although the theoretical studies above were at a standstill, experimental studies have found the novel Phenomena 1-15. It should be noted that they cannot be described by conventional optical theories. This is because these theories treat only photons in a vacuum (free photons) and in a macroscopic material, whose dispersion relation is given by the mass-shell ("on-shell" for short). It has been popularly known that massless particles with non-zero spin, such as free photons, cannot be localized in space in the sense that the position operator cannot be defined [1]. However, it turns out to be natural to consider localized photons when the effective mass of photons, created by light–matter interactions, is taken into account. Especially in the case of NPs, space–time localization and energy–momentum fluctuations constitute novel aspects of light. A photon in such a context is called a DP.

For a theoretical definition of the DP and for describing the Phenomena 1-15 above, the "off-shell" nature of the interaction has to be considered [2]. That is, the DP is an off-shell quantum field that conspicuously deviates from the mass-shell. As has been well known, quantum field theories cannot be formulated without off-shell entities. In other words, the traditional particle description has failed to treat the quantum field of a composite system. Hence, DPs must be entities that are very different from Einstein's quanta of light or free photons.

Here, a fundamental question arises: How can the DP be described as an individual entity? As long as one sticks to the notion of individual entities as irreducible on-shell particles, it is impossible to treat the DP as an individual entity. However, a more general perspective, advocated by Ojima [3], has shown that macroscopic physical phenomena can emerge out of a condensation of microscopic off-shell entities.

By following this perspective, a basic idea can be proposed: In the interaction between photons and NPs, certain families of modes of the composite system will behave as individuals. This behavior suggests that the DP is the quantum field of a

composite system in which an electromagnetic field and an electron (or an exciton) interact in a nanometer-sized space. Furthermore, it is a virtual field localized in the nanometer-sized space within a short time duration. Thus, the DP is a quantum field whose nature is contrary to that of an on-shell photon. This means that conventional optical theories are incapable of giving a systematic description of Phenomena 1-15. Fortunately, however, several hints have been given to construct novel theories for describing the phenomena above by noting that the virtual photon plays an essential role in the electromagnetic Coulomb interactions. They are:

[A] The longitudinal mode of an electromagnetic field (the longitudinal wave) contributes to the Coulomb interaction [4].

[B] The field interaction accompanies the 4-momentum [5].

[C] Although the spacelike field is not spatially localized because it behaves as a stable wave, it becomes unstable and can localize if it interacts with a timelike field [6].

By referring to these hints, novel theoretical studies have commenced based on spatio-temporal vortex hydrodynamics supported by the relativity theory [7,8]. They are reviewed in Section 7.1.

Furthermore, mathematics-based theoretical studies are in progress that will serve as invaluable guides for gaining a deep understanding of the concepts of the physics-based theories for the phenomena that originate from the DP [9]. Examples of these theories are the quantum probability theory and the quantum measurement theory. Also demonstrated is a theory based on micro–macro duality, which serves as a foundation for embarking on theoretical studies of off-shell science. They are reviewed in Section 7.2.

One of the promising future direction of DP science is to propel the theoretical studies above in collaboration with experimental ones. By using the fruits of these studies, further developments of application technologies are expected, resulting in further disruptive innovations.

7.1 Theory based on spatio-temporal vortex hydrodynamics

This section starts by presenting the reason why the on-shell scientific method does not meet the requirement mentioned in Section 1.1. Next, novel theoretical studies based on spatio-temporal vortex hydrodynamics are reviewed for describing the DPs by using off-shell scientific methods [10].

7.1.1 Reasons why the on-shell scientific method does not meet the requirement

As was pointed out at the end of Section 1.1, novel theories on light-matter interactions are required to analyze Phenomena 1-15. However, Haag's theorem describes the reasons why this requirement has not been met by on-shell science [11]. The claims resulting from this theorem are summarized as follows:

(1) The off-shell and on-shell quantum fields cannot be mutually transformed by a unitary transformation. This means that there is a theoretical gap between nanometer-sized and macroscopic quantum fields, and thus, they are incompatible with each other.

(2) The quantum field created by the interaction among multiple elementary particles in a nanometer-sized complex system is a non-particle field[1)] that is unrelated to the fields of its constituent particles. This means that this quantum field cannot be represented by the superposition of the modes of free quantum fields.

(3) It is not possible to describe the temporal and spatial behaviors of the quantum field by linear equations. This impossibility is equivalent to the limit of applicability of the conventional quantum theories for describing the interaction[2)].

However, conventional quantum field theories can be easily used for describing quite a large number of optical phenomena by neglecting Haag's theorem and its claims **(1)–(3)** above. An example of such easy use is found in representing the quantum field by superposing the modes of the on-shell quantum field (eqs.(2.1) and (2.2)). Here, it should be noted that this expansion is allowed only when the bases (modes of the on-shell quantum field) form a complete set. However, the intrinsic problem is that the timelike and lightlike components, popularly used in on-shell science, are not sufficient to form this set. The Greenberg–Robinson's theorem [12] claims that the spacelike components in the 4-momenta field are indispensable for this formation[3)] (Minkowski spacetime: Fig. 7.1).

It has been experimentally found that a DP is created and localized at the position where a field varies discontinuously, for example, at the apex of a fiber probe or at a boron (B) atom (Phenomena 1 and 7). High-wavenumber modes must be involved in the mode-superposition when a step-function is used to represent this discontinuous electromagnetic field. However, the use of modes of the timelike and lightlike components in the 4-momenta field is insufficient because the energies of the high-wavenumber modes are much higher than that of the photon of the visible light that serves as a source for creating the DP. The high-wavenumber modes of the spacelike components are required because their energy is sufficiently low to be safely used. This is the reason, found in experimental studies, why the spacelike components of the 4-momenta field are required to represent the creation and localization of the DP.

The next section reviews the creation and localization of the DP by referring to the spacelike components of the 4-momenta field, for which the Clebsch dual (CD) field is used.

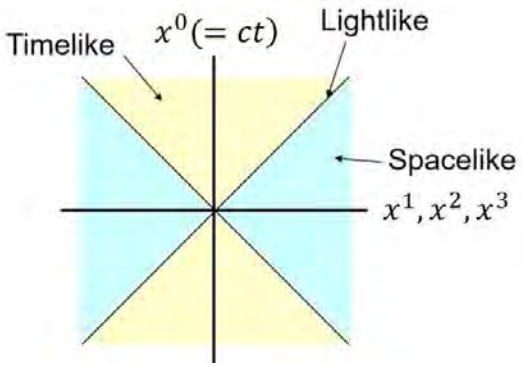

Fig. 7.1 Minkowski spacetime.

7.1.2 Description of DPs by the off-shell scientific method

Off-shell scientific studies on the mechanism of DP creation have recently made progress by carefully examining the interaction between electromagnetic fields and matter fields [13]. They are summarized as follows (Appendix B gives some supplementary explanations):

Step 1: Spacelike components in the 4-momenta field play indispensable and essential roles in the quantum field interaction.

Step 2: The quantum field of the spacelike components is expressed by the CD field.

Step 3: The CD field corresponds to a vector boson that is composed of a set of Majorana fermion fields.

Supplementary explanations of **Steps 1–3** are given in the following:

Step 1: This step corresponds to the claim given by the Greenberg-Robinson theorem [12] mentioned above. This theorem relies on the axiomatic quantum field theory and indicates the indispensable and essential roles of the spacelike components.

Step 2: Detailed analyses of Maxwell's equations based on relativistic theory have found that the spacelike electromagnetic field is expressed by the CD field. Here, the CD field is given by the external product of two gradient vectors (C_i, L_i) that are mutually orthogonal (Fig. 7.2). When the vector potential is lightlike (that is, a null vector), C_i corresponds to the lightlike longitudinal electric field. This fact indicates that the

longitudinal electric field is involved in the interaction of **Step 1** above[4]. On the other hand, L_i is a spacelike vector and is normal to the vector C_i, by which L_i is regarded as representing the magnetic field. This fact indicates that the CD field is a spacelike electromagnetic field[5]. By surveying the energy-momentum tensor of the CD field, it has been found that the wave representation and particle representation of the CD field are equivalent to each other. The particle representation is given by $\rho C_i C_k$, which is isomorphic to the energy-momentum tensor of the free fluid. The quantity ρ corresponds to the fluid density, which is given by $L^m L_m$. It should be pointed out that this quantity ρ takes a negative value, and therefore, it has been considered as a non-physical quantity. This non-physical nature indicates the reason why the longitudinal electric field has been excluded over a period of many years from the on-shell scientific studies on quantizing the electromagnetic field under the Lorentz-covariance condition[6]. However, thanks to the recent progress made in off-shell scientific studies, it was found that such a non-physical mode is required for describing the interaction, and in addition, that the spacelike components of the 4-momenta field are required (**Step 1**).

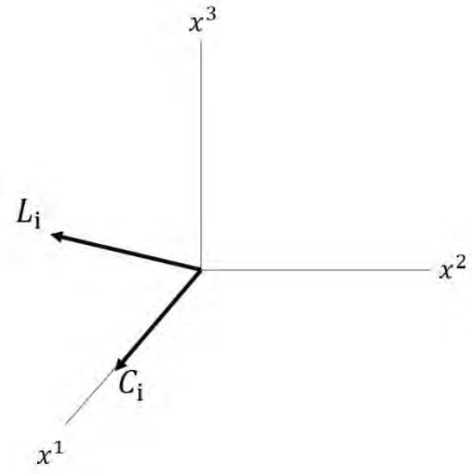

Fig. 7.2 Four-dimensional vectors C_i and L_i displayed in (x^1, x^2, x^3)-space.

The 0-th axis x^0 is not shown. The field propagates along the x^1 -axis.

Step 3: The spacelike components above can be represented by the spacelike Klein-Gordon's (KG) equation, which is derived by replacing the effective mass term m in the timelike KG equation by $i\kappa_0$. By noting that Dirac's equation corresponds to the

square root of the KG equation, the equation for the Majorana fermion (MF) is derived by replacing m in the timelike Dirac's equation by $i\kappa_0$. The MF represents an electrically neutral quantum field whose particle and antiparticle components are represented by identical equations. From the relations among the timelike KG equation, the spacelike KG equation, and Dirac's equation above, it was found that the quantum mechanical expression of the spacelike CD field was equivalent to that of the MF field.

By referring to the discussions in **Steps 1–3**, the mechanism of DP creation was described from the viewpoint of the interaction, specifically: the spacelike CD field (MF field) interacts with the timelike components of the 4-momenta field [7], and the MF field subsequently creates a timelike particle and antiparticle forming a pair. This pair is annihilated promptly because of its non-propagating nature[8]. However, a non-propagating electromagnetic field remains in the interacting system, which is the very field of the DP[9].

In summary, this section reviewed the recent progress made in theoretical studies on mechanisms of DP creation by focusing on the light–matter interaction in a nanometer-sized space. First, it was pointed out that the conventional on-shell scientific method has intrinsic problems in describing the above interaction. Second, the off-shell scientific method, which can overcome these problems, was reviewed, and it was demonstrated that the CD field can be appropriately used for the description. The mechanisms of DP creation, identified by theoretical analysis using the CD field, are: the spacelike CD field (MF field) interacts with the timelike components of the 4-momenta field, and the MF field subsequently creates a timelike particle and antiparticle forming a pair. This pair is annihilated promptly because of its non-propagating nature. However, a non-propagating electromagnetic field remains, and this is the very field of the DP.

The energy–momentum tensor of the CD field is isomorphic to the left-hand side of the Einstein field equation represented as a Ricci curvature tensor defined in terms of a contracting Riemann tensor, thus suggesting an interpretation wherein the energy–momentum tensor of a virtual photon field carries a part of the energy–momentum of "vacuum", as in classical space-time. It also suggests that it may represent a so-far unidentified energy field similar to the controversial dark energy in cosmology, since, corresponding to its space-like characteristics, the associated scalar curvature is negative. According to a quantum mechanical point of view, a vacuum is considered as a fluctuating energy field where creation and annihilation of a variety of virtual particles occur incessantly.

1) Such a field has been called the Heisenberg field.

2) For example, let us consider the case of exciting a free quantum field by injecting energy to the system under study. The excited field interacts with the existing field, and this interaction is described by Newton's equation of motion in the classical theory. Although this equation is linear as long as the magnitude of the injected energy is low, it becomes nonlinear when the energy is increased. Here, the problem is that such nonlinear equations have never been derived in quantum theory.

3) In the conventional theories of elementary particles, the spacelike component of the 4-momenta field has been excluded from the theoretical model because of its superluminality and thus, non-physical nature.

4) As an example, a longitudinal electric field is involved in the well-known Coulomb interaction.

5) This indication is based on the fact that the vector potential satisfies the spacelike Proca's equation even though it is a null vector.

6) By noting that the quantum field with an infinite degree of freedom is composed of multiple sectors [14], it can be realized that the non-physical longitudinal electric field exists in such a sector that is disjoint with the sector to which the conventionally approved transverse electromagnetic field belongs.

7) By irradiating an NP with light, CD fields are excited simultaneously with the timelike components of the 4-momenta field. These CD fields are the basic modes for creating the fields of the spacelike components. Since the CD fields correspond to the MF fields (**Step 3**), these MF fields interact with the timelike components at the NP.

8) Its spatial extent is expressed as the Yukawa function (eq.(2.5)).

9) In the case where the spins of the particle and antiparticle are parallel to each other, a zero-spin electric DP is created. In the case where they are anti-parallel, on the other hand, a magnetic DP whose spin is unity is created.

7.2 Theories having a mathematical basis

It is expected that mathematics-based theories will serve as invaluable guides for gaining a deep understanding of the concepts of the physics-based theories for the phenomena that originate from the DP [15]. Examples of these theories are the quantum probability theory and the quantum measurement theory, which are reviewed in this section. Also demonstrated is a theory based on micro–macro duality, which serves as a foundation for embarking on theoretical studies of off-shell science.

7.2.1 Quantum probability theory

Quantum probability theory has been constructed by noting a large uncertainty Δp in

the DP momentum [16]. This theory focuses on the families of the higher and lower energy–momentum modes for investigating phenomena that cannot be analyzed by conventional on-shell theories. The family of higher modes of the composite system is created as a result of light–matter interaction and behaves like an individual entity. This entity can be defined as the DP. The family of lower modes serves as a kind of heat-bath.

Since no a priori strict boundary between the higher and lower modes exists, it is required to investigate the asymptotic behavior of modes where the energy–momentum becomes large. In other words, the core of a mathematical theory for the DP is nothing but a kind of quantum-classical correspondence for describing an asymptotic state that appears as its quantum number increases to infinity. Hence, some general frameworks are required for both quantum/micro and classical/macro systems. Fortunately, a mathematical theory that meets this requirement has been constructed, that is, the quantum probability theory. The intermediate realm, appearing between the micro- and the macro-systems, has been successfully described by this theory.

As has been popularly known, a quantum harmonic oscillator with a large quantum number behaves very much like a classical harmonic oscillator. The composite system created by light–matter interaction is considered to be a typical example of such a quantum harmonic oscillator. This consideration and the definition of the DP above lead to the fact that the time averaged distribution of the position of the DP can be governed by an arcsine law. Note that each mode of the DP gains an effective mass by the interaction between the light and nano-material, and thus, it is not paradoxical to consider the position of the DP. Moreover, since the size of the nano-material is much less than the wavelength of light, the variance of the distribution will be determined by this size. The stronger the interaction, the higher the energy at a suitable boundary between the family of the higher mode (DP) and that of the lower mode (heat bath). Hence, it is expected that the arcsine law will represent a sufficiently accurate distribution of the DP when the interaction is sufficiently strong.

Since the arcsine function has a twin-peaked profile, the probability of finding the DP will be the highest at the singular point, which is the reason why localization of the DP occurs at the boundary. This localization feature is quite consistent with the experimental results acquired so far [17].

Here, let us take as the most fundamental example the localization of the DP in a fiber probe [18]. The three-dimensional density of the DP can be expressed by an arcsine function

$$f(x) = C\frac{1}{S(x)\sqrt{2-x^2}}, \tag{7.1}$$

where C and $S(x)$ respectively denote the normalization constant and the cross-sectional area of the fiber probe on which the DP is created. The localization of the DP at the tip of the fiber probe, and furthermore, at the position of the impurity atoms in the material were successfully described based on the twin-peaked spatial feature (peaks at $x = \pm\sqrt{2}$ in eq. (7.1)) [16].

In conjunction with the quantum probability theory above, a quantum walk model was used to mathematically describe Phenomena 1, 4,6, and 7. It was also used to analyze the dynamic behavior of the composite system created as a result of the interaction between multiple quantum fields. Furthermore, it was aimed at exploring the master equation for describing the dynamics of the DP by noting that their behaviors are similar to those of the quantum walk. It has been experimentally confirmed that these behaviors exhibited inherent characteristics that corresponded to those of the quantum walk [19]: The temporal behavior of the DP energy transfer between the two NPs was least-squares fitted to an exponentially decaying function $\exp(-t/\tau)$, where t and τ represent time and the time constant of the phenomena, respectively (Section 2.3). This exponential decay corresponds to the quantum walk (QW) dynamics.

By referring to the arcsine law above, the quantum probability theory has been applied to analyze several phenomena that originate from the DP. They are:

a. Numerical simulation for the fiber-to-fiber system

Numerical simulations were carried out to analyze the creation of the DP and its energy transfer in a fiber probe-to-fiber probe system. As is schematically explained by Fig. 7.3 (a), two fiber probes served as a sender and a receiver of the DP energy under collective excitation by conventional propagating light.

Two assumptions were made for this analysis. They were: **(a1)** The sender fiber probe was coherently excited by the incident light. **(a2)** The created DP hopped from one atom to an adjacent atom in a coherent manner, which corresponded to the quantum walk process. The analysis described three energy dissipation phenomena caused by the energy conversion from the DP to the conventional propagating light: **(d1)** The conversion to a conventional electromagnetic field to be guided backward to the main body of the sender fiber probe. **(d2)** The conversion to a conventional electromagnetic field to be guided forward to the main body of the receiver fiber probe. **(d3)** The conversion to a conventional electromagnetic field that propagates out from the tapered

part of the fiber probe to the outer free space. As a result, it was confirmed that, among all of the created DPs, the one created by the pair of anti-parallel electric dipoles was localized at the tip of the fiber probe without being dissipated through phenomena **(d1) – (d3)**.

Figures 7.3(b) and (c) show the calculated results for the single-tapered and double-tapered fiber probes, respectively [20]. They demonstrate that the double-tapered fiber probe concentrated the DP energy at its tip more efficiently than that at the single-tapered one. This suggests that the double-tapered fiber probe is more advantageous for creating/measuring the DP with higher efficiency, which is consistent with the experimental results (refer to Fig.1.5) [21].

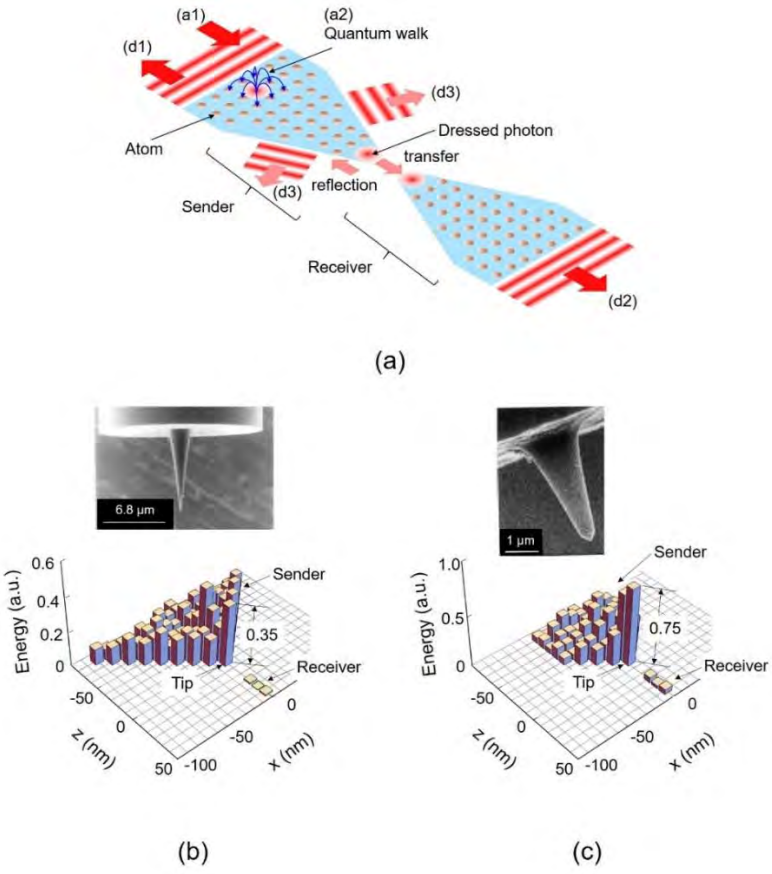

Fig7.3 Simulation by a quantum walk model.

(a) The fiber probe-to-fiber probe system. (a1) and (a2) represent the two assumptions. (d1)-(d3) are the energy dissipation phenomena. (b) and (c) represent the calculated results for single-tapered and double-tapered fiber probes, respectively. The photos show scanning electron microscopic images of these fiber probes.

b. Quantum walk model for the DP energy transfer

Figure 7.4 shows the QW model that corresponds to the experimental system in Fig. 2.6 used for demonstrating the temporal behavior of DP energy transfer. Two semiconductor NPs played the roles of nodes 1 and 2. The DP, transferred between these NPs bidirectionally, played the role of a link. The light incident into and emitted from the NPs played the role of the input and output signals, respectively.

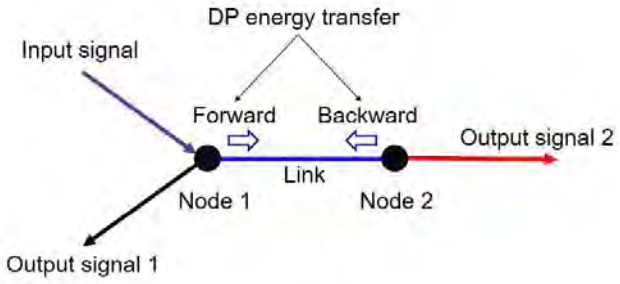

Fig. 7.4 The QW system to be experimentally realized in the present paper.

As a result of the planned strategies **(S1)** and **(S2)** in Section 2.3, the system of Fig. 2.6(b) exhibited the following differences **(D1)** – **(D3)** from the system of Fig.7.4 [22]. They were:

(D1) Node 2 was split into three because of the triple degeneracy of the exciton state in NP_L.

(D2) A part of the DP energy dissipated at node 2 due to the non-radiative relaxation of the exciton in NP_L .

(D3) Since the effective side lengths ($a_{S,\mathrm{eff}}$ and $a_{L,\mathrm{eff}}$) of NP_S and NP_L were different from each other, the magnitudes of the created DP energies and their spatial extents, represented by a Yukawa function $V(r)$ (eq.(2.5)), were different. Thus, their DP energy transfer times, being inversely proportional to $V(r)$, were different. That is, since $a_{S,\mathrm{eff}} < a_{L,\mathrm{eff}}$, the transfer time of the forward path of the link (from NP_S to NP_L) was longer than that of the backward path (from NP_L to NP_S).

By noting the differences **(D1)** - **(D3)**, Fig. 7.4 was revised to Fig. 7.5(a). However, for a basic discussion of the QW process, it should be possible to approximate Fig. 7.5(a) by the simpler system of Fig. 7.5(b) because of the sufficiently low magnitude of the energy dissipation in **(D2)**.

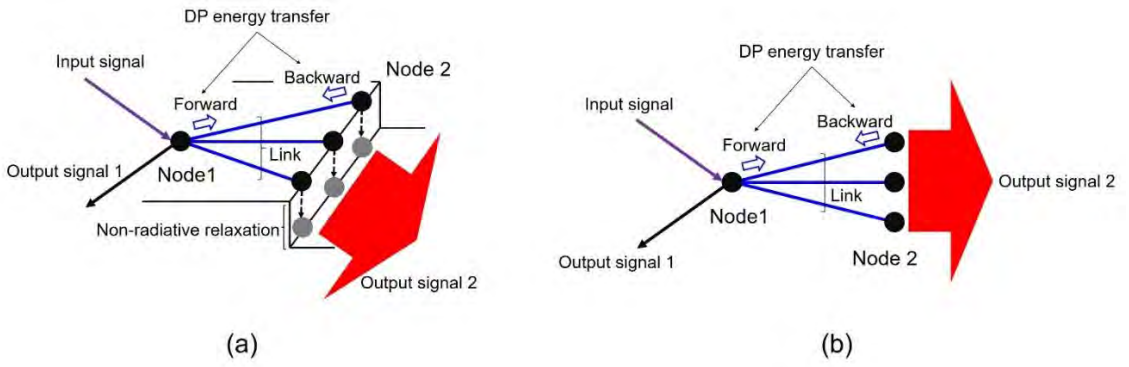

Fig. 7.5 The revised QW system.

c. Grover walk model on semi-infinite jellyfish graphs for the dressed photon

A Grover walk model on jellyfish graphs has been proposed to analyze the behavior of DPs [23]. This proposal focused on the quantum walks (QWs) on a kind of graph called a jellyfish graph, which was used to construct a toy model of the phenomena that originate from the DPs. This model was composed of a finite connected graph and a finite number of half-lines attached to it. It was formulated by referring to the physical system of Fig. 3.4.

The idea of a Grover walk corresponded to the idea of scattering the quantum field induced by the DP energy transfer. Higuchi and Segawa [24] derived a basic theorem of the limit amplitudes of the Grover walks on jellyfish graphs. This theorem indicated that the NP and the half-lines corresponded to a vertex of the Grover walk and the arrows incident on the vertex, respectively, when viewed from the far field and sufficiently after transferring the DP energy.

By using the Kirchhoff-type theorem given in [24], a new theorem was derived for the limit amplitudes of QWs on jellyfish graphs. After defining the net amplitudes of the DPs around the vertices, this theorem was used to analyze QWs on jellyfish graphs that corresponded to the physical model of Fig. 3.4. As a result, it was found that the DPs clustered around vertices that subsequently emitted a large amount of outflow to the far field. In other words, the DPs gathered autonomously at the vertices which dissipated the energy to the far field (refer to **{1}** and **{2}** in Section 2.2.2).

If further progresses can be made in the study of the Grover walk, it is expected that the origins of Phenomena 1, 4, 7, and 9 can be qualitatively and quantitatively discussed.

7.2.2 Other basic theories having a mathematical basis

a. Quantum measurement theory

A theoretical description of Phenomenon 3 is essential for understanding the process of measuring the DP. Here, the problem is how to describe the dynamics of the DP energy transfer that occurs during the measurement. To solve this problem, quantum measurement theory, a branch of algebraic quantum theory, is under construction based on the theory of operator algebra, especially, C^*-algebra. C^*-algebraic quantum theory is advantageous because it can explicitly describe macroscopic classical levels of quantum systems.

Mathematical issues for constructing the algebraic quantum measurement theory for the DP have been surveyed [25,26]. They are:

(1) Two methods are possible. Their mathematical issues are:

[For the top-down method] After the mathematical model is built based on the universal gauge principle of quantum electrodynamics, several approximations should be made depending on the scale of the system or the properties of the material fields.

[For the bottom-up method] This method is advantageous to build a mathematical model for describing the properties of the energy–momentum and the properties of localization of the DP. This model should be built by considering the ability to extend and scale it.

(2) Mathematical modeling should start from the space-time area $\mathcal{O}$ in which nano-materials are provided. Here, a sub-space of the real space can work as the area $\mathcal{O}$. Next, an algebra $\mathcal{A}(\mathcal{O})$, composed of physical quantities in the area $\mathcal{O}$, is considered. Then, the temporal evolution $\alpha_t^{\circ} \cap \mathcal{A}(\mathcal{O})$ is considered for each area $\mathcal{O}$. Microscopic physical quantities, representing the boundary conditions (the lattice defects, as an example), can be included in α_t°. For this consideration, the measurement process can be represented by the inclusion relation $\mathcal{O} \subset \mathcal{O}_2$, where $\mathcal{O}_2$ represents the space-time domain under study. Finally, the measurement theory is expected to be established by the algebra $\mathcal{A}(\mathcal{O}_2)$.

b. Theory based on micro–macro duality

Based on an algebraic quantum field theory, micro–macro duality theory has been constructed as a powerful mathematical guide for analyzing the nature of the DP [27]:

Symmetry breaking in the algebra in a microscopic area can produce multiple sector spaces. Some physical quantities in these sector spaces satisfy the commutativity requirement, and the quantity named the center can be used to classify the sector spaces. That is, a commutative observable classical system and a non-commutative quantum system can coexist in each sector space, and this provides the basic structure for quantum-classical correspondence.

The sector space can be interpreted also as a mathematically symmetric space. It has been found through this interpretation that the automorphic form plays an essential role. Several discussions were made by taking a fiber probe as a test system: In order to construct a consistent theory for describing the DP, it will be a crucial breakthrough to faithfully reproduce its proper dynamic functions. This reproduction forms the micro–macro boundary level described by a symmetric space arising from a broken symmetry, which is possible by projecting the *s*-channel structure at the invisible micro-level to the spacelike *t*-channel. If suitable automorphic forms defined on this symmetric space are successfully identified, it will become possible to describe any of non-trivial dynamic phenomena caused by the DP. In particular, the automorphic factor appearing in the definition of an automorphic form will play an important role as a cocycle carrying the dynamic properties of the invisible micro-level. In the context of the DP, this will perhaps justify an analogy with the dynamic behavior played by the Regge trajectories, which carry spacelike momenta in the hadronic scattering processes originating from the dual resonance structure.

As is shown by Fig. 7.6, the theory based on micro–macro duality serves as a foundation of the theories reviewed in this article. This figure also summarizes the principal characteristics of the DP, the developed theories, their physical and/or mathematical methods, and information derived by these theories. The red double-pointed arrows indicate the topics commonly described by the multiple theories. By noting these arrows, correlations between the theoretical studies can be clearly recognized. Successful construction of off-shell science, guided by systematic studies on the DP, is expected by analyzing these correlations. It is also expected that the micro–macro duality theory will serve as a guide to this development.

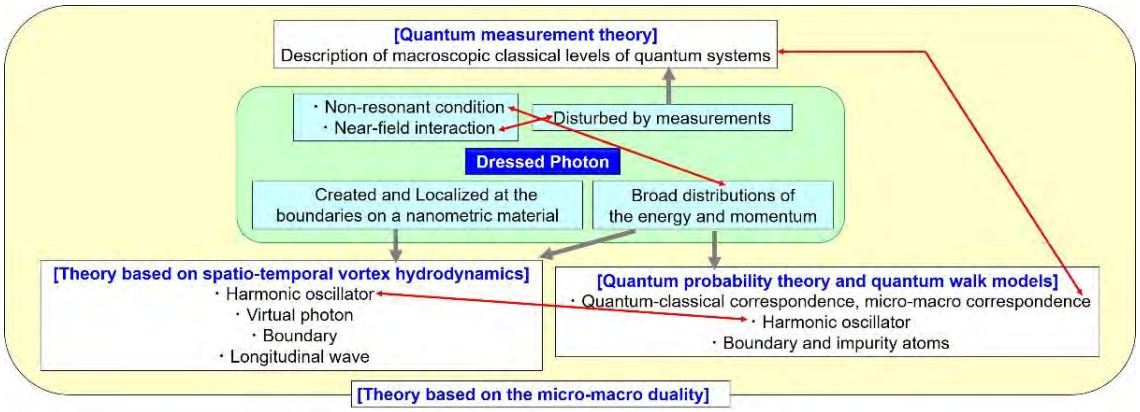

Fig.7.6 The principal characteristics of the DP, developed theories, their physical and/or mathematical methods, and information from the theoretical studies.

Red double-pointed arrows indicate the topics common to the adjacent theories.

Appendix A Present status of numerical simulation techniques and their problems

In order to describe the autonomy observed in DP energy transfer and its measurement process, numerical simulations have been carried out by using a random walk model relying on statistical mechanics and complex-systems science.

This appendix reviews the results of these simulations and presents the problems associated with them [1]. It also presents possible directions for solving these problems, which could promote advances in off-shell science.

A.1 Nano-droplets

The experimental results in Section 5.1.2 have been analyzed by the following numerical simulations:

<<Fabrication>> The numerical simulation confirmed that the rate of pairing NP1 and NP2 was

(1) highest when their sizes were equal (Fig. A.1(a)),

and

(2) higher when the liquid temperature was higher (Fig. A.1(b)) [2].

Finding **(1)** originated from the size-dependent resonance of the DP momentum. Finding **(2)** was because the rate at which NP1 and NP2 encountered each other depended on the random walk velocity of the Brownian motion of the NPs in the liquid UV-setting resin. These two findings were consistent with the experimental results.

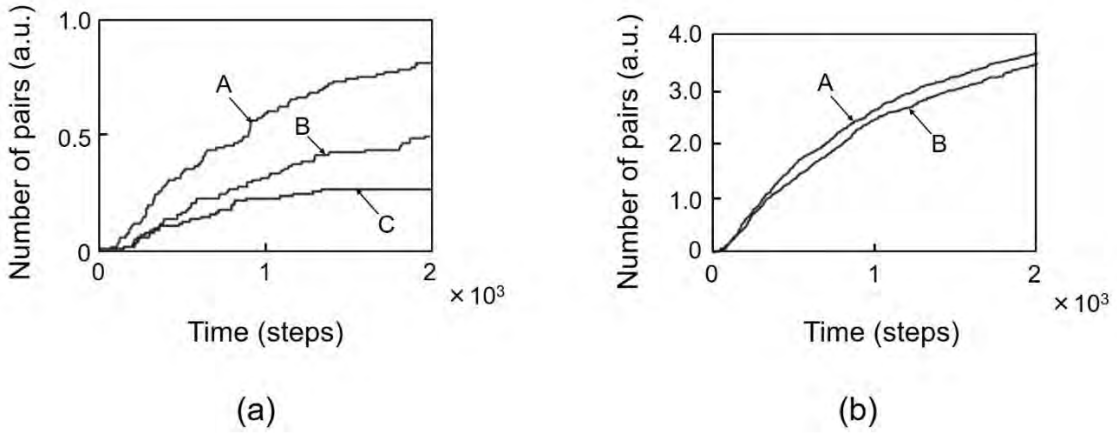

Fig.A.1 Temporal increases in the number of pairs (Fig. 7 in ref.[2]).

(a) Dependence on the ratio of the sizes a_{NP1} and a_{NP2} of the two NPs. The curves A, B, and C represent the results for a_{NP1} / a_{NP2} = 1, a_{NP1} / a_{NP2} < 1, and a_{NP1} / a_{NP2} > 1, respectively. (b) Dependence on the temperature of the liquid UV-setting resin. The curves A and B represent the results for high- and low-temperature liquids, respectively.

<<Operation>> The validity of the present numerical simulation has been confirmed because the experimentally evaluated magnitude of the spectral peak shift of the light emitted from the CdSe (NP1) was consistent with the simulated temporal behavior of the NP-pair formation rate (Figs. A.1(a) and (b)).

However, it should be pointed out that findings **(1)** and **(2)** above could be presumed by simply evaluating the experimental results. This means that the simulation was not essential for analyzing the experimental results. Furthermore, several problems were found with the simulation, including:

(p1-1) The simulation employed a one-dimensional model.

(p1-2) The simulation did not analyze the case of $N_2 / N_1 \neq 1$ (where $N_1 \gg 1$ and $N_2 \gg 1$) even though experiments have demonstrated that large numbers of NP1 ($N_1 \gg 1$) and NP2 ($N_2 \gg 1$) were confined in the fabricated NDs. Furthermore, their ratio N_2 / N_1 was not unity in the experiments.

(p1-3) The simulation did not introduce the deceleration of the Brownian motion of the NPs that originated from temporal hardening of the liquid UV-setting resin during the light irradiation.
(p1-4) The simulation did not introduce the recoiling of NP1 from NP2 that originated from the exchange of their momenta during the DP energy transfer.

A.2 Photovoltaic devices having a silver electrode with a unique surface morphology

During the DP-assisted material formation process of a granular Ag film with a unique surface morphology, the photovoltaic device, reviewed in Section 5.2, was open to the environment and thus involved energy flow and was subjected to environmental fluctuations. A two-dimensional nonequilibrium statistical mechanics model was used to describe the nonequilibrium dynamics [3]. In this model, it was assumed that two stochastic variables (i.e., the number of deposited Ag-NPs and the amount of electrical charge) dynamically coupled at each site of a two-dimensional square lattice and evolved with time.

The temporally varying magnitude of the repulsive Coulomb potential at each site caused by the charges was calculated in order to simulate the drift and deposition processes of Ag particles. The contribution of the DP was included by introducing irradiation light power b per site on the lattice. By regarding b as an external control parameter, it was shown that as b increased, a transition of the surface morphology occurred at a critical value b_c. That is, when $b \le b_c$, the DPs were not created effectively, and random Ag deposition was maintained as long as the simulation was continued (**State I**). When $b > b_c$, on the other hand, the DPs were created effectively, and Ag deposited autonomously, resulting in the formation of a unique surface morphology of the Ag film (**State II**). It was found that the transition from **State I** to **State II** was similar to the equilibrium second-order phase transitions.

As a result of this simulation, a configuration of Ag clusters on the surface was reproduced in the stationary state. Figure A.2 shows the cluster size distribution in **State II**. As indicated by a downward arrow, a bump was found at size 11, which was consistent with the experimentally observed bumps identified by the downward arrows in Figs. 5.12(b) and (c). However, several problems were found with the simulation:

(p2-1) The maximum size of the DP (Phenomenon 10) was neglected even though it has been experimentally found [4].
(p2-2) The size-dependent resonance effect of the DP energy transfer (Phenomenon 5) was not correctly considered.

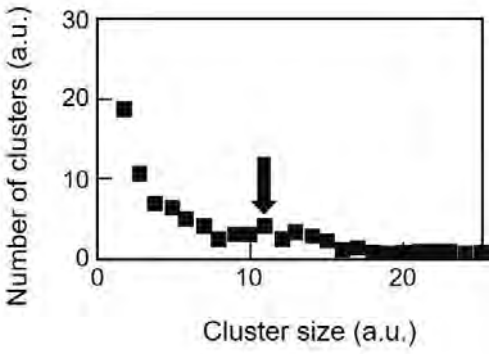

Fig.A.2 Relation between the size and the number of clusters in the steady state in state II. The downward arrow represents a bump on this relation.

A.3 Light-emitting diodes using silicon crystals

The origin of the PB effect in the Si-LED, reviewed in Section 6.1, was that the spatial distribution of B atoms played the role of genes. That is, this distribution bore the generic information and autonomously varied depending on the photon energy and polarization of the light irradiated during the DP-assisted annealing, eventually reaching a stationary state. The stable spatial distribution of B atoms was reproduced, and the characteristics of the emitted light were simulated by a numerical simulation using a nonequilibrium statistical mechanical model [5].

For this simulation, a two-dimensional square lattice was assumed to represent the pn-junction in which the B atoms existed, and the thermally diffusing behavior of the B atoms was represented by a random walk of the B atoms on the lattice. By using an injected current, I, and an irradiation light power, P^0, as external control parameters, a simulation model composed of seven steps was formulated:
(Step 1) A random walk of B atoms forming B atom pairs with length d (=3a) on the square lattice was introduced, where a is the lattice constant of the Si crystal (Phenomenon 12).
(Step 2) A random variable X was generated in order to represent the number of electrons for generating the Joule energy. Its distribution followed a Poisson process whose average was proportional to I.
(Step 3) Another random variable Y was generated that also followed a Poisson

process. Its average was proportional to P, where P $(=P^0+P^{PB})$ was the sum of the power, P^0, of the light irradiated during the DP-assisted annealing and the power, P^{PB}, of the emitted light. By adding the spontaneously emitted light power to Y, the total number of virtual photons Y^* $(=Y+1)$ that contributed to producing the PB effect was derived.

(Step 4) By means of the balance between the numbers of electrons and photons, being injected and irradiated during the DP-assisted annealing, respectively [6,7], a value $Z=\min(X,Y^*)$ was derived to represent the number of photons created by the B atom pair.

(Step 5) By executing **Steps 1-4** for all the B atom pairs, the values Z were summed to represent the value P^{PB}.

(Step 6) In the case where $Z \geq 1$, the random walker was regarded as being inactivated. This was because the created photon with power P^{PB} propagated out from the Si crystal, and as a result, the thermal energy was lost. At that moment, the simulation was terminated.

(Step 7) In the case where $Z < 1$, the random walker was still active and hopped to the adjacent site, and the simulation was repeated by returning to **Step 1**.

The results obtained by the numerical simulation were as follows:

<<Fabrication>> The regions A and B in Figure A.3 show the temporal variation of the simulated power, P^{PB}, of the light emitted during the DP-assisted annealing [8]. In region A, the power increased immediately after the DP-assisted annealing started. Then it showed relaxation oscillation, such that the amplitude of the oscillation decreased with time. Subsequently, in region B, the power reached the stationary state after a certain time and showed a relatively small fluctuation.

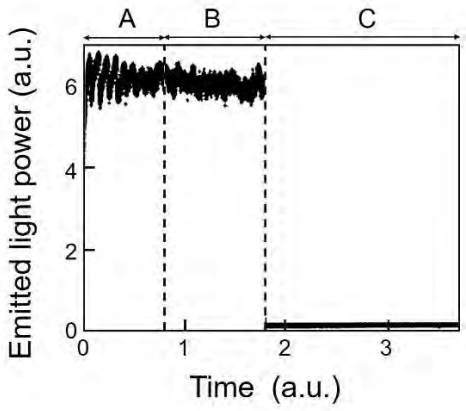

Fig. A.3 Output power of photon emitted from the device.

The regions A and B represent the state of transition and a stationary state during the device fabrication.

The region C is the output power emitted during the device operation. The values used for the simulations were l =40 and P^0 =80 in regions A and B. They were l =4 and P^0 =0 in region C.

<<Operation>> Region C in Fig. A.3 shows the power P^{PB} emitted during the device operation. Its value was smaller than those in regions A and B because of the smaller injection current than those injected for the DP-assisted annealing. However, it was stable over time. This was because the spatial distribution of the B atom pairs in the Si crystal was fixed, and random walks of the B atoms were suppressed.

The PB effect with respect to polarization has been also experimentally observed. In this effect, the polarization of the emitted light was equivalent to that of the light irradiated during the DP-assisted annealing [9]. Numerical simulations reproduced this effect by counting the number of created photon pairs that were orthogonally polarized. Here, it was assumed that the B atom pairs followed two independent Poisson distributions depending on the orientation of the B atom pairs on the square lattice.

Although the results of the numerical simulations above were consistent with most of the experimental results, several problems were found, including:

(p3-1) The simulation employed a two-dimensional model.

(p3-2) It was not straightforward to describe the details of the PB effect when using the conventional nonequilibrium statistical mechanical model, which relied on the temperature-dependent thermal diffusion. Novel models that incorporate theories of stochastic processes and quantum probability are required.

A.4 Problems in conventional numerical simulations

The essential feature, common to the fabrication process of the devices described in Sections A.1 – 3 (devices 1–3, respectively), was that the spatial distributions of the DPs were autonomously optimized by means of the external control parameters in order to realize the largest contribution of the DPs to the device operation. As summarized in Table A.2, these parameters increased the number of relevant NPs in device 1 during its fabrication, whereas they remained constant in devices 2 and 3. By referring to this table, problems in conventional numerical simulations and suggestions for solving them are presented in this section.

Table A.2 Fabrication processes for the three devices.

	NPs used	Temporal variation of the number of the NPs	Motions of NPs	External control parameters
Device 1	NP1 (made of CdSe), NP2 (made of ZnO or CdS)	Maintained constant	Pairing to form an ND	Irradiated light and resin temperature
Device 2	Ag atoms	Increased	Depositing on the surfaces of Ag grains	Irradiated light and applied voltage
Device 3	B atoms	Maintained constant	Forming pairs	Irradiated light and injected current

The conventional numerical simulations relied on the theories of statistical mechanics and complex-system science, which are branches of traditional on-shell science. Although they succeeded in reproducing most of the experimental results, there were several problems that remain to be solved to explore future directions:

[1] In the conventional simulations, the numerical values were carefully selected in order to fit the results to the experimental results. However, the essential problem in these simulations was not a quantitative comparison with the experimental results, but identifying the origins of the DP creation and the autonomous energy transfer of the DP. That is, we need to answer the questions "What is the DP?" and "What are the intrinsic features of the DP?" The answers to these questions have not yet been given.

[2] The answer to the question "What is the nature of the interaction between nanometer-sized materials via the DP?" has not yet been given either. The absence of an answer originates in the intrinsic nature of on-shell science. One example was that even if infinite numbers of electromagnetic modes in the on-shell region were superposed, this superposition cannot represent the off-shell electromagnetic field that plays an essential role in the interaction. The off-shell field is unrelated to and completely different from the on-shell field. The problem is how to develop off-shell scientific theories that are indispensable for finding the answer to this question.

Possible suggestions for finding the solutions are:

{1} (For device 1; refer to **(p1-1)** – **(p1-4)** at the end of Section A.1) A theoretical expression for the size-dependent resonance should be introduced into the model.

{2} (To problem **[1]** in Section A.2) A maximum size of the DP (Phenomenon 10) should be introduced to establish a three-dimensional model.

{3} (To problem **[2]** in Section A.2) The concepts of "interaction" and "off-shell field" should be introduced.

{4} (For device 2; refer to **(p2-1)** and **(p2-2)** at the end of Section A.2) It should be advantageous to introduce a function $\mathbf{1}(\alpha)$ in order to represent the maximum size of the DP, where

$$\mathbf{1}(\alpha)=\begin{cases}1 & ;\alpha \le \alpha_{\mathrm{DP\,max}} \\ 0 & ;\alpha > \alpha_{\mathrm{DP\,max}}\end{cases}$$

where $\alpha_{\mathrm{DP\,max}}$ is the maximum size of the DP. Experimental and theoretical values are 50–70 nm [4] and 38 nm [10], respectively. By using this function, the effective potential of the DP can be revised to $V_{\mathrm{eff,rev}}(r)=\mathbf{1}(\alpha)\cdot\exp(-r/\alpha)/r$.

{5} (For device 3; refer to **(p3-1)** and **(p3-2)** at the end of Section A.3) A three-dimensional model should be established.

Several discussions have been made recently by following suggestions **{1}**-**{5}** above, and it has been suggested that it was advantageous to employ a quantum walk (QW) model in the numerical simulations for solving problems **[1]** and **[2]** above [11]. This simulation is expected to give the answers for describing the off-shell scientific phenomena by developing a QW model with an infinite number of degrees of freedom. Based on this description, it is expected that it will be possible to find the origin of the interaction between the quantum fields by introducing a spacelike field into the QW model. The line-graph method [12] could be advantageously used for this. Furthermore, this method could succeed in introducing the phase of the Yukawa function (, the effective potential of the DP) to the simulation. This is expected to result in a description of the mechanical phenomena generated by the DP, such as the recoil effect* [13,14], as discussed at the end of Section A.1.

(*) It has been experimentally demonstrated that freely moving atoms in a vacuum were deflected or trapped by a DP.

Appendix B Supplementary explanation: Theory based on spatio-temporal vortex hydrodynamics

Large uncertainties Δp in the DP momentum suggest that the inequality $E < cp$ holds (E, c, and p are the energy, speed, and momentum of an electromagnetic field, respectively), which means that the field can exist in the spacelike domain of the Minkowski spacetime. In addition, the hint **[B]** in Section 7 suggests that a timelike-support and spacelike-support of the 4-momenta are required to describe the interacting fields. By referring to these suggestions and also to the hint **[C]**, it can be conjectured that the DP can be created by the interaction between the fields in the timelike and the spacelike domains.

Prompted by this conjecture, a novel theory has been constructed by focusing on the similarity in formulation between vortex hydrodynamics and electromagnetics [1]. For this construction, it was also noted that the contribution of the spacelike momenta was indispensable for the interaction between the quantum fields to occur [2].

Conventional classical theories have claimed that the Coulomb mode played a principal role in the electromagnetic interaction and that the longitudinal wave was a physically existing mode [3-6] (refer also to the hint **[A]**). In contrast, conventional theories of quantum electrodynamics have excluded the longitudinal wave as a "non-physical mode" even though it had a close relation with the Coulomb mode. Instead, they have introduced the exchange of virtual photons into the theoretical model for describing the electromagnetic interaction. This contrast suggests that a rift exists between the classical and quantum explanations above. This problem should be solved to draw a consistent physical picture of the DP that exists in an intermediate area between the classical and quantum worlds.

It should be pointed out that the theory of micro-macro duality (Section 7.2.2b) has already explained how to connect the classical and quantum worlds, by which a clue to solve the problem above can be found. The principal advantage of this theory is the capability of analyzing versatile structures of quantum fields with infinite degrees of freedom. This theory has demonstrated that the two worlds above coexist in the sense that the classical–quantum correspondence is mathematically guaranteed. The main purpose of the present subsection is to describe the electromagnetic interaction by adopting the micro–macro duality theory. It is expected that this description can systematically demonstrate the contributions of the longitudinal wave and the spacelike 4-momenta for drawing a physical picture of the DP.

For this demonstration, a novel mathematical expression, called the Clebsch representation, is adopted for the 4-vector potential of the electromagnetic field [7]. The Clebsch representation is a method involving the use of Clebsch variables for representing the velocity vector field v_μ that is introduced to analyze the Hamiltonian of a barotropic fluid. It should be noted here that the mathematical structure (eq. (B.1a)) of the 4-vector potential $\boldsymbol{A}$ of the skew-symmetric electromagnetic field is similar to that of the equation of motion (eq. (B.1b)) for a barotropic fluid based on relativity theory:

$$F_{\mu\nu}\partial^\nu\phi = 0\,, \tag{B.1a}$$

$$\omega_{\mu\nu}v^\nu = 0\,, \tag{B.1b}$$

where $F_{\mu\nu}$ denotes the skew-symmetric transverse electromagnetic field, and $\omega_{\mu\nu}$ is the skew-symmetric vorticity defined by the rotation of the velocity field v^ν. This similarity is due to the fact that the scalar field $\phi\left(=\partial_\nu A^\nu\right)$ satisfies the wave equation and its gradient vector $\partial_\nu\phi$ is parallel to the propagation direction of the wave (normal to the electric and magnetic fields).

Next, using the two-variable (λ and ϕ) Clebsch representation ($U_\mu = \lambda\partial_\mu\phi$), the v^ν in eq. (B.1b) is regarded as the vector potential of the electromagnetic field. Here, U_μ denotes the Clebsch parameterized 4-vector potential that is parallel to the 4-Poynting vector. Since $\omega_{\mu\nu}$ in eq. (B.1b) can also be regarded as denoting the electromagnetic field, it is represented by the skew-symmetric field

$$S_{\mu\nu} = \partial_\mu U_\nu - \partial_\nu U_\mu\,. \tag{B.2}$$

Furthermore, the following two equations are derived, whose mathematical structure is similar to that of the Maxwell equation:

$$\partial^\nu\partial_\nu\lambda^\mu - \kappa^2\lambda^\mu = 0\,, \tag{B.3a}$$

$$\partial^{\nu}\lambda\partial_{\nu}\phi = 0 . \qquad \text{(B.3b)}$$

Here, eqs. (B.3a) and (B.3b) indicate that λ follows a spatial Klein-Gordon (KG) equation, and that the two vectors ($\partial^{\nu}\lambda$ and $\partial_{\nu}\phi$) are normal to each other, respectively.

Using the vector U_{ν}, these equations can be rewritten as

$$\partial^{\nu}\partial_{\nu}U^{\mu} - \kappa^{2}U^{\mu} = 0 . \qquad \text{(B.4)}$$

The field, represented by U_{μ}, can be called the Clebsch dual (CD) field by comparison with A^{μ} that satisfies the Proca equation

$$\partial^{\nu}\partial_{\nu}A^{\mu} + \kappa^{2}A^{\mu} = 0 . \qquad \text{(B.5)}$$

The energy-momentum tensor T_{μ}^{ν} for $S^{\mu\nu}$ is expressed as

$$T_{\mu}^{\nu} = -S_{\mu\sigma}S^{\nu\sigma} = \rho C_{\mu}C^{\nu} , \qquad \text{(B.6)}$$

where $\rho \equiv -\partial^{\mu}\lambda\partial_{\mu}\lambda$ denotes a spacelike vector, being proportional to the spacelike momentum. $C_{\mu} \equiv \partial_{\mu}\phi$ represents a longitudinal wave. The middle part of eq. (B.6) has the same form as that of the conventional electromagnetic field. The right-hand side is given by the product of ρ and $C_{\mu}C^{\nu}$, which shows that the Clebsch representation succeeded in including two essential elements (the spacelike momentum and the longitudinal wave) in the equations.

Although U_{μ} was a null vector in the discussion above, it can be extended to the spacelike domain so that T_{μ}^{ν} can be represented by

$$T_{\mu}^{\nu} = -S_{\mu\sigma}S^{\nu\sigma} + S_{\alpha\beta}S^{\alpha\beta}g_{\mu}^{\nu} . \qquad \text{(B.7)}$$

The mathematical form of the right-hand side is equivalent to the curvature term in the Einstein equation. It should be pointed out that this equivalency was derived by breaking the U(1) gauge symmetry for extending the CD field to the spacelike domain. Equation

(B.7) is acceptable because the CD field plays the role of the basic mode to represent the spacelike 4-momenta of the interacting fields and because the inherent feature of the relativistic field is represented by its space-time structure.

In order to apply the concept of the CD field above to draw the physical picture of the DP, several points should be noted: The spatially homogeneous spacelike momentum field becomes unstable if it interacts with the timelike momentum field, as was shown in the hint **[C]** in Section 7. By such an interaction, the timelike and spacelike momentum fields can be transformed between each other, and, as a result, the spatial structures of the fields are significantly deformed. Although such a transformation occurs throughout the whole of the interacting area, it occurs more conspicuously at a singular point of the material, such as at the surface of the material or at the impurity atoms in the material (Phenomena 1 and 7).

Several discussions were made to describe this transformation: When the timelike momentum vector satisfies the timelike KG equation, its solution takes the form of a homogeneous wave. Such a homogeneous wavy solution can be also derived from the spacelike KG equation satisfied by the spacelike momentum vector. Since the constants in the KG equation represent the physical quantities of the material under study, the transformation between the timelike and spacelike vectors can be expressed by reversing the signs of these constants.

The information derived by these discussions is:

1) The complex-conjugate amplitudes

$$S_{0r}^{\dagger} = \frac{\omega}{c} R' \exp\left[\frac{\omega}{c} x^0 \right], \quad S_{0r} = -\frac{\omega}{c} R' \exp\left[-\frac{\omega}{c} x^0 \right] \qquad \text{(B.8)}$$

of the derived CD field correspond to the creation ($\hat{a}^{\dagger}$) and annihilation ($\hat{a}$) operators of the quantum harmonic oscillator, respectively. Here, ω is the angular frequency. R' is the radial component of the solution of the KG equation. This correspondence enabled the definition of the normal mode of the electromagnetic field in a sub-wavelength-sized field, which had been impossible with the previous theory (Sections 2.1 and 2.2).

2) The CD field represents a longitudinal wave (the complex-conjugate amplitudes C_{μ} and C_{μ}^{*}) that is accompanied by the components ($L_{\mu} (= \partial_{\mu} \lambda)$ and L_{μ}^{*}) satisfying the KG equation in the spacelike domain (Fig. 7.2).

3) The components (L_μ and L^*_μ) become temporally unstable due to the interaction with the field in the timelike domain. As a result, they are created or annihilated within a very short duration, which means that the CD field corresponds to a virtual photon.
4) The transverse wave of the CD field is converted to a longitudinal wave at the material surface. This means that the material surface serves as the source of a longitudinal wave, thus successfully describing Phenomena 1 and 7.
5) The spatial profile of the field is described by a Yukawa function, which can be understood by replacing x^0 in S_{0r} of eq.(B.8) by x^1, x^2, or x^3. As a result, Phenomena 1 and 11 were also described. This means that the DP is a localized quantum field, created as a result of the transformation of the spacelike momentum field to the timelike field at a singular point of the material.
6) The DP can be represented by the superposition of the longitudinal waves of the CD field. This representation is possible because these waves behave as normal modes. It should be pointed out that the virtual photon behavior of the components (L_μ and L^*_μ), accompanying this longitudinal wave, is nothing less than the origin of this successful representation.

Future progress is expected to explain Phenomena 4 and 6, and also to establish the theory of the fully quantum optical version.

References

[Section 1]

[1] M. Ohtsu, History, current developments, and future directions of near-field optical science, *Opto-Electronic Advances*, **3** (3) (2020) 190046.

[2] K. Kobayashi and M. Ohtsu, "Quantum theoretical approach to a near-field optical system," *Journal of Microscopy*, **194** (1999) pp.249-254.

[3] K. Kobayashi, K., S. Sangu, S., H. Ito, and M. Ohtsu, "Near-field optical potential for a neutral atom," *Physical Review A*, **63** (2001) pp.1-9.

[4] H. Ito, T. Nakata, K. Sakaki, and M. Ohtsu, "Laser Spectroscopy of Atoms Guided by Evanescent Waves in Micron-Sized Hollow Optical Fibers," *Physical Review Letters*, **76** (1996) pp.4500-4503.

[5] M. Ohtsu, K. Kobayashi, T. Kawazoe, S. Sangu, and T. Yatsui, "Nanophotonics: Design, Fabrication, and Operation of Nanometric Devices Using Optical Near Fields," *IEEE J. of Selected Topics in Quantum Electron.*, **8** (2002) pp.839-862.

[6] M. Ohtsu (ed.), *Handbook of Nano-Optics and Nanophotonics* (Springer, 2013).

[7] M. Ohtsu, in *Progress in Nanophotonics* 4 (ed.Yatsui, T.)Ch.1 (Springer, 2018).
[8] H.Sakuma, I. Ojima, and M. Ohtsu: "Dressed photons in a new paradigm of off-shell quantum fields," Progress in Quantum Electronics, **55**, (2017) pp.74-87.
[9] M. Ohtsu (ed.): *Near-Field Nano/Atom Optics and Technology* (Springer, Tokyo, 1998) pp.15-100.
[10] M. Ohtsu and H. Sakuma, "Creation and Measurement of Dressed Photons: A Link to Novel Theories," *Off-shell Archive* (December, 2017) Offshell:1712R.001.v1.
DOI: 10.14939/1712R.001.v1. http://offshell.rodrep.org/?p=89
[11] M. Ohtsu and K. Kobayashi: *Optical Near Fields* (Springer, Berlin, 2004) p.23.
[12] T. Yatsui and M. Ohtsu: "High-Throughput Probes for Near-Field Optics and Their Applications," *Prog. in Nano-Electro-Optics I* (ed. M. Ohtsu) (Springer, Berlin, 2003) p.12.
[13] M. Ohtsu and K. Kobayashi: *Optical Near Fields* (Springer, Berlin, 2004) pp.29-30.
[14] M. Ohtsu, T. Kawazoe, and H. Saigo: "Spatial and Temporal Evolutions of Dressed Photon Energy Transfer," *Off-shell Archive* (October, 2017) Offshell:1710R.001.v1.
DOI: 10.14939/1710R.001.v1. http://offshell.rodrep.org/?p=79.
[15] M. Ohtsu: *Dressed Photons* (Springer, Heidelberg, 2014) pp.18-36.
[16] A. Taflove: *Computational Electrodynamics* (*The Finite-Difference Time-Domain Method*) (Artech House, Boston, 1995).
[17] I. Banno and M. Ohtsu, "Irrationality of the Permittivity in Non-resonant Near-field Optics," Abstract of the 11th Asia-Pacific Conference on Near-Field Optics, July 10-13, 2017, Tainan, Taiwan, p.35.
[18] H. Sakuma, I. Ojima, and M. Ohtsu: "Gauge symmetry breaking and emergence of Clebsch-dual electromagnetic field as a model of dressed photons," Appl. Phys. *A* (2017) 123:750.
[19] I. Ojima: "Micro-macro duality in quantum physics," *Statistic Analysis: Classical and Quantum – Perspectives of White Noise Theory* (ed. T. Hida) (World Scientific, Singapore, 2005) pp.143-161.
[20] O. Bratteli and D.W. Robinson: *Operator Algebras and Quantum Statistical Mechanics* (2nd ed.), vols.1 and 2 (Springer, Berlin, 1987,19977).

[Section 2]

[1] M. Ohtsu, in *Progress in Nanophotonics 4* (ed.Yatsui, T.)Ch.1 (Springer, 2018).
[2] M. Ohtsu: *Dressed Photons* (Springer, Heidelberg, 2014) p.3.
[3] Y. Tanaka and K. Kobayashi, "Spatial localization of an optical near field in one-dimensional nanomaterial system," *Physica*, **E40** (2007) pp.297-300.
[4] K. Kobayashi and M. Ohtsu, "Quantum theoretical approach to a near-field optical system," *Journal of Microscopy*, **194** (1999) pp.249-254.
[5] S. Sangu, K. Kobayashi, and M. Ohtsu, "Optical near fields as photon-matter interacting systems," *J. Microscopy*, **202** (2001) pp. 279-285.
[6] M. Ohtsu: *Dressed Photons* (Springer, Heidelberg, 2014) p.31.

[7] S. Sangu, K. Kobayashi, and M. Ohtsu, “Optical near fields as photon-matter interacting systems,” *J. Microscopy*, **202** (2001) pp. 279-285.

[8] *S. A. Maier, M. L. B*rongersma, P. G. Kik, S. Meltzer, A. A. G. Requicha, and H. A. Atwater, *“Plasmonics—a route to nanoscale optical devices*,” *Advanced Materials*, **13** (2001) pp.1501-1505.

[9] M. Ohtsu, “Indications from dressed photons to macroscopic systems based on hierarchy and autonomy,” *Off-shell Archive* (June, 2019) Offshell: 1906R.001.v1. **DOI:** 10.14939/1906R.001.v1. http://offshell.rodrep.org/?p=201

[10] M. Ohtsu and H. Sakuma, “Creation and Measurement of Dressed Photons: A Link to Novel Theories,” *Off-shell Archive* (December, 1017) Offshell: 1712R.001.v1.
DOI: 10.14939/1712R.001.v1. http://offshell.rodrep.org/?p=89

[11] M. Ohtsu and K. Kobayashi: *Optical Near Fields* (Springer, Berlin, 2004) pp.29-30.

[12] M. Naya, S. Mononobe, R. Uma Maheswari, T. Saiki, and M. Ohtsu, “Imaging of biological samples by a collection-mode photon scanning tunneling microscope with an aperture probe,” Opt. Commun., **124** (1996) pp.9-15.

[13] N. Tate, M. Naruse, T. Yatsui, T. Kawazoe, M. Hoga, Y. Ohyagi, T. Fukuyama, M. Kitamura and M. Ohtsu, ”Nanophotonic code embedded in embossed hologram for hierarchical information retrieval,” *Optics Express*, **18** (2010) pp.7497-7505.

[14] M. Ohtsu and T. Kawazoe, “Experimental estimation of the maximum size of a dressed photon,” *Off-shell Archive* (February, 2018), Offshell: 1802R.001.v1. **DOI**:10.14939/1802R.001.v1. http://offshell.rodrep.org/?p=98

[15] M. Ohtsu and T. Kawazoe, “Nutation in energy transfer of dressed photons between nano-particles,” *Off-shell Archive* (May, 2020) OffShell: 2005O.001.v1.
DOI: 10.14939/2005O.001.v1. http://offshell.rodrep.org/?p=274

[16] T.Kawazoe, K. Kobayashi, J. Lim, Y. Narita, and M. Ohtsu, "Direct Observation of Optically Forbidden Energy Transfer between CuCl Quantum Cubes via Near-Field Optical Spectroscopy,” Phys. Rev. Lett., **88** (2002) 067404.

[17] M. Ohtsu, T. Kawazoe, and H. Saigo, "Spatial and Temporal Evolutions of Dressed Photon Energy Transfer,” *Off-shell Archive* (October, 1017) Offshell:1710R.001.v1.
DOI: 10.14939/1710R.001.v1. http://offshell.rodrep.org/?p=79

[18] M. Ohtsu, **“**New Routes to Studying the Dressed Photon,” *Off-shell Archive* (September, 2017) OffShell: 1709R.001.v1.
DOI: 10.14939/1709R.001.v1. http://offshell.rodrep.org/?p=4

[19] N. Konno, *Quantum Walk*, Chapter 8, Quantum Potential Theory, ed. by U. Franz and M. Schürmann, (Springer, Heidelberg, 2008) pp.309-452.

[20] M. Ohtsu, “Dressed photon phenomena that demand off-shell scientific theories,” *Off-shell Archive* (November, 2019) OffShell: 1911.R.001.v1. **DOI:** 10.14939/1911.R.001.v1.

http://offshell.rodrep.org/?p=232

[21] A. Neogi, H. Morkoç, A. Tackeuchi, T. Kuroda, M. Ohtsu, and T. Kawazoe, "Near Field Optical Spectroscopy of GaN/AlN Quantum Dots," *Abstract of the Conf. on Lasers and Electro-Opt*.(16–21 May 2004, San Francisco, USA) IThM2.

[22] A. Neogi, B. P. Gorman, H. Morkoç, T. Kawazoe, and M. Ohtsu, "Near-field optical spectroscopy and microscopy of self-assembled GaN/AlN nanostructures," *Appl. Phys. Lett*., **86** (2005) 043103.

[23] T. Yatsui, W. Nomura, T. Mano, H. T. Miyazaki, K. Sakoda, T. Kawazoe, and M. Ohtsu, "Emission from a dipole-forbidden energy state in a GaAs quantum-ring induced by dressed photon," *Appl. Phys. A,* **115** (2014) pp.1-4.

[Section 3]

[1] M. Ohtsu, T. Kawazoe, and H. Saigo, "Spatial and Temporal Evolutions of Dressed Photon Energy Transfer," *Off-shell Archive* (October, 1017) Offshell:1710R.001.v1.

DOI: 10.14939/1710R.001.v1. http://offshell.rodrep.org/?p=79

[2] S. Sangu, K. Kobayashi, S. Shojiguchi, and M. Ohtsu, "Logic and functional operations using a near-field coupled quantum-dot system," *Phys.B*, **69** (2004) 115334.

[3] T. Kawazoe, M. Ohtsu, S. Aso, Y. Sawado, Y. Hosoda, K. Yoshizawa, K. Akahane, N. Yamamoto, and M. Naruse, "Two-dimensional array of room-temperature nanophotonic logic gates using InAs quantum dots in mesa structures," *Appl. Phys. B*, **103** (2011) pp. 537-546.

[4] T. Kawazoe, M. Ohtsu, S. Aso, Y. Sawado, Y. Hosoda, K. Yoshizawa, K. Akahane, N. Yamamoto, and M. Naruse, "Two-dimensional array of room-temperature nanophotonic logic gates using InAs quantum dots in mesa structures," *Appl. Phys. B*, **103** (2011) pp. 537-546.

[5] M. Naruse, K. Leibnitz, F. Peper, N. Tate, W. Nomura, T. Kawazoe, M. Murata, M. Ohtsu, "Autonomy in excitation transfer via optical near-field interactions and its implications for information networking," *Nano Communication Networks*, **2** (2011) pp.189-195.

[6] T. Kawazoe, S. Tanaka, M. Ohtsu, "A single-photon emitter using excitation energy transfer between quantum dots," J. Nanophotonics, **2** (2008) 029502.

[7] M. Naruse, P. Holmstrom, T. Kawazoe, K. Akahane, N. Yamamoto, L. Thylen, and M. Ohtsu, "Energy dissipation in energy transfer mediated by opticalnear-field interactions and their interfaces with optical far-fields," *Appl. Phys. Lett*., **100** (2012) 241102.

[8] M. Naruse, N. Tate, M. Aono, and M. Ohtsu, "Information physics fundamentals of nanophotonics," *Rep. Prog. Phys.*, **76** (2013) pp. 1-50.

[9] S.-J. Kim, M. Naruse, M. Aono, M. Ohtsu, and M. Hara, "Decision Maker based on Nanoscale Photo-excitation Transfer," *Scientific Report*, **3** (2013) pp. 1-6.

[10] M. Aono, M. Naruse, S-J. Kim, M. Wakabayashi, H. Hori, M. Ohtsu, and M. Hara, "Amoeba-Inspired Nanoarchitectonic Computing: Solving Intractable Computational Problems Using Nanoscale

Photoexcitation Transfer Dynamics," *Langmuir*, **29** (2013) pp. 7557-7564.

[11] N. Tate, H. Sugiyama, M. Naruse, W. Nomura, T. Yatsui, T. Kawazoe, and M. Ohtsu, "Quadrupole-Dipole Transform based on Optical Near-Field Interactions in Engineered Nanostructures," *Optics Express*, **17** (2009) pp. 11113-11121.

[12] N. Tate, M. Naruse, T. Yatsui, T. Kawazoe, M. Hoga, Y. Ohyagi, T. Fukuyama, M. Kitamura, and M. Ohtsu, "Nanophotonic code embedded in embossed hologram for hierarchical information retrieval," *Optics Express*, **18** (2010) pp. 7497-7505.

[13] T. Kawazoe, K. Kobayashi, and M. Ohtsu, "Optical nanofountain: A biomimetic device that concentrates optical energy in a nanometric region", *Appl. Phys. Lett.* **86** (2005) 103102.

[14] H. Imahori, "Giant Multiporphyrin Arrays as Artificial Light-Harvesting Antennas," *J. Phys. Chem. B*, **108** (2004) pp.6130–6143.

[15] M. Naruse, T. Kawazoe, R. Ohta, W. Nomura, M. Ohtsu, "Optimal mixture of randomly dispersed quantum dots for optical excitation transfer via optical near-field interactions, " *Phys. Rev. B*, **80** (2009) 125325.

[16] N. Johnson, *Simply Complexity*, (Oneworld Publications, Oxford, 2007).

[17] W. Nomura, T. Yatsui, T. Kawazoe, M. Naruse, and M. Ohtsu, "Structural dependency of optical excitation transfer via optical near-field interactions between semiconductor quantum dots, " *Appl. Phys. B*, **100** (2010) pp. 181-187

[18] M. Ohtsu, "Indications from dressed photons to macroscopic systems based on hierarchy and autonomy," *Off-shell Archive* (June, 2019) Offshell: 1906R.001.v1.

DOI 10.14939/1906R.001.v1. http://offshell.rodrep.org/?p=201

[19] M. Naruse, W. Nomura, M. Aono, M. Ohtsu, Y. Sonnefraud, A. Drezet, S. Huant, and S.-J Kim, "Decision making based on optical excitation transfer via near-field interactions between quantum dots," *J. Appl. Phys.*, **116** (2014) 154303.

[20] M. Ohtsu, "Novel functions and prominent performance of nanometric optical devices made possible by dressed photons," *Off-shell Archive* (April, 2019) Offshell: 1904R.001.v1.

DOI: 10.14939/1904R.001.v1. http://offshell.rodrep.org/?p=190

[21] T. Kawazoe, K. Kobayashi, K. Akahane, M. Naruse, N.Yamamoto and M. Ohtsu," Demonstration of nanophotonic NOT gate using near-field optically coupled quantum dots," *Applied Physics B*, **84** (2006) pp. 243－246.

[22] R. Hambury Brown, R.Q. Twiss, "The Question of Correlation between Photons in Coherent Light Rays," *Nature*, **178** (1956) pp.1447–1448.

[23] L.B.Kish, "Moore's Law and the energy requirement of computing versus performance, " *IEE Proc. - Circ.Dev.Syst.*, **151** (2004) pp.190–194.

[24] F. Moll, M. Roca, E. Isern, "Analysis of dissipation energy of switching digital CMOS gates with coupled outputs," *Microelectronics Journal*, **34** (2003) pp. 833-842.

[25] M. Ohtsu, “Nanophotonics: Devices, fabrications, and systems”, *RLNR/Tokyo-Tech 2003 International Symposium on Nanoscience and Nanotechnology on Quantum Particles*, Tokyo, paper number I-3.

[26] N. Streibl, K.-H. Brenner, A. Huang, J. Jahns, J. L. Jewell, A. W. Lohmann, D.A.B. Miller, M. Murdocca, M. E. Prise, T. Sizer,”Digital Optics,” *Proc. IEEE*, **77** (1989) pp. 1954-1969.

[Section 4]

[1] M. Ohtsu and T. Kawazoe, “Experimental estimation of the maximum size of a dressed photon,” *Off-shell Archive* (February, 2018) Offshell:1802R.001.v1.

DOI: 10.14939/1802R.001.v1. http://offshell.rodrep.org/?p=98

[2] M. Ohtsu, “History, current developments, and future directions of near-field optical science,” *Opto-Electronic Advances*, **3** (2020) 190046.

[3] T. Kawazoe, K. Kobayashi, S. Takubo, and M. Ohtsu, “Nonadiabatic photodissociation process using an optical near field,” *J. Chem. Phys.* **122** (2005) 024715.

[4] S. Mononobe and T., T. in *Near-Field Nano/Atom Optics and Technol*.(ed Ohtsu, M.) (Springer Tokyo, 1998) Chs.3 and 4.

[5] T. Pangaribuan, K. Yamada, S. Jian, H. Ohasawa, and M. Ohtsu, “Reproducible fabrication technique of nanometric tip diameter fiber probe for photon scanning tunneling microscope,” *Jpn. J. of Appl. Phys*, **31** (1992) pp. L1302-L1304.

[6] T. Kawazoe, K. Kobayashi, and M. Ohtsu, “Near-field optical chemical vapor deposition using $Zn(acac)_2$ with a non-adiabatic photochemical process,” *Appl. Phys. B*, **84** (2006) pp. 247-251.

[7] J. Lim, T. Yatsui, and M. Ohtsu, “Observation of Size-Dependent Resonance of Near-Field Coupling between a Deposited Zn Dot and the Probe Apex during Near-Field Optical Chemical Vapor deposition,” *IEICE Trans. Electron.,* **E88-C** (2005) pp. 1832-1834.

[8] S. Sangu, K. Kobayashi, and M. Ohtsu, “Optical near fields as photon-matter interacting systems,” *J. Microscopy,* **202** (2001) pp. 279-285.

[9] V. V. Polonski, Y. Yamamoto, M. Kourogi, H. Fukuda, and M. Ohtsu, “Nanometric patterning of zinc by optical near-field photochemical vapour deposition,” *J. Microscopy*, **194** (1999) pp. 545-551.

[10] H. Yonemitsu, T. Kawazoe, K. Kobayashi, and M. Ohtsu, “Nonadiabatic photochemical reaction and application to photolithography,” *Journal of Photoluminescence,* **122-123** (2007) pp. 230-233.

[11] Y. Inao, S. Nakasato, R. Kuroda, and M. Ohtsu, “Near-field lithography as prototype nano-fabrication tool,” *Microelectronic Engineering*, **84** (2007) pp. 705-710.

[12] T. Kawazoe, K. Kobayashi, K. Akahane, M. Naruse, N.Yamamoto and M. Ohtsu," Demonstration of nanophotonic NOT gate using near-field optically coupled quantum dots," *Applied Physics B*, **84** (2006) pp. 243－246.

[13] T. Kawazoe, T. Takahashi, and M. Ohtsu, “Evaluation of the dynamic range and spatial resolution of

nonadiabatic optical near-field lithography through fabrication of Fresnel zone plates," *Appl. Phys.* B, **98** (2010) pp. 5-11.

[14] M. Koike, S. Miyauchi, K. Sano, and T. Imazono, in *Nanophotonics and Nanofabrication*, (ed. Ohtsu, M.), Ch.9 (Wiley-VCH, 2009).

[15] K. Hirata, "Realization of high-performance optical element by optical near-field etching," *Proc. SPIE,* **7921** (2011) 79210M.

[16] T. Yatsui, W. Nomura, and M. Ohtsu. "Realization of Ultraflat Plastic Film using Dressed-Photon–Phonon-Assisted Selective Etching of Nanoscale Structures," *Advances in Optical Technologies*, **2015** (2015) 701802.

[17] D.W. Allan, "Statistics of Atomic Frequency Standards," *Proc. IEEE,* **54** (1966) pp.221-230.

[18] T. Yatsui, K. Hirata, Y. Tabata, Y. Miyake, Y. Akita, M. Yoshimoto, W. Nomura, T. Kawazoe, M. Naruse, and M. Ohtsu, "Self-organized near-field etching of the sidewalls of glass corrugations," *Appl. Phys. B*, **103** (2011) pp. 527-530.

[19] R. Teki, A. J. Kadaksham, M. House, J. H. Jones, A. Ma, S. V. Babu, A. Hariprasad, P. Dumas, R. Jenkins, J. Provine, A. Richmann, J. Stowers, S. Meyers, U. Dietze, T. Kusumoto, T. Yatsui, M. Ohtsu, and F. Goodwin, "Alternative Smoothing Techniques to Mitigate EUV Substrate Defectivity," *Proc. Soc. of Photo-optical Instrum. Eng. (SPIE)*, SPIE, February 12-16, 2012, San Jose, CL, USA, Vol. 8322, pp. 1-12.

[20] T. Yatsui, W. Nomura, F. Stehlin, O. Soppera, M. Naruse, and M. Ohtsu, "Challenge in realizing ultraflat material surfaces," *Beilstein J. Nanotechnol*., **4** (2013) pp.875–885.

[21] W. Nomura, T. Yatsui, Y. Yanase, K. Suzuki, M. Fujita, A. Kamata, M. Naruse, and M. Ohtsu, "Repairing nanoscale scratched grooves on polycrystalline ceramics using optical near-field assisted sputtering," *Appl. Phys. B*, **99** (2010) pp. 75-78

[22] T. Yatsui, W. Nomura, M. Naruse, and M. Ohtsu, "Realization of an atomically flat surface of diamond using dressed photon-phonon etching," *J. Phys. D*, **45** (2012) 475302.

[Section 5]

[1] T. Kawazoe, H. Fujiwara, K. Kobayashi, and M. Ohtsu, "Visible light emission from dye molecular grains via infrared excitation based on the nonadiabatic transition induced by the optical near field," *J. of Selected Topics in Quantum Electronics*, **15** (2009) pp.1380-1386.

[2] H. Fujiwara, T. Kawazoe, and M. Ohtsu, "Nonadiabatic multi-step excitation for the blue–green light emission from dye grains induced by the near-infrared optical near-field," *Appl. Phys. B*, **98** (2010) pp. 283-289.

[3] H. Fujiwara, T. Kawazoe, and M. Ohtsu, "Nonadiabatic nondegenerate excitation by optical near-field and its application to optical pulse-shape measurement", *Appl. Phys*. *B*, **100** (2010) pp.85-91.

[4] M. Ohtsu, T. Kawazoe, and H. Saigo, "Spatial and Temporal Evolutions of Dressed Photon Energy Transfer," *Off-shell Archive* (October, 2017) Offshell: 1710R.001.v1. **DOI:** 10.14939/1710R.v1. http://offshell.rodrep.org/?p=79

[5] T. Kawazoe, A. Mizushima, K. Matsue, and M. Ohtsu: "A wavelength conversion film using energy transfer via dressed photon," *Abstract of the 60th JSAP Spring Meeting*, March 2013, Atsugi, Japan, paper number 28p-A1-11.

[6] T. Kawazoe, K. Matsue, and M. Ohtsu: "Fabrication of ZnO-QDs for wavelength conversion film using a dressed photon," *Abstract of the 74th JSAP Autumn Meeting*, September 2013, Kyoto, Japan, paper number 18p-C14-16.

[7] T. Kawazoe, K. Matsue, and M. Ohtsu: "Size control of ZnO quantum dots in a wavelength conversion film using a dressed photon for a solar cell," *Abstract of the 61st JSAP Spring Meeting*, March 2014, Sagamihara, Japan, paper number 18a-F12-6.

[8] T. Kawazoe, C. Amagai, and M. Ohtsu: "High-effectiveness of crystalline silicon solar cell by a wavelength conversion film using a dressed photon," *Abstract of the 62th JSAP Spring Meeting*, March 2015, Hiratsuka, Japan, paper number 11p-A12-7.

[9] M. Ohtsu, "Dressed photon phenomena that demand off-shell scientific theories," *Off-shell Archive* (November, 2019) OffShell: 1911.R.001.v1. **DOI:** 10.14939/1911.R.001.v1. http://offshell.rodrep.org/?p=232

[10] N. Tate, Y. Liu, T. Kawazoe, M. Naruse, T. Yatsui, and M. Ohtsu, "Fixed-distance coupling and encapsulation of heterogeneous quantum dots using phonon-assisted photo-curing," *Appl. Phys. B,* **110** (2013) pp. 39-45.

[11] N. Tate, Y. Liu, T. Kawazoe, M. Naruse, T. Yatsui, and M. Ohtsu, "Nanophotonic droplet: a nanometric optical device consisting of size- and number-selective coupled quantum dots," *Appl. Phys. B,* **110** (2013) pp. 293-297.

[12] N. Tate, M. Naruse, Y. Liu, T. Kawazoe, T. Yatsui, and M. Ohtsu, "Experimental demonstration and stochastic modeling of autonomous formation of nanophotonic droplets," *Appl. Phys. B,* **112** (2013) pp. 587-592.

[13] N. Tate, W. Nomura, T. Kawazoe, and M. Ohtsu, "Novel wavelength conversion with nanophotonic droplet consisting of coupled quantum dots," *Opt. Express,* **22** (2014) pp. 10262-10269.

[14] S. Yukutake, T. Kawazoe, T. Yatsui, W. Nomura, K. Kitamura, and M. Ohtsu, "Selective photocurrent generation in the transparent wavelength range of a semiconductor photovoltaic device using a phonon-assisted optical near-field process," *Appl. Phys. B***, 99** (2010) pp. 415-422.

[15] H. Tanaka, T. Kawazoe, and M. Ohtsu, "Increasing Si photodetector photosensitivity in near-infrared region and manifestation of optical amplification by dressed photons," *Appl. Phys*. *B***, 108** (2012) pp. 51-56.

[16] M. Ohtsu, “The present and future of numerical simulation techniques for off-shell science,” *Off-shell Archive* (March, 2020) OffShell: 2003R.001.v1. **DOI** 10.14939/2003R. 001.v1
[17] M. Ohtsu, *Silicon Light-Emitting Diodes and Lasers* (2016, Springer) pp.8-10.

[Section 6]

[1] K.D. Hirschman, L.Tysbekov, S.P. Duttagupta, and P.M. Fauchet, “Silicon-based visible light emitting devices integrated into microelectronic circuits,” *Nature*, **384** (1996) pp. *338*-341.
*[2] Z.H. Lu, D.J. Lockwood, and J.M. Baribeau, “*Quantum confinement and light emission in SiO_2/Si superlattices,” *Nature*, **378** (1995) pp. *258*–260.
[3] M.M. Milošević, X. Chen, W. Cao, A.F.J. Runge, Y. Franz, C.G. Littlejohns, S. Mailis, A.C. Peacock, D.J. Thomson, and G.T. Reed, “Ion Implantation in Silicon for Trimming the Operating Wavelength of Ring Resonators,” *IEEE J. Sel. Top. Quant*., **24** (2018) 8200107.
[4] T. Kawazoe, M.A. Mueed, and M. Ohtsu, “Highly efficient and broadband Si homojunction structured near-infrared light emitting diodes based on the phonon-assisted optical near-field process,” *Appl. Phys.B*, **104** (2011) pp.747-754.
[5] M. Ohtsu, “History, current developments, and future directions of near-field optical science,” *Opto-Electronic Advances*, **3** (2020) 190046.
[6] J.H. Kim, T. Kawazoe, and M. Ohtsu, “Optimization of dressed-photon—phonon-assisted annealing for fabricating GaP light-emitting diodes.” *Applied Physics A*, **121** (2015) pp. 1395-1401.
[7] M. Yamaguchi, T. Kawazoe, and M. Ohtsu, “Evaluating the coupling strength of electron–hole pairs and phonons in a 0.9 μm-wavelength silicon light emitting diode using dressed-photon–phonons,” *Appl. Phys. A*, **115** (2013) pp. 119-125.
[8] N. Wada, M.-A. Tran, T. Kawazoe, and M. Ohtsu, “Measurement of multimode coherent phonons in nanometrics spaces in a homojunction-structured silicon light emitting diode,” *Appl. Phys. A*, **115** (2014) pp. 113-118.
[9] M. Ohtsu, M. and T. Kawazoe, “Principles and practices of Si light emitting diodes using dressed photons,” *Adv. Mat. Letters*, **10** (2019) pp.860-867.
[10] Y. Tanaka.Y and K. Kobayashi, “Optical near field dressed by localized and coherent phonons,” *J. Microscopy*, **229** (2007) pp. 228-232.
[11] T. Kawazoe, K. Nishioka, and M. Ohtsu, “Polarization control of an infrared silicon light-emitting diode by dressed photons and analyses of the spatial distribution of doped boron atoms,” *Applied Physics A*, **121** (2015) pp.1409-1415.
[12] M.A. Tran, T. Kawazoe, and M. Ohtsu, “Fabrication of a bulk silicon p-n homojunction-structured light emitting diode showing visible electroluminescence at room temperature,” *Appl. Phys. A*, **115** (2014) pp. 105-111.
[13] M. Yamaguchi, T. Kawazoe, T. Yatsui, and M. Ohtsu, “Spectral properties of a lateral p-n

homojunction-structured visible silicon light-emitting diode fabricated by dressed-photon—phonon-assisted annealing," *Appl. Phys. A*, **121** (2015) pp. 1389-1394.

[14] Ohtsu, M. *Silicon Light-Emitting Diodes and Lasers* Ch.6 (Springer, 2016) pp.83-101.

[15] D. Liang and J. E. Bowers, "Recent progress in lasers on silicon," Nat. Photonics, **4** (2010) pp.511-517.

[16] H. Rong, R. Jones, A. Liu, O. Cohen, D. Hak, A. Fang, and M. Paniccia, "A continuous-wave Raman silicon laser," *Nature*, **433** (2005) pp.725-728.

[17] S. Saito, Y. Suwa, H. Arimoto, N. Sakuma, D. Hisamoto, H. Uchiyama, J. Yamamoto, T. Sakamizu, T. Mine, S. Kimura, T. Sugawara, and M. Aoki, "Stimulated emission of near-infrared radiation by current injection into silicon (100) quantum well," *Appl. Phys. Lett*., **95** (2009) 241101.

[18] G.A Bernard and G. Duraffourg, "Laser Conditions in Semiconductors," *Phys. Status Solidi*, **1** (1961) pp.699-703.

[19] M. Ohtsu and T. Kawazoe, "High-Power Infrared Silicon Light-emitting Diodes Fabricated and Operated using Dressed Photons," *Off-shell Archive* (April, 2018) Offshell: 1804O.001.v1.

DOI: 10.14939/1804O.001.v1. http://offshell.rodrep.org/?p=109

[20] T. Kawazoe, M. Ohtsu, K. Akahane, and N. Yamamoto, "Si homojunction structured near-infrared laser based on a phonon-assisted process," *Appl. Phys. B*, **107** (2012) pp. 659-663.

[21] H. Tanaka, T. Kawazoe, M. Ohtsu, and K. Akahane, "Decreasing the threshold current density in Si lasers fabricated by using dressed-photons," *Fluoresc. Mater.,* **1** (2015) pp.1-7.

[22] M. Ohtsu, *Silicon Light-Emitting Diodes and Lasers* (Springer, Heidelberg, 2016) pp.16-19.

[23] M. Ohtsu, Y. Teramachi, and T. Miyazaki, "Mode stability analysis of nearly single-longitudinal-mode semiconductor lasers," *IEEE J. Quantum Electron.*, **24** (1988) pp.716-723.

[24] M. Ohtsu and Y. Teramachi, "Analysis of mode partition and mode hopping in semiconductor lasers," *IEEE J. Quantum Electron*., **25** (1989) pp.31-38.

[25] H. Tanaka, T. Kawazoe, and M. Ohtsu, "Increasing Si photodetector photosensitivity in near-infrared region and manifestation of optical amplification by dressed photons" *Appl. Phys. B*, **108** (2012) pp. 51-56.

[26] H. Tanaka, T. Kawazoe, M. Ohtsu, K. Akahane, and N.Yamamoto, "Evaluation of optical amplification properties using dressed photons in a silicon waveguide," *Applied Physics A*, **121** (2015) pp.1377-1381.

[27] Z. I. Kazi., T.Egawa, T. Jimbo, and M. Umeno, "Gain coefficient, quantum efficiency, transparency current density, and internal loss of the AlGaAs-GaAs-based lasers on Si substrate," *IEEE Photonics Technol. Lett.,* **11** (1999) pp. 1563-1565.

[28] H. Tanaka, T. Kawazoe, and M. Ohtsu, Abstract of the 63st JSAP Spring Meeting, March 2016, Tokyo, Japan, paper number 19a-S622-8.

[29] H. Tanaka, T. Kawazoe, M. Ohtsu, K. Akahane, and N. Yamamoto, Abstract of the 76th JSAP Autumn Meeting, September 2015, Nagoya, Japan, paper number 16p-2G-8.

[30] T. Kawazoe, K. Hashimoto, and S. Sugiura, "High-power current-injection type Silicon laser using nanophotonics," *Abstract of the EMN Nanocrystals Meeting*, October 17-21, 2016, Xi'an, China, pp.9-11 (paper number 03).

[31] T. Kawazoe, S. Sugiura, and M. Ohtsu, *Abstract of the 64th JSAP Spring Meeting*, March 2017, Yokoyama, Japan, paper number 15a-F202-9.

[32] T. Kawazoe, K. Hashimoto, and S. Sugiura, "High Power Homojunction Silicon Laser," *Abstract of the 65th JSAP Spring Meeting*, March 2018, Tokyo, Japan, paper number 19p-F310-14.

[33] M. Ohtsu, *Silicon Light-Emitting Diodes and Lasers* (Springer, Heidelberg, 2016) pp.83-101.

[34] M. Ohtsu, *Coherent Quanatum Optics and Technology* (KTK Scientific and Kluwer Academic, Tokyo, Dordrecht, Boston, London, 1992) pp.49-81.

[35] M. Ohtsu, *Highly Coherent Semiconductor Lasers* (Artech House, Boston, 1992) pp.7-60.

[36] J.R. Singer (ed.), *Advances in Quantum Electronic*s, (Columbia University Press, New York, 1961) pp.456-506.

[37] W.P. Dumke, "Interband Transitions and Maser Action," *Phys. Rev*., **127**, (1962) pp.1559-1563.

[38] M. Ohtsu, T. Kawazoe, "Gigantic Ferromagnetic Magneto-Optical Effect in a SiC Light-emitting Diode Fabricated by Dressed-Photon–Phonon-Assisted Annealing," *Off-shell Archive* (September, 2018), OffShell: 1809R.001.v1. **DOI:** 10.14939/1809R.001.v1. http://offshell.rodrep.org/?p=161

[39] *Chronological Scientific Tables*, the 77th edition, (ed)National Astronomical Observatory of Japan, Maruzen Co., Tokyo, Japan (2004) p.449

[40] T. Kawazoe, N. Tate, and M. Ohtsu, "SiC magneto-optical current-transformer applicable to a polarization rotator using dressed photons," Abstract of the 22nd International Display Workshops, Dec. 9-11, 2015, Otsu, Japan, PRJ3-5L.

[41] M. Ohtsu, *Silicon Light-Emitting Diodes and Lasers*, Springer, Heidelberg (2016) p.136.

[42] T.H. Upton, "Low-lying valence electronic states of the aluminum dimer," *J. Phys. Chem*., **90** (1986) pp.754-759.

[43] A. Rajca, "Organic Diradicals and Polyradicals: From Spin Coupling to Magnetism?, " *Chem. Rev*., **94** (1994) pp.871-893.

[44] N. Tate, T. Kawazoe, W. Nomura, and M. Ohtsu, "Current-induced giant polarization rotation using ZnO single crystal doped with nitrogen ions, ". *Scientific Reports,* **5** (2015) 12762.

[Section 7]

[1] Newton, T.D. & Wigner, E. P. Localized States for Elementary Systems. *Rev. Mod. Phys.*, **21** (1949) pp.400-406.

[2] M. Ohtsu, "History, current developments, and future directions of near-field optical science," *Opto-Electronic Advances*, **3** (2020) 190046.

[3] I. Ojima, “Micro-macro duality in quantum physics,” in *Stochastic Analysis: Classical and Quantum Perspectives of White Noise Theory*, (ed. T. Hida) Ch.12 (World Scientific, 2005).

[4] I. Ojima, “Nakanishi-Lautrup *B*-field, Crossed Product & Duality,” *Research on Quantum Field Theory*, *RIMS Workshop*, Abstr.**1524** (2006) pp.29-37.

[5] G.F. Del’Antonio, “Support of a field in *p* space,” *J. Math. Phys*., **2** (1961) pp.759-766.

[6] Y. Aharanov, A. Komar, and L. Susskind, “Superluminal Behavior, Causality, and Instability,” *Phys. Rev.*, **182** (1969) pp.1400-1403.

[7] Yatsui, T. (ed). P*rogress in Nanophotonics*, **5** (Springer, 2018) pp.53-77.

[8] M. Ohtsu, I. Ojima, and H. Sakuma, in *Progress in Optics*, **64** (ed. Visser, T.D.) Chapter 2 (Elsevier, 2019).

[9] Yatsui, T. (ed). *Progress in Nanophotonics **5*** (Springer, 2018) pp.79-167.

[10] M. Ohtsu, “Progress in off-shell science in analyzing light–matter interactions for creating dressed photons,” *Off-shell Archive* (April, 2020) OffShell: 2004R.001.v1.**DOI** 10.14939/2004R.001.v1. http://offshell.rodrep.org/?p=268

[11] R.F.Streater and A.S. Wightman, *PCT, Spin and Statistics, and All That* (Princeton Univ. Press, Princeton and Oxford, 1964) pp.163-165.

[12] R. Jost, *The General Theory of Quantized Fields* (Lectures in Applied Mathematics, Volume IV) XV + 157 S. (American Mathematical Society, Providence, 1965).

[13] M. Ohtsu, I. Ojima, and H. Sakuma, “Dressed Photon as an Off-Shell Quantum Field,” *Progress in Optics 64* (ed. T.D. Visser) (Elsevier, Amsterdam, 2019) pp.45-97.

[14] I. Ojima,“A Unified Scheme for Generalized Sectors Based on Selection Criteria: Order Parameters of Symmetries and of Thermality and Physical Meanings of Adjunctions,” *Open Systems & Information Dynamics*, **10** (2003) pp. 235-279.

[15] M. Ohtsu, “Embarking on theoretical studies for off-shell science,” *Off-shell Archive* (November, 2018), Offshell: 1811R001.v1. **DOI** 10.14939/1811R.001.v1. http://offshell.rodrep.org/?p=176

[16] H. Saigo, “Quantum Probability for Dressed Photons: The Arcsine Law in Nanophotonics,” *Progress in Nanophotonics 5* (ed. T. Yatsui) (Springer, Heidelberg, 2018) pp.79-106.

[17] M. Ohtsu, *Dressed Photons*, Springer, Heidelberg (2014) pp.89-246.

[18] M. Ohtsu (ed.), *Near-Field Nano/Atom Optics and Technology*, Springer, Tokyo (1988) pp.15-100.

[19] M. Ohtsu, T. Kawazoe, and H. Saigo, “Spatial and Temporal Evolutions of Dressed Photon Energy Transfer,” Offshell: 1710R,001.v1 (2017).
[20] S. Sangu, H. Saigo, M. Ohtsu, “Simulation of Dressed Photon Energy Transfer based on Quantum-Walk Model,” *Abstracts of the 79th Jpn. Soc. Appl. Phys. Autumn Meeting*, September 2018, Nagoya, Japan, paper number 19a-437-7.
[21] M. Ohtsu (ed.), *Near-Field Nano/Atom Optics and Technology*, Springer, Tokyo (1988) pp.71-87.
[22] M. Ohtsu and T. Kawazoe, “Nutation in energy transfer of dressed photons between nano-particles,” *Off-shell Archive* (May, 2020) OffShell: 2005O.001.v1. **DOI** 10.14939/2005O.001.v1
http://offshell.rodrep.org/?p=274
[23] M. Hamano and H. Saigo “Quantum Walk and Dressed Photon,” *Electron. Proc. in Theoretical Compt. Sci*. (EPTCS), **315** (2020) pp.93-99.(G. Di Molfetta, V. Kendon and Y. Shikano (Eds.): 9th International Conference on Quantum Simulation and Quantum Walks (QSQW 2020))
DOI:10.4204/EPTCS.315.9
[24] Y. Higuchi and E. Segawa, “A dynamical system induced by quantum walk,” *J. Phys.A*, **52** (39) (2019) 697702.
[25] K. Okamura, “An Approach from Measurement Theory to Dressed Photon,” *Progress in Nanophotonics 5* (ed. T. Yatsui) (Springer, Heidelberg, 2018) pp.137-167.
[26] K. Okamura, “An approach from measurement theory to dressed photon,” *Abstracts of the 79th Jpn. Soc. Appl. Phys. Autumn Meeting*, September 2018, Nagoya, Japan, paper number 19a-437-4.
[27] I. Ojima, “Control over Off-Shell QFT via Induction and Imprimitivity,” *Progress in Nanophotonics 5* (ed. T. Yatsui) (Springer, Heidelberg, 2018) pp.107-135.

[Appendix A]

[1] M. Ohtsu, “The present and future of numerical simulation techniques for off-shell science,” *Off-shell Archive* (March, 2020) OffShell: 2003R.001.v1. **DOI:** 10.14939/2003R. 001.v1
http://offshell.rodrep.org/?p=259
[2] N. Tate, M. Naruse, Y. Liu, T. Kawazoe, T. Yatsui, and M. Ohtsu, “Experimental demonstration and stochastic modeling of autonomous formation of nanophotonic droplets,” *Appl. Phys. B,* **112** (2013) pp.587-592.
[3] K. Takahashi, M. Katori, M. Naruse, and Motoichi Ohtsu, “Stochastic model showing a transition to self-controlled particle-deposition state induced by optical near-fields,” *Appl. Phys. B*, **120** (2015) pp.247-254.
[4] M. Ohtsu and T. Kawazoe, “Experimental estimation of the maximum size of a dressed photon,” *Off-shell Archive* (February 2018) Offshell: 1802R.001.v1. **DOI:** 10.14939/1802R.001.v1, http://offshell.rodrep.org/?p=98

[5] M. Katori and H. Kobayashi, in *Prog. Nanophotonics 4* (ed. M. Ohtsu and T. Yatsui) (Springer, Heidelberg, 2017) pp.19-55.
[6] M. Ohtsu and T. Kawazoe, "Principles and Practices of Si Light Emitting Diodes using Dressed Photons," *Off-shell Archive* (May 2018) Offshell: 1805R.001.v1. **DOI:** 10.14939/1805R.001.v1,
[7] J. H. Kim, T. Kawazoe, and M. Ohtsu, "Optimization of dressed-photon—phonon-assisted annealing for fabricating GaP light-emitting diodes," *Appl. Phys. A*, **121** (2015) pp.1395-1401.
[8] M. Ohtsu and M. Katori, "Complex System of Dressed Photons and Applications," *The Review of Laser Engineering*, **45** (2017) pp.139-143 (in Japanese).
[9] T. Kawazoe, K. Nishioka, and M. Ohtsu, "Polarization control of an infrared silicon light-emitting diode by dressed photons and analyses of the spatial distribution of doped boron atoms," *Appl. Phys.A*, **121** (2015) pp.1409-1415.
[10] H. Sakuma, "On the problem of quantization of Clebsch dual field and a quantized representation of dressed photon," *Proc. of the Workshop on Basic Mathematic-Physical Studies on Dressed Photon* (ed. by T. Takiguchi), *Mathematics for Industry Research* No.14, Inst. Mathematics for Industry, Kyushu Univ., (February 2019) pp.127-148.
[11] H. Saigo, "Dressed Photon and Quantum Walk," *Abstracts of the 66th Jpn. Soc. Appl. Phys. Spring Meeting*, March 2019, Tokyo, Japan, paper number 10p-W621-13.
[12] E. Segawa, S. Sangu, and M. Ohtsu, "An expression for dressed photon by quantum walks on line graphs," *Abstracts of the 80th Jpn. Soc. Appl. Phys. Spring Meeting*, September 2019, Sapporo, Japan, paper number 19p-E314-5.
[13] H. Ito, T. Nakata, K. Sakaki, and M. Ohtsu, "Laser Spectroscopy of Atoms Guided by Evanescent Waves in Micron-Sized Hollow Optical Fibers," *Phys. Rev. Lett.,* **76** (1996) pp.4500-4503.
[14] M. Ohtsu, "Near-Field Optical Atom Manipulation: Toward Atom Photonics," Chapter 11 in *Near-Field Nano/Atom Optics and Technology*, (Springer, Tokyo, 1998) pp.217-266.

[Appendix B]

[1] H. Sakuma, "Virtual Photon Model by Spatio-Temporal Vortex Dynamics," *Progress in Nanophotonics 5* (ed.T. Yatsui) (Springer, Heidelberg, 2018) pp.53-77.
[2] R. Jost, "The General Theory of Quantized Fields," in *Lectures in Applied Mathematics*, Volume IV, XV + 157 S. Providence, Rhode Island, 1965, American Mathematical Society.
[3] I. Ojima, "Nakanishi-Lautrup B field, crossed product and duality," in R*esearch on Quantum Field Theory*, RIMS Workshop, Kyoto, 2006, pp.29-37.
[4] H. Sakuma, I. Ojima, and M. Ohtsu, "Gauge symmetry breaking and emergence of Clebsch-dual electromagnetic field as a model of dressed photons," *Appl. Phys. A* (2017) 123:750.
[5] H. Sakuma, I. Ojima and M. Ohtsu, "Dressed photons in a new paradigm of off-shell quantum

fields," *Progress in Quantum Electronics*, **55** (2017) pp.74-87.

[6] L. Cicchitelli, H. Hora, and R. Postle, "Longitudinal field components for laser beams in vacuum," *Phys. Rev. A*, **41** (1990) pp.3727-3732.

[7] M. Ohtsu, "Embarking on theoretical studies for off-shell science guided by dressed photons," *Off-shell Archive* (November, 2018) Offshell: 1811R.001.v1. **DOI:** 10.14939/1811R. 001.v1. http://offshell.rodrep.org/?p=176

Progress in off-shell science in analyzing light–matter interactions for creating dressed photons

M. Ohtsu

Research Origin for Dressed Photon,
3-13-19 Moriya-cho, Kanagawa-ku, Yokohama, Kanagawa 221-0022 Japan

Abstract

This article reviews the recent progress in theoretical studies on mechanisms of creating dressed photons (DPs) by focusing on the light–matter interactions in a nanometer-sized space. First, the intrinsic nature of the DP is reviewed, and fifteen experimentally observed phenomena are described. Second, it is pointed out that the conventional on-shell scientific method has intrinsic problems in describing these interactions. Finally, the off-shell scientific method, which can overcome these problems, is reviewed, and it is demonstrated that this method, relying on the Clebsch dual (CD) field, has succeeded in identifying the mechanism of creation of the DP, specifically: the spacelike CD field (Majorana fermion (MF) field) interacts with the timelike components of the 4-momenta field, and the MF field subsequently creates a timelike particle and antiparticle forming a pair. This pair is annihilated promptly because of its non-propagating nature. However, a non-propagating electromagnetic field remains in the interacting system, which is the very field of the DP.

1. Introduction

A dressed photon (DP) is a quantum field created by light–matter interaction in a nanometer-sized space. More specifically, it is the quantum field of a composite system composed of photons, electrons, and phonons [1]. In other words, it is not a solitary free photon. DP energy transfer among nanometer-sized materials (NMs) originates also from this interaction. A variety of experimental results involving this interaction have been observed and reviewed in the *Off-shell Archive* series [2-11]. By referring to these articles, the present paper reviews the recent progress in theoretical studies on the mechanism of DP creation. Section 2 reviews the intrinsic nature of the DP and presents experimental evidence. Section 3 points out that the conventional quantum field theories have intrinsic problems in describing the above interaction. Section 4 introduces off-shell scientific methods and reviews the Clebsch dual field as a promising theoretical model for overcoming these problems.

2. Experimental demonstration of novel phenomena originating from dressed photons

The straight line and curves in Fig. 1 represent the dispersion relation between the momentum and energy of a free photon that propagates through a macroscopic-sized vacuum and a material, respectively. They have been derived by quantum field theory and represent what is called the mass shell. That is, a free photon is an on-shell quantum field, and the science of studying this field has been called on-shell science.

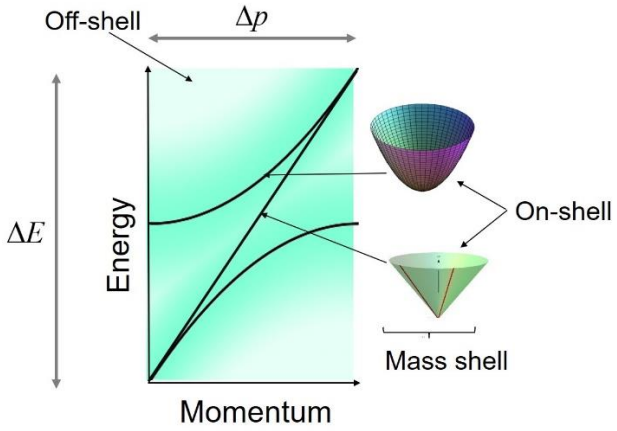

Fig. 1 On-shell (on the mass shell) and off-shell in the dispersion relation.

It should be noted that a DP is created by a light–matter interaction in a nanometer-sized space. In other words, it is created by the exchange of momenta and energies among photons incident on a nanometer-sized material (NM), electrons (or excitons) and phonons in the NM. The created DP localizes at the NM, and its spatial extent is equivalent to the size a of the NM. The DP has been called an optical near field due to this localized feature.

Since a is much smaller than the wavelength λ of the incident light, Heisenberg's uncertainty principle indicates that the uncertainty Δp of the DP momentum p is large ($\Delta p \gg p$). Furthermore, since the energy E depends on the momentum, the large uncertainty Δp indicates a large uncertainty of the energy ($\Delta E \gg E$). It is also indicated by Heisenberg's uncertainty principle that the DP is a virtual photon because the duration Δt ($= h / \Delta E$, where h is Planck's constant) of the DP is short.

In summary, the DP has the natures of both an optical near field and a virtual photon. It should be noted here that its dispersion relation deviates from the mass shell due to the large uncertainties Δp and ΔE. That is, the DP is an off-shell quantum field that exists in the green area in Fig. 1. The science of studying this field has been called off-shell science. The off-shell quantum field can never be represented by the superposition of the electromagnetic modes of the on-shell free photons.

This indicates that off-shell and on-shell sciences do not overlap, as indicated by Fig. 1. They play complementary roles in modern science.

Conventional optical science falls under the category of on-shell science and treats the response of a macroscopic vacuum or material to the propagating free photons. The particle natures of these photons have been studied by using the conventional quantum theory of light in which the light–matter interaction has been described by a perturbative method using a virtual photon model. However, this method is incapable of describing the DP, which is an off-shell quantum field of a nanometer-sized complex system.

Table 1 summarizes novel phenomena originating from DPs, observed in the author's experimental studies [12]. Even though novel theories on light–matter interactions are required to analyze these phenomena, on-shell science has never met this requirement [1)].

Table 1 Novel phenomena originating from dressed photons

No	Phenomena
1	An off-shell field is created and localized on a sub-wavelength material.
2	The DP energy transfers back and forth between two NMs.
3	The DP field is conspicuously disturbed and demolished by inserting NM2 for detection.
4	The efficiency of the DP energy transfer between two NMs is highest when the sizes of the NMs are equal.
5	An electric-dipole forbidden transition is allowed in off-shell science.
6	The DP energy transfers among NMs autonomously.
7	The DP energy transfer exhibits hierarchical features.
8	The photon energy $h\nu$ can be lower than the excitation energy of the electron $E_{ex} - E_g$, where E_{ex} and E_g are the energies of the excited and ground states of the electron, respectively.
9	The maximum size $a_{DP,Max}$ of the DP is 50–70 nm.
10	The DP is created and localized at a singularity such as a nanometer-sized particle or impurity atom in a material.
11	The spatial distribution of B atoms varies and reaches a stationary state autonomously due to DP-assisted annealing, resulting in strong light emission from the Si crystal.
12	The length and orientation of the B atom pair in a Si crystal are autonomously controlled by DP-assisted annealing.
13	A light emitting device fabricated by DP-assisted annealing exhibits photon breeding (PB) with respect to photon energy; i.e., the emitted photon energy $h\nu_{em}$ is equal to the photon energy $h\nu_{anneal}$ used for the annealing.
14	By DP-assisted annealing, a Si crystal works as a high-power light emitting device even though it is an indirect transition-type semiconductor.
15	A semiconductor SiC crystal was made to behave as a ferromagnet as a result of DP-assisted annealing and exhibited a gigantic magneto-optical effect in the visible region.

3. Reasons why the on-shell scientific method does not meet the requirement

Haag's theorem describes the reasons why the requirements mentioned at the end of Section 2 have not been met by on-shell science [13]. The claims resulting from this theorem are summarized as follows:

(1) The off-shell and on-shell quantum fields cannot be mutually transformed by a unitary transformation. This means that there is a theoretical gap between nanometer-sized and macroscopic quantum fields, and thus, they are incompatible with each other.

(2) The quantum field created by the interaction among multiple elementary particles in a nanometer-sized complex system is a non-particle field[2)] that is unrelated to the fields of its constituent particles. This means that this quantum field cannot be represented by the superposition of the modes of free quantum fields.

(3) It is not possible to describe the temporal and spatial behaviors of the quantum field by linear equations. This impossibility is equivalent to the limit of applicability of the conventional quantum theories for describing the interaction[3)].

However, conventional quantum field theories can be easily used for describing quite a large number of optical phenomena by neglecting Haag's theorem and its claims (1)–(3) above. An example of such easy use is found in representing the quantum field by superposing the modes of the on-shell quantum field [14]. Here, it should be noted that this expansion is allowed only when the bases (modes of the on-shell quantum field) form a complete set. However, the intrinsic problem is that the timelike and lightlike components, popularly used in on-shell science, are not sufficient to form this set. The Greenberg–Robinson's theorem [15] claims that the spacelike components in the 4-momenta field are indispensable for this formation[4)] (Fig. 2).

It has been experimentally found that a DP is created and localized at the position where a field varies discontinuously, for example, at the apex of a fiber probe or at a boron (B) atom. High-wavenumber modes must be involved in the mode-superposition when a step-function is used to represent this discontinuous electromagnetic field. However, the use of modes of the timelike and lightlike components in the 4-momenta field is insufficient because the energies of the high-wavenumber modes are much higher than that of the photon of the visible light that serves as a source for creating the DP. The high-wavenumber modes of the spacelike components are required because their energy is sufficiently low to be safely used. This is the reason, found in experimental studies, why the spacelike components of the 4-momenta field are required to represent the creation and localization of the DP.

The next section reviews the creation and localization of the DP by referring to the spacelike components of the 4-momenta field, for which the Clebsch dual (CD) field is used.

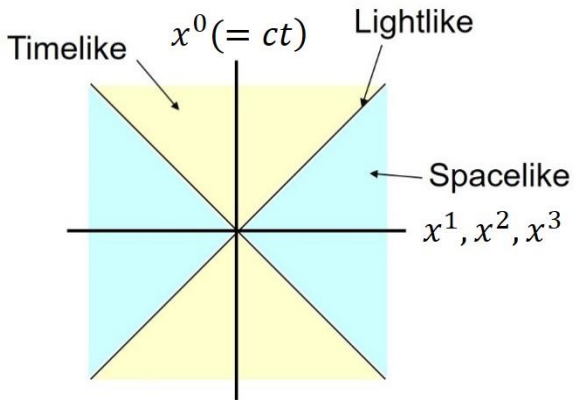

Fig. 2 Minkowski spacetime.

4. Description of dressed photons by the off-shell scientific method

Off-shell scientific studies on the mechanism of DP creation have recently made progress by carefully examining the interaction between electromagnetic fields and matter fields. Details have been published in [16]. They are summarized as follows:

Step 1: Spacelike components in the 4-momenta field play indispensable and essential roles in the quantum field interaction.

Step 2: The quantum field of the spacelike components is expressed by the CD field.

Step 3: The CD field corresponds to a vector boson that is composed of a set of Majorana fermion fields.

Supplementary explanations of **Steps 1–3** are given in the following:

Step 1: This step corresponds to the claim given by the Greenberg-Robinson theorem [15] mentioned in Section 3. This theorem relies on the axiomatic quantum field theory and indicates the indispensable and essential roles of the spacelike components.

Step 2: Detailed analyses of Maxwell's equations based on relativistic theory have found that the spacelike electromagnetic field is expressed by the CD field. Here, the CD field is given by the external product of two gradient vectors (C_i, L_i) that are mutually orthogonal (Fig. 3). When the vector potential is lightlike (that is, a null vector), C_i corresponds to the lightlike longitudinal electric field. This fact indicates that the longitudinal electric field is involved in the interaction of **Step 1** above[5)]. On the other hand, L_i is a spacelike vector and is normal to the vector C_i, by which L_i is regarded as representing the magnetic field. This fact indicates that the CD field is a

spacelike electromagnetic field[6]. By surveying the energy-momentum tensor of the CD field, it has been found that the wave representation and particle representation of the CD field are equivalent to each other. The particle representation is given by $\rho C_i C_k$, which is isomorphic to the energy-momentum tensor of the free fluid. The quantity ρ corresponds to the fluid density, which is given by $L^m L_m$. It should be pointed out that this quantity ρ takes a negative value, and therefore, it has been considered as a non-physical quantity. This non-physical nature indicates the reason why the longitudinal electric field has been excluded over a period of many years from the on-shell scientific studies on quantizing the electromagnetic field under the Lorentz-covariance condition[7]. However, thanks to the recent progress made in off-shell scientific studies, it was found that such a non-physical mode is required for describing the interaction, and in addition, that the spacelike components of the 4-momenta field are required (**Step 1**).

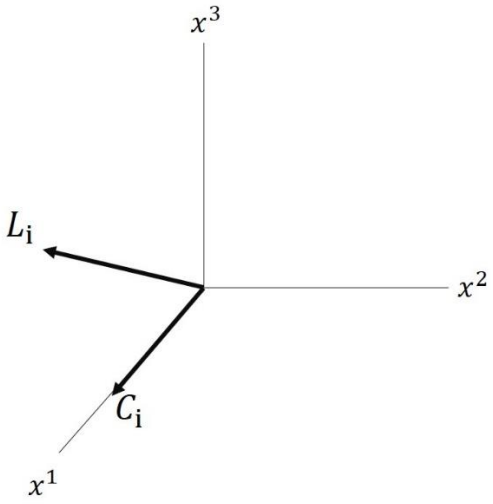

Fig. 3 Four-dimensional vectors C_i and L_i displayed in (x^1, x^2, x^3)-space.

The 0-th axis x^0 is not shown. The field propagates along the x^1-axis.

Step 3: The spacelike components above can be represented by the spacelike Klein-Gordon's (KG) equation, which is derived by replacing the effective mass term m in the timelike KG equation by $i\kappa_0$. By noting that Dirac's equation corresponds to the square root of the KG equation, the equation for the Majorana fermion (MF) is derived by replacing m in the timelike Dirac's equation by $i\kappa_0$. The MF represents an electrically neutral quantum field whose particle and antiparticle components are represented by identical equations. From the relations among the timelike KG equation, the

spacelike KG equation, and Dirac's equation above, it was found that the quantum mechanical expression of the spacelike CD field was equivalent to that of the MF field.

By referring to the discussions in **Steps 1–3**, the mechanism of DP creation was described from the viewpoint of the interaction, specifically: the spacelike CD field (MF field) interacts with the timelike components of the 4-momenta field [8)], and the MF field subsequently creates a timelike particle and antiparticle forming a pair. This pair is annihilated promptly because of its non-propagating nature[9)]. However, a non-propagating electromagnetic field remains in the interacting system, which is the very field of the DP[10)].

5. Summary

This article has reviewed the recent progress made in theoretical studies on mechanisms of DP creation by focusing on the light–matter interaction in a nanometer-sized space. First, the intrinsic nature of the DP was reviewed, and fifteen experimentally observed novel phenomena were described. Second, it was pointed out that the conventional on-shell scientific method has intrinsic problems in describing the above interaction. Finally, the off-shell scientific method, which can overcome these problems, was reviewed, and it was demonstrated that the Clebsch dual (CD) field can be appropriately used for the description. The mechanisms of DP creation, identified by theoretical analysis using the CD field, are: the spacelike CD field (Majorana fermion (MF) field) interacts with the timelike components of the 4-momenta field, and the MF field subsequently creates a timelike particle and antiparticle forming a pair. This pair is annihilated promptly because of its non-propagating nature. However, a non-propagating electromagnetic field remains, and this is the very field of the DP.

Footnotes

(1) Since conventional optical theory is a branch of on-shell scientific theories, it does not explain the nature of the DP. For example, this theory claims that the zero-mass photon with a non-zero spin cannot be spatially localized in the sense that its position operator cannot be defined.

(2) Such a field has been called the Heisenberg field.

(3) For example, let us consider the case of exciting a free quantum field by injecting energy to the system under study. The excited field interacts with the existing field, and this interaction is described by Newton's equation of motion in the classical theory. Although this equation is linear as long as the magnitude of the injected energy is low, it becomes nonlinear when the energy is increased. Here, the problem is that such nonlinear equations have never been derived in quantum theory.

(4) In the conventional theories of elementary particles, the spacelike component of the 4-momenta field has been excluded from the theoretical model because of its superluminality and thus, non-physical nature.

(5) As an example, a longitudinal electric field is involved in the well-known Coulomb interaction.

(6) This indication is based on the fact that the vector potential satisfies the spacelike Proca's equation even though it is a null vector.

(7) By noting that the quantum field with an infinite degree of freedom is composed of multiple sectors [17], it can be realized that the non-physical longitudinal electric field exists in such a sector that is disjoint with the sector to which the conventionally approved transverse electromagnetic field belongs.

(8) By irradiating an NM with light, CD fields are excited simultaneously with the timelike components of the 4-momenta field. These CD fields are the basic modes for creating the fields of the spacelike components. Since the CD fields correspond to the MF fields (**Step 3**), these MF fields interact with the timelike components at the NM.

(9) Its spatial extent is expressed as the Yukawa-type function $\exp(-r/a)/r$, where a is the size of the NM, as was given in Section 2.

(10) In the case where the spins of the particle and antiparticle are parallel to each other, a zero-spin electric DP is created. In the case where they are anti-parallel, on the other hand, a magnetic DP whose spin is unity is created.

Acknowledgements

The author thanks D. H. Sakuma (Research Origin for Dressed Photon) for his valuable comments and discussions.

References

[1] M. Ohtsu, Dressed Photons (Springer, Heidelberg, 2014), pp.1-315.

[2] M. Ohtsu,"New Routes to Studying the Dressed Photon," *Off-shell Archive* (September, 2017) OffShell: 1709R.001.v1, http://offshell.rodrep.org/?p=42,**[DOI]** 10.14939/1709R.001.v1

[3] M. Ohtsu, T. Kawazoe, and H. Saigo, "Spatial and Temporal Evolution of Dressed Photon Energy Transfer," *Off-shell Archive* (October, 2017) Offshell: 1710R.001.v1, http://offshell.rodrep.org/?p=79,**[DOI]** 10.14939/1710R.001.v1

[4] M. Ohtsu and H. Sakuma, "Creation and Measurement of Dressed Photons: A Link to Novel Theories," *Off-shell Archive* (December, 2017) Offshell: 1712R.001.v1, http://offshell.rodrep.org/?p=89,**[DOI]** 10.14939/1712R.001.v1

[5] M. Ohtsu and T. Kawazoe, "Experimental estimation of the maximum size of a dressed photon," *Off-shell Archive* (February, 2018) Offshell: 1802R.001.v1, http://offshell.rodrep.org/?p=98,**[DOI]** 10.14939/1802R.001.v1

[6] M. Ohtsu,"Embarking on theoretical studies for off-shell science guided by dressed photons," *Off-shell Archive* (November, 2018) Offshell: 1811R.001.v1, http://offshell.rodrep.org/?p=176,**[DOI]** 10.14939/1811R.001.v1

[7] M. Ohtsu, "Novel functions and prominent performance of nanometric optical devices made possible by dressed photons," *Off-shell Archive* (April, 2019) Offshell: 1904R.001.v1, http://offshell.rodrep.org/?p=190,**[DOI]** 10.14939/1904R.001.v1

[8]┫ M. Ohtsu, "Indications from dressed photons to macroscopic systems based on hierarchy and autonomy," *Off-shell Archive* (June, 2019) Offshell: 1906R.001.v1, http://offshell.rodrep.org/?p=201,**[DOI]** 10.14939/1906R.001.v1

[9] M. Ohtsu,"Dressed photon phenomena that demand off-shell scientific theories," *Off-shell Archive* (November 2019) OffShell: 1911.R.001.v1,
http://offshell.rodrep.org/?p=232,**[DOI]** 10.14939/1911.R.001.v1
[10] M. Ohtsu,"History, current developments, and future directions of near-field optical science," *Off-shell Archive* (December 2019) OffShell: 1912R.001.v1, http://offshell.rodrep.org/?p=241,**[DOI]** 10.14939/1912R.001.v1
[11] M. Ohtsu, "The present and future of numerical simulation techniques for off-shell science," *Off-shell Archive* (March, 2020) OffShell: 2003R.001.v1.
http://offshell.rodrep.org/?p=259,**[DOI]** 10.14939/2003R.001.v1,
[12] M. Ohtsu,"History, current development, and future directions of near-field optical science," Opto-Electronic Advances, Vol.3, No.3 (2020)190046.
[13] R.F.Streater and A.S. Wightman, *PCT, Spin and Statistics, and All That* (Princeton Univ. Press, Princeton and Oxford, 1964) pp.163-165.
[14] M. Ohtsu, *Dressed Photons* (Springer, Heidelberg) pp.11-18.
[15] R. Jost, *The General Theory of Quantized Fields* (Lectures in Applied Mathematics, Volume IV) XV + 157 S. (American Mathematical Society, Providence, 1965).
[16] M. Ohtsu, I. Ojima, and H. Sakuma, "Dressed Photon as an Off-Shell Quantum Field," *Progress in Optics* Vol.64, (ed. T.D. Visser) (Elsevier, 2019) pp.45-97.
[17] I. Ojima,"A Unified Scheme for Generalized Sectors Based on Selection Criteria: Order Parameters of Symmetries and of Thermality and Physical Meanings of Adjunctions," *Open Systems & Information Dynamics*, Vol.10, No.3, (2003) pp. 235-279.

The present and future of numerical simulation techniques for off-shell science

M. Ohtsu

Research Origin for Dressed Photon,

3-13-19 Moriya-cho, Kanagawa-ku, Yokohama, Kanagawa 221-0022 Japan

Abstract

The first part of this article presents experimental results on novel devices that were fabricated and operated by utilizing dressed photons. The fabricated devices were photovoltaic devices having an Ag-electrode with a unique surface morphology, light-emitting diodes using silicon crystals, and nano-droplets in which pairs of nanometer-sized semiconductor particles were confined. The second part reviews the results of the numerical simulations for these devices using a random walk model. This model relies on statistical mechanics and complex-systems science. The third part describes the problems with these simulations and presents some suggestions for solving them. Finally, the need for a three-dimensional off-shell scientific model that takes account of interactions in a nanometric space is pointed out.

1. Introduction

The dressed photon (DP) is a quantum field that is created as a result of interactions among photons, electrons (excitons), and phonons in a nanometric space. The DP has been intensively studied as a representative topic of off-shell science [1-3]. Novel theories of the DP have been developed and used as a guide to support experimental studies, including a variety of advanced technologies [1].

A principal difficulty of developing these theories is that the size of the DP is much smaller than the wavelength of light. This means that the electromagnetic modes of the DP cannot be defined by the theories of conventional optical science (on-shell science). In order to overcome this difficulty, the DP has been expressed as a superposition of an infinite number of electromagnetic modes in the on-shell region, which allowed derivation of creation and annihilation operators for the DP. The operators representing the coupled state of a DP and phonons were also derived. Furthermore, theoretical analysis of a microscopic system surrounded by a macroscopic system yielded a Yukawa-type function for representing the spatially localized nature of the DP energy.

After this, the remaining theoretical problem to be solved was how to describe the autonomy observed in DP energy transfer and its measurement process [1,4]. For this description,

numerical simulations have been carried out by using a random walk model relying on statistical mechanics and complex-systems science.

Section 2 of this article reviews experimental results that have been reproduced by numerical simulations. Section 3 reviews the results of these simulations and presents the problems associated with them. Section 4 presents possible directions for solving these problems, which could promote advances in off-shell science. Section 5 presents a summary of this article.

2. Experimental results for novel devices fabricated and operated based on dressed photons

This section reviews experimental results for three novel devices that have been fabricated and operated by using DPs.

2.1 Photovoltaic devices having a silver electrode with a unique surface morphology

Photovoltaic devices convert optical energy to electrical energy and have been used as solar cell batteries. Here, a device using organic molecules of poly(3-hexylthiophene) (P3HT) are reviewed as an example. Autonomously created DPs were utilized for fabrication and operation of this device in order to realize a high conversion efficiency. The details of the fabrication and operation have been described in [5]. They can be summarized as follows:

Fabrication

A P3HT film was used as a p-type semiconductor having a bandgap energy, E_g, of 2.18 eV, and therefore, the cutoff-wavelength, λ_c, for optical to electrical energy conversion was 570 nm. A ZnO film was used as an n-type semiconductor (E_g=3.37 eV, λ_c=367 nm). A transparent ITO film and an Ag film were used as two electrodes. The principal features of this photovoltaic device originated from the P3HT because a depletion layer of the pn-junction was formed inside the P3HT. Films of ITO, ZnO, P3HT, and Ag were deposited successively on a sapphire substrate to thicknesses of 200 nm, 100 nm, 50 nm, and several nm, respectively, in order to make a preliminary device (Fig. 1).

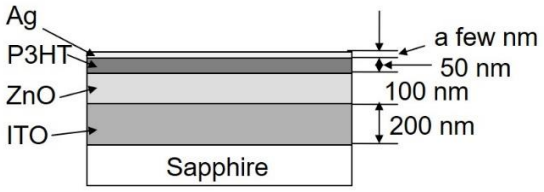

Fig. 1 Preliminary photovoltaic device using an Ag film as an electrode.

On the Ag film of the preliminary device, Ag particles were deposited by the method shown in Fig. 2: While Ag particles were being deposited by RF-sputtering, the surface of the Ag film was irradiated with light to create DPs, and a reverse bias voltage, V_b, was applied to the pn-junction. Here, the wavelength λ_0 of the irradiation light was longer than λ_c. As an example, λ_0 was set to 660 nm, and V_b was -1.5 V.

The fabrication principle was such that the autonomously created DPs and the reverse bias voltage controlled the amount of Ag particles that flew into and out of the Ag film surface. The fabrication process was as follows:

(1) Creation of electron–hole pairs by the DPs (Fig. 3(a)): The DPs were created at bumps on the Ag film surface by the irradiation light. If the field of the DPs extended to the pn-junction, electrons were excited to create electron–hole pairs even though the photon energy of the irradiation light was lower than E_g. This unique excitation was possible due to the contribution of the energy of the phonon that was a constituent element of the DP.

(2) Charging the Ag film (Fig. 3(b)): The created electron–hole pairs were annihilated by the electric field generated by the reverse bias voltage, and the positive holes were attracted to the Ag film electrode. As a result, the Ag film was positively charged.

(3) Autonomous control of Ag particle deposition (Fig. 3(c)): The Ag particles striking the Ag film surface were positively charged because they passed through an Ar plasma for RF-sputtering. Therefore, these Ag particles were repulsed from the area of the Ag film surface that was locally positively charged as a result of efficient creation of DPs in steps **(1)** and **(2)**. As a result, the repulsed Ag particles were deposited on other areas of the Ag film surface.

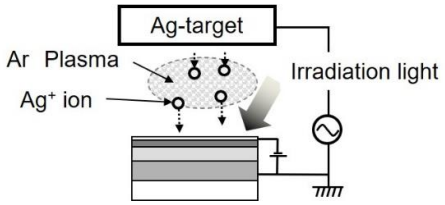

Fig. 2 Deposition of Ag particles by RF-sputtering under light irradiation.

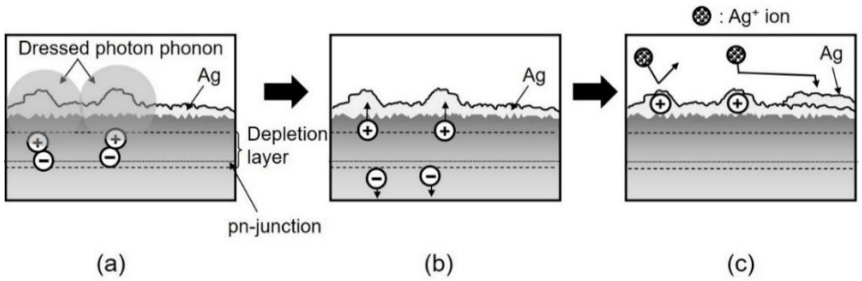

Fig. 3 Principle of controlling the amount of Ag particles that flew into and out of the Ag film surface.
(a), (b), (c) represent the creation of electron-hole pairs by the DP, charging of the Ag film, and autonomous control of the Ag particle deposition, respectively.

By steps **(1)**–**(3)**, a unique surface morphology was formed on the Ag film, which was governed by the spatial distribution of the DPs. The fabrication process finished autonomously once the spatial distribution of the created DPs reached a stationary state.

Table 1 summarizes the values of the irradiation light power, P, and the reverse bias voltage, V_b, for three devices A, B, and C. Figure 4 shows scanning electron microscope (SEM) images of the Ag film surfaces. The images show that the surfaces of devices B and C (Fig. 4(b) and (c)) were rougher than that of device A (Fig. 4(a)) due to the larger Ag grains grown on the surface. The lower parts in Figs. 4(b) and (c) show histograms of the distribution of grain diameters, derived by assuming spherical grain shapes. The solid curves are lognormal functions fitted to these histograms. In Fig. 4(b), the average and the standard deviation of the diameter were 90 nm and 64 nm, respectively, whereas they were respectively 86 nm and 32 nm in Fig. 4(c). By comparing these values, it was found that the standard deviation decreased with increasing light power, P, which meant that a surface morphology with unique-sized grains was autonomously formed due to the high irradiation power. A unique feature of the histograms in Figs. 4(b) and (c) was the bumps, identified by downward arrows, that deviated from the lognormal functions.

Table 1 The values of the irradiation light power, P, and the reverse bias voltage, V_b, for device fabrication.

Name of device	Irradiation light power, P	Reverse bias voltage, V_b
A(1)	0	0
B	50 mW	-1.5 V
C	70 mW	-1.5 V

(1) A is a reference device that was fabricated to compare its performance with that of devices B and C.

Operation

To operate the device fabricated above, it was irradiated with light from the rear surface of the sapphire substrate (Fig. 5). Since the spatial distributions of the DPs created on the Ag grains in Figs. 4(b) and (c) depended on the grain sizes (the average diameters of the grains were 90 nm and 86 nm, respectively), the DP fields of devices B and C extended to the pn-junctions because the sum of the thicknesses of the Ag film and the P3HT was less than 70 nm. As a result, electron–hole pairs were created by these DPs when the device was irradiated with light*. Even though the photon energy of the irradiation light was lower than E_g, optical to electrical energy up-conversion was expected thanks to the energy of the phonons, constituent elements of the DP. Furthermore, it was expected that the efficiency of creating the electron–hole pairs would be highest when the irradiation light wavelength was equal to the wavelength, λ_0, of the light irradiated during the

fabrication process. This phenomenon is called the photon breeding (PB) effect [6], and will be reviewed also in Section 2.2.

(*) In the case of device A, on the other hand, the field of the DPs did not reach the pn-junction because the Ag film was too thick (800 nm) to allow electron–hole pairs to be created.

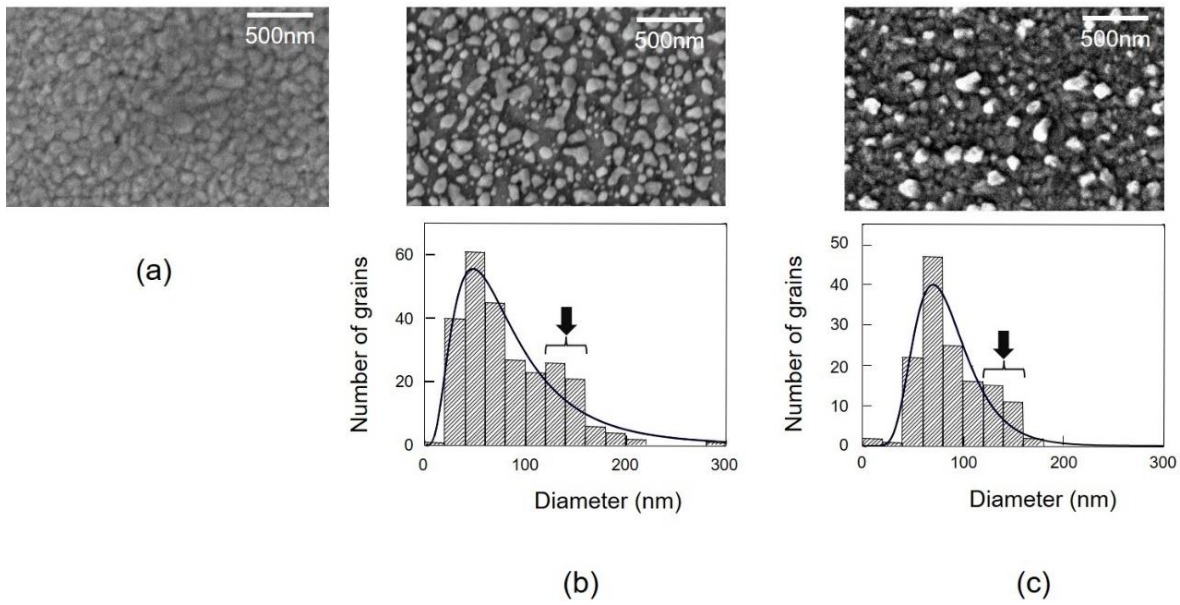

Fig. 4 Scanning electron microscopic images of Ag film surfaces.
(a), (b), and (c) show images of devices A, B, and C, respectively. Lower parts of (b) and (c) show histograms of the distribution of the Ag grain diameters. The downward arrows represent the bumps on the histograms.

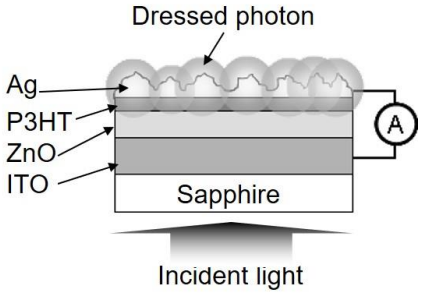

Fig. 5 Operation of the fabricated photovoltaic device.

Figure 6 shows the measured dependence of the generated photocurrent density on the irradiation light wavelength. The wavelength range of the measurement was 580–670 nm, which was longer than the wavelength λ_c (=570 nm) of the P3HT. Curve A in this figure shows a very

low photocurrent density generated from device A. Curves B and C are for devices B and C, respectively. They show that photocurrents were generated even with irradiation light wavelengths longer than λ_c.

Curve C has a peak at 620 nm*, clearly confirming the PB effect. Wavelength selectivity was not so clearly seen in curve B (device B) compared with curve C, because of the lower light power (50 mW) irradiated during the fabrication process for device B. The clear wavelength selectivity of curve C was due to the efficient creation of DPs by the higher irradiation power (70 mW).

(*) The peak wavelength (620 nm) of curve C was 40 nm shorter than the wavelength, λ_0 (=660 nm), of the irradiation light used in the fabrication process. This difference in wavelength originated from the DC Stark effect induced by the reverse bias voltage, V_b, applied during the fabrication process.

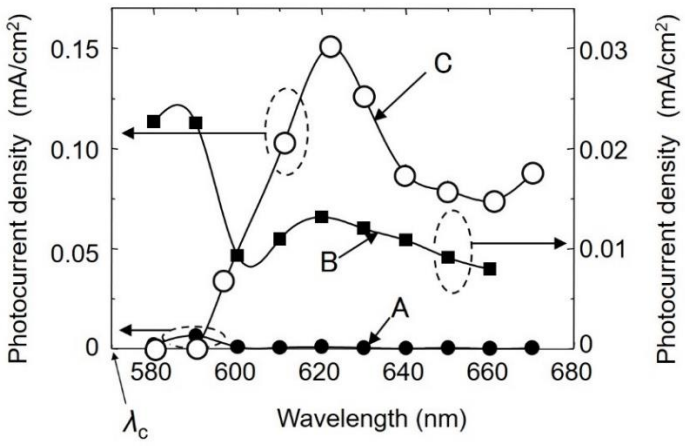

Fig.6 Relation between the incident light wavelength and the photocurrent density.
Curves A, B, and C represent the measured results for devices A, B, and C, respectively.

2.2 Light-emitting diodes using silicon crystals

This section reviews novel light-emitting diodes (LEDs) made of silicon (Si) crystal. Even though Si is an indirect-transition-type semiconductor, it emitted light due to the momentum exchange between a multi-mode coherent phonon in the DP and an electron in the conduction band of the Si. The details of the fabrication and operation of these LEDs have been described in [6-8]. They can be summarized as follows:

Fabrication

To fabricate an LED, as the first step, the surface of an n-type Si crystal was doped with boron (B) atoms to transform it to a p-type layer, thereby forming a pn-homojunction. As the second step, the crystal was annealed using a novel method named DP-assisted annealing [1,6]. This annealing process was:

(1) By means of current injection, the Si crystal was heated by Joule energy to diffuse the B atoms. During this heating, the Si crystal surface was irradiated with light (photon energy: $h\nu_{\text{anneal}}$) to create DPs at the B atoms.

(2) The electrons injected into the conduction band exchanged momenta with the phonons in the created DPs, thus recombining with positive holes and emitting light. This emission process was stimulated emission because it was triggered by the irradiation light.

(3) The emitted light propagated outside the Si crystal, which meant that a part of the Joule energy for heating was dissipated out in the form of optical energy. This dissipation locally cooled the region of the crystal at which the DP was created. As a result, the diffusion rate of the B atoms decreased locally.

(4) By means of a balance between heating by the Joule energy and cooling by the optical energy dissipation, the spatial distribution of B atoms varied autonomously and reached a stationary state.

Such a stationary distribution of B atoms could be the optimum for spontaneous emission because its probability was proportional to the probability of the stimulated emission in step **(2)** above.

Operation

The fabricated device emitted photons in response to current injection. The emitted photon energy $h\nu_{\text{em}}$ depended on $h\nu_{\text{anneal}}$ of the light irradiated during the DP-assisted annealing. From high-resolution analysis of the B atom distribution, it was found that two B atoms formed a pair whose length was n-times the lattice constant of the Si crystal. It was also found that the emitted photon energy $h\nu_{\text{em}}$ was equal to $E_{\text{g}} - nE_{\text{phonon}}$, where E_{g} and E_{phonon} are the bandgap energy of Si and the phonon energy, respectively. This formula indicates that the integer n, representing the length of the B atom pair as shown above, corresponds to the number of phonons that contributed to the momentum exchange with electrons for the photon emission. The emitted photon energy, $h\nu_{\text{em}}$, coincided with $h\nu_{\text{anneal}}$, an effect that is called the photon breeding (PB) effect.

2.3 Nano-droplets

Nano-droplets (NDs) are novel optical energy down-conversion devices that have been used to increase the conversion efficiency of solar cell batteries. The details of their fabrication and operation have been described in [9-13]. They can be summarized as follows:

Fabrication

Two kinds of nanometer-sized particles (NP1 and NP2) were dispersed into a liquid ultraviolet (UV)-setting resin. For example, a CdSe nano-crystal was used as NP1, while a ZnO or a CdS nano-crystal was used as NP2. Subsequently, the liquid was irradiated with visible light (photon energy: 2.33 eV) to create DPs selectively on the surface of NP1s. The energy of the created DP transferred to the neighboring equal-sized NP2s due to the size-dependent resonance of the DP momentum [9,14]. These NP2s created DPs whose energies were as high as the UV photon energy thanks to the contribution from the phonon energy in the DP. Finally, these DPs cured the liquid UV-setting resin around NP1 and NP2, resulting in the formation of an ND in which NP1 and NP2 were confined.

Operation

For operation, the fabricated ND was irradiated with UV light whose photon energy was tuned to the electron energy in NP2 in the ND (3.06 eV). Then, a DP was created on NP2, and its energy was transferred from NP2 to NP1, enabling visible light emission (2.08 eV) from NP1. This emission process corresponds to optical energy down-conversion.

3. Results of numerical simulations and associated problems

This section reviews numerical simulations that have been carried out for the three devices described in Section 2.

3.1 Photovoltaic devices having a silver electrode with a unique surface morphology

During the DP-assisted material formation process of a granular Ag film with a unique surface morphology, the photovoltaic device was open to the environment and thus involved energy flow and was subjected to environmental fluctuations. A two-dimensional nonequilibrium statistical mechanics model was used to describe the nonequilibrium dynamics [15]. In this model, it was assumed that two stochastic variables (i.e., the number of deposited Ag grains and the amount of electrical charge) dynamically coupled at each site of a two-dimensional square lattice and evolved with time.

The temporally varying magnitude of the repulsive Coulomb potential at each site caused by the charges was calculated in order to simulate the drift and deposition processes of Ag particles. The contribution of the DP was included by introducing irradiation light power b per site on the lattice. By regarding b as an external control parameter, it was shown that as b increased, a transition of the surface morphology occurred at a critical value b_c. That is, when $b \le b_c$, the DPs were not created effectively, and random Ag deposition was maintained as long as the simulation was continued (**State I**). When $b > b_c$, on the other hand, the DPs were created effectively, and Ag deposited autonomously, resulting in the formation of a unique surface morphology of the Ag film (**State II**). It was found that the transition from **State I** to **State II** was similar to the equilibrium second-order phase transitions.

As a result of this simulation, a configuration of Ag clusters on the surface was reproduced in the stationary state. Figure 7 shows the cluster size distribution in **State II**. As indicated by a downward arrow, a bump was found at size 11, which was consistent with the experimentally observed bumps identified by the downward arrows in Figs. 4(b) and (c). However, several problems were found with the simulation:

(p1-1) The maximum size of the DP was neglected even though it has been experimentally found [16].

(p1-2) The size-dependent resonance effect of the DP energy transfer was not correctly considered.

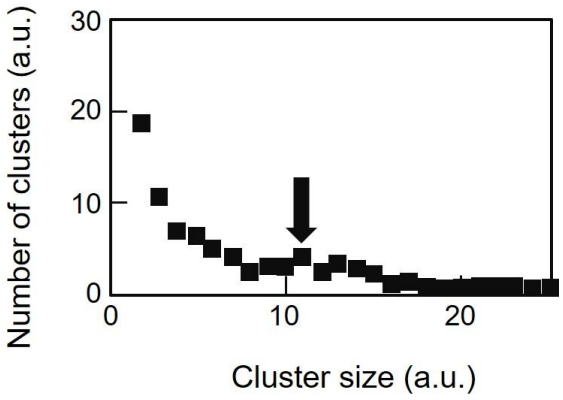

Fig.7 Relation between the size and the number of clusters in the steady state in state II.
The downward arrow represents a bump on this relation.

3.2 Light-emitting diodes using silicon crystals

The origin of the PB effect in the Si-LED was that the spatial distribution of B atoms played the role of genes. That is, this distribution bore the generic information and autonomously varied depending on the photon energy and polarization of the light irradiated during the DP-assisted annealing,

eventually reaching a stationary state. The stable spatial distribution of B atoms was reproduced, and the characteristics of the emitted light were simulated by a numerical simulation using a nonequilibrium statistical mechanical model [17].

For this simulation, a two-dimensional square lattice was assumed to represent the pn-junction in which the B atoms existed, and the thermally diffusing behavior of the B atoms was represented by a random walk of the B atoms on the lattice. By using an injected current, I, and an irradiation light power, P^0, as external control parameters, a simulation model composed of seven steps was formulated:

(Step 1) A random walk of B atoms forming B atom pairs with length d (=3a) on the square lattice was introduced, where a is the lattice constant of the Si crystal.

(Step 2) A random variable X was generated in order to represent the number of electrons for generating the Joule energy. Its distribution followed a Poisson process whose average was proportional to I.

(Step 3) Another random variable Y was generated that also followed a Poisson process. Its average was proportional to P, where P ($= P^0 + P^{PB}$) was the sum of the power, P^0, of the light irradiated during the DP-assisted annealing and the power, P^{PB}, of the emitted light. By adding the spontaneously emitted light power to Y, the total number of virtual photons Y^* ($= Y + 1$) that contributed to producing the PB effect was derived.

(Step 4) By means of the balance between the numbers of electrons and photons, being injected and irradiated during the DP-assisted annealing, respectively [7, 18], a value $Z = \min(X,Y^*)$ was derived to represent the number of photons created by the B atom pair.

(Step 5) By executing **Steps 1-4** for all the B atom pairs, the values Z were summed to represent the value P^{PB}.

(Step 6) In the case where $Z \geq 1$, the random walker was regarded as being inactivated. This was because the created photon with power P^{PB} propagated out from the Si crystal, and as a result, the thermal energy was lost. At that moment, the simulation was terminated.

(Step 7) In the case where $Z < 1$, the random walker was still active and hopped to the adjacent site, and the simulation was repeated by returning to **Step 1**.

The results obtained by the numerical simulation were as follows:

Fabrication

The regions A and B in Figure 8 show the temporal variation of the simulated power, P^{PB}, of the light emitted during the DP-assisted annealing [19]. In region A, the power increased immediately after the DP-assisted annealing started. Then it showed relaxation oscillation, such that the amplitude of the oscillation decreased with time. Subsequently, in region B, the power reached the stationary state after a certain time and showed a relatively small fluctuation.

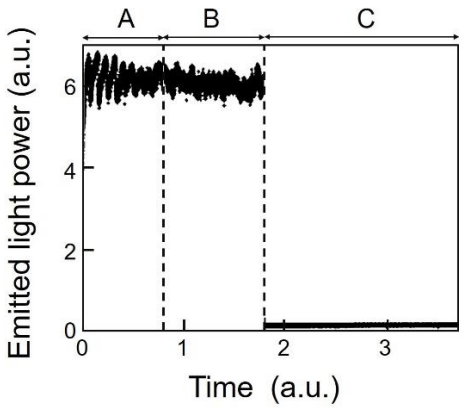

Fig. 8 Output power of photon emitted from the device.

The regions A and B represent the state of transition and a stationary state during the device fabrication. The region C is the output power emitted during the device operation. The values used for the simulations were I =40 and P^0 =80 in regions A and B. They were I =4 and P^0 =0 in region C.

Operation

Region C in Fig. 8 shows the power P^{PB} emitted during the device operation. Its value was smaller than those in regions A and B because of the smaller injection current than those injected for the DP-assisted annealing. However, it was stable over time. This was because the spatial distribution of the B atom pairs in the Si crystal was fixed, and random walks of the B atoms were suppressed.

The PB effect with respect to polarization has been also experimentally observed. In this effect, the polarization of the emitted light was equivalent to that of the light irradiated during the DP-assisted annealing [20]. Numerical simulations reproduced this effect by counting the number of created photon pairs that were orthogonally polarized. Here, it was assumed that the B atom pairs followed two independent Poisson distributions depending on the orientation of the B atom pairs on the square lattice.

Although the results of the numerical simulations above were consistent with most of the experimental results, several problems were found, including:

(p2-1) The simulation employed a two-dimensional model.

(p2-2) It was not straightforward to describe the details of the PB effect when using the conventional nonequilibrium statistical mechanical model, which relied on the temperature-dependent thermal diffusion. Novel models that incorporate theories of stochastic processes and quantum probability are required.

3.3 Nano-droplets

The experimental results in Section 2.3 have been analyzed by the following numerical simulations:

Fabrication

The numerical simulation confirmed that the rate of pairing NP1 and NP2 was **(1)** highest when their sizes were equal (Fig. 9(a)), and **(2)** higher when the liquid temperature was higher (Fig. 9(b)) [12]. Finding **(1)** originated from the size-dependent resonance of the DP momentum. Finding **(2)** was because the rate at which NP1 and NP2 encountered each other depended on the random walk velocity of the Brownian motion of the NPs in the liquid UV-setting resin. These two findings were consistent with the experimental results.

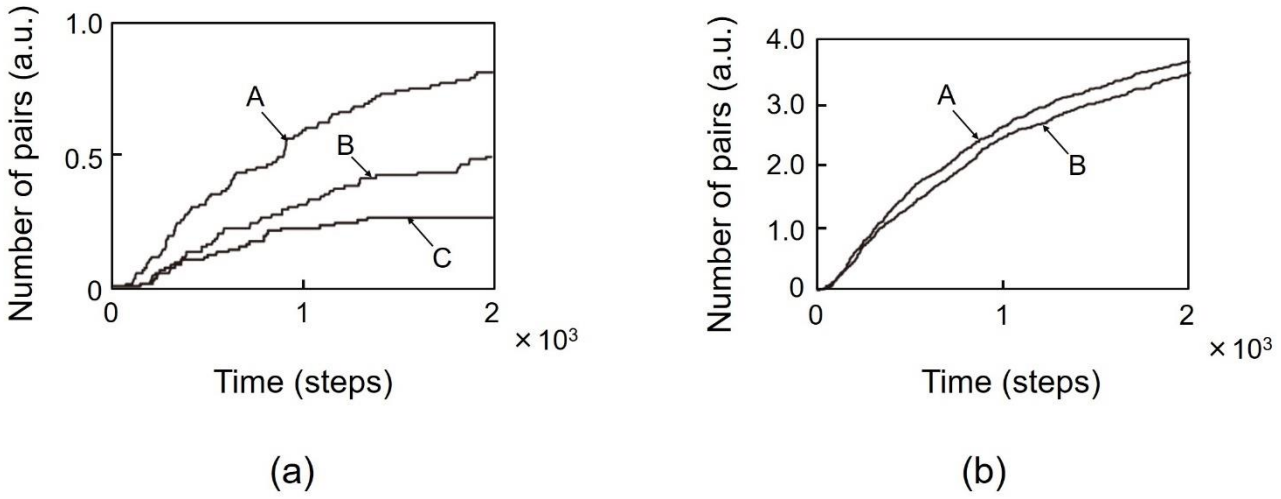

Fig.9 Temporal increases in the number of pairs (Fig. 7 in ref.[12]).

(a) Dependence on the ratio of the sizes a_{NP1} and a_{NP2} of the two NPs. The curves A, B, and C represent the results for a_{NP1} / a_{NP2} = 1, a_{NP1} / a_{NP2} < 1, and a_{NP1} / a_{NP2} > 1, respectively. (b) Dependence on the temperature of the liquid UV-setting resin. The curves A and B represent the results for high- and low-temperature liquids, respectively.

Operation

The validity of the present numerical simulation has been confirmed because the experimentally evaluated magnitude of the spectral peak shift of the light emitted from the CdSe (NP1) was consistent with the simulated temporal behavior of the NP-pair formation rate (Figs. 9(a) and (b)).

However, it should be pointed out that findings **(1)** and **(2)** above could be presumed by simply evaluating the experimental results. This means that the simulation was not essential for analyzing the experimental results. Furthermore, several problems were found with the simulation, including:

(p3-1) The simulation employed a one-dimensional model.

(p3-2) The simulation did not analyze the case of $N_2 / N_1 \neq 1$ (where $N_1 \gg 1$ and $N_2 \gg 1$) even though experiments have demonstrated that large numbers of NP1 ($N_1 \gg 1$) and NP2 ($N_2 \gg 1$) were confined in the fabricated NDs. Furthermore, their ratio N_2 / N_1 was not unity in the experiments.

(p3-3) The simulation did not introduce the deceleration of the Brownian motion of the NPs that originated from temporal hardening of the liquid UV-setting resin during the light irradiation.

(p3-4) The simulation did not introduce the recoiling of NP1 from NP2 that originated from the exchange of their momenta during the DP energy transfer.

4. Future directions

The essential feature, common to the fabrication process of the devices described in Sections 2.1 to 2.3 (devices 1–3, respectively), was that the spatial distributions of the DPs were autonomously optimized by means of the external control parameters in order to realize the largest contribution of the DPs to the device operation. As summarized in Table 2, these parameters increased the number of relevant NPs in device 1 during its fabrication, whereas they remained constant in devices 2 and 3. By referring to this table, problems in conventional numerical simulations and suggestions for solving them are presented in this section.

Table 2 Fabrication processes for the three devices.

	NPs used	Temporal variation of the number of the NPs	Motions of NPs	External control parameters
Device 1	Ag atoms	Increased	Depositing on the surfaces of Ag grains	Irradiated light and applied voltage
Device 2	B atoms	Maintained constant	Forming pairs	Irradiated light and injected current
Device 3	NP1 (made of CdSe), NP2 (made of ZnO or CdS)	Maintained constant	Pairing to form an ND	Irradiated light and resin temperature

4.1 Problems in conventional numerical simulations

The conventional numerical simulations relied on the theories of statistical mechanics and complex-system science, which are branches of traditional on-shell science. Although they succeeded in reproducing most of the experimental results, there were several problems that remain to be solved to explore future directions:

[1] In the conventional simulations, the numerical values were carefully selected in order to fit the results to the experimental results. However, the essential problem in these simulations was not a quantitative comparison with the experimental results, but identifying the origins of the DP creation and the autonomous energy transfer of the DP. That is, we need to answer the questions "What is the DP?" and "What are the intrinsic features of the DP?" The answers to these questions have not yet been given.

[2] The answer to the question "What is the nature of the interaction between nanometer-sized materials via the DP?" has not yet been given either. The absence of an answer originates in the intrinsic nature of on-shell science. One example was that even if infinite numbers of electromagnetic modes in the on-shell region were superposed, this superposition cannot represent the off-shell electromagnetic field that plays an essential role in the interaction. The off-shell field is unrelated to and completely different from the on-shell field. The problem is how to develop off-shell scientific theories that are indispensable for finding the answer to this question.

4.2 Suggestions for finding solution

Possible suggestions for finding the solutions described in the previous sections are:

{1} (To problem **[1]** in Section 4.1) A maximum size of the DP should be introduced to establish a three-dimensional model.

{2} (To problem **[2]** in Section 4.1) The concepts of "interaction" and "off-shell field" should be introduced.

{3} (For device 1; refer to **(p1-1)** and **(p1-2)** at the end of Section 3.1) It should be advantageous to introduce a function $\mathbf{1}(\alpha)$ in order to represent the maximum size of the DP, where

$$\mathbf{1}(\alpha)=\begin{cases}1 & ;\alpha \le \alpha_{\mathrm{DP\,max}} \\ 0 & ;\alpha > \alpha_{\mathrm{DP\,max}}\end{cases}$$

where $\alpha_{\mathrm{DP\,max}}$ is the maximum size of the DP. Experimental and theoretical values are 50–70 nm [16] and 38 nm [21], respectively. By using this function, the effective potential of the DP can be revised to $V_{\mathrm{eff,\,rev}}(r)=\mathbf{1}(\alpha)\cdot\exp(-r/\alpha)/r$.

{4} (For device 2; refer to **(p2-1)** and **(p2-2)** at the end of Section 3.2) A three-dimensional model should be established.

{5} (For device 3; refer to **(p3-1)** – **(p3-4)** at the end of Section 3.3) A theoretical expression for the size-dependent resonance should be introduced into the model.

Several discussions have been made recently by following suggestions **{1}**-**{5}** above, and

it has been suggested that it was advantageous to employ a quantum walk (QW) model in the numerical simulations for solving problems **[1]** and **[2]** in Section 4.1 [22]. This simulation is expected to give the answers for describing the off-shell scientific phenomena by developing a QW model with an infinite number of degrees of freedom. Based on this description, it is expected that it will be possible to find the origin of the interaction between the quantum fields by introducing a spacelike field into the QW model. The line-graph method [23] could be advantageously used for this. Furthermore, this method could succeed in introducing the phase of the Yukawa-type function (, the effective potential of the DP) to the simulation. This is expected to result in a description of the mechanical phenomena generated by the DP, such as the recoil effect[*][24,25], as discussed at the end of Section 3.3.

(*) It has been experimentally demonstrated that freely moving atoms in a vacuum were deflected or trapped by a DP.

5. Summary

The first part of this article presented experimental results on novel devices that were fabricated and operated by using dressed photons. These devices were photovoltaic devices having an Ag electrode with a unique surface morphology, light-emitting diodes using Si crystals, and nano-droplets in which pairs of nanometer-sized semiconductor particles were confined. The second part reviewed the results of numerical simulations for these devices by using a random walk model relying on statistical mechanics and complex-systems science. It also described the problems with these simulations and presented some suggestions for solving them. Finally, it was pointed out that a three-dimensional off-shell scientific model that takes account of the interaction in a nanometric space should be developed, and it was suggested that the line-graph method of the quantum walk model could be advantageously used.

Acknowledgements

The author thanks Prof. N. Tate (Kyushu Univ.) for his collaboration in the experimental and theoretical studies on nano-droplets.

References

[1] M. Ohtsu, *Dressed Photons* (Springer, 2014).

[2] M. Ohtsu, I. Ojima, and H. Sakuma, “Dressed Photon as an Off-Shell Quantum Field,” *Progress in Optics* Vol.64, (ed. T.D. Visser) pp.45-97 (Elsevier, 2019).

[3] M. Ohtsu, “Embarking on theoretical studies for off-shell science guided by dressed photons,” *Off-shell Archive* (November 2018) Offshell: 1811R.001.v1. **DOI** Offshell: 1811R.001.v1, http://offshell.rodrep.org/?p=176
[4] M. Ohtsu, “Indications from dressed photons to macroscopic systems based on hierarchy and autonomy,” *Off-shell Archive* (June, 2019) Offshell: 1906R.001.v1. **DOI** 10.14939/1906R.001.v1, http://offshell.rodrep.org/?p=201
[5] S. Yukutake, T. Kawazoe, T. Yatsui, W. Nomura, K. Kitamura, M. Ohtsu, “Selective photocurrent generation in the transparent wavelength range of a semiconductor photovoltaic device using a phonon-assisted optical near-field process,” *Appl. Phys.* B **99**, 415 (2010) pp. 415-422.
[6] M. Ohtsu, *Silicon Light-Emitting Diodes and Lasers* (2016, Springer).
[7] M. Ohtsu and T. Kawazoe, “Principles and Practices of Si Light Emitting Diodes using Dressed Photons,” *Off-shell Archive* (May 2018) Offshell: 1805R.001.v1. **DOI** Offshell: 1805R.001.v1, http://offshell.rodrep.org/?p=129
[8] M. Ohtsu and T. Kawazoe, “Principles and practices of Si light emitting diodes using dressed photons,” *Advanced Materials Letters*, **10** (2019) pp.860-867.
[9] M. Ohtsu, “Dressed photon phenomena that demand off-shell scientific theories,” *Off-shell Archive* (November 2019). Offshell: 1911R.001.v1. **DOI** Offshell: 1911R.001.v1, http://offshell.rodrep.org/?p=232
[10] N. Tate, Y. Liu, T. Kawazoe, M. Naruse, T. Yatsui, and M. Ohtsu, “Fixed-distance coupling and encapsulation of heterogeneous quantum dots using phonon-assisted photo-curing,” *Appl. Phys.* B, **110** (2013) pp.39-45.
[11] N. Tate, Y. Liu, T. Kawazoe, M. Naruse, T. Yatsui, and M. Ohtsu, “Nanophotonic droplet: a nanometric optical device consisting of size- and number-selective coupled quantum dots,” *Appl. Phys.* B, **110** (2013) pp.293-297.
[12] N. Tate, M. Naruse, Y. Liu, T. Kawazoe, T. Yatsui, and M. Ohtsu, “Experimental demonstration and stochastic modeling of autonomous formation of nanophotonic droplets,” *Appl. Phys.* B, **112** (2013) pp.587-592.
[13] N. Tate, W. Nomura, T. Kawazoe, and M. Ohtsu, “Novel wavelength conversion with nanophotonic droplet consisting of coupled quantum dots,”*Opt. Express*, **22** (2014) pp.10262-10269.
[14] S. Sangu, K. Kobayashi, and M. Ohtsu, “Optical near fields as photon-matter interacting systems,” *J. Microsc*. **202** (2001) pp.279-285.
[15] K. Takahashi, M. Katori, M. Naruse, and M. Ohtsu, *Appl. Phys.* B, **120** (2015) pp.247-254.
[16] M. Ohtsu and T. Kawazoe, “Experimental estimation of the maximum size of a dressed photon,” *Off-shell Archive* (February 2018) Offshell: 1802R.001.v1. **DOI** 1802R.001.v1, http://offshell.rodrep.org/?p=98
[17] M. Katori and H. Kobayashi, in *Prog. Nanophotonics* 4 (ed. by M. Ohtsu and T. Yatsui) (Springer, Heidelberg, 2017) pp.19-55.
[18] J. H. Kim, T. Kawazoe, and M. Ohtsu, “Optimization of dressed-photon—phonon-assisted annealing for fabricating GaP light-emitting diodes,” *Appl. Phys*. A **121** (2015) pp.1395-1401.
[19] M. Ohtsu and M. Katori, “Complex System of Dressed Photons and Applications,” *The Review of Laser Engineering*, **45** (2017) pp.139-143 (in Japanese).
[20] T. Kawazoe, K. Nishioka, and M. Ohtsu, “Polarization control of an infrared silicon light-emitting diode by dressed photons and analyses of the spatial distribution of doped boron atoms,” *Appl. Phys.*A, **121** (2015) pp.1409-1415.

[21] H. Sakuma, “On the problem of quantization of Clebsch dual field and a quantized representation of dressed photon,” *Proc. of the Workshop on Basic Mathematic-Physical Studies on Dressed Photon* (ed. by T. Takiguchi), *Mathematics for Industry Research* No.14, Inst. Mathematics for Industry, Kyushu Univ., (February 2019) pp.127-148.
[22] H. Saigo, “Dressed Photon and Quantum Walk,” *Abstracts of the 66th Jpn. Soc. Appl. Phys. Spring Meeting*, March 2019, Tokyo, Japan, paper number 10p-W621-13.
[23] E. Segawa, S. Sangu, and M. Ohtsu, “An expression for dressed photon by quantum walks on line graphs,” *Abstracts of the 80th Jpn. Soc. Appl. Phys. Spring Meeting*, September 2019, Sapporo, Japan, paper number 19p-E314-5.
[24] H. Ito, T. Nakata, K. Sakaki, and M. Ohtsu, “Laser Spectroscopy of Atoms Guided by Evanescent Waves in Micron-Sized Hollow Optical Fibers,” *Phys. Rev. Lett.* **76** (1996) pp.4500-4503.
[25] M. Ohtsu, “Near-Field Optical Atom Manipulation: Toward Atom Photonics,” Chapter 11 in *Near-Field Nano/Atom Optics and Technology*, (Springer, Tokyo, 1998) pp.217-266.

[V] PUBLISHED BOOKS

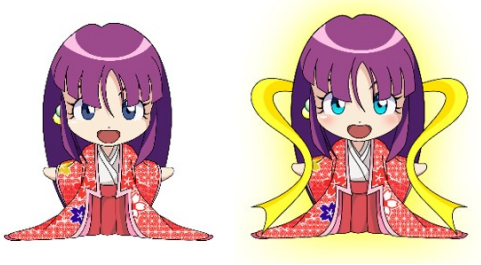

ここからはじまる量子場

ドレスト光子が開く
オフシェル科学

9784254131338
1923042038000
ISBN978-4-254-13133-8
C3042　¥3800E
定価（本体3800円+税）

ここからはじまる量子場
ドレスト光子が開くオフシェル科学
大津元一
小嶋　泉
[編著]

ここからはじまる量子場

ドレスト光子が開くオフシェル科学

大津元一
小嶋　泉
[編著]

西郷甲矢人
岡村和弥
佐久間弘文
安藤浩志
[著]

朝倉書店

[VI] PRESENTATIONS

IN DOMESTIC CONFERENCES

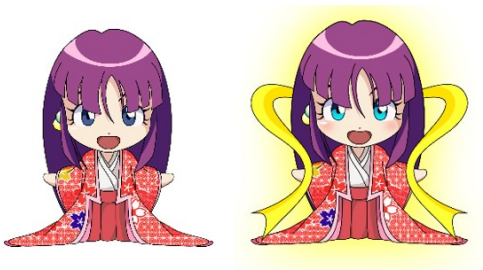

ドレスト光子による磁気光学効果を使った SiC 偏光回転素子

SiC polarization rotator using a magneto-optical effect induced by dressed photons

○門脇 拓也[1]，川添 忠[1]，大津 元一[2]

○Takuya Kadowaki [1], Tadashi Kawazoe [1], Motoichi Ohtsu [2]

日亜化学工業(株)[1]，(一社)ドレスト光子研究起点[2]

Nichia Corporation [1], Research Origin for Dressed Photon [2]

E-mail: takuya.kadowaki@nichia.co.jp

1. Introduction

光情報処理技術の著しい進展に伴って、これまでに比べさらに性能の高い光デバイスの実現が熱望されている。その中でも磁気光学効果を使った代表的な光デバイスとして、磁気光学空間変調器や光アイソレータがある。このようなデバイスには一般的に強磁性材料が使われるが、可視光領域での吸収の問題や低い偏光回転特性の問題がある。このため、可視領域で吸収が低く、偏光回転特性が高い材料は依然として存在しない。

一方で我々は、Al 原子をイオン注入した間接遷移型半導体の SiC 単結晶を使い、可視域で動作する新規の透過型の偏光回転素子を作製した。この素子は、ドレスト光子(DP)と呼ばれるナノ寸法領域での光子、電子の結合状態により磁場との相互作用が顕著になることで誘起される磁気光学効果によって動作する[1, 2]。また、外部コイルによる巨大な磁場や外付けのバルク磁石を必要とせず、素子表面のリング電極に発生する mT オーダーの小さな磁場で動作する。測定結果から、SiC 素子は、既存の材料と比較して巨大な磁気光学効果を示した。その Verdet 定数は、入射光波長 450 nm において 9.51×10^4 rad/T.m であった。

本発表では、その基本原理とともに、作製方法および特性評価について報告する。また、偏光回転のメカニズム解明に向けて SQUID 装置で評価した SiC 結晶の磁化特性についても報告する。

2. Experimental results and discussions

今回作製した透過型の偏光回転素子の構造を Fig.1 に示す。n 型の 4H-SiC 結晶の(0001)面に Al 原子をイオン注入法で打ち込み p 型に変換した。その後、電極を形成し、SiC 素子としてチップ化、実装した。作製したデバイスの p 層表面に対して波長 405 nm パワー20 mW のレーザー光を照射しつつ、両電極間に順方向電圧 19V (0.022A/mm^2)を印加してジュール熱による加熱を行った。これは、Al ドーパントの拡散および再配置により DP を高効率で生成するためのプロセスである。作製した素子を Fig.2(a)に示す一般的なクロスニコルの偏光実験の測定系で評価した。デバイス表面のリング型電極の中心に波長 450 nm の直線偏光を入射し、リング型電極に電流を印加したときの、透過光の強度変化を測定した。Fig.2(b)にピーク電流が 600 mA の三角波電流を注入したときの透過光強度の時間変化の測定値を示す。内挿図にスクリーンに集光して投影した透過光像を示す。電流注入時のクロスニコル透過光の明るいスポットから偏光回転が確認された。グラフは三角波電流値の変換に追随して透過光の強度が変化しているが、この結果から透過光の偏光の回転角の値を定量的に評価することができる。これらの結果をもとに、偏光回転の指標である Verdet 定数を算出すると、9.51×10^4 rad/T.m であった。これは、可視域の光アイソレータで使われる既存の材料と比較して、10^2 倍高い値である。

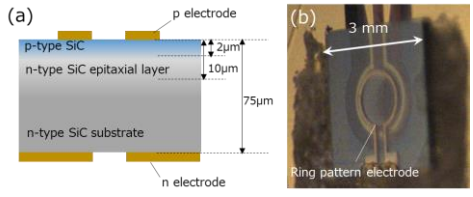

Fig.1 SiC 偏光回転素子の構造.(a)断面模式図. (b)顕微鏡写真.

このデバイスは、光情報処理システムなどへの広い応用可能性を秘めていると考えている。

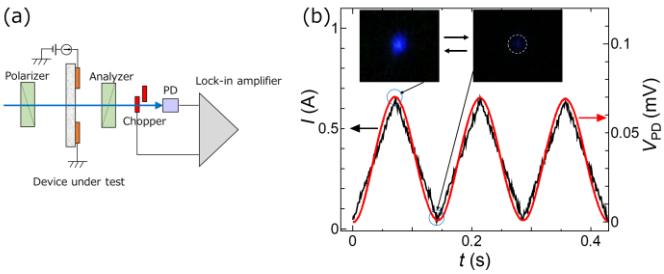

Fig.2 (a)測定系. (b)三角波電流(I)を注入したときの透過光強度(V_{PD})の時間変化.

【参考文献】

[1] M. Ohtsu, “History, current development, and future directions of near-field optical science,” *Opto-Electronic Advances*, **3**, 190046 (2020).

[2] 門脇他, 2019 年応用物理学会秋季学術講演, 19p-E314-8

ドレスト光子と物質系の非相対論性

Dressed Photons and Non-relativistic Nature of Material System

○ 坂野　斎[1]、大津元一[2]

(1. 山梨大院、2. ドレスト光子研究起点)

○Itsuki Banno[1], Motoichi Ohtsu[3]

(1.Univ. of Yamanashi, 2. Research Origin of Dressed Photon)

E-mail: banno@yamanashi.ac.jp

ドレスト光子（DP）は物質に内在するオフシェル（分散関係を満たさず伝搬しない）電磁場で，エネルギー非共鳴条件下でその効果は顕著になる．川添・大津らが行った非金属ナノ構造と近接場光を用いたエネルギー非共鳴条件下での一連の実験 [1] の特異な現象；間接遷移型半導体の発光，不十分な光子エネルギーでの近接場光化学反応，ナノ構造による周波数上方変換などは，DP が不足の運動量やエネルギーを補償する役目を担っている考えられる．このような DP 系を記述するために，私たちは，内在・外来全自由度のスカラーポテンシャル（SP）とベクトルポテンシャル（VP）を対等に扱う応答理論 [2] を構築した．それによれば線型・非線型感受率は，① 作用積分の SP・VP の汎関数微分から導出される，② 電荷保存則とゲージ変換不変性を自動的に保証する，③ VP のみが関わるエネルギー非共鳴条件下で強調される寄与；非共鳴項と SP と VP が対等に関わるエネルギー共鳴条件下で強調される寄与；共鳴項からなる．特に③で線型・非線型感受率の非共鳴項に VP のみが関わる（例えば，線型感受率の非共鳴項はロンドン方程式を導く）ことから，非共鳴項が支配する DP 系は，超伝導体系やアハラノフ-ボーム効果の系のように電場・磁場の概念が破綻する系であり，未認知の光学のレジームにあること（2018 秋 19a437-1 と-2）を強調したい

ここで，線型・非線型感受率の非共鳴項における SP と VP の不平等性は，非相対論系の作用積分やハミルトニアン中の SP と VP の依存性の違いから生じている．換言すれば，DP 系の現象には非相対論性が根本の原因として関与している．DP 系における非相対論性の役割の理解を目的として，この発表では，非相対論系の電荷密度と電流密度それぞれと結合する電磁場自由度を新たに SP と VP として再定義し，それで記述した作用積分を出発点とする．次に上記に倣って作用積分の SP・VP による汎関数微分によって物質場である電荷密度・電流密度を決める線型・非線型感受率と電磁場を決める波動方程式を導出する．その結果，以下がわかった：新たな線型・非線型感受率には SP と VP が対等に関与すること，作用積分から導出される SP・VP の波動方程式は VP に関して非線型であること，電荷保存則と互換性のあるゲージはクーロンゲージであること．なお，再定義した SP・VP と，それに伴う線型・非線型感受率は，従前に誘導電流密度・誘導電荷密度を不変に保つ非線型変換によって導いた「非共鳴描像」のもの（2019 春，10p-W621-9）に一致する．

謝辞

ドレスト光子研究起点 (RODreP) での数理物理的な議論について次の方々に感謝いたします：小嶋泉博士 (RODreP)，佐久間弘文博士 (RODreP)，川添忠博士 (東京電機大学)，西郷甲矢人博士 (長浜バイオ大学)，岡村和弥博士 (名古屋大学)，安藤浩志博士 (千葉大学)，瀬川悦生博士 (横浜国立大学)，松岡雷士博士 (広島工業大学)．この研究の一部は光科学技術研究振興財団からの援助（2018-2019）を受けています．

参考文献

[1] M. Ohtsu, ”Progress in Dressed Photon Technology and the Future”, in *Progress in Nanophotonics* **4** eds. by M. Ohtsu and T. Yatsui (Springer, 2017) Chap. 1 .

[2] I. Banno: ”Response Theory Supporting Dressed Photons”, in *Progress in Nanophotonics* **5**, ed. by T. Yatsui (Springer Nature, 2018) Chap. 6; I. Banno: ”Theory of Single Susceptibility for Near-field Optics Equally Associated with Scalar and Vector Potentials”, http://arxiv.org/abs/1807.10992 .

量子場理論に対する問題提起としてのドレスト光子研究

Dressed photon study as the touchstone of developing quantum field theory

ドレスト光子研究起点　○佐久間弘文、小嶋泉、大津元一

Research Origin for Dressed Photon, ○Hirofumi Sakuma, Izumi Ojima, Motoichi Ohtsu

E-mail: sakuma@rodrep.or.jp

これまでの２年間の発表において、発表者は未解明のドレスト光子（DP）現象に対して、特にその発生メカニズムに焦点した新しい理論の構築を行って来た。その研究は、新設された「ドレスト光子研究起点」（RODreP）の研究グループで共有されている認識：「ドレスト光子は新たなオフシェル科学を拓く突破口」を強く反映するものである。オフシェルとは、量子場理論の言葉で、存在形態としては非常に限定的ではあるが、その概念的重要性の為にこれまで専ら注目を集めたオンシェルモードの対極的概念として存在するものである。日常的な言葉で例えるなら、海洋に浮かぶはっきりとした輪郭を持った氷山がオンシェル場に対応し、オフシェル場は流動する氷山を背景場として支える海洋そのものであると言える。

公理的量子場理論が示す重要な帰結として、量子場の相互作用を４運動量 (p) 空間で表現した時、 p としては時間的、光的なものの他に、空間的なものを含めたすべての関与が必須である事が示される。この数学的帰結は非常に重要だと思われるが、現在も未解決のままである量子場理論のこれまでの取り組みにおいては、この事は明示的に取り込まれていない。言うまでもなく、オフシェル科学への挑戦においては、量子場理論の再考は避けて通れない問題である。しかしながら、非自明な相互作用を記述する量子場理論の構築という「大問題」が一朝一夕には達成できないであろうことも確かである。この「大問題解決」を登山における登頂に例えるなら、そこへたどり着くルートも複数であるに違いない。発表者が、これまでに取り組んで来た空間的運動量に焦点した Clebsch 双対場 [1] もその様なルートの一つであるが、主に DP の現象的振る舞いを入り口としたアプローチも RODreP においては、量子ウォーク研究 [2] や格子ゲージ理論を参照する形で積極的に行われている。

前々回と前回の発表においては、Clebsch 双対場の基本的構造を調べて行くと、全く分野の異なる宇宙論（そこでは重力場が重要な役割を占める）の未解決問題に繋がる可能性がある事を示した。分野は大きく隔たるものの、古典場としての電磁場と重力場が同様な性質を示す事は、Coulomb 力と万有引力の相似性として良く知られている。

今回の発表においては、前回発表した宇宙論関連の議論をより発展させる事により得られた（４階のテンソル場としての）Weyl 場に関しての新たな発見（式 (1)）に基づき、Clebsch 双対場を導入した元々の動機としての「場の相互作用には、時間的、光的及び空間的運動量の全てが必須」という数学的帰結の “具体例” が実は、古典的重力場の中にも存在している事を示す。

$$g_{ab} = 4W_{acde}W_b^{cde}/W_{ijkl}W^{ijkl}. \qquad (1)$$

この様な電磁場と重力場との比較を通して、電磁場におけるドレスト光子の特異な位置づけが、スケールは全く異なるものの、重力場が主役となる天体力学ではどの様なものに対応付けられるのかという事を示し、且つドレスト光子の尋常ならぬ未知の力学的振る舞いがどの様なものであるかを、重力場の例を通して推察する。

謝辞：本研究の一部は（公財）光科学技術研究振興財団の研究助成によるものである。

参考文献

[1] Sakuma, H. Virtual Photon Model by Spatio-Temporal Vortex Dynamics. In Progress in Nanophotonics, vol. 5, pp. 53-77, 2018

[2] 西郷甲矢人、量子確率論からドレスト光子へ、ドレスト光子に関する基礎的数理研究 マス・フォア・インダストリ研究所 No.14, 2019

量子ウォークによるドレスト光子のエネルギー移動の自律性について

A quantum walk simulation of autonomy in dressed photon energy transfer

横浜国立大 [1], 広島工業大 [2], 長浜バイオ大 [3], (株) リコー [4], ドレスト光子 [5],
瀬川 悦生 [1○], 松岡 雷士 [2], 西郷 甲矢人 [3], 三宮 俊 [4], 大津 元一 [5]
Yokohama Nat. Univ.[1], Hiroshima Inst Tech[2], Nagahama BioSci Tech[3], Ricoh Co., Ltd[4], Dressed Photon[5],
○Etsuo Segawa[1], Leo Matsuoka[2], Hayato Saigo[3], Suguru Sangu[4], Motoichi Ohtsu[5]
E-mail: segawa-etsuo-tb@ynu.ac.jp

量子ウォーク (QW) は, グラフの各有向辺で生成される線形空間上のユニタリ作用素で, 離散的に時間発展をする. そして幾つかの代表的な量子的ダイナミクスの離散的類推を与えるので, 量子デバイス上でのシミュレーターとしての応用が期待されている. この研究では, この単純な QW モデルを通じてナノ物質上のドレスト光子のエネルギ推移の自律性 [1] と QW の挙動の比較検討することで, ドレスト光子というものを深く理解するための手がかりを探す.

時間発展作用素は, 与えられたグラフの対称有向辺の集合 A に対する二つの同値関係から誘導される, 二つのユニタリ作用素の積 $U = SC$ と記述される. 一つ目の同値関係による商集合をベースにして QW を読み治すと, 自然に各辺に, 2 つの状態を付随した $\ell^2(E;\mathbb{C}^2)$ のように空間を記述できる. このことをラインググラフ化と呼ぶ. このように頂点そのものよりも, むしろその頂点間の接続関係をベースにした考察が QW の特徴の一つである.

そこでまず半無限システムにおける QW の定常性を利用する. この QW における定常状態は背後にあるランダムウォークの可逆性が反映され, 電気回路で表現される [2]. しかしながら, その入射が時刻に依存して振動するような場合は, グラフの内部構造の推定や最適化に有用であることが期待されているにも関わらず, ほとんど何も知られていない. そこでまず手始めに 1 次元有限パスの場合の散乱に関する明示的な表示が得られたので報告する. M 個の微小な粒子がパス上に並んでおり, パスの左端からレーザーを照射し続け, ドレスト光子のエネルギーの推移が自発的に連鎖することにより, 反対側のパスの右端で, どのような応答を得られるかを考える. 各微小粒子におけるエネルギー推移のルールは行列式 Δ の 2 次元ユニタリ行列 $C = \begin{bmatrix} a & b \\ c & d \end{bmatrix}$ によって与えられるものとする. すると, パスの数え上げの母関数を用いることによって, 次のような結果が得られた：

定理: $M \geq 2$ とする. 位相が時間に依存する量子ウォーカーを左端から $\alpha_L e^{i\xi n}$, 右端から $\alpha_R e^{i\xi(n-M+1)}$ ($\xi \in \mathbb{R}$, α_L, $\alpha_R \in \mathbb{C}$) で入射し続け, 十分に時刻 n が経過したときの応答をそれぞれ β_L, β_R とすると,

$$e^{i\xi} \begin{bmatrix} \beta_R \\ \beta_L \end{bmatrix} = \Sigma_M(\xi) \begin{bmatrix} \alpha_R \\ \alpha_L \end{bmatrix}. \tag{1}$$

ここで, $\tilde{U}_n(\xi) := U_n\left(\frac{\cos\eta}{|a|}\right)$ (第二種チェビシェフ多項式), $\eta := \arg(\Delta)/2 - \xi$ として, ユニタリ行列 $\Sigma_M(\xi)$ は,

$$\frac{1}{\tilde{U}_{M-1}(\xi) - |a|e^{i\eta}\tilde{U}_{M-2}(\xi)} \begin{bmatrix} \Delta^{1/2}|a|\left(\frac{a\Delta^{-1/2}}{|a|}\right)^M & b\tilde{U}_{M-1}(\xi) \\ c\tilde{U}_{M-1}(\xi) & \Delta^{1/2}|d|\left(\frac{d\Delta^{-1/2}}{|d|}\right)^M \end{bmatrix}.$$

この明示公式から, 例えば任意の M において, 透過量 (対角成分) を最大 (完全透過) にするパラメータをコントロールすることができ, 実装の際に有用であることが期待される.

謝辞: 本研究の一部は (一社) ドレスト光子研究起点の助成を受けた.

参考文献: [1] M. Ohtsu, T. Kawazoe, H. Saigo, Spatial and temporal evolutions of dressed photon energy transfer, OffShell: 1710R.001.
[2] Yu. Higuchi and E. Segawa, J. Phys. A 52 (39) (2019).

ドレスト光子エネルギー移動における定常状態への収束過程

Convergence Process to Steady States in Dressed-photon Energy Transfer

(株) リコー[1]，長浜バイオ大[2]，ドレスト光子研究起点[3]
○三宮 俊[1]，西郷 甲矢人[2]，大津 元一[3]

Ricoh Co., Ltd.[1], Nagahama Inst. Bio-Sci. Tech.[2], Res. Origin Dressed Photon[3],
°Suguru Sangu[1], Hayato Saigo[2], Motoichi Ohtsu[3]
E-mail: suguru.sangu@jp.ricoh.com

1. はじめに

ナノ領域において発現する特異な現象[1]の解明やその応用に向け、物質や環境の影響を取り込んだ「ドレスト光子」の数値シミュレーションの研究開発を進めている。これまで量子密度行列を用いた計算手法の検討を進め、物理イメージの取得や膨大な計算量の観点から、ドレスト光子を記述する特徴的な基底状態を得たいという要求に至っている[2]。

一方、局在性や高速性といったドレスト光子の特徴を、グラフ上の量子ウォークを用いてモデル化する理論検討が進められている。特に、定常状態の解析により、グラフ構造の尖った（出力端の少ない）部分においてドレスト光子の存在確率が高くなるといった法則が見出されている[3]。

本発表では、定常状態に着目し、これを固有モードに分解した状態をドレスト光子の基底状態と捉え、定常状態に収束する際の基底状態間の遷移ダイナミクスについて議論を行う。

2. 固有モードと収束過程の計算結果

量子密度行列のマスター方程式より定常解を数値的に求め、得られた量子密度行列の対角化を行うことで固有モードが算出できる。得られた固有モードを改めて基底状態とし、各固有モードの時間発展を得る。

Fig. 1 に、テイパー構造からなる二次元物質（46 ノード）の固有モードに対する量子密度行列を時間発展の初期、中期、終期（定常状態付近）について図示する。対角成分は各固有モードの存在確率、非対角成分は固有モード間の遷移確率であり、寒～暖色で大きさを表現している。見やすさのために、確率 0.01%以下を同色となるように閾値表示している。また、図中に主要な固有モードの幾つかを可視化表示した。各固有モードにおいて収束速度の異なる様子がうかがえる。

3. まとめ

上記結果より、採用した基底状態において量子密度行列が時間発展の初期より比較的疎な行列要素で記述できることが分かる。これは数値シミュレーションにおける計算量の低減可能性を示唆している。また、さらなる検討として、媒介する固有モードの空間的特徴やナノ物質の形状に対する依存性に関しても本発表にて議論する予定である。

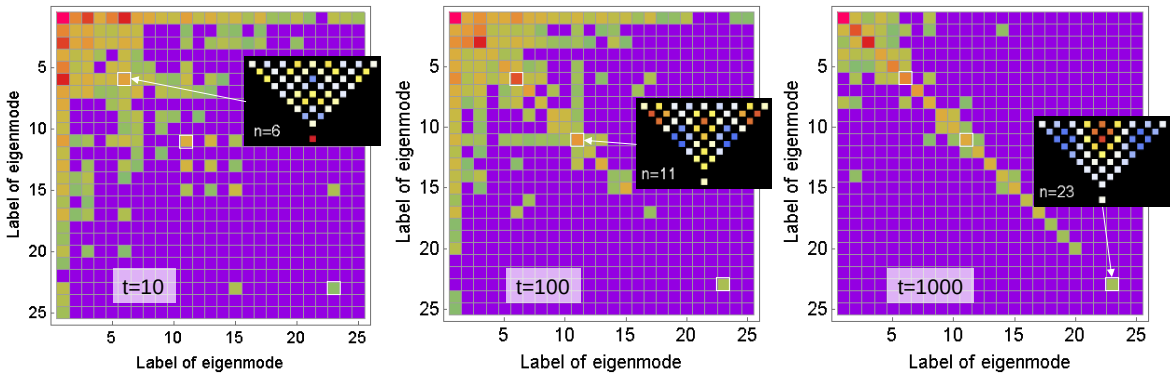

Fig. 1: 固有モードに展開した量子密度行列の時間発展（挿入図：固有モードの例）

参考文献

[1] 例えば、川添・他, 光学 43(8) 366 (2014); 八井, OPTRONICS 35(413) 204 (2016).
[2] 三宮・他、第 80 回応用物理学会秋季学術講演会 19p-E314-6 (2019).
[3] 瀬川・他, 第 80 回応用物理学会秋季学術講演会 19p-E314-5 (2019).

ドレスト光子を用いた波長 2μm の Si 発光ダイオードの作製と評価

Fabrication and evaluation of Si light-emitting diode of 2 μm-wavelength using dressed photons

日亜化学工業(株)[1]，東京電機大[2]，ドレスト光子研究起点[3]
○門脇 拓也[1]，川添 忠[2]，大津 元一[3]
Nichia Corporation[1], Tokyo Denki University[2], Research Origin for Dressed Photon[3]
○Takuya Kadowaki[1], Tadashi Kawazoe[2], Motoichi Ohtsu[3]
E-mail: takuya.kadowaki@nichia.co.jp

1. はじめに

近年、ドレスト光子技術により間接遷移型半導体の Si 結晶を用いた多様な発光素子(LED、LD など)が報告されている[1]。これらは従来の直接遷移型とは異なりドレスト光子フォノン(DPP)の中間準位(コヒーレントフォノン準位)を介した伝導帯中の電子との運動量授受により発光する。

結晶中に DPP を効率よく発生させるには DPP アニールと呼ばれる製作法が使われる。これは所望の発光光子エネルギー(発光波長)に相当する光を照射しながら電流注入によるジュール熱で結晶中のドーパント原子を拡散させ、最適なドーパント分布の自律的形成を促すもので、その結果発光波長は半導体のバンドギャップではなく照射光波長で決まる(光子ブリーディング(PB)効果)。

今回は PB デバイスの例として Si LED を取り上げる。これまでの DPP アニール時の通電による素子電極への損傷などの問題[2]を避けデバイス性能・信頼性をさらに向上させるため、電極形成前にプローバーを用いて DPP アニールする手法を考案し Si LED を作製した。そのうえで波長 2 μm 帯の発光スペクトル特性を評価した。これにより PB の機構へのフォノンの寄与を確認したので報告する。

2. 素子作製

n 型の Si 基板に対して、B 原子をイオン注入法で打ち込み p 型に変換した。波長 2.0 μm で発光させることを目指し、フォノンの寄与を勘案して波長 1.3 μm のレーザー光(パワー1 W)を p 層表面に照射しつつ、両電極間に順方向電流 1.0 A/mm^2 を印加して DPP アニールを行い B 原子を拡散・再配置させた。その後 Fig.1(a)に示すメッシュ状電極を形成し、□1 mm のチップ化および実装を行い Si LED を作製した(Fig.1 (b))。

3. 結果と考察

作製した Si LED の I-V、I-L 特性の測定結果および発光像を Fig.1(c)に示す。I-L 曲線はスーパーリニア特性を示した。これは発光機構が DPP による誘導放出に起因することを表す独特な結果である。次に、液体窒素冷却の分光器を用いてフォノンに起因する側波帯を高感度評価した。Fig.2(a)の EL スペクトルの結果から波長 1.3 μm と 2.0 μm に明瞭なピークが確認できた(図中の↓)。これらのピークは、DPP アニールによる PB 効果の現れである(1.9 μm の凹部(図中の↑)は大気中の H_2O による吸収に起因)。すなわち 1.3 μm のピーク波長は DPP アニール時に照射した波長と一致している。さらに 2.0 μm のピーク波長は今回目指したもので、結晶中の B 原子濃度で決まる Weibull 分布から計算される波長とよく一致している。これらは運動量保存則を満足するために、Fig.2(b)に示す光学フォノン(エネルギー57 meV) 3 個および 9 個(前者の 3 次高調波[3])の寄与による側波帯の発光であることが確認された。

今後は各種パラメータの調整により Fig.2(a)の 2 つのピーク特性などのさらなる制御自由度の増加が期待される。

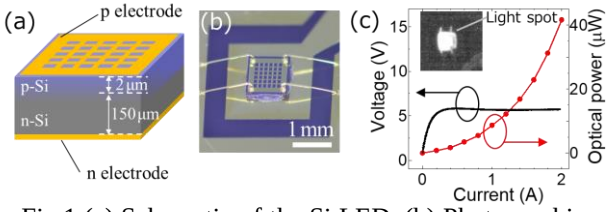

Fig.1 (a) Schematic of the Si LED. (b) Photographic profile. (c) I-V and I-L curves. The *inset* shows the emitted light spot.

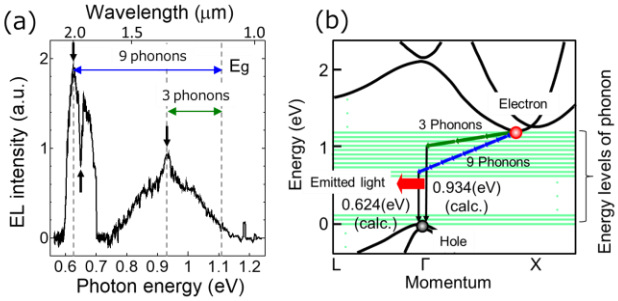

Fig.2 (a) The EL spectrum under a current of 1.5A. (b) The energy band structure of Si for schematically explaining light emission.

【参考文献】

[1] M. Ohtsu, *Silicon Light-Emitting Diodes and Lasers*, Springer, Heidelberg (2016)
[2] 川添, 門脇, 大津, 第 66 回応物講演会(2019 年 3 月), 10p-W621-16
[3] M. Ohtsu and T. Kawazoe, Adv. Mat. Letters, **10** (2019) pp.860-867

シリコン結晶製の高光パワー発光素子は LED? レーザー？

---いや、それはドレスト光子が創る新しい PBD---

大津元一
(一般社団法人)ドレスト光子研究起点　代表理事
(東京大学および東京工業大学　名誉教授)
〒221-0022　神奈川県横浜市神奈川区守屋町 3－13－19

1 まえがき：奇異な点

本フォーラムの参加各位は本講演の次の内容を容認しないであろう。

(1)半導体発光デバイスについて述べる。これは従来の LED、レーザーとは異なる。それは PBD((Photon Breeding Device：光子ブリーディングデバイス)と呼ばれている[1]。

(2)間接遷移型半導体を使う。一例として Si、SiC の例を示す。もちろんこれは従来の光デバイスに使われている直接遷移型半導体(化合物半導体)ではない。

(3)上記の基礎概念はオフシェル科学に基づく。これは従来のオンシェル科学ではない[2,3]。

以下ではまず(1)、(2)の実験事実を提示し、次に(3)を解説する。そして将来展望の後にまとめを記す。付録には「容認」されない理由の本質を略記する。

2 実験事実は？

1 節(1)、(2)の内容が容認されないのは Si、SiC が間接遷移型半導体だからである。また (3)の内容を容認されないのは SiC は強磁性体ではないからである。仮にこれらが容認されても極めて奇異に感じられるのは、これらの結果を説明する理論を持たないからである。しかし(1)-(3)に関し既に下記の表 1 に示す実験事実がある。

表 1　これまでの実験事実

PBD の種類	使用材料	性能
LED 型	Si[4]	発光波長は 0.9～2.5μm、パワー2.0W
	SiC[1]	発光色は緑、青、紫色、白色
レーザー型	Si[1,5]	[単一モード型]波長 1.3～1.4μm、しきい値電流密度 40 A/cm^2 [高パワー型]波長≒2μm(多モード)、パワー100 W
偏光回転子型	SiC[1,6]	波長 405nm にてベルデ定数 660 (deg/A)、ファラディ回転角 2480(deg/cm)

3　なぜ？

2 節の表 1 に示した性能が現れる理由はオフシェル科学の概念を使っているからである。これはナノ領域での光・物質相互作用の扱いを可能とする。これが扱う量子場の際立った特徴はその運動量とエネルギーの間の関係が分散関係から逸脱していることである。一方、従来の光科学はオンシェル科学の概念を使っている。それは「自由場」としての光に対する物質の応答を扱う。そこでは運動量とエネルギーの間の

分散関係は確定し相互作用を「仮想光子」などのモデルなどにより摂動的に表す。

しかし上記のナノ領域での光・物質相互作用はまだ証明されていないことに注意されたい[7]。そればかりかオフシェルの量子場（ナノ寸法）とオンシェルの自由量子場（巨視的寸法）の間のユニタリ変換が存在しないことも古くから指摘されているのである(Haag の定理)[8]。即ち両者間にはギャップがあり、相容れない。以上からわかるようにオンシェル科学はナノ領域での光・物質相互作用を扱うには無防備である（末尾の「**付録**」参照)。オフシェル科学はオンシェル科学と直交し、補完関係にあるため従来の光科学の教育カリキュラムに含まれておらず、従って表記のように「容認」しないという強い意思が働く。

4　謎解き

表 1 の性能を得るためにはドレスト光子（DP）と呼ばれるナノ寸法の量子場を生成して使う。DP はナノ領域での光子と電子の相互作用により生成される量子場であり、そのエネルギーの空間的広がりは DP が生成されるナノ寸法物質の寸法程度である。[2]。寸法が自由場の光波長以下なのでその運動量は不確定であり、従って分散関係から逸脱している。すなわちこれはオフシェル領域の量子場であることを表している。なお、生成された DP はさらにフォノンと結合する。

Si 結晶のような間接遷移型半導体の伝導帯中の電子は DP を構成するフォノンと運動量を授受し電子正孔再結合して発光する。これが 2 節(1)、(2)の起源である。これを可能にするには「物質中にいかに DP を生成するか？」が必須である。それは次の DP 援用アニールと呼ばれる製造法により実現している [1-4]

n 型 Si 結晶表面に p 型ドーパントの B 原子をイオン注入し pn ホモ接合を形成する。それに順方向電流を注入しジュール熱により B 原子を拡散させる。その際、外部から光(光子エネルギー$h\nu_{anneal}$)を照射する。この光により B 原子に DP が生成される。さらに対をなす B 原子があると DP はそこにコヒーレントフォノンが励起され、DP はそれと結合する。その DP の場の中に伝導帯の電子が入り込むと、この電子は DP 中のフォノンと運動量を授受し正孔と再結合して発光する（光の誘導放出の一形態)。生成された光子は伝搬光として Si 結晶外部に伝搬する。すなわち上記の発熱のためのジュールエネルギーの一部は光エネルギーとして外部に散逸されるため、DP が発生した部位の発熱は抑制される。こうしてジュール熱による拡散、光エネルギー散逸によるその抑制と相まって B 原子の数の空間分布は自律的に変化し、定常状態へと達する。

以上で DP 援用アニールは終了であるが、その後の B 原子数の空間分布は動作時に高い発光効率を与えるための最適分布になっている。なぜなら LED 動作のための自然放出確率は上記の誘導放出の確率と比例するからである。

5 そして PBD とは？

DP 援用アニールにより製造したデバイスは LED 型の動作をする。すなわち順方向電流を注入すると発光する。その光子エネルギー$h\nu_{em}$は照射光エネルギー$h\nu_{anneal}$に相当する（Si のバンドギャップエネルギーE_gではない)。これは DP 援用アニールの結果、照射光の複製の光子が生成されることを意味している。これが光子ブリーディング（PB）と呼ばれる現象であり、このデバイスは PBD と呼ばれている。言い換えると、所望の$h\nu_{em}$をもつ光を発生するデバイスを作るにはそれと同等の照光子エネ

ルギーをもつ光を照射して製作すればよい。これは所望の光子エネルギーに相当する E_g をもつ新規物質を探索する従来技術とは無縁である。

なお PB は光子エネルギーの複製のみでなく、光子のスピン（偏光）も複製する。例えば直線偏光の光を照射して製作すると、動作時の発光は同様に直線偏光する [9]。さらに Si 結晶に光導波路やファブリペロー共振器を作り付けるとレーザー型の動作が実現する。また、電極構造を修正し電流注入により磁場を発生させると巨大磁気光学効果を示し入射光の偏光方向を回転させる。すなわち偏光回転子型の動作が実現する。表 1 は以上のデバイスの性能を列挙している。

6　将来展望

4、5 節の内容は従来の光技術とは直交する。従来技術は物質科学に立脚し、分散関係を活用したオンシェル科学だからである。それに対し今回紹介した話題はナノ領域での光・物質相互作用にかかわり、分散関係とは無縁のオフシェル科学である。今後は必要に応じて両者を補完的に利用すればよかろう。

DP は光波長以下の寸法のナノ領域に局在した量子場であるため、オンシェル科学で常用されている電磁場モードを定義できない。そうなるとこれは無限数のモードの重ね合わせで表されると考えられるかもしれない。実際その考え方でこれまでの理論が展開されたが、それは正確ではない。オンシェル科学の概念に立脚する限り、相互作用の概念が扱えないからである。DP は上記のような重ね合わせで表されれるようなものでは決してない。オンシェル科学の手法を借りる限り、それは応急処置にすぎず、オフシェル状態の量子場としての DP は従来の量子力学、量子場理論、電磁気学、光学に使われている基本方程式の修正では記述できないのである（末尾の「**付録**」参照）。しかしこれまでに多くの実験研究により DP の性質についての知見が積み上げられている。またここで取り上げた発光素子以外にも表 2 の包括的な応用技術が開発されている[2]。この状況下でオフシェル科学の理論手法の開拓が不可欠になっていることから、最近では理論研究が加速している[8]。

表 2 DP による包括的な応用技術

技術分野	技術項目
微細加工技術	光化学気相堆積、光リソグラフィ、光エッチングまたは光堆積による物質表面平坦化など。
ナノ寸法の光デバイス	光パルス発生器、光スイッチ、光論理ゲート、光 DA 変換器、光周波数上方変換器、光バッファメモリ、ナノ集光器、光エネルギー移動路など。
光システム	高分解能の顕微鏡・分光システム、光ルーターシステム、光パルス形状測定システム、光情報セキュリティシステム、高密度磁気記録システムなど。
エネルギー変換	光/光エネルギー変換、光/電気エネルギー変換、電気/電気エネルギー変換

7　まとめ

ここで紹介した PB の現象は従来のデバイスでは見られない。なぜなら従来素子はオンシェル科学の基盤の上に設計製作されたものだからである。そこでは微小領域での複数の光子、電子の相互作用はブラックボックスに封じ込め、遠方で観測される

光波の特性のみを議論している。それに対しオフシェル科学ではこのブラックボックスを開け、その内部を議論するのである。光科学のみでなく素粒子物理学、量子場物理学などでもこのブラックボックス内をつまびらかに垣間見たことは無かった。奇しくもDPの実験研究の結果、このブラックボックスが開いたので中を覗いてみるとそこにはオフシェル科学が存在し、その基礎となる理論が著しく不足していることがわかったのである。これはオンシェル科学で忌避されてきたパンドラの箱を開けたことに相当している。

光技術は1990年代前半に成熟して久しいが、本講演で扱う話題が今後の別位相の発展、ブレークスルーを実現するためのヒントとなれば幸いである。

謝辞

研究協力を賜る次の皆様に感謝します(敬称略)：小嶋泉 (RODreP)、佐久間弘文(RODreP)、岡村和弥 (RODreP)、西郷甲矢人 (長浜バイオ大学)、安藤浩志 (千葉大学), 瀬川悦生 (横浜国立大学), 松岡雷士 (広島工業大学)、三宮俊 (リコー) 、坂野斎 (山梨大) 、川添忠 (東京電機大学)。

参考文献

[1] M. Ohtsu, *Silicon Light-Emitting Diodes and Lasers* (Springer, Heidelberg, 2016).

[2] M. Ohtsu, *Dressed Photons* (Springer, Heidelberg, 2014).

[3] M. Ohtsu, I. Ojima, and H. Sakuma, "Dressed Photon as an Off-Shell Quantum Field," in *Prog. Opt.* **64** (ed. by T.D. Visser) (Elsevier, Amsterdam, 2019) pp.45-97.

[4] M. Ohtsu and T. Kawazoe, "Principles and practices of Si light emitting diodes using dressed photons," *Advanced Materials Letters*, **10** (2019) pp.860-867.

[5] M. Ohtsu and T. Kawazoe, "Infrared lasers using silicon crystals," *Off-shell Archive* (August, 2019) Offshell: 1908R.001.v1.
DOI 10.14939/1908R.001.v1, http://offshell.rodrep.org/?p=214

[6] M. Ohtsu and T. Kawazoe "Gigantic Ferromagnetic Magneto-Optical Effect in a SiC Light-emitting Diode Fabricated by Dressed-Photon-Phonon Assisted Annealing," *Off-shell Archive* (September 2018) Offshell: 1809R.001.v1.
DOI 10.14939/1809R.001.v1, http://offshell.rodrep.org/?p=161

[7] 大津元一(編著)、*ここからはじまる量子場* (朝倉書店、東京、2020年)、第3章.

[8] R.F.Streater and A.S. Wightman, *PCT, Spin and Statistics, and All That* (Princeton Univ. Press, Princeton and Oxford, 1964) pp.163-165.

[9] T. Kawazoe, K. Nishioka, and M. Ohtsu, "Polarization control of an infrared silicon light-emitting diode by dressed photons and analyses of the spatial distribution of doped boron atoms," *Applied Physics* A, **121** (2015) pp.1409-1415.

付録：容認されない理由の本質

オフシェルとは量子場理論の用語である。そして分散関係を満たす自由場の粒子をオンシェルモードとして捉えた時、その様なモードとして表現できない場がオフシェル場である。一組の異なる素粒子と素粒子が強く相互作用している場合の場は、もちろんどちらの粒子の場とも異なる言わば“非粒子”の場で、その様な場は一般にハイゼンベルグ場と呼ばれ、自由場とはユニタリ変換で結ぶ事ができない事が知られている（Haag の定理）[8]。

ここで自由場について考える。系にエネルギーを注入すると場が励振され、既存の場と相互作用する。この相互作用は古典論ではニュートン力学により記述され、エネルギーが小さい時は線形の波動方程式で与えられる。大きい時は非線形方程式となる。しかし量子場についてはそのような相互作用を記述する一般的理論が未発見なのである。3 節で記した Haag の定理[8]は、非線形相互作用の結果生じている場は波が線形波動方程式によって変化して行く形では決して表現できないという事に対応し、それは取りも直さず既存の量子論の限界を示している。

既存の量子場理論は、この様な限界を持っているにもかかわらずしばしばその限界を忘れ、より一般の場合に適用する危うさを持つ。その代表例が 6 節で記したように場を自由場のモードで展開してしまう事である。このモード展開は、任意の関数がフーリエモードで展開できるという数学定理を真似たものであるが、それが正当化されるのは基底（今の場合自由場モード）の完備性がある場合のみである。この点に関しては、量子場の相互作用を 4 運動量で表現するには Timelike、Lightlike、 Spacelike の要素が必要である事に注意されたい（Greenberg and Robinson の定理[10]）。既存の素粒子物理学において、Spacelike 運動量成分はしばしば「Spacelike 運動量→超光速→非物理」という形式的理解に基づき議論から排除されてきたが、上記の定理は Timelike、Lightlike 運動量だけでモード展開しても相互作用を表せないことを意味している。

DP はファイバープローブの先端や不純物表面といった場の不連続性が核となって生じるが、ステップ関数をモード展開した場合一般に高波数成分の寄与無しにはその様な場は表現できない。Timelike、Lightlike 運動量で高波数成分を実現しようとすれば必然的に高エネルギーを伴う事になるが、Spacelike 運動量ならばその定義より低いエネルギーでも高波数成分を持つのは明らかである。従って場の不連続性を持つ相互作用において Spacelike 運動量成分が特に重要な寄与をすると考えるのは自然であり、その意味において DP の因子としての Clebsch 双対場が重要であることが指摘されている[7]。以上のように DP 研究がきっかけとなり量子場の見直しの必要性がようやく浮かび上がってきたのである。

[10] R. Jost, *The General Theory of Quantized Fields* (Lectures in Applied Mathematics, Volume IV) XV + 157 S. (American Mathematical Society, Providence, 1965).

Dressed photon phenomena that demand off-shell scientific theories

M. Ohtsu

Research Origin for Dressed Photon,
3-13-19 Moriya-cho, Kanagawa-ku, Yokohama, Kanagawa 221-0022 Japan

Abstract:
This presentation reviews experimental results on dressed photon (DP) phenomena that demand the quantum field measurement theory and quantum walk theory. In relation to the quantum field measurement theory, it is shown that disturbance of the DP momentum was observed. It is also shown that the linear relation between the cause and effect of the DP energy measurement is lost. An electric-dipole forbidden transition becomes an allowed transition, and the energy disturbance is enhanced by decreasing the probe–specimen distance. In relation to the quantum walk theory, it is shown that energy transfer of the DP and the Brownian motion of nanometer-sized particles were autonomously controlled.

１．まえがき

オフシェル科学の一つのトピックスとして研究されているドレスト光子（DP）はナノ領域における光子と電子(励起子)との相互作用により生ずる量子場である[1-3]。それは各種の応用に用いられている[1]。これらの応用の指導原理としての理論がいくつか開発された。その詳細は文献[1]にあるが、その概略は次のとおりである：その開発の際の本質的困難はDPの場の寸法が光波長よりずっと小さいことであった。これはDPの場の電磁モードが従来の光科学（オンシェル科学）の理論では定義できないことを意味する。この困難を一時的に回避するため、無限数の電磁モードの重ね合わせとしてDPの場が表された。これをもとにDPの生成、消滅を表す量子演算子が導出された。さらにDPとフォノンとの結合も説明された。一方、DPのエネルギーの空間的局在性を表すため、巨視系に囲まれた微視系を取り扱い、湯川関数が導出された。

残されている問題はDPのエネルギー移動の自律性の性質とその観測[1,4]をいかに説明するかである。その説明の為、これまでに統計力学、複雑系科学の考え方に基づき、

ランダムウオークモデルを使った数値シミュレーションが行われている。本稿ではまず2節で関連する実験結果を概説する。次に3節でこれらの数値シミュレーションの方法と結果を紹介し、それらの抱える問題を提示する。4節ではその解決の指針を提示し、オフシェル科学を進展させるために必要な数値シミュレーションの方向について提言する。最後に5節でまとめる。

2　DPによる新奇デバイスに関する実験結果

本節ではDPによって製作され動作する3つの新奇デバイスに関する実験結果を概説する。ここでは次節の数値シミュレーションのために必要な内容のみを記す。

2.1 特殊な表面形状の銀電極を持つ光起電力デバイスの製作とデバイス動作

ここで取り扱うのは光起電力デバイスである。これは光エネルギーを電気エネルギーへ変換するデバイスであり、太陽電池などに応用されている。ここでは有機分子(Poly(3-hexylthiophene、以下ではP3HTと略記)の薄膜を用いたデバイスを例にとる[5]。その製作、動作にDPを使う。

【製作】

使用する材料は次のとおりである。

[p 型半導体] P3HT 薄膜。バンドギャップエネルギーE_g=2.18eV（光電変換の遮断波長λ_c=570nm)。pn接合の空乏層はP3HT内に形成されるのでデバイスの主要な性質はP3HTに依存する。

[n型半導体] ZnO薄膜。E_g＝3.37eV（遮断波長λ_c= 367nm)。

[二つの電極] ITO薄膜、Ag薄膜。

図 1 に示すようにサファイア基板上に ITO 薄膜（厚さ 200nm)、ZnO（厚さ 100nm)、の P3HT（厚さ 50nm)、Ag 薄膜（厚さ数 nm）をつける。次に Ag 薄膜表面に Ag 微粒子を吹きつける（RF スパッタリングによる）（図 2)。その際 Ag 薄膜表面に光を照射（照射光の波長 λ_0=660nm：上記の遮断波長λ_cより長い値）して DP を生成する。かつ P3HT と ZnO からなる pn 接合に逆バイアス電圧 V_bを印加する。ここでは表 1 に示すように照射光パワー、逆バイアス電圧の値を設定して 3 種類のデバイス A,B,C を製作した。

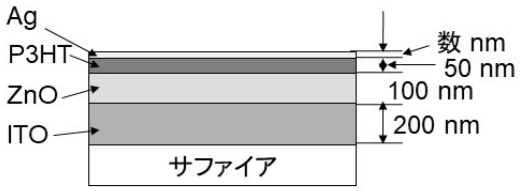

図 1　 Ag 薄膜を電極として予備的に作った光起電力デバイス

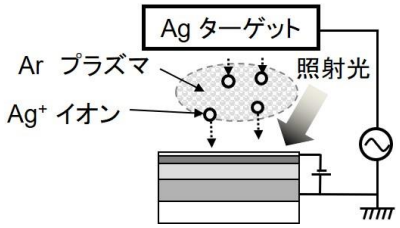

図 2　 光照射下での RF スパッタリングによる Ag 微粒子の吹きつけ

表 1　デバイス作製に用いた照射光パワー*P*、バイアス電圧 V_bの値
(*)デバイス A はデバイス B、C の性能との比較のための参照用

デバイス名	照射光パワー*P*	バイアス電圧 V_b
A(*)	0	0
B	50mW	-1.5V
C	70mW	-1.5V

上記のように生成された DP と逆バイアス電圧によって Ag 薄膜表面の各位置に飛来する Ag 微粒子の流入・流出量を次のように自律的に制御する（図 3)。

(1)（図 3 左）DP による電子・正孔対の生成

光照射により Ag 薄膜表面の突起部に DP が生成される。その DP の場の空間的広がりが pn 接合部に達していれば電子が励起され pn 接合部には電子・正孔対が生成される。

(2) （図 3 中）Ag 薄膜の帯電

生成された電子・正孔対は電子と正孔とに分離する（逆バイアス電圧による電場のため)。正孔は電極である Ag 薄膜に引きつけられ、Ag 薄膜は正に帯電する。

(3) （図 3 右）Ag 微粒子の流入・流出量の自律的制御

Ag 薄膜表面に飛来する Ag 微粒子は正に帯電したイオン Ag+なので､Ag 薄膜表面のうち上記(2)に記した局所的に正に帯電している部分から反発を受ける。従って Ag 微粒子は Ag 薄膜表面のうち DP が生成している部分を避け、別の部分に堆積する。その結果、DP のエネルギーの空間分布に依存して独特の表面形状をもつ Ag 薄膜が形成される。この Ag 薄膜の形状は時間とともに自律的に変化し、やがて独特の表面形状になる。

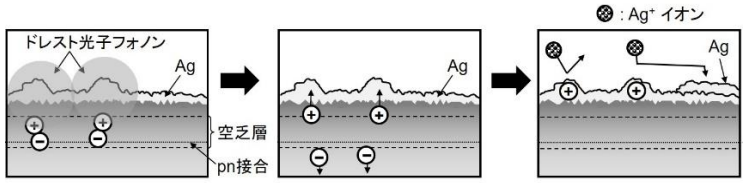

図 3　DP による電子・正孔対の生成（左）、Ag 薄膜の帯電（中）、Ag 微粒子の流入・流出量の自律的制御（右）

図 4 は表 1 の 3 つのデバイスの Ag 薄膜表面の走査型電子顕微鏡(SEM)像である[5]。デバイス B、C の表面形状（図 4 (b)、(c)の SEM 像）はデバイス A（図 4(a)）に比べ粗く、大きな塊を含む。さらに両図の塊の寸法は互いに異なるので、寸法の分布の測定値のヒストグラムおよびそれにあてはめた曲線を図 4 (b)、(c)の下半分に示す。図 4 (b)に示す分布から塊の直径の平均値 90nm、標準偏差値 64nm を得る。一方図 4(c)に示す分布から塊の直径の平均値 86nm、標準偏差値 32nm を得る。図 4(b)、(c)を比べると塊の寸法の標準偏差値は照射光パワーの増加とともに減少していることがわかるが、これは独特の寸法の塊をもつ表面が自律的に形成されたことを意味する。

デバイス B,C の Ag 塊(図 4(b)、(c))に発生する DP の場は pn 接合部に達している。（∵DP の場の平均直径（90nm、86nm）は Ag 薄膜と P3HT を併せた厚み（70nm 以下）より大きいから）。従って DP により pn 接合部に電子・正孔対が生成される。なお、デバイス A では Ag

薄膜の厚みは 800nm なので、DP が発生したとしてもその場は pn 接合部には達しない。従って電子・正孔対は生成されない。

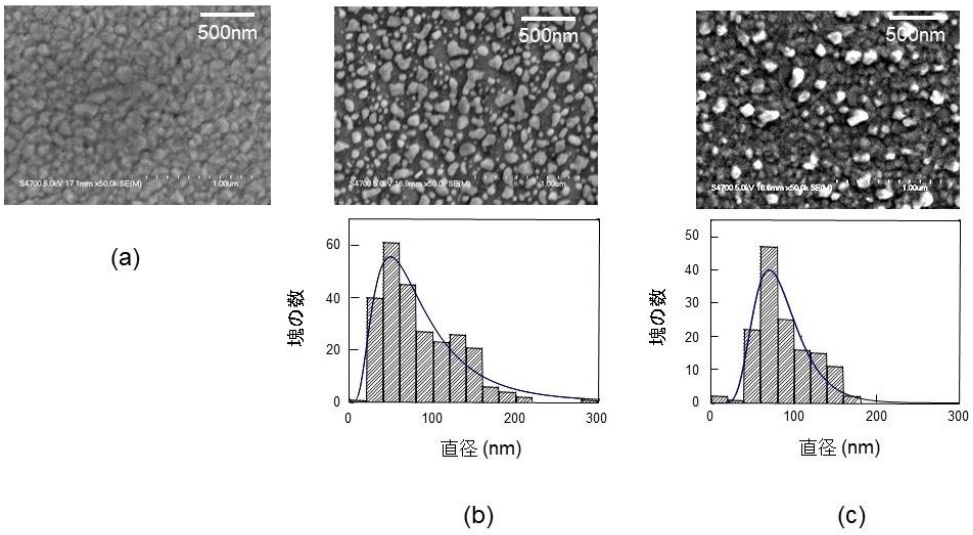

図 4　作製された光起電力デバイスの Ag 薄膜表面の走査型電子顕微鏡（SEM）像。
(a)、(b)、(c)はデバイス A、B、C の場合。(b)、(c)の下半分は塊の直径の分布を表す。

【動作】

Ag 薄膜を電極として用いる。サファイア基板の後ろ側から光を入射すると（図 5）Ag 電極表面に DP が効率よく発生し、pn 接合部に電子・正孔対が生成する。ここで入射光波長が製作の際の照射光の波長 λ_0 に等しいとき電子・正孔対の生成効率は最高になり、従って光電流発生効率は波長 λ_0 において最大となることが期待される。これは 2.2 節のデバイスでも観測されている光子ブリーディング（PB）効果である[6]。このような波長選択性を図 6 に示す。これは光照射により発生する電流密度の測定結果である。曲線 A はデバイス A から発生する非常に小さい光電流密度の値を表す。これに対し、曲線 C（デバイス C の値）の値は大きく、かつ波長 620nm*で最大値をとる。これは上記の PB 効果を表している。曲線 B（デバイス B の値）では波長選択性は曲線 C ほど顕著ではない。これは表 1 に示す様に製作用の照射光パワー（50mW）が十分には大きくない事に起因する。

(*)この値は Ag 薄膜表面形状の制御用照射光の波長 λ_0(=660nm)より 40nm 短い。この短波長シフトは逆バイアス電圧 V_b(=-1.5V)により誘起された直流シュタルク効果に起因する。

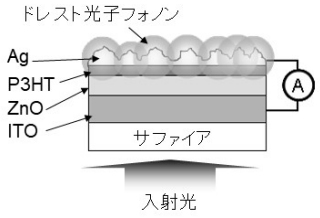

図 5　出来上がった光起電力デバイスの構造。

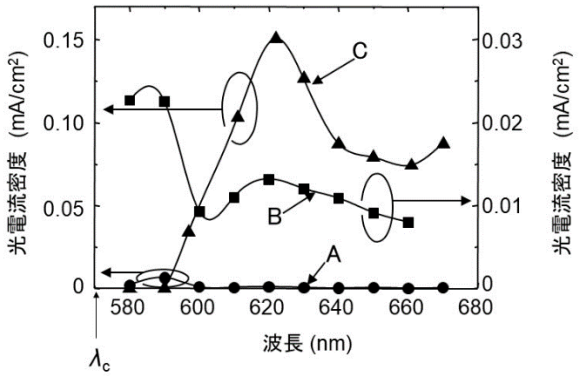

図 6　入射光波長と光電流密度との関係。
曲線 A、B、C は各々デバイス A、B、C の場合。

2.2 シリコン発光素子の製作とデバイス動作

シリコン発光素子の代表例として発光ダイオード（LED）を取り上げる。その製作と動作の概略は次の通りである。詳細については文献[6-8]を参照されたい。

【製作】

p 型層を形成するために Si 結晶中に B 原子をドープする。DP を生成するため DP 援用アニールと呼ばれる方法を使う[1,6]。その過程は次のとおりである：

(1) 順方向電流を注入しジュール熱を発生させてB原子を拡散させその空間分布を変える。同時に光(光子エネルギー$h\nu_{anneal}$)を照射し、B 原子に DP を生成する。B 原子が対をなすとき、DP によりそこに局在フォノンが生成し DP と結合する。

(2) 電流注入により伝導帯に生成された電子がその DP の場に流入すると、電子と上記のフォノンとの間で運動量を交換するので電子は正孔と再結合して光子を生成する。この現象は照射光に起因する光の誘導放出である。

(3) 生成された光子は自由光子として Si 結晶外部に伝搬する。すなわち B 原子拡散用のジュールエネルギーの一部は光エネルギーとして外部に散逸する。したがって光子を生成した局所的な空間領域でのジュール熱は減少し、B 原子の拡散が抑圧される。

(4) 引き続く電流注入と光照射により B 原子の空間分布は変化し、その分布は外部から加えられたジュールエネルギーと散逸する光エネルギーのつり合いにより定常状態へと達する。

この定常状態は LED としての動作に最適な B 原子分布を自律的に形成すると考えられる。なぜならば光の自然放出確率は上記の誘導放出確率と比例するからである。さらに、LED 動作時の放出光の光子エネルギー$h\nu_{em}$は上記の照射光の光子エネルギー$h\nu_{anneal}$と等しい（PB 効果）ことが期待される。

【動作】

製作されたデバイスに電流を流すと、Si は間接遷移型半導体であるにもかかわらず発光し、その光子エネルギー$h\nu_{em}$は Si のバンドギャップエネルギーE_gではなく上記の照射光のそれ$h\nu_{anneal}$に依存した。また、結晶中の B 原子は対を形成していることが確認された。その対の長さは Si 結晶の格子定数の整数 n 倍であり、発光の光子エネルギー$h\nu_{em}$は $h\nu_{anneal} - nE_{phonon}$で与えられた。ここではフォノンのエネルギーであり、整数 n は B 原子対の長さを表すとともに、電子との運動量授受に寄与したフォノンの数を表す。この式は $h\nu_{anneal}$ の値に等しく、PB 効果の証左となっている。

2.3 ナノドロップレットの製作とデバイス動作

ナノドロップレット（ND）はDPによる光エネルギー下方変換を行うデバイスであり、太陽電池の光電変換効率向上などに応用されている。その製作方法と動作の概略は次のとおりである。詳細については[9-13]を参照されたい。

【製作】

CdSe、ZnO, CdSなどのナノ寸法の粒子（NP）を液体状の紫外線硬化樹脂または熱硬化樹脂に分散し、可視光を照射する。NP表面に発生したDPはDPの寸法依存共鳴の性質[9,14]により、同じ寸法をもつNPに移動する。その結果二つの異種のNPは対を作り、紫外線と同等の光子エネルギーを持つDPを生成する。このDPは周囲の液体を硬化させ、これらの対は樹脂の中に封じ込められる。これがNDである。

【動作】

製作されたNDに紫外線を照射すると、その中のNP間のDPエネルギー移動により可視光を生成する。すなわち光エネルギー下方変換が実現する。

3 数値シミュレーションの結果とその問題

上記の3種類のデバイスに関し統計力学・熱力学の考え方に基づき、下記のようにランダムウオークモデルを使った数値シミュレーションが行われている。

3.1 特殊な表面形状の銀電極を持つ光起電力デバイスの製作とデバイス動作

このデバイスの電極として使われるAg薄膜の形成の基本物理過程はナノ寸法での光・物質相互作用が関与する。この系は環境に開いており、従ってエネルギー流と環境揺らぎを伴うので、その非平衡動力学を記述するために、新しい統計力学的モデルが使われている[15]。このモデルでは有限寸法の二次元正方格子中の各サイトにおいて、離散時刻ステップでの

堆積された粒子の数と電荷量を確率過程変数と考えた。そして格子上の全電荷に起因する各サイトでの反発クーロンポテンシャルを時間ステップごとに計算した。その際、格子上の各サイトあたりの入射光パワーを表すパラメータb、および物質上のDPの寸法依存共鳴効果を表す関数$f(s)$を導入することにより生成するDPの寄与を含めた。さらにbをモデルの外部制御パラメータと見なし、表面のAg+の初期堆積のしきい値エネルギーE_{th}を考慮した。Ag+がAg膜表面の局所的に正に帯電している部分から反発をうける確率はE_{th}とbの値に依存すると考えた。これらの考察のもとにAg+のドリフトと堆積の過程の数値シミュレーションが行われた。その結果、臨界値b_cにおいてパターン形成の表面状態の転移が起こることが示された。すなわち$b \leq b_c$の場合、DPは有効に誘起されない（**状態B**）。一方$b > b_c$の場合、効率よく誘起されAg堆積過程は自律的となる（**状態A**）。**状態A**ではAg薄膜は独特の表面形状となり、状態Bではシミュレーションを続ける限りランダムなAg堆積が続く。さらに臨界現象を持つ平衡第二次相転移との類推により状態Bから状態Aへの遷移が議論された。

このシミュレーションの結果、**状態A**において自律的に形成されたAg薄膜表面形状の構造が再現された。図7には状態Aにおける定常状態での表面上の２次元Ag塊の寸法の分布を示す。これは図7の下向き矢印で示す塊寸法(値は11付近)にピークをもっている。これは実験結果[5]と整合している。

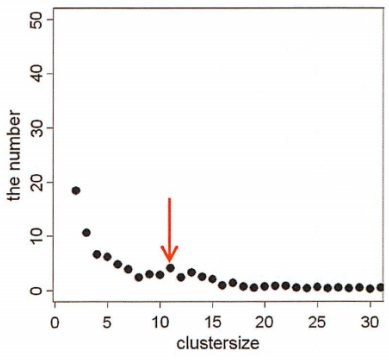

図７　状態 A における定常状態での表面上の２次元 Ag 塊の寸法の分布

以上のように数値シミュレーションの結果は実験結果と整合するが、次の問題が指摘されている。

(p1-1) DP の最大寸法は未考慮

(p1-2) 寸法依存共鳴の考慮の方法十分適当とは言えない。

3.2 シリコン発光素子の製作とデバイス動作

このデバイスが PB 効果を発現するのは B 原子の空間分布と配置が遺伝子の役割を担っているからである。すなわち「遺伝情報」である B 原子配置は DP 援用アニール照射光の波長や偏光に応じて自律的に応答し、PB を可能とする B 原子配置が形成され安定化する。B 原子配置の形成とそれに基づく発光の特性が複雑系科学に基づく数値シミュレーションによって次のように再現されている[16]。

B 原子が存在する層を有限寸法の二次元正方格子で表し、B 原子の熱拡散を、この格子上の複数の粒子のランダムウオークにより表した。二つの外部パラメータ I, P^0(各々順方向電流の大きさ、照射光の強度を表す)を導入し、次の数理モデルが考案された：

(ステップ 1)B 原子のランダムウオークの結果、格子上に長さ d(=3a)を持つ B 原子の対ができたと仮定する（a は Si 結晶の格子定数)。

この仮定のもとに各 B 原子対の位置において以下の**ステップ 2-7** に進む。

(ステップ 2) I に比例する平均値を持つポアッソン分布に従って、PB 効果に関与する電子の数を表す乱数 X を生成する。

(ステップ 3)PB 効果を示す光の強度 P^{PB} と上記の P^0 を足し合わせ、この値に比例した平均値を持つポアッソン分布に従い、ステップ 2 とは独立にもう一つの乱数 Y を生成する。これに自然放出光の強度も加えた値（$Y^*=Y+1$)を、PB 効果を示す仮想光子の数と見なす。

(ステップ 4)DP 援用アニールにおける電子数と光子数との釣り合い[7,17]を考慮し、

Z=min(X, I^*)を求める。これはB原子対に複製された光子の個数を表す。

(ステップ 5)以上の**ステップ 1-4** をすべての B 原子対に対して実行し、得られた Z の数を全て加え合わせ、その値を P^{PB} とする。

(ステップ 6)強度 P^{PB} をもつ複製された光は伝搬し、系の外にエネルギーを放出する。複製光子数 Z が 1 以上の B 原子対においては、B 原子対を形成していたランダムウォーカーはエネルギーを失い不活性化するとみなす。

(ステップ 7)依然として活性状態にあるランダムウォーカーをホッピングさせ、**ステップ 1** に戻る。

以上のステップでは格子上の長さ d(=3a)の B 原子対が形成されることがフォノン生成、および複製光子生成の過程を表す。この意味でこのステップそのものが DP とフォノンとの結合過程と考えられる。このステップが d(=3a)を持つ B 原子対という局所的な構造の上で巡回することが DP の局所性(湯川関数で表される)に対応する。

数値シミュレーションの結果は次のとおりである。

【製作】

図 8 は発光強度 P^{PB} の時間依存性を表す[18]。すなわち DP 援用アニール開始直後に指数関数的に増加し、振動を伴いながら大きな値を持つ平衡値に達し(領域 A)、その後は平衡値の周りで小さく揺らぐ（領域 B)。

【動作】

LED の動作時には P^{PB} の値は B 原子のランダムウオークは生じない。なぜならば動作のためには、製作時よりも小さな電流を流せばよいからである。その結果 B 原子対構造は凍結され存在し続け、その上で**ステップ 2-5** が繰り返される。

実験では偏光に関する PB 効果（DP 援用アニール時の照射光の偏光状態が動作時の発光の偏光状態に遺伝する効果）が確認されている[19]。この効果は上記**ステップ 3** で扱う仮想光子に二つの偏光成分を仮定し、正方格子上の B 原子対の配向き方向に応じて二つ

の独立なポアッソン分布を用いて二つの光子の発生個数を別々に数えることにより再現された。

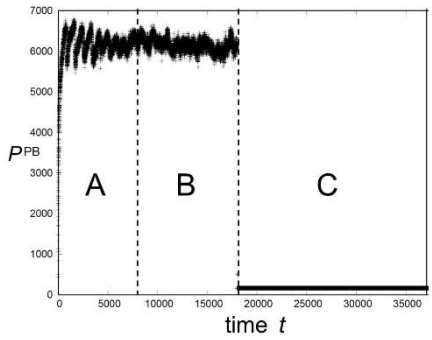

図 8　Si-LED に対する数値シミュレーションの結果
A. 製作時における過渡状態。B. 製作過程における平衡状態。C. 動作時。
使用した数値は：　製作過程では P^0=80、I=40。動作時では P^0=0、I=4。

以上の数値シミュレーションの結果は実験結果と整合するが、次の問題が指摘されている。

(p2-1) 二次元モデルである。

(p2-2) 温度や熱拡散といった既存の概念だけで PB 効果の詳細を説明することは適切でない。すなわち従来の熱力学には無かった視点（たとえば情報理論的な視点）も必要となる。

3.3 ナノドロップレットの製作とデバイス動作

2.3 節の実験により確認された次の現象が数値シミュレーションにより検討されている。

【製作】

NP の対形成の効率は

(1) 両 QD の寸法が等しい時に高い[12]（図 9(a)）

(2) 溶液が高温の方が高い[12]（図 9(b)）

事が確認された。(1) は寸法依存共鳴に起因し、(2) は二つの異種の NP(NP1, NP2) の遭遇の頻度が溶液中の NP のブラウン運動のランダムウォーク速度に依存することに起因している。

これらは実験結果と整合している。

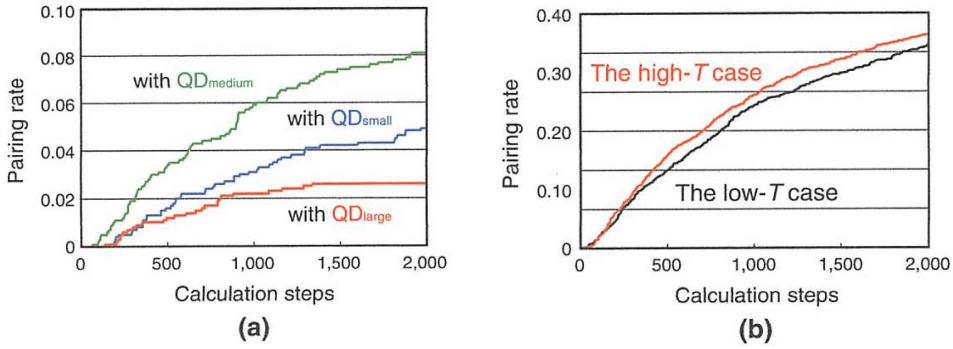

図9　二つの異種のNPの対形成率（参考文献[12]の図7）（横軸は時間）

(a)NP1に対するNP2の寸法への依存性。緑：両寸法等しい。青：NP2が大きい。赤:NP2が小さい。

(b)溶液の温度依存性。赤：高温。黒：低温。

【動作】

CdSe（NP1)の発光スペクトルのピークのシフト量がこのナノ粒子の寸法に依存する性質がNP対の形成率の時間依存性（図9(a),(b)）と整合することをもって、シミュレーションの正当性の根拠としている。

しかし上記の結果(1),(2)は数値シミュレーションをするまでもなく、実験結果を見れば推察できることを指摘したい。さらに次の問題が指摘されている。

(p3-1) 1次元モデルである。

(p3-2) 両NPの数が各々1つではなく、複数:複数の場合も扱う必要がある。

(p3-3) UV硬化高分子が次第に硬化するためにNPの速度が減速する現象を取り入れる必要がある。

(p3-4) DPエネルギー移動の際のDP運動量授受によりNP1がNP2から反発される事（反跳効果）を取り入れる必要がある。

4. 今後の方向

2.1 - 2.3 節の 3 つのデバイス（各々デバイス 1-3 と記す）の製作と動作では DP の生成、DP のエネルギーの空間局在性、DP のエネルギー移動の自律性、PB 効果などの特徴が顕著に表れている。これらのデバイス間の共通点は製作時に外部制御変数によって DP を効率よく生成し、DP の効果を最適化していることである。差異はデバイス 1 では外部制御変数によって関連するナノ粒子数が時間的に増加すること、一方デバイス 2,3 ではそれらが一定であることである。これらの共通点、差異を表 2 にまとめる。以下では、従来の数値シミュレーションの持つ問題、その解決のための指針について概説する。

表 2　三つのデバイスの製作、動作時の比較。

デバイス	ナノ物質	ナノ物質数の時間変化	ナノ物質の動き	制御のための外部物理量
1 (2.1 節)	Ag^+、Ag 塊	増加	Ag^+が Ag 塊表面に堆積 (Ag 塊寸法増加)	照射光、電圧
2 (2.2 節)	B 原子、B 原子対	不変	B 原子が対形成 (Si 結晶中)	照射光、電流
3 (2.3 節)	ナノ粒子 (NP) (CdSe, ZnO, CdS)	不変	NP が対*となり ND 形成	照射光、熱

4.1 従来の数値シミュレーションの持つ問題

従来の数値シミュレーションでは統計力学・熱力学という既存の理論(オンシェル科学、物質科学)をモデルの基礎とするのに留まっている。また、従来の数値シミュレーションで注目している相転移などの議論は統計力学の側からの興味に過ぎず、重要ではない。デバイス 1-3 に関する数値シミュレーションの持つ共通の問題は次のとおりである。

[1] 従来の数値シミュレーションでは自分流のモデルを使い、その結果が実験結果と合うように使用数値を選んでいる。いわゆるフィッテイングをしている。しかしここで要求さ

れるのは、「実験結果とよく合った」、ではなく

1.「ドレスト光子とは何か？」(DP の生成の起源と検出過程)

2.「ドレスト光子の特徴は？」(DP のエネルギー移動とその自律性の起源)

の問題を解くことである。これまではこの二点についての解は与えられていない。すなわち、DP の本質的問題（生成と消滅、空間・時間的特性、エネルギー移動の自律性）の解がない。

[2]より本質的な問題は「そもそもナノ物質間の DP による相互作用とは何か？」について答えていないことである。

[2]の答えが無い理由は次のとおり： オンシェル科学の概念ではこれに答えることはできない。なぜなら相互作用に関する理論は無いからである。すなわちオフシェル領域の電磁場はオンシェル領域の電磁場のモードの線形重ね合わせでは表されない。両者は全く別物である。今後はオフシェル科学が必要なのである。

4.2 解決のための指針

4.1 節の問題を解決するための指針を以下に提案する：

[1] 4.1 節の問題[1]の解を得るには DP の最大寸法に関する議論、3 次元モデルの構築、などが必要である。

[2] 4.1 節の問題[2]の解を得るには「相互作用」、「オフシェル科学」に注目した数値シミュレーションを進めるべきである。

[3] デバイス 1 の場合の問題(3.1 節末尾に記載)を解決するための第一歩として、 DP の有効ポテンシャルを表す湯川関数 $V_{\mathrm{eff}}(r) = e^{-r/\alpha}/r$ (相互作用長 α～ナノ物質（ここでは Ag

塊）の寸法）に、DP には最大寸法があることを表す関数

$1(\alpha)=1;\ \alpha \leqq \alpha_{DPmax}$、

$=0;\ \alpha > \alpha_{DPmax}$

α_{DPmax}：ＤＰの場の最大寸法（=50～70 nm: 実験結果[20]）（=38 nm: 計算結果[21]）

を組み合わせ $V_{eff}(r) = e^{-r/\alpha}/r \cdot 1(\alpha)$

とするのが有利である。

[4] デバイス 2 の場合の問題(3.2 節末尾に記載)を解決するための第一歩として、 モデルを 3 次元化する必要がある。

[5] デバイス 3 の場合の問題（3.3 節末尾に記載)を解決するための第一歩として、 NP 間の寸法依存共鳴の効果を考慮する必要がある。

4.3 オフシェル科学進展のための量子ウオーク（QW）モデルの採用

4.1 節の問題を解決するための数値シミュレーションの基礎として、最近 QW モデル[22]が検討されている。この数値シミュレーションが解くべき問題は次のとおりである。

[1] 無限自由度系に対するQWモデルを開拓しオフシェル科学の物理的現象の対応を明らかにする。

それと関連し、次の問題を解決する。

[2] 量子場の相互作用を明らかにする。

[3] 相互作用にはSpacelikeの縦波が必須なので、QWにこれを導入する。その糸口としてline graph[23]を活用するのが有利である。

[4] DP の有効ポテンシャルを表す湯川関数の絶対値のみでなく、位相に関する情報も取り

入れる。これにより 3.3 節末尾の反跳効果のみでなく、従来観測されている DP の力学的効果(運動量) *[24,25]の説明も可能となると期待される。

(*)真空中におかれたナノ物質の表面に生成される DP による自由運動原子の飛行方向の偏向、捕獲。

5. まとめ

本記事ではまずドレスト光子による新規なデバイス（特殊な表面形状の銀電極を持つ光起電力デバイス、Si 発光デバイス、ナノドロップレット）の製作とデバイス動作に関する実験結果を紹介した。ここでは数値シミュレーションに関連する話題のみを取り上げた。次にこれら 3 つのデバイスの製作、動作に関する数値シミュレーションについて概説した。これには統計力学、複雑系科学に基づくランダムウオークモデルを使った。さらにこれまでに行われた数値シミュレーションの問題を示し、その解決の方針を記した。特にナノ物質間の DP による相互作用に注目し、オフシェル科学に基づく三次元モデルを開発することが重要であることを主張した。その開発にはラングラフを足掛かりにした QW モデルを使うのが有望であろう。

文献

[1] M. Ohtsu, *Dressed Photons* (Springer, 2014).
[2] M. Ohtsu, I. Ojima, and H. Sakuma, “Dressed Photon as an Off-Shell Quantum Field,” *Progress in Optics* Vol.64, (ed. T.D. Visser) pp.45-97 (Elsevier, 2019).
[3] M. Ohtsu, “Embarking on theoretical studies for off-shell science guided by dressed photons,” *Off-shell Archive* (November 2018) Offshell: 1811R.001.v1. **DOI** Offshell: 1811R.001.v1, http://offshell.rodrep.org/?p=176
[4] M. Ohtsu, “Indications from dressed photons to macroscopic systems based on hierarchy and autonomy,” *Off-shell Archive* (June, 2019) Offshell: 1906R.001.v1. **DOI** 10.14939/1906R.001.v1, http://offshell.rodrep.org/?p=201
[5] S. Yukutake, T. Kawazoe, T. Yatsui, W. Nomura, K. Kitamura, M. Ohtsu, “Selective photocurrent generation in the transparent wavelength range of a semiconductor photovoltaic device using a phonon-assisted optical near-field process,” *Appl. Phys.* B **99**, 415 (2010) pp. 415-422.

[6] M. Ohtsu, *Silicon Light-Emitting Diodes and Lasers* (2016, Springer).
[7] M. Ohtsu and T. Kawazoe, "Principles and Practices of Si Light Emitting Diodes using Dressed Photons," *Off-shell Archive* (May 2018) Offshell: 1805R.001.v1. **DOI** Offshell: 1805R.001.v1, http://offshell.rodrep.org/?p=129
[8] M. Ohtsu and T. Kawazoe, "Principles and practices of Si light emitting diodes using dressed photons," *Advanced Materials Letters*, **10** (2019) pp.860-867.
[9] M. Ohtsu, "Dressed photon phenomena that demand off-shell scientific theories," *Off-shell Archive* (November 2019). Offshell: 1911R.001.v1. **DOI** Offshell: 1911R.001.v1, http://offshell.rodrep.org/?p=232
[10] N. Tate, Y. Liu, T. Kawazoe, M. Naruse, T. Yatsui, and M. Ohtsu, "Fixed-distance coupling and encapsulation of heterogeneous quantum dots using phonon-assisted photo-curing," *Appl. Phys.* B, **110** (2013) pp.39-45.
[11] N. Tate, Y. Liu, T. Kawazoe, M. Naruse, T. Yatsui, and M. Ohtsu, "Nanophotonic droplet: a nanometric optical device consisting of size- and number-selective coupled quantum dots," *Appl. Phys.* B, **110** (2013) pp.293-297.
[12] N. Tate, M. Naruse, Y. Liu, T. Kawazoe, T. Yatsui, and M. Ohtsu, "Experimental demonstration and stochastic modeling of autonomous formation of nanophotonic droplets," *Appl. Phys.* B, **112** (2013) pp.587-592.
[13] N. Tate, W. Nomura, T. Kawazoe, and M. Ohtsu, "Novel wavelength conversion with nanophotonic droplet consisting of coupled quantum dots,"*Opt. Express*, **22** (2014) pp.10262-10269.
[14] S. Sangu, K. Kobayashi, and M. Ohtsu, "Optical near fields as photon-matter interacting systems," *J. Microsc*. **202** (2001) pp.279-285.
[15] K. Takahashi, M. Katori, M. Naruse, and M. Ohtsu, *Appl. Phys.* B, **120** (2015) pp.247-254.
[16] M. Katori and H. Kobayashi, in *Prog. Nanophotonics* 4 (ed. by M. Ohtsu and T. Yatsui) (Springer, Heidelberg, 2017) pp.19-55.
[17] J. H. Kim, T. Kawazoe, and M. Ohtsu, "Optimization of dressed-photon—phonon-assisted annealing for fabricating GaP light-emitting diodes," *Appl. Phys*. A **121** (2015) pp.1395-1401.
[18] M. Ohtsu and M. Katori, "Complex System of Dressed Photons and Applications," *The Review of Laser Engineering*, **45** (2017) pp.139-143 (in Japanese).
[19] T. Kawazoe, K. Nishioka, and M. Ohtsu, "Polarization control of an infrared silicon light-emitting diode by dressed photons and analyses of the spatial distribution of doped boron atoms," *Appl. Phys.*A, **121** (2015) pp.1409-1415.
[20] M. Ohtsu and T. Kawazoe, "Experimental estimation of the maximum size of a dressed photon," *Off-shell Archive* (February 2018) Offshell: 1802R.001.v1. **DOI** 1802R.001.v1, http://offshell.rodrep.org/?p=98
[21] H. Sakuma, "On the problem of quantization of Clebsch dual field and a quantized representation of dressed photon," *Proc. of the Workshop on Basic Mathematic-Physical Studies on Dressed Photon* (ed. by T. Takiguchi), *Mathematics for Industry Research* No.14, Inst. Mathematics for Industry, Kyushu Univ., (February 2019) pp.127-148.
[22] H. Saigo, "Dressed Photon and Quantum Walk," *Abstracts of the 66th Jpn. Soc. Appl. Phys. Spring Meeting*, March 2019, Tokyo, Japan, paper number 10p-W621-13.
[23] E. Segawa, S. Sangu, and M. Ohtsu, "An expression for dressed photon by quantum walks on line graphs," *Abstracts of the 80th Jpn. Soc. Appl. Phys. Spring Meeting*, September 2019, Sapporo, Japan, paper number 19p-E314-5.
[24] H. Ito, T. Nakata, K. Sakaki, and M. Ohtsu, "Laser Spectroscopy of Atoms Guided by Evanescent Waves in Micron-Sized Hollow Optical Fibers," *Phys. Rev. Lett.* **76** (1996) pp.4500-4503.
[25] M. Ohtsu, "Near-Field Optical Atom Manipulation: Toward Atom Photonics," Chapter 11 in *Near-Field Nano/Atom Optics and Technology*, (Springer, Tokyo, 1998) pp.217-266.

[VII] AWARDS

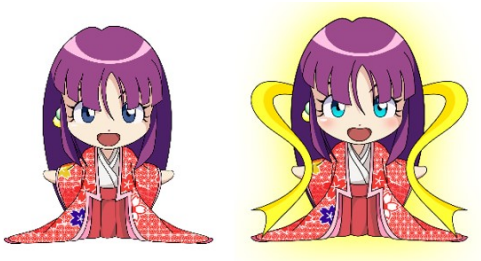

[VIII] APPENDIX

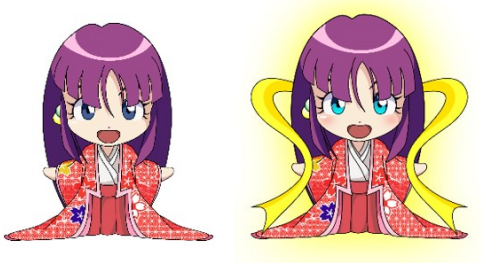

Quantum Walk and Dressed Photon

Misa Hamano
Nagahama Institute of Bio-Science and Technology
Nagahama, Japan
misa.flute617klfx@gmail.com

Hayato Saigo
Nagahama Institute of Bio-Science and Technology
Nagahama, Japan
harmoniahayato@gmail.com

A physical model called dressed photon, a composite system of photons and excitation of electrons in the nano-particles, is effectively used in the realm of near-field optics. Many interesting behaviors of dressed photons are known, especially the rapid energy transfer and the accumulation to singular points, e.g., points with strong dissipation. We propose a new modelling of dressed photons based on quantum walks, especially Grover walks on semi-infinite graphs which we call jellyfish graphs, and show a universal accumulation phenomena around the point with strong dissipation.

1 Introduction

The subject of this paper is to analyze the behavior of dressed photons [10] using quantum walks. In this section, we briefly review what quantum walks and dressed photons are, and then describes the structure of this paper.

Quantum walks are, in a nutshell, "quantum version of the random walk" (see [1], for example). More specifically, we generally consider the complex "probability amplitudes" and the unitary evolution of them. Here, the probability amplitude is a quantity which the probability can be obtained by squaring its absolute value, and the unitary evolution is the time evolution by a reversible linear mapping which keeps "sum of the squares of the absolute values of the probability amplitudes".

In general, the sum of the probabilities is normalized to be 1, but it is convenient not to normalize such a value when the quantum beam is constantly incident and emitted as the phenomena focused in this paper, and we simply call them "amplitudes". Where the square of the absolute value of amplitudes is high, the probability is relatively high.

Quantum walks seem to have an analogous definition to random walks, but in reality there are major differences in nature. For example, the average travel distance of a random walk is generally proportional to the "square root" of time, while that of a quantum walk is proportional to the time itself. Quantum walks are "rapid" compared to random walks. Because of this nature, quantum walks are considered as the basis for more efficient search and computing.

The quantum walk can also be seen as a toy model of the quantum field (see [2], for example). As is well known, quantum phenomena should be considered as the behaviors of fields as system with spatial and temporal extent, but in measurement they appear as local and particle-like phenomena. Mathematical models for such system are called "quantum fields", which is defined as a system of quantities spread from place to place, from which the expectation values of the measurements of those quantities are determined (for each interaction with the environment). Such a correspondence from quantity to expectation value is called "state". It is known that any state in this meaning can generally be expressed as a vector of Hilbert space. In short, a quantum field is considered as a system composed of algebras of physical quantities and states (or "local states" [7]) on them.

Quantum fields defined in this way are the most central concept in modern physics, but their analysis requires sophisticated mathematical techniques. It is also known that, apart from free fields, no such

G. Di Molfetta, V. Kendon & Y. Shikano (Eds.): 9th International Conference on Quantum Simulation and Quantum Walks (QSQW 2020)
EPTCS 315, 2020, pp. 93–99, doi:10.4204/EPTCS.315.9

non-trivial mathematical model can be constucted that satisfies the "seemingly natural" axioms.

Therefore, it is interesting to use "Quantum walk on the graph" in which the amplitude is defined on each arrow at each time as a simple model, breaking the basic properties assumed in the conventional quantum field theory. In particular, this modeling is suitable for modeling the light as a quantum field that interacts with nanoparticles called "dressed photon".

The dressed photon [10] is a useful concept to consider the behavior of a quantum field formed by combining a photon field and an electron (excitation of) field of a nanoparticle. It has an overwhelmingly larger number of modes (momentum and energy) than the incoming light itself. Of these modes, the momentum and energy "relatively high" modes manifest themselves as "a small grain of light" localized to the "interval" of the nanoparticle. This is the dressed photon ("relatively low" modes are thought to function as a kind of heat bath). Simply put, the dressed photons are a new kind of quantum created "between" nanoparticles when light combines with the nanoparticle system.

The main subject of this paper is to analyze the behavior of dressed photons using "Grover walks on jellyfish graphs" as a first step, or a toy model, toward such a theoretical foundation. After the preliminaries (section 2), modelling based on concepts such as jellyfish graphs and Grover walks on them are introduced in section 3. In section 4, the main theorem of the present paper are introduced based on these preparations. In Section 5, we discuss the physical meaning of the theorem.

2 Preliminaries

2.1 Directed Graph

Simply put, a directed graph is a figure consisting of "vertices" and "arrows" connecting them. Mathematically correct definition is as follows.

Definition 1 (Directed Graph) *A directed graph (or a digraph) G is a quadruple (V_G, A_G, o_G, t_G) composed of a set V_G, a set A_G, a mapping $o_G : A_G \longrightarrow V_G$ and a mapping $t_G : A_G \longrightarrow V_G$. The elements of V_G and of A_G are called vertices and arrows, respectively. For an arrow a, $o_G(a)$ is called the origin of a and $t_G(a)$ is called the target of a.*

With regard to directed graphs, the concept of "path" is important.

Definition 2 *A path in a directed graph G is a (finite) sequence of arrows $a_1, a_2, ..., a_n$ in G such that $o_G(a_{i+1}) = t_G(a_i)$ holds for any i. $o(a_1)$ is called the origin of the path and $t(a_n)$ is called the target of the path.*

In this paper, "connected" directed graphs play an important role. The connectivity of a graph is defined as follows using the concept of "path".

Definition 3 *A directed graph is called connected if for any two vertices v, v' there is some path whose origin is v and whose target is v'.* [1].

2.2 Symmetric Simple Directed Graph

This paper deals with "symmetric simple directed graphs". The symmetry and the simplicity of directed graphs are defined as follows:

[1] Although the notion of connectivity defined here is usually called "strongly connected", no confusion will be occurred by this abuse of the term for the kinds of graphs treated in the present paper.

Definition 4 *A directed graph $G = (V_G, A_G, o_G, t_G)$ is called symmetric if there exist a mapping $\bar{(\ )} : A_G \longrightarrow A_G$ such that $o_G(\bar{a}) = t_G(a), t_G(\bar{a}) = o_G(a)$ holds.*

Definition 5 *A directed graph $G = (V_G, A_G, o_G, t_G)$ is called simple if for any $v, v' \in V_G$ there exists at most one $a \in A_G$ such that $v = o_G(a), v' = t_G(a)$ hold and for any $a \in A_G$, $o_G(a) \neq t_G(a)$ holds.*

Hereafter, in this paper, "a graph" simply means "a symmetric simple directed graph". Such graph can also be considered as "a directed graph obtained from simple undirected graph by replacing each edge by the pair of opposite arrows". The notion of simple undirescted graph can be defined as follows:

Definition 6 *A pair of sets $\Gamma = (V_\Gamma, E_\Gamma)$ is called a simple undirected graph if any of elements of E_Γ is a set composed of two elements of V_Γ. An element of V_Γ is called a vertex of Γ, and an element of E_Γ is called an edge of Γ. An edge e is called incident to a vertex v if $v \in e$. The number of edges incident to a vertex v is called the degree of v and denoted as $deg(v)$.*

Since the graphs (symmetric simple directed graphs) can be considered as essentially the same as simple undirected graphs, we apply the terms originally defined for the latter to the former. Also, we often omit the indices indicating the name of graphs, especially for the targets and origins.

3 Modelling

3.1 Jellyfish Graphs

The main focus of this paper is quantum walks on a kind of graphs, called "jellyfish graphs" defined below, which is useful for constructing a toy model of the dressed photon phenomenon. In short, a jellyfish graph is a graph composed of a finite connected graph and a finite number of "half-line" attached to it. More precisely, it is defined as follows.

Definition 7 *A graph G is called a jellyfish graph if it is the union of a finite number of graphs*

$$G^{(0)}, l^{(1)}, l^{(2)}, ...$$

which satisfy the following conditions:

- *$G^{(0)}$ is finite connected graph, i.e., connected graph composed of a finite number of vertices and arrows. For simplicity, we identify the set of vertices with the set $\{1, 2, 3, ..., n\}$, where n denotes the number of vertices.*
- *Each $l^{(i)}$ is a half-line graph, i.e., a connected graph such that degree of any vertex v is 2 except for one vertex called the endvertex of $l^{(i)}$ which is the unique common vertex of $l^{(i)}$ and $G^{(0)}$.*

3.2 Quantum Walks on Jellyfish Graphs

A toy model of dressed photon phenomena can be formulated as a quantum walk on a jellyfish graph, based on the picture that the light is injected to a nanoparticle system from a distance, and it becomes a dressed photon between the nanoparticles for a while, and then emitted as light from there.

Although the term "jellyfish graph" itself is introduced in this paper, Feldman and Hillery already considered the discrete time quantum walk on this kind of graph[4] and continuous time quantum walk had been considered by Farhi and Gutmann[3]. Higuchi and Segawa [6] also study this type of graph and showed the following theorem (We modify the statement with our terminology).

Theorem 8 *Consider a quantum walk on jellyfish graph being free on each half-line $l^{(i)}$, i.e., a quantum walk satisfying the condition that for any arrow a in $l^{(i)}$ and any arrow a' in $l^{(i)}$ such that $o(a') = t(a), t(a') \neq o(a)$*

$$\psi_{t+1}(a') = \psi_t(a)$$

holds, where $\psi_t(a)$ and $\psi_{t+1}(a')$ denotes the amplitude of a and a' at the time t and $t+1$, respectively.

If such quantum walk starts from the initial condition with

- *constant amplitudes $\alpha^{(i)}$ on the arrows in each half-line $l^{(i)}$ directed to the end vertex*
- *amplitude* 0 *on other arrows*

then the amplitude $\psi_t(a)$ converges to the limit amplitude $\psi_\infty(a)$ when t tends to infinity.

3.3 Grover Walks on Jellyfish Graphs

The theorem above holds for general quantum walks. If we focus on the typical concrete quantum walks called Grover walks, we obtain more detailed results. Here, Grover walk means the quantum walk such that the amplitudes in time t of arrows $a, a', a'', ...$ with the common target determines the ones in time $t+1$ of $\bar{a}, \bar{a'}, \bar{a''}, ...$, and the relation ship between these amplitudes are given by

$$\begin{bmatrix} \beta \\ \beta' \\ \beta'' \\ \vdots \end{bmatrix} = \begin{bmatrix} 2/r-1 & 2/r & \cdots & 2/r \\ 2/r & 2/r-1 & \cdots & 2/r \\ \vdots & \vdots & \ddots & \vdots \\ 2/r & 2/r & \cdots & 2/r-1 \end{bmatrix} \begin{bmatrix} \alpha \\ \alpha' \\ \alpha'' \\ \vdots \end{bmatrix}$$

where r denotes the degree of the common vertex.

Physically speaking, the idea of a Grover walk corresponds to the idea of "scattering in the absence of potential" but it is also considered to be the first step in considering the energy transport of dressed photons (In the sense that we first consider the case where there is no potential, and then make corrections as necessary).

Higuchi and Segawa [6] showed the following fundamental theorem about the limit amplitudes of the Grover walks on jellyfish graphs.

Theorem 9 *Let $\alpha^{(i)}$ denotes the constant amplitude of a in $l^{(i)}$ and $\beta^{(i)} = \psi_\infty(\bar{a})$ denotes the limit amplitude of a, which is shown to be constant for each $l^{(i)}$. The relation between these amplitudes are given as follows:*

$$\begin{bmatrix} \beta^{(1)} \\ \beta^{(2)} \\ \beta^{(3)} \\ \vdots \end{bmatrix} = \begin{bmatrix} 2/r-1 & 2/r & \cdots & 2/r \\ 2/r & 2/r-1 & \cdots & 2/r \\ \vdots & \vdots & \ddots & \vdots \\ 2/r & 2/r & \cdots & 2/r-1 \end{bmatrix} \begin{bmatrix} \alpha^{(1)} \\ \alpha^{(2)} \\ \alpha^{(3)} \\ \vdots \end{bmatrix}$$

Simply put, this theorem means that when viewed "from far away and after enough time", the nanoparticle system itself appears to be as if a "vertex" of the Grover walk, with the half-line viewed as if the arrows incident to the vertex.

In [6], the following "Kirchhoff type" theorem is also proved:

Theorem 10 *Let $J(a)$ be the quantity defined as*

$$J(a) := \psi_\infty(a) - ave(\alpha^{(1)}, \alpha^{(2)}, \cdots, \alpha^{(m)}),$$

where $ave(\alpha^{(1)}, \alpha^{(2)}, \cdots, \alpha^{(m)})$ denotes the average of $\alpha^{(1)}, \alpha^{(2)}, \cdots, \alpha^{(m)}$. The following equations hold:

- $J(a) + J(\bar{a}) = 0$.
- *For any $v \in V_G$,* $\sum_{a \in A_G, t(a)=v} J(a) = 0$.

This is nothing but the "Kirchhoff's current law" for the quantity $J(a)$. Similarly, a law corresponding to the "Kirchhoff's voltage law" is also shown, but it is omitted here. It is important to note that these law on $J(a)$ allows us to calculate the limit amplitudes.

In the next section, we use the theorem introduced in this section to describe a new theorem for the limit amplitudes of quantum walks on jellyfish graphs.

4 Result

We made the following speculation based on the physical insight of the dressed photons and the analogy with the quantum walk:

> Consider the Grover walk on a jellyfish graph with the initial amplitudes $\alpha^{(1)}, \alpha^{(2)}, ...\alpha^{(m-1)}$ on the arrows in $l^{(1)}....l^{(m-1)}$ directed to $G^{(0)}$. Then the difference between the sum of the square of the absolute value of limit amplitudes on arrows into a vertex and the one on arrows out of it, which will correspond to the (not normalized) probability "around the vertex", will be maximized at the vertex with the maximum sum of the amplitudes of arrow out of it into the exterior of $G^{(0)}$.

Based on this speculation, we obtain the following simple theorem. The physical meaning of quantity $P^0(v)$ defined in the statement is the net amplitude of dressed photon around the vertex v (For the detailed physical interpretation of the theorem, see the next section) .

Theorem 11 *Let $P^{(0)}(v)$ be the quantity defined as*

$$P^{(0)}(v) = \sum_{t(a)=v, a \in G^{(0)}} |\psi(a)|^2 - \sum_{t(a)=v, a \in G^{(0)}} |\psi(\bar{a})|^2.$$

For any $v \in V_{G^{(0)}}$

$$P^{(0)}(v) = 4ave(\alpha^{(1)}, \alpha^{(2)}, \cdots, \alpha^{(m)}) J^{out}(v)$$

holds, where $\alpha^{(1)}, \alpha^{(2)}, \cdots, \alpha^{(m)}$ are real numbers and $J^{out}(v)$ denotes the quantity defined as

$$J^{out}(v) = \sum_{o(a)=v, a \in G/G^{(0)}} J(a)$$

which is equal to $\sum_{t(a)=v, a \in G^{(0)}} J(a)$ *by Kirchhoff's law.*

Proof.

Let us denote $ave(\alpha^{(1)}, \alpha^{(2)}, \cdots, \alpha^{(m)})$ as ave.

$$
\begin{aligned}
&P^{(0)}(v) = \sum_{t(a)=v, a\in G^{(0)}} |\psi(a)|^2 - \sum_{t(a)=v, a\in G^{(0)}} |\psi(\bar{a})|^2 \\
&= \sum_{t(a)=v, a\in G^{(0)}} \{|J(a)+ave|^2 - |-J(a)+ave|^2\} \\
&= \sum_{t(a)=v, a\in G^{(0)}} \{(J(a)^2 + 2J(a)ave + ave^2) - (J(a)^2 - 2J(a)ave + ave^2)\} \\
&= \sum_{t(a)=v, a\in G^{(0)}} \{J(a)^2 + 2J(a)ave + ave^2 - J(a)^2 + 2J(a)ave - ave^2\} \\
&= \sum_{t(a)=v, a\in G^{(0)}} 4J(a)ave \\
&= 4ave \sum_{t(a)=v, a\in G^{(0)}} J(a) \\
&= 4aveJ^{out}(v) = 4ave(\alpha^{(1)}, \alpha^{(2)}, \cdots, \alpha^{(m)})J^{out}(v). \quad \blacksquare
\end{aligned}
$$

Remark 12 *We can easily generalize the theorem and proof above for any complex amplitudes.(Omitted here for simplicity.)*

5 Discussion

Let us consider the physical meaning of the theorem above.

Quantum walks on jellyfish graphs are considered to correspond to a physical model in which light enters a nanoparticle system from a distance, becomes a dressed photon for a while, and then emitted into far field.

If this modeling is appropriate, then the above theorem means:

Dressed photons cluster around vertices that emit a large amount of outflow into the distance.

In other words, the dressed photons gather "in a self-compensating manner" where there is a large "dissipation"(into the far field).

In fact, many phenomena being coherent to the result above have been confirmed experimentally. For example, a fiber probe used as a "generator" of the dressed photons receives light from its root and emits light to the external environment mostly at its surface, especially at its tip, where it is experimentally known that the density of dressed photons are known highest[5].

Similarly, when visible light (not ultraviolet light,) enters the surface of a substance in contact with a gas such as chlorine or oxygen, a chemical reaction that cannot occur at the original frequency due to low energy occurs at the tip of a nanostructure similar to a fiber probe, and the sharp part is polished autonomously[9]. It has also been put to practical use as a nanometer scale polishing technology. Another example is a device called "optical nanofountain" that uses nanoparticles of different sizes[8]. By limiting the place where the light is emitted, energy is allowed to flow into the place autonomously by the movement of the dressed photons. If we assume that modeling as a quantum walk on a jellyfish graph is appropriate, these phenomena can be understood as a consequence of the theorem presented above, not only qualitatively but also quantitatively.

On the other hand, these phenomena cannot be understood as "random walk". This is because when we consider the "random walk" on a jellyfish graph, the probability in the limits is equal on all edges (The amount J is, so to speak, the amount of deviation from "random walk" and it can be said that it measures

a kind of "symmetry breaking"). Then, only the number of edges to which the vertices are connected, or "degree" is important, which contradicts the importance of dissipation. This also contradicts the fact that the density of the dressed photons is high at "vertices with rather small degrees", such as the endpoints. These phenomena suggest that the model of quantum walk on a jellyfish graph is appropriate for the analysis of the behavior of dressed photons.

Acknowledgment

The authors thank Prof. Motoichi Ohtsu and Prof. Izumi Ojima for the fruitful discussions on dressed photons and quantum fields. They also thank Mr. Suguru Sangu and Mr. Etuso Segawa for the discussions on the modelling by quantum walks. This work was supported by Research Origin for Dressed Photon.

References

[1] A. Ambainis (2003): *Quantum walks and their algorithmic applications*. International Journal of Quantum Information 1(4), pp. 507–518, doi:10.1142/S0219749903000383. Available at https://arxiv.org/abs/quant-ph/0403120.

[2] G.M. D'Ariano (2012): *Physics as quantum information processing: Quantum fields as quantum automata*. Phys. Lett. A 376, p. 697702, doi:10.1016/j.physleta. Available at https://arxiv.org/abs/1110.6725.

[3] E. Farhi & S. Gutmann (1998): *Quantum computation and decision trees*. Phys. Rev. A 58, p. 915928, doi:10.1103/PhysRevA.58.915. Available at https://arxiv.org/abs/quant-ph/0403120.

[4] E. Feldman & M. Hillery (2005): *Quantum walks on graphs and quantum scattering theory*. Contemp. Math. 381, p. 7196, doi:10.1090/conm/381/07092. Available at https://arxiv.org/abs/quant-ph/0403066.

[5] V. Polonski Y. Yamamoto M. Kourogi H. Fukuda & M. Ohtsu (1999): *Nanometric patterning of zinc by optical near-field photochemical vapour deposition*. Journal of Microscopy 194(2-3), pp. 545–551, doi:10.1046/j.1365-2818.1999.00497.x. Available at https://onlinelibrary.wiley.com/doi/abs/10.1046/j.1365-2818.1999.00497.x.

[6] Yu. Higuchi & E. Segawa (2019): *A dynamical system induced by quantum walk*. Journal of Physics A: Mathematics and Theoretical 52(39), p. 697702, doi:10.1088/1751-8121/ab370b. Available at https://arxiv.org/abs/1812.04730h.

[7] K. Okamura I. Ojima & H. Saigo (2016): *Local State and Sector Theory in Local Quantum Physics*. Letters in Mathematical Physics 106(6), pp. 741–763, doi:10.1007/s11005-016-0841-y. Available at https://arxiv.org/abs/1501.00234.

[8] T. Kawazoe K. Kobayashi & M. Ohtsu (2005): *Optical nanofountain: A biomimetic device that concentrates optical energy in a nanometric region*. Applied Physics Letters 86(10), p. 103102, doi:10.1063/1.1875734. Available at https://aip.scitation.org/doi/10.1063/1.1875734.

[9] T. Yatsui W. Nomura M. Naruse & M. Ohtsu (2012): *Realization of an atomically flat surface of diamond using dressed photonphonon etching*. Journal of Physics D: Applied Physics 45(47), p. 475302, doi:10.1088/0022-3727/45/47/475302. Available at https://iopscience.iop.org/article/10.1088/0022-3727/45/47/475302.

[10] M. Ohtsu (2014): *Dressed Photons*. Springer-Verlag, Berlin Heiderberg, doi:10.1007/978-3-642-39569-7.

2020 International Symposium on Nonlinear Theory and Its Applications,
NOLTA2020, Virtual, November 16-19, 2020

On the measurement of dressed photon

Kazuya Okamura† ‡

†Research Origin for Dressed Photon, 3-13-19 Moriya-cho Kanagawa-ku, Yokohama, 221-0022, Japan
‡Graduate School of Informatics, Nagoya University, Furo-cho, Chikusa-ku, Nagoya 464-8601, Japan
Email: k.okamura.renormalizable@gmail.com

Abstract—Quantum measurement theory has been studied since Heisenberg and von Neumann. I propose an extension of quantum measurement theory to describe measuring processes of dressed photons. To perform such an attempt, I use a mathematical modeling of dressed photons. The unstable aspects of dressed photons are used for measurement.

1. Introduction

In this paper, we discuss the modeling and measurement process of dressed photons (See [1] for details on dressed photons). In other words, our goal is to formulate interacting systems between the electromagnetic field and nonuniform materials at scales below the wavelength, and to systematize the measurement theory for them. We adopt the concept of "local net" to formulate quantum fields as a starting point for this attempt. In algebraic quantum field theory (AQFT) [2, 3], a family of algebras of observables in bounded regions is called a local net. We then adopt the formulation of the measurement in terms of "completely positive (CP) instruments" defined on C*-algebras. An instrument introduced by Davies and Lewis [4] is a map describing probability weighted state changes caused by the measurement, which is compatible with the statistical aspect of the measurement. It is known that every CP instrument, its special case, can be modeled by a quantum system. In the future, it is necessary to describe the measurement consistent with the description of dressed photon as an open system, but in the paper, we aim to establish a C*-algebraic formulation, which is an extension of previous theoretical investigations, as a first step.

2. Local nets and Open system

2.1. C*-algebraic quantum theory

As mentioned in [5], all the statistical aspects of a physical system **S** are registered in a C*-probablity space $(\mathcal{X}, \omega)$. Observables of **S** are described by self-adjoint elements of the C*-algebra $\mathcal{X}$. On the other hand, the state ω on $\mathcal{X}$ statistically correponds to a physical situation (or an experimental setting) of **S**. We state that every quantum system is described in the language of noncommutative (quantum) probability theory (See [6] for an introduction to noncommutative probability theory, and [7, 8] for details on operator algebras).

2.2. Local net and open system

To begin with, we define the concept of local net in order to describe quantum fields algebraically.

We suppose that M is a manifold or a graph. M describes the space-time or the space under consideration. $\mathcal{R}$ denotes the set of bounded regions of M, which satisfies $\cup\mathcal{R} = M$. $M \in \mathcal{R}$ is assumed when M is bounded.

Definition 1 (local net)**.** *A family $\{\mathcal{A}(O)\}_{O\in\mathcal{R}}$ of C*-algebras are called a local net on M if it satisfies the following conditions:*
(*i*) *For every inclusion $O_1 \subset O_2$, we have $\mathcal{A}(O_1) \subset \mathcal{A}(O_2)$.*
(*ii*) *For O_1 and O_2 are causally separated, then* $[\mathcal{A}(O_1), \mathcal{A}(O_2)] = \{AB - BA | A \in \mathcal{A}(O_1), B \in \mathcal{A}(O_2)\} = \{0\}$.

For every local net $\{\mathcal{A}(O)\}_{O\in\mathcal{R}}$ on M, there exists a C*-algebra

$$\mathcal{A} = \overline{\bigcup_{O\in\mathcal{R}} \mathcal{A}(O)}^{\|\cdot\|}, \tag{1}$$

called the global algebra of $\{\mathcal{A}(O)\}_{O\in\mathcal{R}}$. If M is bounded, then $\mathcal{A} = \mathcal{A}(M)$ since $M \in \mathcal{R}$ and $O \subset M$ for all $O \in \mathcal{R}$. To describe the statistical aspect of quantum fields by a local net $\{\mathcal{A}(O)\}_{O\in\mathcal{R}}$, states on the global algebra $\mathcal{A}$ or "local states" [9] are used.

In describing the measurement of dressed photons, only the use of the local net first adopted is not enough. In fact, to detect (the effect of) dressed photons, we need an operation that we bring some probe closer to the spatial scale at which dressed photons are generated. We introduce an extension of a local net to mathematically describe the operation.

Definition 2. *Let $\{\mathcal{A}(O)\}_{O\in\mathcal{R}_1}$ and $\{\mathcal{B}(O)\}_{O\in\mathcal{R}_2}$ be local nets on M_1 and M_2, repectively. $\{\mathcal{B}(O)\}_{O\in\mathcal{R}_2}$ is an extension of $\{\mathcal{A}(O)\}_{O\in\mathcal{R}_1}$ if it satisfies the following conditions:*
(*i*) $M_1 \subset M_2$. (*ii*) $\mathcal{R}_1 \subset \mathcal{R}_2$. (*iii*) $\forall O \in \mathcal{R}_1$, $\mathcal{A}(O) \subset \mathcal{B}(O)$.

The reason why we use extensions of a local net is that the construction of the composite system of the system of interest and a measuring apparatus is not so simple. In particular, the construction of the composite system by the tensor product is not always applicable to quantum fields.

3. Completely positive instrument

Here, we analyze the concept of CP instrument defined on C*-algebra. In previous investigations [4, 10, 11, 12], it has been examined in the von Neumann algebraic formulation. The generalization to C*-algebra is realized in terms of central subspaces of the dual of a C*-algebra. Our approach enables us to unify the measurement theory with sector theory developed by Ojima [13, 14].

3.1. Definition

Let $\mathcal{X}$ be a C*-algebra and $(\pi, \mathcal{H})$ a representation of $\mathcal{X}$. Let $\mathcal{M}$ be a von Neumann algebra on a Hilbert space $\mathcal{K}$. $\mathcal{Z}(\mathcal{M})$ denotes the center of $\mathcal{M}$. $\mathcal{M}_*$ denotes the set of ultraweakly continuous linear functionals on $\mathcal{M}$.

A subspace $\mathcal{L}$ of $\mathcal{X}^*$ is called a central subspace of $\mathcal{X}^*$ if there exists a central projection C of $\mathcal{X}^{**}$, i.e., $C \in \mathcal{Z}(\mathcal{X}^{**})$, such that $\mathcal{L} = C\mathcal{X}^*$. A central subspace $\mathcal{L}(= C\mathcal{X}^*)$ is said to be σ-finite if its dual $\mathcal{L}^*(\cong C\mathcal{X}^{**})$ is a σ-finite W^*-algebra.

Example 3 (See [8, Chapter III] for example)**.** *Let $\mathcal{M}$ be a von Neumann algebra on a Hilbert space $\mathcal{H}$. There exists a central projection C of $\mathcal{M}^{**}$ such that $\mathcal{M}_* = C\mathcal{M}^*$.*

Let $\mathcal{M}$ and $\mathcal{N}$ be W^*-algebras. $P(\mathcal{M}_*, \mathcal{N}_*)$ denotes the set of positive linear maps of $\mathcal{M}_*$ into $\mathcal{N}_*$. Also, $\langle \cdot, \cdot \rangle$ denotes the pairing of $\mathcal{M}_*$ and $\mathcal{M}$.

Definition 4 (instrument)**.** *Let $\mathcal{X}$ be a C*-algebra and $(S, \mathcal{F})$ a measurable space. $\mathcal{I}$ is called an instrument for $(\mathcal{X}, S)$ if it satisfies the following three conditions:*
(1) *$\mathcal{I}$ is a map of $\mathcal{F}$ into $P(\mathcal{V}_{\text{in}}, \mathcal{V}_{\text{out}})$ for some σ-finite central subspaces $\mathcal{V}_{\text{in}}$, $\mathcal{V}_{\text{out}}$.*
(2) *$\langle \mathcal{I}(S)\rho, 1\rangle = \langle \rho, 1\rangle$ for all $\rho \in \mathcal{V}_{\text{in}}$.*
(3) *For every $\rho \in \mathcal{V}_{\text{in}}$, $M \in \mathcal{V}_{\text{out}}^*$ and mutually disjoint sequence $\{\Delta_j\}_{j\in\mathbb{N}}$ of $\mathcal{F}$, $\langle \mathcal{I}(\cup_j \Delta_j)\rho, M\rangle = \sum_{j=1}^{\infty} \langle \mathcal{I}(\Delta_j)\rho, M\rangle$. An instrument $\mathcal{I}$ for $(\mathcal{X}, S)$ is said to be completely positive (CP) if $\mathcal{I}(\Delta)$ is completely positive for all $\Delta \in \mathcal{F}$.*

When we would like to emphasize that an instrument $\mathcal{I}$ for $(\mathcal{X}, S)$ is a map of $\mathcal{F}$ into $P(\mathcal{V}_{\text{in}}, \mathcal{V}_{\text{out}})$, we say that $\mathcal{I}$ is an instrument for $(\mathcal{X}, \mathcal{V}_{\text{in}}, \mathcal{V}_{\text{out}}, S)$. In particular, when $\mathcal{V}_{\text{in}} = \mathcal{V}_{\text{out}} = \mathcal{V}$, it is called an instrument for $(\mathcal{X}, \mathcal{V}, S)$

For every CP instrument $\mathcal{I}$ for $(\mathcal{X}, \mathcal{V}_{\text{in}}, \mathcal{V}_{\text{out}}, S)$ and normal state φ on $\mathcal{V}_{\text{in}}^*$, we define the probability measure $\|\mathcal{I}\varphi\|$ on $(S, \mathcal{F})$ by $\|\mathcal{I}\varphi\|(\Delta) = \|\mathcal{I}(\Delta)\varphi\|$ for all $\Delta \in \mathcal{F}$.

For every instrument $\mathcal{I}$ for $(\mathcal{X}, S)$, the dual map $\mathcal{I}^* : \mathcal{V}_{\text{out}}^* \times \mathcal{F} \to \mathcal{V}_{\text{in}}^*$ of $\mathcal{I}$ is defined by $\langle \mathcal{I}(\Delta)\rho, M\rangle = \langle \rho, \mathcal{I}^*(M, \Delta)\rangle$ for all $\rho \in \mathcal{V}_{\text{in}}$, $M \in \mathcal{V}_{\text{out}}^*$ and $\Delta \in \mathcal{F}$. From now on, $\mathcal{I}$ denotes the dual map $\mathcal{I}^*$ of an instrument $\mathcal{I}$ for $(\mathcal{X}, S)$.

3.2. Central decomposition of states via CP instrument

Let $C : \mathcal{F} \to \mathcal{Z}(\mathcal{V}^*)$ be a projection valued measure (PVM). A CP instrument $\mathcal{I}_C$ for $(\mathcal{X}, \mathcal{V}, S)$ is defined by $\mathcal{I}_C(\Delta)\rho = C(\Delta)\rho$ for all $\rho \in \mathcal{V}$ and $\Delta \in \mathcal{F}$.

For every $M_1, M_2 \in \mathcal{V}^*$ and $\rho \in \mathcal{V}$, we define $M_1\rho M_2 \in \mathcal{V}$ by $\langle M_1\rho M_2, M\rangle = \langle \rho, M_2 M M_1\rangle$ for all $M \in \mathcal{V}^*$.

Theorem 5. *$\mathcal{I}_C$ satisfies the following conditions:*
(1) *$\mathcal{I}_C(S)\rho = \rho$ for all $\rho \in \mathcal{V}$.*
(2) *It is repeatable, i.e., it satisfies $\mathcal{I}_C(\Delta)\mathcal{I}_C(\Gamma) = \mathcal{I}_C(\Delta\cap\Gamma)$ for all $\Delta, \Gamma \in \mathcal{F}$.*
(3) *For every $\rho \in \mathcal{V}_+ := \mathcal{V} \cap \mathcal{X}_+^*$ and $\Delta \in \mathcal{F}$, $\mathcal{I}_C(\Delta)\rho$ and $\mathcal{I}_C(\Delta^c)\rho$ are mutually disjoint.*
(4) *For every $\Delta \in \mathcal{F}$, $\mathcal{I}_C(\Delta)$ is $\mathcal{V}^*$-bimodule map, i.e., for every $\Delta \in \mathcal{F}$, $\rho \in \mathcal{V}$ and $M_1, M_2 \in \mathcal{V}^*$,*

$$\mathcal{I}_C(\Delta)(M_1\rho M_2) = M_1(\mathcal{I}_C(\Delta)\rho)M_2. \tag{2}$$

Conversely, if an instrument $\mathcal{I}$ for $(\mathcal{X}, \mathcal{V}, S)$ satisfies the conditions (2) *and* (4)*, then there exists a spectral measure $C : \mathcal{F} \to \mathcal{Z}(\mathcal{V}^*)$ such that $\mathcal{I} = \mathcal{I}_C$.*

An instrument $\mathcal{I}$ for $(\mathcal{X}, \mathcal{V}, S)$ is said to be subcentral if it satisfies the conditions (2) and (4) in Theorem 5. An instrument $\mathcal{I}$ for $(\mathcal{X}, \mathcal{V}, S)$ is said to be central if it is the maximum in the set of subcentral instruments for $(\mathcal{X}, \mathcal{V}, S)$, where the maximum is due to the (pre)order $\prec$ on instruments defined as follows: For instruments $\mathcal{I}_1$, $\mathcal{I}_2$ for $(\mathcal{X}, \mathcal{V}, S_1)$ and $(\mathcal{X}, \mathcal{V}, S_2)$, respectively, $\mathcal{I}_1 \prec \mathcal{I}_2$ if $\mathcal{I}_1\rho \subset \mathcal{I}_2\rho$ for all $\rho \in \mathcal{S}(\mathcal{X}) \cap \mathcal{V}$, where $\mathcal{I}_i\rho$, $i = 1, 2$, is the subset of $\mathcal{V}_+$ defined by $\mathcal{I}_i\rho = \{\mathcal{I}_i(\Delta_i)\rho \mid \Delta_i \in \mathcal{F}_i\}$.

Theorem 6. *$\mathcal{I}_C$ is central if and only if the abelian von Neumann algebra generated by $\{C(\Delta) \mid \Delta \in \mathcal{F}\}$ is isomorphic to $\mathcal{Z}(\mathcal{V}^*)$.*

By [7, Theorem 4.1.25], for every state ω on $\mathcal{X}$, there exist a probability Borel measure μ_ω on $\mathcal{S}(\mathcal{X})$ and a *-isomorphism $\kappa_\omega : L^\infty(\mathcal{S}(\mathcal{X}), \mu_\omega) \to \mathcal{Z}_\omega(\mathcal{X})$ such that

$$\langle \Omega_\omega | \kappa_\omega(f)\pi_\omega(X)\Omega_\omega\rangle = \int_{\mathcal{S}(\mathcal{X})} f(\rho)\, \hat{X}(\rho)\, d\mu_\omega(\rho) \tag{3}$$

for all $f \in L^\infty(\mathcal{S}(\mathcal{X}), \mu_\omega)$ and $X \in \mathcal{X}$, where $\hat{X}(\rho) = \rho(X)$ for all $\rho \in \mathcal{X}^*$ and $\mathcal{Z}_\omega(\mathcal{X}) = \pi_\omega(\mathcal{X})'' \cap \pi_\omega(\mathcal{X})'$. μ_ω is called the central measure of ω. We then have the following.

Theorem 7. *Let $\mathcal{V}$ be a σ-finite central subspace of $\mathcal{X}^*$. For every normal faithful state ω on $\mathcal{V}^*$, there exists a central instrument $\mathcal{I}$ for $(\mathcal{X}, \mathcal{V}, \mathrm{supp}(\mu_\omega))$ such that $\|\mathcal{I}\omega\| = \mu_\omega$.*

This theorem shows that the central decomposition of a state is given by a central instrument, and that the concept of sector is also natural in quantum measurement theory. The author thinks that the concept of posterior states [15, 11] is applicable to sector theory beyond the above theorem.

3.3. Measuring processes

A measuring process is a quantum mechanical modeling of the probe part of a measuring apparatus and is defined as follows.

Definition 8 (Measuring process)**.** *A 4-tuple $\mathbb{M} = (\mathcal{K}, \sigma, E, U)$ is called a measuring process for $(\mathcal{X}, \mathcal{V}, S)$*

if it satisfies the following conditions: (1) $\mathcal{K}$ *is a Hilbert space.* (2) σ *is a normal state on* $\mathbb{B}(\mathcal{K})$. (3) $E : \mathcal{F} \to \mathbb{B}(\mathcal{K})$ *is a spectral measure.* (4) U *is a unitary operator on* $\mathcal{H}\otimes\mathcal{K}$. (5) $\{\mathcal{I}_{\mathbb{M}}(M,\Delta) \mid M \in \mathcal{V}^*, \Delta \in \mathcal{F}\} \subset \mathcal{V}^*$, *where* $\mathcal{V}$ *is a* σ*-finite central subspace of* $\mathcal{X}^*$, $\mathcal{H}$ *is a Hilbert space on which faithfully represents elements of* $\mathcal{V}^*$ *as bounded operators and* $\mathcal{I}_{\mathbb{M}} : \mathbb{B}(\mathcal{H}) \times \mathcal{F} \to \mathbb{B}(\mathcal{H})$ *is defined by*[1] $\mathcal{I}_{\mathbb{M}}(X,\Delta) = (\mathrm{id}\otimes\sigma)[U^*(X\otimes E(\Delta))U]$ *for all* $X \in \mathbb{B}(\mathcal{H})$ *and* $\Delta \in \mathcal{F}$.

An instrument $\mathcal{I}$ for $(\mathcal{X}, S)$ is said to be discrete if there exist a countable subset S_0 of S and $T : S_0 \to P(\mathcal{V}_{\mathrm{in}}, \mathcal{V}_{\mathrm{out}})$ such that $\mathcal{I}(\Delta) = \sum_{s\in S_0\cap\Delta} T(s)$ for all $\Delta \in \mathcal{F}$. The following theorem gives the necessary and sufficient condition for the realization of a central instrument by a measuring process.

Theorem 9. *Let* $(S,\mathcal{F})$ *be a standard Borel space. A repeatable CP instrument for* $(\mathcal{X},\mathcal{V},S)$ *is realized by a measuring process for* $(\mathcal{X},\mathcal{V},S)$ *if and only if is discrete.*

4. Discussion and perspective

We have discussed local net, its extension, and CP instruments defined on C*-algebras. In the setting of AQFT, we use a local net $\{\mathcal{A}(O)\}_{O\in\mathcal{R}_1}$ on a space M_1 in order to describe the dressed photon phenomena. However, as mentioned before, we have to use extensions of $\{\mathcal{A}(O)\}_{O\in\mathcal{R}_1}$ to detect (the effect of) dressed photons.

Let $\{\mathcal{B}(O)\}_{O\in\mathcal{R}_2}$ be a local net on M_2 and an extension of $\{\mathcal{A}(O)\}_{O\in\mathcal{R}_1}$. Here, we suppose that M_1 is bounded and M_2 is unbounded. described by $\{\mathcal{B}(O)\}_{O\in\mathcal{R}_2}$. The composite system of the original system and a probe, which is close to the original system on the spatial scale where dress photons are generated, is described by $\{\mathcal{B}(O)\}_{O\in\mathcal{R}_2}$ as a quantum field. Furthermore, the material system, which is part of the composite system, is assumed to be localized in the neighborhood of M_1. In the composite system, the generation and annihilation of dressed photons constantly occur near non-uniform materials in the unstable situation where light continues to incident constantly. By measuring the emitted light at regions far from M_1, we check (or estimate) the effect of dressed photons generated in M_1.

In the future, we should realize the description of the measurement by CP instruments when the composite system is treated as an open system. Moreover, constructing the concrete model of dressed photons is a future task in order to connect experiments of dressed photons with the theory.

Acknowledgments

This work is supported by Research Origin for Dressed Photon.

[1] Let $\mathcal{M}$ and $\mathcal{N}$ be von Neumann algebras. For every $\sigma \in \mathcal{N}_*$, we define $\mathrm{id}\otimes\sigma : \mathcal{M}\,\overline{\otimes}\,\mathcal{N}$ by $\langle\rho\otimes\sigma, X\rangle = \langle\rho, (\mathrm{id}\otimes\sigma)(X)\rangle$ for all $\rho \in \mathcal{M}_*$ and $X \in \mathcal{M}\,\overline{\otimes}\,\mathcal{N}$.

References

[1] M. Ohtsu, *Dressed Photons*, (Springer, Berlin, 2014).

[2] H. Araki, *Mathematical theory of quantum fields*, (Oxford UP, Oxford, 1999).

[3] R. Haag, *Local quantum physics: Fields, Particles, Algebras*, 2nd ed., (Springer, Berlin, 2012).

[4] E.B. Davies & J.T. Lewis, "An operational approach to quantum probability," *Commun. Math. Phys.* **17** (1970), 239–260.

[5] I. Ojima, K. Okamura & H. Saigo, "Derivation of Born Rule from Algebraic and Statistical Axioms," *Open Sys. Inform. Dyn.* **21** (2014), 1450005.

[6] A. Hora & N. Obata, *Quantum probability and spectral analysis of graphs*, (Springer, Berlin, 2007).

[7] O. Bratteli & D. W. Robinson, *Operator Algebras and Quantum Statistical Mechanics* Vol.1 (2nd printing of 2nd ed.), (Springer, 2002).

[8] M. Takesaki, *Theory of Operator Algebras I*, (Springer, Berlin, 1979).

[9] I. Ojima, K. Okamura & H. Saigo, "Local state and sector theory in local quantum physics," *Lett. Math. Phys.* **106** (2016), 741–763.

[10] M. Ozawa, "Quantum measuring processes of continuous obsevables," *J. Math. Phys.* **25** (1984), 79–87.

[11] K. Okamura & M. Ozawa, "Measurement theory in local quantum physics," *J. Math. Phys.* **57** (2016), 015209.

[12] K. Okamura, "Measuring processes and the Heisenberg picture." In: *Nagoya Winter Workshop: Reality and Measurement in Algebraic Quantum Theory*, edited by M. Ozawa et. al., (Springer, Singapore, 2018), pp.361–396.

[13] I. Ojima, "A unified scheme for generalized sectors based on selection criteria –Order parameters of symmetries and of thermality and physical meanings of adjunctions–," *Open Sys. Inform. Dyn.* **10** (2003), 235–279.

[14] I. Ojima, "Micro-Macro Duality in Quantum Physics,"pp.143–161 in *Proc. Intern. Conf. on Stochastic Analysis, Classical and Quantum*, (World Scientific, 2005), arXiv:math-ph/0502038.

[15] M. Ozawa, "Conditional probability and a posteriori states in quantum mechanics," *Publ. RIMS* **21** (1985), 279–295.

2020 International Symposium on Nonlinear Theory and Its Applications,
NOLTA2020, Virtual, November 16-19, 2020

Development of a Mathematical Model Describing Dressed Photon Phenomena Based on Quantum Walks on Self-Expanding Complex Networks

Leo Matsuoka[1], Etsuo Segawa[2], Kazuya Okamura[3,4], Suguru Sangu[5] and Hayato Saigo[6]

[1] Faculty of Engineering, Hiroshima Institute of Technology
2–1–1 Miyake, Saeki-ku, Hiroshima 731-5193, Japan
[2] Graduate School of Environment and Information Sciences, Yokohama National University
79–7 Tokiwadai, Hodogaya-ku, Yokohama, Kanagawa 240-8501, Japan
[3] Research Origin for Dressed Photon
3-13-19 Moriya-cho Kanagawa-ku, Yokohama, 221-0022, Japan
[4] Graduate School of Informatics, Nagoya University
Furo-cho, Chikusa-ku, Nagoya 464-8601, Japan
[5] Ricoh Institute of Technology, Ricoh Company, Ltd.
2-7-1 Izumi, Ebina, Kanagawa 243-0460, Japan
[6] Faculty of Bioscience, Nagahama Institute of Bio-Science and Technology
1266 Tamura-cho, Nagahama, Shiga 526-0829, Japan
Email: r.matsuoka.65@cc.it-hiroshima.ac.jp, segawa-etsuo-tb@ynu.ac.jp, k.okamura.renormalizable@gmail.com,
suguru.sangu@jp.ricoh.com, h_saigoh@nagahama-i-bio.ac.jp

Abstract—The photon breeding process used in the production of Si-LED can be considered an autonomous structure optimization led by the dressed photon phenomena. This study develops a mathematical model describing the photon breeding process based on a steady-state quantum walk in a network. We propose a concept of self-expansion process of the network corresponding to the dynamics of the quantum walk. The concept is based on a natural extension of the BA model that is a production method of a scale-free network to the steady-state quantum walks.

1. Introduction

Optical science of dressed photons (DPs) that originates from studies on optical near fields, is rapidly advancing with several practical applications [1]. Examples of applications are nano-fabrication, photo-diode, light-emitting diodes, and other novel optical devices. Regardless of the concrete physical system, DPs often show unexpected autonomy that optimizes the system composed of atoms or nanoparticles [2, 3]. In particular, the photon breeding (PB) process observed in the DP-assisted annealing is a typical example of autonomous optimization. The PB process is a phenomenon in which the energy and the polarization of the emitted photon from the LED become identical to those used for the annealing [2]. As in the PB processes, the autonomous structure optimization is studied using stochastic models [2, 3]. The characteristic features in a material are reproduced from the evolution of the stochastic systems. However, the source of the autonomous features of the DPs is unclear because the micro nature of the system is simplified to manage the macro system in the simulations.

Currently, a new theory of the DPs that considers the DPs as some quantum field is being developed. The quantum walk models have significant roles in the theory. The quantum walk that is studied as a quantum counterpart of the random walk is a promising toy-model that expresses some features of the quantum field. Recently, Higuchi and Segawa proposed a model of quantum walk on a connected finite graph with two tails to consider steady injection and corresponding emission to/from the system [4, 5]. This model is referred to as steady-state quantum walk because it can express the steady-state of the finite system with consecutive injection and emission that is not the focus of conventional stochastic processes. This model has a high affinity with a representation of the dressed photon phenomena because it accurately expresses some qualitative features of DPs. Furthermore, studies on quantum walks are an interface between the mathematics of the quantum field and the dressed photon phenomena, and can lead to further extensions of the theoretical understandings.

This study proposes a mathematical model that describes the photon breeding process on the framework of steady-state quantum walk. Assuming the toy-model of the quantum walk on the network accurately expresses the feature of the dressed photon phenomenon, the structure optimization in the photon breeding will be modeled by the autonomous optimization of the connection structure of the network. Initially, toward expressing the autonomous optimization, we propose a method for expanding the network according to the dynamics of the steady-state quantum walk. Beginning with a brief introduction of the steady-state quantum walk, we discuss an extension of the Barabási-Albert (BA) model [6] to the steady-state quantum walk. The BA model is a well-known production method of a scale-free network (a complex network). Our model is a counterpart of the BA

model in the field of quantum walk.

2. Steady-State Quantum Walk on a Network

We briefly introduce an example of the steady-state quantum walk on a graph (or network) for the foundation of our proposal. Alternate to the form in the original article, we show this from the perspective of computational simulations. The base network consists of nodes and directed edges connecting them (Fig.1a). Although a pair of nodes can be connected by directed edges, the counter-directing edge connecting the same pair of nodes is necessary. Two or more pairs of edges are connected to the exterior of the system, to implement injection and emission of the "walkers". Each directed edge has a complex amplitude, and its square expresses the density of the "walkers". The density of "walkers" is defined on the directed edges and not nodes.

As a typical rule of time-evolution, we focus on the Grover walk. Figure 1(b) depicts a Grover walk rule on a node where d is the "degree" of the node. If an amplitude "1" reaches a node with degree d, "$\frac{2}{d} - 1$" is reflected and "$\frac{2}{d}$" is transmitted to each edge other than the reflecting passage. The density given by the sum of the squares of the complex amplitudes is preserved through each evolution. If we assume a consecutive injection of "1" from the exterior of the system and the corresponding emission through the other exits, then the distribution of the density exhibits the steady-state. Hamano and Saigo indicated that the maximum density in the steady-state is observed near the exit edge [7]. Furthermore, they indicated that the feature accurately emulates the density distribution of the dressed photons that maximizes near the "dissipation".

3. Concept of Self-Expansion of the Network Assisted by the Steady-State Quantum Walk

The quantum walk model emulates the features of the dressed photon phenomenon. In this model, the "walkers" corresponds to the dressed photon, and the network corresponds to the material structure. Assuming the dressed photons are playing the principal role in optimizing the structure of the material, we discuss a new toy-model where the network expands following the dynamics of the "walkers". Herein, we propose a new concept of the self-expansion of a network of quantum walk beginning with a well-known model.

Our model is based on the Barabási-Albert (BA) model that is a production scheme of a scale-free network. In the scale-free network, the degree distribution follows a power law. The BA model produces the scale-free structure using the "preferential attachment". If a new node is attached to the network, the nodes in the network accept an edge from the new one with the probability proportional to their respective degrees (Fig. 2a).

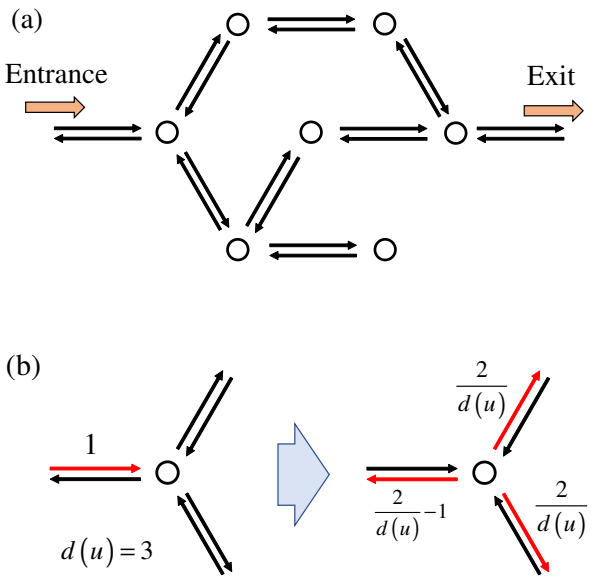

Figure 1: (a) An example of the network structure of the steady-state quantum walk. The structure is fully artificial. (b) An example of Grover walk's evolution around a node with degree three.

Before applying the BA model to the steady-state quantum walk, we indicate a BA model concept relevant to the classical random walk. Let the random walk simulation be performed on the network. After infinity time-evolution, the probability distribution converges where the probability is proportional to the degree of each node, whereas the preferential attachment in the BA model is determined by the degree of each node. Therefore, the limit distribution of the random walk can be used as the indicator of the strength of the preferential attachment.

The quantum-walk-based counterpart of the BA Model is considered by replacing the random walk with the steady-state quantum walk. Although the complex amplitudes are defined on directed edges, the densities on the nodes are calculated by the square sum of the amplitudes on the edges directed into the node. In the steady-state quantum walk, the density approaches the network exit. Accordingly, the new node will be attached preferentially to the network exit (Fig.2b). From the figure, the exit edge is ruled to move to the newly attached node. However, other rules are also applicable. The structure of the network that results in the attachment is different from the conventional scale-free network.

In this model, the prototype concept of the interaction between quantum walk dynamics and network structure was naturally introduced. The method of extension of the network is intuitively consistent with the energy transfer of the dressed photons because the most preferential node in the network is positioned near the exit. Now, the concrete meanings or real counterparts of the nodes, edges, and walkers are not defined. They can be the nanoparticles,

dressed photons, or the points placed in the Fourier Space. The concrete parameter to be optimized autonomously according to the composition of the network is unclear. The initial interest is the concrete structure of the network formed by this process. Numerical and mathematical analyses of the present model will be performed.

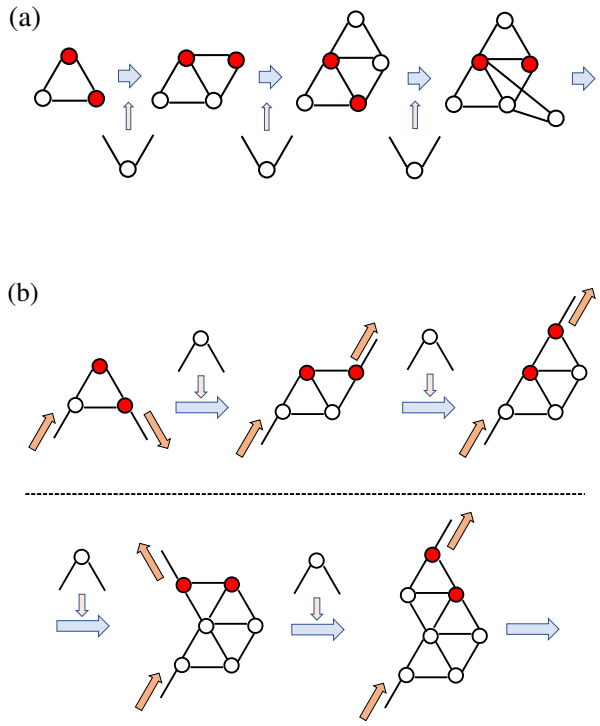

Figure 2: (a) An example of the network composition by the BA model. In this example, each new node has two edges. The nodes accepting the new edges are marked by red and were selected with the probability proportional to their "degrees". (b) An example of the network composition by the concept presented. The directions of edges have been omitted for simplicity. The nodes accepting the new edges are selected with probability proportional to the density distribution of the steady-state quantum walk. The exit edge always moves to the newly attached node in this example.

4. Summary

A new concept of the self-expanding network according to the dynamics of the steady-state quantum walk is presented. The BA model of the scale-free network was naturally extended to the steady-state quantum walk. The correspondence with the dressed photon phenomena will be investigated by further numerical and mathematical analyses.

Acknowledgments

This work was supported by Research Origin for Dressed Photon.

References

[1] M. Ohtsu, "History, current developments, and future directions of near-field optical science" *Opto-Electron. Adv.*, vol. 3, 190046, 2020.

[2] M. Katori and H. Kobayashi, "Nonequilibrium Statistical Mechanical Models for Photon Breeding Process Assisted by Dresssed-Photon-Phonons" in *Prog. Nanophotonics*, 4, ed. T. Yatsui (Springer, Heidelberg), pp.19–55, 2017.

[3] K. Takahashi, M. Katori, M. Naruse, M. Ohtsu, "Stochastic model showing a transition to self-controlled particle-deposition state induced by optical near-fields" *Appl. Phys. B*, vol.120, pp.247–254, 2015.

[4] Y. Higuchi and E. Segawa, "A dynamical system induced by quantum walk" *J. Phys. A: Math. Theor.*, vol. 52, 395202, 2019.

[5] Y. Higuchi, M. Sabri, E. Segawa "Electric circuit induced by quantum walk" *arXiv:* 2002.05261v2 [quant-ph], 2020.

[6] A. -L. Barabási and R. Albert, "Emergence of Scaling in Random Networks" *Science*, vol. 286, pp. 509–512, 1999.

[7] M. Hamano and H. Saigo, "Quantum Walk and Dressed Photon" *Electronic Proceedings in Theoretical Computer Science*, vol. 315, pp. 93–99, 2020.

2020 International Symposium on Nonlinear Theory and Its Applications,
NOLTA2020, Virtual, November 16-19, 2020

A discontinuity of dressed photon energy in the internal graph predicted by a quantum walk simulation

Etsuo Segawa† and Leo Matsuoka‡

†Graduate School of Environmental Sciences, Yokohama National University
Hodogaya, Yokohama 240-8501, Japan
‡Faculty of Engineering, Hiroshima Institute of Technology
Saeki-ku, Hiroshima 731-5193, Japan
Email: segawa-etsuo-tb@ynu.ac.jp, r.matsuoka.65@cc.it-hiroshima.ac.jp

Abstract—The quantum walks on networks expanded to a bounded state space is a promising model to describe dressed photon phenomena. The scattering on the surface of the graph can be observed while detailed behaviors of the internal of the networks are generally difficult to be observed. In this study, we consider a quantum walk on the one-dimensional lattice, and obtain an explicit expression of the relative distribution in the internal region, and also found a discontinuity of the energy in the internal region with respect to the output which looks like that of the Dirichlet function and suggests instability of the stationary state in the special output cases.

1. Introduction

Quantum walks have been studied intensively since the beginning of 2000's from the view point of quantum information see [1] and its references therein. One of the reasons for the studies on quantum walks is now not only the efficiency on quantum search algorithm but also application as a quantum simulator of quantum phenomena (on a quantum device) envisioned by Feynman [2] because of its universality of the quantum computation [3], for example: a simulator of the Dirac equation, quantum graphs, light energy transfer system in photosynthesis and a topological insulator and so on see [4] and its references therein, for example. The dressed photon is the off-shell quantum field with the correlation between a photon field and an electron (excitation) field of a nanoparticle. In this talk, we attempt to apply it to simulate the energy transfer of the dressed photon in nano materials which accomplishes the autonomous optimization [5, 6]. To detect the dressed photon, the energy transfer and the dissipation processes are need. Very recently, such experimental results on the temporal behavior of dressed photon energy transfer are presented by [7]. To this end, we apply a line graph concept focusing on a relation rather than vertices itself to realize the eternal provide of an incident source and also the dissipation [8, 9]. It is known that the steady state of quantum walk model can be obtained [8, 10].

In this paper, for simplicity, the network is one-dimensional lattice. We compute the response to the input considering not only its scattering on its surface, but also the "energy" in the internal region, which is expected to promise the localization of the dressed photon around a nano material and also to be a new observation. This graph is quite simple but some appropriate designs of the local time evolution operators, called quantum coins, make it possible to realize quantum walks on some graphs having some symmetricities. This reduction to a finite path graph will be useful to reduce the problem considered by [9] studying the energy transfer of the dressed photon. In this talk, we simply set the quantum coins uniformly in the perturbed region to focus on the property of the discontinuity of the energy.

2. Setting

We assign a 2×2 unitary matrix to each $x \in \mathbb{Z}$ so called local quantum coin

$$C_x = \begin{bmatrix} a_x & b_x \\ c_x & d_x \end{bmatrix}.$$

The two-dimensional internal state may reflect the interaction between a photon and excitation in a quite simplified realization in the dressed photon. Putting $|L\rangle := [1,0]^\top$, $|R\rangle := [0,1]^\top$ and $\langle L| = [1,0]$, $\langle R| = [0,1]$, We define the following matrix valued weights associated with moving to left and right from x by

$$P_x = |L\rangle\langle L|C_x, \quad Q_x = |R\rangle\langle R|C_x,$$

respectively. Then the time evolution operator on $\ell^2(\mathbb{Z};\mathbb{C}^2)$ is described by

$$(U\psi)(x) = P_{x+1}\psi(x+1) + Q_{x-1}\psi(x-1)$$

for any $\psi \in \ell^2(\mathbb{Z};\mathbb{C}^2)$. To extract a "relationship" between quantum walk's state assigned at vertices, it is useful to see this model by the arc based expression, say $A = \{(x;R),(x;L) \mid x \in \mathbb{Z}\}$, which seems to be compatible to the off-shell science: the expression on $\ell^2(A)$ is described by

$$(U'\phi)(x;L) = a_{x+1}\phi(x+1;L) + b_{x+1}\phi(x+1;R),$$
$$(U'\phi)(x;R) = c_{x-1}\phi(x-1;L) + d_{x-1}\phi(x-1;R)$$

for any $\psi \in \ell^2(A)$. We call a_x and d_x the transmitting amplitudes, and b_x and c_x the reflection amplitudes at x, respectively [1]. Remark that U and U' are unitarily equivalent such that letting $\eta : \ell^2(\mathbb{Z};\mathbb{C}^2) \to \ell^2(A)$ be

$$(\eta\psi)(x;R) = \langle R|\psi\rangle, \quad (\eta\psi)(x;L) = \langle L|\psi\rangle$$

then we have $U = \eta^{-1}U'\eta$. The free quantum walk is the quantum walk where all local quantum coins are described by the identity matrix i.e.

$$(U_0\psi)(x) = \begin{bmatrix} 1 & 0 \\ 0 & 0 \end{bmatrix}\psi(x+1) + \begin{bmatrix} 0 & 0 \\ 0 & 1 \end{bmatrix}\psi(x-1).$$

Then the walker runs through one-dimensional lattices without any reflections in the free case.

In this paper we set "impurities" on

$$\Gamma_M := \{0, 1, \ldots, M-1\}$$

in the free quantum walk on one-dimensional lattice; that is,

$$C_x = \begin{cases} \begin{bmatrix} a & b \\ c & d \end{bmatrix} & : x \in \Gamma_M, \\ \\ I_2 & : x \notin \Gamma_M. \end{cases}$$

We put $\Delta = ad - bc$. We consider the initial state Ψ_0 as follows.

$$\Psi_0(x) = \begin{cases} e^{i\xi x}|R\rangle & : x \le 0; \\ 0 & : \text{otherwise}, \end{cases}$$

where $\xi \in \mathbb{R}/2\pi\mathbb{Z}$. Note that this initial state belongs to no longer ℓ^2 category. The region Γ_M is obtain a time dependent inflow $e^{-i\xi n}$ from the negative outside. On the other hand, if a quantum walker goes out side of Γ_M, it never come back again to Γ_M. We can regard such a quantum walker as an outflow from Γ_M. Roughly speaking, in the long time limit, the inflow and outflow are balanced and obtain the stationary state with some modification. Indeed the following statement holds.

Proposition 2.1 *[8]*

(1) This quantum walk converges to a stationary state in the following meaning:

$$\exists \lim_{n\to\infty} e^{i(n+1)\xi}\Psi_n(x) =: \Phi_\infty(x).$$

(2) This stationary state is a generalized eigenfunction satisfying

$$U\Phi_\infty = e^{-i\xi}\Phi_\infty.$$

[1] If we put $a_x = d_x = 1$ and $b_x = c_x = \sqrt{-1} = i$, then the primitive form of QW in [11] is reproduced.

3. Main result

Set $\omega := e^{i\xi}\Delta^{-1/2}$ which corresponds to the $\Delta^{-1/2}$-rotated incident flow, and divide the unit circle in the complex plain into three parts by

$$\begin{aligned} B_{in} &:= \{\omega \in \mathbb{C} \mid |\omega| = 1,\ |\mathrm{R}(\omega)| < |a|\}, \\ B_{out} &:= \{\omega \in \mathbb{C} \mid |\omega| = 1,\ |\mathrm{R}(\omega)| \ge |a|\}, \\ \partial B &:= \{\omega \in \mathbb{C} \mid |\omega| = 1,\ |\mathrm{R}(\omega)| = |a|\}. \end{aligned}$$

Since there is a one-to-one correspondence between ω and ξ, in the following, we use the parameter ω on the unit circle instead of $e^{i\xi}$ as the representative of the initial state.

First, let us consider the transmitting and reflecting rate denoted by

$$R(\omega) = |\langle L, P_0\Phi_\infty(0)\rangle|^2, \quad T(\omega) = |\langle R, Q_{M-1}\Phi_\infty(M-1)\rangle|^2.$$

By the unitarity of the walk, $T + R = 1$ holds. Then we have the following.

Proposition 3.1 *Assume $abcd \neq 0$. For any $\omega \in \mathbb{C}$ with $|\omega| = 1$, we have*

$$\begin{aligned} T(\omega) &= \frac{|a|^2}{|a|^2 + |b|^2\zeta'^2_M}, \\ R(\omega) &= \frac{|b|^2\zeta'^2_M}{|a|^2 + |b|^2\zeta'^2_M}, \end{aligned}$$

where $\zeta'_M = U_{M+1}((\omega + \omega^{-1})/(2|a|))$. Here $U_n(\cdot)$ is the Chebyshev polynomial of the second kind.

We define $\theta \in (0, \pi)$ by

$$\begin{cases} \cos^{-1}((\omega + \omega^{-1})/(2|a|)) & : \omega \in B_{in}, \\ \cosh^{-1}((\omega + \omega^{-1})/(2|a|)) & : \omega \in B_{out}. \end{cases}$$

From this proposition, we can obtain a useful condition for the perfect transmitting; that is, $T = 1$ as follows.

Corollary 3.1 *Assume $abcd \neq 0$. The perfect transmitting happens if and only if $\omega \in B_{in}$ and*

$$\theta \in \left\{ \frac{\ell}{M}\pi \mid \ell \in \{0, 1, \ldots, (M-1)\} \right\}.$$

Secondly, let the internal energy with the inflow represented by ω in the internal region Γ_M be defined by

$$\mathcal{E}_M(\omega) = \sum_{x\in\Gamma_M} \|\Phi_\infty(x)\|^2.$$

Then let us consider the asymptotics of the energy for sufficiently large M. It is shown that $\|\Phi_\infty(x)\|^2$ is invariant under the map $\omega \mapsto \omega^{-1}$, which implies that the relative probability can be further represented by θ instead of $\omega \in B_{in}$. Note that $\theta \to 0$ or π means ω closes to ∂B from B_{in}. and

$\theta \to 0$ implies also ω closes to ∂B from B_{out}. We design θ if $\omega \in B_{in} \cup B_{out}$ by

$$\theta = \theta(M) = \frac{x\pi}{M}$$

with the parameters $\theta \in (0, M) \in \mathbb{R}$ and $\alpha > 0$. We obtain the following theorem, which is our main statement.

Theorem 3.1

(1) If $\omega \in \partial B$, then $\mathcal{E}_M(\omega) \in O(M)$.

(2) If $\omega \in B_{out}$, then

$$\mathcal{E}_M(\omega) \in \begin{cases} O(1) & : 1 \ll x \asymp M \\ O(M) & : \textit{otherwise} \end{cases}$$

(3) If $\omega \in B_{in}$, $x' = \min\{x, M - x\} \in \mathbb{N}$ and $x' \in O(M^\beta)$, $\beta \in [0, 1]$, then

$$\mathcal{E}_M(\omega) \in O(M^{3-2\beta}).$$

(4) If $\omega \in B_{in}$, $x' = \min\{x, M - x\} \notin \mathbb{N}$, then

$$\mathcal{E}_M(\omega) \in O(M).$$

Corollary 3.2 *Assume $abcd \neq 0$. If $\omega \in B_{in}$ and $x' = \min\{x, M - x\} \asymp 1$, then*

$$\mathcal{E}_M(\omega) \in \begin{cases} O(M^3) & : x' \textit{ is natural number and } \alpha \geq 1, \\ O(M) & : \textit{otherwise.} \end{cases}$$

We can compute the coefficient of the main term in Corollary 3.2 by $|b|^2/(|a|\theta_*)^2$, where $\sin\theta_* \sim |\sin M\theta|$. Then combining it with Corollary 3.2, we obtain the following formula which is similar to the Dirichlet function in the limit of large M.

Corollary 3.3 *Let all the setting be the same as Corollary 3.2 and $|\sin M\theta| \sim |\sin\theta_*|$. We define*

$$\kappa(x') := \frac{|a|^2\theta_*^2}{|b|^2} \lim_{M\to\infty} \frac{\mathcal{E}_M(\omega)}{M^3}.$$

Then we have

$$\kappa(x') = \begin{cases} 1 & : x' \textit{ is natural number,} \\ 0 & : \textit{otherwise,} \end{cases}$$

for any $x' \geq 0$.

Remark that the condition of $x' \in \mathbb{N}$ coincides with the perfect transmitting condition in Corollary 3.1. This non linearity of the energy in the internal region is suggested by the experimental result in [12]. To clarify this relationship is one of the interesting future's problem.

Acknowledgments

This work was supported by Research Origin for Dressed Photon. E.S. acknowledges financial supports from the Grant-in-Aid of Scientific Research (C) Japan Society for the Promotion of Science (Grant No. 19K03616)

References

[1] R. Portugal, Quantum Walk and Search Algorithms, 2nd Ed., Springer Nature Switzerland (2018).

[2] R. P. Feynman, Simulating physics with computers, Int. J. Theor. Phys. 21 (1982) 467-488.

[3] A. Childs, Universal computation by quantum walk, Phys. Rev. Lett. 102 (2009) 180501.

[4] Y. Ide and N. Konno, 量子ウォークの新展開—数理構造の深化と応用, 培風館 2019 (omnibus style by 21 authors in Japanese).

[5] T. Kawazoe, K. Kobayashi, S. Sangu, and M. Ohtsu, Demonstration of a nanophotonic switching operation by optical near-field energy transfer, Appl. Phys. Lett., **82** (2003) 2957-2959.

[6] M. Ohtsu, T. Kawazoe, H. Saigo, Spatial and temporal evolutions of dressed photon energy transfer, OffShell: 1710R.001.

[7] M. Ohtsu and T. Kawazoe, Nutation in energy transfer of dressed photons between nano-particles OffShell: 2005O.001.v1

[8] Yu. Higuchi and E. Segawa, Dynamical system induced by quantum walks, Journal of Physiscs A: Mathematical and Theoretical **52** (2009) 395202.

[9] M. Hamano and H. Saigo, Quantum Walk and Dressed Photon, Electronic Proceedings in Theoretical Computer Science **315** (2020) pp.93-99.

[10] H. Morioka, Generalized eigenfunctions and scattering matrices for position-dependent quantum walks, Rev. Math. Phys., **31** (2019) 1-37.

[11] R. P. Feynman and A. R. Hibbs, Quantum Mechanics and Path Integrals, Dover Publications, Inc., Mineola, NY, emended edition (2010).

[12] W. Nomura, T. Yatsui, T. Kawazoe, M. Naruse, M. Ohtsu Appl. Phys. B **100** (2010) pp.181187

2020 International Symposium on Nonlinear Theory and Its Applications,
NOLTA2020, Virtual, November 16-19, 2020

Numerical Analysis of Dressed-Photon Dynamics toward Its Control

Suguru Sangu†, and Hayato Saigo‡

†Ricoh Institute of Technology, Ricoh Company, Ltd.
2-7-1 Izumi, Ebina, Kanagawa 243-0460, Japan
‡Faculty of Bioscience, Nagahama Institute of Bio-Science and Technology
1266 Tamura-cho, Nagahama, Shiga 526-0829, Japan
Email: suguru.sangu@jp.ricoh.com, harmoniahayato@gmail.com

Abstract– Several attractive phenomena originating from dressed photons have been reported experimentally. On the other hand, knowledge for designing functional devices and materials has not yet been established. In this paper, a simulation model that expresses the characteristics of dressed photons is proposed, and a method for controlling spatial localization is discussed. Specifically, by constructing a unitary transformation matrix from a stationary solution in a certain matter structure, control factors of dressed photons are identified, and the enhancement of localization nature is verified numerically.

1. Introduction

Light-matter interaction has been payed attention for many years from the viewpoints of natural physics and industrial applications. Thanks to advanced micro-fabrication and microscopic observation technologies, the subject of interest is shifting to the interaction in a scale less than optical wavelength. In such situations, several optical phenomena cannot be explained in terms of conventional optical theory. For example, light emission by Si material that is an indirect transition semiconductor [1], nano-structure selective etching with autonomy [2], and high-speed energy transfer imitating photosynthesis [3] have been experimentally demonstrated. While such experimental results with large physical impacts have emerged, expansion or proposal of novel concept in the optical theory is still in the stage of development. We aim to establish the concept of dressed photons and explain above attractive optical phenomena.

Characteristic behavior of dressed photons is breaking of the energy and momentum conservation laws satisfied in conventional optical theory, that causes such as spatial localization and high-speed energy transfer in the nanometer range. In other words, the dressed photon can exist in the off-shell region or outside region of the light cone surface that is known as the dispersion relation between light and matter.

While research for constructing the dressed-photon theory is important, approach by numerical simulation is also practically meaningful in accelerating theoretical studies and applying it to engineering. At present, there is no method to design functional nanophotonic device based on dressed-photon technologies. Although several ideal theories focused on unique properties of dressed photons in a nanometer scale have been published [4], they are inadequate for describing actual experimental situations. One of reasons is that expression of continuous connection from the microscopic to the macroscopic systems has not been founded. This is a problem to be solved with the help of numerical approaches.

Against the above background, a qualitative model of dressed photons for numerical simulation is proposed in this paper, that operates on a rather large scale, and one of methods for defining appropriate bases of dressed photons is developed, that identifies energy-transfer paths to access a specific basis to be controlled by matter structures.

2. Model of Dressed Photons

The dressed photons show characteristic features such as enhancement of existence probability (localization) at the edge of the matter as well as high-speed energy transfer in a nanometric matter. Focusing on the localization, such a property is analogous to the behavior of harmonic oscillator with highly excited states, where the probability approaches asymptotically the arcsine law. In order to reproduce the localization in a free-form matter, a continuous object is described as a set of discrete nodes, and the dressed photon is a simple two-level system, and is bounded at a node, where the two-level system corresponds to a light-matter coupled state. The localization originates from superposition of high-order oscillation modes in collective motion of two-level systems. Figure 1(a) represents the schematic illustration of the dressed-photon system. Energy transfer among the nodes takes place through creation and annihilation of dressed photons, which can be expressed as

$$\hat{H}_{\mathrm{int}} = \sum_{i \neq j} U\left(|\boldsymbol{r}_i - \boldsymbol{r}_j|\right)\left(\hat{A}_i^{\dagger}\hat{A}_j + \hat{A}_i\hat{A}_j^{\dagger}\right), \qquad (1)$$

where $\hat{A}_i^{\dagger}$ and $\hat{A}_j$ represent creation and annihilation operators, and the coupling strength U is dependent on distance between two nodes labeled i and j. In the following calculation, the coupling strength is given by Yukawa function, $U(r) \propto \exp(-m_{\mathrm{eff}}r)/r$, that has been derived by considering environment-assisted energy and momentum not-conserved interaction between two bodies [4]. Ideally, the deviation from energy and momentum conservation laws in conventional optics should be exposed, but in this stage, a system is expressed as the dispersion relation

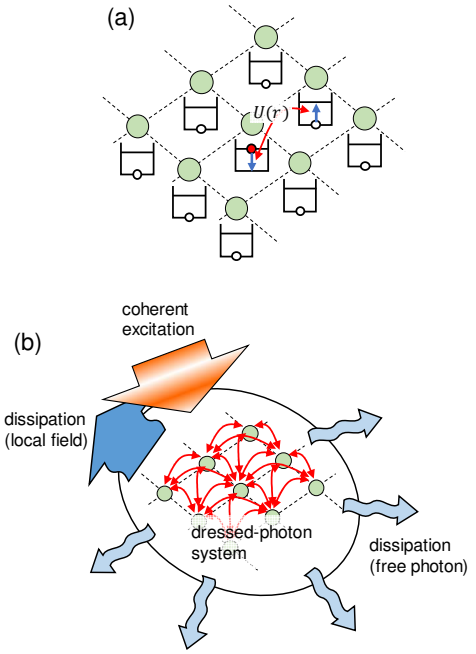

Figure 1: Schematic illustrations of dressed-photon system. (a) Model of dressed photon that is bounded on a node and moved via inter-node coupling, and (b) the operation system with excitation and dissipation processes.

modified. In future study, we aim to construct the light-matter interaction with spatial and temporal variations.

For driving the above dressed-photon system, it is necessary to add an input and dissipation mechanisms, that means considering a nonequilibrium open system where input and output are balanced. Here, coherent excitation is assumed, that is given by

$$\hat{H}_{\mathrm{exc}} = \sum_{i\in(\mathrm{input})} \mu_i\left(\hat{A}_i^{\dagger} + \hat{A}_i\right), \qquad (2)$$

where μ_i denotes the strength of excitation at predetermined nodes (input boundary). While, the dissipation is approximately expressed in the following Liouville equation that describes the dynamics of dressed photons,

$$\begin{aligned}\frac{d\hat{\rho}(t)}{dt} &= -\frac{i}{\hbar}\left[\hat{H}_0 + \hat{H}_{\mathrm{int}} + \hat{H}_{\mathrm{exc}}(t), \hat{\rho}(t)\right] \\ &+ \frac{\gamma_{\mathrm{wg}}}{2}\sum_{i,j\in(\mathrm{edge})}\left\{2\hat{A}_i\hat{\rho}(t)\hat{A}_j^{\dagger} - \hat{A}_i^{\dagger}\hat{A}_j\hat{\rho}(t) - \hat{\rho}(t)\hat{A}_i^{\dagger}\hat{A}_i\right\} \\ &+ \frac{\gamma_{\mathrm{f}}}{2}\sum_{i,j}\left\{2\hat{A}_i\hat{\rho}(t)\hat{A}_j^{\dagger} - \hat{A}_i^{\dagger}\hat{A}_j\hat{\rho}(t) - \hat{\rho}(t)\hat{A}_i^{\dagger}\hat{A}_j\right\}. \qquad (3)\end{aligned}$$

The equation represents time evolution of density matrix operator, $\hat{\rho}(t)$, and the Lindblad-type formulation which is based on the Born-Markov approximation [5] is adopted for the dissipation terms in the second and third lines in Equation (3). Furthermore, it should be emphasized that the two types of dissipation are considered, that the one returns to input edge (relaxation constant: γ_{wg}) and the other radiates toward the outer field as free photons (relaxation constant: γ_{f}).

Before moving on to the discussion of numerical analysis, a correspondence relation between the above model and the quantum walk will be touched upon. Our model, where the dressed-photon system is expressed as collection of nodes and the carrier exists only on the nodes, is easily associated with the quantum walk in which a walker moves in a quantum stochastic manner on a graph with nodes and branches. The large difference between the two is whether the time evolution is dealt with continuously or step by step. Identities in both have been mathematically proven [6]. In such simplified models of the quantum walk, steady-states solution has been already derived [7, 8]. There is a possibility that the complicated dressed-photon dynamics derived numerically can be easily interpreted using the words of quantum walk, which is interesting research subject as future studies.

3. A Description of Dressed-Photon Bases

The dressed-photon dynamics can be calculated by solving Equation (3) numerically. While the existence probability of dressed photons in a steady state shows a characteristic spatial distribution, it is hard to capture physical meaning from such distribution. In this section, the proposed unitary transformation inspired by stationary solution is explained, and the paths that reaches specific localization states will be considered.

3.1. Steady State by Node-Bound Bases

At first, spatial distribution of dressed photons described by node-bound basis is discussed for intuitive understanding. The model is a two-dimensional tapered structure, and the result for the steady state is visualized in Figure 2. In this calculation, only one particle states are considered for simplicity, and thus, the interaction among plural dressed photons, that induces non-linear effect, is not taken into consideration. Figure 2 shows the existence probability of dressed photons on the nodes, where the magnitude of the probability is displayed in color from blue to red in Figure 2(a), and the absolute value of the probability on the center axis (x = 0) is shown in Figure 2(b). Localization of the dressed photons can be confirmed at the tip and the slope of the taper structure. The result suggests a tendency to approach the arcsine law. Although we would like to infer a structure that emphasizes localization of dressed photons on the tip, it is hard to improve the taper shape from this result.

3.2. Basis Transformation Constructed by Steady State

The result in Figure 2 is a steady state in a nonequilibrium open system, and there is no time evolution of the spatial distribution for the probability. That means the existence of the optimal basis that the off-diagonal matrix elements of the density matrix become zero in the steady state. Specifically, the unitary transformation is carried out by using the matrix that diagonalizes the steady-

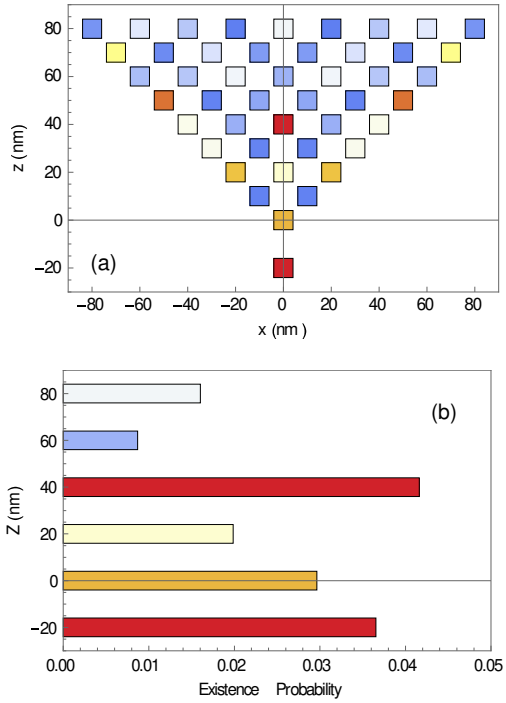

Figure 2: Visualization of dressed-photon steady state. (a) Spatial distribution of existence probability of dressed photons. The dressed photons tend to stay at the tip and the slope in the taper structure, that seem asymptotic signs of the arcsine law. (b) Cross-sectional view of existence probability on the center line ($x = 0$ in Figure 2(a)).

state density matrix for the node-bound basis. Figure 3(a) shows the result of the unitary transformation from the node-bound basis to the new one, in which the color map represents the values of the density matrix with 47 × 47 elements before and after transformation. For visual understanding, some typical bases are reproduced on the nodes of taper structures as shown in Figure 3(b).

Using this unitary transformation matrix, the process of time evolution can be calculated at arbitrary times, that the density matrices are shown in Figure 4. The existence of temporarily involved states is confirmed from the appearance of off-diagonal matrix elements that are the transition probability between different bases. By cutting or enhancing these, it is possible to control the localization of dressed photons in the steady state.

3.3. Characteristics of Temporarily Mediated Basis

In this subsection, contribution of the off-diagonal elements of the density matrix to a specific localization state is evaluated. In order to quantify the contribution, the following cumulative function is defined,

$$C_{f,m}(t) = \int_0^t |\langle f|\hat{\rho}(t')|m\rangle| dt', \qquad (4)$$

that is time integration of an off-diagonal element with the temporarily involved state $|m\rangle$ and target state $|f\rangle$. In Figure 5, the contribution is plotted for several strongly

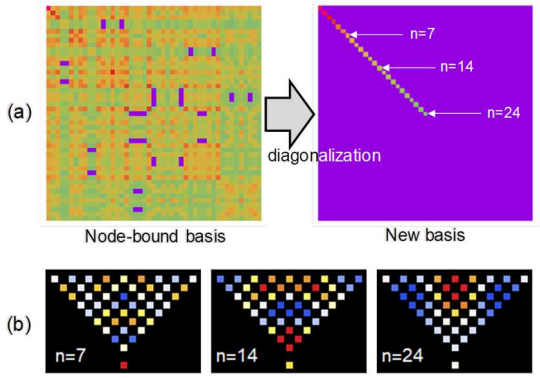

Figure 3: Visual expression of proposed basis transformation. (a) Color maps of density matrix elements (absolute values) before and after transformation. (b) Spatial distribution of several bases, corresponding to the label in the upper-right map.

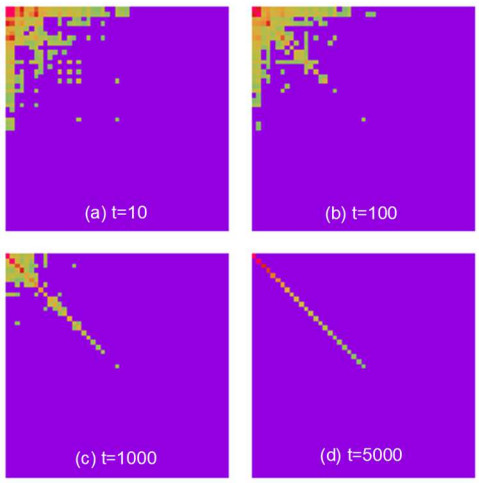

Figure 4: Snapshots of density matrix elements (absolute values) at the time steps (a) t =10, (b) 100, (c) 1000, and (d) 5000.

contributing bases, where the target basis is set as $n = 7$ (see Figure 3(b)). From this convergence values of the contributions, the bases $n = 2$ and 3 play a role of propagation paths to the localization state. The difference in the rise time among these bases should be noted, that seems to be involved in the difference of typical sizes of the excited states, that seems to relate connection between the bases with micro and macro scales.

In this way, temporarily involved bases can be selected that should be adjusted to control the localization.

4. Control of Dressed-Photon Dynamics

To verify the possibility for controlling dressed-photon distribution, structural defects are introduced to prevent the temporarily involved states. Reflecting the result in Figure 5, taper structures are slightly modified with reference to the bases $n = 2$ and 3, shown at upper part in Figure 6, and labelled as Type 1 and 2. The defects are located so as to

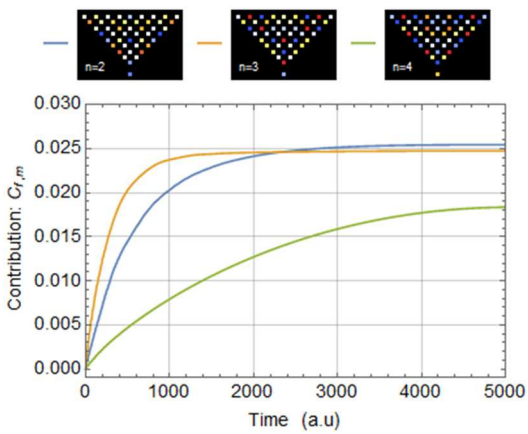

Figure 5: Contribution of temporarily involved bases, that is defined in Equation (4), for three components with higher values.

cancel the spatial distribution in these bases. Figure 6 shows comparison of existence probabilities in three different structures, that before modification, Type 1, and Type 2. The existence probability at the tip position is enhanced approximately twice as expected in the case of Type 2, and the spatial distribution (inset in Figure 6) approaches that of the target basis (n = 7).

In the above discussion, the matter structure is given by removing certain nodes for simplicity. Naturally, it can be done by the expansion and contraction of the shape, that means to change coupling strength among the corresponding nodes. It is necessary to develop more appropriate method for describing matter structures in future studies.

5. Summary

A simulation model of dressed photons that the carrier is dealt with collective motion of plural two-level systems, has been proposed, and stationary solution as well as time evolution of dressed photons have been numerically derived. For controlling the spatial distribution of dressed photons, unitary transformation which is constructed by using numerical stationary solution in a certain system has been performed, and the convergence process to the steady state has been traced. As a result, it is found that the localized states can be controlled by identifying and modulating the temporarily involved bases. Numerical evaluation shows expected enhancement in localization of dressed photons under slight structural changes.

To apply the proposed method to a system showing autonomous structure formation via dressed photons is one of attractive applications. It may be useful in understanding phenomena as mentioned at the beginning part in this paper, that cannot be explained by conventional optics. In the future, we would like to expand this simulation and analysis method to more actual device and material design.

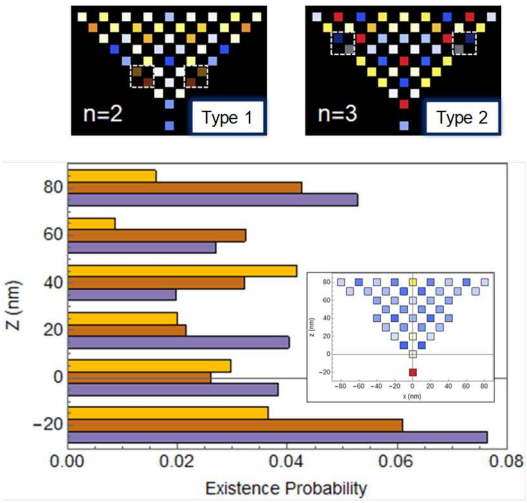

Figure 6: Existence probabilities on the center lines in three taper structures: (a) before modification (orange, same as that in Figure 2), (b) Type 1 (brown), and (c) Type 2 (purple). The top color maps are the bases of attention in the structural deformations, and the removing parts are shown by dotted rectangular areas.

Acknowledgments

The authors would like to thank Profs. M. Ohtsu, I. Ojima (Research Origin for Dressed Photon), Drs. E. Segawa (Yokohama Nat. Univ.), K. Okamura (Nagoya Univ.), and L. Matsuoka (Hiroshima Inst. Tech.) for their fruitful discussions on the context of dressed photons.

References

[1] M. Ohtsu, *Silicon Light-Emitting Diodes and Lasers* (Springer), 2016.

[2] T. Yatsui and K. Nobusada, "Near-field assisted chemical reactions and its applications," in *Prog. Nanophotonics 4*, eds. M. Ohtsu and T. Yatsui (Springer), pp.57–85, 2017.

[3] T. Kawazoe, et.al., "Optical nanofountain: A biomimetic device that concentrates optical energy in a nanometric region," *Appl. Phys. Lett.* vol.86, 103102, 2005.

[4] M. Ohtsu, *Dressed Photons* (Springer, Berlin), 2014.

[5] H. J. Carmichael, *Statistical Methods in Quantum Optics 1* (Springer, Berlin), 1999.

[6] H. Saigo and H. Sako, "Space-homogeneous quantum walks on Z from the viewpoint of complex analysis," *arXiv:*1802.01837 [math-ph], 2018.

[7] Y. Higuchi and E. Segawa, "A dynamical system induced by quantum walk," *J. Phys. A: Math. Theor.*, vol.52, 395202, 2019.

[8] M. Hamano and H. Saigo, "Quantum walk and dressed photon," *Proc. 9th Int. Conf. on Quantum Simulation and Quantum Walks,* vol.315, pp.93–99, 2020.

Dissipativity and Visibility of Macro

Izumi OJIMA
Research Origin for Dressed Photon

Virtual QBIC Workshop 2020 on 14 October, 2020

Abstract

In this talk, we try to understand the essential mechanism of the visualization processes from Microscopic to Macroscopic levels in relation with dissipativity and the roles played by dressed photons.

Gauge Invariance, Dissipativity & Visibility of Macro

The contrast and mutual relations between [**invisible Micro**] & [**visible Macro**] in algebraic QFT & in quantum gauge theory play crucially important and interesting roles:

The essence of **Visible Macro** in gauge theory is boiled down into the notion of **gauge invariance** formulated in terms of **subsidiary condition** to specify physical states and observables.

In AlgQFT, Micro-Macro relation is controlled by **duality**:

$$(\mathfrak{F} \curvearrowleft G) \rightleftarrows (\mathfrak{A} \curvearrowleft \widehat{G}),$$

between Microscopic field algebra $\mathfrak{F}$ (Micro $\mathfrak{F}$, in brief) acted by group G of symmetry and Macroscopic observable algebra $\mathfrak{A}$ (Macro $\mathfrak{A}$) acted by dual $\widehat{G}$ of G.

Micro-Macro Duality

Here, the essence of duality is the mutual relation between Micro $\mathfrak{F}$ & Macro $\mathfrak{A}$ given by

$$\mathfrak{A} \hookrightarrow \mathfrak{F} = \mathfrak{A} \rtimes \widehat{G};$$
$$\mathfrak{F} \overset{\Lambda}{\twoheadrightarrow} \mathfrak{A} = \mathfrak{F}^{G},$$

where $\mathfrak{A} \rtimes \widehat{G}$ is the crossed product of $\mathfrak{A}$ with the dual $\widehat{G}$ of G which acts on $\mathfrak{A}$: $\mathfrak{A} \curvearrowleft \widehat{G}$, and $\mathfrak{F}^{G}$ is the fixed-point subalgebra of $\mathfrak{F}$ under the action $\mathfrak{F} \curvearrowleft G$ of G on $\mathfrak{F}$.

Note that discussions in this standard setting in terms of the above four ingredients, $\mathfrak{F}, \mathfrak{A}, G, \widehat{G}$, have so far been **static** ones, without touching upon dynamical nature of the basic structure/process of the system!

How to Visualize Macro?

For instance, a quantity $A \in \mathfrak{A}$ belonging to observable algebra $\mathfrak{A}$ is supposed **by definition** to be visible as observable, without asking how and why it is so.

To provide scientific explanation for the mutual relation between Micro $\mathfrak{F}$ & Macro $\mathfrak{A}$, we should be serious about the question as to how Macro $\mathfrak{A}$ becomes **visible** in invisible Micro $\mathfrak{F}$. For this purpose, we need to discuss **dynamical processes** taking place between $\mathfrak{F}$ and $\mathfrak{A}$ involving G and $\widehat{G}$, which **visualize** Macro $\mathfrak{A}$ physically.

As a conditional expectation, the map $\Lambda : \mathfrak{F} \twoheadrightarrow \mathfrak{A}$ to project out a Macro subalgebra $\mathfrak{A} = \mathfrak{F}^G \subset \mathfrak{F}$ in Micro $\mathfrak{F}$ is naturally dissipative. Thus, the **visibility** of Macro $\mathfrak{A}$ is closely related with the dissipativity involved in the duality $\mathfrak{F} \rightleftarrows \mathfrak{A}$.

Dissipativity vs. Visualization

In this way, **visibility of Macro** $\mathfrak{A}$ is to be understood as a result of the **visualization process** of invisible Micro $\mathfrak{F}$ involving some kind of **dissipativity**.

The dissipativity of Λ itself is, however, **not** sufficient for Macro $\mathfrak{A}$ to be **visualized**. It is really a non-trivial question to clarifiy **why & how Macro** $\mathfrak{A} = \mathfrak{F}^{\mathcal{G}}$ **becomes visible** in the context of Micro-Macro duality in AlgQFT, which has **never been questioned nor answered so far**.

To solve the question, we recall here the simple common knowledge that the actor playing the vital roles in the context of whether visible or invisible should just be the **light** arising from the **electromagnetic degrees of freedom**. Thus, the essential point here is **how to attach gauge field= electromagnetic field, on the "surface" of Macro** $\mathfrak{A}$ for the sake of visibility!

Visualization caused by Light

However again!: Paying enough attention to the **long-range tails** of usual photons as quasi-free modes in ordinay quantum electromagnetism, our desire to attach the electromagnetic modes on the "surface" of Macro $\mathfrak{A}$ turns out to be impossible!!

To solve this difficulty, we remark here the **dressed photons** whose remarkable feature is found to be the small size of their elementary excitations at the **nano-scale orders**. which sounds like a saviour! Owing to the roles played by dressed photons attached to the "surface" of Macro $\mathfrak{A}$, we can rely on the visibility of Macro world. Since dressed photons are just electromagnetic field in special modes of gauge invariance, our solution for visibility of Macro $\mathfrak{A}$ can solve simultaneously the visibility question of gauge invariant modes in local gauge theory which cannot be solved in itself without being combined with AlgQFT.

How to Visualize Macro by Dressed Photons

Dressed photons appearing here are very interesting photon modes, systematically investigated by Prof. Motoichi Ohtsu (Prof. Emeritus at Univ. of Tokyo) in his indefatigable research.

Aside from the small size of their elementary excitations at the **nano-scale orders** mentioned above, they have very special and interesting spectrum in the sense that energy-momentum (p_μ) is always purely spacelike! In view of this feature, the use of ζ-function with (p_μ) as prime ideals may be of interest for measuring and recording the behaviours of dressed phtons.

Thus, the remaining task in this direction would be to construct a unified theoretical framework for accommodating the above three mathematical ingredients in the form of AlgQFT, local gauge theory adapted to dressed photons, and the physiology combined with information theory for the sensory organ to count dressed photons by means of a ζ-function.

ドレスト光子と測定過程

Dressed photon and measuring processes

ドレスト光子研究起点，　岡村 和弥

Research Origin for Dressed Photon,　Kazuya Okamura

E-mail: k.okamura.renormalizable@gmail.com

ドレスト光子のモデリングと測定過程の関係についての発表を行う。ドレスト光子の拡張可能性をもつモデリングに基づいて，ドレスト光子が発生する状況での測定過程を代数的量子場理論の局所ネットの観点から定式化を行う。

局所ネット [1, 2] とは，基となる時空 M の有界領域のなす（半順序) 集合 $\mathcal{R}$ の元 O から作用素代数 $\mathcal{A}(O)$ への対応で以下の条件を満たすものである：(i) $O_1 \subset O_2$ ならば，$\mathcal{A}(O_1) \subset \mathcal{A}(O_2)$。($ii$) O_1 と O_2 が「空間的」ならば，$\mathcal{A}(O_1)$ と $\mathcal{A}(O_2)$ は可換である。すなわち，有界領域で扱える物理量の集まりを定めるのが局所ネットであり，代数的量子場理論は局所ネットに基づいて理論展開されている。局所ネットから大域的物理量代数 $\mathcal{A} = \overline{\cup_{O\in\mathcal{R}}\mathcal{A}(O)}^{\|\cdot\|}$ が構成され，$\mathcal{A}$ を用いて系の状態が定義される。

量子測定理論における重要な概念は「インストルメント」および「測定過程」である [3, 4]。インストルメントは統計的な意味付けがされている一方，測定過程は測定装置の量子力学的モデリングである。$\mathcal{H}$ を対象系のヒルベルト空間，$(S, \mathcal{F})$ を可測空間とする。測定過程 $\mathbb{M} = (\mathcal{K}, \xi, E, U)$ とは，ヒルベルト空間 $\mathcal{K}$, $\mathcal{K}$ の単位ベクトル ξ，スペクトル測度 $E : \mathcal{F} \to \boldsymbol{B}(\mathcal{K})$ および $\mathcal{H}\otimes\mathcal{K}$ 上のユニタリー作用素 U からなる 4 つ組を意味する。

本講演の要点は以下の 3 つである：

1. 非一様な物質構造がある状況での量子電磁場を代数的量子場の 1 つの定式化である局所ネットの観点から考察する。自由場のときとは異なり，オンシェルでの生成・消滅演算子に基づいた理論展開ができない状況であることに基づく考察である。

2. その上で，ドレスト光子が発生する状況での測定過程の一般的枠組みを定式化する。インストルメント概念および測定過程が機能する状況を再吟味するという意義があり，現状の量子測定理論の枠組み [3, 4, 5] を超える状況を取り込む試みである。

3. また，有界領域における測定可能な物理量と $U(1)$-ゲージ不変性に関する考察を行う。

謝辞：　本研究の一部は (一社) ドレスト光子研究起点の助成を受けた。

参考文献

[1] R. Haag and D. Kastler, An algebraic approach to quantum field theory, J. Math. Phys. **5**, 848–861 (1964).
[2] R. Haag, *Local quantum physics: Fields, particles, algebras*, 2nd rev. and enlarged ed., (Springer, Berlin, 1996).
[3] M. Ozawa, Quantum measuring processes of continuous observables, J. Math. Phys. **25**, 79-87 (1984).
[4] M. Ozawa, Uncertainty relations for noise and disturbance in generalized quantum measurements, Ann. Phys. (N.Y.) **331**, 350–416 (2004).
[5] K. Okamura and M. Ozawa, Measurement theory in local quantum physics, J. Math. Phys. **57**, 015209 (2016), doi: 10.1063/1.4935407.

ドレスト光子と不定形量

Dressed photons and indefinite metric

○ 安藤 浩志 (千葉大理)

○Hiroshi Ando

E-mail: hiroando@math.s.chiba-u.ac.jp

ドレスト光子は電磁場がナノ物質中の電子と電磁相互作用する際に生じる準粒子である。そのエネルギー・運動量は、空間的局在性と短時間で生成・消滅される事から大きな不確定性を持っている。従ってドレスト光子は分散関係が質量殻上ではなく、広がりを持った領域を占めている。そのような量子電磁場のモデルの構築が目標であるが、現状様々な困難が知られている。電磁場の共変的量子化に於いては不可避的に不定計量状態空間が生じる。Gupta–Bleurer–Nakanishi–Lautrup の処方により、正のノルムを持つ物理的状態空間が選ばれ、その部分空間（の商の完備化) として得られる Hilbert 空間にだけ着目すれば良い。この定式化に於いてスカラーポテンシャル A_0 と、ベクトルポテンシャルの縦運動量成分 A_{L} の物理的状態空間の元への作用は相殺され、非物理的な自由度であると考えられる。しかし小嶋のミクロ・マクロ双対性に基づく研究 ([1, 2] 等を参照) において、これらの成分が粒子モードを励起する事はないが、infrared Coulomb tail 等を介してマクロ現象に寄与するが、その機構の理解に代数的レベルにおけるゲージ不変性、作用素レベルでのゲージ不変性を区別して考察する事が重要である事が明らかにされた。A_0, A_{T} は粒子的モードのセクターとは無縁な古典的モードのセクターに対応した表現を持つ [2, 3]. 本発表では A_0, A_{T} の理的状態空間の外での振る舞いを調べてみる事で、そのセクターのあるべき性質を推定できないか考察した事を述べる。佐久間らによる Clebsch 双対場を用いたドレスト光子モデル [5, 6] やその量子化との関係も考察したい。

謝辞

本研究は (社) ドレスト光子研究起点の助成を受けています.

参考文献

[1] I. Ojima, Micro-Macro Duality in Quantum Physics, pp.143-161, in Proc. Intern. Conf.“Stochastic Analysis: Classical and Quantun”, World Scientific, 2005.

[2] I. Ojima, Nakanishi–Lautrup B-field, crossed products and duality, RIMS 講究録 1524 巻 (2016), 29–37.

[3] 小嶋泉, 量子場とミクロ・マクロ双対性 (丸善出版), 2013.

[4] 大津元一, ドレスト光子 (朝倉書店), 2013.

[5] H. Sakuma, Virtual Photon Model by Spatio-Temporal Vortex Dynamics, Progress in Nanophotonics 5 (2018), 53–77.

[6] H. Sakuma, I. Ojima and M. Ohtsu, Dressed photons in a new paradigm of off-shell quantum fields, Progr. Quantum Electron. 55 (2017), 74–87.

CdSe 量子ドット間のドレスト光子を介したエネルギー移動の時間分解計測

Time-resolved Measurement of Energy Transfer between CdSe Quantum Dots via Dressed photons

電機大, ○川添 忠
TDU, ○Tadashi Kawazoe
E-mail: kawazoe@mail.dendai.ac.jp

量子ドット(QD)の吸収波長および発光波長は材料組成を変えることなくその寸法によって制御可能であり(量子サイズ効果)、例えばセレン化カドミウム(CdSe)を用いた量子ドットのでは可視光帯域すべてをその寸法のみでカバーすることが可能である。この特性を生かし QD を分散した樹脂、ガラスなどの材料は波長選択フィルター、ディスプレイ、太陽電池などに広く利用されている。これらの応用には単一でも現れる QD 自身の特性が注視されており、QD 間の光学的相互作用はあまり議論されていない。対して我々は QD 間の相互作用に注目し、新しい物理現象[1]や高性能化[2]、新しい応用[3]を模索して研究を行っている。

Fig.1 に 1.0×10^{18}/cm^3 と 1.5×10^{16}/cm^3 の密度で無秩序に分散させた場合の隣接 QD 間距離の分布(ワイブル分布)を示す。均一濃度で分散した場合、量子ドット間距離はそれぞれ 10nm、40nm に相当する濃度であるが、無秩序分散の場合、それぞれ約 5nm、20nm の隣接量子ドット間距離に配置されるものが多くなる。また、それ以下の距離に隣接する QD も多数存在し、比較的低密度であっても QD 間の相互作用は無視できないと思われる。

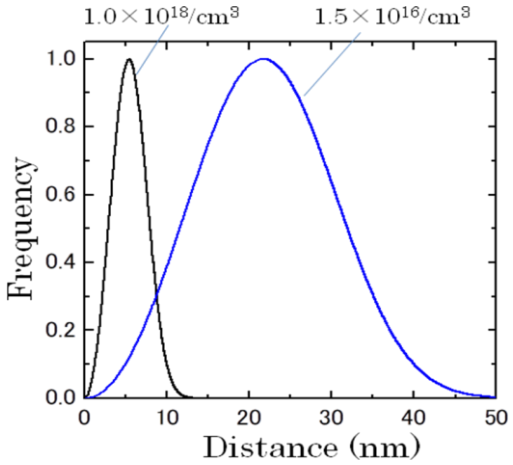

Fig.1.

Fig.2 に 1.0×10^{18}/cm^3 と 1.5×10^{16}/cm^3 の密度で UV 硬化樹脂中に分散した平均粒径 2.2nm の CdSe 量子ドットの発光寿命計測結果を示す。発光波長は両者とも 540nm であったが、発光寿命は濃度に依存して著しく変化しそれぞれ 2.2ns と 5.5ns であった。より低密度(～10^{14}/cm^3)では室温で 20ns、低温(10K)で 1 μs という報告もあり[4]、QD 間の相互作用が強まった結果であると考えられる。

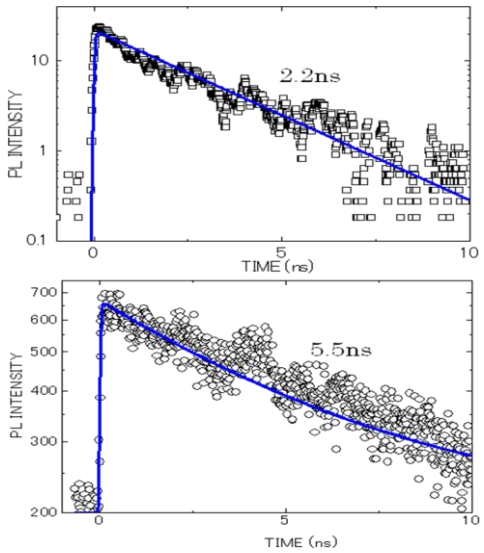

Fig.2

CdSe はウルツ鉱型結晶の構造を持ち、バンド構造が複雑でバンド端には多くの縮退準位が存在するがその多くは禁制された遷移である。Fig.2 に示したような高密度化に伴う発光寿命の短縮は禁制遷移の許容化[1]にあると考えている。そのため高密度化によって発光スペクトルも変化する。しかしながら吸収スペクトル計測では Lambert–Beer の法則にほぼ一致する振る舞いを示した。この矛盾はドレスト光子相互作用が隣接 QD 間に働くと考えることで説明可能になる。この相互作用が発現するには光子の存在が欠かせない。すなわち、QD に励起子などの光学的エネルギーが存在する時により強く相互作用が働くため単なる吸収スペクトルには濃度による変化が現れなかったと思われる。

発表では、寸法の異なる 2 種類の QD を混合することでドレスト光子を介したエネルギー移動がより明瞭に現れる実験を行ったのでその詳細を報告する。

[1] T. Kawazoe et al., Phys. Rev. Lett. **88**, 6, 067404 (2002).
[2] 田中尚裕、川添忠、野村航、田所貴志川添忠、大津元一、日本応用物理学会(2018)年秋季学術講演会[19a-437-10]
[3] M. Ohtsu et al., IEEE Journal of Selected Topics in Quantum Electronics, Vol. 14, No. 6, December 2008, pp. 1404-1417.
[4] C. M. Donega et al., Phys Rev B **74** 085320 (2006).

ナノドロップレット光波長変換膜による a-Si 太陽電池の発電効率向上

Improvement of power generation efficiency of amorphous silicon solar cell by wavelength conversion film with nano-droplets

電機大　○野村 航，冨田 嘉崇，川添 忠，田所 貴志

TDU,　°Wataru Nomura, Yoshitaka Tomita, Tadashi Kawazoe, Takashi Tadokoro

E-mail: wnomura@mail.dendai.ac.jp

アモルファスシリコン(a-Si)太陽電池は結晶シリコン太陽電池に比べ分光感度が可視域で高く、低消費電力のデバイスの屋内使用に適している。一方で我々の研究グループではこれまでにドレスト光子(DP)の原理に基づく量子ドット(QD)と色素間のエネルギー移動を利用した光波長変換材料[1]と、それを微小な球状に固形化させ変換効率等の諸特性を高めたナノドロップレット[2]を開発している。この波長変換材料およびナノドロップレットは材料となる色素の選択で変換波長を調整可能である。今回、既存の a-Si 太陽電池の発電効率向上のため室内光源用にナノドロップレットを調整し、これを含む波長変換膜を作製することで発電量の向上を目指した。

試料として、酸化亜鉛 QD と有機色素 Coumarin 461 (Exciton 社製)からなるドロップレットを作製した。ドロップレットは真球状であり(Fig.1 a)、光学顕微鏡で観察された平均寸法は直径 4.9 μm、最大 10.7 μm であった。このドロップレットをシリコーン樹脂に混合し、カバーガラスに膜厚約 500 μm で塗布し硬化させることで波長変換膜を作製した。また、発電効率評価用に AM1.5 基準で発電効率 3.6 %の市販の a-Si 太陽電池を採用し、Fig.1 b に示すように変換膜を前面に乗せた場合の発電効率の変化を評価した。

蛍光灯照射下で測定した a-Si 太陽電池の I-V 特性を Fig.2 に示す。黒で示す太陽電池単体に比べ赤で示す波長変換膜を乗せた場合では短絡電流の向上が見られた。同様の測定をソーラーシミュレータ、LED デスクライト、蛍光灯の 3 つの光源で行い、最大出力電力の増加率を評価したところ、それぞれ平均 + 3.2 %、+ 3.6 %、+ 6.3% であった。設計通り室内光源使用時に高い発電効率の向上が見られ、特に紫外光を含む蛍光灯照射下で顕著な効果が得られる事が確かめられた。

参考文献　[1] 川添他、2017 年秋応物講演会、15a-F202-10　[2] 田中他、2018 年秋応物講演会、19a-437-10

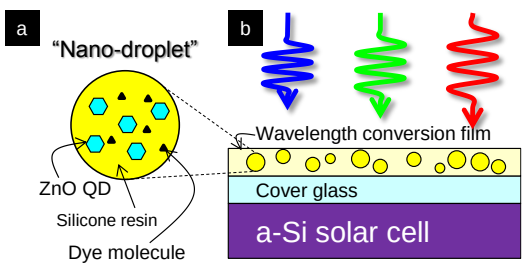

Fig.1 Schematic images of (a) a nano-droplet and (b) the solar cell with a conversion film.

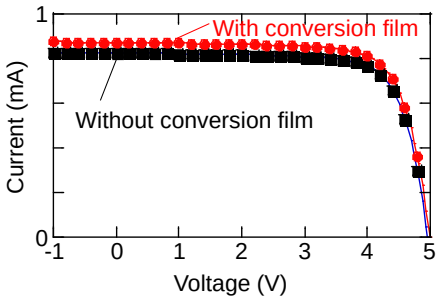

Fig.2 I-V curves of the a-Si solar cell under fluorescent light irradiation.

Correlation analysis of the size-resonanced near-field optical signals for advanced physical security

Naoya Tate
ISEE, Kyushu University

Abstract:
With the increasing popularity of the Internet of Things (IoT), there are considerable demands to improve the performance of physical security systems owing to the increase in edge devices. In recent years, fabrication and measurement techniques used by attackers are continuously improving, and it is difficult to ensure the security of edge devices by conventional approaches. To go against variable attacks in this background, we propose the *Nano-opt metric system*, which is based on a functional collaboration of existing physical security and near-field optical techniques. In this presentation, we report the results of quantitative evaluations of obtained optical signals due to near-field optical interactions between *target* and *reader* from the viewpoint of physical security. Additionally, interpretation of the signals based on size-resonance effect of the interactions will be discussed.

Dynamics of Micro-Macro Duality

Izumi Ojima
Research Origin for Dressed Photon

Abstract
The Micro-Macro Duality consists of two kinds of dualities, the duality between the system algebra (Alg) and its state space (States) and the duality from the spectrum (Spec) to the system dynamics (Dyn), In view of the difference between these two kinds of dualities, the repetition of the cycle, Dyn → Alg → States → Spec → Dyn → ... can become delicate at the stage of Spec → Dyn, which is the important target in the dynamics of Micro-Macro Duality.

Dressed photons and Electromagnetic fields from operator algebraic viewpoint

Hiroshi Ando
Department of Mathematics and Informatics, Chiba University

Abstract:
Dressed photons are considered to be associated with quantum fields with off-shell dispersion relations. Especially it is of interest to consider how to specify a state which describes an interaction of electromagnetic fields with electrons trapped in nano materials. We discuss how to model such fields, focusing on an operator algebra (or representation theoretic) viewpoint.

Dressed Photon and Quantum Walk

Hayato Saigo
Nagahama Institute of Bio-Science and Technology

Abstract:
Dressed photon is a useful physical concept for understanding the behavior of the light as quantum field interacting with nanomaterials. Recently, it has been proposed to use the notion of quantum walk, a mathematical concept that originated from the idea of "quantum version of the random walk", as the mathematical tool to analyze dressed photons. In this talk, I will explain why it seems meaningful to model dressed photons in terms of quantum walks, showing some elementary properties of Grover walks on certain kind of graphs and its physical implications. This talk is based on the joint work with M. Hamano, S. Sangu, E. Segawa and M. Ohtsu.

Dynamics of dressed-photon population from the perspective of convergence to steady state

Suguru Sangu
Ricoh Institute of Technology, Ricoh Company, Limited

Abstract:
A mechanism of localization and dissipation in steady state of dressed photon is becoming clear with the help of mathematical approaches, such as a quantum-walk picture. In this study, generating process of population for specific bases, that are given by diagonalization of steady-state solution of quantum master equation in a nonequilibrium open system, is visualized numerically, and energy transfer among the bases will be discussed. Purpose of this approach is to clear up a major part of object nodes for giving and receiving dressed photons locally as well as the role of a minor one. Knowledge gained from this study will be useful for reducing calculation volume in dressed-photon simulation, and optimizing geometrical structures of nanometric systems.

Measurement of Dressed Photon

Kazuya Okamura
Research Origin for Dressed Photon

Abstract:
We present a categorical framework for measurement theory of dressed photon. The concept of local net is effectively used.

Review on Clebsch dual field and on the parallel between dynamical behavior of dressed photon and gravitational pseudo-energy field.

Name: Hirofumi Sakuma
Research Origin for Dressed Photon

Abstract
In our effort of developing a new model of dressed photon (DP), we have introduced a notion of Clebsch dual electromagnetic wave field to cover the spacelike counterpart of Maxwell's equation. Brief review of this notion is given focusing on the generating mechanism of dressed photon. As an extension of the study on DP-genesis, we discuss the dynamical behaviors of generated dressed photons in reference to the elusive behavior of gravitational pseudo energy-momentum.

Non-relativistic Nature in Material Systems and the Dressed Photons

Itsuki Banno
Interdisciplinary and engineering researches, Yamanashi University

Abstract:
Dressed photon (DP) is the off-shell electromagnetic field existing inherently in the material systems, and stands out under the non-resonant condition. Such the non-resonant effects originate from the non-relativistic nature of the material systems, and this presentation will discuss on the relationship between the non-linear non-resonant response and the symmetry breaking from the relativistic system.